ISSN 2188-5001

MATERIALS DESIGN AND
CHARACTERIZATION LABORATORY

SUPERCOMPUTER CENTER

ACTIVITY REPORT 2013

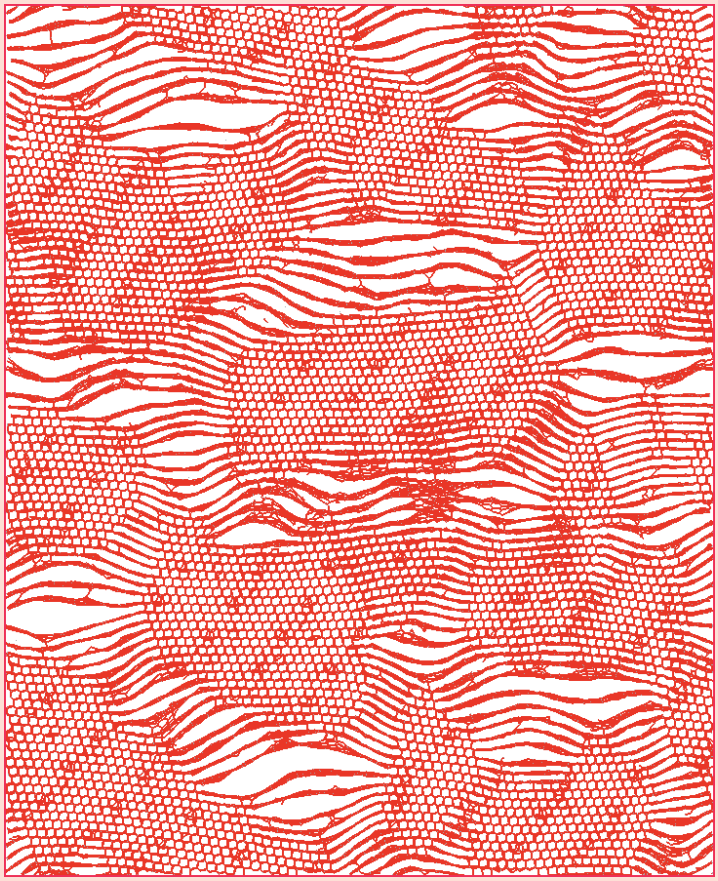

INSTITUTE FOR SOLID STATE PHYSICS
THE UNIVERSITY OF TOKYO

Materials Design and Characterization Laboratory (MDCL)

The MDCL was established as the third research facility of the Institute for Solid State Physics (ISSP) when the latter was reorganized in May 1996. Its aim is to promote material science with an emphasis on the "DSC cycle", where DSC stands for design, synthesis and characterization, three processes for developing new materials.

The MDCL consists of two sections, Materials Design (MD) section and Materials Synthesis and Characterization (MSC) section. The Supercomputer Center of the ISSP (SCC-ISSP) is placed in the MD section, while in the MSC section there are six laboratories for joint use; Materials Synthesis Laboratory, Chemical Analysis Laboratory, X-ray Diffraction Laboratory, Electron Microscope Laboratory, Electromagnetic Measurement Laboratory, and Spectroscopy Laboratory.

Almost all the facilities of the MDCL are open to scientists in Japan through the User Programs conducted by two steering committees of the MDCL. One is the steering committee of the SCC-ISSP, under which the Supercomputer Project Advisory Committee is placed for reviewing proposals. The other is the steering committee of the MSC facilities. More than half of the members of these committees are from the outside of ISSP.

PREFACE

The Supercomputer Center (SCC) is a part of the Materials Design and Characterization Laboratory (MDCL) of ISSP. Its mission is to serve the whole community of computational condensed-matter physics of Japan providing it with high performance computing environment. In particular, the SCC selectively promotes and supports large-scale computations. For this purpose, the SCC invites proposals for supercomputer-aided research projects and hosts the Steering Committee, as mentioned below, that evaluates the proposals.

he ISSP supercomputer system consists of three subsystems: System A, which is intended for a parallel computation with relatively smaller number of nodes connected tightly, and System B, which is intended for more nodes with relatively loose connections. In July, 2010, the SCC replaced the two supercomputer subsystems. The current system B is SGI Altix ICE 8400EX, which consists of 30 racks or 15360 cores whereas the system A is NEC SX-9, which consists of 4 nodes or 64 cpus. They have totally 200 TFlops. System C - FUJITSU PRIMEHPC FX10 was installed in April, 2013. It is highly compatible with K computer, the largest supercomputer in Japan. System C consists of 384 nodes, and each node has 1 SPARC64TM IXfx CPU (16 cores) and 32 GB of memory. The total system achieves 90.8 TFlops theoretical peak performance.

The hardware administration is not the only function of the SCC. The ISSP started hosting Computational Materials Science Initiative (CMSI), a new activity of promoting materials science study with next-generation parallel supercomputing. This activity is financially supported by the MEXT HPCI strategic program, and in CMSI, a number of major Japanese research institutes in various branches of materials science are involved. The SCC supports the activities of CMSI as its major mission.

All staff members of university faculties or public research institutes in Japan are invited to propose research projects. The proposals are evaluated by the Steering Committee of SCC. Pre-reviewing is done by the Supercomputer Project Advisory Committee. In school year 2013 totally 245 projects were approved for ISSP joint research projects and 16 for CMSI projects.

The ISSP joint research projects are roughly classified into the following three (the number of projects approved):

First-Principles Calculation of Materials Properties (107)
Strongly Correlated Quantum Systems (30)
Cooperative Phenomena in Complex, Macroscopic Systems (86)

All the three involve both methodology of computation and its applications. The results of the projects are reported in the present volume of 'Activity Report 2013' of the SCC. Every year 3-4 projects are selected for “invited papers” and published at the beginning of the volume. This year’s invited papers are the following three:

"One-hundred-million-atom electronic structure calculations on the K computer", Takeo HOSHI

"Strong correlation of electrons studied by computational approaches—Physics of superconductors and topological phases",
Shiro SAKAI, Takahiro MISAWA, Youhei YAMAJI, Mayuru KURITA, and Masatoshi IMADA

"Coarse-Grained Simulation of Surfactant Membrane",
Hayato SHIBA and Hiroshi NOGUCHI

We hope this volume will give you a good overview on recent activities in computational condensed matter physics in Japan.

May 19, 2014
Hiroshi Noguchi
(Chairman of the steering committee, SCC, ISSP)

CONTENTS

1 Outline

1.1 Supercomputer System

In SY 2013, the ISSP supercomputer center provided users with three supercomputing systems: NEC-SX9 (System A), SGI Altix ICE 8400EX (System B), and FUJITSU PRIMEHPC FX10 (System C) (Fig. 1). Systems A and B began service on July 1, 2010. In addition, FUJITSU PRIMEHPC FX10 (System C) entered service at the beginning of SY 2013. The three systems are all installed in the main building of ISSP.

System A - NEC SX9 is a vector computer with 4 nodes (64 CPUs). Vectorization and parallelization between CPUs can automatically be done by the C/Fortran compilers. One node contains 1 TB of shared memory, and the total system achieves 6.5 TFlops theoretical peak performance. All the nodes are connected to a 13 TB storage system with high throughput.

System B - SGI Altix ICE 8400EX is a massively-parallel supercomputer with 1,920 nodes (3,840 CPUs / 15,360 cores) achieving 180.0 TFlops theoretical peak performance. Each node has 24 GB of memory (46 TB in total) and two Intel Xeon X5570 CPUs running at 2.93 GHz connected by dual QPI links (2×25.6 GB/sec). Up to 128 nodes are connected by enhanced hypercube 4×QDR InfiniBand networks with 40 GB/s bisection bandwidth. A 110 TB Lustre file system is connected to the entire system also with InfiniBand, realizing I/O throughput on the order of GB/sec.

System C - FUJITSU PRIMEHPC FX10 is highly compatible with K computer, the largest supercomputer in Japan. System C consists of 384 nodes, and each node has 1 SPARC64TM IXfx CPU (16 cores) and 32 GB of memory. The total system achieves 90.8 TFlops theoretical peak performance.

For further details, please contact ISSP Supercomputer Center (SCC-ISSP).

[Correspondence: center@issp.u-tokyo.ac.jp]

1.2 Project Proposals

The ISSP supercomputer system provides computation resources for scientists working on condensed matter sciences in Japan. All scientific staff members (including post-docs) at universities or public research institutes in Japan can submit proposals for projects related to research activities on materials and condensed matter sciences. These proposals are peer-reviewed by the Advisory Committee members (see Sec. 1.3), and then the computation resources are allocated based on the review reports. The leader of an approved project can set up user accounts for collaborators. Other types of scientists, including graduate students, may also be added. Proposal submissions, peer-review processes, and user registration are all managed via a web system.

The computation resources are distributed in a unit called “point”, determined as a function of available CPU utilization time and consumed disk resources. There

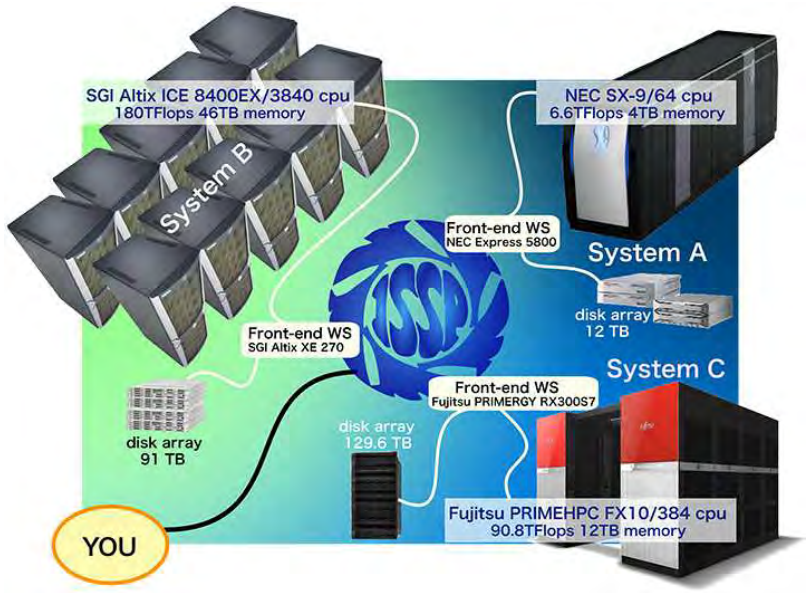

Figure 1: Supercomputer System at the SCC-ISSP

were six classes of research projects in SY 2013. The number of projects and the total number of points that were applied for and approved in this school year are listed in Table 1.

In addition, from SY 2010, ISSP Supercomputer is providing 20% of its computational resources for Computational Materials Science Initiative (CMSI), which aims at advancing parallel computations in condensed matter, molecular, and materials sciences on the 10-PFlops K Computer. The points for projects run by CMSI are distributed in accord with this policy. Computer time has also been alloted to Computational Materials Design (CMD) workshops run by CMSI.

- Proposals for projects in Classes B (small), C (mid-size), E (large-scale), and S (exceptional) can be submitted twice a year. Approved projects in Classes A, B, C, E, and S continue to the end of the school year.

- In Class D, projects can be proposed on rapidly-developing studies that need to perform urgent and relatively large calculations. An approved project continues for 6 months from its approval.

- Class S is for projects that are considered extremely important for the field of condensed matter physics and requires extremely large-scale computation. The project may be carried out either by one research group or cooperatively by several investigators at different institutions. A project of this class should be applied with at least 10,000 points; there is no maximum. We require group leaders applying for Class S to give a presentation on the proposal to the Steering Committee of the SCC-ISSP.

- Project leaders can apply for points so that the points for each system do not exceed the maximum point shown in this table.

Table 1: Classes of research projects in SY 2013

Class	Max. Point			Application
	Sys–A	Sys–B	Sys–C	
A	100	100	100	any time
B	2k	1k	500	twice a year
C	20k	10k	2.5k	twice a year
D	20k	10k	2.5k	any time
E	–	30k	2.5k	twice a year
S	(Sys-A+B)>10k		–	twice a year

Class	# of Proj.	Total points					
		Applied			Approved		
		Sys–A	Sys–B	Sys–C	Sys–A	Sys–B	Sys–C
A	10	350	850	500	350	850	500
B	56	40.7k	45.0k	6.6k	28.7k	29.8k	5.8k
C	130	793.5k	1043.0k	146.9k	486.5k	391.0k	98.6k
D	3	0	22.0k	0	0	19.0k	0
E	24	–	653.0k	43.8k	–	283.5k	36.6k
S	0	0	0	0	0	0	0
CMSI	22	–	–	–	–	–	92.5k

1.3 Committees

In order to fairly manage the projects and to smoothly determine the system operation policies, the Materials Design and Characterization Laboratory (MDCL) of the ISSP has organized the Steering Committee of the MDCL and the Steering Committee of the SCC-ISSP, under which the Supercomputer Project Advisory Committee (SPAC) is formed to review proposals. The members of the committees in SY 2013 were as follows:

Steering Committee of the MDCL

HIROI, Zenji	ISSP (Chair person)
KATO, Takeo	ISSP
KAWASHIMA, Naoki	ISSP
NOGUCHI, Hiroshi	ISSP
SUGINO, Osamu	ISSP
SUEMOTO, Toru	ISSP
TSUNEYUKI, Shinji	Univ. of Tokyo
MIYASHITA, Seiji	Univ. of Tokyo
KIMURA, Kaoru	Univ. of Tokyo
KAWAKATSU, Toshihiro	Tohoku Univ.
SAWA, Hiroshi	Nagoya Univ.

KAGEYAMA, Hiroshi	Kyoto Univ.
OGUCHI, Tamio	Osaka Univ.
NOHARA, Minoru	Okayama Univ.

Steering Committee of the SCC-ISSP

NOGUCHI, Hiroshi	ISSP (Chair person)
KAWASHIMA, Naoki	ISSP
SUGINO, Osamu	ISSP
TAKADA, Yasutami	ISSP
TOKUNAGA, Masashi	ISSP
TSUNETSUGU, Hirokazu	ISSP
SHIBA, Hayato	ISSP
WATANABE, Hiroshi	ISSP
KASAMATSU, Shusuke	ISSP
HATANO, Naomichi	Univ. of Tokyo
IMADA, Masatoshi	Univ. of Tokyo
MIYASHITA, Seiji	Univ. of Tokyo
NAKAJIMA, Kengo	Univ. of Tokyo
TSUNEYUKI, Shinji	Univ. of Tokyo
KAWAKATSU, Toshihiro	Tohoku Univ.
OTSUKI, Tomi	Sophia Univ.
SHIRAISHI, Kenji	Nagoya Univ.
OGUCHI, Tamio	Osaka Univ.
SUZUKI, Takafumi	Univ. of Hyogo
YOSHIMOTO, Yoshihide	Tottori Univ.
YATA, Hiroyuki	ISSP
FUKUDA, Takaki	ISSP

Supercomputer Project Advisory Committee

NOGUCHI, Hiroshi	ISSP (Chair person)
KAWASHIMA, Naoki	ISSP
SUGINO, Osamu	ISSP
TAKADA, Yasutami	ISSP
TOKUNAGA, Masashi	ISSP
TSUNETSUGU, Hirokazu	ISSP
SHIBA, Hayato	ISSP
WATANABE, Hiroshi	ISSP
KASAMATSU, Shusuke	ISSP
AOKI, Hideo	Univ. of Tokyo
ARITA, Ryotaro	Univ. of Tokyo
HATANO, Naomichi	Univ. of Tokyo
HUKUSHIMA, Koji	Univ. of Tokyo
IKUHARA, Yuichi	Univ. of Tokyo

IMADA, Masatoshi	Univ. of Tokyo
IWATA, Jun-Ichi	Univ. of Tokyo
MIYASHITA, Seiji	Univ. of Tokyo
MOTOME, Yukitoshi	Univ. of Tokyo
NAKAJIMA, Kengo	Univ. of Tokyo
OGATA, Masao	Univ. of Tokyo
OSHIYAMA, Atsushi	Univ. of Tokyo
TSUNEYUKI, Shinji	Univ. of Tokyo
WATANABE, Satoshi	Univ. of Tokyo
NEMOTO, Koji	Hokkaido Univ.
YAKUBO, Kosuke	Hokkaido Univ.
AKAGI, Kazuto	Tohoku Univ.
KAWAKATSU, Toshihiro	Tohoku Univ.
KURAMOTO, Yoshio	Tohoku Univ.
SHIBATA, Naokazu	Tohoku Univ.
YANASE, Yoichi	Niigata Univ.
ISHIBASHI, Shoji	AIST
MIYAMOTO, Yoshiyuki	AIST
OTANI, Minoru	AIST
KOBAYASHI, Kazuaki	NIMS
TATEYAMA, Yoshitaka	NIMS
HATSUGAI, Yasuhiro	Univ. of Tsukuba
KOBAYASHI, Nobuhiko	Univ. of Tsukuba
OKADA, Susumu	Univ. of Tsukuba
YABANA, Kazuhiro	Univ. of Tsukuba
HIDA, Kazuo	Saitama Univ.
NAKAYAMA, Takashi	Chiba Univ.
FURUKAWA, Nobuo	Aoyama Gakuin Univ.
MATSUKAWA, Hiroshi	Aoyama Gakuin Univ.
TAKANO, Hiroshi	Keio Univ.
YAMAUCHI, Jun	Keio Univ.
YASUOKA, Kenji	Keio Univ.
OTSUKI, Tomi	Sophia Univ.
OBATA, Shuji	Tokyo Denki Univ.
ANDO, Tsuneya	Tokyo Inst. Technology
TADA, Tomofumi	Tokyo Inst. Technology
HOTTA, Takashi	Tokyo Metropolitan Univ.
OKABE, Yutaka	Tokyo Metropolitan Univ.
WATANABE, Kazuyuki	Tokyo Univ. of Sci.
HAGITA, Katsumi	National Defense Academy
INOUE, Junichiro	Nagoya Univ.
KONTANI, Hiroshi	Nagoya Univ.
OKAMOTO, Yuko	Nagoya Univ.
SHIRAISHI, Kenji	Nagoya Univ.
TANAKA, Yukio	Nagoya Univ.

ODA, Tatsuki	Kanazawa Univ.
SAITO, Mineo	Kanazawa Univ.
ARAKI, Takeaki	Kyoto Univ.
KAWAKAMI, Norio	Kyoto Univ.
MASUBUCHI, Yuichi	Kyoto Univ.
TOHYAMA, Takami	Kyoto Univ.
YAMAMOTO, Ryoichi	Kyoto Univ.
KASAI, Hideaki	Osaka Univ.
KAWAMURA, Hikaru	Osaka Univ.
KUROKI, Kazuhiko	Osaka Univ.
KUSAKABE, Koichi	Osaka Univ.
MORIKAWA, Yoshitada	Osaka Univ.
OGUCHI, Tamio	Osaka Univ.
SHIRAI, Koun	Osaka Univ.
YOSHIDA, Hiroshi	Osaka Univ.
YUKAWA, Satoshi	Osaka Univ.
HARIMA, Hisatomo	Kobe Univ.
SUGA, Seiichiro	Univ. of Hyogo
SUZUKI, Takafumi	Univ. of Hyogo
TATENO, Masaru	Univ. of Hyogo
SAKAI, Toru	Japan Atomic Energy Agency
HOSHINO, Kozo	Hiroshima Univ.
HOSHI, Takeo	Tottori Univ.
YOSHIMOTO, Yoshihide	Tottori Univ.
YASUDA, Chitoshi	Univ. of the Ryukyus
KATO, Takeo	ISSP
TODO, Synge	ISSP

1.4 Staff

The following staff members of the SCC-ISSP usually administrate the ISSP Supercomputer.

NOGUCHI, Hiroshi	Associate Professor (Chair person)
KAWASHIMA, Naoki	Professor
SUGINO, Osamu	Associate Professor
WATANABE, Hiroshi	Research Associate
KASAMATSU, Shusuke	Research Associate
NOGUCHI, Yoshifumi	Research Associate
SHIBA, Hayato	Research Associate
MORITA, Satoshi	Research Associate
YATA, Hiroyuki	Technical Associate
FUKUDA, Takaki	Technical Associate
ARAKI, Shigeyuki	Technical Associate

2 Statistics (School Year 2013)

2.1 System and User Statistics

In the following, we present statistics for operation time taken in the period from April 2013 to March 2014 (SY 2013). In Table 2, we show general statistics of the supercomputer system in SY 2013. The total number of CPUs in System A, B, and C is 64, 3840, and 384 respectively. Consumed disk points amount to about 4%, 5%, and 1% of the total consumed points in System A, B, and C respectively.

In the left column of Fig. 2, availabilities, utilization rates, and consumed points in each system are plotted for each month. Throughout the school year, the utilization rates were high enough. Especially in System B, they were exceeding 90% throughout most of the year. In System C, roughly half of the total utilized resources were used by CMSI projects. This amounts to about 20% of the total usage of the computational resources in this school year. The user statistics are shown in the right column of Fig. 2. The horizontal axis shows the rank of the user/group arranged in the descending order of the execution time (hour×CPU). The execution time of the user/group of the first rank is the longest. The vertical axis shows the sum of the execution time up to the rank. From the saturation points of the graphs, the number of "active" users of each system is around 50 and 220 for System A and B, respectively. The maximum ranks in the graphs correspond to the number of the users/groups that submitted at least one job.

2.2 Queue and Job Statistics

Queue structures of System A, B, and C in SY 2013 are shown in Table 3. In each system, the queues are classified by the number of CPUs the user can use and the maximum duration of each submitted job. In System A, in addition to the usual P class jobs, there is a queue "D1" for debugging, and "L1" for jobs which require only one CPU but quite a long time. Parallel jobs are executed with "P4" and "P16", 16 CPUs being available at maximum with one job using "P16".

In System B, a highly detailed classification is adopted. The biggest portion (20 racks out of 30 in total) of the resources is allotted for "F256", which mainly uses 128 or 256 CPUs at once. "F16", "F32", and "F64" are for smaller-scale jobs using 16, 32, and 64 CPUs respectively. The elapsed-time limit of the above queues is 24 hours for one job, while it is set smaller for smaller-scale queues ("F4" and "F8") to speed up their rotation. For time-demanding jobs, L-type queues are also introduced, whose time limit is set longer than F-type queues. "P64" queue is set up to accept jobs which require any number of CPUs more than 1 and not exceeding 64. "i32" is a queue for debugging, which corresponds to interactive mode in the previous system. In "i32", users can execute their jobs using up to 16 nodes at once from the command line, as if they were logging into the calculation node.

In System C, the "F" and "L" queues are set up similarly to System B. In addition, a debug queue is set up for short debugging jobs utilizing 1 to 4 CPUs, and an interactive queue that can use 1 to 4 CPUs is also available.

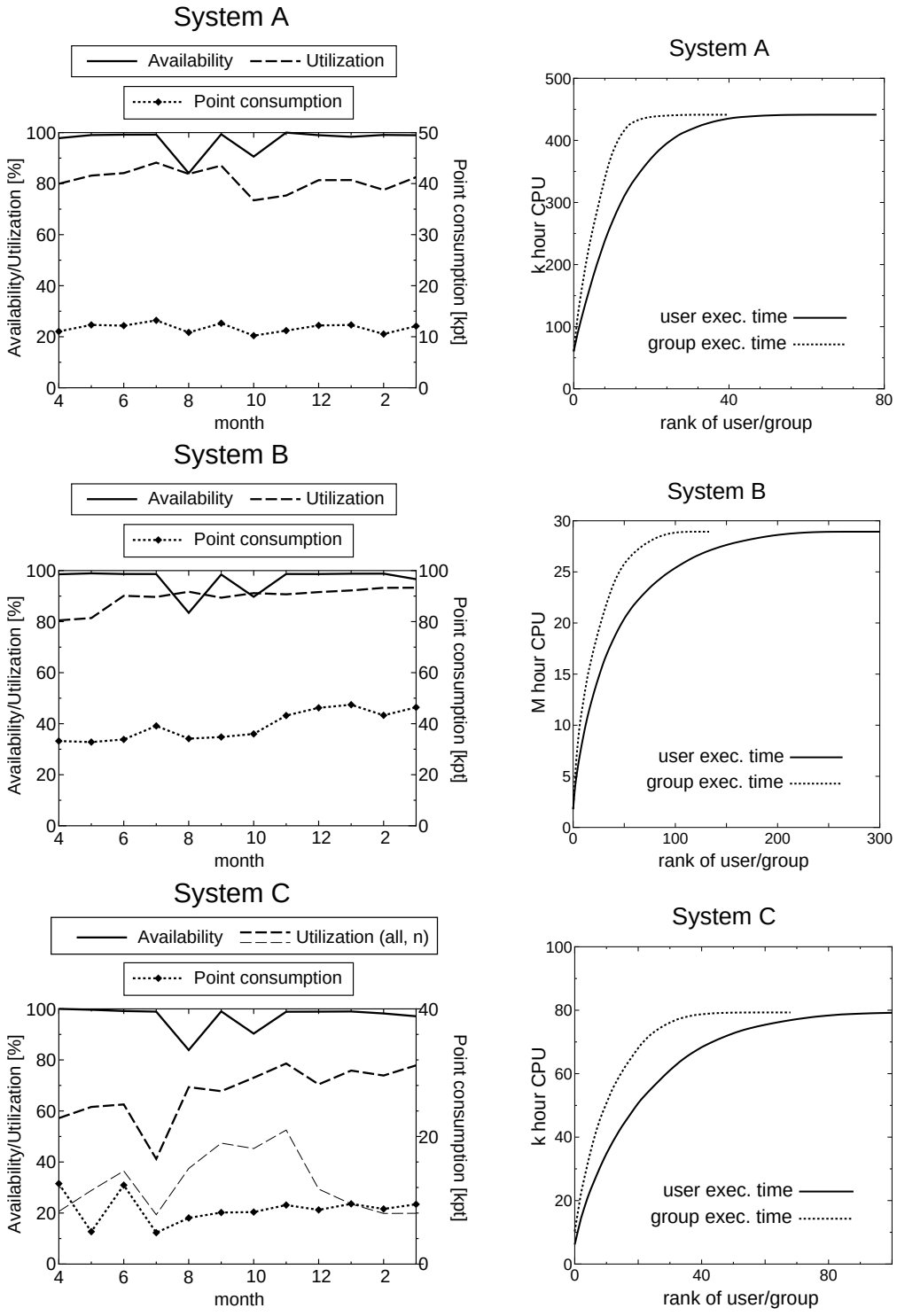

Figure 2: Left: Availabilities, utilization rates and point consumptions of each month during SY 2013. For System C, the utilization by CMSI projects (denoted by "n") is plotted in addition to the total utilization. Right: User statistics. The horizontal axis shows the rank of the user/group arranged in the descending order of the execution time (hour×CPU). The vertical axis shows the sum of the execution time up to the rank.

Table 2: Overall statistics of SY 2013

	System-A	System-B	System-C
total service time (k hour × CPU)	541.0	32301.1	3243.4
number of executed jobs	27196	189954	29182
total consumed points (k point)	140.7	470.5	85.9
CPU points (k point)	134.8	445.8	84.8
disk points (k point)	5.9	24.7	1.1
points consumed by CMSI (k point)	–	–	42.9
total exec. time (k hour × CPU)	438.8	28931.4	2184.1
availability	97.0 %	96.5%	96.9%
utilization rate	81.1 %	89.6%	67.3%

The CPU points are set smaller for larger-scale queues for System B as shown in Table 3, while it is more uniform in System A. To prevent overuse of the storage, points are charged also for usage of disk quota in the three systems, as shown in Table 4. Disk points are revised often for optimal usage of the resources by examining usage tendencies each year.

Although we do not mention here in detail, to promote utilization of the massively parallel supercomputer, background queues ("B16", "B32", "B64", and "B256"), which charge no CPU points for the jobs, have also been open in System B.

The ISSP Supercomputer also supports large-scale jobs, which use tens of thousands of cores at once by exclusively using the necessary number of CPUs. In-advance application is necessary to execute this type of job. Large-scale jobs can be executed in queues "P512", "P1024", "P2048", and "P3840" just after the scheduled monthly maintenance. However, since such large-scale jobs are now covered by the K Computer, no jobs were executed in these queues in SY2013.

The number of jobs, average waiting time, and total execution time in each queue are shown in Table 5. In System A, the average waiting times of P4 and P16 are a bit long compared with the elapsed-time limit (24 hours). This is because a few active users tend to submit many jobs at once. Because fair-share scheduling is adopted, the waiting time is considered to be appropriate for fair distribution of computational resources. We will continue to look for more appropriate queue settings also in the next school year to meet the user's tendency of resource usage.

In System B, a large portion of jobs have been executed in queues "F16", "F32", "F64", and "F256". As we intended, most of the execution time has been consumed in "F256" and "L256". In all of these queues, the queue settings meet the user's tendencies in that the waiting times are on the order of the elapsed-time limit.

In System C, the waiting times for the "F" queue jobs are less than twelve hours. The "L96" queue has a waiting time of nearly five days, owing to the large amount of resources the jobs occupy when run in this queue.

Table 3: Queue structures in SY 2013

System–A

queue name	Elapsed time limit (min)	# of CPU /Job (n)	# of CPU /queue (p)	memory size	CPU points / (CPU·day)
D1	15	1	2	60GB	7.776
L1	7200	1	4	60GB	7.776
P1	1440	1	10-30	60GB	7.776
P4	1440	4	16-32	240GB	7.776
P16	1440	16	16	960GB	6.048

System–B

queue name	Elapsed time limit (min)	# of CPU /Job (n)	# of CPU /queue (p)	CPU points /(CPU·day)
P1	720	1	32	0.690
P64	720	2-64	64	0.518
F4	720	4	96	0.518
F8	720	8	96	0.518
F16	1440	16	1024	0.518
F32	1440	32	1024	0.518
F64	1440	64	1024	0.518
L16	7200	16	64	0.518
L32	7200	32	64	0.518
L64	7200	64	64	0.518
i32	20	1-32	64	0.518
F256	1440	65-256	2560	0.358
L256	7200	65-256	512	0.358
P512	–	128-512	512 or 1024	0.358
P1024	7200	384-1024	3072	0.358
P2048	–	128-2048	2048	0.358
P3840	1440	1024-3840	3840	0.358

* The available memory size is limited to 21 GB per one node.

* P queues require in-advance application (see main text). The elapsed-time limit for P512 and P2048 queues is determined on a per-application basis.

System–C

queue name	Elapsed time limit (min)	# of CPU /Job (n)	# of CPU /queue (p)	CPU points /(CPU·day)
debug	30	1-4	24	1
interactive	30	1-4	24	1
F12	1440	2-12	60	1
F96	1440	2-12	288	1
L12	7200	24-96	24	1
L96	7200	24-96	192	1

* The available memory size is limited to 28 GB per one CPU.

Table 4: Disk points of System A, B, and C

		point/day
System A	`/home`	$0.0125 \times \theta(q-2)$
	`/work`	$0.005 \times \theta(q-30)$
System B	`/home`	$0.05 \times \theta(q-2)$
	`/work`	$0.005 \times \theta(q-30)$
System C	`/home`	$0.05 \times \theta(q-5)$
	`/work`	$0.005 \times \theta(q-60)$

* q is denoted in unit of GB.
* $\theta(x)$ is equal to the Heaviside step function $H(x)$ multiplied by x, i.e., $xH(x)$.

Acknowledgments

The staffs would like to thank Prof. Takafumi Suzuki (now at University of Hyogo) for developing WWW-based system (SCM: SuperComputer Management System) for management of project proposals, peer-review reports by the SPAC committee, and user accounts. We also thank Ms. Reiko Iwafune for creating and maintaining a new WWW page of the ISSP Supercomputer Center.

Table 5: Number of jobs, average waiting time, total execution time, and average number of used CPU's per job in each queue.

System-A

queue	# of Jobs	Waiting Time (hour)	Exec. Time (k CPU × hour)	# of CPU
D1	6103	0.02	0.30	1.00
P1	15131	29.56	177.65	1.00
L1	1042	7.50	16.90	1.00
P4	3898	26.62	134.10	3.97
P16	978	39.60	109.89	16.00

System-B

queue	# of Jobs	Waiting Time (hour)	Exec. Time (k CPU × hour)	# of CPU
P1	71590	14.56	199.37	1.0
P64	20873	24.07	346.00	4.7
F4	16364	21.36	287.23	4.0
F8	11125	9.18	376.86	8.0
F16	20226	13.98	2575.80	16.0
F32	8990	12.66	2099.62	32.0
F64	5044	29.79	2561.01	64.0
L16	302	44.99	135.22	16.0
L32	85	94.65	160.05	32.0
L64	21	123.45	32.07	64.0
i32	20178	0.02	42.05	21.8
F256	10712	20.09	15405.86	198.3
L256	210	31.35	1737.60	209.9
P512	0	0	0.00	0
P1024	0	0	0.00	0
P2048	0	0	0.00	0
P3840	0	0	0.00	0

System-C

queue	# of Jobs	Waiting Time (hour)	Exec. Time (k CPU × hour)	# of CPU
F12	9084	5.08	309.69	6.4
F96	6900	11.97	1592.51	40.1
L12	408	9.74	49.80	4.9
L96	146	64.67	222.04	30.8
debug	8887	0.04	1.53	2.0
interactive	3165	0.00	0.82	1.2

3 RESEARCH REPORTS

3.1 Invited Articles

One-hundred-million-atom electronic structure calculations on the K computer

Takeo HOSHI[1,2]
[1] *Department of Applied Mathematics and Physics, Tottori University*
Koyama Minami, Tottori 680-8550, Japan
[2] *Japan Science and Technology Agency, Core Research for Evolutional Science and Technology (JST-CREST), 5, Sanbancho, Chiyoda-ku, Tokyo 102-0075, Japan*

Abstract

One-hundred-million atom (100-nm-scale) electronic structure calculations were realized on the K computer. The methodologies are based on inter-disciplinary collaborations among physics, mathematics and the high-performance computation field or 'Application-Algorithm-Architecture co-design'. Novel linear-algebraic algorithms were constructed as Krylov-subspace solvers for generalized shifted linear equations ($(zS - H)\boldsymbol{x} = \boldsymbol{b}$) and were implemented in our order-N calculation code 'ELSES' with modeled (tight-binding-form) systems. A high parallel efficiency was obtained with up to the full core calculations on the K computer. An application study is picked out for the nano-domain analysis of sp^2-sp^3 nano-composite carbon solid. Future aspects are discussed for next-generation or exa-scale supercomputers. The code for massive parallelism was developed with the supercomputers, the systems B and C, at ISSP.

1 Introduction

The current or next generation computational physics requires 'Application-Algorithm-Architecture co-design', or inter-disciplinary collaborations among physics, mathematics and the high-performance computation field.

Our recent papers [1, 2] report that electronic structure calculations with one-hundred-million atoms were realized on the K computer and the methodologies are based on the Application-Algorithm-Architecture co-design with novel linear algebraic algorithms [3, 4]. The calculations are called '100-nm-scale', because one hundred million atoms are those in silicon single crystal with the volume of $(126\text{nm})^3$. The calculations were realized by our electronic structure calculation code 'ELSES' [5] and the computational cost is order-N or proportional to the number of atoms N. The code uses modelled (tight-binding-form) Hamiltonians based on *ab initio* calculations. Since the fundamental methodologies are purely mathematical, they are applicable both to insulating and metallic cases. Moreover, they are applicable also to other physics problems amang and beyond electronic structure calculations.

Fig. 1 illustrates our basic strategy for large-scale calculations with the Application-Algorithm-Architecture co-design. The essential concept is to combine new ideas among the three fields for a breakthrough. The possibility of sharing the mathematical solvers among applications will be discussed in the last section.

The present paper is organized as follows; Section 2 explains the fundamental mathematical theory. Section 3 is devoted to the computational procedures and benchmarks. Sec-

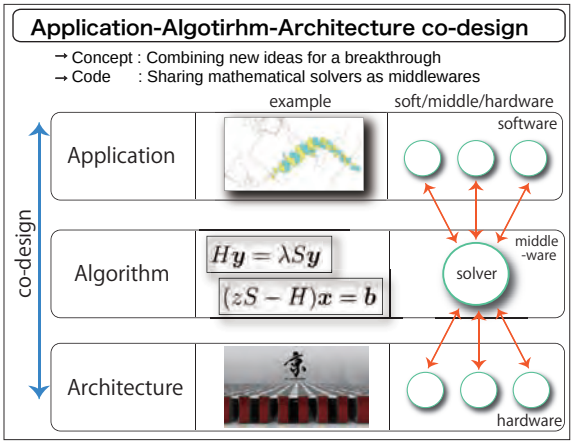

Figure 1: Application-Algorithm-Architecture co-design, our basic strategy for large-scale calculations.

tion 4 describes an application study on a nano-domain analysis of nano-composite carbon solids. Summary and future aspects are given in the last section.

2 Fundamental mathematical theory

Our fundamental mathematical theory is novel linear-algebraic algorithms with Krylov subspace.

Krylov subspace [6] is a general mathematical concept and gives the foundation of various iterative linear-algebraic solvers. such as the conjugate gradient method. A Krylov subspace is denoted as $K_\nu(A; \boldsymbol{b})$ with a given integer ν, a square matrix A and a vector $\boldsymbol{b}$, and means the linear (Hilbert) space that spanned by the ν basis vectors of $\{\boldsymbol{b}, A\boldsymbol{b}, ..., A^{\nu-1}\boldsymbol{b}\}$:

$$K_\nu(A; \boldsymbol{b}) \equiv \mathrm{span}\{\boldsymbol{b}, A\boldsymbol{b}, ..., A^{\nu-1}\boldsymbol{b}\}. \quad (1)$$

Usually, the subspace dimension ν is the iteration number of the iterative computational procedures and a matrix-vector multiplication with a vector of $\boldsymbol{v}$ ($\boldsymbol{v} \Rightarrow A\boldsymbol{v}$) governs the operation cost at each iterate.

A mathematical foundation of electronic state calculations is a generalized eigen-value equation

$$H\boldsymbol{y}_k = \varepsilon_k S\boldsymbol{y}_k. \quad (2)$$

The matrices H and S are Hamiltonian and the overlap matrices, respectively. These matrices are $M \times M$ real-symmetric (or Hermitian) matrices and S is positive definite. In this paper, the real-space atomic-orbital representation is used and the matrices are sparse real-symmetric ones. Large-matrix calculations with the conventional solvers for Eq. (2) give huge operation cost and difficulty in massive parallelism.

For years, we have constructed novel linear algebraic solvers for large-system calculations, in stead of the conventional generalized eigenvalue equation in Eq. (2). They are commonly based on linear equations in the form of

$$(zS - H)\boldsymbol{x} = \boldsymbol{b}. \quad (3)$$

Here z is a (complex) energy value and the matrix of $(zS-H)$ can be non-Hermitian. The vector $\boldsymbol{b}$ is an input and the vector $\boldsymbol{x}$ is the solution vector. The set of linear equations in Eq. (3) with many energy values is called 'generalized shifted linear equations'. A recent preprint [2] contains the complete reference list of our novel solvers and the present paper picks out two methods [7, 3].

The use of Eq. (3) results in the Green's function formalism, since the solution $\boldsymbol{x}$ of Eq. (3) is written formally as $\boldsymbol{x} = G\boldsymbol{b}$ with the Green's function $G = G(z) \equiv (zS - H)^{-1}$.

These solver algorithms are purely mathematical and applicable to large-matrix problems in many computational physics fields. Our study began for our own electronic structure calculation code and, later, grew up into more general one. For example, the shifted Conjugate Orthogonal Conjugate Gradient (sCOCG) algorithm [7], one of our algorithms, is based on a novel mathematical theorem, called collinear residual theorem [8]. After the application study on our electronic structure calculations [7], we applied

the sCOCG algorithm to a many-body problem for $La_{2-x}Sr_xNiO_4 (x = 1/3, 1/2)$, since a large-matrix problem with the matrix size of 64 millions appears. [9] The sCOCG algorithms were applied also to the shell model calculation [10] and a real-space-grid DFT calculation [11]. Other applications with the collinear residual theorem [8] are found, for example, in a QCD problem [8] and a electronic excitation (GW) calculation [12].

3 Computational procedures and benchmarks

This section is devoted to the computational procedure of our electronic structure calculation and their benchmarks for the order-N scaling [3] and the parallel efficiency [1, 2]. In all the results of the present paper, the multiple Arnoldi method [3] is used as the solver for Eq. (3), since it is suitable for a molecular dynamics simulation [3]. Equation (3) is solved with the multiple Krylov subspaces of $\mathcal{L} \equiv K_p(H; \boldsymbol{b}) \oplus K_q(H; S^{-1}\boldsymbol{b})$. The subspace dimension ν is $\nu \equiv p + q$. The second term is introduced, so as to satisfy some physical conservation laws exactly. The multiple Arnoldi method gives the Green's function G.

The procedures for calculating physical quantities are briefly explained. In general, a physical quantity is defined as

$$\langle X \rangle \equiv \sum_k f(\varepsilon_k)\, \boldsymbol{y}_k^{\mathrm{T}} X \boldsymbol{y}_k \tag{4}$$

with a given matrix X and the occupation number in the Fermi function $f(\varepsilon)$. The case in $X = H$, for example, gives the electronic structure energy

$$E_{\mathrm{elec}} \equiv \sum_k f(\varepsilon_k)\, \varepsilon_k. \tag{5}$$

A quantity in Eq.(4) is transformed into the trace form of

$$\langle X \rangle = \mathrm{Tr}[\rho X] \tag{6}$$

with the density matrix

$$\rho \equiv \sum_k f(\varepsilon_k)\, \boldsymbol{y}_k\, \boldsymbol{y}_k^{\mathrm{T}}. \tag{7}$$

The density matrix is given by the Green's function as

$$\rho = \frac{-1}{\pi} \int_{-\infty}^{\infty} f(\varepsilon)\, G(\varepsilon + i0)\, d\varepsilon, \tag{8}$$

because of

$$G(z) = \sum_k \frac{\boldsymbol{y}_k\, \boldsymbol{y}_k^{\mathrm{T}}}{z - \varepsilon_k}. \tag{9}$$

The energy integration in Eq. (8) is carried out analytically in the multiple Arnoldi method. The chemical potential μ appears in the Fermi function $f(\varepsilon)$ and is determined by the bisection method. The computational workflow is summarized as

$$(H, S) \Rightarrow G \Rightarrow \mu \Rightarrow \rho \Rightarrow \langle X \rangle. \tag{10}$$

Several points are discussed; (i) If the matrix X is sparse, the physical quantity $\mathrm{Tr}[\rho X] = \sum_{i,j} \rho_{ji} X_{ij}$ is contributed only from the selected elements of ρ_{ij} where $X_{ij} \neq 0$ and, therefore, we should calculate only these elements of the density matrix (ρ_{ij}) and the Green's function (G_{ij}) in the workflow of Eq. (10). The above fact is a foundation of the order-N property. (ii) The trace in Eq. (6) is decomposed into

$$\mathrm{Tr}[\rho X] = \sum_j^M \boldsymbol{e}_j^{\mathrm{T}} \rho X \boldsymbol{e}_j, \tag{11}$$

where $\boldsymbol{e}_j \equiv (0, 0, 0, ...1_j, 0, 0, ..., 0)^{\mathrm{T}}$ is the j-th unit vector. The quantity $\boldsymbol{e}_j^{\mathrm{T}} \rho X \boldsymbol{e}_j$ is called 'projected physical quantity' and is computed in parallelism. (iii) The Green's function is used also for calculating other quantities, such as the density of states and the crystalline orbital Hamiltonian population (See the next section).

Figures 2 (a) and (b) show benchmarks. The calculated systems are amorphous-like

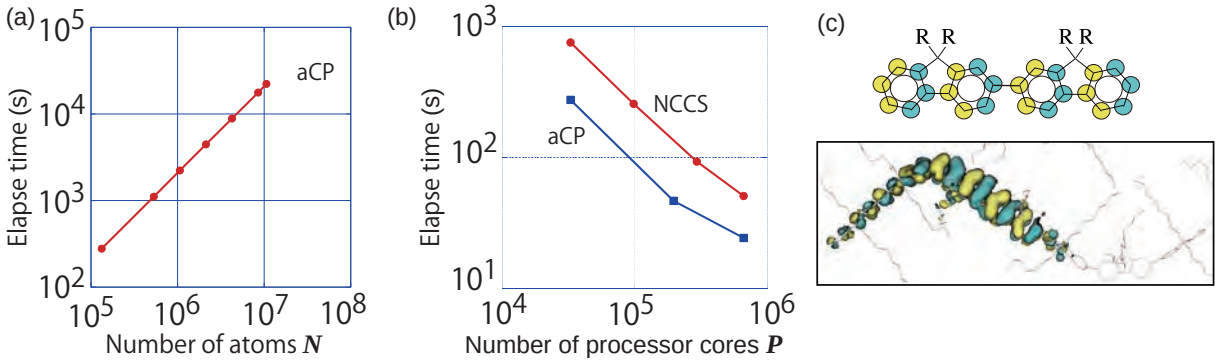

Figure 2: (a) Benchmark for the order-N scaling. [3] The calculated system is amorphous-like conjugated polymer (aCP), poly-(9,9 dioctyl fluorene). (b) Benchmark for the parallel efficiency, the 'strong scaling', on the K computer with one hundred million atoms. [1, 2] The calculated systems are aCP and an sp^2-sp^3 nano-composite carbon solid (NCCS). (c) A typical π wavefunction in aCP [1]. The upper panel is a schematic figure for two successive monomer units with R≡C_8H_{17}. The lower panel is a simulation result, where only C-C bonds are drawn for eye-guide.

conjugated polymer (aCP), poly-(9,9 dioctyl-fluorene) [3, 1, 2] and an sp^2-sp^3 nano-composite carbon solid (NCCS). [4, 1]. Figure 2(a) shows that the calculation has the order-N scaling property [3] in the aCP systems. Figure 2(b) shows the parallel efficiency on the K computer with one hundred million atoms. The MPI/OpenMP hybrid parallelism is used. The results are shown for the NCCS system with $N = 103,219,200$ [1] and the aCP system with $N = 102,238,848$ [2]. The elapse time T of the electronic structure calculation for a given atomic structure is measured as the function of the number of used processor cores P ($T = T(P)$), from $P = P_{\rm min} \equiv 32,768$ to $P_{\rm all} \equiv 663,552$, the total number of processor cores on the K computer. The parallel efficiency is defined as $\alpha(P) \equiv T(P)/T(P_{\rm min})$ and such a benchmark is called 'strong scaling' in the high-performance computation field. The measured parallel efficiency among the NCCS systems is $\alpha(P = 98,304) = 0.98$, $\alpha(P = 294,921) = 0.90$ and $\alpha(P = P_{\rm all}) = 0.73$. The measured parallel efficiency among the aCP systems is $\alpha(P = 196,608) = 0.98$ and $\alpha(P = P_{\rm all}) = 0.56$.

The high parallel efficiency stems not only from the fundamental mathematical theory but also from detailed techniques in the high-performance computation field or the information science [4]. These techniques do not affect the numerical results. In particular, techniques were developed in (i) programing techniques for saving memory and communication costs (ii) a parallel file I/O technique, and (iii) an original visualization software called 'VisBAR' for a seamless procedure between the numerical simulation and visualization analysis (See the next section).

Physical points are briefly discussed for the calculated systems. A typical π wave function of the aCP system is shown in Fig. 2(c). The π wavefunction is terminated at the boundary region between monomer units, unlike one in an ideal chain structure, because the two monomer units are largely twisted and the π interaction between the monomer units almost vanishes. The physical property of NCCS will be discussed in the next section.

4 Nano domain analysis of nano-composite carbon solid

This section picks out an application study on nano-composite carbon solid (NCCS). A recent preprint [2] gives a review of another recent study with our code for battery-related materials [13] and earlier studies.

4.1 Analysis methods

In general, large-system calculations result in complicated nano structures with many domains and domain boundaries. Novel methods are required for the post-simulation analysis of these structures with huge electronic structure data distributed among computer nodes.

Here such analysis methods are presented with the real-space atomic-orbital representation of the Green's function; crystalline orbital Hamiltonian population (COHP) method [14], and its theoretical extension called πCOHP method [4].

The original COHP [14] is defined as

$$C_{IJ}(\varepsilon) \equiv \frac{-1}{\pi} \sum_{\alpha,\beta} H_{J\beta;I\alpha} \mathrm{Im}\, G_{I\alpha;J\beta}(\varepsilon + \mathrm{i}0), \quad (12)$$

with the atom suffixes, I and J, and the orbital suffixes, α and β. The energy integration of COHP, called ICOHP, is also defined as

$$B_{IJ} \equiv \int_{-\infty}^{\infty} f(\varepsilon) C_{IJ}(\varepsilon) d\varepsilon. \quad (13)$$

Since a large negative value of B_{IJ} $(I \neq J)$ indicates the energy gain for the bond formation between the (I, J) atom pair, B_{IJ} is understood as the local bonding energy. The sum of B_{IJ} is the electronic structure energy

$$E_{\mathrm{elec}} \equiv \sum_k f(\varepsilon_k)\, \varepsilon_k = \sum_{I,J} B_{IJ}. \quad (14)$$

A theoretical extension of COHP, πCOHP, is proposed [4]. Since the present Hamiltonian contains s- and p-type orbitals, off-site Hamiltonian elements are decomposed, within the Slater-Koster form, into σ and π components $(H_{J\beta;I\alpha} = H^{(\sigma)}_{J\beta;I\alpha} + H^{(\pi)}_{J\beta;I\alpha})$. From the definitions, the off-site COHP and ICOHP are also decomposed into the σ and π components

$$C_{IJ}(\varepsilon) = C^{(\sigma)}_{IJ}(\varepsilon) + C^{(\pi)}_{IJ}(\varepsilon), \quad (15)$$

$$B_{IJ} = B^{(\sigma)}_{IJ} + B^{(\pi)}_{IJ}. \quad (16)$$

The decomposed terms are called 'σ(I)COHP' and 'π(I)COHP' and the original (I)COHP is called 'full (I)COHP'.

By the σ(I)COHP and π(I)COHP, σ and π bonds can be distinguished energetically. A large negative value of $B^{(\sigma)}_{IJ}$ or $B^{(\pi)}_{IJ}$ indicates the formation of a σ or π bond between the atom pair, respectively.

The analysis method is suitable to the present massively parallel order-N method, because the full, σ, and π(I)COHP can be calculated from the Green's function without any additional inter-node data communication.

4.2 Nano domain analysis

The (π)COHP analysis method is applied to an early-stage study [4] on the formation process of the nano-polycrystalline diamond (NPD), a novel ultrahard material produced at 2003 [15]. NPD is obtained by direct conversion sintering process from graphite under high pressure and high temperature and has characteristic 10-nm-scale lamellar-like structures. NPD is of industrial importance, because of its extreme hardness and strength that exceed those of conventional single crystals. Sumitomo Electric Industries. Ltd. began commercial production from 2012. Similar properties are observed also in nano-polycrystalline SiO_2 [16].

Our simulation is motivated by the investigation of possible precursor structures in the formation process of NPD and the structures should be nano-scale composites of sp^2 (graphite-like) and sp^3 (diamond-like) domains.

Figures 3 shows the result of nano-domain analysis on sp^2-sp^3 nano-composite carbon solid (NCCS) [4]. The system is a result

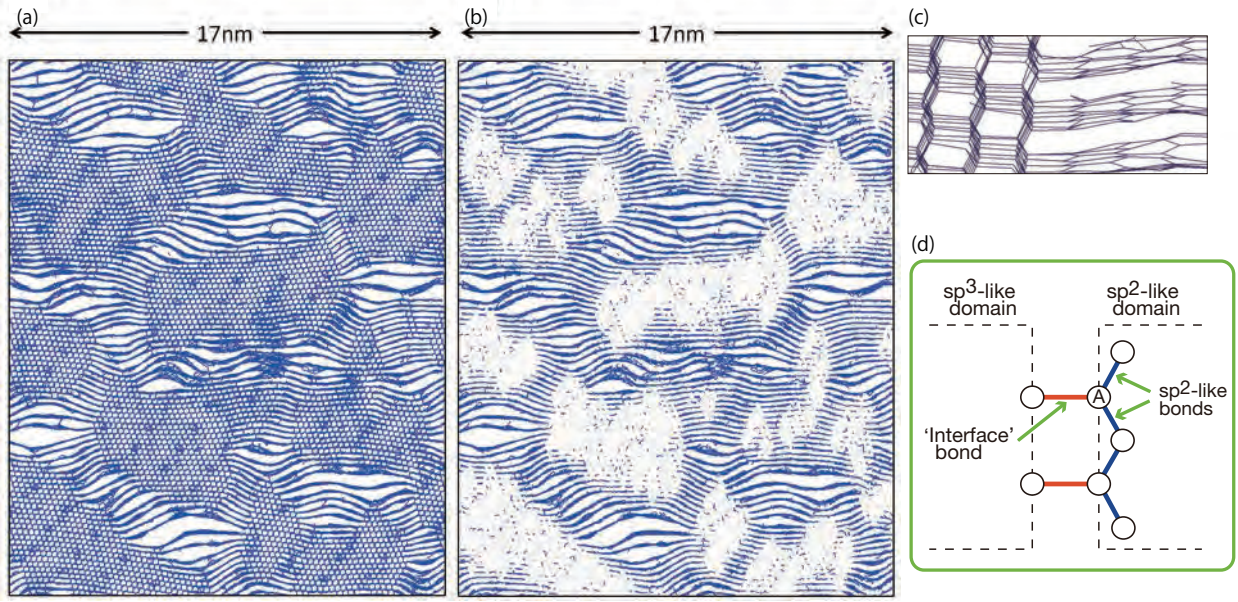

Figure 3: Nano-domain analysis of sp^2-sp^3 nano-composite carbon solid (NCCS) visualized with the COHP or πCOHP analysis [4]. The sp^2 (graphite-like) and sp^3 (diamond-like) domains are visualized in (a), while only the sp^2-like domains are visualized in (b). A closeup of a sp^2-sp^3 domain boundary is shown in (c). The atoms at a typical domain boundary are shown in (d).

of our finite-temperature molecular-dynamics simulation with a periodic boundary condition. The (π)COHP analysis is used, because sp^2 domains can be distinguished from sp^3 domains by the presence of π bonds. Figures 3(a) and (b) are drawn by the bond visualization by the full ICOHP and the πICOHP, respectively. In Fig. 3(a), a bond is drawn for an (I, J) atom pair, when its ICOHP value satisfies the condition $B_{IJ} < B_{\rm th} \equiv -9$ eV. Bond visualization by the full ICOHP indicates the visualization of both sp^2 and sp^3 bonds. In Fig. 3(b), on the other hand, a π bond is drawn, when its π ICOHP value satisfies the condition $B_{IJ}^{(\pi)} < B_{\rm th}^{(\pi)} \equiv -1.5$ eV. Bond visualization by the πICOHP indicates the visualization of only sp^2 bonds.

The analysis concludes that layered domains are sp^2 domains and non layered domains are sp^3 domains. Figure 3(c) is a close-up of a domain boundary between sp^2 and sp^3 domains, which shows that a layered domain forms a graphite-like structure and a non layered domain forms a diamond-like structure, as expected from the (π)ICOHP results.

A typical domain interface, schematically shown in Fig. 3(d), is analyzed for the nature of each bond, so as to clarify how the (π)COHP analysis works well. The atom labeled 'A' in Fig. 3(d) is focused on. The atom has three bonds that are painted blue or red in Fig. 3(d). The (π)ICOHP analysis shows that the two 'blue' bonds contain π bonds, while the 'red' bond dose not. The analysis result is consistent to the fact that the 'blue' bonds are those within an sp^2 domain, while the 'red' bond is an 'interface' bond or a bridge between sp^2 and sp^3 domains.

5 Summary and future aspects

The present paper reports our methods and results of large-scale electronic structure calculations based on our novel linear algebraic

algorithms. The mathematical algorithms are applicable to various computational physics problems among and beyond electronic structure calculations. A high parallel efficiency was observed for one-hundred-million-atom (100-nm-scale) systems with up to all the built-in cores of the K computer. An application study of nano-domain analysis on nano-composite carbon solids is shown as an example.

Finally, three future aspects are discussed; (I) Material: The present methodologies are general and an important application should be one for organic materials, since non-ideal 100-nm-scale structures are crucial for devices. Preliminary calculations are shown for amourphous-like conjugated polymers in this paper. (II) Theory: Large-system calculations for transport and optical properties should be next stages and these calculations are reduced to large-matrix problems beyond the present formulations. A central mathematical issue is the internal eigen-value problem in which we calculate only the selected eigen values and eigen vectors near the HOMO and LUMO levels or the Fermi level. Recently, a novel two-stage algorithm was proposed for the internal eigen-value problem with Sylvester's theorem of inertia [17]. (III) Code development style: As shown in Fig. 1, novel mathematical solvers can be shared as middlewares, among many application softwares or computational physics fields, because of their generality. 'Mini applications' should be also developed with the solvers, so as to clarify their mechanism and efficiency. An alpha version of such a mini application with eigen-value solvers was prepared and is now being extended [18]. Such solvers and mini applications will play a crucial role in the Application-Algorithm-Architecture co-design among next-generation or exa-scale computational physics.

Acknowledgements

The fundamental mathematical theory was constructed in the collaboration mainly with T. Sogabe (Aichi Prefectural University), T. Miyata, D. Lee and S.-L. Zhang (Nagoya University). The basic code was developed in the collaboration mainly with S. Yamamoto (Tokyo University of Technology), S. Nishino and T. Fujiwara (University of Tokyo). The code for massive parallelism was developed with the supercomputers, the systems B and C, at ISSP. The K computer was used in the research proposals of hp120170, hp120280 and hp130052. Several structure data of amorphous-like conjugated polymers were provided by Y. Zempo (Hosei University) and M. Ishida (Sumitomo Chemical Co. Ltd.). Figures 2(c) and 3 were drawn by our original Python-based visualization software 'VisBAR' [4, 2].

References

[1] T. Hoshi, K. Yamazaki, Y. Akiyama, JPS Conf. Proc., **1** (2014) 016004.

[2] T. Hoshi, T. Sogabe, T. Miyata, D. Lee, S.-L. Zhang, H. Imachi, Y. Kawai, Y. Akiyama, K. Yamazaki and Seiya Yokoyama, Proceedings of Science, in press; Preprint : `http://arxiv.org/abs/1402.7285/`

[3] T. Hoshi, S. Yamamoto, T. Fujiwara, T. Sogabe, S.-L. Zhang, J. Phys.: Condens. Matter **21** (2012) 165502.

[4] T. Hoshi, Y. Akiyama, T. Tanaka and T. Ohno, J. Phys. Soc. Jpn., **82** (2013) 023710.

[5] ELSES (= Extra Large-Scale Electronic Structure calculation): http://www.elses.jp/

[6] See mathematical textbooks, such as H. A. van der Vorst *Iterative Krylov Meth-*

ods for Large Linear Systems, Cambridge Univ. Pr., (2009).

[7] R. Takayama, T. Hoshi, T. Sogabe, S.-L. Zhang, and T. Fujiwara, Phys. Rev. B **73** (2006) 165108.

[8] W. A. Frommer, Computing **70** (2003) 87; For a review, T. Sogabe and S.-L. Zhang, Bull. JSIAM **19**, 163 (2009) (in japanese).

[9] S. Yamamoto, T. Fujiwara, and Y. Hatsugai, Phys. Rev. B **76** (2007) 165114; S. Yamamoto, T. Sogabe, T. Hoshi, S.-L. Zhang and T. Fujiwara J. Phys. Soc. Jpn. **77** (2008) 114713

[10] T. Mizusaki, K Kaneko, M. Honma, T. Sakurai, Phys. Rev. C **82**, (2010) 024310.

[11] Y. Futamura, H. Tadano and T. Sakurai, JSIAM Letters **2** (2010) 127.

[12] F. Giustino, M. L. Cohen, and S. G. Louie, Phys. Rev. B **81** (2010) 115105.

[13] S. Nishino, T. Fujiwara, H. Yamasaki, S. Yamamoto, T. Hoshi, Solid State Ionics **225** (2012) 22; S. Nishino, T. Fujiwara, S. Yamamoto, and H. Yamasaki, *8th Pacific Rim International Congress on Advanced Materials and Processing*, Hawaii, 4-9. August, 2013

[14] R. Dronskowski and P. E. Blöchl: J. Phys. Chem. **97** (1993) 8617; `http://www.cohp.de/`

[15] T. Irifune, A. Kurio, A. Sakamoto, T. Inoue, and H. Sumiya, Nature **421** (2003) 599.

[16] N. Nishiyama, S. Seike, T. Hamaguchi, T. Irifune, M. Matsushita, M. Takahashi, H. Ohfujia and Y. Kono, Scripta Materialia **67** (2012) 955.

[17] D. Lee, T. Miyata, T. Sogabe, T. Hoshi, S.-L. Zhang, Japan J. Indust. Appl. Math. **30**, (2013) 6255; in *International Workshop on Eigenvalue Problems: Algorithms; Software and Applications, in Petascale Computing (EPASA2014)*, Tsukuba-city, Japan, 7-9, Mar. 2014.

[18] `http://www.damp.tottori-u.ac.jp/~hoshi/eigen_test/`; T. Hoshi, H. Imachi, Y. Kawai, Y. Akiyama, K. Yamazaki, S. Yokoyama, in *International Workshop on Eigenvalue Problems: Algorithms; Software and Applications, in Petascale Computing (EPASA2014)*, Tsukuba-city, Japan, 7-9, Mar. 2014.

Strong Correlation of Electrons Studied by Computational Approaches – Physics of Superconductors and Topological Phases

Shiro SAKAI, Takahiro MISAWA, Youhei YAMAJI, Moyuru KURITA and Masatoshi IMADA

Department of Applied Physics, University of Tokyo, 7-3-1, Hongo, Bunkyo-ku, Tokyo 113-8786, Japan

Strong electron correlation is a source of rich and marvelous phenomena, functions and concepts in condensed matter. However, it has hampered reliable treatments by theoretical approaches for a long time and still continues to be a challenge, where the mean-field and single-particle type approximations do not work in many cases. Numerical approaches offer promising tools for this challenge, while the numerical accuracy has to be kept sufficiently high because various orders are severely competing and the systems are often under large quantum fluctuations. Partly thanks to rapid progress in computer power, several numerical methods have been developed for this purpose recently. Here, we focus on the cluster extension of the dynamical mean-field theory (CDMFT) and the multi-variable variational Monte Carlo method (mVMC). The CDMFT has been applied to understanding of the mechanism of the high-temperature superconductivity for the model of the cuprate superconductors, particularly to reveal the origin of the pseudogap phenomena. The CDMFT has made it possible to clarify physics of the anomalous metallic phase of the Hubbard model in two dimensions as relevant to the cuprates. The structure of the pseudogap revealed here as a nodeless gap is essentially important in understanding the superconducting mechanism as well. The mVMC has been applied to understand physics of another family of high-T_c superconductors, iron-based superconductors, where the role of electron correlation effects had been controversial before the studies we review here. A key role of the strong electron correlation has become revealed with the help of supercomputers. The topological phases are the subject of extensive studies for two-dimensional electrons under strong magnetic fields as well as for materials with strong spin-orbit interactions. Recent mVMC calculations revealed an intriguing interplay of the spin-orbit interaction and the electron correlation effect. The possibility of the topological phase purely driven by the electron correlation effect without spin-orbit interactions is another hot subject of the numerical approaches. We here review these numerical studies at frontiers of efforts to understand nature of strongly correlated electrons.

1 Pseudogap in high-T_c cuprates

Despite the intensive studies in the last few decades, high-T_c cuprate superconductors still defy a comprehensive understanding. A key to the superconducting mechanism is in the anomalous "normal state", from which the superconductivity emerges. In particular, in underdoped cuprates, various experimental probes have observed a gap (pseudogap) behavior in the single-electron excitation spectra as well as in the two-particle responses such as magnetic and transport measurements at temperatures above T_c. Although vast amounts of experimental data have been accumulated to date, the origin of the pseudogap and its relationship to the superconductivity are still controversial.

From a theoretical point of view, the difficulty in studying the cuprates is in the fact that the superconductivity occurs in the carrier-doping region sandwiched by the Mott insulating state and the Fermi liquid state, which are the states of two different limiting cases. The former is a manifestation of the localizing nature of the strongly correlated electrons while the latter manifests the itinerancy of the electrons. This requires a theory for the cuprates to describe the dual character of the electrons simultaneously in a unified fashion. In terms of the quantum field theory, the itinerancy of the electrons is described by the presence of poles of the single-electron Green's function G at the Fermi level; that is, a metal is defined by the presence of the Fermi surface. On the other hand, the locality of the electrons is described by the presence of zeros of G (i.e., poles of the self-energy Σ) at the Fermi level, as it induces a gap in the excitation spectra [1]. Thus the duality of the electrons is translated into the presence of (or proximity to) both poles and zeros in G at low energy.

In order to take into account both poles and zeros at the same time, we need a non-perturbative approach. The cluster dynamical mean-field theory (CDMFT) [2,3] is one of such schemes with a capability to provide information on dynamical properties. It maps in a self-consistent way the original lattice model, like the Hubbard model, onto an effective cluster impurity model comprised of a finite-size interacting cluster and infinite number of non-interacting bath sites. The cluster impurity problem is then solved by an accurate numerical scheme such as the exact diagonalization method and the quantum Monte Carlo (QMC) method. The CDMFT takes into account all the correlation effects within the cluster, so that it can capture in an accurate way the physics caused by short-range electronic correlation effects.

Using the CDMFT, we have explored the two-dimensional Hubbard model in the region of the hole- or electron-doped Mott insulators. At small dopings and at zero temperature, both poles and zeros coexist at the Fermi level, which is a new metallic state of matter. We have shown that its electronic structure indeed accounts for various experimental results found in the anomalous metallic (pseudogap) state of the cuprates (Sec. 1.1). Our result furthermore shows an unprecedented momentum structure of the pseudogap on the positive-energy side, which has been elusive in experiments (Sec. 1.2).

1.1 Pole-zero structure of Green's function

We have first studied the zero-temperature electronic structure underlying the pseudogap state, by applying the CDMFT to the two-dimensional Hubbard model on the square lattice [4,5]. We employed a 2×2 square cluster, and solved the effective cluster impurity problem with the exact diagonalization method. In order to capture the electronic structure in the full momentum space, we took advantage of a truncated Fourier transformation of the cumulant [6], $M = (\omega + \mu - \Sigma)^{-1}$, where ω, μ, Σ are frequency, chemical potential and the self-energy, respectively. Since the cumulant is a well localized quantity in the proximity to the Mott insulator, the Fourier transformation truncated at the cluster size is expected to give a good approximation in that region. This argument was indeed confirmed by our subsequent study on the cluster-size dependence, up to 4×4, with the CDMFT + continuous-time QMC (CTQMC) [7] method [8].

Figure 1 (reproduced from Fig. 2(a) in Ref. 4) shows the electronic structure which we obtained in the region slightly hole-doped to the Mott insulator. Around the middle (red) $G = 0$ surface, spectral function is small because of the large scattering (imaginary part of the self-energy) there. Hence this surface induces a gap behavior in the spectral function, which is identified with the pseudogap found in preceding CDMFT studies [9,10]. Since the $G = 0$ surface crosses the Fermi level around (π, π), its large real part of the self-energy deforms the Fermi surface into a pocket around the nodal point. The presence of the singular surface of the self-energy at the Fermi level indicates that a non-Fermi-liquid ground state underlies the pseudogap phase. The metallic

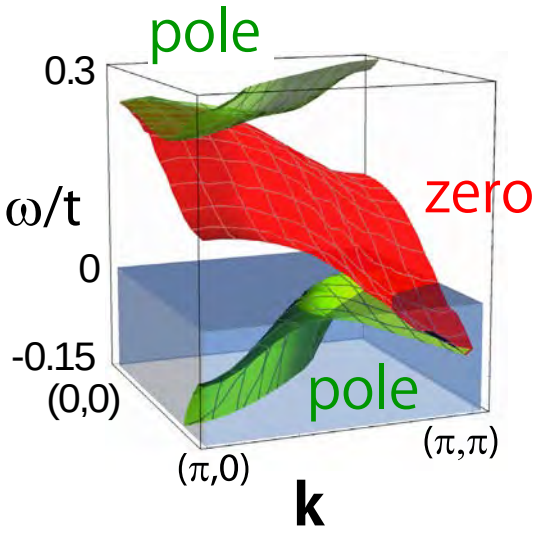

Figure 1: Pole-zero structure of G underlying pseudogap state at temperature $T = 0$ for on-site interaction $U = 8t$ and 9% hole doping to the half filling of two-dimensional Hubbard model, calculated by CDMFT + exact diagonalization method.

state with coexisting pole and zero surfaces also connects the electronic structure of the Mott insulating state at zero doping, where only a zero surface exists around the Fermi level, and the Fermi liquid state at large dopings, where only a pole surface exists.

Furthermore, the spectral function calculated for this pole-zero structure shares many anomalies with what have been experimentally observed in the pseudogap state of the cuprates [5]. The anomalies are attributed to the interference effect between the poles and zeros in the energy-momentum space, that is, the large self-energy around the zero surface deforms and broadens the pole surface into spectra which are out of the standard theory of metals. For example, the Fermi arc [11], back-bending dispersion [12], and the electron-hole asymmetry [13–16] are well reproduced by our CDMFT results.

1.2 *s*-wave pseudogap

Another remarkable feature of the structure in Fig. 1 is that the gap (pseudogap) opens everywhere in the momentum space [4, 5]. This is distinct from the conventionally-assumed *d*-wave structure of the pseudogap. Nevertheless, the calculated spectra are fully consistent with hitherto known ARPES experimental results, as we have mentioned in the previous section, since the gap *below* the Fermi level closes in the nodal direction. Namely, while the gap is around the Fermi level in the antinodal region, it shifts to higher energy as going to the nodal region and eventually locates itself at *above* the Fermi level in the nodal direction. We call this "*s*-wave" pseudogap in the sense that the gap amplitude is finite in the whole momentum space, although the strong momentum dependence of the energy location of the gap discriminates it from the standard *s*-wave gap structure.

Since our *s*-wave pseudogap structure is obtained by an accurate numerical simulation without any assumption on the symmetry or structure of the pseudogap, we took the result seriously and reexamined whether the common belief that the pseudogap is *d*-wave is really founded. In fact, in contrast to the superconducting gap, whose *d*-wave symmetry is firmly evidenced by the SQUID experiments [17,18], there are no phase-sensitive experimental evidences on the *d*-wave symmetry of the pseudogap. The common belief relies on the ARPES results, which have observed a *d*-wave-like structure of the pseudogap. However, as already discussed above, it cannot be an evidence since only with the occupied spectra observed by ARPES we cannot distinguish the *d*-wave and our *s*-wave pseudogaps. Since the symmetry of the pseudogap is a building block of a number of phenomenological theories, the distinction should play a crucial role in understanding the high-T_c superconductivity.

In order to distinguish the *d*-wave and our *s*-wave pseudogaps in experiments, we need information on the spectra *above* the Fermi level, especially in the nodal region of the momentum space. The momentum structure of the unoccupied spectra has, however, been elusive in experiments. In Ref.19, we explored this dark (unoccupied) side, by combining the electronic Raman spectroscopy experiments and a theoretical analysis based on the cluster dy-

namical mean-field theory. The advantage of the Raman spectroscopy is that it reflects both the occupied and unoccupied parts of the spectra and has a selectivity of momentum area through exploiting the photon polarizations. In the CDMFT analysis, since a better momentum resolution is required, we employed a 16-site cluster and solved the effective cluster impurity problem with the CTQMC method, which also allows us to study the properties at finite temperatures.

Then we observed the following anomalous behavior in the temperature dependence of the Raman response for underdoped samples. (i) As temperature is lowered from a high temperature, a depression at low frequencies, due to the pseudogap opening, first occurs in the antinodal response. (ii) At a lower temperature, the nodal response begins to decrease in an *intermediate*-frequency region while it increases at around zero energy. These behaviors were indeed well reproduced by our CDMFT Raman calculation, and thereby attributed to the s-wave pseudogap state: (i) is consistent with the fact that the pseudogap in the single-particle spectra opens first in the antinodal region, and (ii) accords with that the pseudogap in the nodal region opens at a lower temperature and above the Fermi level while the quasiparticle peak develops at the Fermi level. The s-wave pseudogap furthermore explains well the electron-hole asymmetry observed in recent ARPES [15, 16] and STM [20] experiments, which would be difficult to be explained within the d-wave pseudogap scenario.

Thus there are mainly two reasons to consider the pseudogap to be the s wave. One is the fact that microscopic numerical simulations, when taking into account all the short-range correlation effects, produce the s-wave structure. The other is the extensive consistency with the experimental observations discussed above. The results impose a strong constraint on our understanding of the pseudogap and of the high-T_c superconducting mechanism in the cuprates.

2 *Ab initio* studies on iron-based superconductors

2.1 Introduction

Iron-based superconductors were discovered in 2008 [21] and the highest critical temperature became above 55 K. It has been shown that most of mother materials of the iron-based superconductors are antiferromagnetic metals [22]. This is in sharp contrast with the other high-T_c superconductors, namely the cuprates, whose mother materials are antiferromagnetic Mott insulators, induced by the strong electron correlation. Thus, at the initial stage of the study, it was not clear whether the electronic correlation is weak or strong in the iron-based superconductors, although it is one of the most important factor to understand the origin of the high-T_c superconductivity.

To clarify the strength of the electronic correlation and its effects on electronic structures such as magnetism and superconductivity in the iron-based superconductors, we applied *ab initio* downfolding scheme [23] to the iron-based superconductors. In this scheme, the global band structures are calculated based on the density functional theory and then the low-energy effective Hamiltonian is obtained by using constrained random phase approximation (cRPA). Finally, we solve the low-energy effective model by employing a high-accuracy low-energy solver such as the multi-variable variational Monte Carlo (mVMC) method and clarify the electronic properties of the target materials in a fully *ab initio* way. In this review, we first explain the basic properties of the low-energy effective model derived for the iron-based superconductors. Then, we will show how the electronic structures of the iron-based superconductors are obtained by solving the low-energy effective models.

2.2 Model

In this report, we consider four iron-based superconductors, namely, LaFePO, LaFeAsO, $BaFe_2As_2$, and FeTe. The obtained low-energy effective model for each iron-based superconductor is a five-orbital Hubbard model and its

form is given as

$$\mathcal{H} = \mathcal{H}_0 + \mathcal{H}_{\rm int} \quad (1)$$

$$\mathcal{H}_0 = \sum_{\sigma}\sum_{i,j}\sum_{\nu,\mu} t_{i,j,\nu,\mu} a^{\dagger}_{i,\nu,\sigma} a_{j,\mu,\sigma} r \quad (2)$$

$$\begin{aligned}\mathcal{H}_{\rm int} &= \frac{1}{2}\sum_{\sigma,\sigma',i,\nu,\mu}\Big\{U_{i,i,\mu,\nu} a^{\dagger}_{i,\nu,\sigma} a^{\dagger}_{i,\mu,\sigma'} a_{i,\mu,\sigma'} a_{i\nu,\sigma} \\ &+ J_{i,i,\mu,\nu}\big(a^{\dagger}_{i,\nu,\sigma} a^{\dagger}_{i,\mu,\sigma} a_{i,\nu,\sigma'} a_{i,\mu,\sigma} \\ &+ a^{\dagger}_{i,\nu,\sigma} a^{\dagger}_{i,\nu,\sigma} a_{i,\mu,\sigma'} a_{i,\mu,\sigma}\big)\Big\}, \end{aligned} \quad (3)$$

where $a^{\dagger}_{i,\nu,\sigma}$ ($a_{i,\nu,\sigma}$) is a creation (annihilation) operator of an electron with spin σ on the νth maximally localized Wannier orbital at the i-th site. $t_{i,j,\nu,\mu}$ contains single-particle levels and transfer integrals. $U_{i,i,\nu,\mu}$ and $J_{i,i,\nu,\mu}$ are screened Coulomb and exchange interactions, respectively. In the actual calculations, we used the transfer integrals up to the fifth neighbors, which well reproduce the band structures by the local density approximation. Off-site interactions are ignored since those are less than a quarter of the onsite parameters.

The derived effective models are defined in three spatial dimensions at this stage. To explicitly reflect the two-dimensionality of the iron-based superconductors, we performed dimensional downfolding [24] and obtained purely two-dimensional low-energy effective models. Our results of the *ab initio* dimensional downfolding for each compound indicate that the screenings from the other layers reduce all the Coulomb interactions uniformly [24]. Based on our calculated *ab initio* results, we subtract the constant values from $U_{\nu,\mu}$'s in the 3D models [25] as follows; 0.44 eV for LaFePO, 0.41 eV for LeFeAsO, 0.38 eV for $BaFe_2As_2$, and 0.40 eV for FeTe, respectively. We note that the exchange interactions $J_{\nu,\mu}$ are not significantly changed by the screenings from the other layers [24]. Details of the interaction as well as the single-particle parameters that we used are shown in the literatures [24–27].

From the *ab initio* derivation of the interaction parameters, we have found that family dependence of the interaction parameter can be well scaled by the single parameter λ [25–27], which is defined as $\mathcal{H} = \mathcal{H}_0 + \lambda\mathcal{H}_{\rm int}$, where $\lambda = 1$ corresponds to the *ab initio* parameters for LaFeAsO. By changing λ, we successfully reproduce the interaction parameters for other materials from those of LaFeAsO. For example, by taking $\lambda \simeq 0.8$, we reproduce the interaction parameters for LaFePO.

2.3 Method

To clarify the electronic structures of the effective models, we employ the mVMC method. Details of the mVMC methods are given in the literature [28]. In the mVMC calculations, we study the ground state properties by employing a generalized Bardeen-Cooper-Schrieffer (BCS) type wave function with the quantum number projection and the Gutzwiller and Jastrow factors;

$$|\psi\rangle = \mathcal{P}_{\rm G}\mathcal{P}_{\rm J}\mathcal{L}^{S=0}|\phi_{\rm pair}\rangle. \quad (4)$$

Here, $\mathcal{L}^{S=0}$ is the spin projection operator to the total spin $S = 0$ subspace; $\mathcal{P}_{\rm G}$ and $\mathcal{P}_{\rm J}$ are the Gutzwiller and Jastrow factors, respectively [28]. The spin projection is performed onto the $S = 0$ singlet subspace. The Gutzwiller factor punishes the double occupation of electrons by $\mathcal{P}_{\rm G} = \exp(-\sum_{i,\nu} g_{i\nu} n_{i\nu\uparrow} n_{i\nu\downarrow})$ where $n_{i\nu\sigma} = a^{\dagger}_{i\nu\sigma} a_{i\nu\sigma}$. The Jastrow factor is introduced up to the next-nearest-neighbor sites as $\mathcal{P}_{\rm J} = \exp(-\frac{1}{2}\sum_{i,j} v_{ij\nu\mu} n_{i\nu} n_{j\nu})$, where $n_{i\nu} = \sum_{\sigma} n_{i\nu\sigma}$. The one-body part $|\phi_{\rm pair}\rangle$ is the generalized pairing wave function defined as $|\phi_{\rm pair}\rangle = (\sum_{\nu,\mu=1}^{5}\sum_{i,j=1}^{N_{\rm s}} f_{ij\nu\mu} a^{\dagger}_{i\nu\uparrow} a^{\dagger}_{i\mu\downarrow})^{N_e/2}|0\rangle$, where N_e (N_s) is the number of electrons (number of sites). In this study, we restrict the variational parameters, $g_{i\nu}$, $v_{ij\nu\mu}$ to have a 2×1 structure, and $f_{ij\nu\mu}$ to have a 2×2 sublattice structure. The number of variational parameters are 10 for $g_{i\nu}$, 220 for $v_{ij\nu\mu}$, and $100N_s$ for $f_{ij\nu\mu}$. All the variational parameters are simultaneously optimized by using the stochastic reconfiguration method [28, 29]. Our variational wave function $|\psi\rangle$ can flexibly describe superconducting (SC), antiferromagnetic (AF), and paramagnetic (PM) phases as well as their fluctuations on an equal footing. The calculations were done up to 8×8 sites.

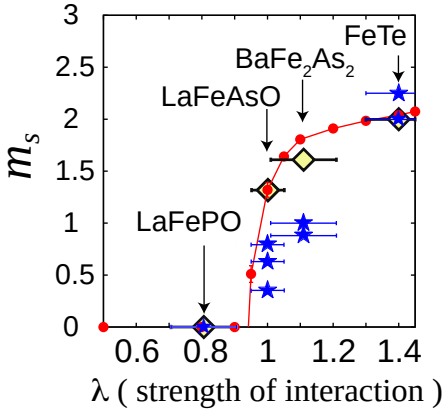

Figure 2: Interaction dependence of magnetic ordered moment m_s [27]. Magnetic ordered moment of each *ab initio* model is represented by (yellow) diamond while experimental magnetic ordered moments for several materials are represented by (blue) stars. By changing the interaction parameter λ for LaFeAsO, we obtain the λ dependence of the magnetic ordered moment [closed (red) circles].

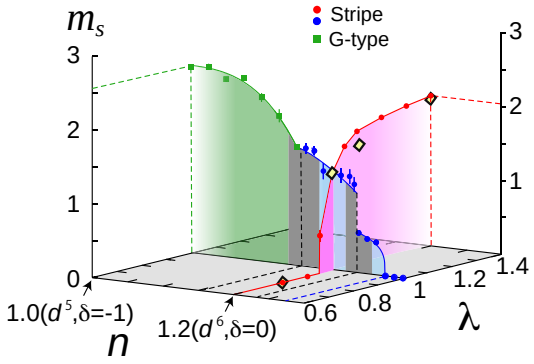

Figure 3: Magnetic ordered moment m_s in the plane of λ and doping concentration δ [27]. The data are plotted in the cross-sections for λ=1 as well as for δ=0. It shows a peak at d^5 (δ=−1.0) and decreases monotonically over d^6 (δ=0), which forms a large half-dome structure peaked at d^5. The mVMC results of the *ab initio* models are shown by (black-framed yellow) diamonds. There exist two first-order transitions (black dashed lines), one indicated by the jumps in the ordered moment around $\delta\sim$0.17 and the other at the transition between the G-type and stripe around $\delta\sim-0.22$, which signals large charge fluctuations under phase-separation effects. In the present short-ranged-interaction model, the phase separation indeed occurs in the gray shaded regions.

2.4 Results

By using this method, we first clarify that the low-energy effective models can reproduce the family dependence of the magnetic ordered moment m_s [27], which is defined as

$$\boldsymbol{S}_{i\nu} = \frac{1}{2}\sum_{\sigma,\sigma'} a^{\dagger}_{i\nu,\sigma}\boldsymbol{\sigma}_{\sigma\sigma'}a_{i\nu,\sigma'}, \quad (5)$$

$$m(\boldsymbol{q}_{\rm peak})^2 = \frac{4}{3N_{\rm s}^2}\sum_{i,j,\nu,\mu}\langle \boldsymbol{S}_{i\nu}\cdot\boldsymbol{S}_{j\mu}\rangle, \quad (6)$$

$$m_s = \lim_{N_s\to\infty} m(\boldsymbol{q}_{\rm peak}), \quad (7)$$

where $\boldsymbol{\sigma}$ represents Pauli matrix, $\boldsymbol{q}_{\rm peak}$ is set to $\boldsymbol{q}_{\rm peak} = (0,\pi)$ (stripe magnetic order). As shown in Fig. 2, We calculated the magnetic ordered moment for LaFePO, LaFeAsO, $BaFe_2As_2$, and FeTe and plot them at corresponding λ, which is a measure of the strength of the interaction parameters. The diverse family dependence of the magnetic ordered moment is well explained from the systematic dependence on the strength of the effective electronic interactions. Our calculation also clarifies that LaFeAsO is very close to an antiferromagnetic quantum critical point and this is the origin of the small magnetic ordered moment observed in the experiment.

In Fig. 3, we show the global phase diagram in the plane of interaction λ and doping concentration δ [27]. Undoped case (six electrons in five orbitals, i.e, d^6 configuration) corresponds to the $n = 1.2$ (red) plane. At $\lambda = 1$, we change the electron density and examine the intrinsic doping effect. By doping electrons, magnetic order vanishes at around 20% doping. In contrast to this, by doping holes, we find unexpected behaviors; magnetic ordered moment becomes larger and larger, and it has a peak at the d^5 configuration. At d^5 configuration, the checkerboard-type (G-type) antiferromagnetic Mott insulator appears. This result indicates that the iron-based superconductors are located on the foot of large dome structures originating from the d^5 Mott insulator.

Here, based on our *ab initio* study, we compare the iron-based superconductors with the other high-T_c superconductors, the cuprates. Both materials are under the proximity effects of the Mott insulator. However, in the iron-based superconductors, due to the multi-orbital effects and the large Hund's rule coupling, the antiferromagnetic dome ranges from d^5 to d^6. This is in sharp contrast with the cuprates, where the proximity effect of the Mott insulator collapses with a small umbrella below 20-30% doping around d^9. In the iron-based superconductors, at the foot of the large d^5 Mott insulator, several intriguing phenomena such as high-T_c superconductivity are found. It is an intriguing issue to reveal the relation between the proximity effects of the d^5 Mott insulator and the high-T_c superconductivity.

3 Correlated Topological Insulators

Emergence of topologically-protected edge states, which are not affected by impurities or imperfection in crystalline electron systems, has been a central issue of quantum Hall insulators realized in two-dimensional electron gases under strong magnetic fields.

Together with pioneering works [30–33], theoretical prediction of quantum *spin* Hall insulators by Kane and Mele [34] has triggered intensive experimental and theoretical studies. Now, the emergence of topologically-protected edge (or surface) states has been recognized as rather universal phenomena: A certain class of insulators, including well-studied polymer polyacetylene and thermoelectric compound Bi_2Te_3, has protected edge/surface states irrespective of their spatial dimensions [35–38].

For essentially non-interacting electron systems, these quantum phases with protected surface states have been classified by using symmetric properties of these systems [36–38].

However, studies on topological states of strongly-correlated electron systems are still ongoing. There are mainly three issues of the studies on topologically non-trivial gapped phases of strongly correlated electron systems:

1. Correlation effects on topological insulators classified in corresponding non-interacting systems.
2. Topological insulators induced by spontaneous symmetry breakings, often called topological Mott insulators.
3. Emergent topological phases of many-body systems that do not appear in non-interacting systems, such as Haldane phases in one-dimensional integer-spin Heisenberg models.

Here, we reiew our numerical study [39] on the first issue in the above list. By using mVMC, we studied a typical model for topologically non-trivial correlated insulators called Hubbard-Kane-Mele model detailed below. The topologically non-trivial phase can in principle be probed by directly calculating the Z_2 topological number. However, it is a formidable computational task. Alternatively and equivalently, the gapless edge probed by the Drude weight concomitant with the gapful bulk state on the cylinder ensures the existence of the topologically nontrivial phase [34]. Our VMC results on the edge Drude weights reveal that the electron correlations enhance spin transports at the edge while charge transports are suppressed. We also give a brief summary of our studies on the second issue.

3.1 Hubbard-Kane-Mele model

We employ a tight binding hamiltonian on the two-dimensional honeycomb lattice proposed by Kane and Mele [34] with inclusion of the spin-orbit coupling as complex hopping terms and the on-site Coulomb interaction, and without the Rashba term to study electron correlation effects on the topological insulator. Hereafter we call this simple model the Hubbard-Kane-Mele model and it is defined as

$$\hat{H} = \hat{H}_{\rm KM} + U \sum_I \hat{n}_{I\uparrow}\hat{n}_{I\downarrow}, \tag{8}$$

with

$$\begin{aligned} \hat{H}_{\rm KM} &= -t \sum_{\langle I,J\rangle\sigma} \hat{c}^\dagger_{I\sigma}\hat{c}_{J\sigma} \\ &+ it_2 \sum_{\langle\langle I,J\rangle\rangle\alpha\beta} \nu_{ij}\hat{c}^\dagger_{I\alpha}[\sigma_z]_{\alpha\beta}\hat{c}_{J\beta}, \end{aligned} \tag{9}$$

where $\hat{H}_{\rm KM}$ is the Kane-Mele hamiltonian, t (t_2) is the nearest-neighbor (next-nearest-neighbor) hopping, and U is the onsite Hubbard interaction. Here we define $\nu_{ij}=\vec{d}_i \times \vec{d}_j / \left|\vec{d}_i \times \vec{d}_j\right|$, and $I=(i,a)$ $(a=A,B)$ (see Fig.4(a)).

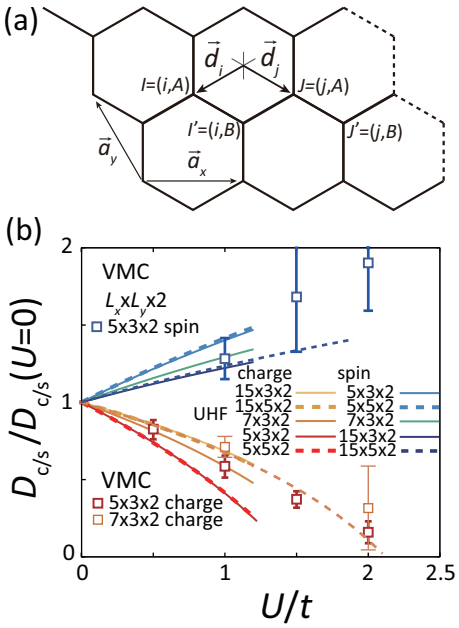

Figure 4: (a) Honeycomb lattice on which the Hubbard-Kane-Mele model is defined. (b) U dependence of charge and spin Drude weights renormalized with the Drude weight for $U=0$. For comparison, we also show the results of a partially unrestricted Hartree-Fock approximation with prohibition of x and/or y components of spin densities, denoted as UHF in the figure.

To carry out VMC calculations of the Hubbard-Kane-Mele model, we employ a variational wave function defined as

$$|\psi\rangle = \mathcal{P}_{\rm G}\mathcal{P}_{\rm J}|\phi_{\rm pair}\rangle, \qquad (10)$$

where $\mathcal{P}_{\rm G}$ and $\mathcal{P}_{\rm J}$ are the Gutzwiller and Jastrow factor, respectively. We impose the Gutzwiller factor on all the sites, whereas introduce the Jastrow factor only along the zigzag edges. The one-body part $|\phi_{\rm pair}\rangle$ is a generalized pairing wave function $|\phi_{\rm pair}\rangle = \left[\sum_{i,j=1}^{N_{\rm s}} f_{ij} c_{i\uparrow}^{\dagger} c_{j\downarrow}^{\dagger}\right]^{N/2}|0\rangle$ with f_{ij} being the complex variational parameters. In this study, we allow f_{ij} to have 2-sublattice ($2\times L_y$-sublattice) structure or equivalently we have $2\times 2\times N_{\rm s}$ ($2\times L_y\times 2\times L_y\times L_x$) variational parameters for the torus (cylinder). All the variational parameters are simultaneously optimized by using the stochastic reconfiguration method generalized for complex variables.

3.2 Charge and Spin Drude Weights

Charge and spin Drude weights are calculated by introducing vector potentials as the Peierls factors,

$$t_{IJ\sigma} \to t_{IJ\sigma}\exp[i\vec{A}_\sigma \cdot \vec{r}_{IJ}], \qquad (11)$$

where $\vec{r}_I = n_I\vec{a}_x + m_I\vec{a}_y$ and $\vec{r}_{IJ} = \vec{r}_I - \vec{r}_J$. Here n_I and m_J are integers, and lattice vectors are $\vec{a}_x$ and $\vec{a}_y$ (see Fig.4(a)). By introducing these Peierls factors, the Drude weights for the charge and spin channels, $D_{\rm c}$ and $D_{\rm s}$, respectively, are calculated from the energy stiffness

$$D_{\rm c} = \frac{1}{2}\frac{d^2E(\vec{A}_\uparrow,\vec{A}_\downarrow)}{d|\vec{A}|^2}\bigg|_{\vec{A}_\uparrow=\vec{A}_\downarrow=|\vec{A}|}, \qquad (12)$$

and

$$D_{\rm s} = \frac{1}{2}\frac{d^2E(\vec{A}_\uparrow,\vec{A}_\downarrow)}{d|\vec{A}|^2}\bigg|_{\vec{A}_\uparrow=-\vec{A}_\downarrow=|\vec{A}|}, \qquad (13)$$

where $E=\langle\psi|\hat{\mathcal{H}}|\psi\rangle/\langle\psi|\psi\rangle$ is the total energy. If we introduce spin-dependent vector potentials, $\vec{A}_\sigma=\sigma\vec{A}$, we obtain the Drude weight for the spin channel, namely the spin Drude weight. To clarify the edge state, we employ a cylinder with sizes $N_s=L_x\times L_y\times 2$, for the honeycomb lattice with two sites on a unit cell and the periodic (free) boundary conditions in the x (y) directions. We have confirmed that the employed width L_y is large enough to make isolated two edges at the two free boundaries at $y=0$ and $y=L_y$. For the bulk properties we employ the torus, where the boundary is periodic for all the directions .

We show our VMC results for the Drude weights for the Hubbard-Kane-Mele model on the cylindrical geometry with two zigzag edges along the x-direction in Fig.4(b). The electron correlations enhance the spin Drude weight $D_{\rm s}$

of the edge states while the electron correlations suppress the charge Drude weight D_c. In other words, the electron-electron interactions induce localization of the charge degrees of freedom and enhance the spin conduction. Our results suggest that pure spin conductions are induced by the electron correlation at the edge/surface of the topological insulators.

3.3 Topological Mott insulator

Both in two and three dimensions, the topological insulators are typically realized in the presence of strong spin-orbit interaction [40–42]. On the other hand, it was suggested that the extended Hubbard model on the honeycomb lattice can generate an effective spin-orbit interaction from a spontaneous symmetry breaking at the Hartree-Fock mean-field level and results in the topologically non-trivial phase [43]. Similar phenomenon has also been proposed on the kagomé, diamond and pyrochlore lattices [44–46]. A common property is that the lattice models which are semimetals in the single particle problem may have topologically non-trivial insulator phases caused by the Coulomb interaction. Therefore, these states are called topological Mott insulators. These proposals offer the possibility of the realization of the topological insulator even in the absence of the spin-orbit interaction.

Theories of the topological Mott insulators also opens a possibility of studying quantum phase transitions with novel criticality [47]. Contrary to the ordinary phase transitions, where the universality class is determined by spatial dimension and the structure of broken symmetries, criticality of the transition to the topological Mott insulator depends on the band dispersion near the Fermi point characteristic of the zero-gap semiconductors. In the topological Mott insulators, the criticality of the system is calculated from a free energy expansion

$$f[\zeta] - f[0] \simeq AQ + BV\zeta^2, \qquad (14)$$

$$Q = \int_0^\Lambda k^{d-1} dk \left[-\sqrt{aV^2\zeta^2 + bk^{2n}} + bk^n \right]. \qquad (15)$$

Here, A, B, a, b are constants depending on the system, V is the control parameter, ζ is the order parameter, Λ is the cut-off wave length, d is the spatial dimension of the system, and n is the exponent which determines the band dispersion near the Fermi point. Therefore, the topological change of the Fermi surface leads to a free-energy singularity $|\zeta|^{d/n+1}$, and generates unconventional universalities characterized by mean-field critical exponents $\beta = n/(d-n)$ and $\delta = d/n$.

For more quantitative estimate of the critical exponents by considering fluctuations, for example, fermionic renormalization group [48] or a renormalization group method applicable to non-analytic free-energy expansions, which may give a modification to our analysis, will be helpful and are left for future studies. These may give a solution for dynamical exponents and upper critical dimensions of the topological Mott transition, and hence give the estimate for quantitative corrections of the other critical exponents as well. Furthermore, strong quantum fluctuations expected around the present topological Mott transition may offer a basis for unprecedented quantum phases mediated by the spin-orbitons.

References

[1] I. Dzyaloshinskii: Phys. Rev. B **68** (2003) 085113.

[2] G. Kotliar, S. Y. Savrasov, G. Palsson, and G. Biroli: Phys. Rev. Lett. **87** (2001) 186401.

[3] T. Maier, M. Jarrell, T. Pruschke, and M. H. Hettler: Rev. Mod. Phys. **77** (2005) 1027.

[4] S. Sakai, Y. Motome, and M. Imada: Phys. Rev. Lett. **102** (2009) 056404.

[5] S. Sakai, Y. Motome, and M. Imada: Phys. Rev. B **82** (2010) 134505

[6] T. D. Stanescu and G. Kotliar: Phys. Rev. B **74** (2006) 125110.

[7] E. Gull *et al.*: Rev. Mod. Phys. **83** (2011) 349. .

[8] S. Sakai *et al.*: Phys. Rev. B **85** (2012) 035102.

[9] B. Kyung, S. S. Kancharla, D. Seńećhal, A.-M. S. Tremblay,M. Civelli, and G. Kotliar: Phys. Rev. B **73** (2006) 165114.

[10] A. Macridin, M. Jarrell, T. Maier, P. R. C. Kent, and E. D'Azevedo: Phys. Rev. Lett **97** (2006) 036401.

[11] M. R. Norman, H. Ding, M. Randeria, J. C. Campuzano, T. Yokoya, T. Takeuchi, T. Takahashi, T. Mochiku, K. Kadowaki, P. Guptasarma, and D. G. Hinks, Nature **392** (1998) 157.

[12] A. Kanigel, U. Chatterjee, M. Randeria, M. R. Norman, G. Koren, K. Kadowaki, and J. C. Campuzano: Phys. Rev. Lett. **101** (2008) 137002.

[13] T. Hanaguri, C. Lupien. Y. Kohsaka, D.-H. Lee, M. Azuma, M. Takano, H.Takagi, and J. C. Davis: Nature **430** (2004) 1001.

[14] P. W. Anderson and N. P. Ong: J. Phys. Chem. Sol. **67** (2006) 1.

[15] H.-B. Yang *et al.*: Nature **456** (2008) 77.

[16] M. Hashimoto *et al.*: Nature Phys. **6** (2010) 414.

[17] D. A. Wollman, D. J. Van Harlingen, W. C. Lee, D. M. Ginsberg, and A. J. Leggett: Phys. Rev. Lett. **71** (1993) 2134.

[18] C. C. Tsuei *et al.*: Nature **387** (1997) 481.

[19] S. Sakai *et al.*: Phys. Rev. Lett. **111** (2013) 107001.

[20] A. Pushp *et al.*: Science **324** (2009) 1689.

[21] Y. Kamihara, T. Watanabe, M. Hirano, and H. Hosono: J. Am. Chem. Soc. **130** (2008) 3296.

[22] G. R. Stewart: Rev. Mod. Phys. **83** (2011) 1589.

[23] For a review, see T. Miyake and M. Imada: J. Phys. Soc. Jpn. **79** (2010) 112001.

[24] K. Nakamura, Y. Yoshimoto, Y. Nohara, and M. Imada: J. Phys. Soc. Jpn. **79** (2010) 123708.

[25] T. Miyake, K. Nakamura, R. Arita, and M. Imada: J. Phys. Soc. Jpn. **79** (2010) 044705.

[26] T. Misawa, K. Nakamura, and M. Imada: J. Phys. Soc. Jpn. **80** (2011) 023704.

[27] T. Misawa, K. Nakamura, and M. Imada: Phys. Rev. Lett. **108** (2012) 177007.

[28] D. Tahara and M. Imada: J. Phys. Soc. Jpn. **77** (2008) 114701.

[29] S. Sorella: Phys. Rev. B **64** (2001) 024512.

[30] B. A. Volkov and O. A. Pankratov : JETP Lett. **42** (1985) 178.

[31] O. A. Pankratov, S. V. Pakhomov, and B. A. Volkov : Solid State Comm. **61** (1986) 93.

[32] E. Fradkin, E. Dagotto, and D. Boyanovsky : Phys. Rev. Lett. **57** (1986) 2967.

[33] F. D. M. Haldane, : Phys. Rev. Lett. **61** (1988) 2015.

[34] C. L. Kane and E. J. Mele : Phys. Rev. Lett. **95** (2005) 146802.

[35] L. Fu, C. L. Kane, and E. J. Mele : Phys. Rev. Lett. **98** (2007) 106803.

[36] A. Kitaev, in Proceedings of the L. D. Landau Memorial Conference "Advances in Theoretical Physics",e-print arXiv:0901.2686.

[37] S. Ryu, A. P. Schnyder, A. Furusaki, and A. W. W. Ludwig : New. J. Phys. **12** (2010) 065010.

[38] X.-G. Wen : Phys. Rev. B **85** (2012) 085103.

[39] Y. Yamaji and M. Imada : Phys. Rev. B **83** (2011) 205122.

[40] B. Andrei Bernevig, Taylor L. Hughes, and S.-C. Zhang: Science **314** (2006) 1757.

[41] M. König, S. Wiedmann, C. Brüne, A. Roth, H. Buhmann, L. W. Molenkamp, X.-L. Qi, and S.-C. Zhang: Science **318** (2007) 766.

[42] D. Hsieh, D. Qian, L. Wray, Y. Xia, Y. S. Hor, R. J. Cava, M. Z. Hasan: Nature **452** (2008) 970.

[43] S. Raghu, X.-L. Qi, C. Honerkamp, and S.-C. Zhang: Phys. Rev. Lett. **100** (2008) 156401.

[44] J. Wen, A. Rüegg, C.-C. J. Wang, and G. A. Fiete: Phys. Rev. B **82** (2010) 075125.

[45] Y. Zhang, Y. Ran, and A. Vishwanath: Phys. Rev. B **79** (2009) 245331.

[46] M. Kurita, Y. Yamaji and M. Imada: J. Phys. Soc. Jpn. **80** (2011) 044708.

[47] M. Kurita, Y. Yamaji and M. Imada: Phys. Rev. B **88** (2013) 115143.

[48] I. F. Herbut, V. Juricic, and O. Vafek, Phys. Rev. B **80** (2009) 075432.

Coarse-Grained Simulation of Surfactant Membrane

Hayato SHIBA and Hiroshi NOGUCHI
Institute for Solid State Physics, University of Tokyo
Kashiwa-no-ha, Kashiwa, Chiba 277-8581

Abstract

We review our recent studies on the structure formation of surfactant membranes using a meshless membrane model, in which a unit particle represent a patch of the bilayer membrane. We revealed aggregation of ligand–receptor sites binding neighboring membranes, microdomain formation induced by grafted polymer chains, and the formation of a rolled lamellar structure under shear flow using massive parallel simulations.

1 Introduction

Amphiphilic molecules, such as lipids and detergents, self-assemble into various structures such as micelles and bilayer membranes, which display a rich variety of rheological properties under flow. In particular, the bilayer membrane is the basic structure of the plasma membrane and intracellular compartments of living cells, where the membranes are in a fluid phase and lipid molecules can diffuse in two-dimensional space.

Cell adhesion is a fundamental process required for the removal of foreign bodies in immune response and for cell motility. It is mediated by specific (ligand–receptor) and non-specific interactions. Recently, lateral interactions between ligand–receptor binding sites in membranes have been received growing attention [1, 2]. The cooperative aggregation of the adhesion sites yields various patterns of adhesion domains and also morphological changes in cells and liposomes.

The membrane height fluctuations yield a repulsive force $f \sim d^{-3}$ between tensionless fluid membranes with a neighboring membrane distance d. Since the adhesion bond holds two membranes close to each other, an effective attraction works between the adhesion sites. If the adhesion sites are aggregated, the rest of the regions of the membranes are allowed to have large height fluctuations. This entropy gain yields an attraction between adhesion sites. Several groups have been investigated this entropic interaction theoretically and via simulations. These studies have reported a weak attraction between adhesion sites, which induces small temporal clusters. However, it has been concluded that this force is too weak to form a large cluster by itself, and thus, the researchers have included additional pairwise interactions to investigate the phase separation. Using ISSP super computer system B, we have clarified the condition that induces aggregation of the adhesion sites purely by entropic interactions [3].

in living cells, it is considered that local microdomains, called lipid rafts, are formed on biomembranes as a platform of many biological functions. Lipid rafts is in diameter of 10 $\sim$ 100 nm, and proteins, cholesterol, and glycosphingolipids are concentrated. We have investigated the membranes with grafted polymer chain such as glycolipids and PEG-conjugated lipids [4]. We found that the polymer grafting can reduce the line tension of the

membrane edges and membrane domains and stabilize small domains.

About 20 years ago, a salient phenomenon has been found in surfactant systems. Applying shear flow to dilute lamellar phases in surfactant-water mixtures in a Couette cell, the found formation of densely packed multilamellar vesicles like onion [5]. Each onion represents a unit cell of the periodic structure and its layer number is larger than a hundred. Although there have been numerous efforts to understand the onion formation mechanism, the problem was revealed to be to difficult for theoretical analysis. Only very recently, a non-equilibrium free energy analysis has revealed the stability of densely packed lamellar under shear flow more than a little [6].

The transition path and dynamics of transition is still under debate. Scattering experiments (SAXS and SANS) has been conducted under shear flow, and a concentric pattern formation of multilamellar layers has been observed as a precursor state of the onion state [7], Because this structure has sum-μm scale structure, electric microscope image cannot capture the arrangement of the layers, and thus, how the structure is arranged is not completely understood. We tackled this problem using massive parallel simulations of a highly coarse-grained membrane model [8, 9].

2 Model

Coarse-grained models pave the way to simulate large molecular assemblies as typified by soft matter including biomembranes, colloids, liquid crystals, and so on. Various coarse-grained models have been developed to simulate a membrane as an assembly of surfactant molecules [10]. Coarse-grained lipid molecules have been proposed with explicit and implicit solvent. A coarse-grained molecular simulation can only reach lamellar phase with around 10 layers with typical computational power [11], and thus, we need a different approach to enter into investigation of collective instability represented in the experiments mentioned above.

Our basic approach is to adopt a model highly coarse-grained to tens of nm scales and realize a large scale simulation to enable numerical analysis of mm scale systems. The model employed in this study is one of the meshless membrane model [12], in which coarse-grained particles self-assemble into a single layer membrane. Because this model is particle-based, the membranes not only deform but also can exhibit topological changes including rupture and reconnection, and thus, dynamics induced by topological defects their time development can be studied with this model.

The interaction potential of the model is given by

$$\frac{U}{k_B T} = \sum_{i<j} U_{\mathrm{rep}} + \sum_i \left(\epsilon U_{\mathrm{att}} + k_\alpha \alpha_{\mathrm{pl}}\right) \quad (1)$$

In Eq. (1), The first term U_{rep} represents short-ranged repulsive interaction energy, which results in two-body forces between all the nearest neighbor pairs. The second term consists of multibody attractive interaction and curvature potential giving rise to bending rigidity: the former attractive interaction is represented using the local density $\rho_i = \sum_i f_{\mathrm{cut}}(r_{ij}/\sigma)$

$$U_{\mathrm{att}} = 0.25 \ln\{1 + \exp[-4(\rho_i - \rho^*)]\} - C. \quad (2)$$

f_{cut} is a cutoff function satisfying C^∞ continuity defined as

$$f_{\mathrm{cut}}(s) = \exp\left[a\left(1 + \frac{1}{(|s|/s_{\mathrm{cut}})^n - 1}\right)\right]. \quad (3)$$

when s is smaller than a cutoff distance s_{cut} and otherwise $f_{\mathrm{cut}}(s) = 0$. ρ^* is optimal local density which is set to 6 in this paper. This potential is a multibody potential and gives rise to attractive interaction between i and others only when the local density is low enough *i.e.* $\rho_i < \rho^*$

The latter term in the 2nd term in Eq. (1) is defined so that it is proportional to "aplanarity" $\alpha_{\rm pl}$. $\alpha_{\rm pl}$ is defined so that it is proportional to local degree of deviation from a planar shape around each particle, using the eigenvalues $\lambda_1,\ \lambda_2,\ \lambda_3$ of local gyration tensor

$$\alpha_{\rm pl} = \frac{9\lambda_1\lambda_2\lambda_3}{(\lambda_1+\lambda_2+\lambda_3)(\lambda_1\lambda_2+\lambda_2\lambda_3+\lambda_3\lambda_1)} \quad (4)$$

When particles are aligned in a planar shape with curvature, the minimum eigenvalue assumes a very small value ($\lambda_1 \ll \lambda_2, \lambda_3$). The minimum eigenvalue corresponds to the deviation from the planar shape, see Ref. [12] for a detailed explanation. Since the representation of Eq. (4) is symmetric with respect to the three eigenvalues, $\alpha_{\rm pl}$ can be easily deduced from three invariants of the gyration tensors of surrounding particles without calculating the eigenvalues.

To simulate the membranes with ligand–receptor adhesion sites and grafted polymers, solvent-free membranes are employed, where solvent effects are implicitly treated as an effective attractive interactions between membrane particles.

To simulate structure formation of multilamellar layers, we extended the meshless membrane model into explicit solvent simulation. Solvent particles interact with other solvent and membrane particles via the repulsive interaction $U_{\rm rep} = \sum_{i<j}(\sigma_{ij}/r_{ij})^{12}$. The system is then composed of membrane ($\mathcal{A}$) and solvent ($\mathcal{B}$) particles. The total number density of the particles fixed at $\phi = N/V = 0.64\sigma^{-3}$, where the total number of the particles $N = N_{\mathcal{A}} + N_{\mathcal{B}} = 960000$. In the following, the composition (almost equal to the volume fraction) of the membrane particles will be denoted as $\varphi = N_{\mathcal{A}}/N$.

3 Simulation method

The above model is simulated in an NVT ensemble. To keep the temperature constant, the equation of motion of the particles are solved using a Langevin thermostat for solvent-free model and a dissipative particle dynamics thermostat for an explicit-solvent model. In the dissipative particle dynamics, a Langevin thermostat is applied to the relative velocities between all the neighbor particle pairs, conserving the momentum to produce hydrodynamics of the solvent.

In the simulations under shear flow, the parallel simulation runs using 256 CPUs (1024 cores) has been conducted on the System B. The parallelization has been coded using the spacial decomposition, and the code has been developed from scratch by the first author. In this parallelization, the total simulation volume is separated into MPI boxes corresponding to rectangular boxes. In each box, the positions and velocities of particles on the edge is transferred to and from its neighboring boxes, as with the usual parallel molecular dynamics scheme (See Fig. 1 (a) for schematic image).7 The main features of this code is the following.

1. Hybrid parallelization

   Each MPI process box are further divided into smaller cells which are used for searching neighbor particle pairs. In calculating the force for each particle $\boldsymbol{f}_i$, the force is accumulated pair by pair, to reduce the total calculation amount.

   $$f_i^x \mathrel{+}= f_{ij}^x = \frac{\partial U}{\partial x_{ij}}, \quad f_j^x \mathrel{+}= -f_{ij}^x \quad (5)$$

   Here, $x_{ij} = x_i - x_j$ and the same pairwise interaction force f_{ij}^x is used for particles i and j. OpenMP thread parallelization of such an arithmetic cannot be implemented in a simple manner, because multiple access to the same memory address for f_x^i can happen. To avoid this, we divided separated cells into the same group, and distributed force-update processing for separated cells to different OpenMP threads.

2. Lees-Edwards boundary condition

To yield the shear flow, Lees-Edwards (LE) boundary condition is adopted. LE boundary condition is a sort of skewed periodic boundary condition, in which particles go out of the peirodic walls in the shear gradient direction (parallel to z-axis), the velocity and the coordinate of the particles are changed as follows:

$$\begin{cases} v_x^{\rm top} = v_x^{\rm bottom} + \dot{\gamma} L_z \\ x^{\rm top} = x^{\rm bottom} + \dot{\gamma} L_z t \end{cases} \quad (6)$$

"top" and "bottom" indicate that the positions of the particles on the boundary at $z = L_z/2$ and $-L_z/2$, respectively.

To keep MPI parallelization efficiency, combinations of neighbor MPI box pairs should be kept, because communication with many far-away processes drag down the simulation speed. In our simulation, the neighbor box pairs between the top and bottom parts are kept by deforming the whole MPI process box and the cells together. When the strain reaches 0.5 *i.e.* its inclination becomes 45-degree, the whole system is converted to the equivalent state with strain -0.5, using all-to-all communication of particle positions between the whole processes. Loss of simulation speed by using this method is less than 10% in our simulation, compared with simulations without shear flow.

4 Results

4.1 Estimation of bending rigidity and surface tension

First, we measured the bending rigidity of the membrane using undulation spectrum analysis and force measurements for implicit-solvent membranes [14, 15]. In the spectrum analysis, undulation spectra of planar strip and cylindrical tube membrane have been calculated to estimate the its bending rigidity. Figure 1 (a) shows a power-spectrum of the height spectrum of a tensionless membrane:

$$\langle |h(q)|^2 \rangle = \frac{k_B T}{\kappa q^4}, \quad (7)$$

where T is the temperature and q is the wavenumber of the spectrum. Various fitting method for estimation of bending rigidity κ has been attempted in the range $0 < q < q_{\rm cut}$ for various cutoff frequencies $q_{\rm cut}$. What is noteworthy in this result is that for various fitting method the estimated bending rigidity provides the same value in the limit of $q_{\rm cut} \to 0$. At high q particle protrusion modes $\langle |h(q)|^2 \rangle \sim q^{-2}$ appears. The influence of the protrusion modes is removed by taking this limit.

Bending rigidity is also estimated by mechanical measurement of cylindrical membrane and buckled membrane. For a cylindrical membrane, it can be estimated using the axial force $f_z = 2\pi\kappa R^{-1}$ [16]. Figure 1 (b) shows the estimation of κ for k_α =5, 10, 20 and $\epsilon = 4$. When the axial length is not too short, κ can be precisely estimated, in agreement with that calculated using Eq. (7) shown in Fig. 1 (a). Asymmetric membranes have a spontaneous curvature. The spontaneous curvature can be also estimated by this force measurement.

We found that buckled fluid membranes have anisotropic mechanical surface tension [15]. Surprisingly, the surface tension perpendicular to the buckling direction shows stronger dependence on the projected area than that parallel to it. This anisoptropty is caused by change of the bending energy as the aspect ratio is varied with a fixed projected area. It can be quantitatively understood by the theoretical analysis of the elastica. The bending rigidity can be also estimated from the area dependence of surface tension.

4.2 Aggregation of adhesion sites

First, we investigate interactions between the adhesion sites binding two membranes, and we confirm the conclusions of previous studies [17]. The adhesion sites are distributed

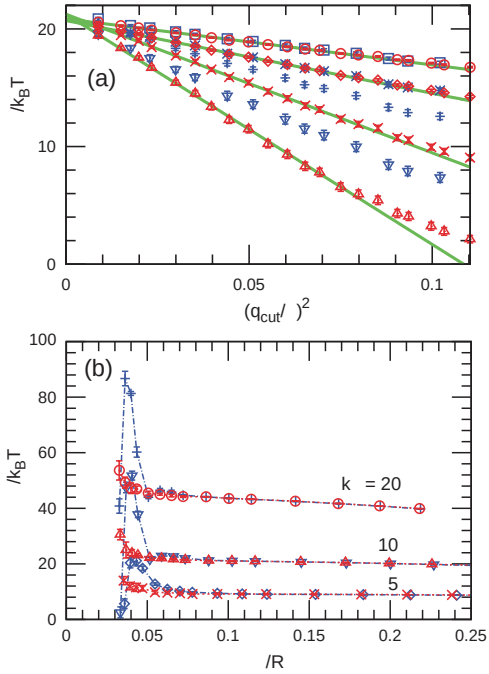

Figure 1: Estimation of the bending rigidity. he data here in is a reprinted from Figs. 3 and 6 of Ref. [14]. (a) Estimated value of the bending rigidity plotted as a function of cutoff frequency of fitting for the implicit-solvent meshless membrane with $k_\alpha = 5$ and $\epsilon = 4$. Different symbols correspond to different fitting method, see Ref. [14] for details. (b) Bending rigidity estimated from axial force measurement of cylindrical membrane, plotted as a function of tube radius R, for $k_\alpha = 5,\ 10, 20$ and $\epsilon = 4$.

throughout the membranes and their small clusters are temporally formed but do not grow into large stable clusters [see Fig. 2(a)]. Even if a simulation is started from a large cluster, it gradually dissolves into the mixed state. The cluster size is almost independent of the mean density of adhesion sites.

In order to produce a large stable cluster, the bending entropy of membranes is enhanced by the addition of more layers of membranes [15]. For triple membranes, the adhesion sites form a single large domain, whose shape shows large fluctuations. A few sites often leave the domain but soon return before moving far

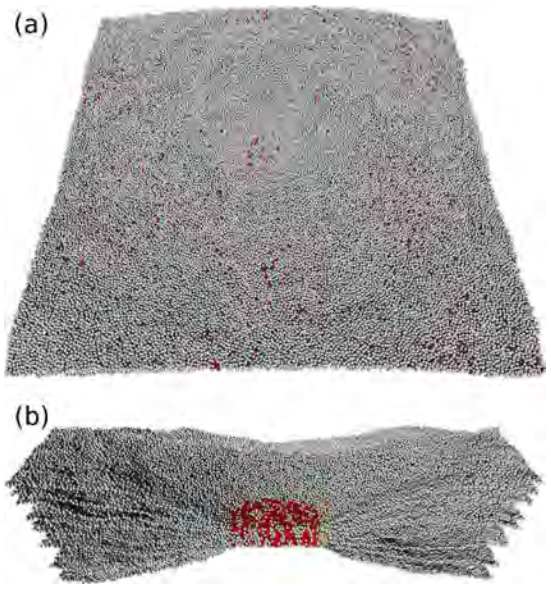

Figure 2: Snapshot of membranes with ligand–receptor adhesion sites. (a) Two membranes are bound. The adhesion sites do not form a large cluster. (b) Eight membranes are bound. The adhesion sites form a circular domain. The front half is removed to show the domain structure. Red (black) and gray spheres represent adhesion sites and membrane particles, respectively.

away, since an isolated site will further suppress the membrane fluctuations of the larger area. With increasing number of the membranes, the domain becomes more compact and circular [see Fig. 2 (b)].

An alternative way to strengthen the entropic force is enhancement of the contribution of each adhesion site [15]. Membrane proteins often modify the structure of surrounding membranes and form an annular shell of specific lipids. Here, we simply consider the effect of the anchor proteins on the main quantity being examined in this study, *i.e.*, bending rigidity. The anchors of ligands or receptors suppress the bending fluctuations of the surrounding membranes. A large stable cluster is successfully formed for a large bending rigidity of the surrounding membranes.

These entropic effects can be understood as

an effective potential in 2D lattice model. Weil and Farago proposed a 2D lattice model to take into account the multibody nature of the interaction [17]. Since local membrane height fluctuations are mainly suppressed by the nearest adhesion site, the entropy of the membrane segment can be expressed by a function of the minimum distance to the nearest site. We have extended their model to take into account multiple membranes and membrane-hardening anchors. Membrane-harding is treated as a similar interaction to the depletion interaction in the Asakura–Oosaka theory. This simple lattice model reproduces our simulation results very well.

These domain formations are different from those of typical phase separation by a pairwise interaction. When two types of molecules are phase-separated in a binary fluid, a small fraction of either type of molecules dissolves in the other phase. In the case of the membrane adhesion sites, the competition between the entropies in the perpendicular direction (height fluctuations) and in the horizontal directions (mixing of the adhesion sites) determines the phase behavior. While a large amount of unbonded membrane particles dissolves in circular domains, no adhesion sites dissolve in the membranes even from largely deformed domains. This asymmetry is caused by the long-range height correlation of the membranes. Such stable domains involving other lipids and proteins may form a good platform for biological functions.

4.3 Membranes with grafted polymers

We investigate the edge line tension with various grafted polymer densities for both ideal chains and excluded-volume chains. A strip of single-phase membrane with grafted polymers is used to estimate the edge tension. The edge tension decreases with increasing polymer density. The reduction for excluded-volume chains is much larger than that for ideal chains. When the polymers stay on the membrane edge, they can have more space to move *i.e.* more conformational entropy. We proposed a mean field theory for the edge line tension reduced by grafted ideal chains, which well reproduces our simulation results.

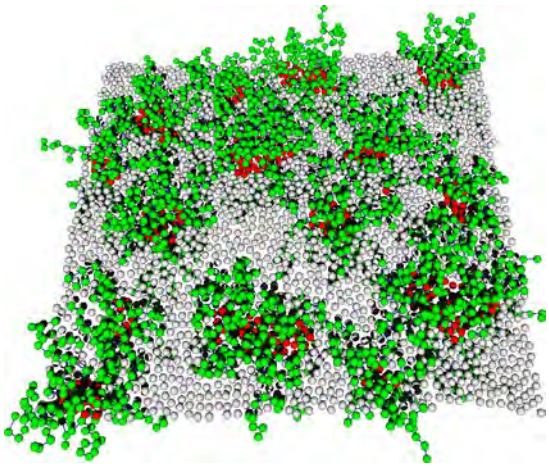

Figure 3: Snapshot of membranes with grafted polymer chains. The membrane consists of two types [red (or dark gray) and light gray] of the membrane particles. The polymer chains are grafted on the (red or dark gray) membrane particles. The polymer grafting induces microdomain formation. Without polymers, a single large domain is formed.

To clarify the polymer effects on the membrane domain, we added grafted polymer into a phase-separated circular domain. As polymer density is increased, the domain shape is fluctuated and subsequently the domain is divided into small domains (see Fig. 3). The line tension between the membrane domains is estimated by two methods using a striped domain and a 2D Laplace pressure of a circular domain. For the membrane without polymer, the obtained values agree with those from the membrane strip very well. However, the values obtained from the Laplace pressure are slightly larger for the polymer-grafted membranes. Thus, more curved domains have lower reduction of the line tension, so that the small domains with a high curvature can have suffi-

ciently large line tension to keep the domain, whereas a large domain is unstable. The entropic effects of glycolipids may play a significant role in stabilizing microdomains $\lesssim$ 100 nm in living cells.

4.4 Concentric structure formation under shear flow

In the absence of shear flow, the membrane structures depend on the membrane volume fraction φ. While at a low volume fraction ($\varphi = 0.0625$), vesicles with around 100 particles appear. Increasing φ, the membrane layer become percolated throughout the system, to form lamellar stack at around $\varphi = 0.25$. At a large scale, orientation of these lamellar stacks are not completely aligned, because the relaxation time to the equilibrium state far exceeds the simulation time.

When apply shear flow to this system, the orientation of the lamellar layers formed at high membrane compositions ($\varphi \geq 0.25$) become aligned in a short time. In Fig. 4, the membrane layers are visualized for $\varphi = 0.3125$, at a shear rate $\dot{\gamma}\tau$ = (a) 2.84×10^{-2} and (b) 14.2×10^{-2}. Here, τ is a typical time scale of this system that is used as a time unit in our simulation. At a low shear rate (a), lamellar layers are aligned in the direction of shear flow over all the system, accompanying defects inside. At higher shear rates, the lamellar layers exhibits concentric instability *i.e.* formation of rolled-up conformation as shown in Fig.4 (b). The membranes layers are completely aligned with the flow directions, and the instability takes place in the direction perpendicular to the shear velocity. Its structure factors are qualitatively in consistency with the precursor state of the onion formation in the time-resolved scattering experiments.

Figure 5 shows the dynamical phase diagram as a function of membrane composition φ and the shear rate $\dot{\gamma}$. At a low shear rate, the system changes from vesicle to aligned lamellar state with increasing φ. At a high membrane

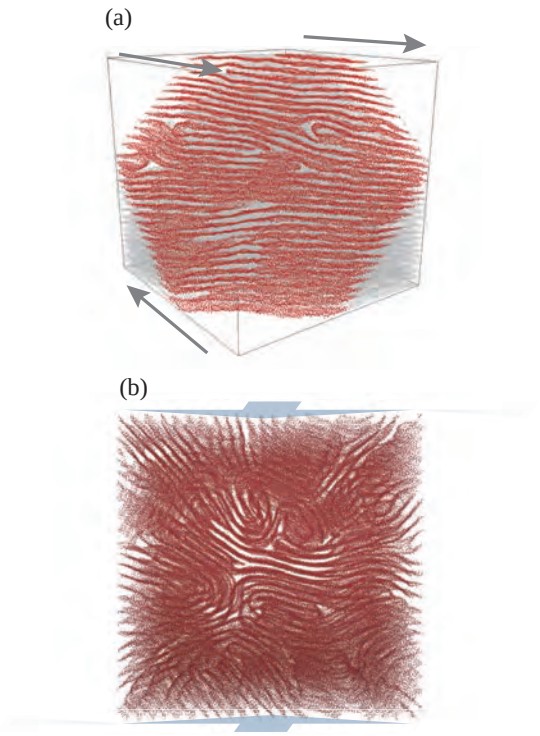

Figure 4: (a) Cross-sectional snapshot in a steady state, at $\varphi = 0.3125$ and $\dot{\gamma}\tau = 2.84 \times 10^{-2}$. This snapshot corresponds to Fig. 7 (a) in Ref. [9]. The arrow indicate the shear flow direction. (b) Snapshot of roll state observed at $\varphi = 0.2125$ and $\dot{\gamma}\tau = 14.2 \times 10^{-2}$.The shear flow is applied in the direction perpendicular direction to the paper. (Reprinted from Ref. [8]. ©2014 The Molecular Simulation Society of Japan)

volume fraction, for example at $\varphi = 0.25$, a transition occurs from lamellar state to rolled up state (at $\dot{\gamma}t = 1.42 \times 10^{-2}$), and then enter into lamellar state takes place again. Although the final onion phase has not been obtained at present, the phase diagram has several common characteristics with the experiments [5]. Remarkable resemblance is seen in a reentrant appearance of the lamellar state as a function of shear rate $\dot{\gamma}$, at large φ region. Moreover, in the lamellar state at low-$\dot{\gamma}$ defect density seems much higher that at high$\dot{\gamma}$, which seems to be in line with the description in Ref. [5]. Thus, our simulation reproduces the a concen-

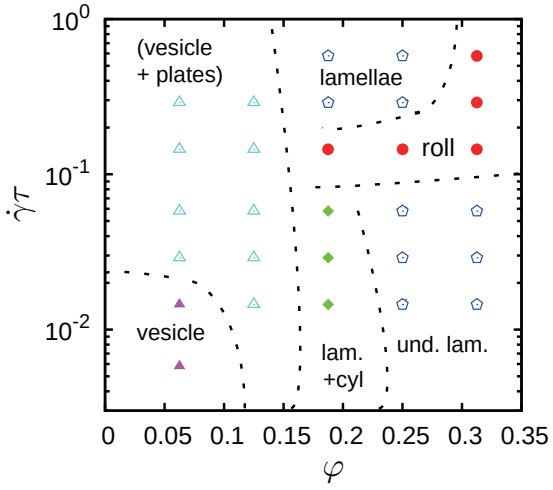

Figure 5: Dynamical phase diagram as a function of the volume fraction φ of the membrane component and the shear rate $\dot{\gamma}$. (Reprinted from Ref. [9]. ©2013 AIP Publishing LLC)

tric structure as a precursor of onion formation, and it is likely that this model will reproduce the onion phase if the simulation condition (including the system size) becomes appropriate.

5 Summary

We have presented the structure formation of the membrane using meshless membrane simulations. Membranes show a rich variety of behavior in thermal equilibrium as well as out of equilibrium. Coarse graining is a powerful tool to investigate membrane dynamics on a micro meter scale. On this scale, a detailed molecular structure can be neglected. The meshless model is suitable to treat topological changes of membranes. In the shear flow, we have found a novel rolled lamellar structures, which capture the feature of the intermediate scattering pattern during the lamellae-to-onion transition. We will further pursue the onion phase and other large scale phenomena using supercomputers.

References

[1] A. -S. Smith, K. Sengupta, S. Goennenwein, U. Seifert, and E. Sackmann, Proc. Natl. Acad. Sci. USA **105**, (2008) 6906.

[2] A. S.Achalkumar, R. J. Bushby, and S. D. Evans, Soft Matter **6** (2010) 6036.

[3] H. Noguchi, EPL **102** (2013) 68001.

[4] H. Wu, H. Shiba, and H. Noguchi, Soft Matter **9** (2013) 9907.

[5] O. Diat, D. Roux, and F. Nallet, J. Phys. II France **3** (1993) 1427.

[6] C.-Y. David Lu, Phys. Rev. Lett. **109** (2012) 128304.

[7] F. Nettesheim, J. Zipfel, U. Olsson, F. Renth, P. Lindner, and W. Richtering, Langmuir **19** (2003) 3603.

[8] H. Shiba and H. Noguchi, Ensemble (Bulletin of Molecular Simulation Society of Japan) **16** (2014) 59. [in Japanese]

[9] H. Shiba, H. Noguchi, and G. Gompper, J. Chem. Phys. **139** (2013) 014702.

[10] H. Noguchi, J. Phys. Soc. Jpn. **78**, (2009) 041007.

[11] H. Guo, K. Kremer, and T. Soddemann, Phys. Rev. E **66** (2002) 061503.

[12] H. Noguchi and G. Gompper, Phys. Rev. E **73** (2006) 021903.

[13] H. Noguchi and G. Gompper, J. Chem. Phys. **125** (2006) 164908.

[14] H. Shiba and H. Noguchi, Phys Rev. E **84** (2011) 031926.

[15] H. Noguchi, Phys Rev. E **83** (2011) 061919.

[16] V. A. Harmandaris and M. Deserno, J. Chem. Phys. **125** (2006) 204905.

[17] N. Weil and O. Farago, Euro. Phys. J. E **33** (2010) 81.

3.2 First-Principles Calculation of Material Properties

First-principles simulations of atomic geometries, electronic properties and chemical reactions at interfaces

Fahdzi MUTTAQIEN, Yuji HAMAMOTO, Kouji INAGAKI, and Yoshitada MORIKAWA

Department of Precision Science and Technology,

Osaka University, Yamada-oka, Suita, Osaka 565-0871

Adsorption and reaction of CO_2 on solid surfaces are attracting growing interest because of their importance in industrial, energy and environmental management[1]. In industry, H_2, CO^2 and CO gas mixtures are used in methanol synthesis by using $Cu/ZnO/Al_2O_3$ catalysts, where CO_2 is considered to be the main carbon source on the basis of the results of an isotope labeling experiment.

Previous studies of CO_2 adsorption on single-crystal Cu surfaces have shown that CO_2 is adsorbed more strongly on defective Cu surfaces than on flat Cu surfaces. On flat copper surfaces, CO_2 is weakly adsorbed molecularly and needs high activation energy to dissociate: 0.69 eV for Cu(110)[2]. Using temperature programmed desorption (TPD) experiment, Fu and Somorjai found that CO_2 is adsorbed and dissociates to CO and O on the Cu(311) surfaces with a 4 L dose at 150 K[3]. Boenicke *et al.* showed by means of thermal desorption spectroscopy (TDS) experiment that CO_2 is chemisorbed and dissociates at 95 K over the Cu(332) surface[4]. Using infrared reflection absorption spectroscopy (IRAS), Koitaya and co-workers recently discovered that CO_2 dissociates on the Cu(997) stepped surface at 83 K[5]. They exposed isotopically labelled $^{13}CO_2$ to the Cu(997) surface at 83 K and observed two absorption peaks at 2050cm^{-1} and 2066 cm^{-1}, which are assigned to the C-O stretching mode of ^{13}CO at terrace and step sites, respectively, clearly demonstrating the dissociation of CO_2. They also discovered that there is no CO_2 dissociation on the Cu(111) surface at 83K.

To investigate the minimum energy pathways of the CO_2 dissociation process, we considered the Cu(111), Cu(221), Cu(211), and Cu(11 5 9) surfaces. We used three close-packed layers for the slab models and a fixed bottom atomic layer. The slab surfaces were constructed by using a calculated equilibrium lattice constant of 3.65Å, which is close to the experimental value of 3.62Å.

The standard GGA Perdew-Burke-Ernzerhof (GGA-PBE) exchange-correlation functional was used for the DFT calculations. The dispersion correction (DFT-D2) proposed by Grimme was used to describe the dispersion interaction between metal atoms and molecules. All calculations were carried out by using the

STATE (Simulation Tool for Atom TEchnology) package, which previously had been applied to the synthesis of formate and its hydrogenation process.

To check the accuracy of our results, we used a van der Waals density functional (vdW-DF) proposed by Dion and co-workers. The vdW-DF calculations were applied to charge density data obtained from standard GGA calculations.

We found that CO_2 is weakly adsorbed on stepped surfaces and that the dissociated products are less stable than the initial ones even if the dissociated CO species are located at the on-top site of copper atoms. The characteristic of CO_2 adsorption in the initial states for all models is identified by its relative distance from the surface (more than 3Å) and its vibrational frequencies, which are close to those in the isolated gas phase.

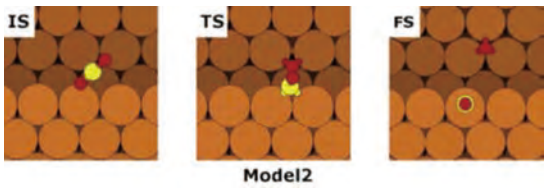

Fig. 1: CO_2 dissociation path on the Cu(221) surface.

We investigated the dissociation process of CO_2 to CO + O on the Cu(111), Cu(221), Cu(211), and Cu(11 5 9) surfaces by using DFT-GGA and vdW-DF calculations. The activation barrier for CO_2 dissociation on the flat Cu(111) surface is 1.33 eV, which agrees well with previous reports. For stepped surfaces, the activation energies are slightly lower, 1.06 eV, 0.67 eV, and 1.02 eV for the Cu(221), Cu(211), and Cu(11 5 9) surfaces, respectively. From our results, we conclude that CO_2 does not dissociate on the flat, stepped or kinked Cu surfaces at low temperature. We attribute the experimentally observed CO_2 dissociation on stepped Cu surfaces below 150 K to other factors such as Cu adatoms, gas phase or condensed CO_2, or other gas phase molecules.

References

[1] H.-J. Freund and M.W. Roberts, Surf. Sci. Rep., **25**, 225 (1996).

[2] J. Nakamura, J.A. Rodriguez, and C.T. Campbell, J. Phys.: Condens. Matter **1**, 149 (1989).

[3] S. Fu and G.A. Somorjai, Surf. Sci. **262**, 68 (1992).

[4] I.A. Boenicke, W. Kirstein, and F. Thieme, Surf. Sci. **307**, 177 (1994).

[5] T. Koitaya, Y. Shiozawa, K. Mukai, S. Yoshimoto, and J. Yoshinobu, "14th International Conference on Vibrations at Surfaces in Kobe", (2012), and personal communication.

Atomic Structures and Electronic Properties of Hard- and Soft-Nanomaterials

Atsushi Oshiyama
Department of Applied Physics, The University of Tokyo
Hongo, Tokyo 113-8656

The two of our achievements in my group are reported in the following.

1. Magic Angle and Height Quantization in Nanofacets on SiC(0001) Surfaces

Nanostructures on surfaces are utilized as templates for subsequent nano-fabrications. A typical example is the faceting that is the unexpected and spontaneous appearance of the small-area surface on the substrate surface. SiC is one of the semiconductors which are most promising in power electronics. The epitaxial growth of SiC films plays a central role in the fabrication of SiC devices. In such epitaxial growth, the (11$\bar{2}$n) nanofacets frequently appear on the (0001) surfaces. Itis observed that such nanofacets consist of bunched atomic steps. Mysteriously, the facet angle φ which is the angle between the (0001) and the (11$\bar{2}$n) planes is insensitive to the crystal polytype and the vicinal angle, being in the range of 12 - 16°, which we call *magic facet angle*. Moreover, the height of the nanofacet along the (0001) direction is interestingly *quantized* to a integer or a half-integer of the unit-cell height.

We have performed large-scale density-functional calculations using our real-space scheme (RSDFT code) [1,2]. We have found that the bunched single-bilayer steps are energetically favorable than equally spaced atomic steps, leading to the formation of the (11$\bar{2}$n) nanofacets with a particular facet angle of $\varphi = 15°$. We find that the balance between two factors, i.e., the step-step repulsive energy and the surface-energy variation, which comes from the different bilayer atomic sequence near the surface, is the reason for the *magic facet angle* and the *quantization* of the facet height.

Figure 1 shows the geometry optimized single-bilayer (SB) step on the 4H-SiC (0001) surface. In the SB step, the Si atom on the upper terrace rebonds with the partner Si atom on the lower terrace at the step edge. The energy gain from this rebonding is 2.1 eV per unit length a_0 ($a_0 = 5.27$ Å) along the step-edge direction. The formation energy for the SB step, λ_{SB}, is 0.31 eV/a_0 in the present LDA calculations. We have also performed geometry optimization for the double-bilayer (DB) and quad-bilayer (QB) steps. On the contrary to the SB step, the rebonding between the upper-terrace and the lower-terrace atoms is unfeasible. As a result of this, the formation energies of the DB step and the QB step, λ_{DB} and λ_{QB}, are larger than λ_{SB} by about 1.8 eV/a_0 and 4.9 eV/a_0, respectively.

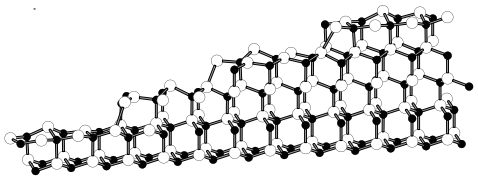

Figure 1: Geometry optimized single-bilayer height step on the 4H-SiC (0001) surface. Large open and small solid circles denote Si and C atoms, respectively. Step edge atoms are either three-fold or four-fold coordinated.

We next explore a possibility of its bunching which leads to the nanofacet. We have constructed the (11$\bar{2}n$) facet ($n = 32, 24, 16, 12, 8, 4$) consisting of the SB steps on the vicinal surface with $\theta = 5.9°$ (968 atoms in a cell of the slab model). The facet angles of these six nanofacets are $\varphi = 5.9$, 7.8, 11.6, 15.3, 22.3, 39.2° respectively. We have performed the geometry optimization and obtained the stable structures for each nanofacet. The total energies of thus obtained nanofacets are plotted as a function of the facet angle in Fig. 2. We have found that there is a particular facet angle of $\varphi_0 = 15°$ which makes the total energy minimum, indicating the existence of the *magic facet angle*. The calculated value $\varphi_0 = 15°$ agrees with the experimental observation.

2. Interstitial Channels that Control Band

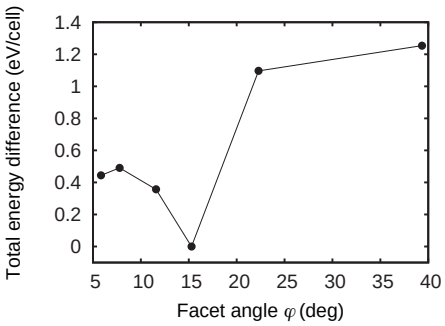

Figure 2: Total energy of the $(11\bar{2}n)$ nanofacet formed on the $4H$-SiC (0001) vicinal surface as a function of the facet angle. The energies are relative to that of the most stable nanofacet with the facet angle $\varphi_0 = 15.3°$ ($n = 12$). The total energy of the geometry optimized equally spaced SB steps (ESS) which corresponds to the facet angle of 5.9° is also shown.

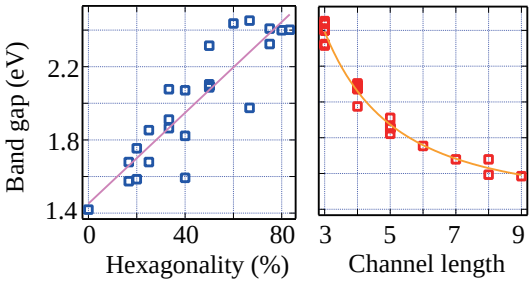

Figure 3: Band gaps for 24 representative SiC polytypes calculated in GGA as a function of the hexagonality (left panel) and a function of the channel length (right panel). In each panel, a fitting function is also shown. Each variance of the fiting is 355 (85) meV for a fitting curve as a function of hexagonality (channel length).

Gaps and Effective Masses in Semiconductors

Most semiconductors, elemental or compound, have the four-fold coordinated tetrahedral structure caused by the hybridization of atomic orbitals. It is written in textbooks that the resultant hybridized sp^3 bonding orbitals constitute valence bands, whereas the anti-bonding counter parts do conduction bands. This is not necessarily true, however: We have recently found that the wave-functions of the conduction-band minima (CBM) of the semiconductors are distributed not near atomic sites but in the interstitial channels [3]. The wave-functions *float* in the internal space, i.e., the channels, inherent to the sp^3-bonded materials.

Another structural characteristic in the semiconductor is the stacking of atomic bilayers along the bond axis direction such as AB (wurtzite) or ABC (diamond or zincblende). The different stacking sequence leads to the different polytype generally labeled by the periodicity of the sequence n and its symmetry, hexagonal (H) or cubic (C). The sequence determines the lengths and the directions of the interstitial channels: e.g., in the $3C$ polytype the channel along $\langle 110 \rangle$ extends infinitely, whereas in the $6H$ polytype the cannel along $\langle 2\bar{2}01 \rangle$ has a finite length of $7a_0$ / 2 $\sqrt{2}$ (a_0: lattice constant). Hence the stacking affects the shapes of the wave-functions of CBMs.

For SiC, dozens of polytypes of SiC are observed and the band gaps vary by 40 %, from 2.3 eV in $3C$ to 3.3 eV in $2H$ despite that the structures are locally identical to each other in the polytypes. This mysterious band-gap variation has been discussed in terms of an empirical quantity, hexagonality, for a half century: A bilayer sandwiched by the two same stacking indexes, as in 2H structure, is called a hexagonal layer and the ratio of the hexagonal layers in whole stacking sequence is called hexagonality; the band-gap variation in the polytypes is argued to be linear with respect to the hexagonality. Yet, the linearity is not satisfactory (see below) and moreover the underlying physics is totally lacking.

We have found, on the basis of the density-functional calculations, that the extent of the internal space, i.e., the length of the interstitial channel, in covalent semiconductors is decisive in the nanoscale shapes of the wave-functions of the CBM and hereby explains the mysterious variation of the band gap in SiC polytypes (Fig. 3). We also find that the observed anisotropy of the effective masses in SiC, and the pressure dependence of the band gaps generally observed in most semiconductors, are naturally explained in terms of the channel length. Further, we find that the stacking control dramatically modifies the electronic properties, leading to generation of low-dimensional electron and hole systems in three-dimensional SiC.

References

[1] K. Sawada, J.-I. Iwata and A. Oshiyama, Proc. ICSCRM **778-780**, 201 (2013).
[2] K. Sawada, J.-I. Iwata adn A. Oshiyama, APL **104**, 051605 (2014); submitted to PRB (2014).
[3] Y. Matsushita and A. Oshiyama, PRL **112**, 136403 (2014); ibid., **108**, 246404 (2012).

First-principles meta-dynamics analysis of Catalytic Referred Etching method (Reaction barrier in etching of GaN, SiC and SiO_2)

Kouji INAGAKI

Graduate School of Engineering, Osaka University

Yamadaoka 2-1, Suita, Osaka 565-0871

Step-and-terrace shaped smooth surfaces of wide-bandgap materials can be easily formed just by wiping the surface by a catalyst plate in an etching solution (named CARE(catalyst referred etching) method[1]), which is promising as an industrial surface finishing technique. To enhance etching rate and to find low-cost catalysts and/or safer etching materials is the current serious issue. In this project, we are investigating the reaction process in the atomic level to give a helping hand to experimentalists.

In this period, we have performed first-principles reaction barrier analysis of the initial stage of the etching process using the program package STATE[2,3] with Pt cluster placed near the reaction region. In the presence of Pt cluster, the energy barrier of dissociative adsorption of the etchant molecule found to become lower, in which the etchant molecule (H_2O or HF) is dissociatively absorbed on the process surface ([OH or F] to [SiC or SiO_2]) and Pt cluster (H to Pt). Figure 1 shows the schematic atomic structure of the intermediate meta-stable state of the reaction. The dissociative adsorption reaction finishes after terminating C atom by H atom through a proton-relay-like reaction shown by arrows in Fig.1. The interaction between Pt (d orbital) and O (p orbital) is also found to be important for reducing the reaction barrier.

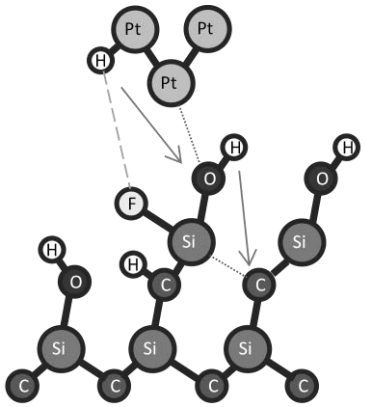

Fig. 1: Schamatic view of the intermediate meta-stable atomic structure in the lower reaction barrier process.

References

[1] H.Hara, et al., J.Electron.Mater. 35 (2006) L11.

[2] Y. Morikawa, Phys. Rev. B 63 (2001) 033405.

[3] T.Hayashi, Y. Morikawa, H. Nozoye, J. Chem. Phys. 114 (2001) 7615.

[4] M.Oue, K.Inagaki, K.Yamauchi, Y.Morikawa, Nanoscale reseach lett. 8(2013) 323.

Ab Initio Study of Excited Electronic States and Nonadiabatic Processes of Nanostructures under External Fields

Kazuyuki WATANABE, Chunping HU, Keisuke TSUBONOYA,
Satoshi HAGIWARA, Taishi HIGUCHI
Department of Physics, Tokyo University of Science
1-3 Kagurazaka, Shinjuku-ku, Tokyo 162-8601

In the project we investigated the following five topics this year. 1) Laser-assisted field emission from silicene nanoribbons by time-dependent density functional theory (TDDFT), 2) Optical properties of boron nitride and graphene nanoribbons by TDDFT, 3) Low-energy electron wavepacket scattering with nanoflakes by TDDFT, 4) Field emission microscopy images of carbon nanotubes by TDDFT, 5) Evaluation of performance of Tamm-Dancoff approximation on nonadiabatic couplings by TDDFT.

1) *Laser-assisted field emission from silicene nanoribbons by TDDFT*:

We explored the laser-assisted field emission (LAFE) from graphene nanoribbons (GNR) in a previous study by the real-time TDDFT simulation, which is one of the most reliable and useful computational methods for describing dynamical phenomena associated with electronic excitations. We have shown the underlying physics of photoemission from GNRs that critically depends on the electric dipole transitions and the electronic properties of emitting states. In this study we further investigated the LAFE from silicene nanoribbons (SiNR) by the TDDFT for comparison with GNRs. The emission currents from SiNR are found to be much larger than from GNR for the same laser parameters in spite of the larger work function of SiNR than that of GNR. We have obtained the detailed results of electron emission and backward currents in real space and time under femtosecond laser pulses of various parameters. Large-scale TDDFT calculations have been performed using System A.

2) *Optical properties of boron nitride and graphene nanoribbons by TDDFT*[1]:

The dielectric functions of the armchair boron nitride nanoribbons with the comparison of their carbon analogues were investigated by the real-time TDDFT in the linear response regime. The energy dependence of dielectric functions changes very dramatically from hexagonal boron nitride to boron nitride white graphene (BNWG), while slightly changes from BNWG to BN nanoribbon (BNR). It was found that a remarkable difference appears in the imaginary part of dielectric function especially in the low energy region between BNR and graphene nanoribbons, which is attributed to the apparent difference in the energy band structures between them. Large-scale TDDFT calculations have been performed using System B.

3) *Low-energy electron wavepacket scattering with nanoflakes by TDDFT*[2]:

Low-energy electron scattering with nanoflakes was investigated using TDDFT simulation in real time and real space. By representing the incident electron as a finite-sized wave packet, we obtained diffraction patterns that show not only the regular features of conventional low-energy electron diffraction (LEED) for periodic structures but also special features resulting from the local atomic inhomogeneity. We also found a signature of π plasmon excitation upon electron impact on a graphene flake. The present study shows the remarkable potential of TDDFT for simulating the electron scattering process, which is important for clarifying the local

and periodic atomic geometries as well as the electronic excitations in nanostructures. Large-scale TDDFT calculations have been performed using System B.

4) *Field emission microscopy images of carbon nanotubes by TDDFT* [3]:

Theoretical field-emission (FE) patterns from pristine and H_2-adsorbed carbon nanotubes (CNTs) was simulated using the real-time TDDFT. The field-emitted electrons are treated in the equal footing with the electrons in the nanotubes and the spatial distributions of FE current densities are calculated directly by the time-propagated Kohn-Sham wave functions. The simulated results of pristine CNTs clearly show either five-fold or six-fold symmetries, corresponding to the symmetries of the features of pentagons on the CNT caps. Further simulations on the H_2 molecule adsorbed CNTs verify that the bright spots in the FE pattern are of signatures of atom adsorption onto CNTs, and the adsorption site should be close to the bright spots. Large-scale TDDFT calculations have been performed using System A.

5) *Evaluation of performance of Tamm-Dancoff approximation on nonadiabatic couplings by TDDFT*[4]:

We performed a systematic evaluation of the performance of the Tamm-Dancoff approximation for the TDDFT calculation of nonadiabatic couplings (NACs) between ground and excited states. In the cases we considered, the TDA performed better than the full TDDFT, contrary to the conjecture that the TDA might cause the NAC results to deteriorate and violate the sum rule. This was conjectured because it is well known that the sum rule of the oscillator strength is lost with the TDA, and the original formulation of NAC is similar to that for oscillator strength. The calculation results in the vicinity of Jahn-Teller and Renner-Teller intersections, as well as in an example of accidental conical intersections, show that the TDA can improve the accuracy of the NAC, since the TDA can give better excitation energies as a result of partially compensating for the LDA error when the intersections are approached. Our work also shows that the good performance of the TDA can only be achieved on the basis of the rigorous TDDFT formulation of NAC. We believe that validation of the good performance of the TDA facilitates future nonadiabatic quantum simulations with TDDFT. Test of the parallel computing has been performed on System B, with the goal to parallelize the density-response calculations over atoms.

References

[1] S. Hagiwara, H. Goto, C. Hu, and K. Watanabe: JPS. Conf. Proc. **1**, 012072 (2014).

[2] K. Tsubonoya, C. Hu, and K. Watanabe, submitted.

[3] C. Hu, R. Mori, and K. Watanabe, JPS Conf. Proc. **1**, 012067 (2014).

[4] C. Hu, O. Sugino, and K. Watanabe, J. Chem. Phys. **140**, 054106 (2014).

First-principles calculation for light-matter interactions

Kazuhiro YABANA

Center for Computational Sciences,

University of Tsukuba, Tsukuba 305-8577

We have been developing a first-principles computational approach to describe electron dynamics in crystalline solid induced by intense and ultra-short laser pulses. We solve the time-dependent Kohn-Sham equation in real time.

This year we conducted a numerical simulation which mimics pump-probe experiments which are standard method to explore interactions between ultrashort laser pulse and matters [1]. It has been considered that the strong laser pulse immediately induces excitations of valence electrons, which bring an ultrafast change of dielectric properties of solids. The change of dielectric function is often modeled by a Drude model added to the dielectric function in the ground state. We numerically achieved pump-probe experiments, solving time-dependent Kohn-Sham equation which includes both pump and probe electric fields as external perturbation. Dielectric properties of excited materials can be examined by the current induced by the probe pulse. From the simulation, we have found that the dielectric properties change immediately after the laser pulse irradiation, and that the change of may be well described by the Drude model for the real part. However, we have found the imaginary part of the dielectric function shows rather complex behavior, sometimes indicating amplification of the probe pulse. We also found there is a substantial difference of the response depending on the relative directions between the pump and probe pulses, although the material is isotropic in the ground state.

We also explore the ultrafast current induced by the strong laser pulse [2]. Recently, it has been found that the laser pulse irradiated on transparent oxide, SiO_2, at the laser intensity close to the threshold of radiation damage induces an electric current in the extremely short time scale. We have explored the mechanism of the generation of the current by the time-dependent density functional theory. We have found that qualitative features of observed current is very nicely reproduced by our calculation.

References

[1] S.A. Sato, K. Yabana, Y. Shinohara, T. Otobe, G.F. Bertsch, Phys. Rev. B89, 064304 (2014).

[2] G. Wachter, C. Lemell, J. Burgdorfer, S.A. Sato, X.M. Tong, K. Yabana, submitted.

Spontaneous Structural Distortion and Quasi-One-Dimensional Quantum Confinement in $LaTiO_{3.4}$

ZHONGCHANG WANG, MITSUHIRO SAITO, YUICHI IKUHARA

WPI, Advanced Institute for Materials Research, Tohoku University, Sendai, Japan

Institute of Engineering Innovation, The University of Tokyo, Tokyo, Japan

Two-dimensional electron gas at heterointerfaces between insulators is currently the subject of intensive research. The confined electrons, which are driven to minimize their free energy, often behave differently than in bulks. All of the unprecedented properties associated with the electrons rely critically on specific crystal structures and local chemistry at heterointerface, which are often not expected in respective bulks. Here we report that a single-phase $LaTiO_{3.4}$ bulk shows a quasi-1D quantum confinement and a fluctuation of valence over individual bulk layers by self-assembled structural distortions. We offer definitive evidence of a delicate structural distortion in the $LaTiO_{3.4}$ bulk unit cells and demonstrate that the energy band gap at Fermi level is almost closed in the spin-majority channel [1].

Figure 1 shows high-angle annular-dark-field (HAADF) image of the monoclinic $LaTiO_{3.41}$ from *a* direction with the corresponding spectrum imaging revealing individual EELS spectrum from the Ti sites 1 to 5. In the HAADF mode, the contrast is proportional to $Z^{1.7}$ (Z: atomic number) at our predefined collection geometry [2]. In this case, the La column appears to be brighter than the Ti column. By acquiring EELS spectrum across the HAADF image, we obtained the elemental mapping of La and Ti at atomic resolution. By examining individual EELS spectrum from the Ti sites 1 to 5, we find that the Ti atoms at the site 3, which has a similar structural environment to that of the $LaTiO_3$, display a 3^+ valence. Ti sites 1, 2, 4 and 5 display a nearly 4^+ valence, since the splitting of L_3 and L_2 peaks are readily visible. However, the valence of Ti at sites 2 and 4 differ that of the Ti in 1 and 5 by revealing a notably lower edge onset energy, indicating the local valence is yet not 4^+, but slightly lower than that, which could be explained by the observed distortion from the HAADF image in comparison to the orthorhombic $LaTiO_{3.1}$. Further DFT calculations reveal that the quasi-1D quantum confinement system shows an extremely small band gap, a ferromagnetic ordering, a strong

anisotropy in the nonequilibrium quasi-1DEG. quantum transport, and a spin-polarized

References

[1] Z.C. Wang, L. Gu, M. Saito, S. Tsukimoto, M. Tsukada, F. Lichtenberg, Y. Ikuhara, and J. G. Bednorz, Adv. Mater. **25** (2013) 2186.

[2] Z. Wang, M. Saito, K. P. McKenna, L. Gu, S. Tsukimoto, A. L. Shluger, and Y. Ikuhara, Nature **479** (2011) 380.

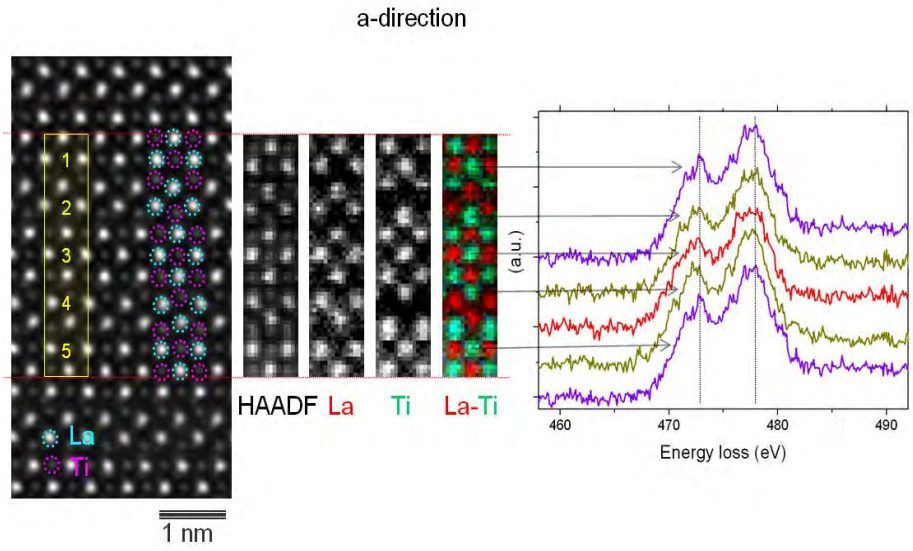

Fig. 1. HAADF and spectrum imaging of $LaTiO_{3.4}$ viewed from *a* direction with individual EELS spectrum from Ti sites 1 to 5.

Theoretical investigation on the magnetic polarization induced at organic/metal interfaces

Susumu YANAGISAWA[1] and Ikutaro HAMADA[2]

[1]*Department of Physics and Earth Sciences, Faculty of Science, University of the Ryukyus, Senbaru 1, Nishihara, Okinawa, 603-0213, Japan*

[2]*International Center for Materials Nanoarchitectonics (WPI-MANA) and Global Research Center for Environment and Energy based on Nanomaterials Science (GREEN), National Institute for Materials Science, 1-1 Namiki, Tsukuba 305-0044, Japan*

There is growing interest in the field of organic spintronics. The spin-valve effect, i.e. charge injection with a preferential spin orientation from a ferromagnetic metal electrode into organic semiconductors has been observed [1]. However, there is a lack of understanding on the mechanism of the spin-valve effect, and thus the effect is hardly reproducible.

Recently, based on experimental results, it was suggested that the formation of spin-polarized hybridization between a ferromagnetic metal and organic molecules play a key role in the spin-valve effect [2].

The interface between Alq_3 molecule and a cobalt surface (Alq_3/Co) has attracted attention for the spin-valve effect [2]. Theoretically, first-principles density functional theory (DFT) calculations indicated formation of hybridized state at the interface [3]. The results indicated decrease in the charge injection barrier, which was induced by the molecular permanent dipole oriented upwardly to the vaccum side, as proposed previously [4]. However, there is no consensus on the electronic mechanism of the preferential spin orientation upon the charge injection.

To clarify the mechanism of the spin-dependent electronic characteristics, we investigate the electronic states of Alq_3/Co interfaces by using spin-polarized DFT calculations. The adsorption configurations of Alq_3 on metal surfaces, i.e. up and down configurations, proposed by the authors in the previous works [4], are taken into account for initial adsorption geometries.

We use the STATE program code [5], with first-principles pseudopotentials for core states and a plane wave basis set for valence states. To optimize the adsorption geometries, we take into account the van der Waals (vdW) interaction in a semi-empirical manner [6].

To eliminate the artificial interaction between the slabs along the surface normal, we use the Effective Screening Medium (ESM) method [7]. By the ESM, the convergence of

DFT self-consistent cycles, which tends to be influenced by the fluctuation of electrostatic potential at the vacuum region, becomes stable. This treatment is advantageous over the conventional slab model or the dipole correction used in the previous similar studies.

First, we investigate the change in adsorption geometry and electronic state in Alq_3 adsorbed on Mg (0001) substrate. Previously, we determined the stable chemisorbed configurations within the conventional GGA-PBE treatment [4]. Here, we find that inclusion of the vdW interaction slightly changes the chemisorption geometry. For the work function shift and the subsequent energy level alignment between the molecular and the substrate states, we find that the present ESM approach reproduces the previous result of the work function shift more efficiently.

Second, using the same methodology, we investigate the adsorption states of Alq_3 on Co. We use the periodic slab model of a hcp Co (0001) surface in a 6×6 superstructure with six atomic-layers. We allow the upper four layers to relax during the optimization, and the lower layers are fixed to the bulk atomic positions. We sample the surface Brillouin zone by a 2×2 or 4×4 **k**-point mesh.

Determination of the adsorption state of Alq_3 on Co(0001) is in progress. After an optimized geometry is obtained, we go on to investigate the spin-dependent energy level alignment at the interface.

References

[1] V. Dediu et al., Solid State Commun. **122**, 181 (2002); Z. H. Xiong, D. Wu, Z. Valy Vardeny, and J. Shi, Nature **427**, 821 (2004).

[2] C. Barraud et al., Nat. Phys. **6**, 615 (2010); S. Steil et al., *ibid*. **9**, 242 (2013).

[3] Y.-P. Wang, X.-F. Han, Y.-N. Wu, and H.-P. Cheng, Phys. Rev. B **85**, 144430 (2012); A. Droghetti et al., *ibid*. **89**, 094412 (2014).

[4] S. Yanagisawa, K. Lee, and Y. Morikawa, J. Chem. Phys. **128**, 244704 (2008); S. Yanagisawa, I. Hamada, K. Lee, D. C. Langreth, and Y. Morikawa, Phys. Rev. B **83**, 235412 (2011).

[5] Y. Morikawa, H. Ishii, and K. Seki, Phys. Rev. B **69**, 041403 (R) (2004).

[6] S. Grimme, J. Comput. Chem. **27**, 1787 (1996).

[7] M. Otani and O. Sugino, Phys. Rev. B **73**, 115407 (2006**).**

Intermolecular interaction as origin of red shifts in absorption spectra of Zinc-Phthalocyanine from first-principles

Susumu YANAGISAWA[1,2], Taiga YASUDA[2], Kouji INAGAKI[2], Yoshitada MORIKAWA[2], Kazuhiro MANSEKI[3] and Shozo YANAGIDA[4]

[1]*Department of Physics and Earth Sciences, Faculty of Science, University of the Ryukyus, 1 Senbaru, Nishihara, Okinawa, 903-0213, Japan*

[2]*Department of Precision Science and Technology, Osaka University, 2-1 Yamada-oka, Suita, Osaka, 565-0871 Japan*

[3]*Graduate School of Engineering, Environmental and Renewable Energy System (ERES) Division, Gifu University, 1-1 Yanagido, Gifu, 501-1193 Japan*

[4] *ISIR, Osaka University, 2-1 Mihoga-oka, Ibaraki, Osaka, 567-0047 Japan*

Zinc-phthalocyanines (ZnPc) have attracted much attention because of their photoelectric properties relevant to energy conversion in dye-sensitized solar cells and organic thin-film solar cells. For optimization of the excitation window, modification of the excited states of a chromophore molecule induced by molecularly stacked aggregation is of primary interest. Two stack configurations, *i.e.*, those with face-to-face cofacial configurations, referred to as H-type aggregates, and slipped-cofacially stacked configurations, known as J-type aggregates, are highlighted.

We investigate electronic origins of a redshift in absorption spectra of a dimerized ZnPc within the density functional theory [1]. We use the Gaussian 09 program code [2] installed on our own pc-cluster to calculate excitation spectra of the ZnPc monomer within the time-dependent density functional theory (TDDFT). We also use the STATE program code [3] on the ISSP systems A and B to optimize the atomic geometry of the dimers of substituted ZnPc's taking into account the van der Waals (vdW) interaction with DFT-D2 [4] method.

In terms of the molecular orbital (MO) picture, the dimerization splits energy levels of frontier MOs such as the highest occupied molecular orbital (HOMO) and the lowest unoccupied molecular orbital (LUMO) of the constituent ZnPc molecules. Consequently, the absorption wavelength seems to become longer than the monomer as the overlap between the monomers becomes larger. However, for a ZnPc dimer configuration with its cofacially stacked monomer arrangement, the calculated absorption spectra within TDDFT indicates no redshift but blueshift in the Q-band absorption spectrum, *i.e.*, a typical H-aggregate.

The origin of the apparently contradictory

result is elucidated by the conventional description of the interaction between monomer transition dipoles in molecular dimers [4]. The redshift is caused by an interaction between the two head-to-tail transition dipoles of the monomers, while the side-by-side arranged transition dipoles result in a blueshift.

By tuning the dipole-dipole interaction based on the electronic natures of the HOMO and the LUMO, we describe a slipped-stacked dimer of unsubstituted ZnPc in which the Q-band absorption wavelength increases by more than 120 nm relative to the monomer Q-band.

However, there has been no experimental report of unsubstituted ZnPc dimer with large redshift. Actually, the binding energy of the slipped-stacked dimer calculated with DFT-D2 indicates that the dimer is meta-stable.

To simulate stable dimers of ZnPc's, we investigate dimer configurations of 1,4,8,11,15,18,22,25-octamethoxy Zinc phthalocyanine.

As a result, we find a stable dimer with a slipped-stack configuration. The binding energy is -2.1 eV. The resulting redshift of the

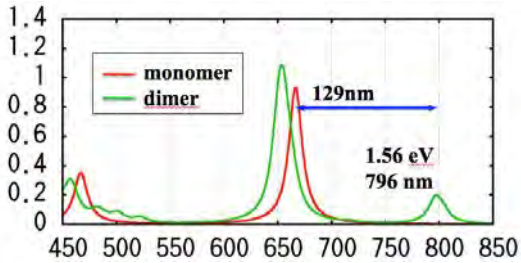

Fig. 1 Absorption spectra of the stable octamethoxy ZnPc with large redshift.

Q-band is 129 nm (Fig. 1). This finding may give us a hint to designing an aggregate of dye molecules with favorable long wavelength absorption.

References

[1] S. Yanagisawa, T. Yasuda, K. Inagaki, Y. Morikawa, K. Manseki, and S. Yanagida, J. Phys. Chem. A **117**, 11246 (2013).

[2] M. Frisch et al., Gaussian 09, revision C.01; Gaussian Inc.: Wallingford CT, 2009.

[3] Y. Morikawa, H. Ishii, and K. Seki, Phys. Rev. B **69**, 041403 (R) (2004).

[4] S. Grimme, J. Comput. Chem. **27**, 1787 (1996).

[5] M. Kasha, Radiat. Res. **20**, 55 (1963).

Analyses on atomic structure, magnetism, and electronic structure in spintronics materials

Tatsuki ODA[1,2], Yuusaku TAGUCHI[2], Daiki YOSHIKAWA[2], Makoto NAKAMURA[2], Nurul IKUSAN[2], Masao OBATA[2]

Institute of Science and Engineering, Kanazawa University, Kanazawa, Ishikawa 920-1192

Graduate School of Natural Science and Technology, Kanazawa University, Kanazawa, Ishikawa, 920-1192

We performed ab-initio electronic structure calculation in Co doped Fe/MgO interface on the basis of density functional theory. Two different slab models are considered, depending on the place of Co atom; at the interface and in the Fe layer. With using atomic forces, we obtained the optimized structure at the interface and discussed the layer distance of interface and the local structure around Co. Spin magnetic moments on Fe and Co atoms are also discussed. In the band dispersion at the Fermi level, distribution of the angular orbital component shows the possibility of perpendicular magnetic anisotropy.

This work takes two minimum slab models; MgO(3ML)/Fe3Co(1ML)/Fe(2ML) and MgO(3ML)/Fe(1ML)/Fe3Co(1ML)/Fe(1ML) (both are 36 atoms in 22 in-plane supercell configuration). In the former, the Co atom is placed at the interface (model A), and in the latter, at the inside of Fe layers (model B). Although the interface Fe/MgO has been fabricated in experiment, the in-plane lattice constant has not been determined even in the clean interface. Therefore, for these slab models, two different in-plane lattice constants 5.74Å (= a_{Fe}) and 5.94Å (= a_{MgO}), which correspond to the bulk lattice constants of Fe and MgO respectively. There is the difference in lattice constant by 3.4%. totally we have four slab models.

For these models, we have carried out first-principles calculation which employs the density functional theory and ultra-soft pseudopotential. Energy cutoffs for electron density and wavefunction are 300Ry and 30Ry respectively. Here we used the 4x4x1 mesh of k space sampling. The generalized gradient approximation was adopted for exchange correlation energy. We optimized electronic wavefunctions and atomic positions by minimizing the total energy functional. The structural optimization has been performed by using atomic forces except for the in-plane lattice constant. The ESM method with zero external electric field condition was used to avoid artificial built-in electric field in the repeated slab model; ESM/vac./slab/vac. For

both vacuum layers, the width of 5.29Å is taken.

We obtained the optimized structure after all the atomic forces reach equilibrium. The interface distance is compared to related works; 2.18Å and 2.16Å for model A with a_{MgO} and a_{Fe} lattice constants, respectively. In these results we observe that the smaller lattice constant produces slightly smaller interface distance. As another interesting point, we found that the Co atom moved from the Fe layer to the magnetic substrate by 0.03A and 0.04A for the model A with a_{MgO} and a_{Fe}, respectively. Even when we put the Co in the middle of Fe layer (model B), still we observed slight contracting distortion of Co to the bottom Fe layer. From these behaviors, we may deduce that Co prefers to be surrounded by Fe. We also observed that the model B has a slightly lower total energy than the model A by 3meV, implying that Co impurities in the middle Fe layer provides more stable system than those at the interface. The total magnetization and atomic magnetic moments were estimated. We observed that the Fe magnetic moment at interface, whose average is 2.8μ_B, is much enhanced from the value of second magnetic layer, the bulk value (2.2μ_B), and the experimental value in the nano clusters. In contrast of this enhancement, the Co magnetic moments are similar to 1.8μ_B. Based on the discussion in the previous work, the enhancement on Fe magnetic moment is not only attributed to the charge transfer to the oxygen at interface, but also understood as surface properties of Fe layer. Indeed, the Co magnetic moment has a similar value obtained by the monolayer model. At surface, electron wavefunction can be localized due to the lack of electron transfer to the open space while the electron transfer to the neighbors makes the wavefunction delocalized in the bulk. This localized electron contributes to larger magnetic moment. Electrons at interface are also easier to be localized compared to the middle layer and therefore, such interface accommodates the magnetic atom to a larger magnetic moment. Discussion mentioned above on delocalized electron also explains the smaller magnetic moment at the smaller lattice constant.

We discussed the possible origin of perpendicular magnetic anisotropy by analyzing the angular component in vicinity of the Fermi level. The angular orbital component in the band structure implies the possible contribution to positive MAE (favor of perpendicular magnetic anisotropy) due to 3d(xy) and 3d(x^2-y^2) orbital coupling below and above the Fermi level, in addition to the origin that the hybridization of 3d($3z^2$-r^2) with oxygen 2p orbital can enhance the favor of perpendicular magnetic anisotropy.

Analyses on magnetic anisotropy and its electric field effect for magnetic thin films

Tatsuki ODA[1,2], Yuusaku TAGUCHI[2], Daiki YOSHIKAWA[2], Makoto NAKAMURA[2], Masao OBATA[2]

Institute of Science and Engineering, Kanazawa University, Kanazawa, Ishikawa 920-1192

Graduate School of Natural Science and Technology, Kanazawa University, Kanazawa, Ishikawa, 920-1192

We have investigated magnetic anisotropy and its electric field (EF) effect in the thin Fe ferromagnetic films by using a first-principles approach of fully relativistic psuedo-potential spinor-planewave method. We have obtained a perpendicular magnetic anisotropy at zero EF for the isolated double Fe atomic layer. Around zero EF, the magnetic anisotropy energy (MAE) indicates a slight increase with respect to the EF. At the large variation to a few V/Å, the MAE decreases with a steep ratio. These behaviors in the EF dependence on MAE possibly explain the disagreement between experimental and theoretical results on the EF dependence for the interface magnetic anisotropy of MgO/Fe system.

For more than a decade, the spintronics has grown up intensively to realistic applications in the technology of magnetic random access memory (MRAM) development. Such development has been remarkable in memory density, reading-writing speed, and non-volatile property in cooperation with the technologies of spin-injection and physics of spin transfer torque. Nowadays, the basic physics about magnetism has been developing in the response to electric field (EF). For thin films both of sensitivity or large response may be required in device applications, where the interface with a few metallic layers is critical to determine the response to the EF. The most promising system is the Fe layer attached with dielectric magerial, for example, MgO/Fe system. The most important microscopic interest is concentrated on the study of interface between Fe and MgO atomic layers.

Although the magnetic anisotropy and its EF effect for MgO/Fe have been already investigated, the part of ingredient layer, namely Fe layer of two atomic layers, was analyzed. The most important point in the computational results is that the largest MAE change is comparable to the corresponding experimental result within a several times. These results on the MAEs and its EF dependences will be contributed at the analysis of magnetic properties in the MgO/Fe interface.

Electronic Properties of Impurity Defects in Organic Molecular Semiconductors

Takashi NAKAYAMA
Department of Physics, Chiba University
1-33 Yayoi, Inage, Chiba 263-8522

Organic molecular semiconductors are key materials for future optical and electronic devices because of their unique characteristics such as softness and light mass. During the device fabrication, a variety of impurity atoms are often incorporated into semiconductor layers. Around metal-electrode interfaces, for example, metal atoms such as Al and Au easily diffuse into semiconductors. These impurities are believed to deteriorate semiconducting properties. However, there have been no systematic studies on how these impurities are located in semiconductors and what electronic states are produced by these impurities. The purpose of this project is to clarify these questions, by using the first-principles calculation based on the density functional theory. In this report, we show some of the results.

We first consider how the metal atoms are incorporated into insulating SAM (self assembled monolayer) film from its surface. Figures 1(a) and 1(b) show the top views of COOK and COOK terminated SAM surfaces, respectively. Adsorbed metal atom diffuses to penetrate the SAM film around crossed points. Figures 1(c) and 1(d) show calculated adiabatic potentials for Au and Al atom diffusions as a function of metal-atom position. It is seen that Au atom can enter the SAM without any potential barrier in case of COOH termination, while the potential has minimum and thus Au atom is trapped around the surface in case of COOK termination. This result well explains the experiments [1]. By analyzing the electronic structure, we found that the potential minimum around the SAM surface is produced by the ionic interaction between positive K and negative Au atoms. In case of Al-atom diffusion, on the other hand, because Al atom has small electronegativity

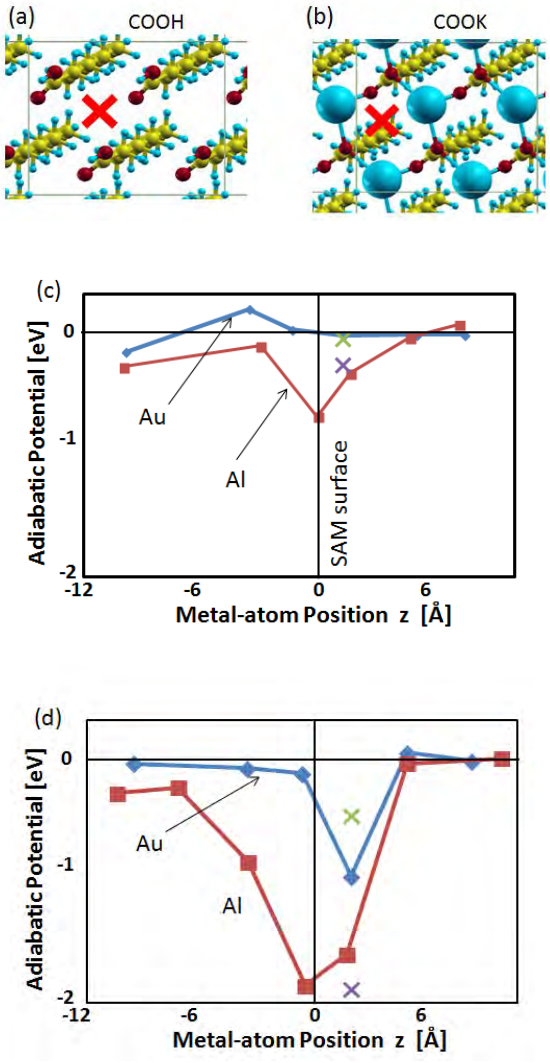

Fig.1. (a) and (b): Top views of COOH and COOK terminated SAM. Adsorbed metal atom diffuses into SAM around crossed point. (c) and (d): Calculated adiabatic potentials for Au and Al atoms around SAM surface. Metal-atom positions, z =0 and z>0, corresponds to SAM surface and vacuum, respectively.

compared to elements of organic molecules, much stronger ionic interaction appears between positive Al and negative O atoms. This is the reason why the potential for Al atom has large minima around

the SAM surface, which again explains the observations [2].

Next, we consider the interaction between metal atoms when metal atoms are located in organic systems. Figure 2(a) shows the calculated interaction energy between two Au (Al) atoms as a function of inter-atomic distance when metal atoms are adsorbed on a graphene sheet. In case of Au, the interaction is attractive and short range. This is because Au atoms are bound to the graphene substrate with weak covalent bonds and do not disturb the electronic states of graphene, thus the Au-Au interaction appearing only when two Au atoms approach nearby to produce a metallic bond [3]. In case of Al, on the other hand, the interaction is repulsive and long range. This is because the electron transfer occurs from Al to graphene due to small negativity of Al, and thus the adsorbed Al atoms are positively ionized. As a result, there appears a repulsive and long-range Coulomb interaction between Al atoms.

Then, we consider the interaction in case of one-dimensional molecule. Figure 2(b) shows the calculated interaction energy between two Au (Al) atoms as a function of inter-atomic distance when metal atoms are adsorbed on a polyacetylene chain. Similar to the case of graphene, roughly speaking, Au and Al atoms have attractive and repulsive interactions, respectively. The most interesting feature is the oscillation of interaction energy as a function of inter-atom distance. This oscillation occurs due to the same scenario as the Peierls transition; when the number of C atoms of polyacetylene skeleton between adsorbed metal atoms is even, the C-C bond shows dimerization and the system becomes stable, promoting negative interaction energy. When the number of such C atoms is odd, there appears no dimerization, thus producing little interaction energy. In this way, the interaction between metal atoms strongly depends on the dimensionality of host molecules.

In order to realize these calculations using the TAPP and xTAPP codes, because the target system

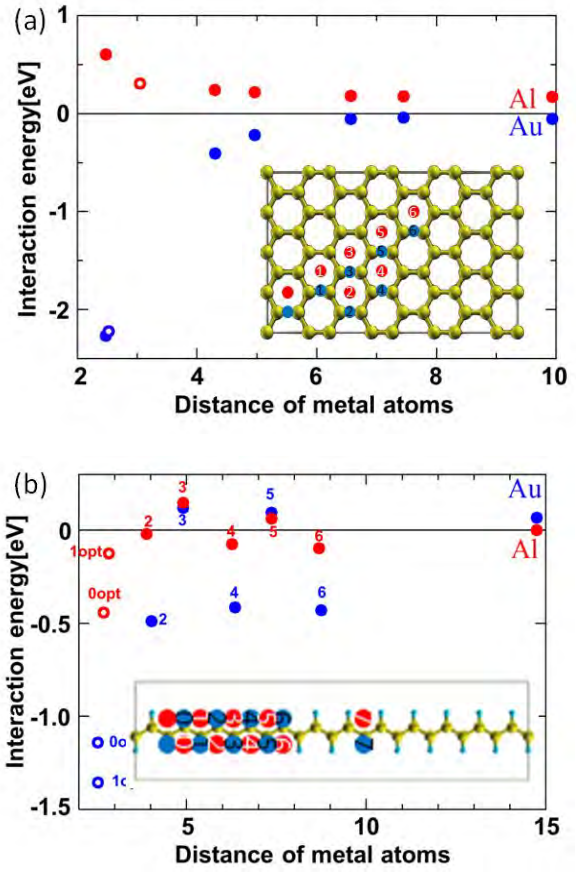

Fig.2. Calculated interaction energy between two metal atoms (a) on a graphene sheet and (b) on a polyacetylene chain as a function of distance, for Au and Al atom cases.

is very large (more than 150 atoms) and has a variety of geometries, the advanced computing facility that has higher-speed CPU than 100GFlops, larger-size memory around 100GB, larger-size strange than 1.0TB, and particularly a multi-task operation is indispensable. These conditions are never prepared in individual research laboratory. Only the present super-computing system of the ISSP can realize these calculations.

References

[1] Z. Zhu et al., J. Am. Chem. Soc. **128** (2006) 13710.

[2] H. Klauk et al., Nature **445** (2007) 745.

[3] T. Park, Y. Tomita, T. Nakayama, Surf. Sci. **621** (2014) 7.

First-principles study of quantum transport in nanostructures

NOBUHIKO KOBAYASHI
Institute of Applied Physics, University of Tsukuba
1-1-1 tennodai Tsukuba Ibaraki 305-8573

Understanding and controlling quantum transport properties in nanostructures from atomistic levels is important for developments of nanoscale devices. A number of experimental studies have been performed on transport properties in nanostructures such as atomic wires, molecules and nano carbon systems to discuss the conductance and the current-voltage characteristics. Quantum nature is essential in nanoscale systems, and atomistic analysis based on detailed electronic states calculations are indispensable to discuss the transport property of such a system theoretically. In order to analyze transport properties, we have developed several methods such as the nonequilibrium Green's function (NEGF) method, and time dependent wave-packet diffusion (TD-WPD) method. Using these methods, we have investigated charge and heat transport properties of atomic wires, organic molecules, nano carbon systems and so on.

We have developed an efficient numerical calculation code for the ab-initio electron transport based on the DFT and NEGF formalism using Fortran and Message Passing Interface(MPI). The parallel computation technique with MPI is employed for efficient computations of density matrix via the the Green's functions, which depend on the energy and two-dimensional wave vectors, as shown in Fig.1. Since each matrix element of the Green's functions depends only on the single energy and two-dimensional wave vector point, it is possible to divide the calculations in the energy and wave vectors, which are carried out separately in each process. As a demonstration of the efficiency of the present code, the numerical calculations of electron transport properties of Al(100)-Si(100)-Al(100) heterostructures are shown in Fig.2. The computational efficiency is seen to improve as the total number of processes becomes larger with the latency by the communication between whole process negligible. For an application, electron transport properties such as transmission spectra and total density of states are investigated for the systems with different thicknesses of Si layers.

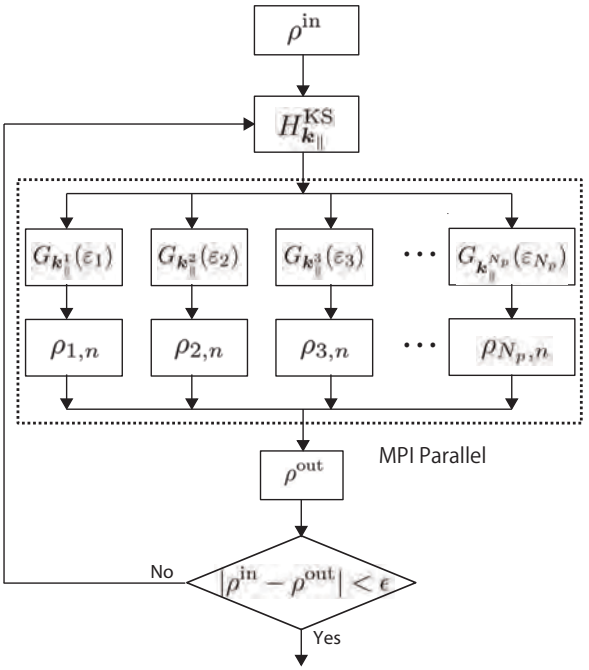

Figure 1: Flowchart of DFT-NEGF calculations with parallelization by MPI.

We have also developed the O(N) TD-WPD method for the quantum transport calculation

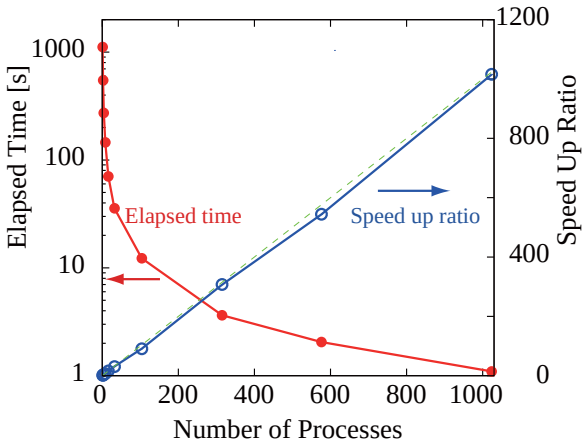

Figure 2: Speed-up ratio of total elapsed time by the parallelization of MPI in the ab-initio electron transport calculations in System B.

of huge systems of up to 100 million atoms.We calculated the conductance and the mobility of the system with micron-order lengths at room temperature based on the Kubo-Greenwood formula. Using this method we can study the transport properties from diffusive to ballistic regimes including the effect of realistic electron-phonon scattering, and determine the mean free path and relaxation time from an atomistic viewpoint. We performed DFT calculations of electronic structures and interactions between molecules of pentacene and rubrene single-crystal organic semiconductors including the effect of the van der Waals interaction, and applied the TD-WPD method to the analysis of transport properties of the organic semiconductors.

The realistic intermolecular-vibration effects on the anisotropic transport properties of pentacene and rubrene single-crystal organic semiconductors were analyzed by the systematic evaluations of the angle-resolved effective mass, mobility, carrier velocity, relaxation time, and mean free path, as shown in Fig. 3 and 4. We find that intermolecular vibrations induce the strong anisotropic relaxation time but moderate the anisotropy of carrier mobility, which increases with temperature, much more than that of inverse effective mass. We also find that the main axis of mobility tensor rotates slightly with temperature in pentacene crystals. This clarifies the mechanism on the deviations of anisotropic ratio of mobility from that of effective mass observed in experiments.

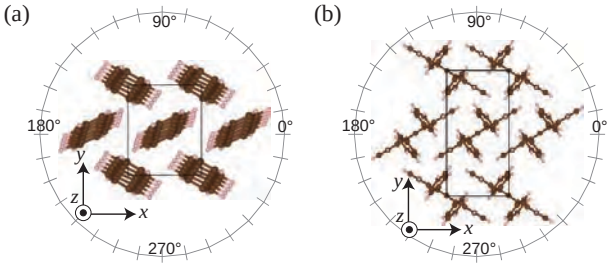

Figure 3: Crystal structures of pentacene (a) and rubrene (b) single-crystal semiconductors.

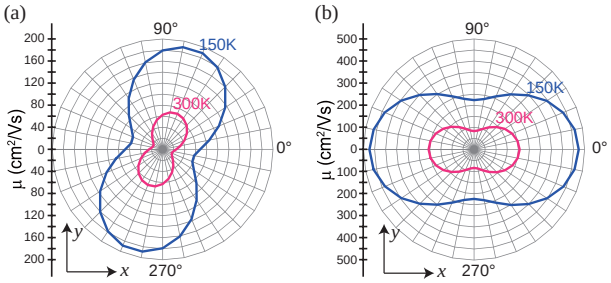

Figure 4: Calculated anisotropic mobilities of pentacene (a) and rubrene (b) single-crystal semiconductors.

References

[1] H. Ishii, N. Kobayashi, K. Hirose, Phys. Rev. B 88 205208 (2013).

[2] K.Yamamoto, H.Ishii, N.Kobayashi, K.Hirose, Nano. Res. Lett. 8 256 (2013).

[3] K.Yamamoto, H.Ishii, N.Kobayashi, K.Hirose, Open J. Comp. Mat. 3 48 (2013).

[4] K.Yamamoto, H.Ishii, N.Kobayashi, K.Hirose, J. Nanomaterials 2013 525070 (2013).

[5] K.Hirose, K.Kobayashi, M.Shimono, H.Ishii, N.Kobayashi, e-Journal Surf. Sci. Nanotechnol. 12 (2014).

DFT statistical mechanics analysis of redox reaction mechanism at interfaces in catalysts and batteries

Y. Tateyama, H. Kino, K. Sodeyama, R. Jono, Z. Futera, L. Szabova, Y. Ootani, J. Haruyama, and K. Aikawa

International Center for Materials Nanoarchitectonics (WPI MANA), National Institute for Materials Science (NIMS) 1-1 Namiki, Tsukuba, Ibaraki 305-0044

We have explored the chemical/redox reactions in solutions and at electrode-electrolyte interfaces via density functional theory based molecular dynamics (DFT-MD) analysis with explicit solvent molecules, for more understanding of cell, battery and catalysis. The advanced techniques for free energy calculations and redox reactions have been also used. Some results are described below.

(1) New reductive decomposition mechanism of carbonate-based electrolyte in Lithium Ion Battery [1]

Solid electrolyte interphase (SEI) on the electrode - electrolyte interfaces formed through the reductive decomposition of organic solvent molecules plays a crucial role in the stability and capability of lithium ion battery (LIB). Additives to the electrolyte often exhibit a large impact on the SEI quality. A typical example is vinylene carbonate (VC) additive to the ethylene carbonate (EC) solvent. Here we investigated the effects of VC additive to the EC solvent on the reductive decomposition and the initial stage of SEI formation. [1] Our focus was put on kinetics as well as thermodynamics of the possible reduction processes. We used DFT-MD with explicit solvent molecules for the equilibrium properties at finite temperature, and carried out the free energy profile calculations along the reaction pathways using the blue-moon ensemble technique.

We found that 1e reduction induces breaking of C_E-O_2 bond in EC to produce o_E-EC^- and CO, while d_{CO}-VC^- and CO are generated from VC through C_C-O_2 bond breaking in contrast to a previous study (Fig. (a)). When another electron is added to the system (2e reduction), EC decomposition produces CO_3^{2-} + C_2H_4 or CO + alkylcarbonate (Fig. (b)), whereas CO production occurs again at the 2e reduction of VC. We then examined the attack of anion radical made by 1e reduction to the nearby intact molecule, and found that the EC radical attack on the intact VC enhances the CO_2 production. These mechanisms on the atomic scale are in good agreement with the experimental observations of the gaseous products. Contrary to the conventional scenario that VC additive is

sacrificially reduced and makes a VC oligomer that seeds SEI formation, the present results provide a completely different mechanism: the VC additive preferentially reacts with the EC anion radical to suppress the 2e reduction of EC, the main initial stage of SEI formation in the VC-free EC electrolyte (Fig. (c)). Because this VC mechanism is realized via 1e reduction, the irreversible capacity at the SEI formation will decrease as well, which is also consistent with the experiments. These results not only reveal the primary role of the VC additive in the EC solvent, but also provide a new fundamental perspective for the reductive decomposition of carbonate-based electrolyte near the negative electrode.

(2) Microscopic mechanism prediction with DFT simulations on unusual phenomena observed in experiments [2-4]

With large-scale DFT-MD simulations and geometry optimizations on supercomputers, we have predicted the mechanisms of unusual swelling of nanosheets with specific electrolyte, unusual high mobility of hole in special organic crystals, and a novel type of molecular switch.

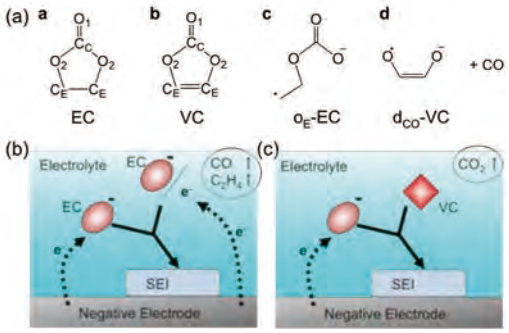

Figure (a) Structures of EC and VC with the atomic labels. Major reductive decomposition products of EC and VC (o_E-EC and d_{CO}-VC) are also displayed. (b) Reductive decomposition mechanism for the electrolyte with EC only, confirmed in this work. (c) Novel reductive decomposition mechanism of the EC electrolyte with VC additives, found in this work.

References

[1] K. Ushirogata, K. Sodeyama, Y. Okuno, Y. Tateyama. *J. Am. Chem. Soc.* **135**, 11967-11974 (2013).

[2] F. Geng, R. Ma, A. Nakamura, K. Akatsuka, Y. Ebina, Y. Yamauchi, N. Miyamoto, Y. Tateyama, and T. Sasaki, *Nature Comm.* **4**, 1632 (2013).

[3] Y. S. Yang, T. Yasuda, H. Kakizoe, H. Mieno, H. Kino, Y. Tateyama, C. Adachi, *Chem. Commun.*, 49, 6483 - 6485, (2013).

[4] G. Pawin, A. Z. Stieg, C. Skibo, M. Grisolia, R. R. Schilittler, V. Langlais, Y. Tateyama, C. Joachim, and J. K. Gimzewski, *Langmuir*, 29, 7309-7317 (2013).

Doping Effect on Magnetism and Transport Property of Heterojunction between Carbon and Boron Nitride Nanotubes

Huy Duy NGUYEN and Tomoya ONO
Department of Precision Science and Technology, Osaka University
Yamada-oka 2-1, Suita, Osaka 565-0871

Honeycomb structures of carbon have emerged as promising candidates for spin-based switches and field-effect devices owing to their weak spin-orbit coupling and high carrier mobility. Theoretical investigations have demonstrated that graphene nanostructures exhibit local spin polarization along their zigzag edges. Recent first-principles calculations based on density functional theory revealed that graphene nanoflakes with a localized magnetic moment along their zigzag edges of carbon exhibit spin-dependent transport behavior (1).

Edge states are also observed in zigzag carbon nanotubes (CNTs). Choi et al. found that the alternate placement of zigzag CNTs and zigzag boron nitride nanotubes (BNNTs), which are possibly fabricated by the laser vaporization method (2), resulted in magnetic ordering by doping electrons or holes, and the magnetic ground states are associated with the zigzag edges of CNTs. However, electron or hole doping is not practical and the rotational symmetry mismatch between the conducting and edge states of a zigzag CNT prevents electron transport (3).

We study the electronic structures and electron-transport properties of the heterojunction formed by alternate placement of CNTs and BNNTs under atom substitutional doping by first-principles calculations using techniques described in Ref. 4. Figure 1 shows the our computational model of (9,0) nanotube and shall be referred as z-C/BNNT. Tetragonal supercells are adopted and periodic boundary conditions are imposed in all directions. The wall-to-wall distance between adjacent nanotubes is chosen so as to exceed 6 Å, which permits tube-tube interactions to be neglected. A grid spacing of 0.17 Å is used.

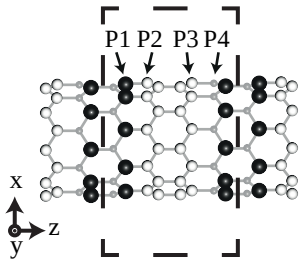

Figure 1: Computational model of a (9,0) z-C/BNNT. White, grey, and black balls are C, N, and B atoms, respectively. P1, P2, P3, and P4 indicate positions at which one B atom is replaced with one C atom, one C atom is replaced with one N atom, one C atom is replaced with one B atom, and one N atom is replaced with one C atom, respectively.

The electronic band structure of a z-C/BNNT is shown in Fig. 2(a). The edge states, which manifest themselves as doubly degenerate flat bands, are observed near the Fermi level. The charge density distributions of these edge states are localized at the zigzag boundaries of the CNT.

Since the edge states in the z-C/BNNT induce a large density of states closest to the

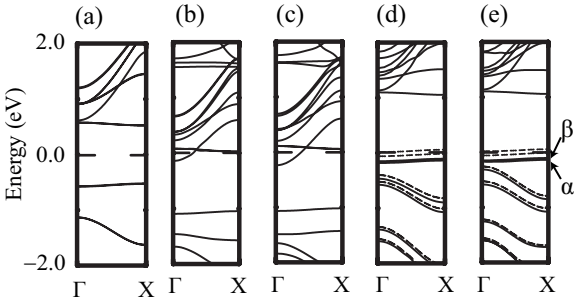

Figure 2: (a) Band structure of z-C/BNNT. (b)-(f) show the band structures of doped nanotubes associated with P1-P4 in Fig. 1. Zero energy was chosen as the Fermi level. Solid (dashed) curves indicate the spin-up (-down) states.

Fermi level, inserting or removing electrons causes spin polarization. We propose the atom substitutional doping, in which one C atom at the CNT/BNNT interface is replaced with one B (N) atom as shown in Fig. 1. As shown in Fig. 2, p-type substitutional doping gives rise to spin polarization with a magnetic moment of 1 μ_B, owing to the variation of the occupation number of the edge states. On the contrary, the $\sigma - \pi$ hybridization due to the curvature pulls down the energetically dispersive states, resulting in the nonmagnetic ground-state electronic structure for the n-type substitutional doping (5).

To study the electron-transport property, we employ a computational model shown in Fig. 3(a). The conductance spectra of the transport model for electrons coming from the left electrode is depicted in Fig. 3(b). Except for the peaks $B_\uparrow$ and $C_\uparrow$, there is a one-to-one correspondence between spin-up and spin-down peaks. By plotting charge density of the scattering waves, we found that these peaks originate from resonant tunneling by the edge states. Although it has been reported that the electron transport through the edge states in CNT is suppressed owing to the symmetry mismatch between the edge states and conducting CNT states. However, our calculation reveals that the fluctuation of the symmetry due to the presence of the doped atom leads to the spin-dependent resonant tunneling through the edge states (5). These results indicate that the atom substitution plays important roles for the electron transport through the edge states in addition to the spin-polarized electronic structure.

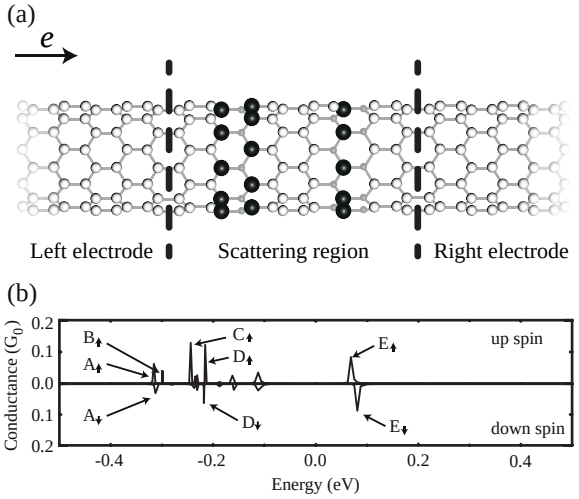

Figure 3: (a) Computational model for transport calculation. Meaning of symbols are the same with those in Fig. 1. (b) Conductance spectra as functions of energy of incident electrons. Zero energy was chosen as the Fermi level.

References

[1] T. Ono, T. Ota, and Y. Egami: Phys. Rev. B **84** (2011) 224424.

[2] S. Enouz, O. Stéphan, J.-L. Cochon, C. Colliex, and A. Loiseau: Nano Lett. **7** (2007) 1856.

[3] T. Ono, Y. Egami, and K. Hirose: Phys. Rev. B **86** (2012) 195406.

[4] K. Hirose, T. Ono, Y. Fujimoto, and S. Tsukamoto, First Principles Calculations in Real-Space Formalism, (Imperial College, London, 2005).

[5] H. D. Nguyen and T. Ono: J. Phys. Chem. C **46** (2013) 117.

Ab-initio search of novel multiferroics based on manganites

Kunihiko Yamauchi[1] and Masayuki Toyoda[1,2]
[1] *ISIR-SANKEN, Osaka University, Ibaraki, Osaka 567-0047*
[2] *CREST, JST, Kawaguchi, Saitama, 332-0012*

By means of density-functional simulations for various transition-metal oxides, we discuss the electronic mechanism of magnetism and ferroelectricity. DFT simulations were performed by using the VASP code and the HiLAPW code within the GGA+U formalism.

Based on multiferroic $HoMnO_3$, where the exchange striction induces the large ferroelectric polarization, we predicted new multiferroic compounds $Ho_{1/2}A_{1/2}MnO_3$ (A = As, Sb, Bi) with enhanced polarization. We found that doping of lone pair cations with different ionic radii, at the A-site of orthorhombic $HoMnO_3$, results in a marked increase of the electronic polarization and its development along the b-axis.[1]

Half-doped manganites are known to exhibit ferroelectricity with CE-type charge-ordered states together with antiferromagnetic spin configuration. In bilayer $PrCa_2Mn_2O_7$, we clarified that the displacement of apical oxygens bonded to either Mn^{3+} or Mn^{4+} ions plays an important role in the rising of ferroelectricity. Importantly, local dipoles due to apical oxygens are also intimately linked to charge and orbital ordering patterns in MnO_2 planes, which in turn contribute to polarization. Besides, an important outcome of our work consists in proposing Born effective charges as a valid mean to quantify charge disproportionation effects, in terms of anisotropy and size of electronic clouds around Mn ions.[2, 3]

A-site-ordered perovskites $AA'_3B_4O_{12}$ are expected to give rise to intriguing magnetic structure, as having magnetic transition-metal ions both at A' site and B site. We comprehensively studied magnetism of $CaCu_3B_4O_{12}$ (B = Ti, Ge, Zr, and Sn) and evaluated the magnetic exchange coupling constants between Cu spins. The experimentally observed magnetic orders of these compounds are reasonably explained by delicate balance of the ferromagnetic nearest coupling and the antiferromagnetic long-range coupling.[4]

参考文献

[1] S. S. Subramanian, K. Yamauchi, T. Ozaki, T. Oguchi and B. Natesan, J. Phys.: Condens. Matter **25**, 385901 (2013).

[2] K. Yamauchi and S. Picozzi, J. Phys. Soc. Jpn. **82**, 113703 (2013).

[3] K. Yamauchi and P. Barone, J. Phys.: Condens. Matter **26**, 103201 (2014).

[4] M. Toyoda, K. Yamauchi, and T. Oguchi, Phys. Rev. B **87**, 224430 (2013).

First-principles studies on a reaction mechanism of Nylon-oligomer hydrolase

Yasuteru SHIGETA

Graduate School of Pure and Applied Sciences,

University of Tsukuba, 1-1-1 Tennodai, Tsukuba, Ibaraki 305-8577

The active site of 6-aminohexanoate-dimer hydrolase, a nylon-6 byproduct-degrading enzyme with a β -lactamase fold, possesses a Ser112/Lys115/Tyr215 catalytic triad similar to the one of penicillin-recognizing family of serine-reactive hydrolases but includes a unique Tyr170 residue [1] as shown in Fig. 1. By using a reactive QM/MM approach [2], we work out its catalytic mechanism and related functional/structural specificities. At variance with other peptidases, we show that the involvement of Tyr170 in the enzyme–substrate interactions is responsible for a structural variation in the substrate-binding state. The acylation via a tetrahedral intermediate is the rate-limiting step, with a free-energy barrier of ~21 kcal/mol (see Fig. 2), driven by the catalytic triad Ser112, Lys115, and Tyr215, acting as a nucleophile, general base, and general acid, respectively. The functional interaction of peculiar Tyr170 with this triad leads to an efficient disruption of the tetrahedral intermediate,

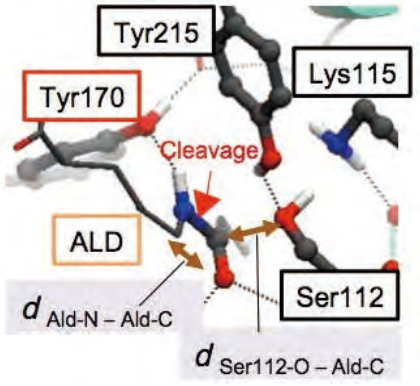

Fig. 1 Active site and reaction coordinates for QM/MM analyses

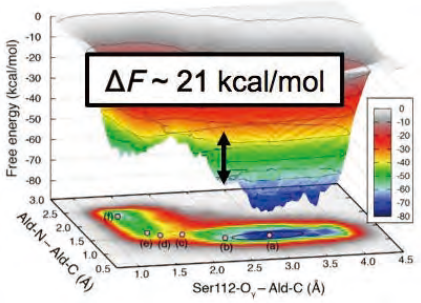

Fig. 2: Free energy surface along two-dimensional reaction coordinates

promoting a conformational change of the substrate favorable for proton donation from the general acid [3].

References

[1] S. Negoro, *et al. J. Mol. Biol.* **370**, 142 (2009).

[2] CPMD ver 3.15 .

[3] K. Kamiya, *et al. J. Phys. Chem. Lett.* **5**, 1210 (2014).

First-principles calculation of electrochemical properties of redox-active monolayers: Counter anion effects

Ken-ichi FUKUI

Department of Materials Engineering Science, Graduate School of Engineering Science, Osaka University, Machikaneyama, Toyonaka, Osaka 560-8531

A microscopic understanding of electrochemical properties is of fundamental importance for future electrochemistry. We have revealed that the electrochemical properties of ferrocene (Fc) terminated self-assembled monolayers (SAMs) can be obtained by first-principles molecular dynamics (FPMD) in the case of hydrophilic environment. In this study, we calculated the hydrophobic systems with including counter anions explicitly.

FPMD calculations were performed using the program "STATE". Fig. 1 shows our Fc SAM systems. Two FPMD runs (more than 0.5 ps) with vertical energy calculations were carried out for neutral (Fc) and positively charged (Fc^+) cases 300 K for each system to estimate the free energy difference ΔA [1].

The obtained values are summarized in Table 1. In contrast to the previous study, FcC4 system showed smaller ΔA value compared to FcC7, indicating that the microscopic environment of the Fc moiety in the FcC4 system is more susceptible to oxidation. This tendency is consistent with the experimental results [2]. These results indicate that the electrostatic interaction between Fc^+ moiety and ClO_4^- in the hydrophobic environment has a significant role in determining ΔA values. Quantitative estimation of anion dependencies is in progress.

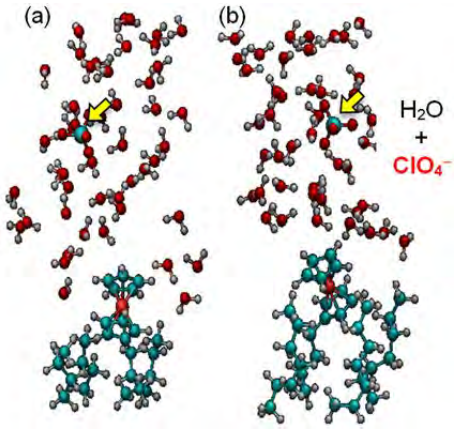

Fig. 1: Snapshots of Fc SAM systems taken from each MD simulation. The Fc-terminated molecule is surrounded by (a) *n*-butane as a standard system (FcC4) and (b) *n*-heptane to represent a hydrophobic environment (FcC7). Each system includes a ClO_4^- anion (see arrows).

Table 1. Values of the free energy difference, ΔA, obtained from MD simulations (unit: eV)

	FcC4		FcC7	
Anion	no	yes	no	yes
ΔA	1.87	1.40	1.73	1.50
$\Delta\Delta A$	-	-	–0.14	+0.10
$\Delta\Delta A$ exp[2]	-	-	-	+0.25

References

[1] Y. Tateyama, et al., J. Chem. Phys., **122**, 234505 (2005).
[2] S. E. Creager, G. K. Rowe, J. Electroanal. Chem., **291**, 420 (1997).

Theoretical Analyses on Electron/Ion/Thermal Transport Properties toward Nano-devices

Satoshi WATANABE
Department of Materials Engineering, the University of Tokyo
7-3-1 Hongo, Bunkyo-ku, Tokyo, 113-8656

1 Introduction

The electrical properties of nanostructures have been extensively investigated in the last few decades. However, further studies on complicated situations and phenomena, such as multi-terminal electronic transport, time-varying electronic transport, and the interplay among electronic, thermal and ionic transport at nanoscale, are strongly desired toward the design and control of nanoscale electronic devices. We have been performing investigations on these topics using theoretical analyses based on atomic/electronic level simulations. In the followings, some of our results in the fiscal year (FY) 2013 are described.

2 AC transient transport in nanostructures

The understanding on responses to AC signals of nanostructures is crucial for realizing next-generation ultrafast devices. So we have been theoretically studying AC transport properties of nanostructures.

Previously, we studied AC transport properties of metallic carbon nanotubes (m-CNTs) with a single atomic vacancy and seamless contact with lead regions using nonequilibrium Green's function (NEGF) method based on simple tight binding calculations [1]. Recently, we have examined the same system more closely, based on the density functional theory (DFT) calculations [2]. In the calculations, we used our homemade code for the NEGF and the SIESTA code. We have found that the two states induced by the vacancy, the π-orbital-origin vacancy state and the σ-orbital-origin dangling-bond state, show different susceptance behaviors at first sight. That is, besides capacitive peaks seen in both of the two states, satellite inductive peaks are clearly seen adjacent to the main capacitive peak only around the dangling-bond state. Our analysis with a simple resonant scattering model reveals that the origin and the magnitude of these satellite inductive peaks can be understood by just one parameter, i.e., the lifetime of electrons at a defect state.

We have also examined AC transport properties of 1, 4-Benzenedithiol molecule sandwiched between semi-infinite one-dimensional gold electrodes using the same method (NEGF based on DFT). In the calculated susceptance spectrum, we have found two types of features; one corresponding to conductance peaks/dips and the other not related to those. We have found that the former can be understood similarly to the case of the above m-CNTs, while the latter, which is seen at the energies having small conductances, correlates with the DOS of the electrodes.

3 Conductive filaments in oxide-based resistive switching devices

Oxide-based resistive switching devices, especially amorphous-TaO_x (a-TaO_x) based ones, have attracted much attention as strong can-

didates of next-generation memory cells. Their switching behavior is understood based on the formation/rupture of conductive filaments (CFs), but microscopic details of the CF structures and their formation/rupture processes have not been well clarified yet.

Previously, we have examined CFs in Cu/a-TaO_x/Pt from first principles within the DFT [3]. Recently, we have examined CFs in Pt/a-TaO_x/Pt heterostructures [4]. Calculations were performed using the VASP. Amorphous TaO_x structures were obtained by simulated annealing method. Since the resistance change of a-TaO_x is controlled by the O concentration, we perform systematic investigation on the structures and properties of a-TaO_x ($0.75 \leq x \leq 2.85$). We have found the strong correlation among Ta/O coordination number, Ta–Ta/Ta–O bond lengths, and O concentration in a-TaO_x. With the decrease of O concentration, Ta atoms tend to merge together and finally form a continued Ta-rich region in a-$TaO_{0.75}$, which suggests that not O vacancies, but the Ta–Ta bonding mainly contributes to the CF in a-TaO_x based resistive switches.

4 Thermoelectric properties of carbon nanostructures

Our previous study on thermal transport properties of various carbon nanostructures, single walled carbon nanotubes (SWNT), graphene nanoribbons (GNR), conical-helix nanofiber (CHNF) and cup-stacked carbon nanofibers (CSNF), by classical nonequilibrium MD simulations revealed that the thermal conductivities of CHNF and CSNF are two orders of magnitude lower than SWNT and GNR [5]. Since the low thermal conductivity is favorable for thermoelectric materials, we have recently investigated the thermoelectric figure of merit, ZT, of conical carbon nanofibers theoretically [6]. We adopted non-equilibrium Green's function (NEGF) method with the semi-empirical Hückel method implemented in the ATK code.

Our results show that the CSNF behaves like a semiconductor while the CHNF is metallic. CSNF electrical conductance is very low at the Fermi-level, which corresponds to remarkably high thermopower of $S > 1.5$ mV/K. The maximum thermopower calculated for CHNF was less than 0.5 mV/K. The estimated values of ZT depend on the Fermi level position, and the maximum values are 5.2 and 2.8 for the CSNF and CHNF, respectively. These high ZT values suggest that further experimental and theoretical studies are worthy.

References

[1] D. Hirai T. Yamamoto and S. Watanabe: Appl. Phys. Express **4** (2011) 075103.

[2] D. Hirai T. Yamamoto and S. Watanabe: J. Appl. Phys., in press.

[3] B. Xiao T. Gu, T. Tada and S. Watanabe: J. Appl. Phys. **115** (2014) 034503.

[4] B. Xiao and S. Watanabe: submitted to Nanoscale.

[5] D. A. Thomas, T. Yamamoto, T. Tada and S. Watanabe: Trans. Mater. Res. Soc. Jpn. **38** (2013) 183.

[6] D. A. Thomas, Doctoral thesis, The University of Tokyo (2014).

Self-Poisoning Dynamical Effects in the Oxygen Reduction Reaction on Pt(111) from a Top-down Kinetic Analysis and First-Principles Calculations

Nicephore Bonnet and Minoru Otani
National Institute of advanced Industrial Science and Technology (AIST), 1-1-1 Umezono, Tsukuba, Ibaaki 305-8568

The oxygen reduction reaction (ORR) is critical to a variety of processes such as combustion, corrosion, energy conversion, and storage. However, the detailed mechanism of the ORR at the atomic level remains unknown owing to the difficulty in probing intermediate species in reactive conditions. Although first-principles techniques have been intensively used to assess different reaction pathways, it is still not possible to rationalize all experimental measurements, which illustrates the persistent difficulties to account for all aspects of the ORR in a first-principles bottom-up approach.

Alternatively, in this project, we have conducted a top-down kinetic analysis of the ORR on Pt(111), in which electrochemical measurements are used to explore the possible reaction pathways at the atomic level, while ensuring that results of this analysis are consistent with first-principles computations, either from existing literature, or performed additionally by using the STATE code on available computational resources.

This dual approach allows us to shed some light on the relative efficacy of the ORR by comparing its free energy landscapes along the alternative associative and dissociative pathways (Fig. 1).

Specifically, we find that although the ORR proceeds preferentially through the associative pathway at high electrode potentials, a dissociative pathway becomes possible at lower potentials. However, the latter is gradually hampered by the products of the oxygen dissociation, such that the associative pathway again becomes dominant in the steady-state regime. The present study thus illustrates the importance of dynamical and self-poisoning effects in the ORR, motivating further characterization by the application of highly space and time-resolved probing techniques. This project also illustrates the intimate synergy between experimental data (here used as the basis for the top-down analysis) and first-principles computations.

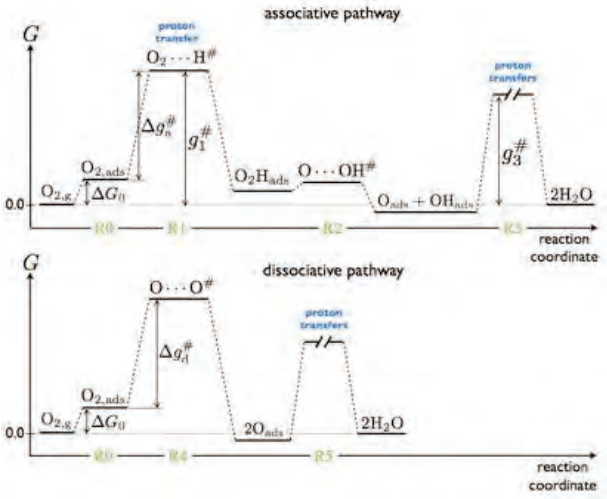

Figure 1: Free energy diagrams of ORR associative (top) and dissociative (bottom) pathways.

[C class; 10000 K (B),2000 K (C)]

First principles calculations on magnetism and transport properties at surfaces/interfaces and in molecules

Kohji NAKAMURA
Department of Physics Engineering, Mie University
Tsu, Mie 514-8507

Progresses on i) perpendicular magnetocrystalline anisotropy (PMA) of 3*d* transition-metal thin films, ii) magneto-transport properties of Fe thin films in an external electric field (*E*-field), and iii) magnetism of metal-phthalocyanine (MPc) molecules, by means of first principles full-potential linearized augmented plane wave method, are presented.[1]

PMA of 3d transition-metal thin films — In searching transition-metal thin films with a large PMA that overcomes the shape in-plane magnetic anisotropy and thermal fluctuations for ultrahigh density and nonvolatile spin-electronics, we systematically calculated the MA energies of Fe-based thin films consisting of magnetic 3*d* elements (Mn, Fe, Co, and Ni). The results predicted that giant PMA can be achieved by tuning the atomic-layer alignments in an Fe-Ni thin film with a bcc-like-layer stacking of $Fe_2Ni/Fe/Ni/Fe_2$, which arises from the spin-orbit coupling interaction between occupied and unoccupied Ni $d_{x^2-y^2,xy}$ bands crossing the Fermi level.

Magneto-transport properties of Fe thin films in an E-field — Magnetism induced by an *E*-field has received much attention as a potential approach for providing a new pathway for controlling magnetism. Here, we investigated the magneto-transport properties in an *E*-field, where the conductivity tensor is obtained by applying the Kubo formula of linear response theory. For the free-standing Fe monolayer, results predict a reduction (enhancement) of the in-plane dc electric and intrinsic Hall conductivities for *E*-field less than about 1 V/Å, due to the change in the band structure around Fermi level (E_F). An abrupt change in these conductivities around 1.1 V/Å appears where the magnetization reorients from the out-of-plane direction to the in-plane direction. The interband conductivity in the low energy region (<0.3 eV from E_F) is modified by the *E*-field. Small changes in the magneto-transport properties were also confirmed in the Fe monolayer on MgO substrate.

Magnetism of MPc molecules — A challenge to miniaturize devices for novel magnetic application now extends to treating the extreme limit of a single atom or molecule. For organometallic molecules with transition-metals, multiplets are essential aspects of their electronic structure. Here, we investigated electronic structures and magnetism of single MPc molecules, in which multiplets are treated by imposing a density matrix constraint on the *d*-orbital occupation numbers. We found that for the MnPc, the ground state is the ${}^4E_g$ (d_{xy}, d_{z^2}, $d^3_{xz(yz)}$) state with the perpendicular magnetic anisotropy with respect to the molecular plane, while for the FePc and CoPc, the ground states are the ${}^3A_{2g}$ (d^2_{xy}, $d^2_{z^2}$, $d^2_{xz(yz)}$) and ${}^2A_{1g}$ (d^2_{xy}, $d^2_{z^2}$, $d^3_{xz(yz)}$) states, respectively, with a planar magnetic anisotropy.

References

[1] K. Hotta et. al., PRL **110** (2012) 267206; K. Nakamura et. al., J. Korean Phys. Soc. **63** (2013) 612; Y. Kitaoka et. al., J. Appl. Phys. **113** (2013) 17E130.

First-principles investigation on thermophysics of nano structures

Shinji TSUNEYUKI[1,2]
[1]*Department of Physics, The University of Tokyo*
Hongo, Bunkyo-ku, Tokyo 113-0033
[2]*Institute for Solid State Physics, The University of Tokyo*
Kashiwa-no-ha, Kashiwa, Chiba 277-8581

Lattice thermal conductivity of crystals is governed by the anharmonicity of interatomic potentials. It is an essential ingredient of the figure of merit for thermoelectric materials, where lower thermal conductivity is preferred. On the other hand, higher thermal conductivity is preferred in electronic devices for thermal stability. From the viewpoint of materials design for these purposes, we have developed a new scheme to calculate lattice thermal conductivity from first principles.

So far three methods have been proposed for computational study of thermal conductivity: a method based on Boltzmann's transport equation and diagrammatic evaluation of lifetime of phonons, molecular dynamics (MD) simulation with the Kubo-Greenwood formula and non-equilibrium MD simulation of heat transfer. In any case, first-principles simulation is highly difficult because of the large system size either in real space or in $\boldsymbol{k}$ space necessary for reliable calculation. Thus we decided to develop an accurate, efficient and versatile method for modelling anharmonic interatomic potentials with first-principles MD based on the density functional theory (DFT).

The model potential is just a Taylor expansion of the total energy of the system calculated by DFT,

$$V(\boldsymbol{u}) = V_0 + \frac{1}{2}\sum_{i,j}\Phi_{ij}u_i u_j + \frac{1}{3!}\sum_{i,j,k}\Phi_{ijk}u_i u_j u_{jk} + \cdots.$$

$\boldsymbol{u} = (u_1, u_2, \cdots)$ are the displacements in xyz direction of each atom from its potential minimum, Φ_{ij} is a harmonic force constant and $\Phi_{ijk\ldots}$ is called an anharmonic force constant. Practically the Taylor expansion is terminated at a low order and the force constants are determined so that the model potential minimizes the deviation from first-principles potential energy for some sampling points under crystalline symmetry constraints [1]. In this study, we adopt up-to the sixth-order force constants for the parameter fitting. For efficient sampling of the potential energy hyper-surface, we use the locus of atoms obtained by first-principles MD at a fixed temperature [2]: the temperature should be high enough to reflect anharmonic character of the potential but low enough to avoid unphysical sampling. We find the third-order force constants determined in this way are comparably accurate as those carefully obtained by numerical differentiation of the potential energy.

Once the force constants are determined, phonon dispersion, group velocity and the lifetime of each phonon mode are calculated, with which lattice thermal conductivity and its temperature dependence is obtained within the relaxation-time approximation. We applied the scheme to Si, Mg_2Si, PbTe, Bi_2Te_3 and $Ba_8Ga_{16}G_{30}$ and found that material dependence and temperature dependence of the thermal conductivity are quantitatively reproduced in a wide range from 10^0 to 10^3 W/mK.

The program package we developed will be published at the portal site for materials science simulation "MateriApps" [3] in FY2014.

References

[1] K. Esfarjani and H.T. Stokes, Phys. Rev. B77, 144112 (2008); Phys. Rev. B86, 019904 (2012).
[2] T. Tadano, Y. Gohda and S. Tsuneyuki, J. Phys. Condens. Matter, in press.
[3] http://ma.cms-initiative.jp/

First-Principles Molecular-Dynamics Study of Structural and Electronic Properties of Covalent Liquids under Pressure

Fuyuki SHIMOJO, Akihide KOURA, Arifin RIZAL, Daiki FUKUNAGA, Kenta IDEUE

Department of Physics, Kumamoto University, Kumamoto 860-8555

To clarify the microscopic mechanism of changes in the structural and dynamic properties of amorphous or liquid covalent materials under pressure, we have carried out first-principles molecular-dynamics simulations [1-3]. To investigate the pressure dependence of the static structure, we obtain the structure factors, the pair distribution functions, and the distribution of the coordination numbers as a function of pressure. The bond-overlap populations and the Mulliken charges as well as the electronic density of states show the change in the covalent character in the materials due to compression.

In the static structure factor of amorphous silica at ambient pressure, there is a first-sharp diffraction peak (FSDP) at a wavenumber of about 1.6 $Å^{-1}$, which indicates the existence of an intermediate-range structural correlation between the tetrahedral units. Our calculations show that FSDP disappears under pressure over 10 GPa, suggesting that the intermediate-range correlation vanishes. Under further compression, the tetrahedral units collapse accompanied with an increase of the coordination number. While the nearest-neighbor distance of the silicon-silicon pair decreases up to 10 GPa, it increases at higher pressures. In the amorphous state, unlike in the crystalline phase, the structural change occurs gradually under pressure.

The concentration dependence of the dynamic properties of liquid thallium-selenium alloys has been also investigated. At low thallium concentrations, fairly long selenium chains exist in the liquid state. Upon the addition of thallium atoms, the self-diffusion coefficients of both selenium and thallium decrease despite the shortening of the selenium chain length. We clarify that this behavior is due to the suppression of self-diffusion by the increase in the strength of electrostatic interactions between thallium and selenium atoms.

References

[1] A. Koura and F. Shimojo: J. Phys. Soc. Jpn. **82** (2013) 094602.

[2] S. Ohmura, *et al.*: J. Phys. Soc. Jpn. **82** (2013) 074602.

[3] A. Koura, S. Ohmura, and F. Shimojo: J. Chem. Phys. **138** (2013) 134504.

Effects of doping on atomic structures and electronic properties of nanocarbon materials

Yoshitaka FUJIMOTO
Depertment of Physics, Tokyo Institute of Technology
Oh-okayama, Meguro, Tokyo 152-8551

Introduction of defects such as atomic vacancies and chemical impurities could often change the electronic properties and enhance chemical reactivity of carbon-based materials. The nitrogen and atomic vacancy complex defects in carbon-based materials has recieved much attention from nanoscience and nanotechnology, and graphene and carbon nanotubes with such nitrogen defects are expected to produce the new device materials used in catalyst for oxgen reduction reactions, capacitors for energy storages and hydrogen storages.

Here, we study the adsorption effects of hydrogens on nitrogen-vacancy complex defects in graphene using a first-principles total-energy calculation within the framework of the density-functional theory. As nitrogen-vacancy complexes, we use two kinds of pyridine-type defects: one is trimerized pyridine-type defects consisting of three nitrogen atoms around a single vacancy and the other is tetramerized pyridine-type defects consisting of four nitrogen atoms around a divacancy [1, 2]. The adsorption energies of hydrogen atoms on N-doped graphene are calculated as a function of the number of hydrogen atom, and it is found that the two hydrogen atoms adsorptions become energetically the most favorable for the trimerized as well as the tetramerized pyridine-type defects.

To discuss the stabilities of H atoms adsorption onto a graphene sheet, the adsorption energy is defined as

$$E_a = E_{tot} - E_{sub} - nE_{\mathrm{H}_2}/2, \qquad (1)$$

where E_{tot} and E_{sub} are total energies of pyridine-type N-doped graphene with and without hydrogen atoms, respectively, E_{H_2} is also total energy of an isolated H_2 molecule, and n is number of adsorbed H atoms.

The adsorption energies of H atoms on N-doped graphene are calculated as a function of number of H atoms. It is found that adsorptions of two H atoms on the trimerized and the tetramerized pyridine-type defects become energetically the most favorable. It is also found that when H_2 molecules are setting near not only the trimerized pyridine-type but also the tetramerized pyridine-type defects, the H_2 molecules are dissociated and two H atoms are adsorbed to N atoms in the pyridine-type defects. Thus, the pyridine-type defects are expected to act as a highly reactive site.

In summary, the adsorptions of hydrogen atoms onto the pyridine-type defects in graphene have been investigated using first-principles density-functional calculations. The dissociative adsorptions of H_2 molecule on the trimerized as well as the tetramerized pyridine-type defects are found to become favorable energetically.

References

[1] Y. Fujimoto and S. Saito, Phys. Rev. B **84**, 245446 (2011).

[2] Y. Fujimoto and S. Saito, Physica E **43**, 677 (2011).

First-principles study on Pt and oxide electrocatalyst

Osamu SUGINO

Institute for Solid State Physics,

The University of Tokyo, Kashiwa-no-ha, Kashiwa, Chiba 277-8581

We have investigated the properties of two different electrocatalysts for the oxidation (reduction) of oxygen/hydrogen molecules, i.e., platinum (Pt) and zirconium oxide (ZrO_2). On the Pt catalyst, despite a large number of theoretical researches the understanding is still far from complete. This is especially the case for the electro-adsorption of hydrogen (H) on Pt(111), which is by far the most studied subject. The research has been hampered by the small difference in the stability among adsorption sites, e.g., top, hollow, and bridge sites and by the limited number of available measurements. In this context, the aim of our study is to overcome this problem by (1) performing an intensive comparison of the adsorption sites within the density functional theory (DFT) and the generalized gradient approximation (GGA) and by (2) utilizing a recent detailed measurement on the effective lateral interaction of the adsorbed H atoms for an honest comparison with the simulation.

It was found that the top site and the fcc hollow site compete with each other as the most stable site, as has been discussed in many researches, but the relative adsorption energy depends very sensitively on the computational parameters, i.e., the thickness of the slab model and the *k*-point used for the Brillouine zone integration. With this in mind we have increased the thickness up to 18 layers and the number of *k*-point up to 24 × 24 per lateral (1 × 1) cell to reach the convergence. The relative energy for the full coverage condition was found to be almost degenerated unless the zero-point energy (ZPE) correction was included but, after including the correction, the fcc hollow site was found more stable by 70 meV. The relative energy is thus originated from the quantum effect.

To investigate the relative energy at lower coverage conditions, we have calculated the DFT-GGA total energy for many different configurations realized within a (3 × 3) lateral cell and mapped the result to a lattice gas model. The model was then used to conduct a Monte Carlo simulation using a (10 × 10) cell. The result was analyzed to obtain the thermally averaged H-H interaction energy, which is called the g-value, to be compared with the measurements. To see a parameter dependence, we have also done the simulation using different set of parameters for the lattice gas model.

The theoretical g-value was found slightly

smaller than the measured one and can be fitted well to the experiment when the H-H interaction parameter was increased by 20 %. This suggests that the interaction is underestimated by DFT-GGA by that amount. Here we admit that our calculation completely neglected the hydration effect considering that the effect has been conjectured small; we cannot therefore exclude the possibility that the hydration effect may play an important role in strengthen the H-H interaction.

Regarding the relative energy of H on the top site and that on the fcc hollow site, the g-value remained unchanged when the fcc hollow site had been virtually lowered in energy and, on the other hand, it deviated from the experiment when the site had been shifted upward. This result can be naturally understood by dominated fcc hollow site in the whole coverages.

This study have advanced a DFT-GGA level description on the H electroadsorption on Pt(111). The theory is found consistent with experiment reasonably well although slight discrepancy from experiment can be seen in the H-H interaction. The next target will be to go beyond the accuracy of DDF-GGA and to take into account the hydration effect.

Regarding the zirconia, we examined the mechanism for oxygen reduction reaction on zirconia surface using first-principles molecular dynamics. In our calculation model, we introduced an oxygen vacancy on tetragonal zirconia (101) surface, adsorbed an oxygen molecule near the vacancy site, introduced water molecules near the surface, and simulated how the system evolves when a hydrogen atom (proton + electron) nears the surface. We found that the oxygen molecule is easily split after being adsorbed at the vacancy site. As a result of this reaction, however, the vacancy is filled by one of the oxygen atoms and thus loses activity as a reaction center. Hydrogen quickly attacks the other oxygen atom and a water molecule is formed when a second hydrogen atom is introduced in the simulation. This suggests that desorption of surface oxygen ions (formation of vacancies) is the rate-limiting step for ORR at the zirconia surface.

References

[1] T. T. H. Tran, Y. Takimoto, and O. Sugino, Surf. Sci. 625, 104 (2014).

Computer Simulations of Nano-Fe Magnetizations

Shuji OBATA
School of Science & Engineering, Tokyo Denki University
Ishizaka, Hatoyama, Hiki, Saitama 350-0394, Japan

Relating with the main subject of the investigations of the electronic states in nano-materials, characteristics of magnetic dipole moment interactions induced from 3d and 4s orbitals in Fe metal are discussed in this work.

Using the ISSP system A (shii), the Fortran programs of the nano-Fe magnetizations are executed by about 500 line programing compiled with sxf90. The used times are about p4- 18 hours par job drawing domain structures and magnetization curves. The magnetic domain structures are determined by the classical dipole moment interactions as shown in Fig. 1. Setting distance vector $\boldsymbol{d}_{ij}=\boldsymbol{e}_{ij}d_{ij}$ between dipole moments at i and j, the interaction energies are equated as

$$W_{ij}=\frac{1}{4\pi\mu_0 d_{ij}^3}\{(\boldsymbol{\mu}_i\cdot\boldsymbol{\mu}_j)-3(\boldsymbol{\mu}_i\cdot\boldsymbol{e}_{ij})(\boldsymbol{\mu}_j\cdot\boldsymbol{e}_{ij})\}. \quad (1)$$

Crystal Fe takes the BCC structure with the lattice constant a=2.86×10^{-10} [m] up to 911 ℃ and have 2 atoms in a lattice. This Fe metal has the dipole moments of $2n_b\mu_0\mu_B$ per a lattice, where n_b=2.22, μ_0 and μ_B are permeability and the Bohr magneton respectively. In our simulations, the magnetic moments are set to have freedom of 26 directions as shown in Fig. 2.[1][2]

The nano-magnets depend on the system structure. The Barkhausen effects are observed in detail magnetization curves as in Fig. 3.

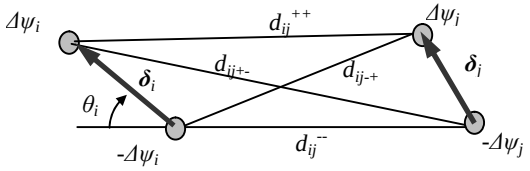

Fig. 1. Two magnetic moment interactions. The dipole moments are equated as $\boldsymbol{\mu}_i=n_b\boldsymbol{\mu}_B^0=\boldsymbol{\delta}_i\Delta\psi$

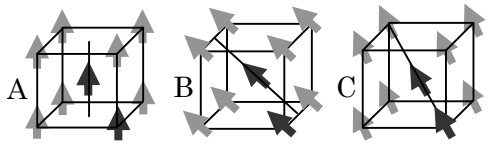

Fig. 2. Magnetic moment directions in a BCC lattice.

The domain structures at the jump points in a circle in Fig. 3 are drawn in Fig. 4. The results in the last year are obtained in the 6 freedoms of the easy axis directions. Comparing to those results, the domain structures in Fig. 4 in 26 freedom directions become a little bit complex, but the Barkhausen effects and the magnetization curves are similarly obtained.

The comparison of BCC & FCC Fe is also investigating now, where the similar results are obtained. The results of Fe_3O_4 are also obtained, where the domain structures are difficult to draw.

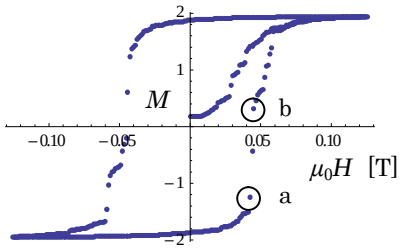

Fig. 3. The magnetization curve in a nano-belt system of the $N_xN_yN_z$=16 × 4 × 64 lattice points in z direction field with n_b=2.0.

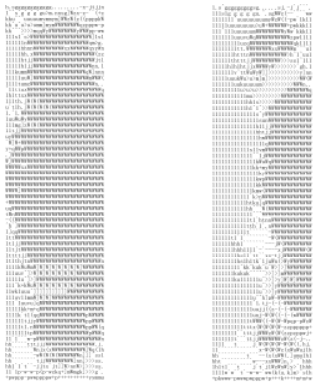

(a) (b)

Fig. 4. The domain structures of the second y layer at the jump points in a circle in Fig. 3. (a)~(d) correspond to a~d respectively.

[1] S. Obata : IEEJ Trans. FM. **133** (2013) 489-499.
[2] S. Obata : Materials Transactions. **54** (2013) 1661-66.

First-Principles Calculation of Transition-Metal Compounds

Tamio OGUCHI, Masayuki TOYODA,
Keisuke ISOYAMA, Masataka DEGUCHI, Akihiro FUJII
Institute of Scientific and Industrial Research, Osaka University, Ibaraki 567-0047

A first-principles density-functional-theory method has been applied to various condensed matter and surface systems for the last few decades. In this project, we study the electronic properties of several transition-metal compounds and explore their chemical trends and effects associated with crystal structure and symmetry. In addition, continuous developments of numerical methods related to the first-principles calculations are also pursued. In FY2013, we mainly studied the electronic structure of transition-metal oxides.

The A-site ordered perovskites $AA'_3B_4O_{12}$ are known to be a derivative of the standard perovskite oxides ABO_3, where relatively large cations occupy the A site while relatively small transition-metal cations are accommodated at the B site. In the A-site ordered perovskites, Jahn-Teller active cations such as Cu^{2+} and Mn^{3+} are located at the A' site with a peculiar square planar coordination. Among them, $CaCu_3B_4O_{12}$ (B=Ti, Ge, Zr, and Sn) (CCBO) consist of non-magnetic B-site ions and may be suitable for a study on the magnetic ordering associated with the A' sites. Magnetic couplings between Cu ions in CCBO were evaluated by total-energy calculations within an effective Heisenberg model [1]. It is found that the nearest and second-nearest neighbor couplings J_1 and J_2 are relatively weak ferromagnetic, almost independent of the B-site ions while the third-nearest neighbor coupling J_3 is also so in B=Ge and Sn but strongly antiferromagnetic in the cases of B=Ti and Zr, leading to the stable antiferromagnetic order. The antiferromagnetic coupling J_3 originates from the long-range superexchange interactions via Cu-O-Ti(Zr)-O-Ti hopping paths. Very strong hybridization between Cu-$d_{x^2-y^2}$ and O-p orbitals is a peculiar feature in these A-site ordered perovskite oxides.

The electronic structure of the A-site ordered perovskite $LaCu_3Fe_4O_{12}$ (LCFO) is also investigated by means of first-principles calculations [2]. LCFO reveals metal-to-insulator and paramegnetic-to-antiferromagnetic transitions with a volume expansion by 1.3% at 393K as temperature decreases. This is believed to be associated with a charge transfer as $3Cu^{2+}+4Fe^{3.75+} \rightarrow 3Cu^{3+}+4Fe^{3+}$, according to a bond distance analysis. We found that the volume change at the transitions is a key for understanding the changes in the electronic structure and magnetism.

Some other first-principles applications to transition-metal compounds have been carried out for $PdCoO_2$[3], $PdCrO_2$[4], $FeTe_{1-x}Se_x$[5], and so on, in collaboration with experimental groups.

References

[1] M. Toyoda, K. Yamauchi, T. Oguchi: Phys. Rev. B **87** (2013) 224430.

[2] K. Isoyama, M. Toyoda, K. Yamauchi, T. Oguchi: JPS Meeting (2014) 28aPS-97.

[3] H. Takatsu, *et al.*: Phys. Rev. Lett. **111** (2013) 056601.

[4] J. M. Ok, *et al.*: Phys. Rev. Lett. **111** (2013) 176405.

[5] H. Okazaki, *et al.*: Euro. Phys. Lett. **104** (2013) 37010.

First-Principles Calculations of Electron and Spin Properties in Solid Materials

Hiroyoshi MOMIDA
Institute of Scientific and Industrial Research, Osaka University
8-1 Mihogaoka, Ibaraki, Osaka 567-0047

We have performed first-principles electronic structure calculations to study material properties of several kinds of solid systems at bulk, surface and interface environments with or without considerations of defect influences. Thanks to the support of computer resources, three refereed papers were published in the fiscal year 2013 [1, 2, 3]. To elucidate the nature of a brittle fracture process in steel materials, we have studied microscopic mechanism of hydrogen-enhanced vacancy embrittlement of grain boundaries in α-Fe [1]. Our computations partly contribute to show x-ray absorption spectra of FeS_2 which is a technologically important material such as secondary batteries [2], and to conduct physical guiding principles for high quality resistive random access memory stack with an Al_2O_3 insertion layer [3].

In the fiscal year 2013, we have mainly used the supercomputers to predict topologically-insulating phases of Sb_2Te-based materials, to study surface band structures of the topological insulator Bi_2Se_3 with several defects, and to estimate magnetic hyperfine interactions at Sn nuclei in Co_2MnSn Heusler alloys. Last two topics are in collaboration with experimental groups. Computations were done using the HiLAPW code which utilizes the all-electron full-potential linearized augmented plane-wave method based on the density functional theory. For the topological insulator systems in which the spin-orbit couplings (SOC) have essential roles on their electronic structures, SOC were included as the second variation procedure. We computed mostly with the MPI-only parallelizations, and code optimizations are still in progress to improve performances.

As a main scientific achievement of this project, we find that Sb_2Te-based materials can have topological insulator phases controlled by external strains or element substitutions. Sb_2Te is known as a semimetal in its equilibrium structure, and the structure has two Sb_2 bilayers between Sb_2Te_3 quintuple layers. Our result shows that an in-plane strain expanding in the layer direction can induce a band gap, and that element substitutions by a larger atom can also induce a band gap. Calculated Z_2 topological invariants of the insulating phases are $Z_2 = 1$ showing that they can be a strong topological insulator.

This work was done in collaboration with Eriko Takasaki, who partly did computations, and Tamio Oguchi. I would like to thank Takahisa Ohno for all of the help and support.

References

[1] H. Momida, Y. Asari, Y. Nakamura, Y. Tateyama and T. Ohno: Phys. Rev. B **88** (2013) 144107.

[2] T. Oguchi and H. Momida: J. Phys. Soc. Jpn. **82** (2013) 065004.

[3] M. Y. Yang, K. Kamiya, B. Magyari-Köpe, H. Momida, T. Ohno, M. Niwa, Y. Nishi and K. Shiraishi: Jpn. J. Appl. Phys. **52** (2013) 04CD11.

First-Principles Calculations Concerning Spintronics

Mineo SAITO

Institute of Science and Technology, Kanazawa University

Kakuma, Kanazawa, 920-1192 Japan

In spintronics, the spin-orbit interaction (SOI) plays an important role. Therefore, fully-relativistic density functional calculations are necessary to evaluate spintronics materials. ZnO forms two-dimensional electron gas which has a good quality and thus its device application is desired. In this study, we carry out first-principles calculations on ZnO which is a wide gap semiconductor.

Since we have studied the conduction band bottom previously [1], we here study the valence band top (Fig. 1). At the Γ point, the highest occupied band belongs to the two-dimensional irreducible representation of E_2 and the next highest occupied band belongs to the irreducible representation of A_1. This energy splitting originates from the crystal field. When the SOI is considered, the E_2 level splits into the upper $E_{1/2}$ level and the lower $E_{3/2}$ level. This energy order was unexpected and thus the negative spin orbit coupling has been considered to occur in this system, previously.

However, we find that this energy order originates from the strong SOI. i.e., we find that two $E_{1/2}$ levels originating from E_2 and A_1 are strongly mixed. This strong mixture can be confirmed that the atomic orbitals of p_x and p_y (E_2) and that of p_z (A_1) are strongly mixed. Therefore, we conclude that the SOI in ZnO is strong. This finding is important in spintronics application of ZnO.

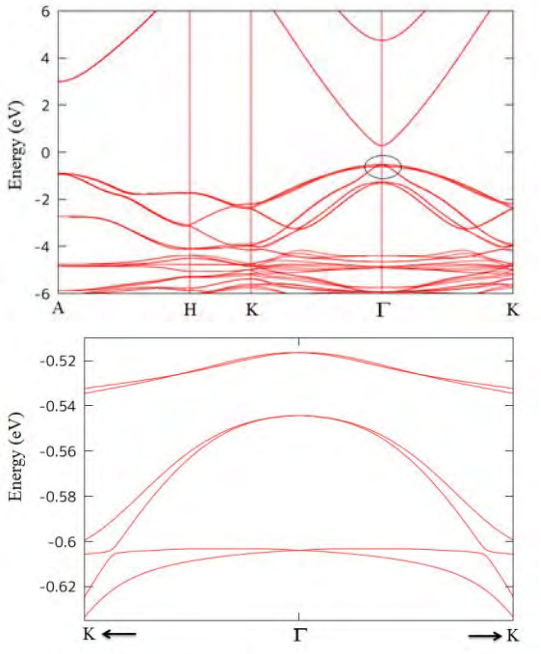

Fig. 1 Band structure of ZnO (SOI is included)

References

[1] M. A. Adhib, H. Kotaka, F. Ishii, and M. Saito: Appl. Phys. Exp. 7 (2014) 053002.

Hybrid *ab initio* QM/MM calculations of biological macromolecular systems

Masaru TATENO

Graduate School of Life Science, University of Hyogo

In this study, hybrid *ab initio* quantum mechanics (QM) / molecular mechanics (MM) calculation was employed to investigate electronic structures of crucial biological macromolecular systems. Here, we used our QM/MM interface program, which connects highly-parallelized engines for QM and MM calculateions. Employing our calculation system, we computationally analyzed catalytic mechanisms of crucial biological macromolecular systems. The followings are parts of the results that we obtained in this FY.

To obtain unknown structures, such as intermediate structures in catalytic reaction processes that are exerted by enzymes, we performed structural modeling to obtain the atomic-resolution structures that are experimentally inaccessible [1]. For the calculations in the modeling, we performed hybrid QM/MM simulations of the enzyme, and thereby built parameter sets of non-standard chemical structures (assigned as the QM regions) that were included in the enzyme, by improving our previous parameter values that were obtained by full QM calculations.

The following is another achievement. For every organism, responses of each cell to signals from the environmental outside are crucial to optimize its states. Thus, the cellular signal transduction systems are essential to the organisms to transduce the outside signal to the nucleus, where genome DNA is located. In fact, the defects of this function lead the system to fatal errors, such as cancer.

The hydrolysis reaction of GTP to GDP by Ras, which is the product of the RAS oncogene (cancer gene), constitutes one of the most critical reactions for cellular signal transduction. Since this hydrolysis reaction, which acts as a crucial switch in various signaling cascades, is activated by binding of the GTPase activating protein (GAP) of Ras, the mechanisms of this reaction by the Ras-GAP complex have intensively been investigated for decades. However, even the reaction scheme has not yet been positively identified.

Last FY, we performed docking simulations of GTP and the Ras-GAP complex by classical MD simulations and hybrid *ab initio* QM/MM MD simulations. In this FY, employing the obtained structural model, we further conducted hybrid *ab initio* QM/MM MD simulations to investigate the catalytic reaction mechanisms [2]. The activation barriers that were estimated

by our computational analysis were comparable with respect to the two reaction pathways, i.e., the dissociative and associative mechanisms (see **Fig. 1**). Thus, we revealed that the catalysis by the Ras•GAP complex operates by both dissociative and associative mechanisms. To our knowledge, this is the first finding of a "dual-mechanism/pathway" hydrolase.

Then, based on the more detailed catalytic processes that were elucidated in the present analysis, we investigated other various hydrolysis reactions by enzymes, with the use of crystal structures that were previously reported. Thereby, we built a novel and simple scheme for identifying the catalytic mechanisms of such various hydrolase reactions, which enabled us to predict the reaction mechanisms of hydrolases. Thus, we can now provide the explanation of the reason why the mechanism operates in a hydrolase. Thus, our present work also provides a solid basis for engineering applications such as enzyme design, etc., based on the detailed hydrolase mechanisms.

References

[1] Kubo, M., etc.: Effective pumping proton collection facilitated by a copper site (Cu_B) of bovine heart cytochrome c oxidase, revealed by a newly developed time-resolved infrared system, *J. Biol. Chem.*, **288** (2013), 30259-69.

[2] Itagaki, T., Kang, J., and Tateno, M.: Dual catalytic reaction mechanisms by the oncogenic Ras and RasGAP complex, *submitted*.

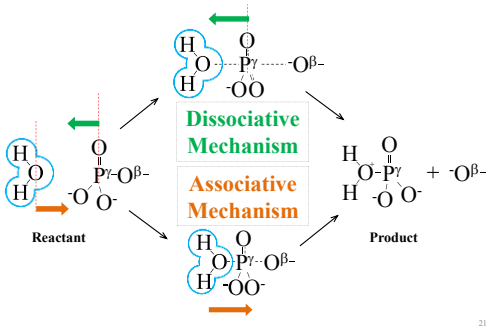

Fig. 1. The fundamental schemes of the catalytic reaction of hydrolysis by various enzymes (hydrolases). The upper and lower represent the dissociative and associative mechanisms, respectively. For the Ras-GAP complex, we investigated whether these two catalytic reaction pathways are plasusible or not, employing hybrid *ab inito* QM/MM MD simulations in this FY [2].

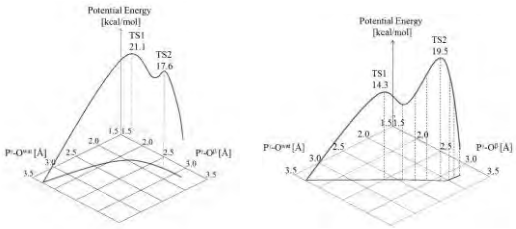

Fig. 2. The energy profiles that were obtained by our hybrid *ab inito* QM/MM MD simulations of the Ras-GAP complex. The analysis revealed that the activation barriers obtained are comparable. Therefore, we concluded that the two reaction pathways are both plausible. This is the first finding that these two catalytic pathways are involved in a hydrolysis reaction by an enzyme (hydrolase).

Theoretical investigation of the initial growth process of organic semiconductor thin films

Kazume NISHIDATE and Masayuki HASEGAWA
Faculty of Engineering, Iwate University
Ueda 4-3-5, Morioka, Iwate 020-8551

A pathway of carriers in an organic semiconductor device is formed at the interface between the organic thin film and the gate insulating thin film. Controlling the arrangement of organic molecule at the first layer on the gate plays a crucial role not only in the device characteristics but also in the crystallinity of the organic thin film.

Pentacene (Pn) is an aromatic molecule composed of five benzene rings. It has been regarded as a very likely candidate for organic semiconductor since it displays high carrier mobility. In recent years, acceleration of the carrier mobility has also been tried by forming Pn layers on a graphene sheet which is placed on the insulating gate.[**?**]

There are two types of interactions between the Pn molecules. One is the long range van der Waals (vdW) interaction, and the other is the repulsive interaction between the outer hydrogen atoms. The competition of the interaction among the Pn molecules result in the formation of the characteristic herringbone pattern of the organic crystal. To assess the early stages of the formation of Pn layers on graphene, we have performed large scale vdW density functional electronic structure calculation (vdW-DFT) of the Pn on graphene system. We also performed the Grimm's D2 calculation (DFT-D2) where vdW force is empirically implemented. Both of the Local density approximation (LDA) as well as the generalized gradient approximation (GGA/PW91) were performed as complement calculations.

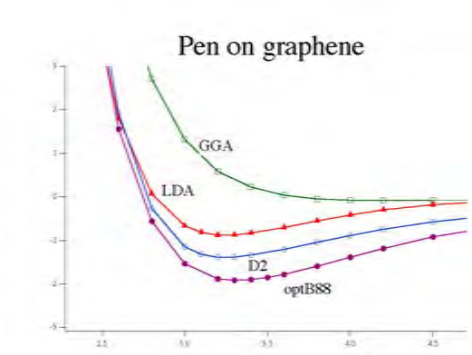

The supercell contains a graphene sheet with the dimensions of 11 × 11 benzene nucleus units. Large vacuum region above the graphene sheet is taken (∼ 15Å) to minimize the unphysical interaction through the boundary. We placed Pn molecule above the graphene sheet with changing the Pn to graphene distance. The configuration is similar to the AB stacking form of graphite; i.e. an apex of the benzen nucleus of Pn is arranged alternately to be on the hole of the benzen nucleus of graphene. The equilibrium distances from Pn to graphene are 3.2 Å(LDA), 3.2 Å(DFT-D2) and 3.3 Å(vdW-DFT). Adsorption energies are -0.87 eV (LDA), -1.38 eV (DFT-D2) and -1.91 eV (vdW-DFT). However, Pn was not adsorbed on the graphene in the GGA computation demonstrating lack of capability to evaluate the long range forces. α

References

[1] Wi Hyoung Lee *et al.*: J. Am. Chem. Soc. **133**, 4447-4454 (2011).

First principles based analysis of reactions on solid surfaces/interfaces

Hideaki Kasai
Department of Applied Physics, Osaka university
Center for Atomic and Molecular Technologies, Osaka university
2-1, Yamadaoka, Suita city, Osaka, Japan, 565-0871

Understanding reactions on surfaces and interfaces is important for developing advanced materials and technologies. Various interesting physical and chemical phenomena are discovered at surfaces and interfaces, ranging from fundamental phenomena like tunneling effects to applications like catalytic reactions and migration of oxygen.

In 2014, several studies on surfaces and interfaces based on density functional theory (DFT) have been carried out in our group [1]. Due to the availability of powerful and useful ISSP computational facilities, it has been possible for us to investigate various interesting and complex problems which can be difficult to deal with experimentally.

Research areas that can be highlighted from our recent works include clean energy related issues such as photocatalysts [2] and solid oxide fuel cells (SOFCs) [3, 4, 5, 6, 7].

The interaction of olefins with various kinds of solid surfaces has been studied extensively over the last few decades. Among many olefin-solid surface interaction systems, ethylene adsorption on solid surfaces is a topic that has attracted a great deal of interest, mainly due to its simplicity in structure and high reactivity. Hence, ethylene adsorption can be regarded as a benchmark study in order to investigate the interaction involving olefin-solid surfaces. It is also worth to be noted that the ethylene interaction with solid surface plays an important role in many kinds of technological, industrial and environmental applications such as separation of light olefins from paraffins, various transformations of hydrocarbons in chemical industries, production of clean transportation fuels, and degradation of various harmful volatile organic compounds (VOCs) derived from ethylene. Therefore, a strong understanding on the physicochemical aspect of olefin-solid surface interaction is necessary. In this work, we investigated the adsorption of C_2H_4 (ethylene) on anatase TiO_2 (001) surface by means of first-principles calculation. Four adsorption configurations that correspond to two main types of interaction of ethylene-solid surface, namely π-bonded and di-σ-bonded interactions, are studied. We found that ethylene adsorbed on top of unsaturated Ti5c (five-fold coordinated Titanium) is the most stable configuration and this configuration corresponds to the π-bonded interaction. In this configuration, the adsorption energy is calculated to be - 0.2 eV and ethylene retains its initial sp^2 planar configuration upon adsorption. Vibrational frequency analysis shows that some small modifications are observed for each reported vibrational modes of ethylene. These findings suggest that ethylene is weakly adsorbed on clean TiO_2 surface and vdW interaction is found to have a significant contribution to the total binding energy of ethylene.

Development of novel fast ion conductors is a crucial issue for SOFCs which can operate at low temperatures. Experimental stud-

ies on fast ion conductors in the recent twenty years have established that rare-earth-based oxides are the most promising materials for solid electrolytes and air electrodes (as cathodes in discharging processes). However, the currently available solid electrolyte materials run at high temperature while one of the main challenges is to reduce the operating temperature below 600°C. Therefore, in our group, we have studied several promising materials that offer possibilities of realizing low operating temperature SOFCs, which includes La_2GeO_5 [3, 4], CeO_2 [3, 5], Pr_2NiO_4 [6], and $LaGaO_3$ [7] as solid electrolyte materials. The studies on La_2GeO_5-based materials are still in the early stage and their properties are being clarified one by one. Here, four of five oxygen atoms are bonded covalently while the other is ionically bonded. This hybrid characteristic is expected to yield in novel ideas that have not been discovered yet. On the other hand, the studies on CeO_2-based materials have entered a mature stage that involved proper conditions of doping and strains toward practical applications. Simple laws are developed on the formation and migration energies and dopant atomic radii. This simpleness is attributed to the ionic nature of O bonding. However, currently we try to increase the complexities of our calculations to also include the description of 4f-electrons in the interaction to gain deeper understanding in the ionic migration. On the other hand, Pr_2NiO_4-based ceramic oxides are known as promising MIEC cathode material for SOFC owing to its experimentally found good ionic and electronic conductivity compared to other known materials. Substitutional doping at the cation site [$Pr_{2-y}RyNi_{1-x-y-z}E_xT_zO_4$ (R=La, and E=Cu and T=Ga)] shows change in both structural and electronic properties. Higher concentration of La doping increases the lattice parameter while maintaining the electronic property of the host system. On the other hand, Cu doping causes tilting of the nickelate octahedral substructures so as to stabilize the whole structure, but is accompanied by emergence of states which contributes to electronic conduction. However, Ga doping has indication of high O ion diffusion and lower electronic conductivity. Lastly, for the case of $LaGaO_3$-based materials, we have investigated the influence of Mg^{2+} doped into Ga^{3+} and Sr^{2+} doped into La^{3+} ions (LSGM). The study is still ongoing and current results indicate that this doped system is semiconductor-like material. Substitution of Ga with Mg weakens the bond leading to the elongating the Mg-O bond length and explains the oxygen migration around Mg dopant.

References

[1] http://www.dyn.ap.eng.osaka-u.ac.jp

[2] Ganes Shukri, et al: Surface Science **619** (2014) 59.

[3] Mamoru Sakaue, et al: ECS Transactions, **57** (2013) 1077.

[4] Tran Phan Thuy Linh, et al: ECS Transactions, **57** (2013) 2411.

[5] Musa Alaydrus, et al: ECS Transactions, **57** (2013) 2753.

[6] Susan Meñez Aspera, et al: ECS Transactions, **57** (2013) 2733.

[7] Triati, et al: ECS Transactions, **57** (2013) 2715.

Density functional theory study of stability and dynamics of metal nanoclusters on a silicon surface

Ikutaro HAMADA
National Institute for Materials Science
Tsukuba 305-0044, Japan

Small atomic clusters are of technological as well as fundamental importances. They are potential components of future microelectronics devices, high density storage devices, and catalysts. Furthermore, it may be possible to realized intriguing physical properties in the small clusters, because of the quantum size effects. Recent progress in scanning probe microscopy enable one to manipulate atoms and molecules one by one, and it is becoming possible to fabricate well defined small atomic clusters on surfaces. Although the control of the number of constituent atoms in the cluster is possible, it is difficult to determine the atomic structures only the experiment. I perform density functional theory calculations of Pb_n (n=1-4) on Si(111)(7×7), to clarify the atomic structures of the Pb_n clusters, and the mechanism of the atomic switching realized by the scanning tunneling microscopy (STM).
All the calculations were performed using the STATE[1] code. We used a plane-wave basis set to expand the wave functions and ultrasoft pseudo potentials to describe electron-ion interactions. The surface was modeled by a slab composed of eight atomic layers, and a thick enough vacuum was inserted between the neighboring slabs. The silicon atoms in the bottom layer are terminated by the hydrogen atoms. The effective screening medium method[2] was used to eliminate spurious electrostatic interactions with the image slabs.

In this work, special attention has been paid for Pb_3, because the atomic switching is induced by STM for Pb_3 . To clarify the mechanism of the atomic switching, it is essential to determine the most stable atomic structure. I have examined more than 20 configurations, and investigated the stable atomic structure of Pb_3. STM topographies for the most stable configuration were simulated by using the Tersoff-Hamann theory[4]. I found that the simulated STM topography for the occupied states is in reasonable agreement with experiment. Simulated topography for unoccupied states is similar to the occupied one. In the experiment, however, STM topography shows significant bias dependence, suggesting that the structures of Pb_3 examined in the calculations so far cannot explain the experimentally observed Pb_3. Further investigation is needed to clarify the structure and dynamics of the Pb_3 cluster on Si(111).

References

[1] Y. Morikawa, H. Ishii, and K. Seki, Phys. Rev. B **69** (2004) 041403(R).

[2] M. Otani and O. Sugino, Phys. Rev. B **73**, (2006) 115407.

[3] I. Hamada, M. Otani, O. Sugino, and Y. Morikawa, Phys. Rev. B **80**, 165411 (2009).

[4] J. Tersoff and D.R. Hamann, Phys. Rev. Lett. **20** (1983) 1998.

First-Principles *GW*+Bethe-Salpeter Calculations for Photoabsorption Spectra of $M^+@C_{60}$

Yoshifumi NOGUCHI

Institute for Solid State Physics,

The University of Tokyo, Kashiwa-no-ha, Kashiwa, Chiba 277-8581

Fullerene is known as a very good acceptor, thereby finding application in organic solar cell. Additionally, recent experiments have shown that metal encapsulation into a fullerene molecule, such as in $Li^+@C_{60}$ enhances its accepting potential owing to the stabilization of the fullerene frame by the metal ion encapsulated inside. A theoretical investigation to understand the structural and optical properties of the $Li^+@C_{60}$ molecule is necessary, for further advances in the field of organic solar cells.

The talented first-principles method, in particular for simulating the optical properties, is a Green's function method based on the many-body perturbation theory (*GW*+Bethe-Salpeter), not a standard DFT-based method. However since the Green's function method is computationally more expensive than DFT, there is a strict limitation on the treatable system size.

Recently, we developed a hybrid (OpenMP and MPI) parallel version of the *GW*+Bethe-Salpeter program code. Fig. 1 shows the result of the benchmark test measured performed on the Fujitsu FX10 supercomputer. The MPI parallel efficiency in weak scaling reaches about 97 % with 1536 MPI parallel execution. With this high parallel efficiency, the present program code can handle systems with more than 100 atoms.

In this study, we employed the first-principles *GW*+Bethe-Salpeter method to calculate the photoabsorption spectra of $M^+@C_{60}$, where M=H, Li, Na, and K. The calculated spectra are in good agreement with the available experiment. We discussed the effect of M^+ encapsulation into fullerene on the photoabsorption spectra [1].

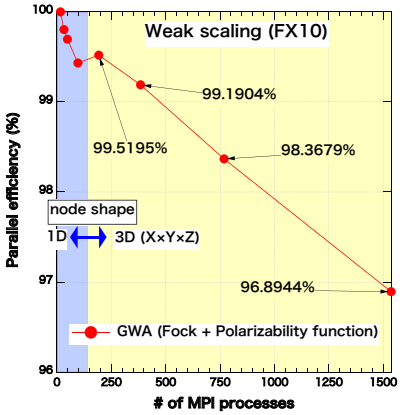

FIG. 1. MPI parallel efficiency.

References

[1] Y. Noguchi, O. Sugino, H. Okada, and Y. Matsuo, J. Phys. Chem. C, **117**, 15362 (2013).

Microscopic Understanding of Electric Double Layer at Solid-Liquid Interfaces

Kazuto AKAGI
WPI-AIMR, Tohoku University
Katahira, Aoba-ku, Sendai, Miyagi 980-8577

H^+ ions play various important roles in functional materials/devices such as catalyst, fuel cell, and also in more complex biological systems. Elucidation of spatial distribution and dynamics of H^+ ions at the interfacial region in these systems is one of the important subjects for computational materials science. In this project, microscopic picture of H^+ ions in an acid aqueous solution is studied based on the first-principles molecular dynamics (MD) calculations and a series of hydrogen-bond network analyses. Each simulation cell has an appropriate size with more than 110 water molecules to describe not an adsorbed water film but a solid-liquid interface. The PBE functional was used at 400K (≈ SPC/E water at 280K) with the plane wave basis set of E_{cutoff} = 400eV and the PAW scheme for valence electrons. 100ps MD trajectories were used for the analysis of each system.

First, the microscopic picture how H^+ ions are bound around counter anions in 2mol/l H_2SO_4 solution was investigated by comparison of the potentials of mean force (PMF) evaluated in two ways: the radial distribution functions and integration of the averaged forces, respectively. It turned out that the picture that a hydrogen ion can be described as a hydronium ion (H_3O^+) is well justified and the typical binding free-energy around HSO_4^- was 4 kcal/mol (Fig.1a). This is almost the same strength as the attractive interaction between Na^+_{aq} and Cl^-_{aq}.

Next, the interfaces between Pt surfaces and

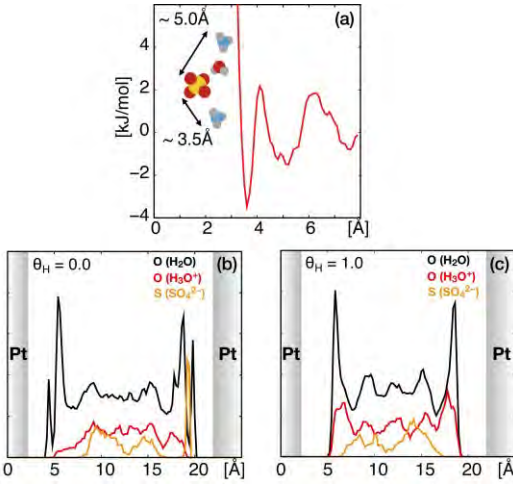

Figure.1 (a) Potential of mean force for H_3O^+ around HSO_4^-/SO_4^{2-}. (b)(c) Spatial distribution of H_2O [black], H_3O^+ [red] and HSO_4^-/SO_4^{2-} [orange] along the depth direction.

2mol/l H_2SO_4 solution were studied. As the Pt(111) surface changed from hydrophilic to hydrophobic with increase in the adsorbed hydrogen atoms, the hydronium ions escaping from the hydrophilic surface (Fig.1b) were getting localized at the most interfacial region with the hydrophobic surface (Fig.1c). They were strongly bound by SO_4^{2-} compared to those in a bulk solution, and their accumulation leads to the stability of adsorbed hydrogen atoms on a Pt surface. While the mechanism of change in spatial distribution of H_3O^+ and HSO_4^-/SO_4^{2-} is still unclear, several interesting relations with the topology of hydrogen-bond network by surrounding water molecules were also found. It will be reported after the detailed analyses are done.

Study on Nano-scale Carbon Materials

Susumu Okada
Graduate School of Pure and Applied Sciences, University of Tsukuba
1-1-1 Tennodai, Tsukuba, Ibaraki 305-8577

Pentagons embedded into hexagonal sp^2 (threefold-coordinated) carbon networks play a crucial role in determining the geometric and electronic properties of the resulting nanoscale carbon allotropes. In the infinite planar hexagonal C network, pentagons should be appeared with the appropriate number of polygons. For example, an isolated pentagon embedded in graphene induces the formation of a heptagon adjacent to it to maintain a planar sp^2 network, as is found in Stone-Wales type and fused pentagon type topological defects. Since pentagons and other polygons disrupt the AB bipartite symmetry of graphene, such topological defects in graphene occasionally induces an unusual electronic structure at or near the Fermi level in addition to the characteristic electronic structure of graphene. Localized states and flat dispersion bands associated with the topological defects are expected to occur around them. Therefore, it is interesting to explore the geometric structure and electronic properties of graphene containing many topological defects. In this study, we explore the geometric and electronic structures of a 2D sp^2 C allotrope consisting of pentagons and dodecagons, as a representative structure of the limit of topological defects in sp^2 networks, based on first-principles total energy calculations.

We found that the 2D sp^2 carbon allotrope retains its planar structure at the equilibrium lateral lattice parameter $a = 7.1$ Å. At the equilibrium lattice constant, the calculated total energy of the sheet is 0.66 eV/atom with respect to the energy of graphene, indicating that the structure is energetically stable. Further *ab initio* molecular dynamics simulations confirmed that the sheet was kinetically stable up to a temperature of 1000K for simulation times of a few picoseconds. We found that the sheet is a metal with a flat dispersion band that crosses the Fermi level. Owing to the flat dispersion band at the Fermi level, the state is split into majority and minority spin states, respectively, leading to spin polarization on the sheet. The polarized electron spin is ferromagnetically ordered and distributed throughout the whole network of the sheet with a magnetic moment of 0.62 μ_B/nm^2. In addition to the magnetism arising from the flat dispersion band, although the network does not contain any hexagonal rings, the sheet still exhibits the characteristics electronic properties of graphite and graphene. The fused pentagon sp^2 C sheet has a pair of massive Dirac dispersion bands at the K point. Detailed analysis on the wave function indicated that the states possess nonbonding π electron nature on the honeycomb network of fused pentagons.

Study on material search and electrode interfaces for next-generation secondary batteries

Yasunobu ANDO
Department of Materials Engineering, The University of Tokyo
7-3-1, Hongo, Bunkyo-ku, Tokyo 113-8656

Basic researches for secondary batteries through the use of computer simulation have been studied actively. Especially, Li-ion batteries have been attracted much interest because of their broad applications. To advance improvements of performance of the batteries, obscure fields such as ion dynamics at electrochemical interfaces should be worked on. In order to understand the nature of ion dynamics at the interfaces, we focus on the functional binders-electrode interfaces. It is reported that functional binders modulate the insertion process that makes us possible to design the performance of batteries.

We model the interfaces including poly(vinylidene fluoride) (PVdF) and single-graphene electrode. *Ab initio* molecular dynamics with electric field is performed by OpenMX (Open source package for Material eXplorer) [1]. Electric field is considered in the system by using Effective Screening Medium (ESM) method. In ESM scheme, atoms must not go across the cell edge along the z-direction because periodic boundary condition is not satisfied. Therefore, we have to impose an artificial wall near the cell edge that is controlled by the value "wall.position" in an input file.

In a process of the research, we find some bugs corresponding to setting the wall position. We have to write "ESM.wall.switch ON" on an input file to valid an ESM wall, which is not written in a official manual. We show the time evolution of position of the topmost H atoms along the z-direction in figure 1. Without the keyword, the topmost atoms expand gradually as is shown by a solid line. On the other hand, with the keyword, the wall is worked appropriately. A broken line in figure 1 suggests that the topmost position is converged to 26.2 Å after about 300 fs. We also find that wall.position is not worked appropriately because actual wall position is relative to the grid origin that is set automatically in the program. All of them have already been reported to developers.

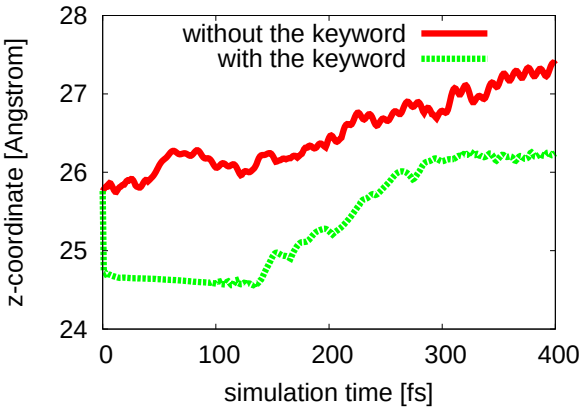

Figure 1: Time evolution of the topmost position of H atoms in PVdF. Solid and broken lines represent the results without and with the keyword "ESM.wall.position ON", respectively.

References

[1] http://www.openmx-square.org

Itinerant electronic states at rare-earth-magnet interfaces

Yoshihiro GOHDA*
Department of Physics, The University of Tokyo
Hongo 7-3-1, Bunkyo-ku, Tokyo 113-0033, Japan

Electrons in rare-earth magnets can be classified as two types: itinerant electrons and localized ones. Fe $3d$ as well as Nd $5d$ electrons are examples of the former, while Nd $4f$ electrons are the latter. In particular, itinerant magnetic states dominate interactions among magnetic sites directly. Thus, itinerant d states are expected to be sensitive to lattice strain, although the current status of the understanding on this issue is being far from complete, in particular for the magnetic anisotropy [1]. In this project, we have investigated strain effects on magnetic properties on the basis of density functional theory. We focused on $Y_2Fe_{14}B$ as shown in Fig. 1 (a), because Y is a prototypical rare earth element without having f electrons. First-principles calculations are performed using the OpenMX code [2], where pseudo-atomic orbitals and norm-conserving pseudopotentials are used.

We changed the lattice constants a and c from the equilibrium values in various manner. We found that the uniform compression enhances the perpendicular magnetic anisotropy. To clarify the origin of this enhancement, we developed a new method to decompose the magnetic-anisotropy energy into contribution from each atomic site as well as from couplings among specific atomic orbitals. This method employs second-order perturbation theory and an on-site approximation for the spin-orbit coupling: the exact form of the scalar triple product of the electric field, the electronic momentum, and the spin direction is approximated as the form of $\xi \boldsymbol{l} \cdot \boldsymbol{s}$ neglecting any off-site interactions. The coupling constant ξ is fixed to the atomic value [3]. The spatial parts of non-perturbed states are Kohn-Sham states obtained by calculations without spin-orbit coupling, whereas the spin part is rotated with the collinearity. As a result, we clarified that the Fe j_2 site plays a significant role in enhancing the magnetic anisotropy. Furthermore, couplings among $3d_{x^2-y^2}$ and $3d_{xy}$ components at this site contribute dominantly, where both the effect of the local density of states shown in Fig. 1 (b) and the matrix elements among atomic orbitals are essential. Our method enables us to study the interface anisotropy quantitatively.

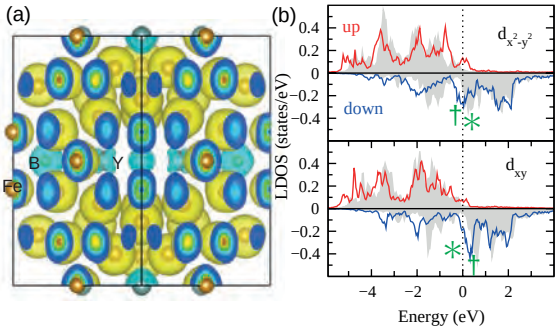

Figure 1: (a) Crystal structure and spin-density distribution of $Y_2Fe_{14}B$. (b) Local density of states (LDOS) projected onto $3d_{x^2-y^2}$ and $3d_{xy}$ components of the Fe j_2 site. The LDOS of the unstrained $Y_2Fe_{14}B$ are depicted by shades, whereas the strained ones are drawn by solid lines. Pairs of † and * indicates anisotropy coupling, respectively.

[1] S. Hirosawa *et al.*, J. Appl. Phys. **59**, 873 (1986).
[2] T. Ozaki, Phys. Rev. B. **67**, 155108 (2003).
[3] Y. Yanase and H. Harima, Solid State Phys. (in Japanese) **46**, 229 (2011).
[4] Z. Torbatian, Y. Gohda, T. Ozaki, and S. Tsuneyuki, in preparation.

*Present address: Department of Materials Science and Engineering, Tokyo Institute of Technology, J1-3, Nagatsuta-cho 4259, Midori-ku, Yokohama 226-8502, Japan

Expansion of the first principle electronic structure calculation with hybrid method

Takeo FUJIWARA
Center for Research and Development of Higher Education, University of Tokyo
Hongo, Bunkyo-ku, Tokyo 113-0033

The aim of our project is the developement of a method applicable to the large-scale molecular dynamics (MD) simulation and investigation of slow dynamics of new materials, such as solid state fast ion conductors.

(I) **Automatic parametrization for tight-binding molecular dynamics simulation method:** We propose the transferable tight-binding parametrization procedure,[1] based on the extended Hückel approximation and the charge self consistent scheme, and applied to the quantum molecular dynamics simulation for long-time dynamics of large-scale systems of liquid and solid fast ion conductors.

We have also developed the algorithm and coding program package for automatic determination of parameters of tight-binding method. This program will be open.

(II) **Dynamical behavior of lithium ions in thio-Lisicon:** Microscopic origin of the high conductivity at room temperatures in lithium superionic conductors has remained the fundamental un-solved problem, though the recent discovery of $Li_{10}GeP_2S_{12}$ took a great step toward the application of solid electrolytes.[1, 2, 3, 4, 5] We achieve long-time (2ns) tight-binding molecular dynamics simulations of $Li_{4-x}Ge_{1-x}P_xS_4$, and observe the diffusion process where lithium atoms collectively hop into neighboring lithium sites by kicking the lithium atoms occupying these sites out. Furthermore, it is found out that excess lithium atoms or doped lithium vacancies trigger a new diffusion process and drastically reduce the activation energy. We discuss the dynamic properties of lithium atoms in these materials, such as the diffusion constant, the activation energy and the diffusion path.

References

[1] S.Nishino and T.Fujiwara: "Parametrization scheme with accuracy and transferability for tight-binding electronic structure calculations with extended Hückel approximation and molecular dynamics simulations", J. Molecular Modelling. **19** (2013) 2363-2373 .

[2] T. Fujiwara, S. Yamamoto, S. Nishino and H. Yamasaki, "Electronic structures and characteristics of Li ionic positions in thio-LISICON by the first principles calculation", The 19th International Conference on Solid State Ionics, Kyoto, Japan, June 2 - 7, 2013.

[3] S. Nishino, T. Fujiwara, H. Yamasaki and S. Yamamoto, "Long Time Tight-Binding Molecular Dynamics Simulations of Li_4GeS_4", The 19th International Conference on Solid State Ionics, Kyoto, Japan, June 2 - 7, 2013.

[4] T. Fujiwara, S. Nishino H. Yamasaki, and S. Yamamoto, "Electronic structures and Li ion dynamics in thio-LISICON, Li_4GeS_4 and Li_3PS_4", International Symposium on Electronic-Structure Theories and Related Experiments, Stuttgart, Germany, 12-15 June 2013.

[5] S. Nishino, T. Fujiwara, S. Yamamoto, and H. Yamasaki, "Lithium Ion Dynamics in Li_4GeS_4 and Li_3PS_4", The 8th Pacific Rim International Congress on Advanced Materials and Processing, August, 2013, Hawaii, USA

[6] 西野信也, 藤原毅夫, 山崎久嗣, "固体電解質 $Li_{4-x}Ge_{1-x}P_xS_4$ におけるリチウム拡散機構", 日本物理学会, 2014 年 3 月 27 日-30 日、東海大学

Development of ab initio GW code

Kazuma Nakamura

Quantum Physics Section, Kyushu Institute of Technology,

1-1 Sensui-cho, Tobata, Kitakyushu, Fukuoka, 804-8550

Using ab initio GW calculations, we study plasmaron states of various materials. The plasmaron state is defined as a coupled state of free electron and plasmon. This state can observe as the ground state in a system which has "isolated low-energy bands" near the Fermi level. Electrons in materials interact via a long-ranged Coulomb interaction with each other, which can generate collective charge excitation, i.e., plasmon excitation. In general, the energy scale of the plasmon excitation is the order of 10 eV and therefore it is believed that such excitations are irrelevant to the low-energy physics of the order of 0.1-1 eV. However, in the isolated-band materials, low-energy bands around the Fermi level tend to isolate from other high-energy bands and, as a result, the Fermi velocity, or equivalently plasma frequency, is dominated by the bandwidth and occupancy of the isolated low-energy bands. Their bandwidth is ~1 eV and the plasma frequency is usually smaller than this value. In this case, this plasmon excitation can renormalize the bare band structure via the self-energy effect and generate a coupled state of free electron and plasmon.

In this report, we present a study for the low-energy plasmaron state of two compounds with the isolated low-energy band structure: One is an organic compound $(TMTSF)_2PF_6$ [1], and the other is the transition metal oxide $SrVO_3$. Both materials are known as a strongly correlated system and effects of onsite Coulomb repulsion on the electronic structure has actively been discussed. On the other hand, for these materials, the low-energy plasmon excitation are experimentally observed in electron energy loss spectroscopy (0.4-1.0 eV for $(TMTSF)_2PF_6$ and 1.4 eV for $SrVO_3$). The bandwidth estimated by density-functional calculations are 1.2 eV for $(TMTSF)_2PF_6$ and 2.7 eV for $SrVO_3$, and thus, the plasmon-excitation energy are smaller than the bandwidth. So, it is interesting to calculate the self-energy effect due to the plasmon excitation with the GW approximation calculations from first principles. To this end, we have developed a GW code based on the plane wave basis set with the pseudopotential approximation, and calculated the spectral function to see the formation of the plasmaron state. The code is massively parallelized, capable to treat huge systems such as organic compounds. All Calculations were done at Supercomputer center at Institute for Solid State Physics, University of Tokyo.

Figure 1 is our calculated reflectance as a function of frequency of $(TMTSF)_2PF_6$ ((a)) and $SrVO_3$ ((b)). The drop from 1 to 0 specifies the plasma frequency. For $(TMTSF)_2PF_6$, the values are 1.0 eV for the E//x polarization right (red) and 0.4 eV for the E⊥x one (green). For $SrVO_3$, the value is 1.4 eV. We found that our spectra well reproduce the experimental ones.

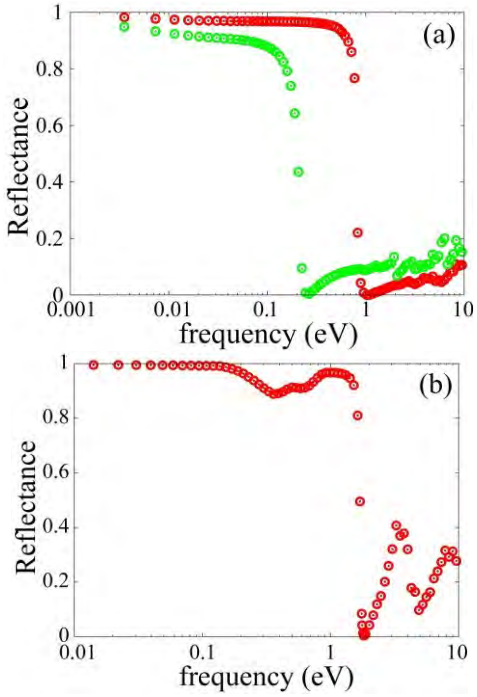

Fig.1 Calculated reflectance of $(TMTSF)_2PF_6$ (a) and $SrVO_3$ (b). In (a), red and green describe results for the E//x and E⊥x polarization rights, respectively.

Figure 2 is the GW spectral function of $(TMTSF)_2PF_6$ ((a)) and $SrVO_3$ ((b)). The density-functional band and the Fermi level are drawn by red and yellow solid lines, respectively. The bright regions below the occupied bands and upper the unoccupied ones indicate the formation of the plasmaron states.

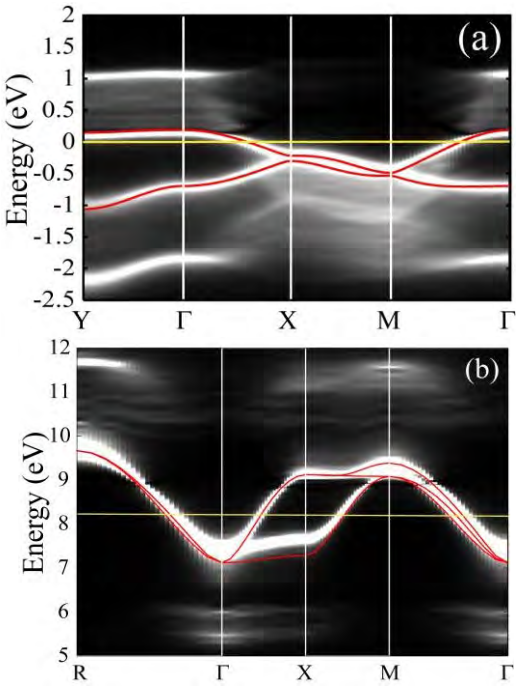

Fig,2 Calculated GW spectral function of $(TMTSF)_2PF_6$ (a) and $SrVO_3$ (b). Red curves is the density-functional results.

In summary, we find low-energy plasmon excitations comparing to the energy scale of the bandwidth for the "isolated-low-energy-band" materials, reproducing experimental reflectance. By calculating GW self energy and spectral function, we find that this low-energy plasmon excitation leads to the formation of the plasmaron states.

[1] K. Nakamura, S. Sakai, R. Arita, and K. Kuroki, Phys. Rev. B 88, 125128 (2013)

Study on physicochemical properties for proton conductivity in lanthanum tungstate

Yohei Shono, Junichiro Otomo

Department of Environment Systems, Graduate School of Frontier Science,

The University of Tokyo, Kashiwa-no-ha, Kashiwa, Chiba 277-8581

Fuel cells have been taught to be a promising alternative power source these days. As commercial products, polymer electrolyte fuel cells (PEFC) and solid oxide fuel cells (SOFC) have been developed in past years, however, both of the fuel cells still have some serious problems in terms of material durability and power generation efficiency. In this sense, intermediate temperature fuel cells (ITFC) with proton conducting solid electrolyte have been proposed, which is expected to have high material durability and power generation efficiency. Nevertheless, there is no promising proton conducting solid electrolyte for ITFC, which should be developed further.

In the previous studies [1-3], there have been some reports about Lanthanum tungstate (LWO) as a promising candidate for proton conducting solid electrolyte for p-ITFC. LWO was reported to have intrinsic oxygen vacancies in its crystal structure, resulting high proton conductivity. Although these reports on crystal structure in LWO, there have been no report on proton conducting mechanism in LWO crystal structure.

In this study, we investigate the proton conducting mechanism in LWO using density functional theory (DFT) and nudged elastic band (NEB) method. DFT calculations were carried out with the SIESTA code [4]. The double-ζ split-valence basis set with polarization orbitals (DZP) was used in the calculations. The generalized gradient approximation (GGA) using the RPBE functional [5] was used as the exchange correlation function, and k-points were sampled with 2×2×2 grids using the Monkhorst–Pack method [6]. Crystal structures were optimized until the maximum atomic forces became smaller than 0.04 eV/Å. We also calculated the proton-conducting barriers in LWO with the NEB method [7] using the revised SIESTA code developed by Ohto et al [8]. Crystal structures were visualized with VESTA software [9]. All calculations in this study were carried out in System B in the super computer center of Institute for Solid State Physics, using 32 to 64 MPI parallel calculations.

Before study on the proton diffusion mechanism in LWO, the crystal structures of LWO70 ($La_{28}W_4O_{56}$) and LWO54 ($La_{27}W_5O_{56}$) were optimized with the conjugated gradient method. The results indicated that the crystal structure of LWO54 is more stable than that of LWO70. This result is consistent with the reported experimental results; LWO can be synthesized only when the La/W ratio is lower than 5.7 [1].

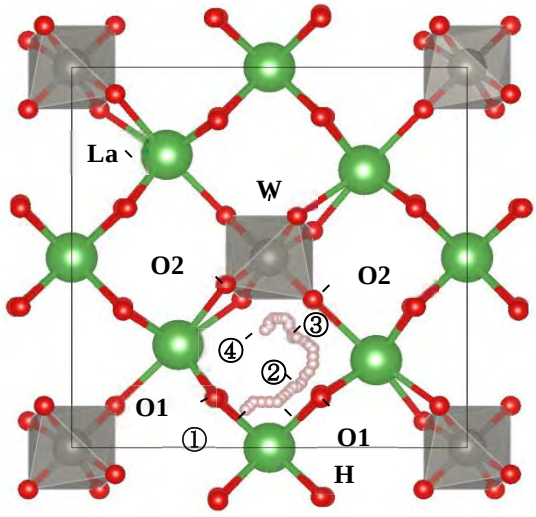

Figure 1. Projected crystal structure of LWO70 with proton diffusion paths calculated in this study.

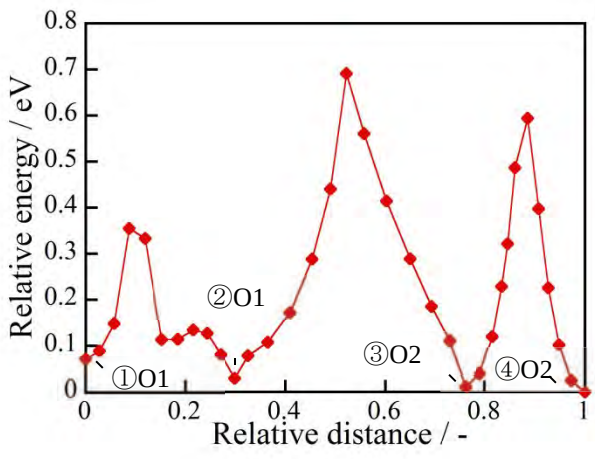

Figure 2. The results of NEB calculation for proton diffusion in LWO70.

To investigate the proton diffusion barrier in LWO, we employed the NEB method and in the LWO70 crystal structure as shown in Figure 1. Because of the locally distorted crystal structure of LWO, there are many possible proton diffusion paths in LWO70. To simplify the calculations, we employed oxygen at the O2 site with average O1–O2 and O2–O2 distances (see Figure 1). Figure 2 shows the results of the NEB calculations. The calculated relative energy was plotted as a function of the relative distance. As shown in Figure 2, the barrier of proton diffusion in the O1–O1 jump is the lowest among the considered paths. This result means that, in the LWO70 crystal structure, long-range proton conduction most likely to occur as O1–O1 jumps, rather than O1–O2 and O2–O2 jumps. Thus, protons in LWO diffuse over a long range through cycles of O1–O1 jumps until becoming trapped in other O2 sites.

The results from the DFT calculations in this study explain the reported experimental observations well. To improve the proton conductivity in LWO, the proton concentration should be increased without disturbing the proton-conducting paths around the O1 sites next to La atoms.

References

[1] A. Magrasó et al.: *Dalton Trans.*, **46,** (2009) 10273-10283.

[2] A. Magrasó et al.: *J. Mater. Chem.*, **22(5),** (2012) 1762-1764.

[3] A. Magrasó et al.: *J. Mater. Chem. A*, **1,** (2013) 3774-3782.

[4] J. M. Soler et al.: *J. Phys.: Condens. Matter.*, **14,** (2002) 2745-2779.

[5] Y. Zhang, W. Yang: *Phys. Rev. Lett.*, **80**(4), (1998) 890.

[6] H. J. Monkhorst and J. D. Pack: *Phys. Rev. B*, **13**, (1976) 5188-5192.

[7] G. Henkelman et al.: *J. Chem. Phys.*, **113 (22),** (2000) 9901-9904.

[8] T. Ohto et al.: *Phys. Rev. B*, **87**, (2013) 205139.

[9] K. Momma, F. Izumi: *J. Appl. Crystallogr.*, **44**, (2011) 1272-1276.

Synthesis of proton conducting electrolyte and evaluation of ion conductivity of interfaces

Aki Iwanaga, Junichiro Otomo

Department of Environment Systems, Graduate School of Frontier Sciences,The University of Tokyo,5-1-5 Kashiwanoha, Kashiwa, Chiba 277-8563, Japan

Proton conducting intermediate temperature fuel cells with proton-conducting solid electrolyte (p-ITFC) have been proposed, which is expected to have high material durability and power generation efficiency. In order to utilize it, it is needed to improve its efficiency. For this mission one of the bottleneck is proton conductivity of electrolyte. To improve proton conductivity, I focused on hetero interface between other kinds of electrolytes. There are some reports that oxide ion conductivity was promoted in hetero interface, so in this study I try to check if promotion of proton conductivity in hetero interface occur or not.

As electrolyte SrZrO3 and SrTiO3 was chosen. To think what happens in hetero structure, there are some phenomenon that affect to proton conductivity. One is segregation of dopant. It was proved by a experiment[1] that dopants segregate in hetero structure. In this study energy level and proton diffusion in SZO was investegated using density functional theory (DFT) and nudged elastic band (NEB) method. DFT calculations were carried out with the SIESTA code[2].The double-ζ split-valence basis set with polarization orbitals (DZP) was used in the calculations. The generalized gradient approximation (GGA) using the RPBE functional[3] was used as the exchange correlation function, and k-points were sampled with 2×2×2 grids using the Monkhorst–Pack method [4].

First, energy level of system in which dopants are segregated and non-segregated were compared. Then proton diffusion barrier was calculated in both system using nudged elastic band method.

Because two electrolytes are also n-type and p-type semiconductor, there is a p-n junction in hetero interface. If the electric field affects level of the system was studied.

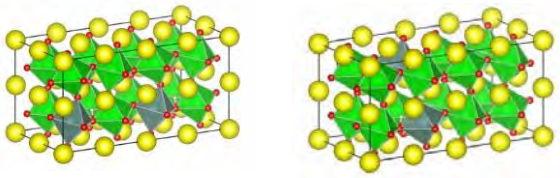

Fig1. 12.5%Ydope SrZrO3; (left) dopant is segregated; (right) Y is not segregatedenergy

sample	DFT total energy (eV)	Potential (eV)	Binding (eV)	Binding/cell (eV)
Non-segregated	-13985.3	-12767.3	-1218.0	-152.2508
segregated	-27970.6	-25534.6	-2436.0	-152.2503

Table 1. energy level of 12.5% Y dope SrZrO3

The picture of the system and their energy level were showed in Fig.1 and Table1. In segregated and non-segregated system, energy levels were almost same. Electric field also did not affect to energy level.

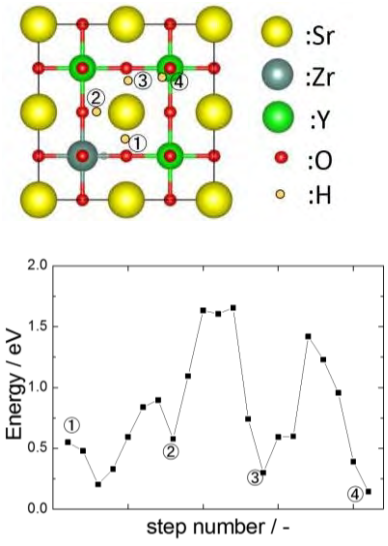

Fig2. Proton diffusion barrior

Proton diffusion barrier is shown in Fig.2. Proton diffusion barrier around dopant is low comparing with other area depart from dopant. From this result, segregated dopant

may have good effect to proton conductivity.

In order to find the reason why ionic conductivity is promoted around hetero interface, further study is needed. Other reasons for promotion of proton conductivity are distortion of lattice structure caused by lattice mismatch, and generation of new diffusion pathway. These possibilities are needed to be checked.

Reference

[1] P.F. Yan et al.:Solid State Ionics 31-37 (2012) 222-223

[2] J. M. Soler et al.: J. Phys.: Condens. Matter., 14, (2002) 2745-2779.

[3] Y. Zhang, W. Yang: Phys. Rev. Lett., 80(4), (1998) 890.

[4] H. J. Monkhorst and J. D. Pack: Phys. Rev. B, 13, (1976) 5188-5192.

[7] G. Henkelman et al.: J. Chem. Phys., 113 (22), (2000) 9901-9904.

First-principles study for adsorbed metallic atoms on quasicrystal surface

Kazuki NOZAWA
Department of Physics, Chuo University
Kasuga, Bunkyo-ku, Tokyo, 112-8551

Quasicrystals (QCs) are long-range ordered materials with rotational symmetries incompatible with the translational symmetry operation. More than 100 binary or ternary metallic QC systems have been found so far, but there is no report about the single-element QC. Recently, it was reported that Pb atoms deposited on a five-fold surface of a ternary QC Ag-In-Yb show different quasiperiodic arrangement depending on deposition time, implying a possibility of forming a multi-layered quasiperiodic film.

We carried out first-principles density functional calculations to determine the adsorption structure of Pb atoms on the Ag-In-Yb QC surface. To handle the aperiodic surface within the first-principles calculation, we used a slab model composed of a disc-shaped cluster with 30Å diameter and 4Å thickness as a model of the five fold surface of the Ag-In-Yb QC. The topmost layer is chosen to intersect the center of the rhombic triacontahedral cluster, which is a structural building unit of this QC, and the atomic positions are extracted from a X-ray diffraction data of isostructural Cd-Yb QC. In order to avoid decreasing accuracy of calculation at the cluster edge, we evaluated adsorption energy as the difference of cohesive energies between adsorbed- and non-adsorbed-systems calculated using a cluster, which is centered at each calculated site. Interactions between ionic cores are approximated using the projector-augmented wave potentials, and the GGA-PBE functional was employed for the exchange-correlation term. A 40Å×40Å×18Å tetragonal super-cell is used to isolate each cluster by sufficient vacuum layer and the gamma point is used for Brillouin-zone sampling. The MPI parallelization method is used to speed up the calculation.

Calculation reveals that experimentally observed quasiperiodic patterns are made from Pb atoms adsorbed at different height from the surface. Additional layers, which were not observed in STM experiments but confirmed by XPS experiment afterward, are found and it was demonstrated that those layers play important role for stabilization of the layered structure. Furthermore, it was determined that the adsorbed Pb atoms occupy the atomic sites of the Ag-In-Yb QC used as a template, meaning Pb atoms are stacking with imitating the crystal structure of the template. Because there are some unoccupied atomic sites, the adsorption height of Pb atoms does not correspond exactly to the atomic sites of QC, but the lateral position is completely agree with the atomic sites of QC. The obtained structure does not have sufficient thickness yet, but this is the first instance of crystal growth of a single element quasicrystal [1].

References

[1] H. R. Sharma, K. Nozawa, J. A. Smerdon, P. J. Nugent, I. McLeod, V. R. Dhanak, M. Shimoda, Y. Ishii, A. P. Tsai, R. McGrath, Nat. Commun., **4**, (2013) 2715.

Local structure of organo-complexes adsorbed on metallic surfaces

Ken-ichi SHUDO

Faculty of Science/Engineering, Yokohama National University

Tokiwadai 79-5, Hodogaya-ku Yokohama 240-8501 JAPAN

Our group observed real-time molecular vibration adsorbed on metal surface using ultrafast pulse lasers. [1] The very high optical sensitivity even at the monolayer film is ascribed to surface enhancement of Raman scattering (SERS) [2] if the substrate surfaces are inhomogenious [3]. Fourier spectra of pyridine adsorbed on Ag nanoclusters (estimated diameter is 50 nm), peaks shifted due to the adsorption and lifetime of the vibronic decay changes according to the colloidal density.

For the cluster models (Fig. 1), we estimated the peak shifts with diagonalization of potential matrices obtained by means of first principles calculation. The eigenfrequencies, corresponding to the experimentally stringest optical peak, shift to the lower energy on the flat surface, while at the vortex site this shifts to the higher energy. This accounts for the observed result that the peak splits into two components.

In the case of 15-carboxyl-1-pentadecanetiol adsorbed to the Ag nanoclusters, transient peak shifts in the time-windowed spectra are suggested to be corresponding to the femtosecond-scale vibronic propagation from Ag to carbon chain, in comparison with the calculated eigenfreqiencies.

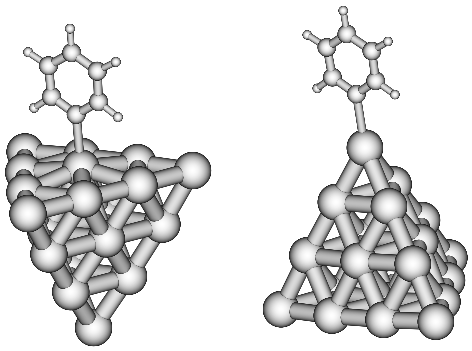

Fig. 1 Cluster model of pyridine adsorbed on a flat surface (left) and at the vortex-atom (right).

References

[1] K. Shudo, I. Katayama, S. Ohno (eds): "Frontiers in Optical Methods: Nano-Characterization and Coherent Control" (2013, Springer-Verlag GmbH, Berlin/ Heidelberg) ISBN 978-3-642-40593-8

[2] J. Takeda, K. Ikufumi, K. Shudo, M. Kitajima: Journal of Luminescence, *in press* (2014).

[3] M. Shindo, T. Sawada, K. Doi, K. Mukai and K. Shudo: J. Phys.: Conf. Ser. **441**, 012044 pp.6 (2013).

First Principles Based Analysis of Electronic Structures and Reactions on Surfaces/Interfaces

Yuji KUNISADA

Center for Advanced Research of Energy and Materials, Faculty of Engineering, Hokkaido University, Sapporo, Hokkaido 060-8628

We investigated the electronic structures and reactions on surfaces/interfaces, with the aid of the first principles calculation based on the density functional theory (DFT). In addition, we developed the quantum state calculation code for atomic nuclei to consider the quantum mechanics behaviors of the hydrogen isotopes (H, D, T, muonium).

At first, we investigated the electronic structures of Pd/ZnO interfaces, which is considered as prospective materials for electronic devices. [1] The full-potential linearized augmented plane wave (FLAPW) calculation based on DFT was carried out through WIEN 2k [2] on F16 queue in system B. We installed parallelized WIEN 2K with Intel® MPI Library and Intel® Math Kernel Library. We calculated the O-K edge electron energy-loss spectra at Pd/ZnO interfaces with the corresponding supercell, which consists of 108 atoms. We found that the sharp peak, which corresponds to the bonding orbitals formed by the overlapping of Pd 4d and O 2p orbitals, appears in the vicinity of 530 eV energy loss. This result shows the good agreement with our experimental O-K edge electron energy-loss spectra. Thus, we could determine electronic structures of Pd/ZnO interfaces from the results from first principles calculation and electron energy-loss spectroscopy (EELS) experiment.

We also investigated the hydrogen isotope adsorption states on fcc Fe(111) surfaces to understand the hydrogen embrittlement mechanism of iron-based steels. We adopted the slab model with 2x2 fcc Fe(111) five atomic layers. We obtained the potential energy surfaces (PES) of H/fcc Fe(111) systems through the repeated ab initio total-energy calculations with various adsorption configurations. We performed the repeated ab initio total-energy calculations with Vienna Ab initio Simulation Package (VASP) [3-6] on P1, F4, F8 and F16 queue in system B. We installed parallelized VASP with Intel® MPI Library and Intel® Math Kernel Library. We consumed most of our budget to obtain the PES, because we have to calculate more than 10,000 ab initio total-energy calculations with various parameters. When we calculated the corresponding PES, we set 12x12 grids for in-plane direction and 26 grids for the direction perpendicular to the surface. We also performed

the quantum state calculations for the hydrogen isotopes to consider the quantum mechanics behaviors of hydrogen isotopes due to their small mass. We adopted the Gaussian basis for the wave function of hydrogen isotopes. [7] In order to obtain the three-dimensional quantum states of hydrogen isotopes on fcc Fe(111) surfaces, we solved the Schrödinger equation for atomic nuclei based on the corresponding PES results. The corresponding eigenstates and eigenenergies includes the influence of non-locality and zero-point energies. The diagonalization of up to 40500x40500 matrix was performed on P1 and F4 queue in system B to obtain the hydrogen isotope adsorption states on 2x2 fcc Fe(111) surfaces. In order to fasten our original code with the large scale diagonalization, we applied appropriate optimization and parallelization with Intel® MPI Library and Intel® Math Kernel Library. From these calculations, we found H and muonium show the delocalized adsorption states on the fcc Fe(111) surfaces.

References

[1] N. Sakaguchi, K. Watanabe, and Y. Kunisada: Kenbikyo **48** (2013) 195.

[2] P. Blaha, K. Schwarz, G. Madsen, D. Kvasnicka, and J. Luitz, WIEN 2k, Augmented Plane Wave + Local Orbitals Program for Calculating Crystal Properties, Vienna, Austria, 2001.

[3] G. Kresse and J. Hafner: Phys. Rev. B **47** (1993) 558.

[4] G. Kresse and J. Hafner: Phys. Rev. B **49** (1994) 14251.

[5] G. Kresse and J. Furthmüller: Comput. Mat. Sci. **6** (1996) 15.

[6] G. Kresse and J. Furthmüller: Phys. Rev. B **54** (1996) 11169.

[7] N. Ozawa, T. Roman, H. Nakanishi, W. A. Diño, and H. Kasai: Phys. Rev. B **75** (2007) 115421.

Dissociation mechanism of multiple-charged molecules irradiated by X-FEL: first-principles molecular-dynamics simulation

Satoshi Ohmura

Department of physics, Kyoto University, Sakyo-ku, Kyoto, 606-8502

With the advent of X-ray free electron laser (X-FEL), many interesting phenomena in which molecules are highly charged due to strong laser fields were observed. The highly charged molecules are quite unstable because of the Coulomb repulsive force and destroyed on a subpicosecond (Coulomb explosion). Recently, dissociation of several highly-charged aromatic molecules has been investigated by position-sensitive time-of-flight measurements. These studies suggest that the momenta of the fragment ions after the explosion reflects the structure of the parent molecules even for the dissociation channels for which the dissociations are not described by the simple Coulomb explosion model. For the application of Coulomb explosion such as Coulomb explosion imaging, it is highly desirable to clarify the charge state dependence of dissociation mechanism in coulomb explosion.

In this study, we performed *ab initio* molecular dynamics simulation to clarify the details of coulomb explosion mechanism of aromatic molecules. We took particular note of the charge-state dependence of the explosion mechanism.

The target system is the 4-bromophenol, in which a bromine atom and a hydroxyl group are located on the opposite sides of the carbon ring. To calculate charged molecular system in reciprocal space, we used cluster boundary conditions imposed with the method of Martyna and Tuckerman [1].

From our simulation, it is found that the dissociation mechanism has charge-state dependence. When the charge state is 6 or 7, one or two hydrogen atoms dissociate in the first stage (at times shorter than 20 fs after the molecule takes charges) while all hydrogen atoms dissociate when the charge state is over 7. After the hydrogen dissociation, the carbon ring breaks up. The mechanism of the carbon-ring breaking also has charge-state dependence. When the charge state is 6 or 7, the ring breaks with molecular expanding. On the other hand, molecule shrinks during the ring breaking when the charge state is over 7.

References

[1] G. J. Martyna, *et al., J. Chem Phys* ***110*** *(1999) 2810*

[2] S. Ohmura *et al., J. Phys.: Conf. Ser. accepted*

Large scale *ab initio* calculations on the fundamental processes of energy convergence devices and on their optimization for high conversion efficiency

Koichi Yamashita

Department of Chemical System Engineering,

The University of Tokyo, Hongo, Bunkyo-ku, Tokyo 113-8656

1. *ab initio* study of fast Na diffusion in Na_3P

Considering the limited resource of lithium, Na ion batteries are the attractive alternative due to the abundant resource of Na. So far the amorphous red P and carbon nanocomposite has been shown to be a very promising anode material for Na ion battery. Ionic conductivity and electronic conductivity are the critical factors that determine the speed of charging and discharging process. In this study, *ab initio* calculation was used to study the ionic conductivity and electron property in the fully charged state of P (Na_3P). This study aims to theoretically estimate the electrochemical performance of P as anode in the discharge process.

The density functional theory (DFT) calculations were performed with VASP. The electron-ion and electron-electron interactions have been described by PAW potentials and the GGA exchange-correlation functional of PBE, respectively. The Nudged Elastic Band method was employed to find the saddle point and minimum energy paths for Na diffusion.

We found that three possible independent and asymmetric Na diffusion paths exist. In the first two, Na diffusion occurs within the same kind of sodium atom; while in the third path, Na diffusion occurs within sodium atoms of different kind. Moreover the activation energies of Na diffusion in the first two paths are much smaller than that of the third. Besides, with the introduction of Na vacancy, a hole state deep in the valence region appears which is responsible for the valence band-edge raising in the center of the Brillouin zone. This sodium vacancy is very likely to play a role in the electron transfer in Na_3P. The fast ionic conductivity and considerable electronic conductivity make P a promising anode material in the first step of Na de-intercalation process.

2. The role of methylammonium cation in the organic-inorganic lead iodide

Several papers have been recently appeared in literature reporting the enhanced photoconversion efficiency (PCE) up to 15% for solar cells formed by sandwiches of perovskite compounds, i.e the light harvester, mesoporous TiO_2, and a polymeric hole conductor. The usage of these 3D $MAPbX_3$ (MA= methylammonium, $CH_3NH_3^+$, X=halide, Cl-, Br-, I-) perovskites, is strictly dependent by

their chemical stability and optimal transport characteristics in the device. It is astonishing, anyway, that materials with so high applicability in PV and with many undisclosed features still find scarce attention among theoreticians. We here disclose and characterize such class of lead-iodide organic-inorganic mixed perovskites.

DFT calculations are performed with VASP and SIESTA . The electron-ion and electron-electron interactions have been described by projector augmented waves potentials and the GGA exchange-correlation functional of Perdew-Burke-Ernzerhof, for the former, Plane Wave based, approach. Atomic Orbitals are at variance used in the case of SIESTA, still through a pseudopotential approach.

We performed a theoretical estimation of effective masses of photocarriers in the pseudocubic $CH_3NH_3PbI_3$, both with and without taking into account spin−orbit coupling effects. Predicted values of photogenerated electrons and holes are comparable to those for silicon used in inorganic commercially available solar cells[1].

3. *ab initio* study on the electronic double layer of transition metal oxide and water interface

Interface structure of electrocatalysts and water plays important role on electrochemical reaction. Attempts to reveal interface structure and distribution of potentials have been made both theoretically and experimentally, however they are still challenges because of the complicated system of electrochemistry. Our research interest lies in an interface structure of RuO_2/water as an (photo)electrocatalysts for oxygen evolution reaction under given pH and electrode potential. The basic concept of the method used in this research is comparing Gibbs Free energies of many different interface structures including effects of pH and electrode potential to find the most stable one.

All the calculations were performed with GPAW Software with PAW setups. We used GGA/RPBE functional. RuO_2/water interfaces are modeled by 4layer slab RuO_2(110) and surface proton concentrations range from 2.0 to 0.0. In case of high coverage conditions, we classified the water structure by their orientations as up (proton is pointing out from the RuO_2 surface), parallel and down (proton is pointing to surface).

The results demonstrated that in the range of low potential region (~0.5 V), almost all surface oxygen atoms become water and in the region around 1.0 V, rapid de-protonation occurs. The difference between acid and base conditions is the water orientation in low potential region. These results are in good agreement with experimental ones. From our studies, it can be proposed that the mechanism of oxygen evolution reaction is different between electrochemical condition (around 1.5 V) and photoelectrochemical condition (expected at low potential region), and between acid and base conditions.

References

[1] G. Giorgi, J.-I. Fujisawa, H. Segawa, K. Yamashita: J. of Phys. Chem. Lett. **4** (2013) 4213.

Theoretical analyses for thermal conductance of interfaces of the gold surfaces and self-assembled monolayers

Koichi Yamashita

Department of Chemical System Engineering,

The University of Tokyo, Hongo, Bunkyo-ku, Tokyo 113-8656

Self-assembled monolayers (SAMs) which have stable and well-order structures are expected as candidates of materials for nanoscale devices. Thermal properties of the interface have particularly attracted attention because they are related to various functions, such as thermal storages and thermal transistors. It is, therefore, required to elucidate the thermal properties of the SAM-metal structures.

This study aims to analyze the structural effects on the thermal properties at the interface of the SAMs sandwiched between gold substrates. For this purpose, we attempted to perform the thermal transport calculations for the SAM-gold-substrate-systems by using the non-equilibrium Green's function (NEGF) method. In particular, we focused on the effects of the anchor atoms sticking to the gold substrates.

In the last year, we investigated of stability of some structures of the SAM-gold-substrate-systems in which sulfur atoms were adopted as the anchor atoms like previous studies [1,2]. For the gold substrates, clean (1 1 1) surfaces were used (Fig. 1). Structural optimizations were performed by using SIESTA [3] with the local density approximation.

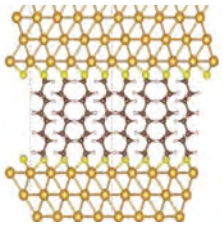

Fig. 1 A structure of the SAM-gold-substrate.

As a result, we have revealed that the adsorption structure is not so stable. Namely, the sandwich structures can be easily collapsed and stable carbon chains are not retained. This instability seems to result from that the van der Waals (VdW) interactions between the carbon chains were not considered explicitly. Therefore, we are planning to investigate VdW effects on the structural stability by using the latest unstable version of SIESTA which is able to consider the VdW interactions explicitly. Then, thermal properties should be investigated by the NEGF.

References

[1] M. D. Losego, M. E. Grady, N. R. Sottos, D. G. Cahill, P. V. Braun: Nat. Mater. **11** (2012) 502.

[2] T. Frederiksen, C. Munuera, C. Ocal, M. Brandbyge, M. Paulsson, D. Sanchez-Portal, A. Arnau: ACS Nano **3** (2009) 2073.

[3] J. M. Soler, E. Artacho, J. D. Gale, A. García, J. Junquera, P. Ordejón, D. Sánchez-Portal : J. Phys. Condens. Mater. **14** (2002) 2745.

First-principles study on the defects in semiconductors

Jun YAMAUCHI
Faculty of Science and Technology, Keio University
3-14-1 Hiyoshi, Kohoku-ku, Yokohama-shi, Kanagawa 223-8522

As the size of devices on integrated circuits decreases, the behavior of dopant atoms make relatively larger effect on the device performance. Especially, it is very important to understand the unfavorable defects including the dopant atoms. The experimental observations on each defect is extremely difficult. One of the major difficulties for detecting dopant configurations is the very weak signals from the defects of very low concentration comparing to those from the matrix semiconductors. However, recently, as a solution for the above problem, it is suggested to use powerful synchrotron radiation facilities to measure the X-ray photoelectron spectroscopy (XPS) signals of defects. On the other hand, there have been few reliable first-principles core-level XPS calculations for impurity defects in semiconductors, because the local potential boundary condition of defect model systems has not yet been sufficiently evaluated. To obtain reliable shifts in the XPS binding energy, it is necessary to take a sufficiently large supercell for a defect.

We carried out a comprehensive study on the arsenic (As) 3d core-level XPS binding energies for As defects in crystalline Si using a first-principles calculation with careful evaluation of the local potential boundary condition for the model system, where convergence within 0.1 eV was confirmed for the supercell size. The code used in this study is xTAPP, which is a hybrid paralleled density functional theory calculation program with plane-wave basis[1]. Figure 1 shows the calculated As 3d core level XPS binding energies for the As defects in silicon crystals. It is found that the experimentally observed spectra (∼1.2 eV) is explained by the combination defects of substitutional As atoms and a vacancy[2].

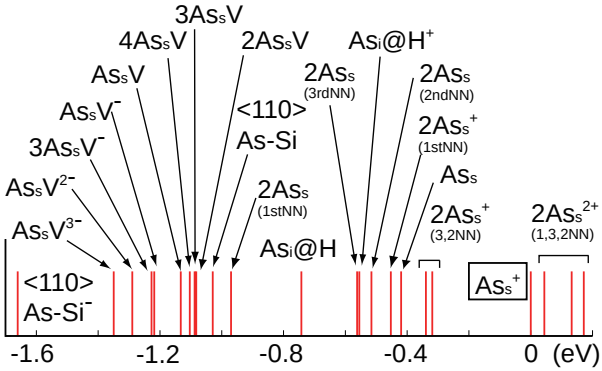

Figure 1: Calculated As 3d core level XPS binding energies for the defects in silicon crystals. The origin of the binding energy is that of the ionized substitutional As, which is surrounded by a square.

References

[1] xTAPP (eXtended Tokyo Ab initio Program Package) (http://frodo.wpi-aimr.tohoku.ac.jp)

[2] H. Kishi, M. Miyazawa, N. Matsushima, and J. Yamauchi: AIP Conf. Proc. **1583** (2014) 226.

Exploring low-dimensional honeycomb nano materials

Noriaki TAKAGI[1], Ryuichi ARAFUNE[2], Mao KANNO[1], and Emi MINAMITANI[3]

[1]*Department of Advanced Materials Science, University of Tokyo*

Kashiwa-no-ha, Kashiwa, Chiba 277-8561,

[2]*International Center for Materials Nanoarchitectonics, National Institute for Materials, Science, 1-1 Namiki, Ibaraki 304-0044,*

[3]*RIKEN, 2-1 Hirosawa, Saitama 351-0198, Japan.*

Since the discovery of exotic graphene, unraveling the hidden properties of honeycomb lattice materials is of great importance. Silicene, a two-dimensional honeycomb sheet of consisting of Si atoms, has attracted lots of attention. It is theoretically predicted that a freestanding silicene possesses Dirac fermion features [1] and that silicene is also topological insulator due to the sizable spin-orbit coupling [2].

We investigated the stability of silicene on Cu(111) covered with a hexagonal boron nitride (h-BN) layer by using density functional theory (DFT) calculations. The DFT calculations were carried out by the plane-wave-based Vienna Ab initio Simulation Package (VASP) [3, 4] with the projected augmented wave method [5]. The silicene on h-BN/Cu(111) was modeled by using a supercell which consists of a silicene layer lying on h-BN layer on top of a 5-layer Cu slab with a vacuum of 15 Å thick along the surface normal. The supercell are composed 35 Cu, 7 B, 7 N and 6 Si atoms. The positions of atoms in silicene, h-BN, and top four layers of Cu slab were optimized without any constraint until the forces on individual atoms were less than 0.01 eV/Å. Inroder to weak interface couplings, van dear Waals correction was included. From the total energy calculations for various configurations of silicene lattice relative to the h-BN lattice, we found that the silicene is stable, and that Dirac fermion feature survives similarly to the freestanding silicene. These results demonstrate that the h-BN/Cu(111) is a promising candidate for realizing Dirac fermion silicene.

Reference

[1] S. Cahangirov et al.: Phys. Rev. Lett. **102**, 236804 (2009).

[2] M. Ezawa, Phys. Rev. Lett. **109**, 055502 (2012).

[3] G. Kresse and J. Furthmüller: Phys. Rev. B **56** (1996) 11169.

[4] G. Kresse and J. Furthmüller: Comput. Mater. Sci. **6** (1996) 15.

[5] P. E. Blöchl: Phys. Rev. B **24** (1994) 17953.

Spin state of organic molecules on solid surfaces

Noriaki TAKAGI[1] , Ryouichi HIRAOKA[1] and Emi MINAMITANI[2]
[1]*Department of Advanced Materials Science, University of Tokyo*
Kashiwa-no-ha, Kashiwa, Chiba 277-8561
[2]*RIKEN, 2-1 Hirosawa, Saitama 351-0198, Japan.*

Manipulating quantum state of matter is central issue in condensed matter physics and material science. Scanning tunneling microscopy (STM) junction where a single molecule connects with two electrodes, i.e., an STM tip and a substrate, is a model of single molecule quantum dot. By changing the tip-molecule distance to tune coupling strengths of the molecule with the two electrodes, the STM junction offers a possibility to manipulate the quantum state of the molecular dot.

We tried to manipulate the Kondo resonance states of iron(II) phthalocyanine (denoted as FePc) on Au(111) [1,2] experimentally by precisely controlling the tip-molecule distance. When the tip was far away from the FePc molecule on Au(111), a Fano-Kondo (F-K) antiresonance was observed. As the tip approached to the central Fe ion of the molecule, the F-K antiresonance gradually became symmetric and a pair of conductance steps appeared in the dI/dV spectrum finally when the tip touched with the molecule. This spectral evolution was reversibly observed when the tip moved away from the molecule. These results indicate that the Hamiltonian of the molecular quantum dot is changed from Kondo-type to the zero field splitting type and vise versa by the perturbation of the tip.

In order to understand the reversible spectral evolution, we calculated the geometric structure, electronic structure and spin state of FePc in the STM junction by the plane-wave-based Vienna Ab initio Simulation Package (VASP) [3, 4] with the projected augmented wave method [5]. The STM junction was modeled by using a supercell. The STM tip was modeled by a 6-layer trigonal pyramid consisting of 56 Au atoms. The FePc molecule is located on a four-layer Au slab. To describe the Coulomb interaction at the Fe ion, we used local density approximation + U method. We calculated two limiting configurations. One is the configuration where the tip is

1.5-nm apart from the molecule such that the coupling of the tip with the molecule is negligible. The other is the configuration where the tip is contacted with the Fe ion in the molecule. When the tip is far away, the position of the Fe ion is slightly displaced into the substrate and the electronic charges are accumulated in between the molecule and Au substrate. In the contact configuration, the Fe ion moves to the tip and the electron charge accumulation is reduced at the molecule-substrate interface and instead appears at the tip-molecule contact region. In addition, the spin states of Fe ion for both configurations are not drastically changed. These calculated results partly explain the spectral evolution observed experimentally, and indicate that the position of the Fe ion is a key to understand the reversible switching of the Hamiltonian.

Reference

[1] N. Tsukahara *et al*.: Phys. Rev. Lett. **106** (2011) 187401.
[2] E. Minamitani *et al*.: Phys. Rev. Lett. **109**, 086602 (2012).
[3] G. Kresse and J. Furthmüller: Phys. Rev. B **56** (1996) 11169.
[4] G. Kresse and J. Furthmüller: Comput. Mater. Sci. **6** (1996) 15.
[5] P. E. Blöchl: Phys. Rev. B **24** (1994) 17953.

First-Principles Study of Magnetic Materials and Magnetism

Takashi MIYAKE
Nanosystem Research Institute, AIST, Umezono, Tsukuba, Ibaraki 305-8568

Rare-earth magnet $NdFe_{11}TiN$ [1]

Performance of a hard magnet is characterized by magnetization and coercivity, and the latter has a strong correlation with the magnetocrystalline anisotropy (MCA) energy. Among rare-earth magnets, $R\mathrm{Fe}_{12-x}M_x$ compounds are potentially strong hard magnets, because large magnetization will be achieved if x can be reduced. Although $R\mathrm{Fe}_{12}$ does not exist, $R\mathrm{Fe}_{12-x}\mathrm{Ti}_x$ is thermodynamically stable for relatively small x 1. Titanium substitution suppresses magnetization significantly. On the other hand, magnetization is enhanced and strong uniaxial anisotropy is induced by interstitial nitrogenation, which makes the compound strong hard magnet.

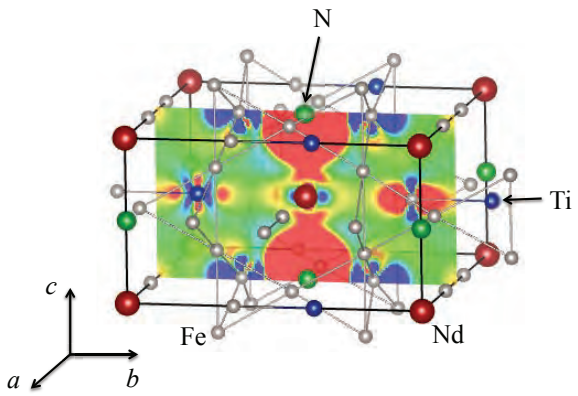

Figure 1: Charge density di erence between $NdFe_{11}Ti$ and $NdFe_{11}TiN$.

We have investigated the e ect of Ti substitution and interstitial nitrogenation on magnetic properties from microscopic viewpoint by means of the density functional theory in the generalized gradient approximation using QMAS [2]. The Nd-f electrons are treated as open-core states. We found that by nitrogenation, electron density is increased in the c direction from Nd (Figure 1). The Nd-f electrons feel repulsive force and extend in the ab directions, leading to large crystal-electric- eld coe cient A_{20}. This is the cause of uniaxial magnetic anisotropy. We also found that virtual bound state appears above the Fermi level by titanium substiturion. Substantial reduction of magnetization is explained by Friedel's sum rule.

Magnetocrystalline anisotropy from transition-metal sublattice [3]

It is widely believed that anisotropy of the orbital moments (OMs) induced by the spin-orbit interaction (SOI) around each atom are physical origin of the MCA. Bruno derived an approximate formula that relates the MCA energy and the OMs by assuming large exchange splitting. However, the MCA energies and OMs of real materials obtained by rst-principles calculations are often inconsistent with Bruno's formula.

We have derived a second-order perturbation formula for the MCA. The energy correction by SOI can be split into the spin-conserving and the spin- ip contributions. We have applied the formula to $L1_0$ alloys. It is found that the formula reproduces qualitatively the behavior of their MCA energies as a function of the lattice constant. While the MCA of FePt, CoPt, and FePd mainly orig-

inates from the spin-conserving contribution, the spin- ip term is major in MnAl and MnGa. In FePt, CoPt, and FePd, the variation of the MCA energy against the lattice constant can be explained from the variation of the spin- ip contribution. These results indicate that not only the anisotropy of OMs but also the spin- ip contributions must be taken into account for the understanding of the MCA of the $L1_0$ alloys.

References

[1] Takashi Miyake, Kiyoyuki Terakura, Yosuke Harashima, Hiori Kino and Shoji Ishibashi: J. Phys. Soc. Jpn. **83** (2014) 043702.

[2] http://qmas.jp/

[3] Taichi Kosugi, Takashi Miyake, and Shoji Ishibashi: J. Phys. Soc. Jpn. **83** (2014) 044707.

Electronic Transport Simulation of Edge-Disordered Graphene Nanoribbons

Takahiro YAMAMOTO

Dept. of Electrical Engineering, Tokyo Univ. of Science Katsushika-ku, Tokyo 125-8585

Graphene is expected to be a channel material of field effect transistors (FETs) because of their high carrier mobility. However no band gap of the graphene is a serious problem for its FET application. One possible way to overcome the gap-opening problem is to process it in the form of a nanometer width ribbon. They have been successfully applied to FETs with high on-off ratio. A recent experiment reported that the resistance of GNRs increases exponentially with their length even at the room temperature [1]. This non-Ohmic behavior is due to the edge-roughness of GNRs. The effects of edge-roughness become more remarkable when the ribbon width becomes narrower in the future.

In this study, we have computationally investigated the coherent electronic transport in narrow edge-disordered armchair GNRs (ED-AGNRs) using the nonequilibrium Green's function method combined with a tight-binding model. We calculated the conductance with various edge-disorder configurations with changing the electron energy from −2eV to 2eV, the amount of edge carbon-pair vacancies from 4% to 30% and the ribbon-width from 0.74 nm to 2.95 nm. We confirmed that the averaged conductance of ED-AGNRs decreased exponentially with their lengths, which is consistent with a previous experimental report [2]. We also examined (i) a relation between the localization length ξ and the edge-vacancy con- centration, and (ii) the ribbon-width dependence of ξ. As is expected, ξ increases with decreasing the edge-vacancy concentration and with increasing the ribbon width.

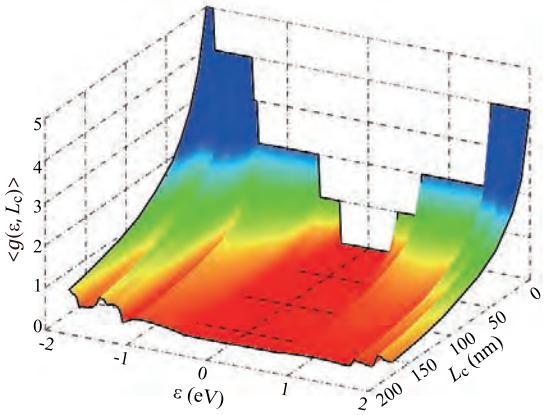

Fig. 1: The length and energy dependences of the averaged conductance of 1.48 nm-width ED-GNRs with 4% edge vacancies.

References

[1] Xu et al., Nano Lett. **11** (2011) 1082.

[2] K. Takashima and T. Yamamoto: Appl. Phys. Lett. **104** (2014) 093105.

Ab initio study of thermoelectric properties of molecules between magnetic electrodes

Tatsuhiko OHTO

Graduate School of Engineering Science,

Osaka University, 1-3 Machikaneyama, Toyonaka, Osaka 560-8531

The molecular junction is a promising system to achieve maximum thermoelectric efficiency due to the quantum confinement of the molecular orbital (MO) into the nanoscale gap [1]. The difference in the energy between the MO and the Fermi level of the electrode is called as the carrier injection barrier. As the Seebeck coefficient S of a molecular junction is related to the differential conductance, smaller carrier injection barrier is desirable. To achieve a small injection barrier, we propose to use molecular junctions with ferromagnetic electrodes as it can induce the spin polarization of MOs. The reduction of the injection barrier due to spin splitting of MOs should be larger than that induced by the change in work functions of metal electrodes. To test this hypothesis, we investigate the transport properties of Ni-benzenedithiol (BDT) -Ni molecular junction with the nonequilibrium Green's function method based on density functional theory. Result revealed that one of the spin split highest occupied MO of BDT appears just above the Fermi level, indicating an increase in the magnitude of S (compared to when Au electrode was used) and a change in the sign as well. We obtained negative and large S for Ni-BDT-Ni junctions. We further investigated the effect of spin configuration of electrodes and surface roughness on S. The structural optimization performed with the SIESTA program [2] on System B was very helpful to advance our research.

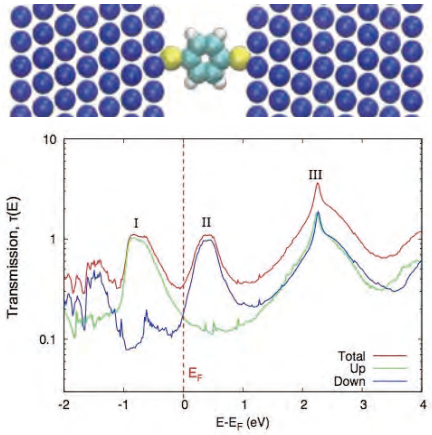

Fig. 1: Structure and transmission coefficient per spin of Ni-BDT-Ni junction.

References

[1] H. Park, Nat. Mater. **6** (2007) 330

[2] J. M. Soler: E. Artacho: J. D. Gale: A. Garcia: J. Junquera: P. Ordejon: D. Sanchez-Portal, J. Phys.: Condens. Matter **14** (2002) 2745

Development and Application of First-Principles Electron-Transport Simulators for Massively Parallel Computer

Yoshiyuki EGAMI
Division of Applied Physics, Faculty of Engineering, Hokkaido University
Kita 13, Nishi 8, Kita-ku, Sapporo, Hokkaido 060-8628

Electron-transport simulations are important to investigate and develop new electronic devices. Recently, to obtain more practical knowledge on electron-transport properties of nanoscale materials, large-scale transport simulations have attracted much interest. In this subject, we developed an efficient first-principles electron-transport simulator systems based on the Lippmann-Schwinger (LS) equation within the framework of the real-space finite-difference scheme[1].

In the conventional LS method, scattering wave functions are expressed in the Laue representation, where a 2-dimensional plane-wave expansion and a real-space discretization are combined. However, one may frequently encounter a numerical problem due to the appearance of evanescent waves exponentially growing and decaying. On the other hand, in our LS method based on the fully real-space algorithm (grid LS), the numerical collapse due to the evanescent waves and the computational costs can be restrained by using the ratio expression of the retarded Green's function obtained analytically or by incorporating the self-energy matrices and the recursive formulas of the ratio matrices[2]. Furthermore, the real-space algorithm is suitable for massively parallel computing.

In order to examine the performance of the grid LS method, the electron-transport simulations for the semiconductor/insulator membranes sandwiched between semi-infinite electrodes are demonstrated on the Sysyem B and/or Systme C of the Supercomputer Center at the Institute for Solid State Physics. Here, the transport properties of electrons flowing across the (001)Si/SiO_2 and (001)Ge/GeO_2 membranes containing danglingbond (DB) defects around interfaces. In each model, one of the DBs is passivated by a hydrogen atom while the other remains with the Si (Ge) atom of the center back-bonded to two neighboring Si (Ge) atoms and an oxygen atom. As the result, the Si/SiO_2 model exhibits much larger currents, while the Ge/GeO_2 membrane avoid serious problems caused by the DB defects and is expected to reduce the leakage current. Consequently, it is confirmed that our procedure can precisely and efficiently extend a knowledge of the physics underlying the transport of electrons through nanoscale structures.

References

[1] K. Hirose et al., First-Principles Calculations in Real-Space Formalism, (Imperial College Press, London, 2005).

[2] Y. Egami, S. Tsukamoto, T. Ono, and K. Hirose, Phys. Rev. B , *submitted*.

First-Principles Calculation of Spin Splitting at Oxide Surfaces and Interfaces

Fumiyuki ISHII
Faculty of Mathematics and Physics, Institute of Science and Engineering, Kanazawa University, Kanazawa, 920-1192, Japan

Felectrics are materials which possess spontaneous electric polarization associated with structural phase transition. The electric polarization in ferroelectrics can be controlled by external electric field and pressure. This electrical feature is applicable to several kind of electronic device such as nonvolatile ferroelectric memory. The ferroelectrics are also potential candidate for spintronics application such as spin field-effect-transistor (spin-FET) made of metal-oxide-semiconductor[1]. In conventional spin-FET, the spin is controlled by the Rashba effect caused by the external electric field [2]. By using the ferroelectrics for spin-FET, the spin can be controlled by electric polarization, i.e., internal electric field.

In this study, we have investigated structure and spin state of ferroelectric oxides $ATiO_3$(A=Pb, Ba) and surface of $PbTiO_3$. We have performed the fully-relativistic first-principles calculations based on the non-collinear spin density functional theory implemented in OpenMX code[3]. We have evaluate the energy barrier for polarization rotation by using nudged elastic band method[4] as show in Fig. 1. By changing the direction of the electric polarization, the spin textures in the Bloch-wave vector space (momentum space) drastically change as show in Fig. 2. Based on the group theory, we also discussed relation between the symmetry of crystal structures and spin textures.

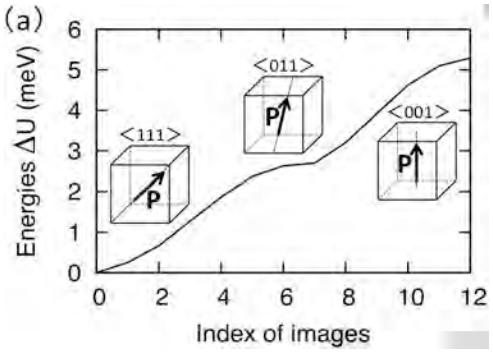

Figure 1: Total energy difference for $BaTiO_3$ with electric-polarization rotation.

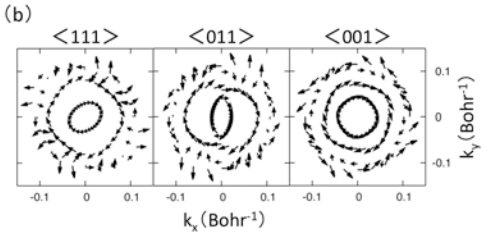

Figure 2: Spin textures for $BaTiO_3$ with electric-polarization rotation.

References

[1] S. Datta and B. Das, Appl. Phys. Lett. **56**, (1990)665.

[2] E. I. Rashba: Sov. Phys. Solid State **2**, (1960)1109.

[3] T. Ozaki et al., http:// www.openmx-square.org/

[4] G. Henkelman and H. Jonsson, J. Chem. Phys. **113**, (2000)9978.

First-Principles Calculation of Transition Metal Oxide Superlattices

Fumiyuki ISHII
Faculty of Mathematics and Physics, Institute of Science and Engineering, Kanazawa University, Kanazawa, 920-1192, Japan

Recently, artificial superlattices are extensively studied for the application to the spintronics device. In particular, heterostructures of perovskite-type transition-metal oxides attract attention because they exhibit a variety of physical properties[1]. For examples, high-mobility electron gas and tunable Rashba spin-splitting caused by internal electric field in nonmagnetic superlattice interface $LaAlO_3/SrTiO_3$ have been reported. Charge-orbital order and magnetic structure in magnetic superlattice $LaMnO_3/SrMnO_3$ were found to be strongly affected by substrate $LaAlO_3$, $La_{0.3}Sr_{1.7}AlTaO_6$ (LSAT) and SrTiO3. The ferromagnetic order were observed in magnetic/nonmagnetic superlattice $(LaMnO_3)_n/(SrTiO_3)_8$ (n=1,2,8). The previous theoretical study clarified that the system $(LaMnO_3)_2/(SrTiO_3)_8$ show half-metallicity. These interesting new properties may originate from the interface of the artificial superlattice. However, the microscopic origin of the phenomenon and the atomic/electronic structure of these interfaces have not been understood sufficiently.

In this study, we clarify the electronic structure and the magnetic stability of artificial superlattice $(LaMnO_3)_n/(SrTiO_3)_m$ by using fully-relativistic first-principles electronic structure calculations. By using OPENMX code[2], we perform fully-relativistic first-principles electronic band structure calculations based on non-collinear spin density functional theory (DFT) within the generalized gradient approximation. Figure 1 shows the atomic structure of the ferromagnetic superlattice $(LaMnO_3)_3/(SrTiO_3)_3$ and the partial density of states (PDOS) of Mn atoms and Ti atoms. While the states of Mn atoms show 100% spin-polarized as like half-metallic states, the states of Ti atoms show metallic by electron doping at the LaO interface. We also investigate the spin states on Fermi surfaces. As a result, we found that the Rashba spin-splitting and spin texture strongly depended on the Fermi surfaces. The Rashba parameters are evaluated by the nearly parabolic band obtained from our first-principles calculation. These results may provide understanding of electrical conductivity of this superlattice interface. We also study the superlattices $LaAlO_3/SrTiO_3$ and $LaMnO_3/SrMnO_3$.

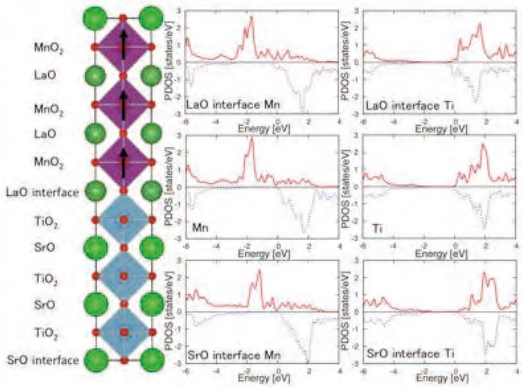

Figure 1: Atomic structure of ferromagnetic superlattice $(LaMnO_3)_3/(SrTiO_3)_3$ and partial density of states of Mn and Ti atoms.

References

[1] H.Y. Hwang et al., Nature Mater. **11** ,(2012)103.

[2] T. Ozaki et al., http:// www.openmx-square.org/

A study of the electron self-energy using GWΓ scheme

Masahiro SAKURAI
Institute for Solid State Physics, University of Tokyo
Kashiwa-no-ha, Kashiwa, Chiba 277-8581

The electron self-energy Σ, which is a fundamental quantity in the many-electron problem, can be determined from the closed set of five equations derived by Hedin that relate the self-energy Σ, the dressed Green's function G, the dynamically screened Coulomb interaction W, the polarization function Π, and the vertex function Γ to each other. Hedin's approach to obtain self-consistent solution to the coupled equations begins with an approximation to the vertex function and it generates the self-energy in a perturbation series in terms of W. Within the lowest level approximation, Γ is taken as unity and Σ is given as a product of G and W. This approximation is called the GW approximation (GWA). The GWA (without self-consistency in practical calculation) has turned out to give an accurate quasiparticle energy for semiconductors and insulators. The GW method, however, has some serious drawbacks. For example, the GWA breaks the exact relation between Σ and Γ known as Ward identity (WI), which results in violation of local electron-number conservation law.

To address this problem, Takada proposed a non-perturbative algorithm yielding exact Σ and formulated self-consistent GWΓ scheme based on it. [1]. In the iterations toward self-consistency, both Σ and Γ are simultaneously revised in such a way as to ensure that they always meet the WI. To perform numerical calculation, we need an approximate functional form for the electron-hole irreducible interaction $\tilde{I} = \delta\Sigma[G]/\delta G$ which is an integral kernel of the Bethe-Salpeter equation to determine Γ. To study the electron gas, we adopted the functional form based on the local-field factor [2]. We developed our GWΓ code using MPI and checked the MPI parallel efficiency on System B (Fig. 1). Computationally heavy multiple summations involved in calculating Σ are parallelized over momentum p and fermion Matsubara frequency $i\omega_n$. Using the improved code, convergence has successfully achieved beyond $r_s = 5.25$ where it appears the dielectric catastrophe associated with negative compressibility κ. We are also developing our code to apply GWΓ scheme to two-dimensional electron gas.

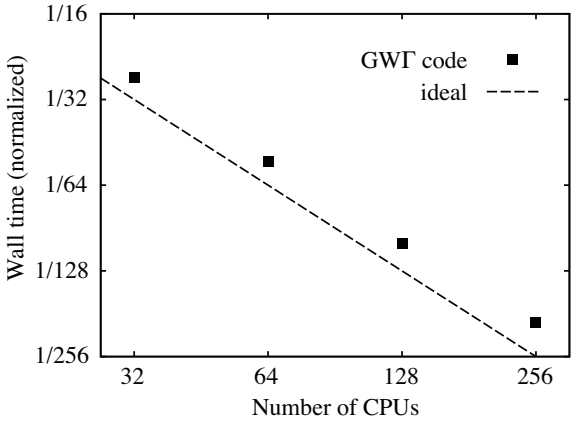

Figure 1: The wall time (normalized to that of 1 CPU) vs. the number of CPUs used for GWΓ calculation on the electron gas ($r_s = 1$).

References

[1] Y. Takada: Phys. Rev. B **52** (1995) 12708; Phys. Rev. Lett. **87** (2001) 226402.

[2] S. Ishii, H. Maebashi, and Y. Takada: arXiv:1003.3342.

Study of hydrogen in intermetallic compound: thermodynamic property of vacancy and hydrogen in tungsten

Kazuhito Ohsawa

Institute for applied Mechanics, Kyushu University

Kasuga-koen 6-1, Kasuga-shi, Fukuoka 816-8580

Hydrogen (H) isotope retention is an important subject for safety operation of future fusion reactors. In particular, tritium (T) is a radioisotope whose physical half-life is about 12 years. Tungsten (W) and its alloys are promising as plasma facing materials installed in the fusion reactors due to the excellent properties, low hydrogen solubility and high melting point etc. However, H isotopes are trapped in vacancy (V) and some sorts of V-H complexes are nucleated. Besides, it has been reported that a maximum of 12 H atoms are trapped in the W vacancy at 0K[1)] according to first-principle calculations, as shown in Fig. 1. In the present work, we investigate thermodynamic properties of the V-H complexes in a bulk W. The V-H complex concentrations are calculated, assuming an equilibrium thermodynamic model. Helmholtz free energy is $F=U-ST$. Internal energy U is composed of binding energy of H to W vacancy and formation energy of the vacancy. Entropy S is derived from the number of possible arrangement of H atoms and V-H complexes in the bulk W, i.e. configurational entropy. V-H complex concentrations are shown in Fig. 2 in a finite temperature. The V-H complex concentrations are equal to thermal vacancy density in the limit of low H concentration. While, the V-H complex concentrations rapidly increase as the H concentration increases. In the limit of high H concentration, the super-abundant vacancy formation induced by H is observed.

References

[1] K. Ohsawa: Phys. Rev. B 82, 184117 (2011)

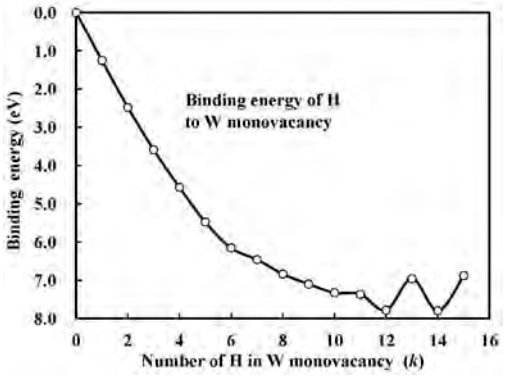

Fig. 1: Binding energy of H to W monovacancy estimated by first-principle calculations.

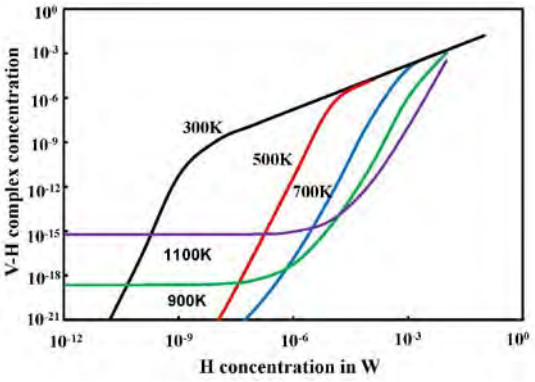

Fig. 2: Dependence of V-H concentration in W on H concentration in a finite temperature.

First-Principles Calculations of Photocatalytic Solid-liquid Interfaces

HIDETOSHI KIZAKI, TAKUYA NISHITANI, and YOSHITADA MORIKAWA

Graduate School of Engineering,

Osaka University, 2-1, Yamada-oka, Suita, Osaka 565-0871

$LaFeO_3$ is a promising material as a photocatalyst possessing a catalytic activity in visible light. In this study, our purpose is to investigate the stoichiometric stabilities under Fe and O vacancies in $LaFeO_3$. The relaxed lattice constants for *a*, *b* and *c* in bulk $LaFeO_3$ correspond to 0.059, 0.574 and 0.792 nm, respectively, which are in reasonable agreement with the experimental values of 0.558, 0.556 and 0.786 nm. At first, we calculated the formation energies of $LaFeO_3$ from La_2O_3 and Fe_2O_3 by GGA and GGA+U, and examined the effect of on-site coulomb U. The calculated formation energy of $LaFeO_3$ by GGA+U (U_{eff} = 3.0 eV) was -0.682 eV in good agreement with the experimental value of -0.669 eV, while it was -0.773 eV by GGA. Then, we modeled many kinds of structures that contained several vacancies of Fe or O, and calculated corresponding formation energies.

Furthermore we have also performed first-principles simulations for solid-liquid interfaces on Pt(322) stepped surface. As a result, we find that a H_2O dissociation and an adsorption of an OH molecule on stepped structure of Pt(322) w/o initial OH adsorptions as shown in Fig. 1. However, in case of the others, we cannot find the H_2O dissociation on not only Pt(111) flat surface w/ and w/o initial OH adsorptions but Pt(322) stepped surface w/ initial OH adsorptions. These results are consistent with the energetics approach of only a hydroxyl adsorption on Pt(322) stepped surface and with experimental data if we consider that our simulation shows on the way to the final water reaction[1].

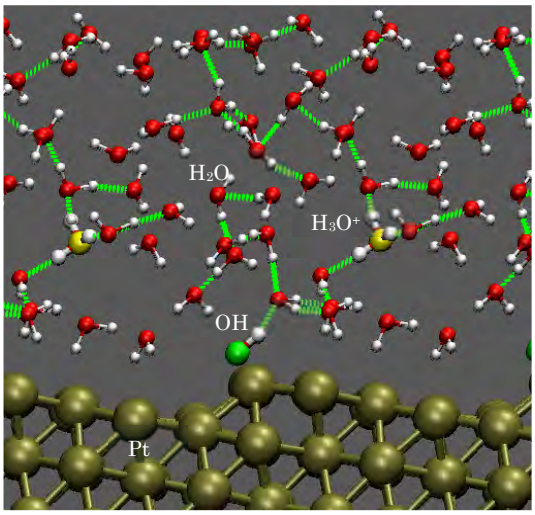

Fig. 1: H_2O dissociation and an adsorption of an OH molecule on Pt(322) stepped surface w/o initial OH adsorptions. Dotted line denotes H-bonding network.

References

[1] Van der Niet, J.T.C Maria et. al. *Cat. Tod.* **2013**, 202, 105.

First principles calculation on defect structures in mixed conducting Perovskite oxides

Koji Amezawa

Institute of Multidisciplinary Research for Advanced Materials,

Tohoku University, 2-1-1 Katahira, Sendai 980-8577

Solid oxide fuel cells (SOFC) are expected as new energy generators due to their high efficiency of energy conversion. In order to realize SOFC operation at middle temperature ranges (773 ~ 973 K), performance of cathode materials need to be improved more. $LaCoO_3$ is one of the candidates as a cathode material [1-2]. In order to understand an origin of good performance of $LaCoO_3$ cathode, we computationally study defect formation behaviors in $LaCoO_3$.

First principles total energy calculations were performed using VASP code. Local density approximation (LDA) and Hubbard *U* potential correction (U_{eff} = 3.8 eV for Co) implemented in VASP code is chosen as an exchange correlation potential for electrons. Cut off energy is set to be 500 eV. Firstly, a primitive cell of rhombohedral $LaCoO_3$ is fully optimized with *k*-point sampling meshes of 5×5×5 until all residual forces acting on each ion become smaller than 0.02 eV/Å. Then, a supercell model containing 320 atoms is constructed. The supercell is optimized under the same condition of residual forces as the primitive cell. Sampling of k-point for the supercell is at Γ point. As defective models, supercells containing an oxide ion vacancy or an interstitial proton are calculated as shown in the figure below.

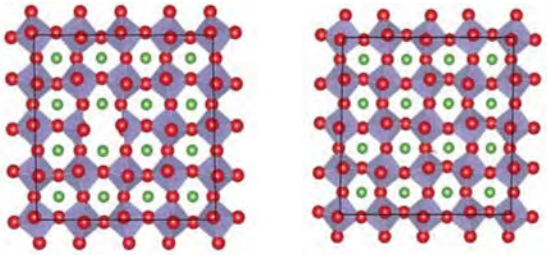

Fig. 1: Supercell models of $LaCoO_3$ with (left) an oxide ion vacancy and (right) an interstitial proton.

From total energy calculations of the supercells with an oxide ion vacancy and an interstitial proton, hydration enthalpy (ΔH_{hyd}) was evaluated. ΔH_{hyd} of $LaCoO_3$ is found to be -0.76 eV. This value is comparable with the case of proton conductive Y-doped $BaZrO_3$, -0.82 eV. This results means that proton solution possibly affect properties of $LaCoO_3$ as a cathode.

References

[1] K. Yashiro, *et al.*, *Electrochem. Solid-State Lett.*, **12**, B135 (2009).

[2] Eva Mutoro, *et al.*, *Energy Environ. Sci.*, **4**, 3689 (2011).

Scanning tunneling microscopy simulation of β-$FeSi_2$(100) surface models

Ken HATTORI
Graduate School of Materials Science, Nara Institute of Science and Technology
Takayama, Ikoma, Nara 630-0192

Total energies of β-$FeSi_2$(100)1x1 with adatoms (66 atoms) and without adatoms (64 atoms) were calculated using Simulation Tool for Atom TEchnology (STATE)-Senri [1]. The substrate structure was assumed to be 1st-layer Si (8 atoms per (100)1x1 unit-cell)/2nd-Fe (2)/3rd-Fe (2)/4th-Si (8)/5th-Fe (4)/6th-Si (8)/7th-Fe (2)/8th-Fe (2)/9th-Si (8)/10th-Fe (4)/11th-Si (8)/12th-H (8). 20 adatom models (two Fe or two Si adatoms on 4 hollow sites, 4 bridge sites and 2 atop sites per (100)1x1 unit-cell) were considered to explain periodical atomic surface-protrusions observed by scanning tunneling microscopy. The in-plane lattice constants b and c, and the atomic positions in the last three layers were fixed to the calculated bulk values or stable surface-adsorption configurations. The film thickness was approximately 22 bohr in the total slab thickness of 60 bohr. The generalized gradient approximation proposed by Perdew, Burke, and Ernzerhof, and Troullier-Martins norm-conserving (Vanderbilt's ultrasoft) pseudo potentials for Fe and Si (H) atoms were used for the density functional theory (DFT) calculations. The wave functions and charge densities are expanded by a plane-wave set with cutoff energies of 25 and 225 Ry, respectively. The spin polarization was not considered. The k-mesh gird was 2x2x1 in the energy estimation. All atoms except the fixed ones were relaxed until all residual force components are less than 0.05 eV/Å.

Two hollow-site models (named as H3 and H4, and they were almost degenerated) were found to be stable for both Fe and Si adatom models. In this stage, the candidate models could be restricted to be WO (without adatoms), Fe-H3, Fe-H4, Si-H3, and Si-H4. Next simulated STM patterns were compared to experimental images at filled ($E_F - 1$ eV) and empty ($E_F + 1$ eV) states. In the STM simulation the k-mesh gird was 5x5x1, and the dipole correction in the vacuum was inserted. The simulation mapped the iso-charge density surfaces at 10^{-8} e/bohr^3.

In the WO model, four Si atoms in the 1st layer were considerably relaxed and form square-like positions, resulting in one protrusion in the STM patterns at both states. The patterns well explained the experimental images. In the Fe-H3/H4 models, one Fe adatom induced one STM protrusion, which were similar to those in the experiments. In the Si-H3/H4 models, Si adatoms also induced STM protrusions in both bias, however, in the empty state 2nd-layer Fe was also participated as brighter protrusions; this was not consistent with the experimental images. Thus, WO and Fe-H3/H4 models were proposed by the DFT calculations.

The calculations were performed in System A. The relaxation calculations were required over 10 hours in P1 process in each model. The dipole-correction calculations were several hours in P1 process. The STM-simulations were in D1 process.

The author thank Prof. Morikawa in Osaka University, Dr. Yanagisawa in Ryukyu University, and Dr. Hamada in NIMS for their great support in STATE-Senri calculations.

References

[1] Y. Morikawa: Phys. Rev. B **63** (2001) 033405, and references therein.

Large scale first principles calculation of core loss spectroscopy

Teruyasu MIZOGUCHI

Institute of Industrial Science, University of Tokyo

Komaba, Meguro, Tokyo 153-8505

To achieve a comprehensive understanding of the chemical reactions, such as catalytic reaction at liquid–solid interfaces, analyses of the liquid properties with improved spatial resolution, temporal resolution, and sensitivity are needed. Among the existing analytical methods, core-loss spectroscopy using electrons or X-rays offers atomic-scale spatial resolution, nanosecond-level time resolution, and high sensitivity. Despite the advantages of core-loss spectroscopy, the practical application of this technique in liquid analysis has been limited, largely due to a lack of suitable theoretical methods for calculating the core-loss spectra of liquids.

In this study, the core-loss spectrum from the liquid was analyzed by combining MD simulations and first-principles band structure calculations in an effective approach for estimating the dynamic behavior of molecules from the core-loss spectrum.

First, two models were constructed for spectral calculations. The first model included an isolated methanol molecule inside a 10 × 10 × 10-Å box (Fig. 1). The methanol structure was optimised, and this model was thereafter called the ‘gas model’ because the methanol molecules were separated from each other. The second model, termed the ‘liquid model’, was constructed from an MD simulation. The validity of the MD simulation was confirmed using simulated melting and boiling temperatures. The liquid model obtained by the MD simulation at 313 K is shown in Figure 1.

The periodic boundary condition was used for the spectral calculations in this study, whereas prior studies used cluster calculations to generate the core-loss spectra of molecules and liquids, and one or several molecules were taken from independent MD calculations. However, the use of the periodic boundary condition was important for reproducing the experimental spectra of liquids.

Through this study, we found that the calculated C-K edge spectrum of the isolated methanol molecule satisfactorily reproduces the experimental spectrum of methanol gas, while it is different from the experimental spectrum of liquid methanol. It was found that the reproducibility of the liquid spectrum is greatly improved by calculating C-K edge of the liquid model. This indicates that the spectral profiles of ELNES/XANES reflect molecule-molecule interactions and local structure fluctuations of molecules, such as stretching and bending [1].

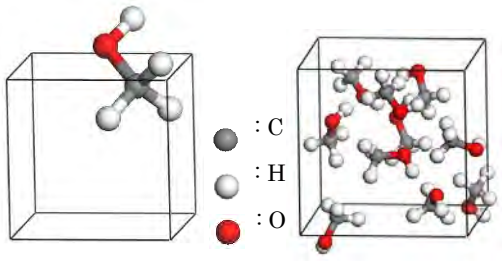

Figure 1: Models for ELNES/XANES calculation. (Left) gas-model and (right) liquid model. The methanol molecule in the gas model has the stable structure, whereas that in the liquid model was obtained by the MD simulation.

References

[1] "An estimation of molecular dynamic behaviour in a liquid using core-loss spectroscopy", Y. Matsui, K. Seki, H. Hibara, T. Mizoguchi, Scientific Reports, 3 (2013) 3503-1-7.

First principles study on homo and hetero interface of photovoltaic materials

Teruyasu MIZOGUCHI

Institute of Industrial Science, University of Tokyo

Komaba, Meguro, Tokyo 153-8505

CIS is a direct energy-gap semiconductor and has a proper band gap for absorbing the solar ray, so it is expected to be the high efficiency photovoltaic cell. To absorb the solar ray more efficiently, the control of the band gap of CIS is indispensable. On the other hand, though the CIS is polycrystalline material and has a lot of GBs, the effect of GB on the band gap property is still under debate. Moreover, the electronic band bending at the GBs has been extensively studied, but many kinds of results were proposed. To clarify the effect of GB, we combined a first-principles calculation and a high-angle annular dark-field scanning transmission electron microscopy (HAADF-STEM).

In this study, we focused on (112)[1$\bar{1}$0] Σ3 twin GB as a model. CIS has chalcopyrite structure which is like diamond structure and zinc-blende structure. Viewing the structure from [1$\bar{1}$0] axis, a dumbbell structure is observed where the dumbbell includes Se column and cation column. In the cation column, Cu and In are arranged in turns in the [1$\bar{1}$0] direction. Using this dumbbell structure, (112)[1$\bar{1}$0] Σ3 twin GB is formed by tilting one side of grain along [1 $\bar{1}$ 0] axis by 35.27° and the other side of grain by -32.27°. The number of atoms in the calculation periodic model was 96.

In STEM observation, HAADF-STEM was used (JEOL ARM-200CF). CIS thin film was deposited on MgO (001) substrate using pulsed laser deposition (PLD) method. In a first principles calculation, projector augmented wave (PAW) method was used within a Perdew-Burke-Ernzerhof (PBE) generalized gradient approximation using the Hubbard U correction (GGA+U) implemented in VASP code. The Heyd-Scuseria-Ernzerhof (HSE) hybrid functional scheme was applied in band gap calculations.

Figure 1 shows HAADF-STEM image of a GB in CIS. Dumbbell structure is clearly observed. From the brightness of those atomic columns, the kinds of the atomic columns can be identified. Thus, it is found that the bondings across the GB are between cation and Se columns. The calculated structure was overplayed on the HAADF-STEM image. It is found that the calculated model is in good agreement with the observed image. Furthermore, similar twin boundary was frequently observed. This result matches the lowness of GB energy in calculation.

The effects of the atomic structure of the GB on the band gap and potential barrier were systematically investigated using hybrid functional calculation [1]. Furthermore, we also investigated the vacancy formation energetics at the GB [2].

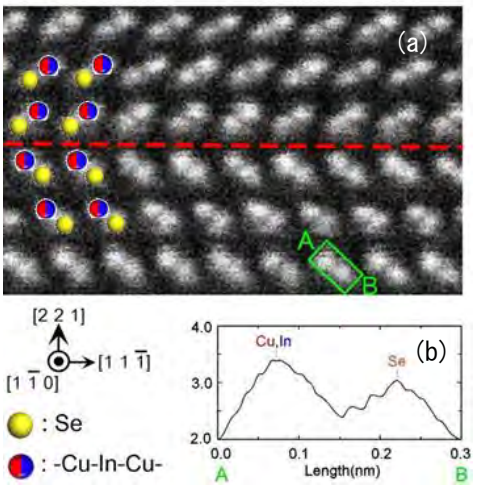

Figure 1: (a) HAADF-STEM images of $CuInSe_2$ and calculated model. The dot line represents the position of Σ3 twin GBs. (b) Intensity profile HAADF image along A-B.

References

[1] "The atomic structure, band gap, and electrostatic potential at the (112)[1-10] twin grain boundary of $CuInSe_2$" H. Yamaguchi, H. Hiramatsu, H. Hosono, and T. Mizoguchi, *Appl. Phys. Lett.*, 104, 153904-1-5 (2014).

[2] "Defect formation energetics at the grain boundary in CuInSe2 using first-principles calculations"

H. Yamaguchi and T. Mizoguchi, *J. Ceram. Soc. Jpn*, in press.

Analysis of the temperature dependence of the magnetic and electronic structures of Mn_3Pt on the basis of the first-principles molecular dynamics theory

Takashi UCHIDA
Hokkaido University of Science
4-1, 7-15, Maeda, Teine-ku, Sapporo 006-8585

The Mn-based ordered alloys Mn_3X (X=Pt, Rh, Ir), which all have Cu_3Au-type crystal structure, are frustrated itinerant magnets with an octahedral configuration of Mn local magnetic moments. Neutron diffraction experiments [1] suggest that at temperatures sufficiently below their Néel temperatures T_N, all these alloys reveal the triangular magnetic structure with Γ_{4g} symmetry (D-phase). On the other hand, it has been suggested that the D-phase of Mn_3Pt changes into collinear magnetic phase (F-phase) at 400 K before changing into paramagnetic phase at $T_N = 475$ K.

To clarify the physical origin of F-phase of Mn_3Pt, we have investigated and compared the temperature dependence of the magnetic and electronic structures of Mn_3Pt and Mn_3Ir by means of the first-principles molecular dynamics (MD) approach for itinerant magnets [2]. The theory is formulated by incorporating the first-principles TB-LMTO Hamiltonian into the MD approach for itinerant magnets on the basis of the functional integral method and the isothermal MD technique. The MD approach allows us to determine automatically the magnetic structure of a large system with several hundred atoms in a unit cell at finite temperatures.

In the first-principles MD approach, we calculate the thermal average of local magnetic moments by solving the isothermal MD equations of motion. The magnetic forces in the MD equations are determined at each time step by calculating the electronic structure by means of the recursion method. We utilize the MPI parallel calculation scheme in the recursion calculation and this is found to be quite effective in saving computing time because more than 90 % of the CPU time concentrates on this process.

We have calculated the electronic and magnetic structure for a system with $4 \times 4 \times 4$ fcc lattice with fixing the crystal structure and lattice constant. At sufficiently low temperatures below T_N, Mn_3Pt and Mn_3Ir both exhibit the triangular magnetic structure (D-phase), being consistent with experiment. With increasing temperature from 25 K, Mn_3Pt exhibits a first-order transition to another ordered phase (F-phase) around 350 K, accompanying a development of Mn-Eg DOS at Fermi energy E_F. Mn_3Ir, on the other hand, shows a continuous decrease of Mn local moments up to T_N, indicating a second-order transition to paramagnetic phase. The Mn-Eg DOS of Mn_3Ir does not show appreciable development up to T_N. We conclude that the enhancement of the ferromagnetic couplings among the second-nearest neighbor Mn local moments (due to Mn-Eg states) are responsible for the emergence of F-phase in Mn_3Pt.

References

[1] T. Ikeda and Y. Tsunoda, J. Phys. Soc. Jpn. **72** (2003) 2614.

[2] T. Uchida and Y. Kakehashi, J. Korean Phys. Soc. **62** (2013) 1748.

First-principles calculations on atomic and electronic structure at oxide grain boundaries

Yukio SATO

Institute of Engineering Innovation,

The University of Tokyo, 2-11-16, Yayoi, Bunkyo, Tokyo 113-8656

Many of practical materials are used in the polycrystalline forms, and the grain boundaries (GBs) often play important roles in obtaining materials function. In the present study, we aim to add electrical conductivity to GBs of alumina (Al_2O_3), which is well-known electrical insulator and therefore used for insulating substrates in electrical circuit. This may allow us to build nano-patterned electrodes embedded within substrate materials. Doping a few 3d transition metal elements such as Co, Ni, and Cu, we tried to modify the electronic states formed in the GBs.

We have chosen an Al_2O_3 single GB for a case study. The GB has the geometrical orientation relationship of Σ13 according to the coincidence site lattice (CSL) theory [1]. The adjacent crystals have common [11-20] axes in parallel and the GB plane is (1-104) [2].

Stable atomic arrangements of the Co, Ni, and Cu-doped Al_2O_3 GBs were simulated by first-principles PAW calculations under GGA approximation. Further, for the density of state calculations, hybrid functional was used for better description. The simulation cells included 120 atoms. All the calculations were done with the VASP code, and oxidation state of all the dopants was assumed to be +3.

Figure 1 shows the stable atomic arrangements of the GBs, where Al atoms at particular sites are replaced by Co, Ni, or Cu. After structural optimization, significant structural relaxation did not occur. On the other hand, there are noticeable differences in the density of states. For all the GBs, dopant elements form additional states in the band gap. Further, the lowest unoccupied levels formed in the Cu-doped case, which may allow us the biggest opportunity to obtain electrically conductive GB.

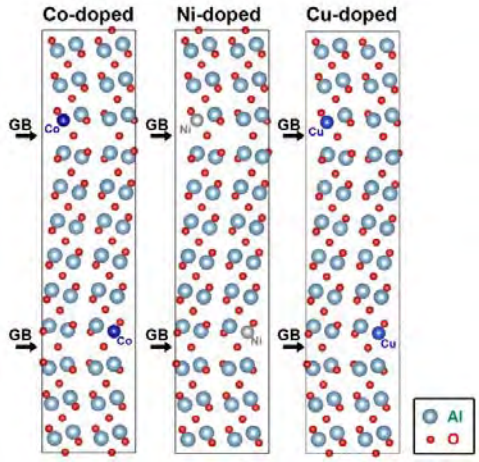

Fig. 1: Stable atomic arrangements in Co-, Ni-, and Cu-doped Al_2O_3 GBs.

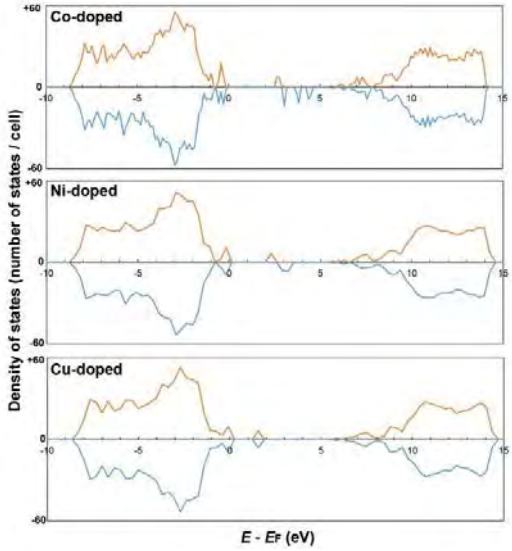

Fig. 2: Density of states of the Co-, Ni-, and Cu-doped Al_2O_3 GB supercells.

References

[1] H. Grimmer, Acta Cryst. A **45** (1989) 505.

[2] S. Fabris and C. Elsässer, Acta Mater. **51** (2003) 71.

First-principles calculations of the atomic arrangement at the interfaces in crystalline solids

Yukio SATO

Institute of Engineering Innovation,

The University of Tokyo, 2-11-16, Yayoi, Bunkyo, Tokyo 113-8656

Polycrystalline zinc oxide (ZnO) ceramics have found the application for varistor devices owing to the high nonlinearity in their current-voltage characteristics. It has been revealed that the nonlinearity is caused by grain boundaries (GBs) in ceramics. On the other hand, in recent years, ZnO films are intensively studied for transparent electrode application. In this case, GB may lower electrical conductivity via the reduction of electron mobility. In order to understand the GB effects on electrical property, we study atomistic structure of a ZnO GB.

We chose ZnO [0001]/(13$\bar{4}$0) symmetric tilt GB for modelling. Simulation cells including the GBs constructed include approximately 210 atoms. First-principles PAW calculations were conducted using the VASP code, where the GGA-PBE exchange correlation potentials were used.

Figures 1 (a)~(d) show stable atomic arrangements of the GB obtained by the first-principles calculations together with their GB energies. The atomic arrangements are periodic as indicated by the dotted lines, and the arrangement are characterized as the combination of five, six, seven or eight-membered rings. Comparison of (a) and (c) reveals that the six- and eight-membered rings exhibit lower energy than the five- and seven-membered ones do. The same conclusion comes out from the comparison of (b) and (d). Existence of dangling bonds in the case of five- and seven-membered rings case [1] would be a cause of extra energies in (c) and (d).

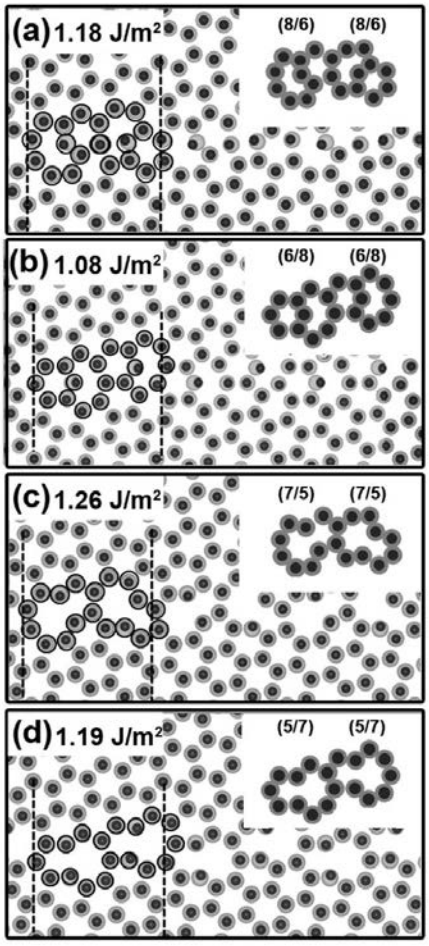

Fig. 1: Some stable atomic arrangements of ZnO [0001]/(13$\bar{4}$0) symmetric tilt GB [1].

Reference

[1] J. Roh *et al.*, J. Am. Ceram. Soc. **97** (2014) 617.

Search for new electronic properties of new nanoscale interfaces

Katsuyoshi KOBAYASHI
Department of Physics, Ochanomizu University
2-1-1 Otsuka, Bunkyo-ku, Tokyo 112-8610

Recently topological insulators are extensively studied. In 2013 we studied the electronic states of bismuth thin films.

It is theoretically predicted that a Bi film of one bilayer (BL) thickness is a two-dimensional topological insulator [1]. There is an experiment using scanning tunneling spectroscopy [2] that shows an evidence for the edge states of 1 BL Bi films. However, the energy range of the edge states observed in this experiment does not match with that of the theoretical calculation [3]. It has not been established that the edge states of 1BL Bi films are experimentally verified.

Another problematic point in 1 BL Bi films is that the dispersion of the edge bands is complex. There are three states in the edge bands that cross the Fermi energy. This property causes back scattering by scatterers with time-reversal symmetry. It makes the quantum spin Hall effect difficult to observe. In order to overcome this difficulty we try two theoretical investigations in 2013. One is making use of interactions with substrates. The other is decoration of the edges of 1 BL Bi films with atoms.

In the first investigation we calculated electronic states of 1BL Bi films on Bi_2Te_3 substrates. 1 BL Bi films have a bilayer structure. When Bi films are placed on substrates, the edge Bi atoms at two sides of wires are not equivalent. Our calculated results show that the degeneracy of the edge states localized at two sides of wires is lifted by the interaction with substrates. However, the splitting of the edge-state bands is not so large that the number of states crossing the Fermi energy changes. This is partially due to the fact that the potential energy at Bi atoms in the 1 BL films is not symmetric.

In the second investigation we calculated electronic states of free standing 1 BL Bi wires with hydrogen atoms at edges. Figure 1 shows a calculated band structure. The band dispersion of the edge states of 1 BL Bi wires with hydrogen atoms are considerably different from those without hydrogen atoms. The former is like an ideal Dirac cone. There is only one state crossing the Fermi energy. Backscattering does not occur by scatterers with time-reversal symmetry. Therefore, the 1 BL Bi wires with hydrogen atoms at edges are promising systems for observing the quantum spin Hall effect.

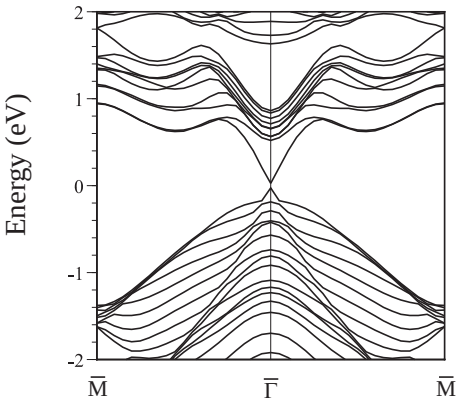

Figure 1: Band structure of a 1 BL Bi wire with hydrogen atoms at edges.

References

[1] S. Murakami: Phys. Rev. Lett. **97** (2006) 236805.

[2] F. Yang *et al.*: Phys. Rev. Lett. **109** (2012) 016801.

[3] M. Wada *et al.*: Phys. Rev. B **83** (2011) 121310(R).

Electronic State and Proximity Effects around Interface in Layered Superlattices

Kunitomo HIRAI
Department of Physics, Nara Medical University
Kashihara, Nara 634–8521

The purpose of the present research is to elucidate characteristics of electronic state in superlattices with layered structures, in particular, to illustrate proximity effects of each layer on adjacent layers in the superlattices. This research of a first-principles electronic structure calculation is performed by means of the Korringa-Kohn-Rostoker (KKR) Green function method within the framework of the local spin density (LSD) functional formalism.

The calculation by means of the KKR method was so far carried out for superlattices of ferromagnetic layers with nonmagnetic spacer layers such as Fe/Cr, Fe/V, Fe/Cu, ... ones, with magnetizations of two successive Fe layers being aligned parallel or antiparallel. Oscillatory interlayer exchange coupling between ferromagnetic layers with respect to spacer thickness was investigated, and relation between bulk effects inherent in the spacer layer and the proximity effects due to the ferromagnetic layers was analyzed. In the calculation, every atom in a monolayer stacked in the superlattices is assumed to be equivalent, and there is one site in each monolayer. This assumption can be justified for the superlattices with ideal interfaces without structure, but not for those with realistic interfaces with structures like steps, islands, or such, and hence there are two or more sites in each monolayer for the superlattices with realistic interfaces.

A need of the calculation for superlattices with more sites in each monolayer arises also for layered superlattices of ordered alloys or compounds, which now attract broad interests particularly in viewpoint of spintronics. We then start preparation of the calculation for superlattices with more sites in each monolayer, which results in increase of the number of atoms in a unit cell and involves vast increase of computation times. In the preparation of the calculation, installation of parallelization with use of the OpenMP into program codes of the KKR methods is intended, together with parallelization with use of the MPI which was already achieved, that is, installation of hybrid parallelization is intended.

The installation of the OpenMP is in progress and will be achieved in due course, and then the proximity effects in the superlattices with realistic interfaces will be investigated to elucidate the roles of the interfaces in the superlattices. The calculation will be carried out for Fe superlattices with steps, and magnetic frustration caused by the steps is investigated, in particular reference to possible mechanism of increase of total magnetization of the Fe layers, where fcc(001) or fcc(111) superlattices are considered together with usual bcc(001) ones and difference between those superlattices is to be analyzed. In addition, the calculation will be carried out for layered superlattices of ordered alloys, such as fcc(001) superlattices consisting of Fe and FePt layers, in particular reference to ferromagnetic or antiferromagnetic coupling between layers and within a monolayer.

First principles calculations of complex defect structures in oxide ceramics

Tetsuya TOHEI

Institute of Engineering Innovation,

The University of Tokyo, Yayoi, Bunkyo-ku, Tokyo 113-8656

α-alumina (alpha-Al_2O_3) is a popular oxide ceramics material with high mechanical strength, toughness, and corrosion resistance up to high temperatures, which are advantageous for application as high temperature structural materials. Rapid short-circuit diffusion process via grain boundaries in alumina is crucial for the material's high temperature properties such as creep deformation, densification in sintering, grain growth, and so on. Although diffusion phenomena along alumina grain boundary (GB) have been extensively studied, many questions remain unresolved [1]. In this study, we investigated atomic structures, vacancy formations and migration behaviors in alumina grain boundary by first principles theoretical calculations in order to understand the defect originated properties such as G.B. diffusion from an atomistic scale. We focused on Al_2O_3 Σ11 (1-210)/[10-11] GB as a model grain boundary. Stable atomic configuration of the GB was firstly searched by the method of rigid body translation employing static lattice calculations. Then accurate atomistic structure of the GB was evaluated by first principles calculations within the framework of density functional theory (DFT). We used plane wave basis PAW method (VASP code) for structure optimization and total energy calculations. Supercells containing about 400 atoms were used for the calculations. Since oxygen diffusion in alpha-alumina is considered to occur mainly via oxygen vacancies, understanding the oxygen vacancy formation behavior is essential. Formation energies of isolated oxygen (O) vacancies were calculated for various atomic sites around the GB and the bulk region. To evaluate atomic diffusion phenomena, we employed two classes of theoretical methods: First we performed classical molecular dynamics (MD) simulations to estimate dominant diffusion paths in alumina Σ11 GB. For the MD calculations extended supercells with the GB and composed of about 3600 atoms were used, with several oxygen vacancies introduced into the atomic sites with low vacancy formation energies at the grain boundary. From the MD trajectories of the oxygen vacancy sites, it was confirmed that diffusion of oxygen vacancies predominantly occurs along the grain boundary. Then accurate geometry and activation energies for the dominant atomic migration paths were calculated by nudged elastic band (NEB) method using the first principles PAW method [2]. Calculations of phonon dispersion relations and phonon density of states were also performed on defect models in α-alumina to consider and discuss the lattice vibrational effects on the defect originated properties and phenomena in the material.

References

[1] A. H. Heuer, J. Eur. Ceram. Soc., **28**, 1495-507 (2008).

[2] N. Takahashi et al., Phys. Rev. B, **82**, 174302 (2010).

Thermo-Chemical Wear Mechanism of Diamond Cutting Tool

Yutaka Uda, Shoichi Shimada

Osaka Electro-Communication University, Hatsu-cho, Neyagawa, Osaka 572-8530

Sakuro Honda

Technology Research Institute of Osaka Prefecture, Ayumino, Izumi, Osaka 594-1157

Demand has been increasing for highly durable molds of heat-resistant materials for complex and precise optical components with high aspect ratio. Diamond is an ideal cutting tool material for high efficient ultraprecision metal cutting of complex three-dimensional metal works. However, it is well known that diamond cutting tool shows severe wear in cutting of heat-resistant materials such as ferrous metals and nickel.

On the other hand, in cutting of electroless nickel deposits (Ni-P), which is used as a material of precision molds of high performance optical components, remarkably less tool wear is observed than in case of pure nickel [1,2]. Phosphorous addition should have an important role for tool wear suppression. However, the essential mechanism of wear suppression has not yet been understood well.

Therefore, to understand the wear mechanism of diamond cutting tool in machining of nickel and ferrous metals is very much meaningful to realize useful fabrication technique of the precise molds of the metals with high accuracy and low cost.

Single grain cutting tests and erosion tests suggest that the wear mechanism is not mechanical but thermo-chemical one [3-5]. Therefore, in order to reveal the mechanisms of the initial stages of wear process and wear suppression by phosphorous addition, ab initio molecular dynamics calculations of chemical reaction on diamond surface in contact with Ni and Ni-P surfaces were carried out using double-grid method for real-space electronic-structure calculations proposed by Dr. T. Ono of Osaka University [6].

The $C_{10}H_{14}$. Cluster is used as a model for a part of diamond (100) surface. Figure 1 shows the optimized atomic configuration of $C_{10}H_{14}$ cluster. The atom at the bottom of the model is the radical carbon interacting with metal surface. The dangling bonds of the other carbon atoms of diamond are terminated by hydrogen

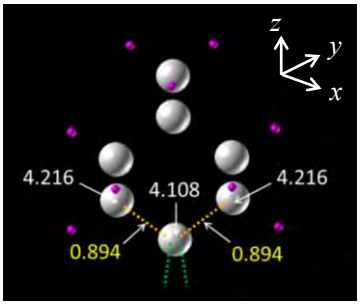

Fig.1. Model of diamond (100) surface

atoms. White and yellow figures express atomic and bond populations, respectively. The atomic population indicates the effective number of electrons belonging to individual atoms. The change between the bond population before and after a chemical reaction is an index of the change in the bond strength in covalent crystal. Figure 2 shows the model of Ni (100) surface. The model have periodic boundaries in *x* and *y* directions and aperiodic boundary in *z* direction. The atomic populations of all Ni atoms are almost 10.0.

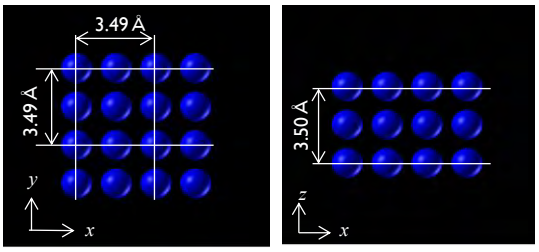

Fig.2. Model of Ni (100) surface

Figure 3 shows the optimized atomic configuration of the diamond cluster interacting with Ni and Ni-12wt%P surfaces. By the interaction with Ni, the atomic population of radical carbon increases to 4.91 from 4.11 and those of Ni decreases to 9.73. The result suggests that the strength of ionic bonding increases between carbon and Ni. The population of back bonds of radical carbon decrease to 0.76 from 0.89. The results suggest that the radical carbon has a chance to dissociate from the diamond surface when it has a large kinetic energy due to cutting temperature. On the other hand, in case of

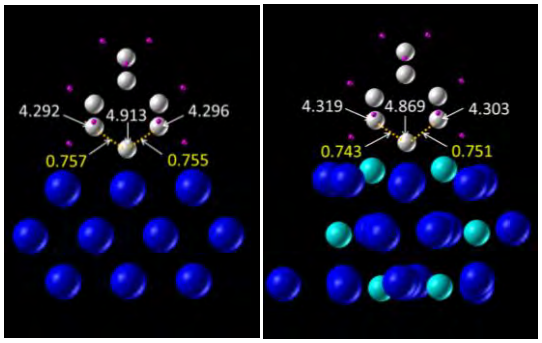

Fig.3. Effect of phosphorous addition to interaction with diamond

interacting with Ni-P, both of decrease of back bond population and increase of atomic population of radical carbon are remarkably suppressed The result suggest that phosphorous addition reduces the dissociation of carbon atoms on diamond surface.

References

[1] C.K. Syn, J.S. Taylor, R.R. Donaldson:Proc. SPIE, **676** (1986) 128.

[2] J.M. Oomen, L. Eisses: Precision Engineering, **14**, (1992) 206.

[3] T. Tanaka, N. Ikawa: Bull. JSPE, **7** (1973) 97.

[4] S. Shimada, H. Tanaka, M. Higuchi, T. Yamaguchi, S. Honda, K. Obata: Annals of the CIRP, **53**, (2004) 57.

[5] N. Furushiro, H. Tanaka, M. Higuchi, T. Yamaguchi, S. Shimada: Annals of the CIRP, **59**, (2010) 105.

[6] T. Ono, K. Hirose: Physical Review Letters, **82** (1999) 5016.

3.3 Strongly Correlated Quantum Systems

Microscopic theory for charge transports of ruthenate

Naoya ARAKAWA
Department of Physics, The University of Tokyo
Bunkyo-ku, Hongo, Tokyo 113-0033

In strongly correlated electron systems near a magnetic quantum-critical point (QCP), many-body effect of electron correlation causes unusual transport properties (TPs) deviating from the Fermi liquid (FL). One of the examples is cuprate: near an antiferromagnetic (AF) QCP, the in-plane resistivity, ρ_{ab}, and Hall coefficient, $R_{\rm H}$, show the T-linear dependence and Curie-Weiss (CW) like T dependence, respectively. Another is ruthenate near an AF or a ferromagnetic QCP: in $Sr_2Ru_{0.075}Ti_{0.025}O_4$, near the AF QCP, ρ_{ab} shows the T-linear dependence; in $Ca_{2-x}Sr_xRuO_4$ around $x = 0.5$, near the FM QCP, ρ_{ab} and $R_{\rm H}$ show the $T^{1.4}$ dependence and CW like T dependence, respectively. Note that ρ_{ab} and $R_{\rm H}$ show the FL behaviors.

For cuprate, the origins of these non-FL behaviors in ρ_{ab} and $R_{\rm H}$ have been clarified by fluctuation-exchange (FLEX) approximation with Maki-Thompson (MT) current vertex correction (CVC), the correction of the current due to MT electron-hole (el-h) four-point vertex function (VF). The T-linear ρ_{ab} arises from the strong T and $\boldsymbol{k}$ dependence of the quasiparticle (QP) damping; the CW like T dependence of $R_{\rm H}$ arises from the strong T and $\boldsymbol{k}$ dependence of MT el-h four-point VF; these dependence of the QP damping and MT el-h four-point VF arise from the CW like T dependence of the spin susceptibility at $\boldsymbol{k} = (\pi, \pi)$.

Although the roles of the QP damping and MT el-h four-point VF will be significant in multiorbital systems, these roles have not been clarified yet due to a large numerical cost arising from the large mesh of the Brillouin zone and the number of the Matsubara frequencies.

In this project, to clarify the roles of the QP damping and the MT el-h four-point VF in the charge transports of ruthenate, I analyze ρ_{ab} and $R_{\rm H}$ for the t_{2g} orbital Hubbard model on a square lattice by the FLEX approximation with the MT CVC [1]; ρ_{ab} and $R_{\rm H}$ (in the weak-field limit) are formulated by using the Kubo formula and considering the most divergent terms with respect to the QP lifetime. Technically, I resolve the numerical difficulty about the large numerical cost explained above by constructing an optimized algorithm, where without using a rotational symmetry, the memory and time of the calculations are about eight times smaller than those for a usual algorithm.

I have revealed the roles and achieved qualitative agreement with experiments. The main contribution arises from the $d_{xz/yz}$ orbital due to the smaller QP damping and larger band velocity of that orbital than those of the d_{xy} orbital. Also, the non-FL like QP damping of the $d_{xz/yz}$ orbital near the AF QCP causes the T-linear ρ_{ab}. Moreover, the MT CVC arising from the non-diagonal spin fluctuation at $\boldsymbol{k} = (0.66\pi, 0.66\pi)$ between the $d_{xz/yz}$ and d_{xy} orbitals causes the negative enhancement and the peak at low T as a result of the sign change and enhancement of the component of the transverse conductivity of the d_{xy} orbital.

References

[1] N. Arakawa, Ph. D. Thesis, The University of Tokyo (2014); in preparation.

Origin of the correlation between the Fermi surface shape and T_c in the cuprate superconductors

KAZUHIKO KUROKI
Department of Physics, Osaka University
1-1 Machikaneyama, Toyonaka, Osaka, 560-0043, Japan

CORRELATION BETWEEN THE FERMI SURFACE SHAPE AND T_c

In 2001, Pavarini *et al.* showed for the cuprate superconductors that there is a correlation between the experimentally observed T_c and the Fermi surface warping[1]. Namely, they have obtained single-orbital tight-binding models for various cuprates to estimate the ratio "r" between the nearest and second-neighbor hoppings, which is a measure of the warping of the Fermi surface. Plotting the experimental T_c against the theoretically evaluated r, they showed that T_c systematically increases with the Fermi surface warping.

In an attempt to investigate the origin of this correlation, we have previously introduced a two-orbital model that explicitly considers the d_{z^2} Wannier orbital on top of the $d_{x^2-y^2}$[2, 3]. There, we showed that ΔE, the level offset between $d_{x^2-y^2}$ and d_{z^2} orbitals, dominates both of the warping of the Fermi surface and T_c. It was shown that La_2CuO_4, despite its less warped (more nested) Fermi surface, has lower T_c than those of $HgBa_2CuO_4$, $Tl_2Ba_2CuO_6$, and $Bi_2Sr_2CuO_6$ due to a strong d_{z^2} orbital mixture on the Fermi surface that degrades T_c. However, among the above mentioned four single-layer cuprates, only La_2CuO_4 has a small ΔE (i.e., a strong d_{z^2} mixture), so that we are still in need of a convincing study as to whether ΔE is systematically controlling T_c in a wider range of cuprates, including the multi-layered ones that were included in Pavarini's plot[1]. Hence, in the present project, we have examined the systematics by extending the analysis to bilayer cuprates as well as those single-layer ones that have relatively lower T_c [4].

MODEL CONSTRUCTION

First-principles electronic structures of the materials are obtained with the VASP package[5], where experimentally determined lattice parameters are adopted. We then employ the $d_{x^2-y^2}$ and d_{z^2} Wannier orbitals as projection functions[6] to model the band structure around the Fermi level. The calculation is performed for single-layer La_2CuO_4, $Pb_2Sr_2Cu_2O_6$, and bilayer $La_2CaCu_2O_6$, $Pb_2Sr_2YCu_3O_8$, $EuSr_2NbCu_2O_8$, $YBa_2Cu_3O_{7-\delta}$(YBCO), $HgBa_2CaCu_2O_6$(HBCO) and $Tl_2Ba_2CaCu_2O_8$. Experimentally, the first five materials are known to have relatively lower T_c's (below 70K), while the last three have higher T_c's (above 90K)[7].

We also construct *single*-orbital models for the above materials so that the main bands intersecting the Fermi level are reproduced with a single Wannier orbital per site. This Wannier orbital mainly consists of the $d_{x^2-y^2}$ orbital, but also has tails with a d_{z^2} orbital character. We can then define the parameter, $r = (|t_2| + |t_3|)/|t_1|$ in terms of the second (t_2) and third (t_3) neighbor hoppings of the single-orbital model, which is a direct measure of the Fermi surface warping[1]. For bilayer materials, r can be defined with hoppings within each layer. Since these materials have two sites per unit cell, with outer and inner Fermi surfaces, so that we can alternatively obtain the respective measures of the warping of the outer and inner Fermi surfaces as $r_{\rm outer,inner} = (|t_2 \pm t_{2\perp}| + |t_3 \pm t_{3\perp}|)/|t_1 \pm t_{1\perp}|$, where $t_{i\perp}$ is the interlayer hopping to the sites vertically above (or below) the i-th neighbor.

FLUCTUATION EXCHANGE ANALYSIS

In the the two-orbital model we consider intra- and inter-orbital electron-electron interactions. The intra-orbital U is considered to be in the range of 7-10t (where $t \simeq 0.45$ eV is the nearest-neighbor hopping) for the cuprates, so we take the intra-orbital $U = 3.0$ eV. The Hund's coupling J and the pair-hopping J' are typically $\sim 0.1U$, so we take $J = J' = 0.3$ eV. Here we observe the orbital rotational symmetry which gives the inter-orbital $U' = U - 2J = 2.4$ eV. We apply FLEX[8] to this multi-orbital Hubbard model, and solve the linearized Eliashberg equation. Its eigenvalue λ increases upon lowering the temperature, and reaches unity at $T = T_c$. Therefore λ at a fixed temperature can be used as a qualitative measure for T_c. The temperature is fixed at $k_{\rm B}T = 0.01$eV in the present calculation. The total band filling (number of electrons /site) is fixed at $n = 2.85$, for which the filling of the main band amounts to 0.85 (15 % hole doping). We take a $32 \times 32 \times 4$ k-point meshes for the three-dimensional lattice with 1024 Matsubara frequencies.

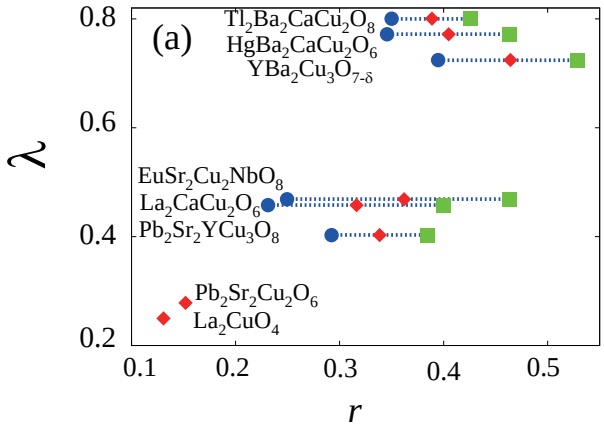

FIG. 1. Eigenvalue of the Eliashberg equation λ obtained for the two-orbital model plotted against r. $r_{\rm inner}$ and $r_{\rm outer}$ are also shown.

In Fig.1, we plot λ (obtained for the two-orbital model) against the measure of the Fermi surface warping r (of the single orbital model). The figure strikingly resembles Pavarini's plot[1] for the experimentally observed T_c against r. This resemblance unambigously shows that the T_c of the cuprates is strongly affected by the d_{z^2} orbital component mixture.

CONCLUSION

To conclude, constructing two- and single-orbital models of various bilayer as well as single-layer cuprates, we have revealed a systematic correlation between the Fermi surface warping and the theoretically evaluated T_c. Its striking resemblance with Pavarini's plot for experimental T_c's[1] unambiguously indicates that the d_{z^2} mixture is indeed a key factor that determines the T_c in the cuprates.

[1] E. Pavarini *et al.*, Phys. Rev. Lett. **87**, 047003 (2001).
[2] H. Sakakibara *et al.*, Phys. Rev. Lett. **105**, 057003 (2010).
[3] H. Sakakibara *et al.*, Phys. Rev. B **85**, 064501 (2012).
[4] H. Sakakibara *et al.*, arXiv : 1403.2497.
[5] G. Kresse and J. Hafner, Phys. Rev. B **47**, 558 (1993); G. Kresse and J. Furthmüller, Phys. Rev. B **54**, 11169 (1996) [http://cms.mpi.univie.ac.at/vasp/vasp/vasp.html]. Here we adopt GGA-PBEsol exchange correlation functional introduced by J. P. Perdew, A. Ruzsinszky, G. I. Csonka, O. A. Vydrov, G. E. Scuseria, L. A. Constantin, X. Zhou, and K. Burke, Phys. Rev. Lett. **100**, 136406 (2008), and the wave functions are expanded with plane waves up to a cut-off energy of 550 eV. 10^3 k-point meshes are used.
[6] N. Marzari and D. Vanderbilt, Phys. Rev. B **56**, 12847 (1997); I. Souza, N. Marzari and D. Vanderbilt, Phys. Rev. B **65**, 035109 (2001). The Wannier functions are generated by the code developed by A. A. Mostofi, J. R. Yates, N. Marzari, I. Souza and D. Vanderbilt, (http://www.wannier.org/).
[7] H. Eisaki *et al.*, Phys. Rev. B **69**, 064512 (2004).
[8] N.E. Bickers, D.J. Scalapino, and S.R. White, Phys. Rev. Lett. **62**, 961 (1989).

Stability of the superfluid state in three components fermionic optical lattices

AKIHISA KOGA
Department of Physics, Tokyo Institute of Technology
Meguro, Tokyo 152-8551, Japan

Ultracold atomic systems provide a variety of interesting topics. One of the active topics is the superfluid (SF) state in ultracold fermions, where interesting phenomena have been observed such as pseudogap behavior and the BCS-BEC crossover. Recently, degenerate multi-component fermionic systems have experimentally been realized,[1, 2, 3] which stimulates further theoretical investigation on the SF state in multi-component fermionic systems.

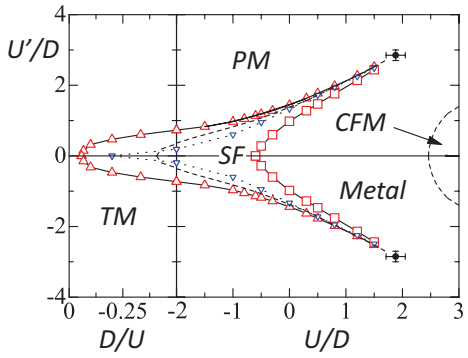

Figure 1: Phase diagram of the system at $T/D = 0.015$. Triangles (squares) represent the phase transition points between the SF and PM (metallic) states. The dashed lines represent the phase boundaries in the paramagnetic system. Dotted lines indicate the ridges of the pair potential in the SF state.

Motivated by this, we have studied low temperature properties of the three-component Hubbard model. By combining dynamical mean-field theory with a continuous-time quantum Monte Carlo method, we have obtained the finite temperature phase diagram, as shown in Fig. 1. We have found that the s-wave superfluid state proposed recently [4] is indeed stabilized in the repulsively interacting case and appears along the first-order phase boundary between the metallic and paired Mott states in the paramagnetic system [5]. Moreover, we have studied low-temperature properties in the BCS and BEC regions. It is found that the BCS state is characterized by the second-order phase transition, while the BEC state is by the first-order one. This is contrast to the two-component system, where the second-order phase transitions occur in both limits. It is also interesting how the SF state is realized in the multi-component fermionic systems for lithium and ytterbium atoms, which is now under consideration.

References

[1] T. B. Ottenstein et al., Phys. Rev. Lett. **101** 203202 (2008).

[2] T. Fukuhara et al., Phys. Rev. Lett. **98**, 030401 (2007).

[3] B. J. DeSalvo et al., Phys. Rev. Lett. **105**, 030402 (2010).

[4] K. Inaba and S. Suga, Phys. Rev. Lett. **108**, 255301 (2012); K. Inaba and S. Suga, Mod. Phys. Lett B **27** 1330008 (2013).

[5] Y. Okanami, N. Takemori and A. Koga: arXiv:1401.5610.

Numerical study of topological order

Y. Hatsugai
Division of Physics
Faculty of Pure and Applied Sciences, University of Tsukuba
1-1-1 Tennodai, Tsukuba 305-8571, Ibaraki, Japan

Numerical studies have been quite successful to describe phases of matter by evaluating correlation functions of local order parameters such as magnetization and pairing amplitudes of superconductors. Recent development of condensed matter physics motivates characterization of quantum phases from different aspects. One of such examples is an anisotropic superconductor where there can be a lot of phases even though all phases are supplemented by the gauge symmetry breaking as superconductivity. It clearly shows that the symmetry breaking is important but not enough. Then structure of the gap nodes of the superconductivity distinguishes the phases which is reflected by boundary states as the Andreev bound states. This is one of the typical examples of the bulk-edge correspondence which was discovered in the study of the quantum Hall effects. Today one may consider non trivial topological phases by the existence of the edges state governed by the bulk-edge correspondence. Then by using this bulk-edge correspondence, we define the topological order. In this sense, the edge states are kinds of order parameters. Then numerical studies are again quite important to directly observe these edge states. Also note that non trivial edge sates implies existence of non trivial Berry connections which characterizes the bulk.

Historical and very well known edge state is a dangling bond of the semiconductors. One may say that the edge states of graphene at the zigzag boundary belongs to this class. To use a symmetry breaking for the characterization of the phases, one needs to treat thermodynamic large systems. Contrary to this, topological order also works for a finite system. In this sense, we investigate topological properties of finite size graphene flakes by using Berry phases. As shown in Fig.1, existence of the dimers along the boundaries of some graphene flakes is clearly described by the Z_2 Berry phases[1].

We have also published several papers using the computer facilities at ISSP. Let us make a list of short descriptions for these works. Ref.[2,3]: calculation of the excitation gap is performed for the spin-resolve chiral condensate state of graphene under a strong magnetic field where many body interaction plays a crucial role. Ref.[4,5,6]: effects of chiral symmetry and randomness are studied numerically for multilayer graphene. Ref.[7-9]: bulk-edge correspondence is studied for massless/massive Dirac fermions.

References

[1] D. Seki, Y. Hamamoto and Y. Hatsugai, JPS Conf. Proc. 1, 012068 (2014)

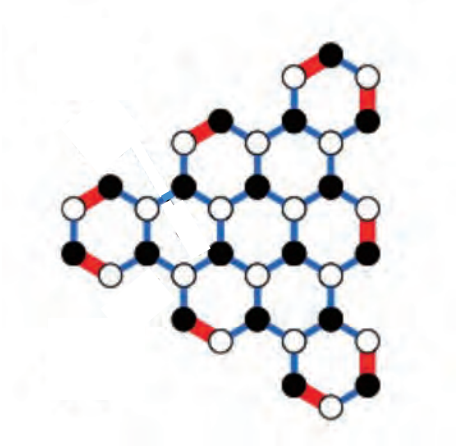

Figure 1: An example of the Z_2 Berry phases for a graphene flake[1]. The red lines correspond to the links with the Berry phase π which implies there is a localized dimer on the link. The other blue links implies the Berry phases of the links are zero.

[2] Y. Hamamoto, T. Kawarabayashi, H. Aoki and Y. Hatsugai, Phys. Rev. B 88, 195141 (2013)

[3] Y.Hamamoto, H. Aoki, T. Kawarabayashi and Y. Hatsugai, J. Phys. Conf. Ser. 456, 012013 (2013)

[4] H. Sakamoto, Y. Hatsugai, H. Aoki and T. Kawarabayashi, JPS Conf. Proc. 1, 012069 (2014)

[5] T. Kawarabayashi, T. Honda, H. Aoki and Yasuhiro Hatsugai, AIP Conf. Proc. 1566, 283 (2013)

[6] T. Kawarabayashi, Y. Hatsugai and H. Aoki, J. Phys. Conf. Ser. 456, 012020 (2103)

[7] T. Kariyado and Y. Hatsugai, JPS Conf. Proc. 1, 012001 (2014)

[8] T. Kariyado and Y. Hatsugai, Phys. Rev. B 88, 245126 (2013)

[9] T. Fukui, K.-I. Imura and Y. Hatsugai, Journal of the Physical Society of Japan 82, 073708 (2013)

Numerical Study of Triangular Hubbard Models

Takami TOHYAMA*
Yukawa Institute for Theoretical Physics, Kyoto University
Kyoto 606-8502

Remarkable observations of a possible spin liquid phase and a new universality class of the metal-insulator transition in organic charge transfer salts have increased interest in these materials. It has been argued that a proper microscopic description of these materials can be given with a Hubbard model on the anisotropic triangular lattice at half filling. Parameters of the model for the description of organic charge transfer salts fall into the regime of strong correlations and significant frustration of antiferromagnetic spin interactions.

In this project, we have investigated two-magnon Raman scattering for organic charge transfer salts in collaboration with an experimental group [1]. Starting with an anisotropic triangular Hubbard model with 1st- and 2nd-neighbour hoppings and on-site Coulomb interaction, we set up an effective spin Hamiltonian after a strong-coupling expansion involving all possible processes up to the fourth order of the hopping terms. The resulting spin Hamiltonian contains all of the 1st-, 2nd-, and 3rd-neighbor exchange interactions together with four-spin ring-type exchange interactions. Performing exact-diagonalization calculations of two-magnon Raman scattering spectrum for a 27-site lattice, we have found that the polarization and material dependence of the spectrum are consistent with experimental data, suggesting a crucial role of frustration in these materials and a possible ground state of spin liquid.

We have also investigated the ground state property of a triangular Hubbard model with isotropic hoppings by density-matrix renormalization group (DMRG). In the ISSP supercomputer, we have performed small-scale calculations, while large scale calculations have been done on K Computer in Kobe. We note that the package of DMRG code for two-dimensional spin and Hubbard systems has been developed and is now available on several platforms including ISSP supercomputer and K computers. We calculated ground-state energy, double occupation number, entangle entropy, and spin-spin correlation function for cylindrical shape of the triangular Hubbard model as well as periodical systems with small system size. A signature of a metal-insulator transition and spin-liquid to order transition has been obtained.

These works were done in collaboration with Y. Nakamura, H. Kishida, S. Sota and J. Kokalj.

参考文献

[1] Y. Nakamura, N. Yoneyama, T. Sasaki, T. Tohyama, A. Nakamura, and H. Kishida: J. Phys. Soc. Jpn. in press.

*Present Address: Department of Applied Physics, Tokyo University of Science, Tokyo 125-8585

Research for Superconductivity in Strongly Correlated Multi-Orbital Systems

Yuji SHIBA and Takashi HOTTA
Department of Physics, Tokyo Metropolitan University
1-1 Minami-Osawa, Hachioji, Tokyo 192-0397

In this research, the effect of the Fermi-surface topology on the emergence of superconductivity is discussed in the two-dimensional $e_{\rm g}$-electron system coupled with Jahn-Teller phonons on the basis of the strong-coupling theory [1]. It is well known that the van Hove singularity occurs in the density of states due to the abrupt change of the Fermi-surface structure, leading to the enhancement of $T_{\rm c}$. We find that $T_{\rm c}$ is increased for the hopping parameters apart from the van Hove singularity point, when the $e_{\rm g}$-electron system possesses disconnected Fermi surfaces in comparison with the case of single Fermi surface. The increase of $T_{\rm c}$ is due to the large pair-hopping amplitude between different Fermi surfaces enhanced by the Jahn-Teller phonons.

We consider the two-dimensional square lattice and the lattice constant is taken as unity. The model Hamiltonian used here is given by

$$H = \sum_{\boldsymbol{k},\sigma,\gamma,\gamma'} \varepsilon_{\boldsymbol{k}\gamma\gamma'} d^{\dagger}_{\boldsymbol{k}\gamma\sigma} d_{\boldsymbol{k}\gamma'\sigma} + \sum_{\boldsymbol{q}} [g_2 \phi_{2\boldsymbol{q}} (\rho^{ab}_{\boldsymbol{q}} + \rho^{ba}_{\boldsymbol{q}}) + g_3 \phi_{3\boldsymbol{q}} (\rho^{aa}_{\boldsymbol{q}} - \rho^{bb}_{\boldsymbol{q}})] + \sum_{\boldsymbol{q}} (\omega_2 a^{\dagger}_{2\boldsymbol{q}} a_{2\boldsymbol{q}} + \omega_3 a^{\dagger}_{3\boldsymbol{q}} a_{3\boldsymbol{q}}), \quad (1)$$

where $d_{\boldsymbol{k}\gamma\sigma}$ denotes an annihilation operator of an $e_{\rm g}$ electron with spin σ and momentum $\boldsymbol{k}$ in the orbital γ (=a and b), a and b indicate x^2-y^2 and $3z^2-r^2$ orbitals, respectively, $\varepsilon_{\boldsymbol{k}aa} = (1/2)[3(dd\sigma) + (dd\delta)](\cos k_x + \cos k_y)$, $\varepsilon_{\boldsymbol{k}bb} = (1/2)[(dd\sigma) + 3(dd\delta)](\cos k_x + \cos k_y)$, $\varepsilon_{\boldsymbol{k}ab} = \varepsilon_{\boldsymbol{k}ab} = -(\sqrt{3}/2)[(dd\sigma) - (dd\delta)](\cos k_x - \cos k_y)$, $(dd\sigma)$ and $(dd\delta)$ denote the Slater-Koster integrals, $a_{2\boldsymbol{q}}$ and $a_{3\boldsymbol{q}}$ are annihilation operators for (x^2-y^2)- and $(3z^2-r^2)$-type Jahn-Teller phonons, respectively, g_2 and g_3 indicate electron-phonon coupling constants, $\phi_{2\boldsymbol{q}} = a_{2\boldsymbol{q}} + a^{\dagger}_{2-\boldsymbol{q}}$, $\phi_{3\boldsymbol{q}} = a_{3\boldsymbol{q}} + a^{\dagger}_{3-\boldsymbol{q}}$, $\rho^{\gamma\gamma'}_{\boldsymbol{q}} = \sum_{\boldsymbol{k},\sigma} d^{\dagger}_{\boldsymbol{k}+\boldsymbol{q}\gamma\sigma} d_{\boldsymbol{k}\gamma'\sigma}$, and ω_2 and ω_3 denote, respectively, Jahn-Teller phonon energies for (x^2-y^2)- and $(3z^2-r^2)$-type modes.

In order to calculate the superconducting transition temperature $T_{\rm c}$, we solve the linearlized gap equation obtained by evaluating both normal and anomalous electron self-energies due to the electron-phonon interaction. Here we consider the spin-singlet s-wave Cooper pair with the even function of frequency. In the second-order perturbation theory in terms of g_2 and g_3, the linearized gap equation at $T = T_{\rm c}$ is given by $\phi_{\mu\nu}(i\omega_n) = -T\sum_{n'}\sum_{\boldsymbol{k}}\sum_{\mu',\nu',\mu'',\nu''} V_{\mu\mu',\nu\nu'}(i\omega_n - i\omega_{n'}) G_{\mu'\mu''}(\boldsymbol{k}, i\omega_{n'}) G_{\nu'\nu''}(-\boldsymbol{k}, -i\omega_{n'}) \phi_{\mu''\nu''}(i\omega_{n'})$, where $\phi_{\mu\nu}(i\omega_n)$ is anomalous self-energy, $\omega_n = (2n+1)\pi T$ with a temperature T and an integer of n, G indicates the normal Green's function, given by $[G(\boldsymbol{k}, i\omega_n)]^{-1}_{\mu\nu} = [G^{(0)}(\boldsymbol{k}, i\omega_n)]^{-1}_{\mu\nu} - \Sigma_{\mu\nu}(i\omega_n)$, $G^{(0)}$ denotes the non-interacting electron Green's function, given by $[G^{(0)}]^{-1}_{\mu\nu} = (i\omega_n + \mu)\delta_{\mu\nu} - \varepsilon_{\boldsymbol{k}\mu\nu}$, μ is a chemical potential determined from the relation of $n = 2T\sum_n \sum_{\boldsymbol{k}} {\rm Tr} G(\boldsymbol{k}, i\omega_n)$, n is electron number per site, $\Sigma_{\mu\nu}(i\omega_n)$ denotes the normal electron self-energy, given by $\Sigma_{\mu\nu}(i\omega_n) = -T\sum_{n'}\sum_{\boldsymbol{k}'}\sum_{\mu',\nu'} V_{\mu\mu',\nu'\nu}(i\omega_n - i\omega_{n'}) G^{(0)}_{\mu'\nu'}(\boldsymbol{k}', i\omega_{n'})$. The phonon-mediated interaction $V_{\mu\mu',\nu\nu'}(i\nu_n)$ with $\nu_n = 2\pi T n$ is given

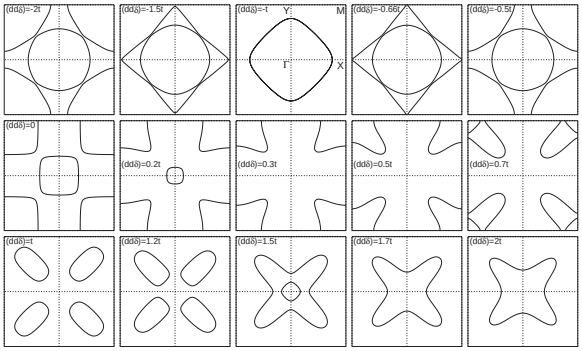

Figure 1: Variation of the Fermi surfaces for $(dd\sigma)/t = -1.0$ depicted in the first Brillouin zone of $-\pi \le k_x \le \pi$ and $-\pi \le k_y \le \pi$ with $\Gamma = (0,0)$, X=$(\pi,0)$, Y=$(0,\pi)$, and M=(π,π).

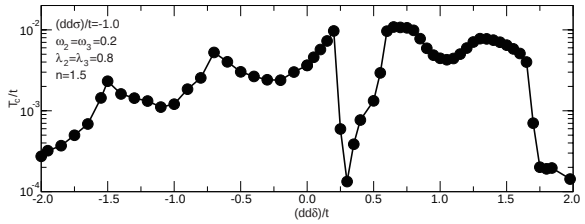

Figure 2: Superconducting transition temperature T_c/t vs. $(dd\delta)/t$ for $(dd\sigma)/t = -1.0$, $\omega_2/t = \omega_3/t = 0.2$, $\lambda_2 = \lambda_3 = 0.8$, and $n = 1.5$ in the range of $-2.0 \le (dd\delta)/t \le 2.0$.

by $V_{aa,aa} = V_{bb,bb} = -V_{aa,bb} = -V_{bb,aa} = g_3^2 D_3$, and $V_{ab,ab} = V_{ab,ba} = V_{ba,ab} = V_{ba,ba} = g_2^2 D_2$, where phonon Green's functions are given by $D_2 = 2\omega_2/[(i\nu_n)^2 - \omega_2^2]$ and $D_3 = 2\omega_3/[(i\nu_n)^2 - \omega_3^2]$.

In the actual calculations, we set $n = 1.5$ and the energy unit t is taken as $t = |(dd\sigma)|$. Note that we set $(dd\sigma) = -t$. For the sum on the imaginary axis, we use 131,072 Matsubara frequencies. As for the phonon energy, we set $\omega_2/t = \omega_3/t = 0.2$. We define the non-dimensional electron-phonon coupling constants as $\lambda_2 = 2g_2^2/(t\omega_2)$ and $\lambda_3 = 2g_3^2/(t\omega_3)$, which are set as $\lambda_2 = \lambda_3 = 0.8$.

In Fig. 1, we show the change of the Fermi surfaces, when we control the Slater-Koster integral $(dd\delta)/t$ from -2.0 to 2.0 for $(dd\sigma)/t = -1.0$. In Fig. 2, we show T_c/t vs. $(dd\delta)/t$. In the region of negative $(dd\sigma)$, we observe the overall tendency of the increase of T_c with the increase of $(dd\delta)/t$ from -2.0 to 0.0, except for the cusps at $(dd\delta)/t = -1.5$ and -0.7 due to the van Hove singularities. When we increase $(dd\delta)$ from zero, T_c is monotonically increased for $0 \le (dd\delta)/t \lesssim 0.2$. For $0.2 \lesssim (dd\delta)/t \lesssim 0.6$, there appears the single Fermi surface and T_c is totally low, since the density of states is suppressed in this region. However, when we increase $(dd\delta)$, T_c is rapidly increased. Around at $(dd\delta)/t = 0.6$, there occurs a new Fermi surface and the Fermi-surface topology is abruptly changed again, leading to the van Hove singularity. For $0.6 \lesssim (dd\delta)/t \lesssim 1.6$, T_c depends on the values of $(dd\delta)$, but we observe that the magnitude of T_c is kept high as $T_c/t = 0.005 \sim 0.01$, even though the Fermi-surface topology is changed in this region. Note that for $1.6 \lesssim (dd\delta)/t \le 2.0$, T_c is totally low and it is difficult to obtain T_c with enough precision in this region, since T_c approaches the lower limit which we can safely calculate.

The enhancement of T_c in the case of the plural numbers of the Fermi surfaces is explained by the enhancement of the pair-hopping attraction between Cooper pairs on different Fermi surfaces due to Jahn-Teller phonons [2]. This pair-hopping attraction does not work for the case of the single Fermi surface. Thus, T_c in the case of the plural numbers of the Fermi surfaces is enhanced in comparison with the case of single Fermi surfce. This enhancement mechanism still works even for the case of small-size pocket-like Fermi surfaces.

References

[1] Y. Shiba and T. Hotta: J. Phys.: Conf. Ser. **428** (2013) 012038.

[2] T. Hotta: J. Phys. Soc. Jpn. **79** (2010) 023709.

Phase formation and dynamics in correlated cold atom systems

NORIO KAWAKAMI
Department of Physics, Kyoto University, Kyoto 606-8502, Japan

In this decade, cold atom systems have attracted much attention as a new field, because of recent rapid progress in cooling and manipulation techniques [1]. The progress in these techniques has enabled experimentalists to cool confined atomic gases to nano-Kelvin temperatures, to make a lattice potential by using interfering laser beams, and also to modify strength and sign of interaction between cold atoms by Feshbach resonance. Further, these system parameters can be adapted in real time or instantaneously, so even the dynamics of cold atom systems is also enthusiastically studied. Therefore cold atom systems are expected to be quantum simulators of model Hamiltonians developed in the field of condensed matter physics.

One of the main issues in our research project is to study non-equilibrium dynamics of cold atom systems. We focus on drag dynamics of a trapped fermion cluster in a fermion cloud, from interest in non-equilibrium dynamics when the system parameters gradually change in real time. These systems are different from quantum quench systems in which the system parameters suddenly change and are fixed after that sudden change.

In this study we simulate the drag dynamics in the following system. Initially a cluster of n fermions is trapped by a harmonic potential within a cloud of the other type of free fermions, where the average fermion density of the cloud is D. The fermion cluster is trapped by a harmonic trap potential, and the interaction exists between two fermions of the different types. Then we suddenly move the trap potential and the cluster by a constant speed for the cluster to push the cloud.

We simulate this dynamics by using time-dependent density matrix renormalization group [2], and calculate the energy of the system. As a result, the moving trap increases the total energy of the system as a linear function of the time approximately. We evaluate the energy increase per unit time P from the energy-time plot.

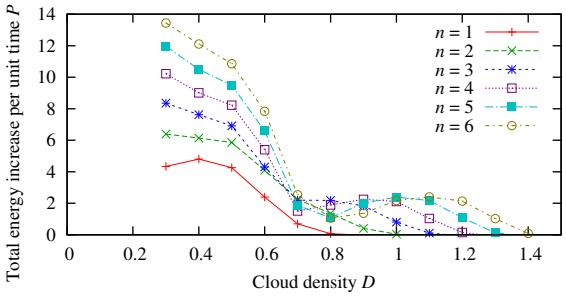

Figure 1: Energy increase per unit time P.

Figure 1 shows how P depends on n and D. In the $n = 1$ case, P has a single peak, but in the $n > 2$ case, P has double peaks. This double-peak structure is explained by our concise model, which includes quantum many-body effects. Our model suggests that the second peak is due to the dynamical collective modes in which momentum is properly distributed [3].

References

[1] D. Jaksch and P. Zoller, Ann. Phys. **315**, 52 (2005).

[2] S. R. White and A. E. Feiguin, Phys. Rev. Lett. **93**, 076401 (2004).

[3] J. Ozaki, M. Tezuka, N. Kawakami, to be published.

Analysis of Topological Phases in Strongly Correlated Systems

NORIO KAWAKAMI
Department of Physics, Kyoto University, Kyoto 606-8502, Japan

Recently, the topological band insulator (TBI) has attracted much interest as a new class of quantum phases, where the spin-orbit coupling plays an essential role. One of the current major issues is the influence of strong correlation effects upon the topological phase because electron correlations are expected to create new topological phases. This issue has further been stimulated by theoretical proposals in d- and f- electron systems [1].

One of the main issues in our research is to study the spatial dependence of electron correlations in these topological phases to clarify the edge state. In this study, we consider a generalized Bernevig-Hughes-Zhang model [2] having electron correlations with the variational Monte Carlo (VMC) method. In order to study how interactions affect the edge states and bulk states respectively, we introduce spatially-dependent variational parameters (Fig. 1).

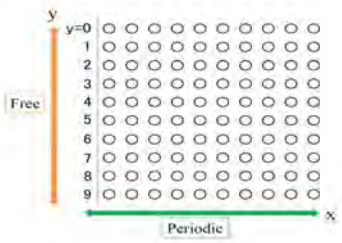

Figure 1: Periodic (free) boundary condition in the x (y) directions. $y = 0$ and $y = 9$ correspond to the boundary in this system.

To perform the large-scale numerical calculation, we have fully made use of the supercomputer resource at ISSP. Namely, we have optimized many spatially-dependent variational parameters efficiently, where we have performed large-scale MPI parallel computing.

Figure 2 shows average electron numbers at each y as functions of the interaction strength U. This result clearly evidences a first-order Mott transition, which is accompanied by a hysteresis. This result also shows that the average electron number at the edge sites ($y = 0$) decreases more rapidly than in the bulk because the coordination number at the edge sites is smaller. In this calculation, however, phase transitions simultaneously occur in the entire system and we cannot find the novel intermediate phase which is expected in some previous works.

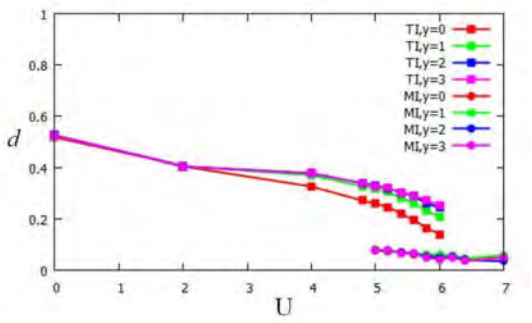

Figure 2: (Color Online). Average electron numbers at each y as functions of interaction strength U. The solid line with square (circles) represents the topological (Mott insulating) state.

We have also calculated the correlation functions to discuss the topological properties of this system. These will be reported elsewhere.

References

[1] T. Yoshida *et al.*, Phys. Rev. B **87**, 165109 (2013).

[2] B. A. Bernevig, T. L. Hughes and S. C. Zhang, Science **314**, 1757 (2006).

Ab initio calculations for iron-based superconductors FeTe and FeSe

Takahiro MISAWA

Department of Applied Physics, University of Tokyo,
7-3-1 Hongo, Bunkyo-ku, Tokyo 113-8656, Japan

Iron-based superconductors have diverse magnetic properties, although most of them have essentially the same band structures. For example, LaFeAsO (called 1111-type) shows the stripe antiferromagnetic (AFS) phase and its magnetic ordered moment is about $0.8\mu_{\rm B}$. The AFS phase is stable not only in the 1111-type compounds but also in the 122-type such as $BaFe_2As_2$. In contrast to this, FeTe (called 11-type) shows bicollinear antiferromagnetic state (AFB) and its ordered moment is about $2.0\mu_B$, while another 11-type compound FeSe does not show any magnetism but superconductivity appears below 10 K. Our previous studies show that this magnetic diversity can not be explained by the band structure alone and it is necessary to consider effects of electronic correlations [1,2].

To study the electronic correlation effects on the magnetism in iron-based superconductors, we employ *ab initio* downfolding scheme (for a review, see [3]). In this scheme, we first obtain the global band structures based on the density functional theory. From the band structures, we derive the low-energy effective models by using constrained random phase approximation. However, it is pointed out that double counting of the electron correlation between the low-energy states exists, and the effects of them are essential especially in the non-degenerate multi-band materials such as the iron-based superconductors [4]. To overcome this problem, constrained self-energy method is proposed, which can eliminate double counting of the electron correlations. In this method, the exchange-correlation energy in the conventional downfolding replaced with the self-energy corrections coming from the eliminated high-energy degrees of freedom as well as from the frequency-dependent part of the partially screened interactions.

In this study, we solve the low-energy effective models for FeTe and FeSe [5]. As a result, we find that the AFB state becomes the ground state in FeTe, while the AFS phase is the ground state in the previous effective model [6]. Moreover, we find that FeSe shows peculiar magnetic degeneracy, i.e., four different magnetic orders including AFS and AFB are energetically degenerate, while the AFS phase is also singled out in the previous model. This degeneracy may explain the absence of magnetic order and superconductivity observed in FeSe.

References

[1] T. Misawa, K. Nakamura, and M. Imada: J. Phys. Soc. Jpn. **80** (2011) 023704.

[2] T. Misawa, K. Nakamura, and M. Imada: Phys. Rev. Lett. **108** (2012) 177007.

[3] T. Miyake and M. Imada: J. Phys. Soc. Jpn. **79** (2010) 112001.

[4] H. Hirayama, T. Miyake, and M. Imada: Phys. Rev. B **87** (2013) 195144.

[5] H. Hirayama, T. Misawa, T. Miyake, and M. Imada: in preparation.

[6] T. Miyake, K. Nakamura, R. Arita, and M. Imada: J. Phys. Soc. Jpn. **79** (2010) 044705.

Effect of fluctuation near the ordered state in strongly correlated electron systems

Tetsuya MUTOU
Interdisciplinary Faculty of Science and Engineering, Shimane University
1060 Nishikawatsu-cho, Matsue, Shimane 690-8584

We studied some theoretical models of strongly correlated electron systems by numerical approach based on the many-body perturbation theory. To solve self-consistent equations in a three- or four-dimensional momentum-energy space, we carried out large-scale numerical calculations mainly on System A of the SCC-ISSP. In practical calculations, we applied simple program parallelizations to numerical integrals in the self-consistent equations.

With applying the fluctuation-exchange approximation to the single-band Hubbard model with realistic tight-binding parameters, we investigated the spin fluctuation effect in spin excitation spectra observed by neutron scattering experiments on electron-doped high-transition-temperature (high-T_c) superconductors [1]. In this study, we showed that the magnetic response of electron-doped high-T_c superconductors can be explained with the conventional Fermi-liquid approach.

The self-consistent second-order perturbation theory (SCSOPT) was applied to the multi-band Hubbard model corresponding to the electron system in bcc iron [2]. It was found that the spin stiffness constant is in good agreement with other theoretical results and it is smaller than the experimental value.

To investigate dynamical spin and density response functions in correlated fermion systems corresponding to two-dimensional (2D) liquid ^{3}He, the SCSOPT was also applied to the Hubbard model with repulsive interactions between fermions on up to fourth-neighbor sites [3]. It was pointed out that it is necessary to treat the large damping effect properly in explaining the propagating mode found in 2D liquid ^{3}He.

We investigated quasiparticle excitations in the periodic Anderson model which is one of models of the heavy Fermion systems by the dynamical mean-field theory with the iterated perturbation theory. We compared the renormalized Fermi energy of the quasiparticle with the effective hybridization energy, and investigated the quasiparticle-formation condition.

References

[1] T. Mutou and D. S. Hirashima: J. Phys. Soc. Jpn. **82** (2013) 094703.

[2] M. Nishishita, D. S. Hirashima, and S. Pandey: J. Phys. Soc. Jpn. **82** (2013) 114705.

[3] A. Kotani and D. S. Hirashima: Phys. Rev. B **88** (2013) 014529.

Numerical study of various phases and non-equilibrium phase transitions in correlated electron systems

Hideo AOKI
Department of Physics, University of Tokyo
Hongo, Tokyo 113-0033

Supersolid phase in electron-phonon systems[1, 2]

Competition and coexistence of various ordered phases are central issues of strongly correlated electron systems. Particularly interesting is the case where the diagonal and off-diagonal long-range order coexist. A primary example is the supersolid (SS) phase, in which superconductivity (SC) and charge order (CO) emerge simultaneously. Supersolid phases have long been pursued both theoretically and experimentally.

We have examined the existence of a supersolid phase in electron-phonon systems, in which a coexistence of e.g. s-wave SC and CO is known to occur in $Ba(Bi,Pb)O_3$ and $(Ba,K)BiO_3$. To this end, we take the Holstein model, one of the simplest and representative models for electron-phonon systems, and solve its ordered phases with the dynamical mean-field theory (DMFT). For the impurity solver of DMFT, we use the numerically exact continuous-time quantum Monte Carlo method, which has been extended so that one can treat SC, CO, and antiferromagnetic (AF) phases without bias[1, 2]. Obtained phase diagram for the intermediate electron-phonon coupling in the BCS-BEC crossover regime is shown in Fig. 1. One can see that SS phase appears between CO and SC phases, where the SS is accompanied by a quantum critical point (QCP) at zero temperature. We have checked that SS phase is indeed stable against phase separation. The transition from SC to SS is continuous with diverging charge fluctuations accompanied by a kink in the superfluid density.

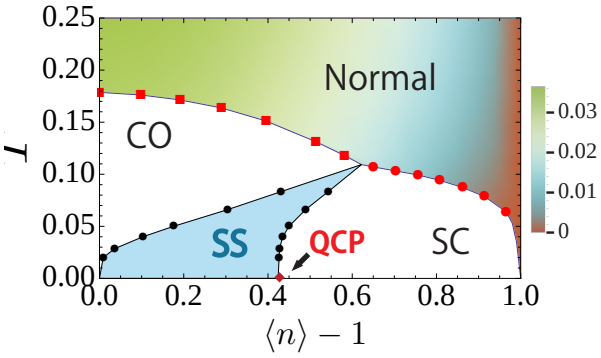

Figure 1: DMFT phase diagram of the Holstein model at the intermediate coupling regime [1]. The colour code in the normal phase represents the dc conductivity.

Nonequilibrium dynamical mean-field theory and its cluster extension[3, 4]

Nonequilibrium dynamical mean-field theory (DMFT) is a well-established approach to simulate nonequilibrium states of correlated many-body systems. It maps the original lattice model to an effective impurity embedded in the self-consistently determined mean-field bath. The essential approximation is to identify the local impurity self-energy with the lattice self-energy, which limits the range of applicability of the nonequilibrium

DMFT. The method has been applied to various systems, and provided fruitful insights for nonequilibrium systems. In view of the recent progress, we have written a review article on the nonequilibrium DMFT and its applications[3].

The local approximation for the self-energy may break down in low dimensional systems, where spatially nonlocal fluctuations play an essential role. To overcome this, we have proposed the nonequilibrium dynamical cluster approximation (DCA) [4], in which the lattice model is mapped to a multi-site cluster rather than a single impurity. As a result, one can take account of short-range correlations within the cluster size. We have applied it to the one- and two-dimensional Hubbard models. In Fig. 2, we plot the time evolution of the double occupancy and the jump of the momentum distribution at Fermi energy after an interaction quench at $t = 0$. We find characteristic momentum-dependent relaxations, which is attributed to the effect of nonlocal correlations.

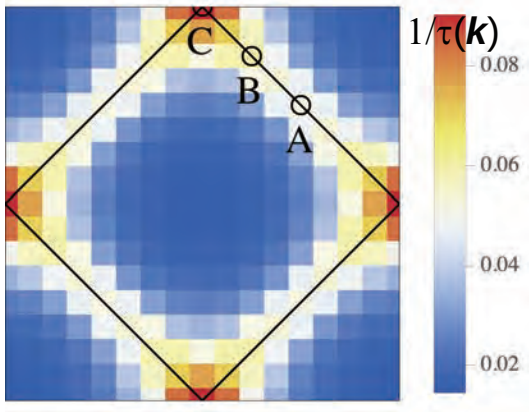

Figure 2: Colour-coded plot of the momentum-dependent quasiparticle lifetime $\tau(k)$ for an interaction quench $U/J = 0 \rightarrow 2$ at $T = 0$. Solid lines indicate the noninteracting Fermi surface.[4]

References

[1] Y. Murakami, P. Werner, N. Tsuji, and H. Aoki: Supersolid phase accompanied by a quantum critical point in the intermediated coupling regime of the Holstein model, arXiv:1402.6456.

[2] Y. Murakami, P. Werner, N. Tsuji, and H. Aoki: Ordered phases in the Holstein-Hubbard model: Interplay of strong Coulomb interaction and electron-phonon coupling, Phys. Rev. B **88**, 125126 (2013).

[3] H. Aoki, N. Tsuji, M. Eckstein, M. Kollar, T. Oka, and P. Werner: Nonequilibrium dynamical mean-field theory and its applications, to be published in Rev. Mod. Phys. (arXiv:1310.5329).

[4] N. Tsuji, P. Barmettler, H. Aoki, and P. Werner: Nonequilibrium dynamical cluster theory, arXiv:1307.5946.

Numerical Studies on Topological and Spin Liquid Phases of Iridium Oxides

Youhei YAMAJI
Department of Applied Physics, University of Tokyo
Hongo 7-3-1, Bunkyo-ku, Tokyo 113-8656

Cooperation and competition between strong electron correlations and spin-orbit couplings have recently attracted much attention. Iridium oxides offer the playgrounds and indeed exhibit intriguing phenomena. Especially, theoretical predictions on realization of novel quantum phases are interesting: The novel phases are condensed-matter realization of Weyl fermions predicted in magnetic phases of pyrochlore iridates $R_2Ir_2O_7$ (R: rare-earth elements) and a quantum spin liquid state with Majorana excitations in honeycomb iridates A_2IrO_3 (A=Na, Li).

The Weyl electrons in the bulk are shown to form metallic surface states called *Fermi arcs*, and to exhibit anomalous transports due to *chiral anomalies*, which have triggered intensive studies on the emergence of the Weyl electrons. However, the Weyl electrons are easily annihilated in pairs. The experimental observation requires fine tunings of the materials.

The spin liquid ground state proven by A. Kitaev for an exactly solvable model, now called Kitaev model, has also inspired extensive studies on A_2IrO_3 as a model system to realize the Kitaev's spin liquid. However, Na_2IrO_3 does not show spin liquid properties experimentally but exhibits a zigzag type magnetic order. A mechanism that stabilizes the zigzag magnetic order and a recipe to realize the Kitaev's spin liquid phase have remained controversial yet.

We revealed that magnetic domain walls in $R_2Ir_2O_7$ host metallic domain-wall states with Fermi surfaces, instead of arcs, even after pair-annihilatin of the Weyl electrons [1]. By using a fully unrestricted Hartree-Fock approximation for a Hubbard-type model of $J_{\rm eff} = 1/2$ states with large supercells at the system B, we show that domain walls perpendicular to $(01\bar{1})$, (100), and (111) directions host metallic domain-wall states. The insertion of the magnetic domain walls induces uniform magnetization. The uniform magnetization enables us to control the metallic domain-wall states with magnetic fields and explains weak ferromagnetism universally observed in $R_2Ir_2O_7$.

We also derived an *ab initio* effective spin model of Na_2IrO_3 [2], which has dominant Kitaev-type couplings together with newly-introduced anisotropy originating from the trigonal distortion. By using Arnoldi methods and thermal pure quantum states [3] at the system B, we show that the magnetic orders, specific heat, and magnetic susceptibilities of the effective spin model are indeed consistent with experiments. We also show how to approach spin liquids.

References

[1] Y. Yamaji and M. Imada: Phys. Rev. X, in press; arXiv:1306.2022.

[2] Y. Yamaji, Y. Nomura, M. Kurita, R. Arita, and M. Imada: arXiv:1402.1030.

[3] S. Sugiura and A. Shimizu: Phys. Rev. Lett. **108** (2012) 240401.

Electronic state calculations of quantum mechanical order appearing in metal compounds

Koichi KUSAKABE
Graduate School of Engineering Science, Osaka University
1-3 Machikaneyama, Toyonaka, Osaka 560-8531

1. Introduction

To derive unified representation of the strongly correlated electron systems (SCES), we need to utilize consistent determination of a basis for expansion of the Hilbert space, keeping description of the quantum fluctuation effects appearing as correlated many-body state vectors and many-body Green's functions. The multi-reference density functional theory[1, 2] gives an answer. For the real applications, we need to set up a good basis. In this study, we mainly focused on creation of a proper basis and estimation of scattering amplitudes appearing for each specific material system.

2. Estimation of electronic parameters and prediction of novel cuprates

A starting expression of the multi-layered cuprate superconductors may be taken as the DFT-GGA description of atomic structures. Actually, we found good convergence in the atomic structure around the experimentally observed structures.[3] We rely on the spin fluctuation mechanism of superconductivity for a judgment of an optimally doped cuprate. Recent confirmation of the correlation between the transition temperature and the Fermi surface shape[4] suggests that, when $3d_{3z^2-r^2}$ orbitals do not have notable contribution at the Fermi level, keeping the energy separation ΔE from $3d_{3z^2-r^2}$ to $3d_{x^2-y^2}$ large around 2eV, then the better Fermi surface nesting, the higher transition temperature appears.

To certify our procedure, we first confirmed that 1) we have small hole-doping dependence of the electronic structure parameters, *i.e.* ΔE and the Fermi surface shape controlling factor $r_{x^2-y^2}$, and 2) these parameters are almost same with little systematic change against the layer number of CuO_2 planes in the unit cell. Following the rule for the orbital distillation effect[6], we try to search for materials which show better sets of $(\Delta E, r_{x^2y^2})$.

We have chosen Hg1223 ($T_c \geq$ 135K) and Tl1223 ($T_c \geq$ 110K) for this optimization. Our analysis suggests that $TlR_2A_2Cu_3O_9$ with R=Li, Y, and A=Li, Na, K, Rb, Cs may appear as stable crystal structures. Among these candidates, we found better conditions on the above parameters for (R, A)=(Y, Li), (Y, Na), and (Y, Rb).[3, 5] When we substitute Cd for Hg in $HgBa_2Ca_2Cu_3O_8$, we have small $r_{x^2-y^2}$, keeping ΔE around 2eV, which is a good condition for the high T_c.

3. Doping mechanism of α-pyridine-TiNCl

The superconductivity in α-MNX compounds attracts interests because of their special two-dimensional electronic structures. Experimentally, origin of the electron carrier was not clarified for pyridine-TiNCl. We have proposed that reduction of pyridine by water molecules could be the solution. We have obtained the electronic structure of pyridinium-ion-doped pyridine-TiNCl. (Fig. 1) The conduction band is doped by pyridinium ion. The

conformation of pyridine layer is affected by the doping, which is though to be origin of change in inter-layer electronic scattering processes. We expect that this non-stoichiometry condition would mediate pair-hopping processes.

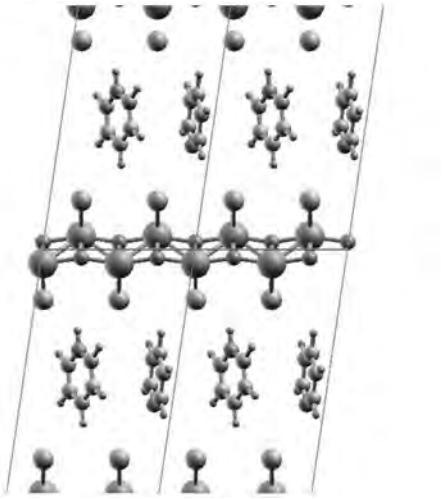

Figure 1: Optimized crystal structures of pyridinium-doped py-TiNCl.

4. Hydrogenated vacancies of graphene

In a recent study on argon sputtering and hydrogenation treatment of graphene, Ziatdinov *et al.* have succeeded in fabrication of various hydrogenated graphene vacancies.[7] They called stable structures V111 for the vacancy with three hydrogen atoms and V211 for the vacancy with four hydrogen atoms. The electronic structure shows a non-bonding localized state around V111, while V211 gives a gap at the Dirac point.

Utilizing the Löwdin charge analysis with the density of states, we concluded that the Fermi level is kept at the Dirac point for charge neutral hydrogenated graphene vacancies. This result suggests existence of a localized spin at V111. In addition, the experimental finding of bias induced carrier doping of graphene device structure suggests a possible Kondo state for V111.

Acknowledgement

The author (K.K.) is grateful to Prof. I. Maruyama, Mr. K. Yamada, Mr. S. Miyao, Mr. S. Gagus Ketut, Mr. Keisuke Iwatani, and Mr. Naoki Morishita for their collaboration. K. K. thanks fruitful collaboration in the study of hydrogenated graphene with Prof. T. Enoki, Prof. T. Mori, Prof. M. Kiguchi, Prof. K. Takai, Prof. S. Fujii, Mr. M. Ziatdinov, and Mr. Y. Kudo. K.K. is grateful to Prof. K. Kuroki, and H. Sakakibara for their collaboration in the study of cuprate superconductors. This work was partly supported by KAKENHI (No. 23540408), and the golbal COE program from MEXT.

References

[1] K. Kusakabe, *et al.*: J. Phys. Condens. Matter **19** (2007) 445009.

[2] K. Kusakabe and I. Maruyam: J. Phys. A: Math. Theor. **44** (2011) 135305.

[3] S. Miyao, *et al.*: arXiv:1304.5043.

[4] H. Sakakibara, *et al.*: arXiv:1403.2497.

[5] S. Miyao, *et al.*: J. Phys. Soc. Jpn. Suppl. **83** (2014) in press.

[6] H. Sakakibara, *et al.*: Phys. Rev. Lett. **105** (2010) 057003 .

[7] M. Ziatodinov, *et al.*: Phys. Rev. B **89** (2014) 155405.

Electronic properties of multi-orbital electronic system with strong spin-orbit coupling

Toshihiro SATO
Computational Condensed Matter Physics Laboratory, RIKEN
Wako, Saitama 351-0198, Japan

The transition-metal oxides have been studied as typical materials of strongly correlated electronic systems. Recent experimental studies have reported interesting behaviors of $5d$ transition-metal Ir oxides, for example Sr_2IrO_4. In these materials, there exists a strong spin-orbit coupling (SOC) with an electron correlation and the SOC splits the t_{2g} bands in the crystal field into the effective local angular momentum $J_{\rm eff}$=1/2 doublet and $J_{\rm eff}$=3/2 quartet bands. In Sr_2IrO_4 with totally five electrons, $J_{\rm eff}$=1/2 antiferromagnetic (AF) insulator has been observed against the expectation from $3d$ and $4d$ transition-metal Ir materials of the similar layered perovskite structure [1, 2, 3], and theoretical understanding in the experimental results has been successful by several numerical methods [1, 4, 5, 6, 7]. However, theoretical understanding of multi-orbital systems with the electron correlation and the SOC systematically is still controversial.

We study electronic and magnetic properties of the three-orbital Hubbard model with the full Hund' rule coupling and the SOC terms at five electrons filling,

$$
\begin{aligned}
H &= \sum_{\langle i,j\rangle,\gamma,\sigma} t^{\gamma} c^{\gamma\dagger}_{i\sigma} c^{\gamma}_{j\sigma} - \sum_{i,\gamma,\sigma} \mu^{\gamma} n^{\gamma}_{i\sigma}, \\
&+ U \sum_{i,\gamma} n^{\gamma}_{i\uparrow} n^{\gamma}_{i\downarrow} + \frac{U'-J}{2} \sum_{i,\gamma\neq\delta,\sigma} n^{\gamma}_{i\sigma} n^{\delta}_{i\sigma} \\
&+ \frac{U'}{2} \sum_{i,\gamma\neq\delta,\sigma} n^{\gamma}_{i\sigma} n^{\delta}_{i\bar{\sigma}} - J \sum_{i,\gamma\neq\delta} c^{\gamma\dagger}_{i\uparrow} c^{\gamma}_{i\downarrow} c^{\delta\dagger}_{i\downarrow} c^{\delta\dagger}_{i\uparrow} \\
&+ J' \sum_{i,\gamma\neq\delta} c^{\gamma\dagger}_{i\uparrow} c^{\gamma\dagger}_{i\downarrow} c^{\delta}_{i\downarrow} c^{\delta}_{i\uparrow} \\
&+ \lambda \sum_{1,\gamma,\delta,\sigma,\sigma'} \langle\gamma|\mathbf{L}_i|\delta\rangle \cdot \langle\sigma|\mathbf{S}_i|\sigma'\rangle c^{\gamma\dagger}_{i\sigma} c^{\delta}_{i\sigma'},
\end{aligned}
$$

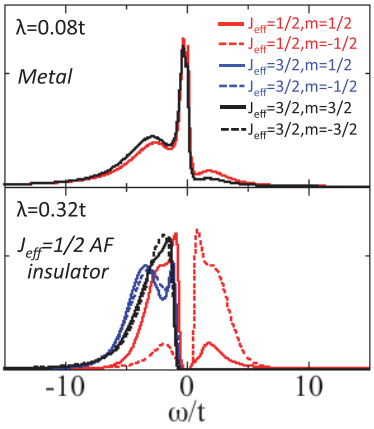

Figure 1: Density of states for two λ's at U=8t and T=0.06t .

where t^{γ} is the nearest-neighbor hopping amplitude with orbital γ=(yz, zx, xy) and μ^{γ} is the chemical potential. U (U') is the intra-orbital (inter-orbital) Coulomb interaction and J (J') is the Hund' s (pair-hopping) coupling, and we set U=U'+2J and J=J'=0.15U. λ is the SOC and $\mathbf{L}_i$ ($\mathbf{S}_i$) is the orbital (spin) angular momentum operator at site i. $c^{\gamma\dagger}_{i\sigma}$ ($c^{\gamma}_{i\sigma}$) is an electron creation (annihilation) operator with spin σ and orbital γ at site i and electron density operator is $n^{\gamma}_{i\sigma} = c^{\gamma\dagger}_{i\sigma} c^{\gamma}_{i\sigma}$. We use the dynamical mean field theory [8] employing a semielliptic bare density of states with the equal bandwidth (t^{γ}=t) for the three orbitals. We calculate the Green's functions inside the orbital by using the continuous-time quantum Monte Carlo solver based on the strong coupling expansion [9]. This numerical calculation was performed by the numerical computations with facilities at Supercomputer Center in ISSP, e.g., for λ=0.1t, U=8t, and T=0.06t, about 10^8 Monte Carlo sweeps

and averaging over 64 samples, and the self-consistency loop of the DMFT converges about 100 hours. We examine λ-dependence of electronic structure at U=8t and T=0.06t fixed, and then confirm the transition from metallic to insulating state with a magnetic order with varying λ as shown in Fig. 1. The insulating state shows $J_{\rm eff}$=1/2 AF insulator, indication of the half-filled $J_{\rm eff}$=1/2 and full-filled $J_{\rm eff}$=3/2 bands. Moreover, we find that excitonic insulating state by the electron-hole paring between $J_{\rm eff}$=1/2 and $J_{\rm eff}$=3/2 bands is induced by λ at larger U, in addition to the $J_{\rm eff}$=1/2 AF insulator.

This work was done in collaboration with Dr. T. Shirakawa and Dr. S. Yunoki.

References

[1] B. J. Kim *et al.*: Phys. Rev. Lett. **101**, (2008) 076402.

[2] B. J. Kim *et al.*: Science **323**, (2009) 1329.

[3] K. Ishii *et al.*: Phys. Rev. B **83** (2011) 115121.

[4] H. Watanabe *et al.*: Phys. Rev. Lett. **105**, (2010) 216410.

[5] T. Shirakawa *et al.*: J. Phys.:Conf. Ser. **273**, (2011) 012148.

[6] C. Martins *et al.*: Phys. Rev. Lett. **107**, (2011) 266404.

[7] R. Arita *et al.*: Phys. Rev. Lett. **108**, (2012) 086403.

[8] G. Kotliar *et al.*: Phys. Rev. Lett. **87**, (2001) 186401.

[9] P. Werner *et al.*: Phys. Rev. Lett. **97**, (2006) 076405.

Quantum Monte Carlo simulation and electronic state calculations in correlated electron systems

Takashi YANAGISAWA
Electronics and Photonics Research Institute
National Institute of Advanced Industrial Science and Technology (AIST)
AIST Central 2, 1-1-1 Umezono, Tsukuba 305-8568

The mechanisms of superconductivity in high-temperature superconductors have been extensively studied using various two-dimensional models of electronic interactions. The CuO_2 plane in cuprates plays an important role for the appearance of superconductivity. It is well known that the parent materials are a Mott insulator and the hole doping leads to superconductivity. In this report we present the results on the Mott transition of high temperature cuprates at half- lling. In the case of cuprates the insulating state is regarded as a charge-transfer insulator, We propose a wave function of Mott state on the basis of an improved Gutzwiller function. To use computers more e ciently, we performed parallel computing with 64 or 128 cores.

The three-band model that explicitly includes Oxygen p orbitals contains the parameters U_d, U_p, t_{dp}, t_{pp}, ϵ_d and ϵ_p. U_d is the on-site Coulomb repulsion for d electrons and U_p is that for p electrons. t_{dp} is the transfer integral between adjacent Cu and O orbitals and t_{pp} is that between nearest p orbitals. The energy unit is given by t_{dp}.

The Gutzwiller wave function is given as $\psi_G = P_G\psi_0$, where P_G is the Gutzwiller projection operator given by $P_G = \prod_i[1 - (1-g)n_{di\uparrow}n_{di\downarrow}]$ with the variational parameter in the range from 0 to unity. P_G controls the on-site electron correlation on the copper site. ψ_0 is a one-particle wave function such as the Fermi sea or the Hartree-Fock state with spin density wave. ψ_0 contains the variational parameters $\tilde{t}_{dp}$, $\tilde{t}_{pp}$, $\tilde{\epsilon}_d$ and $\tilde{\epsilon}_p$: $\psi_0 = \psi_0(\tilde{t}_{dp}, \tilde{t}_{pp}, \tilde{\epsilon}_d, \tilde{\epsilon}_p)$. In the non-interacting case, $\tilde{t}_{dp}$ and $\tilde{t}_{pp}$ coincide with t_{dp} and t_{pp}, respectively. In this report, we consider the Gutzwiller function with an optimization operator:

$$\psi = \exp(\lambda K)\psi_G, \tag{1}$$

where K is the kinetic part of the total Hamiltonian H_{dp} and λ is a variational parameter. This type of wave function is an approximation to the wave function in quantum Monte Carlo method[1, 2, 3]. The computations were performed by using the variational Monte Carlo method.

The above wave function of course can be regarded as a wave function for the Mott state of the single-band Hubbard model. We rst show the results for the single-band Hubbard model. In Fig.1 we show the energy per site as a function of U. The Gutzwiller parameter g is shown in Fig.2 which indicates that g vanishes at a critical value U_c. The state with vanishing g would be an insulating state because of vanishingly small double occupancy. It is seen from Fig.1 that the energy changes the curvature near $U \quad U_c$. The energy is well approximated by a function of C/U with a constant C when U is large:

$$\frac{E}{N} \quad -C\frac{t^2}{U} \propto -CJ. \tag{2}$$

This means that the energy gain mainly comes from the exchange interaction which is of the order of $1/U$.

The gure 3 exhibits the ground state energy per site $E/N - \epsilon_d$ as a function of $\Delta_{dp} \equiv \epsilon_p - \epsilon_d$ for the d-p model. We can nd that the curvature of the energy, as a function of Δ_{dp}, is changed near $\Delta_{dp} \quad 2$. The energy is well

tted by $1/\Delta_{dp}$ shown by the dashed curve in Fig.3 when Δ_{dp} is greater than a critical value. This is because the most energy gain comes from the exchange interaction between nearest neighbor d and p electrons. This exchange interaction, denoted by J_K, is given by $J_K = t_{dp}^2(1/\Delta_{dp} + 1/(U_d - \Delta_{dp}))$. In the low carrier limit with large level di erence Δ_{dp}, the second term in the exchange coupling gives a negligible contribution. Thus, the effective exchange coupling J_K is approximated as $J_K = t_{dp}^2/\Delta_{dp}$. In the insulating state the energy gain is proportional to J_K,

$$\Delta E = \frac{E}{N} - \epsilon_d \simeq -C\frac{t_{dp}^2}{\Delta_{dp}} = -CJ_K, \qquad (3)$$

for a constant C. The critical value of Δ_{dp} is $(\Delta_{dp})_c \simeq 2t_{dp}$. When t_{dp} 1.5eV, the charge-transfer gap is about 3eV.

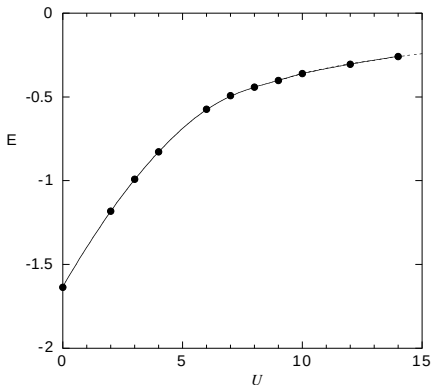

Figure 1: Ground state energy of the 2D Hubbard model as a function U at half- lling. The system size is 6 6.

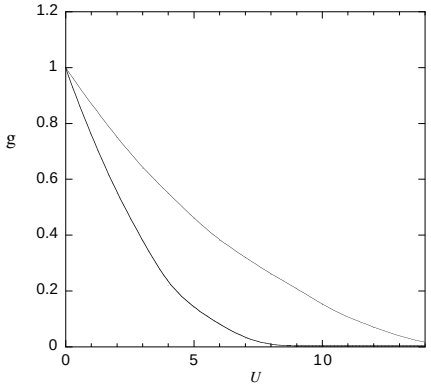

Figure 2: Gutzwiller parameter g as a function of U at half- lling. The parameter g almost vanishes at U 8 showing a transition to an insulating state. The upper line is for $\lambda = 0$ (Gutzwiller function).

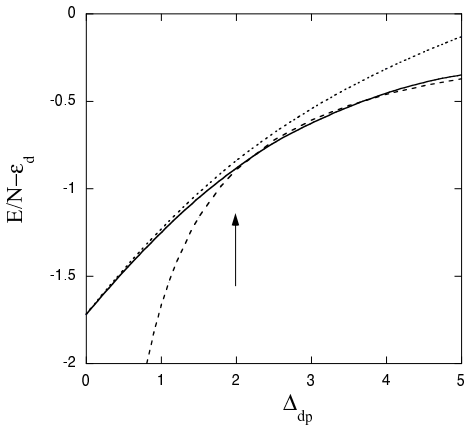

Figure 3: Ground state energy of the 2D d-p model as a function of Δ_{dp} for $t_{pp} = 0.4$ and $U_d = 8$ (in units of t_{dp}) in the half- lled case. The calculations were performed on 6 6 lattice. The arrow indicates a transition point, where the curvature is changed. The dotted curve is for the Gutzwiller function ($\lambda = 0$). The dashed curve indicates a curve given by a constant times $1/(\epsilon_p - \epsilon_d)$.

References

[1] T. Yanagisawa, Phys. Rev. B**75**, 224503 (2007) (arXiv: 0707.1929).

[2] T. Yanagisawa, New J. Phys. 15, 033012 (2013).

[3] T. Yanagisawa and M. Miyazaki, preprint (2014).

Dynamical Jahn-Teller Effect in Spin-Orbital Coupled System

Sumio ISHIHARA
Department of Physics, Tohoku University
Sendai 980-8578

No signs for long-range magnetic ordering down to the low temperatures, termed the quantum spin-liquid (QSL) state, are one of the fascinating states of matter in modern condensed matter physics. A number of efforts have been made to realize the QSL states theoretically and experimentally. A transition-metal oxide, $Ba_3CuSb_2O_9$ [1, 2], is a new candidate of the QSL state, in which S = 1/2 spins in Cu^{2+} ions are responsible for the magnetism. Almost isotropic g factors observed in ESR provide a possibility of no static long-range orbital orders and novel roles of orbital on the QSL.

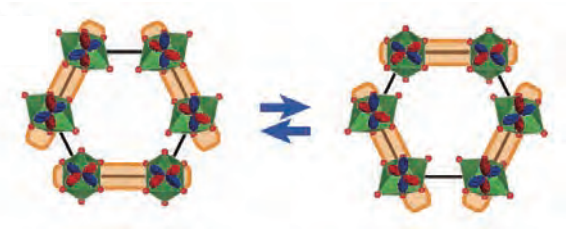

Figure 1: A schematic picture for the SORS. Shaded bonds represent the spin-singlet and parallel-orbital bonds.

We examine a possibility of the QSL state in a honeycomb-lattice spin-orbital (SO) system [3]. Beyond the previous theories for QSL in quantum magnets with the orbital degree of freedom, the present study focuses on the dynamical Jahn-Teller (DJT) effect, which brings about a quantum tunneling between stable orbital-lattice states. We suggest that a spin-orbital resonant state (SORS), where the two degrees of freedom are entangled with each other (see Fig. 1), is induced by the DJT effect.

First, we derive the low-energy electron-lattice model where the super-exchange interaction, the JT effect, and the lattice dynamics are taken into account, that is, $\mathcal{H} = \mathcal{H}_{\rm exch} + \mathcal{H}_{\rm JT}$. The Hamiltonian is analyzed by the exact-diagonalization method combined with the mean-field approximation, and the quantum Monte Carlo simulation with the mean-field approximation.

The phase diagram on a plane of the J_{DJT}-J_{SE} is shown in Fig. 2, where J_{DJT} and J_{SE} are amplitudes of the DJT effect and the super-exchange interaction, respectively. The spin-orbital resonant state appears in intermediate region of J_{DJT} and J_{SE}, that is, this quantum resonant state is realized by interplay of the two interactions. An obtained schematic picture for the spin-orbital resonant state is presented in Fig. 1 where the spin-singlet states and the parallel-orbital states occurs cooperatively.

To demonstrate the spin-orbital entanglement from the viewpoint of dynamics, we show, in Fig. 2, the dynamical spin-correlation function $K_s(\omega)$ and the dynamical orbital correlation function $K_\tau(\omega)$ calculated by using the Lanczos method in finite size clusters. Gapped spin excitations and low-lying orbital excitations are seen in the spin-orbital resonant state. In the resonant phase, in contrast to the orbital-ordered phase, an intensive or-

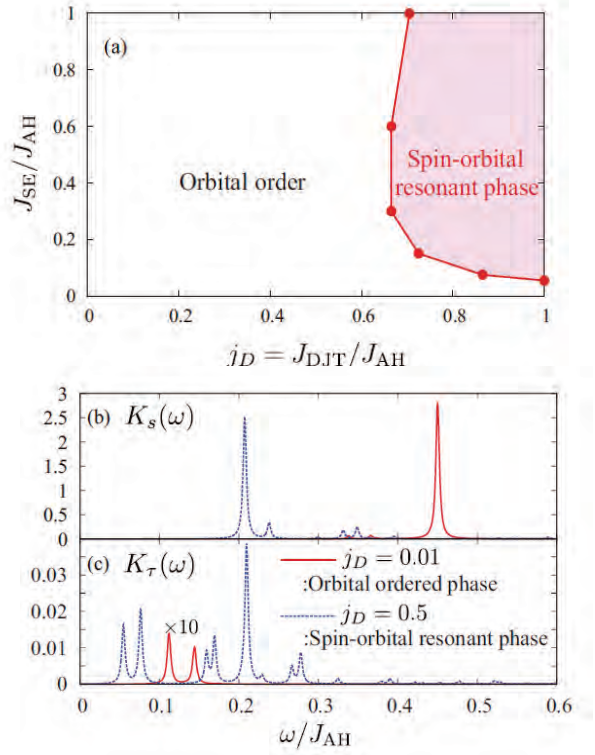

Figure 2: Upper: Phase diagram on the plane of J_{DJT}/J_{AH} and J_{SE}/J_{AH}. Lower: The dynamical spin-correlation function $K_s(\omega)$, and the dynamical orbital-correlation function $K_\tau(\omega)$ in the orbital ordered phase and in the SO resonant phase.

bital excitation is seen around the lowest spin-excitation energy.

The present theory provides a number of forceful predictions in $Ba_3CuSb_2O_9$. There will be a crossover frequency/magnetic field in ESR, corresponding to J_{DJT} and J_{SE}, where the anisotropy in the g factor is changed qualitatively. Dynamics of the orbital-lattice coupled vibronic excitation is expected to be observed directly by inelastic light/x-ray scattering spectra around 1$\sim$ 10 meV.

This work was supported by KAKENHI from MEXT and Tohoku University “ Evolution ” program. Parts of the numerical calculations are performed in the supercomputing systems in ISSP, the University of Tokyo.

References

[1] S. Nakatsuji, K. Kuga, K. Kimura, R. Satake, N. Katayama, E. Nishibori, H. Sawa, R. Ishii, M. Hagiwara, F. Bridges, T. U. Ito, W. Higemoto, Y. Karaki, M. Halim, A. A. Nugroho, J. A. Rodriguez-Rivera,M. A. Green, and C. Broholm, Science **336**, 559 (2012).

[2] Y. Ishiguro, K. Kimura, S. Nakatsuji, S. Tsutsui, A. Q. R. Baron, T. Kimura, and Y. Wakabayashi, Nat. Commun. **4**, 2022 (2013).

[3] J. Nasu and S. Ishihara, Phys. Rev. B **88**, 094408 (2013).

An Efficient Impurity Solver for Tomonaga-Luttinger Liquids

Kazumasa HATTORI

Institute for Solid State Physics,

University of Tokyo, Kashiwa-no-ha, Kashiwa, Chiba 277-8581

Continuous-time quantum Monte Carlo (CTQMC) methods have been developed and widely used for solving quantum impurity problems in strongly correlated electron systems in recent years [1]. They are numerically exact methods and used for not only fermionic systems but also bosonic ones including fermion-boson mixtures.

In this study, we have developed a CTQMC for bosonized Tomonaga-Luttinger (TL) liquids in one-dimensional systems. Technically, this is rather different from existing bosonic CTQMC, because of the dual (fermion/boson) nature of one-dimensional electron systems, which is highlighted in the existence of the Klein factors, various vertex operators relevant to interesting physical quantities, and ultraviolet cutoff (a) that is essentially infinity (i.e., continuous limit).

For a short summary of our results, we here show results for a back-scattering potential model in a spinless-fermionic system investigated by Kane and Fisher [2]. Figure 1 shows imaginary-time (τ) dependence of (left-moving) electron Green's function (G) calculated in the bosonization scheme in the CTQMC with several different values of a, the TL parameter g, and the inverse of temperature β. This clearly indicates that the asymptotic form of G is $\sim 1/\tau^{1/2g}$, which supports a prediction by Furusaki [3].

Since our method can be applicable to other models easily, we expect that various non-trivial physics in impurity problems in TL liquids will be clarified in future investigations.

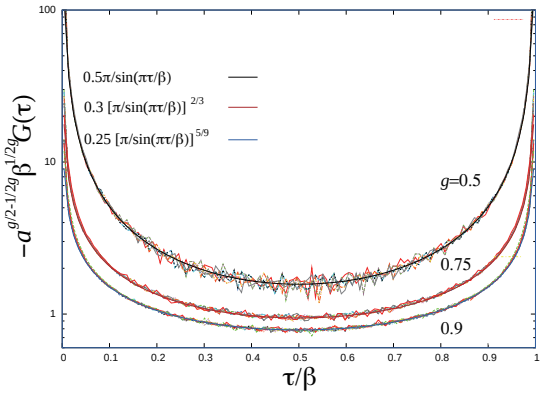

Fig. 1: G vs. τ for g = 0.9, 0.75, and 0.5, with three sets of cutoff a =1, 0.5, 0.25 and β = 200, 400, and 800. For large τ ($\sim\beta/2$), all the data are scaled into the functional form indicated in the figure.

References

[1] See for a review: E. Gull et al,: Rev. Mod. Phys. **83** (2011) 349.

[2] C. L. Kane and M. P. A. Fisher: Phys. Rev. Lett. **68**, (1992) 1220.

[3] A. Furusaki: Phys. Rev. B **56** (1997) 9352

Multiple enhancement mechanism of the dynamic spin-fluctuation in the iron based superconductors

Hayato ARAI, Yuki FUSEYA
University of Electro-Communications
1-5-1 182-0021 Chofugaoka, Chofu, Tokyo

Since the iron based superconductor LaFeAsO was found in 2008, many scientists have discussed about its mechanism of superconductivity. First, a mechanism of the phonon mediated superconductivity was proposed[1]. Then, a mechanism of the spin-fluctuation mediated superconductivity was proposed [2]. After that, a mechanism of the orbital fluctuation mediated superconductivity was proposed[3] in order to explain the impurity effect of iron based superconductors. However, we have not reached a consensus on the mechanism of the iron based superconductor yet. Our purpose is to clarify the mechanism of superconductivity of the iron pnictide on the basis of the spin-fluctuation mechanism. The reason why we focus on the spin-fluctuation mechanism is the fact that the superconducting phase locates next to the antiferromagnetic phase.

We adopted a multi-orbital Hubberd model in order to consider the complicated inter-orbital interactions of the iron pnictide. We constructed the five energy band model of LaFeAsO based on the first principle calculation and the most localized Wannier functions. We apply the FLuctuation EXchange (FLEX) approximation to this model. This calculation solves the multi-orbital Dyson equation self consistently and gives Green's functions that include the effect of interactions. T_c is calculated by solving the linearized Eliashberg equation with this Green's functions. We need to calculate the process using ISSP since we should vectorize the large matrix multiplication in order to reduce the calculation time. The accurate results we required need some self-consistent calculations with $32 \times 32 \times 1$ k-points, 5×2 orbitals and 4096 Matsubara frequency system size in system-B. We cannot consider the scale calculations without the ISSP system.

We have already known some results of the T_c measurement and the low-energy spin-fluctuation by the NMR experiment of $LaFeAs_{1-x}P_xO_{1-y}F_y$[4]. It is known that the P-doping distorts the crystal structure. The degree of this distortion can be parameterized by the Fe-As-Fe bond angle α. We calculated the orbital dependent dynamic spin-susceptivity and solved the linearized Eliashberg equation as a function of α.

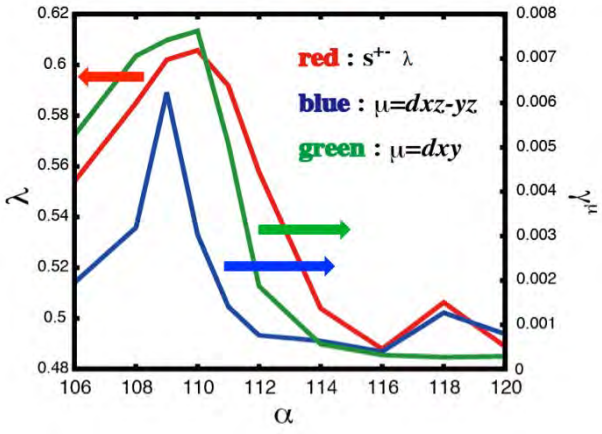

FIG. 1. Eigenvalue λ and low-energy spin-fluctuation γ versus Fe-As-Fe bond angle α. μ denotes the orbital.

The calculated results of the low-energy spin-fluctuations (γ^μ ; μ denotes the orbital

dependence) and the eigenvalue of the linearized Eliashberg equation (λ), which are shown in Fig 1. There is a clear correlation between λ and γ^{μ}. It is found that λ exhibits a double-peak structure : the peak of λ around 110° is due to the spin-fluctuation of both γ^{dxz-yz} and γ^{dxy} while the peak around 118° is due to that of only γ^{dxz-yz}. We conclude that the present theoretical results can give an interpretation of the experimental results that T_c exhibits the double peak structure as a fundtion of P-doping.

[1] L. Boeri, O. V. Dolgov, and A. A. Golubov, Phys. Rev. Lett. **101**, 026403 (2008).

[2] I. Mazin, D. J. Singh, M. D. Johannes, and M. H. Du, Phys. Rev. Lett. **101**, 057003 (2008).

[3] H. Kontani and S. Onari, Phys. Rev. Lett. **104**, 157001 (2010).

[4] H. Mukuda, *et al*, J. Phys. Soc. Jpn. **89**, 064511 (2014).

Development of Nonlocal Dynamical CPA and Numerical Study of Long-Range Magnetic Correlations

Yoshiro KAKEHASHI, M. Atiqur R. PATOARY, and Sumal CHANDRA
Department of Physics and Earth Sciences, Faculty of Science, University of the Ryukyus, 1 Senbaru, Nishihara, Okinawa, 903-0213, Japan

Development of the theory to describe nonlocal electron correlations is one of the central issues in condensed matter physics. Although the effective medium approaches such as the dynamical cluster approximation and the cluster dynamical mean field theory have been developed and can treat nonlocal correlations self-consistently, the range of nonlocal correlations are limited. In order to take into account the long-range inter-site correlations systematically, we developed the dynamical cluster CPA. The theory is an extension of the dynamical CPA [1] and takes into account the long-range nonlocal correlations by making use of the off-diagonal effective medium and the incremental cluster expansion.

The thermal averages of the physical quantities are obtained by solving the isothermal molecular-dynamics (MD) equations for the field variables $\{\xi_i\}$.

$$\dot{\xi}_i = \frac{1}{\mu_{\rm LM}} p_i, \tag{1}$$

$$\dot{p}_i = \frac{1}{2} U\Big(\langle m_i(\xi)\rangle - \xi_i\Big) - \eta_i\, p_i, \tag{2}$$

$$\dot{\eta}_i = \frac{1}{Q}\Big(\frac{p_i^2}{\mu_{\rm LM}} - k_{\rm B}T\Big). \tag{3}$$

Here U is the Coulomb energy parameter, p_i is the momentum being conjugate to the fictitious local moment variable ξ_i on site i, η_i is the friction variable on site i, $\mu_{\rm LM}(Q)$ is a mass for local moment (friction variable), and $m_i(\xi)$ is the average magnetic moment given by

$$m_i(\xi) = \frac{1}{\beta}\sum_{\sigma}\sigma\sum_{l=-\infty}^{\infty}\tilde{G}_{ii\sigma}(\xi, l), \tag{4}$$

$\tilde{G}_{ii\sigma}(\xi, l)$ being a Green function projected onto the static field variable $\{\xi_i\}$.

Figure 1 shows a numerical example of magnetization vs temperature curve for the single-band Hubbard model on the fcc lattice in the high-temperature approximation. Although the accuracy is not enough because of a small number of MD steps (typically 3000 steps), calculated $T_{\rm C}$ is about 0.085. It indicates that the Curie temperature is reduced by 50% by means of the long-range nonlocal correlations.

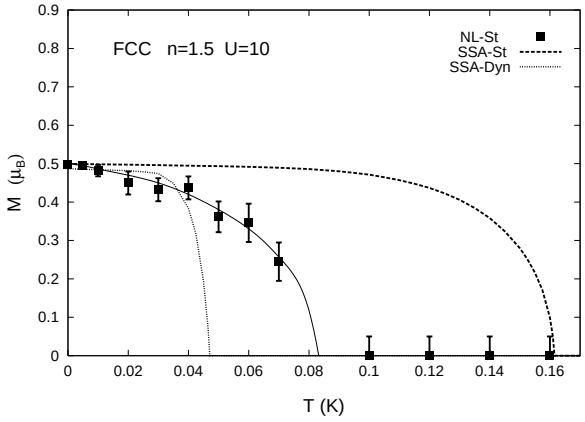

Figure 1: Calculated magnetization vs. temperature curves for the single-site static CPA (dashed-line), dynamical CPA (dotted curve), and the nonlocal dynamical CPA with static approximation (closed circles with error bars and thin line).

References

[1] Y. Kakehashi: Adv. Phys. **53**, (2004) 497; 'Modern Theory of Magnetism in Metals and Alloys' (Springer, Heidelberg, 2013).

Quantum Monte Carlo Approach to Odd-Frequency Superconductivity

Shintaro HOSHINO
Department of Basic Science, The University of Tokyo, Meguro, Tokyo 153-8902, Japan

Strongly correlated electron systems show a variety of intriguing phenomena including unconventional superconductivity. Especially we address the odd-frequency (OF) superconductivity, which is characterized by the pairing amplitude that is an odd function with respect to time. Such exotic pairing state is first proposed by Berezinskii for ^{3}He, and has been attracting attention as a candidate mechanism for unconventional superconductivities [1, 2].

The concrete realization of the OF superconductivity has been theoretically discussed in a variety of electron systems. One of possible realizations is proposed in the two-channel Kondo system by Emery and Kivelson using the impurity model [3]. In higher dimensions, the two-channel Kondo lattice (TCKL), where the periodically aligned localized spins couple to conduction electrons with two degenerate channels, has been investigated by using the dynamical mean-field theory (DMFT) [4]. However the divergent pairing susceptibility has not yet been found, and the existence of the OF superconductivity has remained unclear.

To clarify whether the OF superconductivity is realized in the TCKL, we have revisited this problem by using the DMFT. In this theory, the periodic system is mapped onto the effective impurity system, where one localized spin interacts with a bath of conduction electrons. We choose the continuous-time quantum Monte Carlo (CTQMC) method as the numerical impurity solver [5]. The algorithm we have used is based on the perturbation expansion of the partition function with respect to the interaction. The physical quantities are then evaluated as a Monte Carlo integration. In the present model, there is no sign problem fortunately. However, the calculation becomes heavy at low temperatures since we have to incorporate the contribution from higher-order perturbations. This difficulty can be reduced by the large-scale parallel calculation using the system B.

With use of the method illustrated above, we have successfully demonstrated the divergence of the OF pairing susceptibility [6]. Figure 1 shows the phase diagram of the TCKL obtained by the CTQMC, where the OF superconductivity is found at low temperatures.

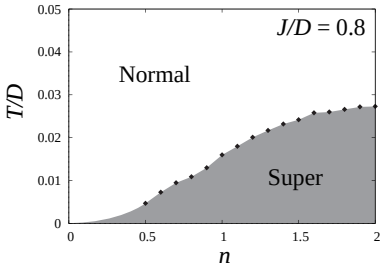

Figure 1: Phase Diagram of the TCKL. Here n, J, D and T are the filling of conduction electrons per site, interaction strength, half band width and temperature, respectively.

References

[1] V. L. Berezinskii: JETP Lett. **20** (1974) 287.

[2] Y. Tanaka, M. Sato, and N. Nagaosa: J. Phys. Soc. Jpn. **81** (2012) 011013.

[3] V. J. Emery and S. Kivelson: Phys. Rev. B **46** (1992) 10812.

[4] M. Jarrell, H. Pang, and D. L. Cox: Phys. Rev. Lett. **78** (1997) 1996.

[5] E. Gull *et al.*: Rev. Mod. Phys. **83** (2011) 349.

[6] S. Hoshino and Y. Kuramoto: Phys. Rev. Lett. **112** (2014) 167204.

3.4 Cooperative Phenomena in Complex Macroscopic Systems

Quantum spin-liquid behavior in the spin-1/2 random Heisenberg antiferromagnet on the triangular lattice

HIKARU KAWAMURA and KEN WATANABE
Faculty of Science, Osaka University
Toyonaka, 560-0043

Experimental quest for the hypothetical "quantum spin liquid" state has recently met a few promising candidate materials including organic salts κ-$(ET)_2Cu_2(CN)_3$ and $EtMe_3Sb[Pd(dmit)_2]_2$, $S = 1/2$ triangular-lattice Heisenberg antiferromagnets consisting of molecular dimers. These compounds exhibit no magnetic ordering nor the spin freezing down to very low temperature, while various physical quantities exhibit gapless behaviors. Recent dielectric measurements revealed the glassy dielectric response suggesting the random freezing of the electric polarization degrees of freedom. Inspired by this observation, we propose as a minimal model of the observed quantum spin-liquid behavior the $S = 1/2$ antiferromagnetic Heisenberg on the triangular lattice with a quenched randomness in the exchange interaction. We study both zero- and finite-temperature properties of the model by an exact diagonalization method.

We consider the AF bond-random $S = 1/2$ quantum Heisenberg model on the triangular lattice whose Hamiltonian is given by

$$\mathcal{H} = \sum_{<ij>} J_{ij} \vec{S}_i \cdot \vec{S}_j - H \sum_i S_i^z, \qquad (1)$$

where $\vec{S}_i = (S_i^x, S_i^y, S_i^z)$ is a spin-1/2 operator at the i-th site on the triangular lattice, H is the magnetic-field intensity, and $J_{ij} > 0$ is the random nearest-neighbor AF coupling obeying the bond-independent uniform distribution between $[(1-\Delta)J, (1+\Delta)J]$, with the mean J. The parameter Δ represents the extent of the randomness: $\Delta = 0$ corresponds to the regular system and $\Delta = 1$ to the maximally random system.

This modelling is motivated by the recent experimental observation on κ-$(ET)_2Cu_2(CN)_3$ that the dielectric degrees of freedom actually exist on each molecular dimer which might be slowed down and tend to be frozen at lower temperatures. The spatially random locations of spin-1/2 carrying electrons from dimer to dimer might gives rise to the effective randomenss for the exchange interaction between dimers: see Fig.1.

By means of an exact diagonalization method, both the zero- and finite-temperature properties of the model are computed for finite lattices. The total number of spins N is $N = 9$, 12, 15, 18, 21, 24, 27, 30 for $T = 0$, and $N = 9$, 12, 15, 18 for $T > 0$, periodic boundary conditions being employed. Sample average is taken over $500(N = 9, 12, 15)$, $250(N = 18, 21)$,$160(N = 24)$, $80(N = 27)$ and $24(N = 30)$ independent bond realizations in the $T = 0$ calculation, while $500(N = 9, 12)$, $80(N = 15)$ and $40(N = 18)$ in the $T > 0$ calculation.

Our $T = 0$ data indicate that the system with strong randomness of $\Delta \geq 0.6$ does not possess the antiferromagnetic long-range order nor the spin-glass-type random order. In that sense, the system is in the randomness-induce quantum spin-liquid state.

In Fig.2(a), we show the temperature dependence of the specific heat per spin C (in units of Boltzmann constant) for the random cases of $\Delta = 0.7$ and 1.0. At lower temperatures $T \lesssim 0.1$, the specific heat exhibits a T-linear behavior $C \simeq \gamma T$, quite different from the behavior of the non-random model. Hence, the spin-liquid phase at $\Delta > \Delta_c$ is characterized by the T-linear specific heat, with the γ-value estimated to be $\gamma \simeq 0.57$ for $\Delta = 0.7$. If we use the experimentally estimated J-value

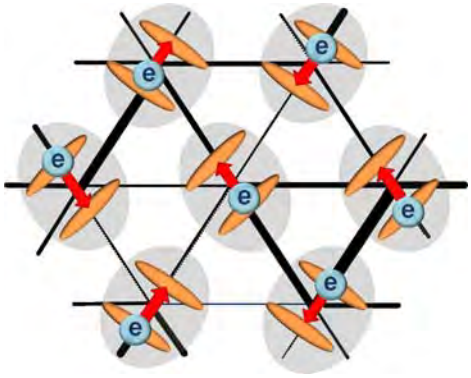

Figure 1: Illustration of the random freezing of the electric polarization at each dimer molecule. The glassy dielectric response experimentally observed in some organic salts suggests the biased position of the spin-carrying electron in a molecular dimer occurring at macroscopic time scales. The electric polarization appears at each dimer molecule in a spatially random manner, as indicated by arrows. This might result in the random modification of the exchange couplings acting between two $S = 1/2$ spins on neighboring dimer molecules, spanning from a weaker J (thin bond) to a stronger J (thick bond).

of κ-$(ET)_2Cu_2(CN)_3$ to be $J \sim 250$K, we get $\gamma \simeq 19\text{mJK}^{-2}\text{mol}^{-1}$ which is not far from the value determined from the specific-heat measurements on the ET salt $\gamma \simeq 12\text{mJK}^{-2}\text{mol}^{-1}$. As shown in the inset, the specific heat turns out to be insensitive to applied fields without any appreciable field dependence up to a field of $0.1J$.

In Fig.2(b), we show the temperature dependence of the magnetic susceptibility per spin χ for several values of Δ. For smaller Δ, the susceptibility goes to zero in the $T \to 0$ limit with a finite gap. At $\Delta = 0.7$, it tends to a finite value, while at $\Delta = 1.0$ it tends to diverge toward $T = 0$ obeying the Curie law $\propto 1/T$. The Curie-like diverging component arises only when a considerable amount of randomness $\Delta > 0.7$ is introduced. The existence of a weak Curie-like component suggests that, in strongly random systems, a small fraction of free spins ($\sim 2\%$) are generated at low temperatures.

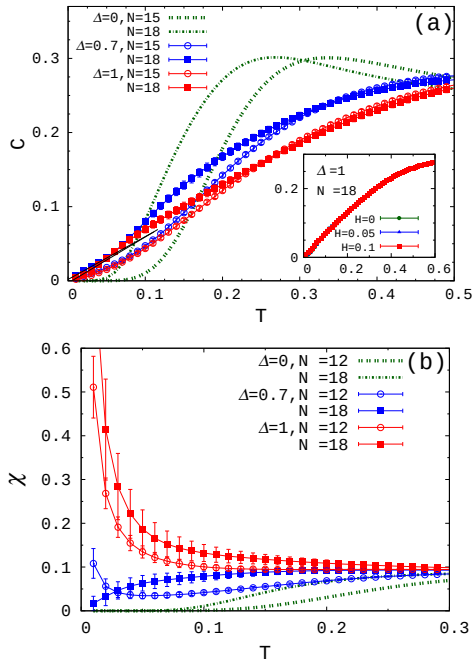

Figure 2: (a) The temperature dependence of the specific heat per spin C for the randomness $\Delta = 0, 0.7$ and 1.0, and for sizes $N = 15$ and 18. The lines are linear fits of the low-temperature data. The inset represents the corresponding data under magnetic fields for the randomness $\Delta = 1.0$ and for the size $N = 18$. (b) The temperature dependence of the uniform susceptibility per spin χ for the randomness $\Delta = 0, 0.7$ and 1.0, and for the sizes $N = 12$ and 18.

Thus, the $S = 1/2$ random AF Heisenberg model with a moderately strong randomness exhibits a spin-liquid ground state, *i.e.*, a state without the conventional Néel ordering nor the spin freezing. This randomness-induced quantum spin-liquid state exhibits gapless behaviors including the temperature-linear specific heat. The results provide a consistent explanation of the recent experimental observations on organic salts.

References

[1] K. Watanabe, H. Kawamura, H. Nakano and T. Sakai, J. Phys. Soc. Jpn. 83, 034714 (2014).

Numerical simulation of the statistical model of earthquakes

HIKARU KAWAMURA and YUSHI UEDA
Faculty of Science, Osaka University
Toyonaka, 560-0043

An earthquake is a stick-slip dynamical instability of a pre-existing fault driven by the motion of a tectonic plate [1]. There is a widespread expectation that a large earthquake might be preceded by a precursory nucleation process which occurs prior to the high-speed rupture of a mainshock. Nucleation process is localized to a compact "seed" area with its rupture velocity orders of magnitude smaller than the seismic wave velocity.

In this year's project, nucleation process of the one-dimensional Burridge-Knopoff model of earthquakes obeying the rate- and state-dependent friction (RSF) law is studied both analytically and numerically [1,2]. The properties of the nucleation dynamics, the nucleation lengths and the duration times are examined together with their continuum limits.

The one-dimensional (1D) BK model consists of a 1D array of identical blocks which are mutually connected with the two neighboring blocks via the elastic springs of the spring stiffness k_c, and are connected to the moving plate via the springs of the spring stiffness k_p [1]. The dimensionless equation of motion can be written as

$$\mathrm{d}^2 u_i/\mathrm{d}t^2 = \nu t - u_i + l^2(u_{i+1} - 2u_i + u_{i-1}) - \phi, \quad (1)$$

where $l \equiv (k_c/k_p)^{1/2}$. The RSF force ϕ reads as $\phi = c + a\log(1 + \frac{v_i}{v^*}) + b\log\theta_i$, where v^* is the dimensionless crossover velocity, and the dimensionless state variable θ_i obeys the aging law, $\mathrm{d}\theta_i/\mathrm{d}t = 1 - v_i\theta_i$.

We observe that the model exhibits qualitatively different behaviors depending on whether the frictional instability is either "weak" or "strong". A slow and long-lasting nucleation process, the quasi-static initial phase, is realized in the former case only. We illustrate in fig.1 typical examples of seismic events realized in the stationary state of the model for each case of (a) the weak, and (b) the strong frictional instability. The model possesses a borderline value of b determined solely by the stiffness parameter l, $b_c(l) = 2l^2 + 1$, which discriminates the strong/weak instability behaviors.

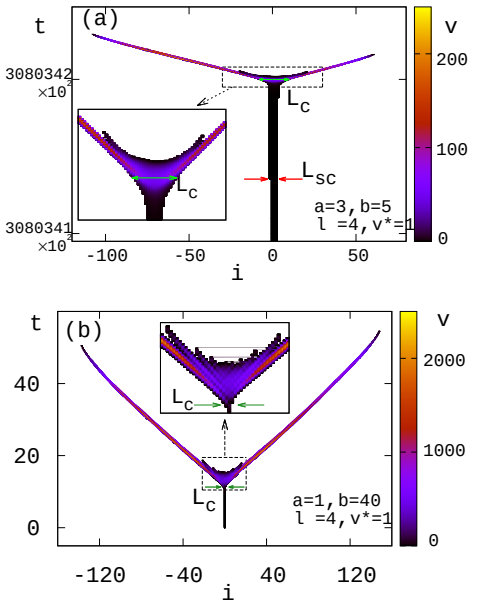

Figure 1: Color plots of typical earthquake nucleation processes depicted in the block-number (position) versus the time plane.

1) H. Kawamura, T. Hatano, N. Kato, S. Biswas and B.K. Chakrabarti, Rev. Mod. Phys. 84, 839 (2012).
2) Y. Ueda, S. Morimoto, S. Kakui, T. Yamamoto and H. Kawamura, arXiv:1401.3247.

Numerical Study on Spin Liquid in Frustrated Systems

Tôru SAKAI[1,2], Hiroki NAKANO[2], Tokuro SHIMOKAWA[3], and Makoto ISODA[4]

[1] *Quantum Beam Science Directorate, Japan Atomic Energy Agency SPring-8, Kouto, Sayo, Hyogo 679-5148, Japan*

[2] *Department of Material Science, University of Hyogo, Kouto, Kamigori, Hyogo 678-1297, Japan*

[3] *Osaka University, Toyanaka, Osaka 560-0043, Japan*

[4] *Faculty of Education, Kagawa University, Takamatsu, Kagawa 760-8522, Japan*

1 Novel Spin Liquid Behavior at 1/3 of the Saturation Magnetization in the S=1/2 Kagome-Lattice Antiferromagnet

The magnetization processes of the S=1/2 isotropic Heisenberg quantum antiferromagnets on the kagome and triangular lattices are studied. Data from numerical-diagonalization method up to 39-spin systems, are reexamined from the viewpoint of the derivative of the magnetization with respect to the magnetic field. We find that for the kagome-lattice antiferromagnet, the behavior of the derivative around the 1/3 height of the magnetization saturation is quite different from the cases of typical magnetization plateaux. This new phenomenon is called the "magnetization ramp"[1]. We also compare it with the 1/3 magnetization plateau of the triangular antiferromagnet. The critical exponent analysis indicates a clear difference between the magnetization plateau and ramp[2]. In order to clarify the difference more, we study a generalized anisotropic triangular-lattice model including the regular-triangular- and the kagome-lattice antiferromagnets in the parameter space. It revealed a quantum phase transition between the triangular- and kagome-lattices at 1/3 of the saturation magnetization[3].

2 Exotic Quantum Spin Liquid Behavior of the Spin Nanotubes

Recently some quantum spin systems on tube lattices, so called spin nanotubes, have been synthesized. They are expected to be interesting low-dimensional systems like the carbon nanotubes. As the first step of theoretical study on the spin nanotube, we investigate the S=1/2 three-leg spin tube, which is the simplest one, using the density matrix renormalization group (DMRG) and the numerical exact diagonalization (ED), conbined with a precise finite-size scaling analysis named level spectroscopy[4]. The spin gap, which is one of the most interesting macroscopic quantum effects, was revealed to be open for any finite rung exchange couplings, in contrast to the three-leg spin ladder system which is gapless. It is consistent with the previous effective Hamiltonian approach. We also found a new

quantum phase transition caused by an asymmetric rung interaction. When one of the three rung coupling constants is changed, the spin gap would vanish. In addition we theoretically predict some new field-induced quantum phase transitions. A chiraliy-mediated novel superconductivity mechanism is also proposed[5, 6, 7, 8].

These results were obtained by the numerical exact diagonalization of the $S = 1/2$ spin tube with 30 spins, using the system A with 8 nodes.

References

[1] H. Nakano and T. Sakai: J. Phys. Soc. Jpn. 79 (2010) 053707.

[2] T. Sakai and H. Nakano: Phys. Rev. B 83 (2011) 100405(R).

[3] T. Saka and H. Nakano: physica status solidi B 250 (2013) 579.

[4] T. Sakai, M. Sato, K. Okunishi, Y. Otsuka, K. Okamoto and C. Itoi: Phys. Rev. B 78 (2008) 184415.

[5] T. Sakai, M. Sato, K. Okamoto, K. Okunishi and C. Itoi: J. Phys.: Condens. Matter 22 (2010) 403201.

[6] K. Okunishi, M. Sato, T. Sakai, K. Okamoto and C. Itoi: Phys. Rev. B 85 (2012) 054416.

[7] T. Sakai and K. Okamoto: JPS Conf. Proc. 2 (2013) 010208.

[8] T. Sakai and K. Okamoto: JPS Conf. Proc. 1 (2013) 012025.

Novel Spin Flop Transition in Low-Dimensional Quantum Spin Systems

Tôru SAKAI[1,2], Hiroki NAKANO[2], Tokuro SHIMOKAWA[3], and Makoto ISODA[4]

[1] *Quantum Beam Science Directorate, Japan Atomic Energy Agency SPring-8, Kouto, Sayo, Hyogo 679-5148, Japan*

[2] *Department of Material Science, University of Hyogo, Kouto, Kamigori, Hyogo 678-1297, Japan*

[3] *Osaka University, Toyanaka, Osaka 560-0043, Japan*

[4] *Faculty of Education, Kagawa University, Takamatsu, Kagawa 760-8522, Japan*

1 Novel Spin Flop Phenomenon in the S=1/2 Square Kagome Lattice Antiferromagnet

Using the large-scale numerical exact diagonalization, we investigated the S=1/2 Heisenberg antiferromagnet on a two-dimensional lattice composed of vertex-sharing triangles called the square kagome lattice. The lattice is similar to the kagome lattice but different from it. We examine the ground-state properties and the magnetization process of this model. We find that a magnetization jump appears at the higher-field-side edge of the magnetization plateau at the one-third height of the saturation. A spin-flop phenomenon is clearly observed at the jump even when the system is isotropic in the spin space[1]

2 Quantum Phase Transition of the S=1/2 Cairo Pentagon Lattice Antiferromangets

The magnetization process of the S=1/2 Cairo Pentagon Lattice is investigated using the large-scale numerical exact diagonalization up to the 36-spin clusters. As a result, we found an interesting quantum phase transition, with respect to the ratio of the two inequivalent antiferromagnetic bonds, between two different magnetization curves around 1/3 of the saturation magnetization. Namely, the magnetization curve with a jump before the 1/3 magnetization plateau changes to the one with a jump after the plateau[2].

These results were obtained by the numerical exact diagonalization of the $S = 1/2$ square-kagome lattice, using the system B.

References

[1] H. Nakano and T. Sakai: J. Phys. Soc. Jpn. 82 (2013) 083709.

[2] H. Nakano, M. Isoda and T. Sakai: to appear in J. Phys. Soc. Jpn.

Slow Dynamical Processes in Nonequilibrium Metastable States

Kazuhiro Fuchizaki, Yuta Asano, and Kazuki Hatsumura
Department of Physics, Ehime University, Matsuyama 790-8577

In FY 2013, we continued pursuing thermodynamic identity of the modified Lennard-Jones (mLJ) system, whose phase diagram has been already reported [1,2]. A shortcut to understanding or predicting thermodynamic outcomes, including the phase behavior, is to establish the equation of state (EOS). To this end, we tried two approaches. One was to construct an approximate EOS using the EOS of the Lennard-Jones (LJ) system as the reference EOS. The procedure and the consequence [3] is briefly outlined below. The other was to set up an EOS as accurate as possible. To realize this latter option, we employed the modified Benedict–Webb–Rubin (mBWR) form, which was created on a phenomenological basis but is known to be able to reproduce the thermodynamic properties of the LJ fluid within a wide temperature (T)–pressure (p)–density (ρ) range. We confirmed that the mBWR EOS can successfully capture mLJ fluid's behavior as well [4]. The way of constructing the EOS is summarized in the following. It should be emphasized that our mBWR EOS was constructed so as to ensure the temperature dependence of the third virial coefficient B_3. The reflection of B_3 on the EOS becomes crucially important when the system approaches the critical point. This aspect, which was not mentioned in our paper [4], is briefly touched on.

Predicting the thermodynamic properties of the mLJ fluid from the LJ EOS [3]

The properties of the mLJ fluid were treated as perturbations of the LJ fluid case, and the discrepancies were expressed as density series expansions. Here, two methods were examined to obtain the series expansions. The first one is rather heuristic; the pressure of the mLJ fluid was expressed by a relationship, which is approximately correct up to $\mathcal{O}(\rho^2)$, by paying attention to the fact that the difference from LJ fluid's pressure is ascribable only to the tail of the LJ potential omitted in the mLJ potential. The second one is systematic; based on a functional derivative of the free energy, we could obtain the expression for mLJ fluid's free energy that is correct up to $\mathcal{O}(\rho)$. A proper approximation was introduced to make the coefficient of the correction term (proportional to ρ) relatively tractable for actual computations. The two methods work equally well. The second virial coefficient of the mLJ fluid was well reproduced by these methods. Reproduction of the liquid–vapor coexisting envelope was also satisfactory, except in the vicinity of the critical point.

mBWR EOS for the mLJ Fluid [4]

Some features of the mLJ fluid behavior were well rationalized by the perturbative treatment mentioned above. Furthermore, we tried to describe the thermodynamic states of the mLJ fluid using the mBWR EOS.

The mBWR EOS contains 32 linear parameters and one nonlinear parameter. Therefore, the major task for us was to find the appropriate values for the parameters with which to capture the thermodynamic behavior of the mLJ fluid over as wide a range as possible. Ten parameters were primarily determined in such a manner that the temperature dependence of B_3 as well as B_2 is reproducible. The remaining parameters were determined so that the resultant EOS became compatible with the extensive set of data for the internal energy and p at given T and ρ. These data, con-

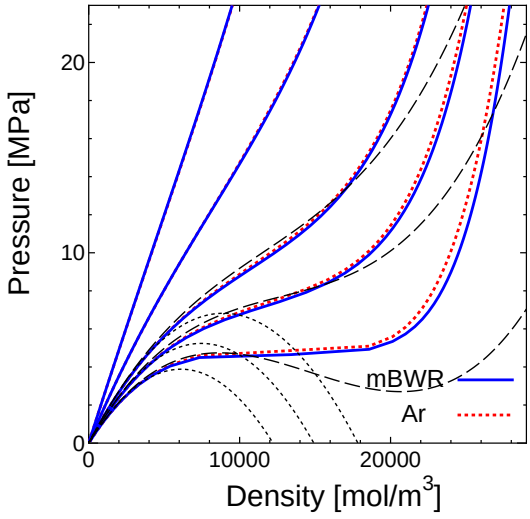

Figure 1: Isotherms of fluid argon near the critical point.

sisting of as many as 677 T–p data points, were prepared by conducting molecular dynamics (MD) simulations over such a wide region, $0.7 \leq T \leq 20$ and $0.001 \leq \rho \leq 1.15$. The mBWR EOS thus constructed satisfactorily reproduces the liquid–gas coexistence envelope, which has been established from the Gibbs ensemble simulation [1].

Recalling that the dominant form of the mLJ potential is basically the same as that of the LJ potential, the substances, whose thermodynamic states are well deducible from the LJ potential, are expected to be describable using the mLJ potential. This expectation was confirmed by finding the mLJ parameters, ϵ and σ, that fit the fluid in question. For example, fluid argon is well described by choosing $\epsilon = 139.8k_{\mathrm{B}}$ J and $\sigma = 3.389$ Å, where k_{B} is Boltzmann's constant. As an example, the pressure variations against density observed for argon along several isotherms are compared with the corresponding variations predicted from the present EOS in Fig. 1. The isotherms delineated by thin dotted and dashed lines are those obtained from the virial expansions up to the terms with B_2 and B_3, respectively. Unless including the effect of B_3, the isotherms no longer show the van der Waals loop behavior. It is thus essential to take the temperature dependence of B_3 into consideration upon construction of the EOS.

Table 1: The updated set of the parameters involved in the mBWR EOS.

i	x_i	i	x_i
1	0.8269(8)	17	162.415(2)
2	3.187(5)	18	-67086.7(7)
3	-7.684(9)	19	33975.3(3)
4	0.409(7)	20	-243048(2)
5	-0.901(3)	21	-18.71(4)
6	0.898(2)	22	-549873(6)
7	5.00(2)	23	36.86(4)
8	-18.85(9)	24	-591544(6)
9	243083(2)	25	-146.839(1)
10	0.311926(3)	26	-366949(4)
11	3.10032(3)	27	-146.453(1)
12	-23.1883(2)	28	-157374(2)
13	20.0562(2)	29	588.307(6)
14	166.922(2)	30	-45105.1(5)
15	-6971.64(7)	31	-1443.50(1)
16	-357.638(4)	32	414.447(4)
		γ	2.2650

Updating the parameters in the mBWR EOS

Although the construction of the EOS for the mLJ fluid is said to be successful, it is still not fully satisfied in that the thermodynamic quantities in the low-temperature and low-density region, which were also employed for determination of the parameters, obtained through the MD simulation were not well equilibrated (as mentioned in Ref. [4]). This insufficiency was covered; the quantities in the region in question were reevaluated after a sufficient equilibration was performed. The 33 parameters were recalculated, using the same procedure as outlined above, but referring to the new set of pressures and internal energies. The values of the parameters thus updated are listed in Table table1. The set of the parameters must be the most refined version to date.

References

[1] Y. Asano and K. Fuchizaki: J. Chem. Phys. **137** (2012) 174502.
[2] K. Fuchizaki and Y. Asano: J. Phys. Soc. Jpn. **82** (2013) 033001.
[3] K. Fuchizaki and Y. Asano: J. Phys. Soc. Jpn. **82** (2013) 124001.
[4] Y. Asano and K. Fuchizaki: J. Phys. Soc. Jpn. **83** (2014) 034601.

Simulation of Cold Atoms with Parallelized Worm Algorithm *

Naoki KAWASHIMA
Institute for Solid State Physics, University of Tokyo
Kashiwa-no-ha, Kashiwa, Chiba 277-8581

The world-line quantum Monte Carlo (QMC) simulation with worm update is very effective for a broad range of the lattice boson/spin problems in condensed matter physics. In particular, recent developments in the experimental technology that made possible to cool atoms down to sub-micro Kelvin temperatures demand more accurate and larger-scale simulations in various setups. While the worm-update QMC is arguably the only method for dealing with systems that are directly comparable to experiments in size, it has been impossible to run it on parallel machines for an obvious reason — the update of the whole system is realized through only one moving object that cannot be split into pieces. In the present project, we aim at developing a new algorithm that can be parallelized and demonstrating its efficiency by applying it to Bose-Hubbard model in 2+1 dimensions.

Here we present a parallelized multiple-worm algorithm (PMWA) for QMC simulations.[1] A PMWA is a generalization of the worm algorithm and it removes the intrinsic drawback due to the serial-operation nature by introducing a large number of worms. With many worms distributed over the system, it is possible to decompose the whole space-time into many domains, each being assigned to a processor. The neighboring processors send and receive updated configurations on their boundaries, once in every few Monte Carlo (MC) steps. Therefore, the time required for communication can be negligible for sufficiently large systems. Moreover, with a PMWA we can measure an arbitrary n-point Green function which is difficult in conventional worm-type algorithms when $n > 4$. The algorithm is based on the directed-loop implementation of the worm algorithm (DLA) that samples from the distribution

$$W(\{\psi_k\}) \equiv \prod_{k=1}^{N_\tau} \langle \psi_{k+1} | 1 - \Delta H_\eta | \psi_k \rangle$$

where $\Delta\tau \equiv \beta/N_\tau$, ψ_k is a basis vector in some complete orthonormal basis set, and $H_\eta \equiv H - \eta Q$ is the Hamiltonian with a fictitious source term ηQ that generates discontinuities of worldlines, namely "worms." A configuration in DLA is characterized by a graph, edges and vertices, and state variables defined on edges in the graph.

The update procedure of the conventional DLA consists of two phases; the worm phase in which the motion of the worm causes changes in the state variables, and the vertex phase in which vertices are redistributed. While the vertex phase in the new algorithm is just the same as the conventional DLA, the worm phase must be modified. In contrast to the conventional DLA, we let the worms proliferate or decrease freely according to the weight controlled by the parameter η. In conventional DLA, therefore, we "wait" for the worms disappear to measure the observables. In the

*This report is based on the collaboration with A. Masaki-Kato, T. Suzuki, K. Harada, and S. Todo published as [1]

present algorithm, we estimate them instead by extrapolation to the $\eta \to 0$. Corresponding to this modification, the worm update is modified in two ways: worms are created and annihilated at many places at the same time, and we introduce a special update procedure for the region near the boundaries. As a result, the worm phase in the new algorithm consists of three steps: worm creation and annihilation, worm scattering, and a domain-boundary update. The last step is necessary only for parallelization, and is not used when the program runs on a serial machine.

The essential difference between the new algorithm and the conventional worm algorithm or DLA is that we regard the parity of the local number of worms as an intermediate representation of the state. To be more specific, for updating a local configuration around a vertex, we simply let a worm scatter at the vertex in the conventional algorithm. In the new algorithm, instead we assign a single-bit variable to each leg of the vertex. If we have even (odd) number of worms on the leg, we assign 0 (1) to it. Then we forget about the specific worm configuration on each leg and consider a stochastic process in terms of these new variables. Once a new configuration (in terms of the parity variables) is selected, we restore a specific worm configuration according to a weight with restriction imporsed by the parity variables. This parity representation is especially useful in handling boundaries, since by it we can avoid a cumbersome "time" ordering of the scattering events that would be necessary to keep the detailed balance condition in the conventional representation.

In order to recover the results in the zero-worm density (or $\eta \to 0$ limit), we have to numerically extrapolate a few sets of finite-η results. In principle, we can do that by using quadratic fitting function. If the system is in the superfluid phase, however, due to the influence of the spontaneous $U(1)$ symmetry breaking that would take place in the thermodynamic limit, there is relatively broad region of η in which the term linear in η is dominating even in finite systems. In such cases, by a linear fitting we can obtain a good approximate value of the thermodynamic limit.

One of the advantage of the present method is that we can directly measure the order parameter $\langle b \rangle$. Moreover, we can measure arbitrary multipoint Green's function simply measuring the product of the local worm densities at the points appearing in the argument of Green's function. For the demonstration of the efficiency of the present algorithm, we carried out a simulation of the systems ranging from $L = 8$ upto $L = 10240$ at fixed $\beta t = 16$. This is much larger than a single processor's memory can accommodate. We successfully equilibrate the whole system and extrapolate to the zero η limit. While this is already something that cannot be done by the conventional method, our code based on the present method showed a reasonably good scaling of the computational time. For an example, in the range between 8 processors to 1024 processors, the estimated statistical error in the energy with fixed system size and the wall time was approximately proportional to $N_p^{-0.41}$ with N_p being the number of processors, when the system is deep in the superfluid phase, whereas $N_p^{-0.5}$ is ideal.

References

[1] Akiko Masaki-Kato, Takafumi Suzuki, Kenji Harada, Synge Todo, Naoki Kawashima: Physical Review Letters **112**, 140603 (2014).

Signatures of 1+continuous replica symmetry breaking around the jamming point

Hajime YOSHINO
School of Science, Osaka University
Machikaneyama 1-1, Toyonaka, Osaka 560-0043

The fate of the super-cooled liquid state at low temperatures or high densities is an important open question in physics. Very recently a notable progress on the theoretical side has been made through the construction of the exact replica mean-field theory (replicated van der waals theory) in the large-dimensional limit [1, 3]. An important new prediction of the theory is that the replica symmetry breaking (RSB) is not limited to the usual 1 step RSB assumed in conventinal view points but is extended to 1+ continuous RSB at high densities around the jamming point.

In the present work we performed extensive MD simulations of the out-of equilibrium dynamics of a densely packed three-dimensional emulsion system (see our previous work [2] for the details) focusing on the fluctuation-dissipation relation (FDR). The purpose of the present work is to clarify if the 1+ continuous structure, which is suggested by the 1+ continuous RSB scenario, appear in FDR in the realistic three-dimensional system.

We measured the shear-stress relaxation taking care of the aging effects. The system is quenched from the liquid state to the working temperature T. After some waiting time $t_{\rm w}$, the shear-strain of small amplitude γ is put to the system via affine transformation. Then relaxation of the shear-stress $\sigma(t)$ is measured as the function of the elapsed time t after the switch-on of the perturbation. We also measured the shear stress auto-correlation function $C(t, t_{\rm w}) \equiv \langle \sigma(t)\sigma(t_{\rm w})\rangle$. In equilibrium, the response $\mu(t, t_{\rm w}) = \langle\sigma(t)\rangle/\gamma$ and $C(t, t_{\rm w})$ are related by the fluctuation dissipation theorem (FDT). In Fig. 1, we show the two data set in a parametric plot which clearly indicated the anticipated 1+continuous FDR.

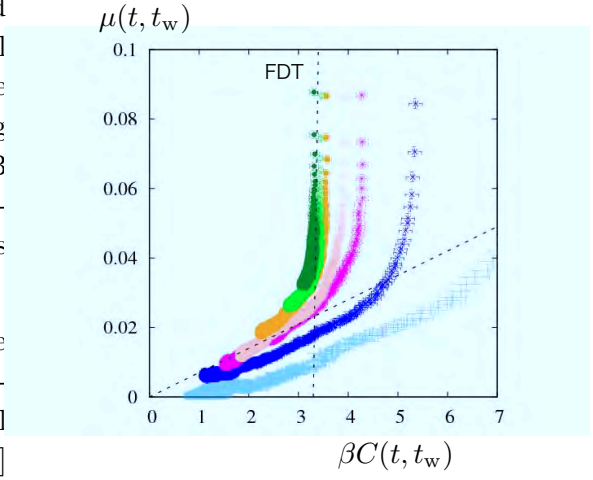

Figure 1: Parametric plot of the response and correlation functions associated with shear at volume fraction$\phi = 0.67$ and $k_{\rm B}T/\epsilon = 10^{-5}$. The waiting times $t_{\rm w}$ as varied as $t_{\rm w} = 10^2, 10^3, 3\cdot 10^3, 10^4, 3\cdot 10^4, 5\cdot 10^4, 10^5$ from the bottom to the top. The two dotted straight lines are the equilibrium FDT line $\mu(t, t_{\rm w}) = \beta C(t, t_{\rm w})$ and and the 1-step extended one $\mu(t, t_{\rm w}) = x\beta C(t, t_{\rm w})$ with $x = 0.007$. It can be seen that a curved, continuously varying regime exists between the two asymptotic regimes.

References

[1] P. Charbonneau, J. Kurchan, G. Parisi, P. Urbani, F. Zamponi, Nature Communications 5, 3725 (2014).

[2] S. Okamura and H. Yoshino, arXiv:1306.2777.

[3] H. Yoshino and F. Zamponi, arXiv:1403.6967.

Simulation studies of near-field hydrodynamic effects in model active suspensions

Akira Furukawa
Institute of Industrial Science, University of Tokyo
Komaba 4-6-1, Meguro-ku, Tokyo 153-8505

Using a fluid-particle dynamics approach [1], which is a hybrid simulation method for the dynamics of complex colloidal suspensions, we numerically studied the effects of hydrodynamic interactions on the collective dynamics of active suspensions within a simple model for bacterial motility: each microorganism is modeled as a stroke-averaged dumb-bell swimmer with prescribed dipolar force pairs. The present study illustrates that hydrodynamic interactions not only affect kinetic pathways in active suspensions, but also cause major changes in their steady state properties.

Simulations of the following issues (i) and (ii) were partially and fully performed at the ISSP Supercomputer Center, respectively. The programs are parallelized with a combination of OpenMP and MPI techniques.

(i) Using both simulations and qualitative arguments, we revealed the following [2].When the separation between swimmers is comparable to their size, the swimmers' motions are strongly affected by activity-induced hydrodynamic forces. To further understand these effects, we investigated semi-dilute suspensions of swimmers in the presence of thermal fluctuations. A direct comparison between simulations with and without hydrodynamic interactions shows these to enhance the dynamic clustering at a relatively small volume fraction; with our chosen model the key ingredient for this clustering behavior is hydrodynamic trapping of one swimmer by another, induced by the active forces. Furthermore, the density dependence of the motility (of both the translational and rotational motions) exhibits distinctly different behaviors with and without hydrodynamic interactions; we argue that this is linked to the clustering tendency.

(ii) In recent experiments on *E. coli* in the presence of additional attractive forces (created via a depletion potential due to polymer additives) it was shown experimentally and by simulation that activity produces a significant shift of the phase boundary compared to that of a passivated system with the same attractions [3]. However the configurations favored by such an attraction need not coincide with those stabilized by the activity-induced hydrodynamic interactions. Moreover, one very recent study suggests a mechanism whereby the equilibrium phase separation caused by attractions is interrupted by activity-induced cluster breakup [4]. We are currently addressing this problem by simulation [5].

References

[1] H. Tanaka and T. Araki, Phys. Rev. Lett. **85**, 1338 (2000).

[2] A. Furukawa, D. Marenduzzo, and M.E. Cates, submitted to Phys.Rev.E.

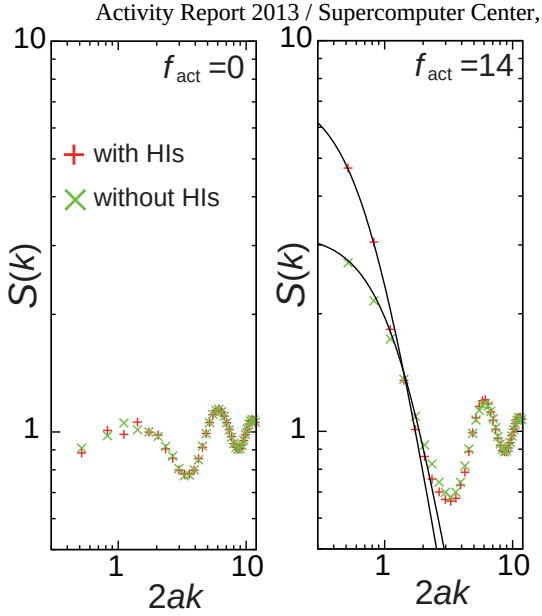

Figure 1: The structure factor $S(k)$ for passive (left panel) and active (right panel) suspensions. In active suspensions, the clustering is evident; the structure factor for $2ak < 1$, where $2a$ is roughly the swimmer size, can be described by the Ornstein-Zernike form, which is represented by the black solid curves in the cases with and without hydrodynamic interactions, respectively. The overall clustering tendency is significantly enhanced by the addition of hydrodynamic interactions.

[3] J. Schwarz-Linek, C. Valeriani, A. Cacciuto, M.E. Cates, D. Marenduzzo, A.N. Morozov, and W.C.K. Poon, PNAS **109**, 4052 (2012).

[4] B. M. Mognetti, A. Šarić, S. Angioletti-Uberti, A. Cacciuto, C. Valeriani and D. Frenkel, Phys. Rev. Lett. **111**, 245702 (2013).

[5] in preparation

Edge state in 2d quantum spin and bosonic systems

Takafumi SUZUKI
Research center for Nano-micro Structure Science and Engineering, University of Hyogo, Shosha, Himeji, Hyogo 671-2280

In this project, we studied (A) edge state of two-dimensional bosonic lattice systems in trapped potentials, (B) edge state of multi-boxies SU(N) Heisenberg model on a square lattice, and (C) magnetic excitations of the Heisenberg-Kitaev model on a honeycomb lattice. The digests of them are shown as follows.

A. Edge state of two-dimensional bosonic lattice systems in confinement potentials

In condensed matter physics, edge state of topological insulators (TIs) has been studied extensively [A1]. The fundamental properties of TIs are that the bulk with an energy gap is characterized by non-local order parameters and a stable metallic state against perturbations breaking specific symmetries appears at the edge of bulk. In quantum spin systems, the Haldane state in the S=1 antiferromagnetic Heisenberg chain [A2] shows the similar properties; a finite spin gap, hidden Z_2 symmetry breaking and free edge spins. Recently, edge/surface states of gapped states in the higher dimensional spin/bosonic systems have been much attracted. To study the higher dimensional spin/bosonic systems, a cold atomic system in optical lattice is one of ideal candidates, because it provides a good controllability for model parameters. However, the presence of confinement potential seems to be an unavoidable problem in experiments, and the effect of confinement potentials (i.e. non-uniformity of systems) on the edge states has not been well studied yet.

In this study, we focused on the effect of the confinement potential in 2D bosonic lattice systems and discussed the edge states of bosonic Mott insulating regions. In order to study it, we treated the rectangular lattice systems, where the chemical potential only changes along a uni-axial (x-axial) direction and open (periodic) boundary condition along the x (y)-axis direction were applied. From the quantum Monte Carlo (QMC) calculations, we discussed the temperature dependence of local helicity modulus and off-diagonal correlation functions by changing the curvature of confinement potential. Since there exists the uni-axial potential, there are three regions in the ground state: $\rho=1$ bosonic Mott insulating region, $\rho \neq 0$ fluid (IC) region, and vacuum region. Here ρ is particle density per site. When width (W) of IC region surrounding the $\rho=0$ (Mott insulating) region, is narrow ($W<10$ sites), off-diagonal correlation shows an exponential decay at a finite temperature. However, when the width W is enough large ($W \sim 20$ sites), we found that the correlation function at edges clearly shows power-law decay below an offset temperature, where the local helicity modulus satisfies the same equation at the KT fixed point of the 2D uniform XY model.

B. Edge state of multi-boxies SU(N) Heisenberg model on a square lattice

The ground state phase diagram of the multibox SU(N) Heisenberg model on a square lattice has been predicted by Read and Sachdev [B1]. This mode is the higher symmetry version of the conventional Heisenberg model for SU(2) spin. For the model with the Young tableaux with m rows and n columns, it was predicted that the N-n phase diagram does not depend on the value m, and has a single line that separates the Neel phase and valence bond solid (VBS) phases. The VBS phases can be also classified into three phases depending on the value of n. The ground state is a nematic VBS order with 180-degree rotational symmetry breakings of lattice for n=2 (mod 4), whereas a columnar order with translational and 90-degree rotational symmetry breakings of lattice is stabilized for n=1 or 3 (mod 4). If n is a multiple of 4, there is no spontaneous breaking of lattice symmetry. Based on the VBS picture, the n=4 state is regarded as the 2D version of the 1D Haldane state.

In this study, we calculated the edge spin correlation of the multibox SU(N) Heisenberg model by QMC method based on the loop algorithm. In Figure 1, the results for the

SU(N=20) and n=2 are shown. We found that, even in the nematic ground state case, the correlation of the edge spins is power-law decay in contrast to an exponential decay of the correlation perpendicular to the edge.

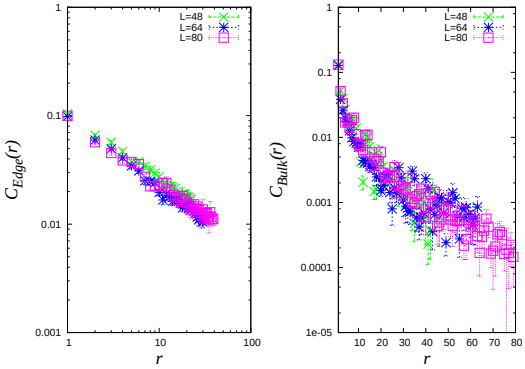

Fig. 1: Spin-spin correlation on the edge for SU(N=20) and (m,n)=(1,2) at the inverse temperature β=32L. Left (Right) hand side is the results on edge sites and Right one is the correlation perpendicular to the edge direction.

C. Magnetic excitations of the Heisenberg-Kitaev model on a honeycomb lattice

In recent years, effects of spin-orbit couplings have much attracted in strongly correlated electron systems. In 5d-transition metal oxides, coulomb repulsion is relatively small against a kinetic energy. This allows us to expect that they show a metallic feature. However, it was reported experimentally that several Iridium oxides, such as Sr_2IrO_4 and A_2IrO_3 (A=Na or Li), show an insulator nature. Theoretically, it was pointed that the presence of the strong spin-orbit coupling is a key to understand the insulating property of those compounds [C3]. For example, Na_2IrO_3 has the small gap 0.35 [eV] [C1] and shows the phase transition to the magnetic ordered state (zigzag order) under T ~ 20[K][C2]. The magnetic moments of Na_2IrO_3 are carried by Ir ions locating at the center of edge-shared IrO_6 octahedrons, and construct the layered honeycomb lattice. The interesting point of this compound is that the interactions between magnetic moments on Ir ions include the Kitaev-type anisotropy in addition to the conventional Heisenberg type interactions because the Ir-O-Ir bond on the interaction path takes almost 90 degree [C3]. In the phase diagram for the Heisenberg-Kitaev model on the honeycomb lattice, three magnetic ordered phases appear by tuning the coupling ratio of the Kitaev and Heisenberg term; the Neel, stripy and spin liquid phase. Several authors have discussed the origin of zigzag order observed in Na_2IrO_3 and proposed the parameter set that can explain experimental observations [C2,C4].

In order to discuss the suitability of proposed parameters, we calculated the spin-wave excitations and dynamical structure factor by the numerical exact-diagonalization method. Via comparisons with inelastic neutron scattering measurements, we discussed the several parameter sets proposed in previous papers [C2,C4].

In this project, we parallelized the Lancsoz code to calculate the dynamic structure factors. In Figure 2, we show a bench march results of our code.

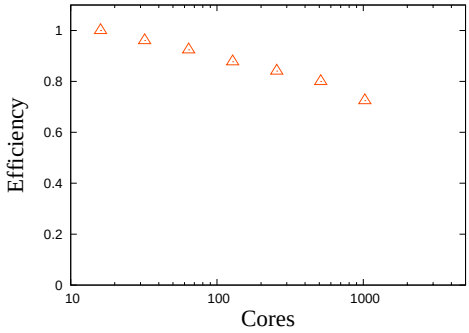

Fig. 2: Strong-scaling results for parallelized Lanczos code. The horizontal axis is the efficiency and the value is scaled by the results for 16 cores. In the ideal case, “efficiency” should keep constant at one. The sampling was performed for the N=32 Heisenberg-Kitaev model on the honeycomb lattice when OpenMP threads were fixed at four, where N is the system size.

References

[A1] M. Z. Hasan and C. L. Kane, Rev. Mod. Phys. **82**, 3045 (2010), X. L. Qi and S. C. Zhang, Rev. Mod. Phys. **83**, 1057 (2011).
[A2] F. D. M. Haldane, Phys. Lett. A **93**, 464 (1983); Phys. Rev. Lett. **50**, 1153 (1983).
[B1] Nucl. Phys. B 316, 609 (1989).
[C1] R. Comin, et al., Phys. Rev. Lett. 109, 266406 (2012).
[C2] S. K. Choi, et al., Phys. Rev. Lett. 108, 127204 (2012); F. Ye, et al., Phys. Rev. B 85, 180403(R) (2012).
[C3] J. Chaloupka, G. Jackeili and G. Khaliullin, Phys. Rev. Lett. 105, 027204 (2010).
[C4] Y. Yamaji, et al., arXiv:1402.1030.

Calculation of dispersion surfaces and rocking curves for X-ray 'In-plane n-beam' cases

Kouhei OKITSU
Institute of Engineering Innovation, University of Tokyo
2-11-16 Yayoi, Bunkyo-ku, Tokyo 113-8656

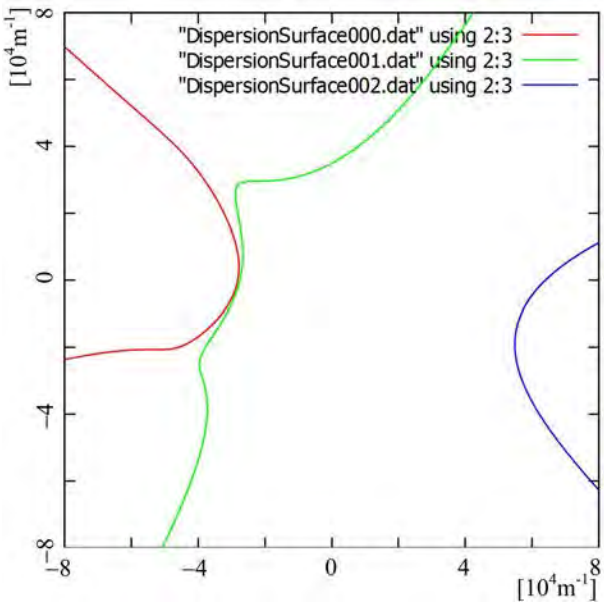

Figure 1: Dispersion surfaces calculated for 0 0 0- (forward-diffracted), 5 1 1- and 3 $\overline{1}$ $\overline{3}$- 'in-plane' three-beam case of silicon crystal.

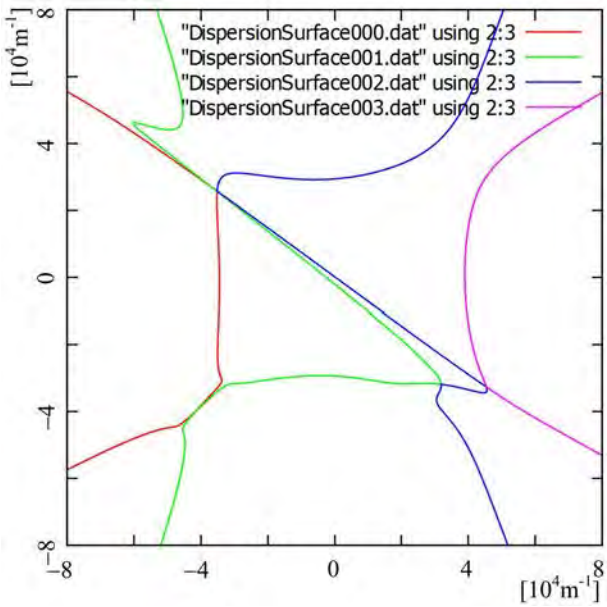

Figure 2: Dispersion surfaces for 0 0 0- (forward-diffracted), 2 2 0-, $\overline{4}$ 2 $\overline{2}$- and 0 6 $\overline{2}$- 'in-plane' X-ray four-beam case of silicon crystal.

A computer program with which dispersion surfaces and X-ray reflection intensities for 'in-plane' n-beam cases has been developed, in which n X-ray beams whose planes of incidence are coplanar are simultaneously strong in the crystal. This case was studied several decades ago before numerical solutions for general n-beam cases were given with Ewald-Laue (E-L) formulation by Colella [1] and with Takagi-Taupin (T-T) formulation by the present author [2-5] since the polarization coupling effect does not have to be considered.

Incidentally, the method to fix the wavelength of the synchrotron X-rays with a monolithic silicon crystal giving two-bounced $\mathbf{h}_1$ and $\mathbf{h}_2$ reflections, is widely used. In this case, $\mathbf{h}_3$ $(= \mathbf{h}_1 + \mathbf{h}_2)$ reflection occurs necessarily. Here, scattering vectors $\mathbf{h}_1$, $\mathbf{h}_2$ and $\mathbf{h}_3$ are coplanar. However, this case was discussed just using the two-beam approximation and the interference effect due to X-rays reflected by $\mathbf{h}_3$ has completely been neglected for many years. The present work is intended precisely to deal with this effect.

Figure 1 shows dispersion surfaces calculated in this work under an assumption that

$\mathbf{h}_1, 5\ 1\ 1$- and $\mathbf{h}_3, 3\ \overline{1}\ \overline{3}$- 'in-plane' three-beam condition is satisfied. The abscissa and ordinate are positions in the reciprocal space in the directions parallel and perpendicular to the crystal surface, respectively. The three curves are loci of initial point of wave vectors of Bloch waves. When selecting $\mathbf{h}_1, 5\ 1\ 1$ reflection as the first reflection and $\mathbf{h}_2, 2\ \overline{2}\ \overline{4}$-reflection as the second one to fix the wavelength of the synchrotron X-rays, $\mathbf{h}_3, 3\ \overline{1}\ \overline{3}$-reflection occurs necessarily, which was neglected completely for several decades.

The program has been coded such that other reflections that simultaneously occurs are searched automatically after the first and second reflection indices are input. Figure 2 shows four dispersion surfaces for a four-beam case by inputting 2 2 0 and $\overline{4}$ 2 2 as the first and second indices. Here, 0 6 $\overline{2}$ has been automatically found as the third reflection. Very complex-shaped dispersion surfaces are found in this figure.

Furthermore, third or more reflection indices are not necessarily coplanar. It has been found with this program that as many as 48 reciprocal lattice nodes can be on the surface of the Ewald sphere, which revealed the importance of consideration on n-beam cases whereas almost all discussions on X-ray diffraction phenomena have been limited to the two-beam cases. Considerations on this situation is important not only for X-ray crystal optical devices designed based on the dynamical diffraction theory but also for crystal structure analysis based on the 'two-beam' kinematical theory almost for a hundred years.

Since the equivalence between the E-L and T-T formulations described with Fourier transform has been explicitly clarified in reference [5], both of them should be properly used for purpose when describing X-ray n-beam cases that is apparently difficult to discuss. The reason why only the two-beam approximation has been used in both dynamical and kinematical theories for a hundred years, is that it was just easy to discuss in spite that there are many problems that should be discussed based on the n-beam approximation.

References

[1] R. Colella: Acta Cryst. A **30** (1974) 413-423.

[2] K. Okitsu: Acta Cryst A **59** (2003) 235-244.

[3] K. Okitsu, Y. Yoda, Y. Imai, Y. Ueji, Y. Urano and X.-W. Zhang: Acta Cryst A **62** (2006) 237-247.

[4] K. Okitsu, Y. Yoda, Y. Imai and Y. Ueji: Acta Cryst A **67** (2011) 550-556.

[5] K. Okitsu, Y. Imai and Y. Yoda: InTech *Recent Advances in Crystallography* (2012) 67-86.

Equilibrium-state calculation in spin-glass models

Koji HUKUSHIMA
Department of Basic Science, University of Tokyo
3-8-1 Komaba, Meguro-ku, Tokyo 153-8902

Mean-field theory of spin glasses has provided a number of novel concepts for understanding of a phase transition in disordered glassy systems. In particular, replica-symmetry breaking (RSB) plays an essential role in describing complex free-energy structure. It turns out that the pattern of RSB is clarified into two distinct classes, full RSB and one-step RSB. Since the mean-field theory has been established, one of the main issues is whether such concepts survive in short-ranged spin-glass models in finite dimensions. Most of the effort has been devoted to examining the issue in an Ising spin glass model in three dimensions, whose corresponding mean field model, i.e., the Sherrington-Kirkpatrick model, exhibits the full RSB. Despite extensive studies including large scale numerical simulations, a definite conclusion has not yet been drawn.

Some mean-field spin-glass models with the one-step RSB have attracted much attention of many researchers in recent years. For instance, p-state Potts glass with $p \geq 3$ belongs to this class. These models are regarded as a prototype of a phenomenological picture of structural glass transition, called random first-order transition (RFOT), which is characterized by a thermodynamic transition with a discontinuous order parameter without latent heat. The advisability of the RSB picture in finite dimensional spin glass models comes to an issue again in the context of the structural glass transition. While the existence of the spin-glass transition of the Potts glass in three dimensions is clarified for $p \leq 6$[1,2], no feature predicted by RFOT based on the one-step RSB is found in numerical simulations and the nature of low temperature phase is not fully understood.

Our purpose is hopefully to detect some evidence of RFOT in a three dimensional Potts glass model by using Monte Carlo simulations. Recently, the fragility of the RFOT feature against finite dimensional fluctuation is discussed in Ref.[3]. According to the argument, if RFOT in finite dimensions is a possibility, the model should take a sufficient large number of states p in high dimensions, say $d \geq 9$ with d being spatial dimension. Instead, our strategy is to take a large number of connectivity up to third neighbor couplings with keeping dimensions three.

We have performed a large scale Monte Carlo simulations based on extended ensemble method for the 7-state Potts glass model in three dimensions with third neighbor couplings. Our findings are as follows[4]: (1) The model exhibits a thermodynamic spin-glass transition at finite temperature T_c, that is in contrast with the fact that the 7-state Potts glass with nearest neighbor couplings has no glassy phase at up to very low temperature. (2) The value of the critical exponent for the correlation length is very close to $2/d$ derived by a heuristic scaling argument based on RFOT. (3) It is strongly suggested that the spin-glass order parameter appears discontinuously at T_c and no latent heat exists. (4) The order-parameter distribution below T_c has double peaks at zero and a finite value corresponding to the self-overlap state. These are fully compatible with those expected from the RFOT picture based on the one-step RSB. Presumably, this is the first numerical evidence showing (one-step) RSB in three dimensional spin-glass models and this also gives the first explicit statistical-mechanical model with RFOT features in three dimensions.

The present work has been done in collaboration with Takashi Takahashi.

[1] L. W. Lee, et al: Phys. Rev. B**74** (2007) 0104416.
[2] A. Cruz, et al: Phys. Rev. B**79** (2009) 184408.
[3] C. Cammarota, et al: Phys. Rev. B**87** (2013) 064202.
[4] T. Takahashi and KH: in preparation.

Clarification of magnon turbulence in nano-contacts.

Katsuyoshi Matsushita
Cybermedia center, Osaka university
Toyonaka, Osaka 560-0043

The response phenomena of magnets have been investigated in order to clarify their potential in the industrial applications. Especially, the instability problem of the microscopic magnetic structure under the electronic current is an important issue related to the availability of the magnetic devices. For example, in the case of the communication device using voltage signals, the instability frequently results in a noisy signal and limits the efficiency of the devices. The further physical understanding the instability is needed to give keys to solve the issue.

In the present work, we shed light on the current induced turbulence in magnetic system as a possible instability in the magnetic system[1]. We have showed that a nanoscopic magnetic system confining a domain wall under current exhibits a transition from a steady state to a turbulence. In the study we conjectured that the critical parameters, namely the critical twist angle of the magnetic system Θ_c and the critical applied current j_c, of the transition only depends on the characteristic length, which depends only on the applied current and the exchange stiffness. To confirm this conjecture, we should determine the main factors of the transition. As a first step of the determination, we concentrate on the effect of the Gilbert damping.

We carried out the numerical simulation of the nanoscopic magnetic wire system under the current where the turbulence appears and evaluate the critical twist angle of the magnetic system. Figure 1 shows the time average magnetization S. The abrupt change of the order

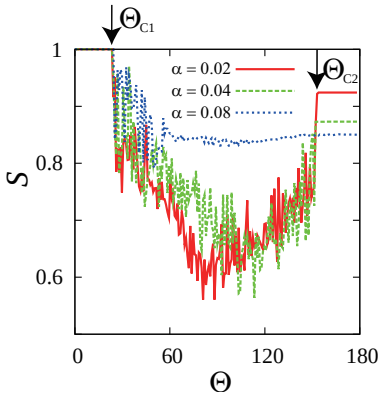

Figure 1: Order parameter as a function of twist angle of magnetic structure (See Ref.1) for $\alpha = 0.02$, 0.04 and 0.08 at around $j \simeq 1.5 j_c$. Θ_{c1} and Θ_{c2}

parameter reflects the transition between the steady state (not fluctuating S) and the turbulence (fluctuating S). The small change in the Gilbert damping constant α does not change the transition twist angles Θ_{c1} and Θ_{c2} for α of realistic small values (0.02 and 0.04). This indicates that the effect of the Gilbert damping is not a main factor for determining the transition points as conjectured previously in the realistic system. However for unrealistically large α (0.08), the turbulence fluctuation is suppressed because of strong damping and thereby Θ_{c2} can not be determined from the simulation.

References

[1] K. Matsushita *et al.*, J. Phys. Soc. Jpn **82** (2013) 033801.

Novel ordering in frustrated spin systems

Tsuyoshi Okubo
Institute for Solid State Physics, University of Tokyo
Kashiwa-no-ha, Kashiwa, Chiba 277-8581

Frustrated spin systems have attracted recent interests. Typical examples of such frustrated systems in two dimension are Heisenberg antiferromagnets on the kagome lattice and the triangular lattice. Recently a new type of frustrated lattice interconnecting the triangular lattice and the kagome lattice has been found in $NaBa_2Mn_3F_{11}$ [1]. In this *kagome-triangular* lattice, a kagome lattice deforms so as to generate the next-nearest (NN) neighbor interactions between three of six NN neighbors on the regular kagome lattice.

The Hamiltonian of the kagome-triangular lattice Heisenberg model is given by

$$\mathcal{H} = J_1 \sum_{\langle i,j\rangle_1} \vec{S}_i \cdot \vec{S}_j + J_2 \sum_{\langle i,j\rangle_2} \vec{S}_i \cdot \vec{S}_j, \qquad (1)$$

where $\vec{S}_i$ is a unit vector with three components, and $\langle i,j\rangle_1$ ($\langle i,j\rangle_2$) represents the sum over the nearest neighbor (NN neighbor) pairs on the kagome-triangular lattice.

Based on an analysis of the Fourier transform of the exchange interactions, we found that typical $q = 0$ state and $\sqrt{3} \times \sqrt{3}$ state appear for antiferromagnetic J_1 with antiferromagnetic J_2 and ferromagnetic J_2, respectively. In contrast, for the case of ferromagnetic J_1 and antiferromagnetic J_2 the wavevector which minimizes the energy appears along the line connecting $q = 0$ and the M point, indicating a possible novel ordered structure.

In order to investigate the ordering of the kagome-triangular lattice Heisenberg model, we performed extensive Monte Carlo simulations. The Monte Carlo simulations were performed based on the standard heat-bath method combined with the over-relaxation method. The lattice is a $L \times L$ kagome-triangular lattice with $24 \leq L \leq 96$ with periodic boundary conditions.

For ferromagnetic J_1 and antiferromagnetic J_2 with $J_2/|J_1| \gtrsim 1$, the ground state is a non-coplaner multiple-q state which is a superposition of three independent wavevectors at the M points. Based on the analysis of snapshots obtained from Monte Carlo simulations, we conclude that this multiple-q state is identical to the 12 sublattices cuboctahedral order found in the conventional J_1-J_2 kagome lattice Heisenberg model[2, 3]. In addition to this cuboctahedral phase, we found a novel incommensurate non-coplaner phase, which did not appear in the conventional kagome lattice J_1-J_2 Heisenberg model, for $1/2 \lesssim J_2/|J_1| \lesssim 1$. Details of this incommensurate phase will be investigated in future works.

References

[1] H. Ishikawa, T. Okubo, Y. Okamoto, and Z. Hiroi: J. Phys. Soc. Jpn. **83** (2014) 043703.

[2] J. C. Domenge, P. Sindzingre, C. Lhuillier, and L. Pierre: Phys. Rev. B **72** (2005) 024433.

[3] J. C. Domenge, C. Lhuillier, L. Messio, L. Pierre and P. Viot: Phys. Rev. B **77** (2008) 172413.

Nonequilibrium phase transitions in Strongly Correlated Electron Systems

Takashi OKA

Department of Applied Physics,

The University of Tokyo, Hongo, Bunkyo-ku,Tokyo 133-8656

Owing to recent developments in experimental techniques such as pump-probe measurements and nonlinear transport, the research of nonequilibrium properties of strongly correlated electron systems is becoming more and more important. From the theory side, the bottleneck of progress is the lack of reliable numerical methods which can be used to study phase transitions that takes place dynamically. Most previous methods such as QMC were developed to study equilibrium time-independent problems. Recently, the dynamical mean field theory (DMFT), a very standard method in correlated electron theory, was extended to nonequilibrium dynamics using the Keldysh green's function method. This method can be applied to models of strongly correlated systems such as the Hubbard model. In collaboration with H. Aoki, N. Tsuji, M. Eckstein, M. Kollar, and P. Werner, I wrote a review article on this topic, which will be published in Review of Modern Physics [1]. The essence of this method is to take into account the local correlation, which is important to describe the Mott physics, by starting from a impurity model represented by

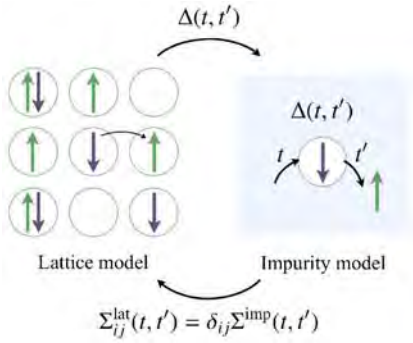

Fig.1 A schematic representation of the algorithm of dynamical mean field theory.

the Anderson model, and incorporate the band effect by performing a self-consistent loop on the green's function (Fig.1). Nonequilibrium DMFT has been applied to several problems such as the photo-induced metallization, dielectric breakdown problem, as well as quantum quench. In the project with the supercomputer in ISSP, I am trying to extend nonequilibrium DMFT to study unconventional superconductivity in cuprates [2]. At present, we have developed the calculation scheme and algorithm and implemented a test program. I expect to report further progress shortly.

References

[1] H. Aoki, N. Tsuji, M. Eckstein, M. Kollar, T. Oka, and P. Werner, "Nonequilibrium

dynamical mean-field theory and its applications", *to appear in* Rev. Mod. Phys.

[2] T. Oka, M. Babadi, and V. Pietila, *in progress*.

The Scaling Law of the Systems with Long-Range Interactions

HYUGA Masahiko

Department of Basic Science, University of Tokyo

3-8-1 Komaba, Meguro, Tokyo 153-8902, Japan

30 April 2014

The systems with long–range interactions are known to exhibit an odd behaviour, such as ensemble inequivalence[1], negative specific heat, and explicit shape– and size–dependency of thermodynamic relations.

Since we should concern all interaction forces of every particle pairs for long–range systems, numerical analysis is more difficult compared to short–range systems. Thus, numerical calculation of long–range systems should be done on super computers.

In this research, we have studied the scaling law of the systems with both long– and short–range interactions. For systems only with a single long–range interactions which scales as $\sim 1/r^{\alpha}$, the scaling law is conjectured by Tsallis[2] and confirmed later by many numerical simulations [3]. In this theory, thermodynamic quantities scale as $E \sim NN^*\mathcal{E}^*, T \sim N^*T^*, V \sim N\mathcal{V}$ where d is a spacial dimension and N^* is given by $N^* = N^{1-\alpha/d}$.

However, for systems with both short– and long–range interactions, N^* should be modified for small system size. We conjectured what formula of N^* should be suited for such systems and confirmed this formula by numerical simulations.

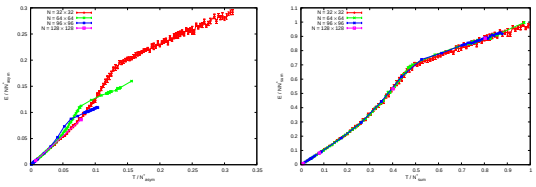

Fig. 1: Left: the relation between energy and temperature for $N^* = N^{1-\alpha/d}$ (previously conjectured formula), and right: our new formula of N^*. You can see four lines lap over each other for bottom figure, which means the scaling factor N^* is correct.

In order to confirm our new formula of N^*, we have numerically simulated a classic lattice system with two potentials whose decaying speed is different each other. This computation requires a lot of computational power, so the super computer was much helpful for this simulation.

The result obtained by our simulation is plotted in Fig.1. Four different lines does not lap over each other for N^* of previous work [left figure], but for newly suggested N^* those lines lap over each other [right figure].

[1] For short–range systems, all the thermodynamic relations calculated from the microcanonical ensemble and the canonical ensemble agrees each other. This property is called the *ensemble equivalence*. However, this property does not hold for some systems with long–range interactions [1].

参考文献

[1] A.Campa, A.Giansanti, D.Mukamel, and S.Ruffo, Physica A **365** (2006) 120–127

[2] C.Tsallis, Fractals **3** (1995) 541–547

[3] See, for example, L.Sampaio, M.Albuquerque, and F. Menezes, Phys. Rev. B **55** (1997) 5611–5614

Molecular Dynamics Simulation Study of Nucleation Mechanism of Calcium Carbonate Crystal in the Presence of Impurities

Hiroki NADA
National Institute of Advanced Industrial Science and Technology (AIST)
Onogawa16-1, Tsukuba, Ibaraki 305-8569

The polymorphism of calcium carbonate ($CaCO_3$) has attracted great interest from long ago. The most thermodynamically stable $CaCO_3$ crystal is calcite. However, the nucleation of metastable vaterite occurs instead of calcite. The nucleation of metastable aragonite or metastable hydrated $CaCO_3$ crystals also occurs in the presence of impurities, such as Mg^{2+} ions. The $CaCO_3$ polymorphism indicates that the nucleation of metastable $CaCO_3$ crystals can be kinetically favored over the nucleation of calcite. However, the cause of the polymorphism remained unclear, because it was difficult to observe the initial stage of nucleation at the atomic scale in solution.

Recently, several experimental studies have reported the nucleation of $CaCO_3$ crystals from amorphous $CaCO_3$ (ACC) particles formed in solution. Therefore, the structure of ACC may be particularly relevant to $CaCO_3$ polymorphism. In this project, we investigated the effects of Mg^{2+} ions and H_2O molecules on the atomic-scale structure of ACC by means of molecular dynamics (MD) simulation [1, 2].

The simulation was performed for bulk ACC. The system for ACC was a cubic consisting of 840 particles, which was the sum of the number of Ca^{2+} ions, Mg^{2+} ions, ${CO_3}^{2-}$ ions and H_2O molecules. Three-dimensional periodic boundary conditions were imposed on the system. The fraction of Mg^{2+} in the system was 0, 0.25, 0.5, 0.75 and 1.0, and the fraction of H_2O molecules in the system was 0, 0.25, 0.5, 0.75. The $CaCO_3$ potential model proposed by Raiteri et al. was used to estimate the $CaCO_3$ interactions in ACC [3]. Mg^{2+} potential parameters were developed in this project [1]. The interaction for the H_2O molecules was estimated using the TIP4P-Ew model [4]. Temperature and pressure were maintained at 300 K and 1 atm, respectively.

The simulation preformed using NEC SX-9 in ISSP provided us the follwing new findings: The structure of pure ACC resembled that of vaterite rather than those of calcite and aragonite. However, Mg^{2+} ions hindered the formation of a vaterite-like structure in ACC. When the fraction of H_2O molecules was high and Mg^{2+} ions were present, the formation of monohydrocalcite-like structure was promoted.

References

[1] H. Tomono et al., J. Phys. Chem. B, **117** (2013) 14849.

[2] F. Zhu et al., Chem. Asian J., **8** (2013) 3002.

[3] P. Raiteri et al., J. Phys. Chem. C, **114** (2010) 5997.

[4] H. W. Horn et al., J. Chem. Phys., **120** (2004) 9665.

Numerical study of quantum liquid phase using tensor network variational method

Kenji HARADA
Graduate School of Informatics, Kyoto University, Kyoto 606-8501, Japan

In the past decade, the disordered behaviors of materials on a layer have been attracting attention. In particular, the possibility of a quantum spin liquid state has been studied. In general, the order of a quantum spin liquid state can be regarded as a topological one which cannot be transformed to a trivial state. However, except for special theoretical models, the evidence of topological order on effective models of materials is poor.

The antiferromagnetic Heisenberg model on a Shastry-Sutherland lattice is an effective model of $SrCu_2(BO_3)_2$. We have an interest in the possibility of intermediate disordered phase between a plaquette valence-bond-solid (VBS) phase and an antiferromagnetic phase on this model. We studied the ground states by using MERA tensor network methods. In our results, the plaquette VBS order is very weak near the antiferromagnetic phase. Thus, the existence of intermediate disorder phase is not clear yet. We continue to improve the numerical precision by applying a new algorithm of tensor networks.

In some cases, to protect the topological state against a trivial state, we need symmetry on models. Then, it is called *symmetry-protected topological order*. The hidden order of quantum spin model on a chain is a striking example of the symmetry-protected topological order[1]. We found the generalized Jordan-Wigner transformation[2] to disentangle the topological order of S=1 bilinear-biquadratic (BLBQ) models on a chain[3]. We successfully extended it to SO(N) BLBQ models[4]. Using this non-local transformation, we can map an SO(N) BLBQ model to a N-color bosonic model. In particular, a symmetry-protected topological order can be transformed to a Landau symmetry-broken order analytically. We can study a symmetry-protected topological state as a conventional symmetry-broken state. In addtion, the negative-sign problem of quantum Monte Carlo (QMC) calculation[5] perfectly disappears. Thus, we can study the topological ordered state by QMC with high precision. Using a worm algorithm on the ISSP super computer system B, we observed the rapid growth of entropy (See Fig. 1) and finite temperature behaviors of topological order parameter (See Fig. 2). The conventional approach cannot calculate these quantities with high precision.

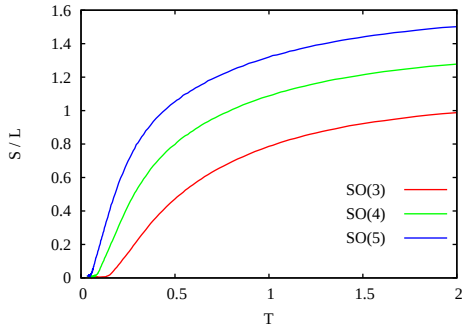

FIG. 1. Entropy per site of SO(3), SO(4), and SO(5) BLBQ models on a chain at the generalized VBS points. The chain length L is 256.

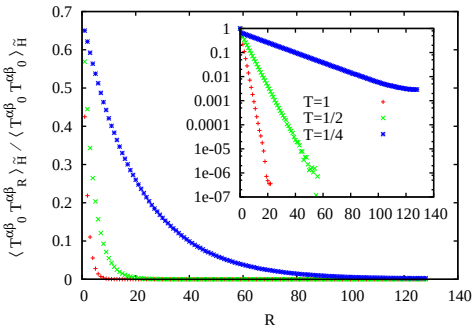

FIG. 2. Two point correlation function of topological order parameter at the AKLT[6] point of S=1 BLBQ model on a chain. The chain length L is 256. The inset is a semi log plot.

[1] F. Pollmann, A. M. Turner, E. Berg, and M. Oshikawa, Phys. Rev. B **81**, 064439 (2010); F. Pollmann, E. Berg, A. M. Turner, and M. Oshikawa, Phys. Rev. B **85**, 075125 (2012).
[2] L. Messio and F. Mila, Phys. Rev. Lett. **109**, 205306 (2012).
[3] K. Okunishi and K. Harada, Phys. Rev. B **89**, 134422 (2014).
[4] H.-H. Tu, G.-M. Zhang and T. Xiang, Phys. Rev. B **78**, 094404 (2008).
[5] K. Harada and N. Kawashima, J. Phys. Soc. Jpn. **70**, 13 (2001).
[6] I. Affleck, T. Kennedy, E. H. Lieb, and H. Tasaki, Phys. Rev. Lett. **59**, 799 (1987).

Numerical study on low-energy states of quantum spin systems

Hiroki NAKANO
Graduate School of Material Science, University of Hyogo
3-2-1 Kouto, Kamigori-cho, Ako-gun, Hyogo 678-1297, Japan

Presice estimation of physical quantities of a quantum spin system is often di cult because the system is a typical many-body problem. Under circumstatnces, importance of numerical approaches, especially, methods beyond any approximations, becomes higher and higher. Computational studies have contributed much for our deep understanding of various quantum spin systems. However, it is still di cult to treat frustrated quantum spin systems in spatial dimensions larger than one. The reason of this di culty is that such systems cannot be treated by the density matrix renormalization group (DMRG) calculations and the quantum Monte Carlo simulations. The numerical diagonalization method based on the Lanczos algorithm is an almost unique way as a valid method for such frustrated quantum spin systems. In this method, unfortunately, only very small system sizes can be treated. To overcome this disadvantage, we have successfully developed a hybrid-type parallelized code of Lanczos diagonalization[1]. Using this Lanczos-diagonalization calculation as a primary approach, we investigate quantum spin systems. We also employ other numerical methods as supplementary ones; we examine quantum spin systems from various points of view.

The primary study of this year in the present project is the magnetization jump in the $S = 1/2$ Heisenberg antiferromagnet on the square-kagome lattice[2]. We nd that the system shows a magnetization plateau at the one-third height of the saturation in its magnetization process; the plateau is accompanied by a magnetization jump at the higher- eld edge. In order to clarify the mechanism of the occurrence of the jump, we observe the local magnetization, capturing the bahavior of the spin- op phenomenon in spite of the fact that the system is isotropic in spin space, where the spin- op phenomenon is widely known to be a phenomenon that occurs when the system includes some anisotropy. The same behavior is observed in the Heisenberg antiferromagnet on the Cairo-pentagon lattice[3].

Properties of other frustrated Heisenberg antiferromagnet were studied by numerical-diagonalization method [4, 5, 6, 7]. Randomness e ect in a frustrated system was also investigated[8]. Our numerical results and theoretical arguments contribute to analyze experiments of various magnetic conpounds[9, 10, 11]. Our studies of quantum spin systems by several numerical approaches including parallelized calculations of Lanczos diagonalization contribute to our understandings of these systems.

References

[1] H. Nakano and A. Terai: J. Phys. Soc. Jpn. **78** (2009) 014003.

[2] H. Nakano and T. Sakai: J. Phys. Soc. Jpn. **82** (2013) 083709.

[3] H. Nakano, M. Isoda, and T. Sakai: J. Phys. Soc. Jpn. **83** (2014) 053702.

[4] H. Nakano and T. Sakai: to be published in JPS Conf. Proc.

[5] T. Shimokawa and H. Nakano: J. Kor. Phys. Soc. **63** (2013) 591.

[6] Toru Sakai and H. Nakano: J. Kor. Phys. Soc. **63** (2013) 601.

[7] H. Nakano, Synge Todo, and Toru Sakai: J. Phys. Soc. Jpn. **82** (2013) 043715.

[8] K. Watanabe, H. Kawamura, H. Nakano and T. Sakai: J. Phys. Soc. Jpn. **83** (2014) 034714.

[9] K. Iwase, H. Yamaguchi, T. Ono, T. Shimokawa, H. Nakano, A. Matsuo, K. Kindo, H. Nojiri, and Y. Hosokoshi: J. Phys. Soc. Jpn. **82** (2013) 074719.

[10] H. Yamaguchi, S. Nagata, M. Tada, K. Iwase, T. Ono, S. Nishihara, Y. Hosokoshi, T. Shimokawa, H. Nakano, H. Nojiri, A. Matsuo and K. Kindo, and T. Kawakami: Phys. Rev. B **87** (2013) 125120.

[11] H. Yamaguchi, K. Iwase, T. Ono, T. Shimokawa, H. Nakano, Y. Shimura, N. Kase, S. Kittaka, T. Sakakibara, T. Kawakami, and Y. Hosokoshi: Phys. Rev. Lett. **110** (2013) 157205.

Dynamical scaling analysis on the low-temperature phase for the RP^2 model in two dimensions

Y. Ozeki[1], A. Matsuda[1], Y. Echinaka[1] and Y. Tomita[2]
[1] *Graduate School of Informatics and Engineering, The University of Electro-Communications*
[2] *College of Engineering, Shibaura Institute of Technology*

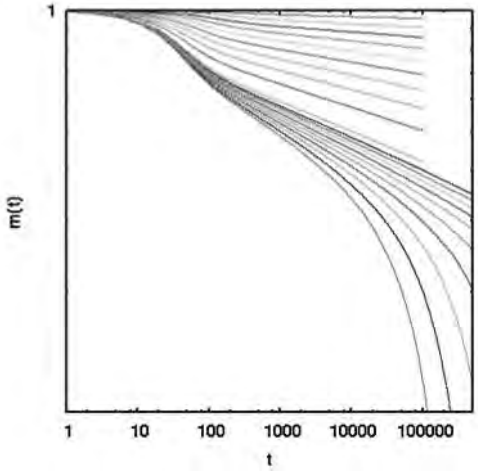

Figure 1: Calculations are made with $\Delta T = 0.05$ for $0.050 \leq T \leq 0.500$, and with $\Delta T = 0.005$ for $0.510 \leq T \leq 0.555$.

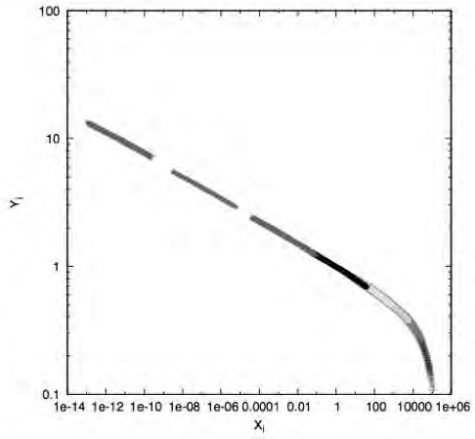

Figure 2: Scaling plot.

We investigate the nature of the phase transition which has been reported to appear in the low-temperature regime for the RP^2 model in two dimensions. [1, 2] They suggested that there exist a topological phase transition like the Kosterlitz-Thouless (KT) one, while, recently, a possibility of no transition has been claimed [3, 4]. We apply the nonequilibrium relaxation (NER) method and examine the improved dynamical scaling analysis [5, 6] for the KT transition by the use of the Bayesian inference and the kernel method, and the relaxation of fluctuations to discuss the critical exponents η and z inside the KT phase.

The Hamiltonian for the RP^2 model is

$$\mathcal{H} = -J \sum_{\langle ij \rangle} \cos^2(\theta_i - \theta_j). \tag{1}$$

We perform Monte Carlo simulation with Metropolis dynamics. First, we estimate the relaxation of the order parameter $m(t) = \langle \sum_i \cos\theta_i \rangle_t / N$ from the all-aligned state, where $\langle \cdots \rangle_t$ represents the dynamical average at t Monte Carlo steps (MCS). Calculations are performed on lattices up to 15001×1500 with skew boundary condition. The averaging is made for 1024 independently chosen samples. The result is shown in Fig. 1; note the unit of temperature is $2J/3k_{\rm B}$ which is used in the Lebwohl-Lasher model.

In the NER analysis of KT transition, it has been a efficient tool due to the finite-time scaling ,

$$m(t, T) = \tau^{-\lambda} \Psi(t/\tau), \tag{2}$$

where $m(t, T)$ is a relaxation of magnetization from the all aligned state. $\tau(T)$ is the relaxation time, which is expected to diverge as

$$\tau(T) \sim \exp(c/\sqrt{T - T_{\rm KT}}) \tag{3}$$

in $T > T_{\rm KT}$. To estimate $T_{\rm KT}$, we fit the data to the above formula using the improved method applying the Bayes inference and the kernel method. [6] In Fig. 2, we show the resulting scaling plot for $X = t/\tau$ vs. $Y = \tau^{\lambda} m(t)$. Furthermore, we apply the algebraic form $\tau(T) \sim |T - T_{\rm c}|^{-z\nu}$ instead of eq.(3), and compare the results. This provides the indication of the KT transition at $T = 0.508$ in the present model.

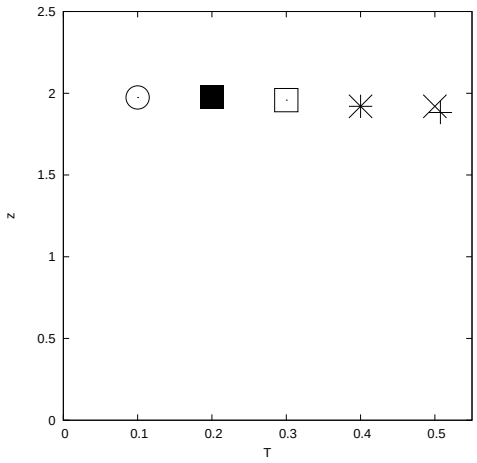

Figure 3: Temperature dependence of the exponent z inside the KT phase.

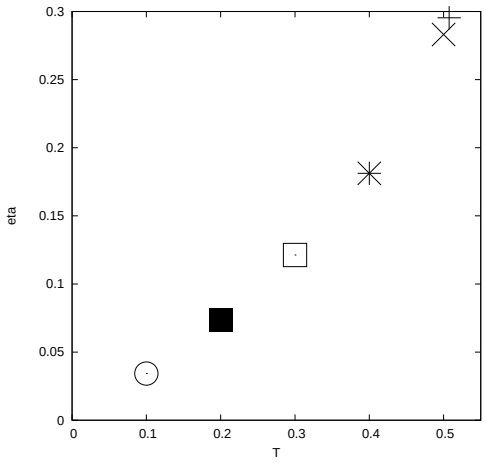

Figure 4: Temperature dependence of the exponent η inside the KT phase.

Next we examine critical exponents at and below the estimated KT transition temperature. We calculate $m(t)$ and

$$f_{mm}(t) \equiv N \left(\frac{\langle m^2 \rangle_t}{\langle m \rangle_t^2} - 1 \right) \tag{4}$$

to estimate these exponents. Calculations are performed on 401×400 lattice. The averaging is made for 4^5 independently chosen samples. From the dynamical scaling argument, the asymptotic forms of these quantities are expected as [5]

$$m(t) \sim t^{-\eta/2z}, \tag{5}$$
$$f_{mm}(t) \sim t^{2/z}. \tag{6}$$

Thus we estimate z and η for several values of temperatures. The results are shown in Figs. 3 and 4. For the dynamical exponent z, which seems to be located around 2 irrespective of temperature. For the static exponent η, which is decreasing linearly in the limit of $T \to 0$. These behaviors are quite similar with the XY model in two dimensions [7] in which the existence of the KT transition has been believed.

The present numerical study indicates that there exists a KT transition in the RP^2 model in two dimensions. In the NER analysis, we observe and analyze relaxations up to an MCS where no size dependence clearly appears. Thus, one may recognize that the observed behavior is that in the thermodynamic limit.

References

[1] H, Kunz and G. Zumbach, Phys. Rev. B **46** 662 (1992).

[2] E. Mondal and S. K. Roy, Phys. Lett. A **312** 397 (2003).

[3] R. Paredes V. *et al*, Phys. Rev. E **78** 051706 (2008).

[4] A. I. Fariñas Sànchez *et al*, Cond. Matter Phys. **13** 13601 (2010).

[5] Y. Ozeki, K. Ogawa and N. Ito, Phys. Rev. E **67** 026702 (2003), Y. Ozeki and N. Ito, J. Phys. A: Math. Theor. **40** R149 (2007);

[6] Y. Ozeki and Y. Echinaka, Activity Report 2012 (Supercomputer Center, ISSP, 2013)

[7] Y. Ozeki, S. Yotsuyanagi, T. Sakai and Y. Echinaka, Phys. Rev. E **89** 022122 (2014).

Novel ordered phase and dynamical response under driving field

Seiji MIYASHITA
Department of Physics, University of Tokyo
7-3-1 Hongo, Bunkyo-ku, Tokyo 113-0033, Tokyo

1 Quantum dynamics under time-dependent external field

1.1 Phase transitions in a cavity driven by an external alternate field

We have studied what kinds of cooperative phenomena take place in systems driven by an external alternate field. In particular, we investigated a cavity system in which a single cavity photon mode couples with many discrete energy systems which we call 'spin' hereafter.[1] The spins are independent of each other but they couple with each other by effective interaction due to the cavity mode. The cavity mode is excited by a resonant external field. The coupling between spin and cavity mode composes a hybrid system where the energy spectrum exhibits an avoided level structure, which has been attracted from a view point of information transfer between photon system and condensed matter.[2] It is known that the coupling causes the so-called Dicke transition where the spontaneous excitation appears even in the ground state, and also that the coupling causes a non-equilibrium phase transition which is called 'optical bistability' as a function of strength of external field.

The system is modeled by the Dicke model or the model with rotation-field approximation (Tavis-Cummings model).

$$\mathcal{H} = \hbar\omega_0 a^\dagger a + \hbar\omega_{\rm A}\sum_{i=1}^{N} S_i^z, \\ +\hbar\hat{g}\sum_{i=1}^{N}(S_i^+ + S_i^-)(a^\dagger + a) + \hat{\xi}(a^\dagger + a)\cos(\omega_{\rm ext}t). \quad (1)$$

where ω_0 is a frequency of the cavity photon, and $\omega_{\rm A}$ denotes the excitation energy of the spin, and g is the strength of the coupling. The last term is the external AC field whose strength is ξ. We study the model with a quantum master equation where we take into account the external driving field and dissipative effect due to a coupling to the thermal bath.

First we drove a quantum master equation in which effects of the interaction in the system is taken into account. This adjustment is necessary to reproduce the spontaneous symmetry breaking phenomena correctly. We also pointed out that the mean-field approximation holds in a proper scaling limits $\hat{g} = g/\sqrt{N}$ and $\hat{\xi} = \sqrt{N}\xi$, and studied cooperative phenomena in the region of strong coupling (g) and the strong driving ξ. We found a new type of symmetry broken state, the region of which is depicted by dots in the phase diagram (Fig. 1).

The mechanism of the new symmetry broken state is given from the view point of the Coherent Destruction of Tunneling (CDT). The lines denote the position where the spin system is expected to show the CDT.

1.2 Landau-Zener dynamics in uniaxial quantum spins

We have studied the Landau-Zener mechanism in isotropic spin systems, where the dynamics is independent of the total spin S. In the case of classical spin in uniaxial spin systems, the so-called Stoner-Wohlfarth mechanism takes place, and the spin dynamics has a

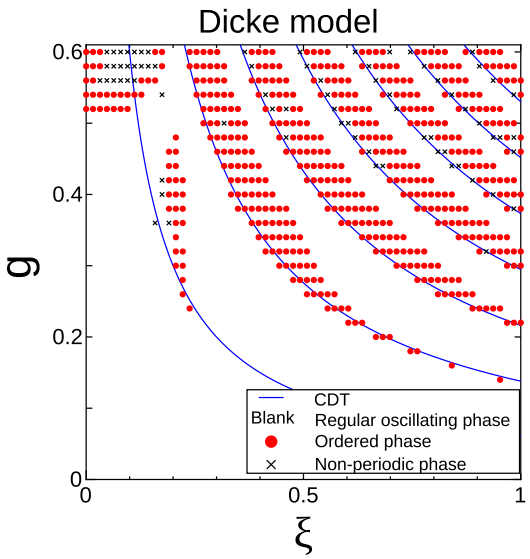

Figure 1: Phase diagram of the driven Dicked model (cited from [1]

threshold phenomenon at which the magnetization jumps. In quantum system similar phenomena takes place, which can be regarded as a first order phase transition in quantum system. We studied the nature of the metastable state associated with the first order phase transition in quantum systems.

2 Other topics

2.1 Phase transitions of systems with bistable states which have different local lattice structures

We have pointed out the effects of long range interaction due to elastic interaction of lattice distortion which is brought by the different local lattice structures of bistable states. This mechanism is relevant in many systems, such as the spin-crossover, Jahn-Teller system, and martensite systems. We studied the effect of long range interaction on the system with short range antiferromagnetic model and obtained full phase diagram for ferro- and antiferromagnetic short range interactions in the elastic model.[3]. We also studied the nature of the domain wall in such system where we found that the width of the domain wall depends on the time scale of spin dynamics[3].

In such systems with long range interaction causes peculiar properties. We found the present model holds the extensivity, but not the additivity[5].

2.2 Phase transition between Mott insulator and Itinerant ferromagnetism

We also studied quantum phase transition of an itinerant ferromagnetism motivated by the Nagaoka ferromagnetism. In the system the electron density is controlled by the chemical potential. The change of the total spin as a function of the chemical potential is obtained by an exact diagonalization and also DMRG method. Various properties, such as magnetization process, the spin-correlation function, and also entanglement entropy was studied[6].

References

[1] T Shirai, T Mori and S Miyashita, Novel symmetry-broken phase in a driven cavity system in the thermodynamic limit, J. Phys. B: At. Mol. Opt. Phys. **47** (2014) 025501 (9pp).

[2] S. Miyashita, T. Shirai, T. Mori, H. De Raedt, S. Bertaina, and I. Chiorescu, Photon and spin dependence of the resonance lines shape in the strong coupling regime, J. Phys. B: At. Mol. Opt. Phys. **45**, 124010(10pp) (2012).

[3] Masamichi Nishino, and Seiji Miyashita, Effect of the short-range interaction on critical phenomena in elastic interaction systems, Phys. Rev. B **88**, 014108 (2013).

[4] Masamichi Nishino, Taro Nakada, Cristian Enachescu, Kamel Boukheddaden, and Seiji Miyashita, Crossover of the roughness exponent for interface growth in systems with long-range interactions due to lattice distortion, Phys. Rev. B **88**, 094303 (2013).

[5] T Mori, Nonadditivity in Quasiequilibrium States of Spin Systems with Lattice Distortion, Phys. Rev. Lett. **111**, 020601 (2013).

[6] H. Onishi and S. Miyashita, "Doping Control of Realization of an Extended-Nagaoka Ferromagnetic State from the Mott state", in preparation.

Transport phenomena in disordered topological insulators

TOMI OHTSUKI[1]
TOHRU KAWARABAYASHI[2]
KEITH SLEVIN[3]
KOJI KOBAYASHI[1]
1) Dept. Phys., Sophia University, Chiyoda-ku, Tokyo 102-8554, Japan
2) Dept. Phys., Toho University, Miyama 2-2-1, Funabashi 274-8510, Japan
3) Dept. Phys., Osaka University, Toyonaka, Osaka 560-0043, Japan

Recent discoveries of two-dimensional quantum spin Hall states and three-dimensional topological insulators (TIs) have inspired extensive research for these novel materials. In the impurity free systems where the translational invariance exists, the topological insulator is characterized by the non-zero topological numbers, which are defined via integral over Brillouin zone. This definition is no longer valid once the translational invariance is broken due to disorder. In this case, we usually use edge/surface states to characterize TIs.

Here we study the bulk properties of the disordered three-dimensional topological insulators numerically, and show how to distinguish TI from ordinary insulators by investigating the transport properties of bulk states. We first calculate bulk conductance via transfer matrix method, from which we draw the phase diagram for disordered TI [1]. Along the phase boundary between different TI phases, we show that the Dirac semimetal emerges even in the presence of disorder. With increase of disorder, the Dirac semimetal undergoes semimetal to metal transition. We propose that the density of states exhibits novel single parameter scaling behavior near the Dirac semimetal to metal transition.

To confirm the scaling behavior, we have performed large scale numerical calculation of the density of states via kernel polynomial method. We consider $200\times200\times200$ cubic systems described by Wilson-Dirac Hamiltonian, which are large enough to discuss approximately the thermodynamic limit. We then estimate the critical exponent ν for the length scale to be $\approx$0.9, and the dynamical exponent z to be $\approx$1.5, significantly different from those of the Anderson transition (in which we obtain $\nu = 1.38 \pm 0.01$ and $z = 3$ [2]). Scaling relations of vanishing density of states, diverging diffusion constant, vanishing conductivity as well as vanishing Dirac electron velocity are derived [3].

References

1. K. Kobayashi, T. Ohtsuki, K.-I. Imura: PRL **110**, 236803 (2013)
2. K. Slevin, T. Ohtsuki: New J. Phys. **16**, 015012 (2014)
3. K. Kobayashi, T. Ohtsuki, K.-I. Imura, I. Herbut: PRL **112**, 016402 (2014)

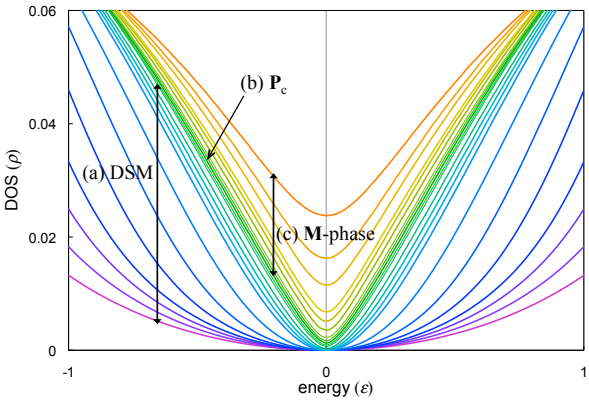

Figure 1: Density of states calculated in different phases: (a) on the boundary, (b) at the tricritical point, and (c) in the metal phase.

Transport phenomena in disordered topological insulators

TOMI OHTSUKI[1]
KEITH SLEVIN[2]
YOSUKE HARASHIMA[2]
1) Dept. Phys., Sophia University, Chiyoda-ku, Tokyo 102-8554, Japan
2) Dept. Phys., Osaka University, Toyonaka, Osaka 560-0043, Japan

In heavily doped semiconductors, a zero temperature metal-insulator transition (MIT) is observed as a function of doping concentration N_d. For samples with doping concentrations below a critical concentration N_c, the conductivity extrapolated to zero temperature $\sigma(T=0)$ is found to be zero, while for samples with concentrations exceeding this critical concentration, $\sigma(T=0)$ is finite.

The object of this study is to understand the MIT in doped semiconductors by determining how the Coulomb interaction affects the critical behaviour of the Anderson transition. We do this by simulating a model of a doped semiconductor that treats on an equal footing both the disorder due to the random spatial distribution of the dopants and the Coulomb interaction between the carriers.

To study a phase transition, we need to consider a reasonably large number of electrons, so exact diagonalization is impractical. Instead we use the Kohn-Sham formulation of density functional theory. The local density approximation (LDA) is adopted. We then observe a localisation-delocalisation transition of the highest occupied Kohn-Sham eigenfunction as a function of donor concentration. Simulations were performed for system sizes in the range $L = 229 \sim 400$ Å and donor concentrations of $N_d = N/L^3 = 0.4 \sim 1.3 \times 10^{18}\mathrm{cm}^{-3}$, which corresponds to $5 \sim 85$ electrons. We set the finite difference grid spacing to 18 Bohr, which is about half of the effective Bohr radius for Si. The donors were randomly distributed on a simple cubic lattice with spacing 36 Bohr. This avoids the situation that two donors are unphysically close. The number of samples for each system size and donor concentration varies between 1500 and 3000.

Applying a multi-fractal finite size scaling method [1], we find that the model exhibits a localization-delocalization transition at approximately the right carrier concentration (see Figure 1) [2]. Moreover, we find that the critical exponent $\nu \approx 1.3$, which is different from that for the standard Anderson transition.

References

1. A. Rodriguez, L. J. Vasquez, K. Slevin, and R. A. Romer: Phys. Rev. Lett. **105** (2010) 046403, Phys. Rev. B **84** (2011) 134209.
2. Y. Harashima, K. Slevin:arXiv:1308.1191

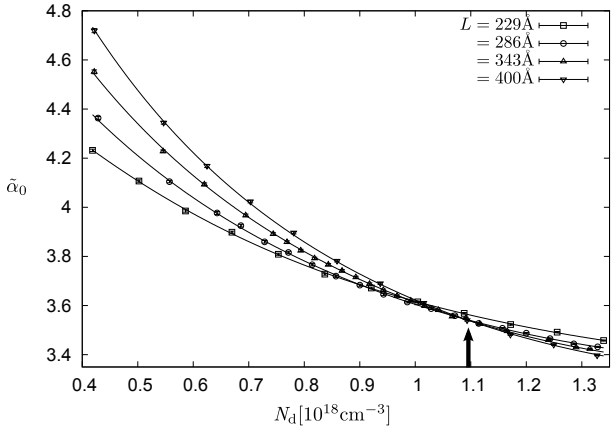

Figure 1: The generalized multi-fractal exponent α_0 as a function of donor concentration for several system sizes. The solid lines are a finite size scaling fit to the data. The critical concentration is indicated by an arrow.

Study on Statistical Physics Based on Quantum Information Theory

Shu TANAKA
Department of Chemistry, The University of Tokyo
7-3-1 Hongo, Bunkyo-ku, Tokyo 113-0033
Yukawa Institute for Theoretical Physics, Kyoto University
Kitashirakawa-Oiwakecho, Sakyo-Ku, Kyoto 606-8502

As a next-generation information technology, quantum information technology has been attracted attention in science. In addition, quantum information science opens a new window on a wide area of physics, *e.g.*, quantum statistical physics. We studied the following two topics in this project[1, 2, 3, 4].

(a) Quantum Annealing for Clustering Problem[1, 2]

In general, it is hard to obtain the best solution of optimization problems. Optimization problems are widespread in science and technology and efficient algorithms have been proposed. Most of combinatorial optimization problems can be mapped onto random Ising model and its generalized model. Thus, development of such algorithms have been done in statistical physics.

In 1998, Kadowaki and Nishimori proposed a versatile algorithm called quantum annealing to obtain the best solution by gradually decreasing quantum fluctuation[5]. The quantum annealing is an alternative to the simulated annealing [6] in which the temperature (*i.e.*, thermal fluctuation) gradually decreases. The efficiency of quantum annealing has been considered for a long time using simple models. In addition, very recently, actual equipment of quantum annealing has been developed[7].

To examine the performance of quantum annealing, we considered quantum annealing to solve a clustering problem which is a typical applicable optimization problem[1]. In our quantum annealing, not only the quantum fluctuation but also the thermal fluctuation are simultaneously controlled. As a result, the efficiency of quantum annealing is better than that of simulated annealing although computational costs of both methods are comparable. In this study, we performed the Monte Carlo simulation based on parallel computation.

The performance of quantum annealing is not good for systems in which phase transition occurs. This fact is known as difficulty in the quantum annealing. In order to avoid the difficulty, we also considered another type of fluctuation to add the Hamiltonian which represents optimization problems[2].

The above studies were done in collaboration with Kenichi Kurihara (Google Inc.), Seiji Miyashita (The University of Tokyo), Hiroshi Nakagawa (The University of Tokyo), Issei Sato (The University of Tokyo), and Ryo Tamura (National Institute for Materials Science).

(b) Entanglement Properties of Two-dimensional Quantum Systems[3, 4]

Entanglement properties have been considered in not only quantum information science but also various fields of physics such as quantum statistical physics. Some beautiful relations between entanglement properties and strongly correlated quantum systems have been found. We have considered entan-

glement properties of two-dimensional quantum systems[3, 4]. A part of this study is now in progress. The obtained results in this study will be reported elsewhere.

The above study was done in collaboration with Hosho Katsura (Gakushuin University, The University of Tokyo) and Ryo Tamura (National Institute for Materials Science).

References

[1] I. Sato, S. Tanaka, K Kurihara, S. Miyashita, and H. Nakagawa: Neurocomputing **121** (2013) 523.

[2] R. Tamura and S. Tanaka: Kinki University Series on Quantum Computing – Vol. 9, "Physics, Mathematics, and All That Quantum Jazz" (World Scientific), in press.

[3] S. Tanaka: Interdisciplinary Information Sciences **19** (2013) 101.

[4] S. Tanaka, R. Tamura, and H. Katsura: Kinki University Series on Quantum Computing – Vol. 9, "Physics, Mathematics, and All That Quantum Jazz" (World Scientific), in press.

[5] T. Kadowaki and H. Nishimori: Phys. Rev. E **58** (1998) 5355.

[6] S. Kirkpatrick, C. D. Gelatt, and M. P. Vecchi: Science **220** (1983) 671.

[7] http://www.dwavesys.com/

Control of Phase Transition Behavior in Lattice Models

Shu TANAKA
Department of Chemistry, The University of Tokyo
7-3-1 Hongo, Bunkyo-ku, Tokyo 113-0033
Yukawa Institute for Theoretical Physics, Kyoto University
Kitashirakawa-Oiwakecho, Sakyo-Ku, Kyoto 606-8502

Investigation of relation between underlying properties in considered models and phase transition behavior is an important topic in statistical physics. In addition, how to control phase transition nature is also an interesting issue. We considered the following two topics in this project[1, 2].

(a) Network growth rule dependence of fractal dimension[1]

It is well-known that conventional percolation transition in static models is continuous phase transition. The critical exponents depending on spatial dimension were investigated. However, there are new type of percolation transitions in dynamical network model. In 2009, Achlioptas et al. proposed a new type of network growth rule and considered percolation transition behavior[3]. They concluded that a discontinuous phase transition occurs using their network growth rule while a continuous phase transition occurs under conventional network growth rules. We constructed a rule that includes the conventional rule and the Achlioptas rule. In our rule, a parameter q which expresses network growth rule is introduced. The relation between the parameter q and geometric properties at the percolation point was investigated using Monte Carlo simulations. In particular, we focused on the fractal dimension of the percolated cluster at the percolation point. As a result, the fractal dimension increases as the network growth rule approaches the Achlioptas rule.

This work was done in collaboration with Ryo Tamura (National Institute for Materials Science).

(b) Relation between the Potts model with invisible states and frustrated spin systems[2]

Recently, frustrated systems where the order parameter is described by the direct product between two groups have been studied. In these systems, unconventional phase transition often occurs. Tamura and Kawashima found that a first-order phase transition with C_3 symmetry breaking occurs in two-dimensional frustrated systems where the order parameter space is $\mathrm{SO}(3) \times C_3$[4, 5]. To explain the phase transition nature qualitatively, the Potts model with invisible states was introduced[6, 7]. By introducing a local parameter in frustrated systems, we considered the relation between the Potts model with invisible states and frustrated spin systems using Monte Carlo simulations. We also estimated the effective interaction of the Potts model with invisible states in frustrated systems using the Curie-Weiss type analysis. This study is closely related to other unconventional phase transition observed in other frustrated systems[8, 9].

This work was done in collaboration with Naoki Kawashima (Institute for Solid State Physics, The University of Tokyo) and Ryo Tamura (National Institute for Materials Sci-

ence).

References

[1] S. Tanaka and R. Tamura: J. Phys. Soc. Jpn. **82** (2013) 053002.

[2] R. Tamura, S. Tanaka, and N. Kawashima: JPS Conf. Proc. **1** (2014) 012125.

[3] D. Achlioptas, R. M. D'Souza, and J. Spencer: Science **323** (2009) 1453.

[4] R. Tamura and N. Kawashima: J. Phys. Soc. Jpn. **77** (2008) 103002.

[5] R. Tamura and N. Kawashima: J. Phys. Soc. Jpn. **80** (2011) 074008.

[6] R. Tamura, S. Tanaka, and N. Kawashima: Prog. Theor. Phys. **124** (2010) 381.

[7] R. Tamura and S. Tanaka: Kinki University Series on Quantum Computing – Vol. 9, "Physics, Mathematics, and All That Quantum Jazz" (World Scientific), in press.

[8] R. Tamura, S. Tanaka, and N. Kawashima: Phys. Rev. B **87** (2013) 214401.

[9] R. Tamura and S. Tanaka: Phys. Rev. E **88** (2013) 052138.

Analysis of Quantum Phase Transitions with Large Finite-Size Effect

Synge Todo
Department of Physics, University of Tokyo, Tokyo 113-0033, Japan

Quantum phase transitions are phase transitions between two different ground states that are triggered by quantum fluctuations at absolute zero temperature. We develop various novel and powerful techniques to tackle various exotic quantum critical phenomena observed in quantum spin systems and performed large-scale and high-precision simulations on the ISSP supercomputer system.

Quantum Monte Carlo simulation with dynamic control of anisotropy [1]

In systems with strong spatial anisotropy, it is often difficult to carry out the conventional finite-size-scaling analysis due to large corrections to scaling. To overcome this difficulty, we develop a novel algorithm where the aspect ratio of the system is optimized dynamically during the Monte Carlo update so that the isotropy is recovered virtually. The optimization is done by the Robbins-Monro machine-learning algorithm. Using this method we can determine the quantum critical points precisely as well as the critical exponents of several physical quantities. We establish that the staggered and columnar dimer models both belong to the conventional $O(3)$ universality class but the optimal aspect ratio of the former model shows the non-monotonic behavior, which comes from the weakly irrelevant cubic term. We also extend out scheme to the quantum critical point with $z > 1$.

Quantum Monte Carlo measurement of local Z_2 Berry phase [2]

We develop a loop cluster algorithm Monte Carlo method for calculating the local Z_2 Berry phase of the quantum spin models. The Berry connection, which is given as the inner product of two ground states with different local twist angles, is expressed as a Monte Carlo average on the worldlines with fixed spin configurations at the imaginary-time boundaries. The "complex weight problem" caused by the local twist is solved by adopting the meron cluster algorithm. We also propose that the gauge-fixed local Berry connection can be an effective tool to estimate precisely the quantum critical point. In addition, we extend the present technique to SU(N) spin models, where N topologically different phases can be distinguished successfully by the local Z_N Berry phase.

BCL: Balance Condition Libray [3]

We have introduced a novel geometric approach that breaks the detailed balance of the Markov chain explicitly (while keeping the (total) balance satisfied) and minimizes (often eliminates) rejection rate. We are now developing the open-source library, BCL (Balance Condition Library), which provides a C++ reference implementation of our algorithm together with the Metropolis-Hasting and Gibbs sampler in Markov Chain Monte Carlo, as well as the API for C, Fortran, Python, etc.

References

[1] S. Yasuda and S. Todo: Phys. Rev. E **88** (2013) 061301(R).

[2] Y. Motoyama and S. Todo: Phys. Rev. E **87** (2013) 021301(R).

[3] http://github.com/cmsi/bcl.

Development and application of a new quantum Monte Carlo Algorithm for lattice bosons

Akiko Masaki

Institute for Solid State Physics,

The University of Tokyo, Kashiwa-no-ha, Kashiwa, Chiba 277-8581

Large-scale computations have the possibility of solving many important remaining problems in quantum many-body physics. Recently high-performance computers, e.g. K-computer, have gained its FLOPS using many cores. Namely the parallelization of algorithms is an effective way to solve these remaining problems. The worm algorithm [1, 2] which has the broad range of applicability is a most efficient global-update algorithm for the world-line quantum Monte Carlo method. However the parallelization of the worm is not straightforward because of the event-driven motions of a worm that is a single-point object in the configuration space.

Based on the directed-loop algorithm [2] we investigated the parallelizable multi-worm algorithm (PMWA) where multiple worms are introduced by an artificial source field η and the configuration space decompose into domains [3]. We estimate physical observables by extrapolation to $\eta = 0$ imit. Introducing multiple-worms requires the different procedure from the conventional worm algorithm so as to satisfy the detailed balance condition. Our algorithm satisfies it. In addition, the propagation of worms between domains and the update of states on domain boundaries are effectively carried out by communications between domains so that the ergodicity is recovered. PMWA is applicable to the soft-core Boson model and the quantum spin model without the negative-sign problem as with the conventional worm algorithm.

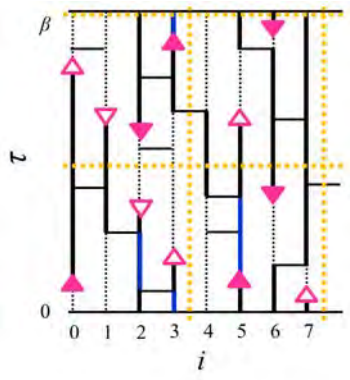

Figure 1: The configuration space of PMWA.

We applied PMWA to the extended Hard-core Bose-Hubbard model on square lattice defined by

$$\mathcal{H} = -t \sum_{\langle i,j \rangle} b_i^\dagger b_j + V \sum_i n_i n_j - \mu \sum_i (n_i + n_j),$$

where b_i ($b_i^\dagger$) is the annihilation (creation) operator at i th site, t is the hopping energy, V

is the nearest-neighbor interaction and μ denotes the chemical potential respectively. Firstly we derived the extrapolation rule to obtain physical quantities at $\eta = 0$. Then we confirmed that extrapolated PMWA result shows the agreement with DLA results.

We accomplished simulations of up to the size of $L \times L \times \beta = 10{,}240 \times 10{,}240 \times 16$ using 3,200 processing cores, where L is the number of the lattice site per spatial direction and β is the inverse of temperature. This size is extremely larger than the workable size of the conventional worm algorithm with single processor. We measured the standard error as a function of the number of domains N to estimate the performance of the algorithm. As a result, we found a weak effect of N for the relaxation time by the simulation with fixed number of the Monte Carlo steps. Moreover, when we compare with the DLA results, PMWA results is more accurate than DLA in fixed wall-clock time with $N > 8$.

References

[1] N. Prokof'ev, B. Svistunov and I. Tupitsyn, Sov. Phys. JETP **87**, 310 (1998).

[2] O. F. Syljuasen and A. W. Sandvik, Phys. Rev. E **66**, 046701 (2012).

[3] Akiko Masaki-Kato, Takafumi Suzuki, Kenji Harada, Synge Todo, Naoki Kawashima, Phys. Rev. Lett. **112**, 140603 (2014).

Morphology of Lipid Vesicles: effects of confinement and genus

Ai Sakashita and Hiroshi Noguchi
Institute for Solid State Physics, University of Tokyo
Kashiwa-no-ha, Kashiwa, Chiba 277-8581

Cell organelles such as Golgi apparatus, endoplasmic reticulum, and mitochondria have very complicated shapes; Among these organelles, mitochondria have a specific feature, *i.e.*, it consists of two bilayer membranes. The nuclear membrane and endoplasmic reticulum are connected and together form complicated shapes. The nucleus is wrapped by two bilayer membranes connected by many lipidic pores. Thus, its shape is considered as a stomatocyte of a high-genus vesicle connected with a tubular network. We focus on geometrical constraints and investigated a vesicle confined in a spherical vesicle [1] and non-zero genus vesicles [2] using the dynamically triangulated surface model.

Figure 1 shows examples of vesicle shapes confined in a sphere [1]. Reduced volume $v_{\rm r}$, area difference Δa, and the volume ratio $v_{\rm con}$ of the inner vesicle to the outer sphere are three parameters to determine the vesicle shape. Under a strong confinement, an additional bud is formed in a stomatocyte in order to fill the volume between the vesicles. In the limit $v_{\rm r} \to 1$, this double stomatycote is the most stable shape. At $v_{\rm r} \simeq 0.9$, other novel shapes can be found in equilibrium. As Δa increases, a stomatocyte transforms into a vesicle with a planar slit and subsequently forms a doublet. As negative values of Δa, the inner bud forms a tubular or discocyte shape. This discocyte bud resembles the crista structures in mitochondria.

For genus-1 toroidal vesicles, we obtained the free-energy profiles using a generalized ensemble Monte Carlo method [2]. At large $v_{\rm r}$, obtained vesicle shapes agree with the previous theoretical results for axisymmetric shapes: double-necked stomatocyte, discoidal toroid, and circular toroid. However, for small $v_{\rm r}$, it is found that a non-axisymmetric discoidal toroid and handled discocyte exist in thermal equilibrium in the parameter range, in which the previous theory predicts axisymmetric shapes. The entropy caused by shape fluctuations slightly modifies the stability of the vesicle shapes.

We have also observed a liposome confined in a spherical liposome and genus-1 and 2 liposomes using a fast confocal laser microscopy. Our simulation results reproduce shape transformations observed in our experiments well.

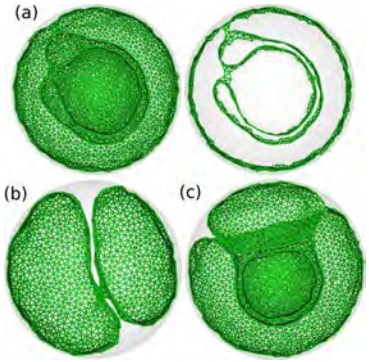

Figure 1: Snapshots of a vesicle confined in a sphere. (a) Double stomatocyte. (b) Doublet. (c) Triplet.

References

[1] A. Sakashita, M. Imai and H. Noguchi: Phys. Rev. E **89** (2014) 040701(R).

[2] A. Sakashita, M. Imai and H. Noguchi: arXiv:1405.3076 [cond-mat.soft].

Efficient sampling simulation of the soft modes significantly contribute to protein properties

Akio KITAO

Institute of Molecular and Cellular Biosciences, University of Tokyo

Biological processes are often associated with significant conformational changes of biomolecules, which are relevant to their functions. The free energy landscape (FEL) along appropriate reaction coordinates provides us essential information to characterize the mechanism of conformational changes and functions. In this sense, efficient and accurate sampling of the conformational space to calculate the FEL is a major topic for molecular dynamics (MD). Let $\boldsymbol{\theta}(\boldsymbol{x})$ be collective variables (CVs) defined as functions of $\boldsymbol{x}$, where $\boldsymbol{x}$ is the Cartesian coordinate of atom. Supposing that $\boldsymbol{z}$ is a particular realization of these CVs, the FEL $F(\boldsymbol{z})$ is defined as:

$$F(\boldsymbol{z}) = -\frac{1}{\beta}\ln\left\{Q^{-1}\int e^{-\beta V(\boldsymbol{x})}\prod_{l=1}^{L}\delta(\theta_l(\boldsymbol{x}) - z_l)\,d\boldsymbol{x}\right\}, \quad (1)$$

where $Q = \int e^{-\beta V(\boldsymbol{x})}d\boldsymbol{x}$, L is the number of CVs, $V(\boldsymbol{x})$ is the potential energy, δ is Dirac's delta function, and $\beta = 1/k_B T$, where k_B is the Boltzmann constant and T is the temperature. If $\boldsymbol{\theta}(\boldsymbol{x})$ can be regard as appropriate reaction coordinate, the goal is to calculate $F(\boldsymbol{z})$.

However, sampling of large conformational space within a limited simulation time is still a challenging problem, because of complexity of FEL and the large gap between simulation time step and time scale of biological process. In order to tackle the difficulty, we proposed a new efficient conformational sampling method, Multi-scale Sampling using Temperature Accelerated and Replica-exchange MD (MuSTAR MD) [1].

MuSTAR MD is an extension of temperature accelerated MD (TAMD) and can also be considered as a variation of replica-exchange MD (REMD). In the MuSTAR MD simulation, each replica contains an all-atom model, at least one coarse-grained model, and a CVs that interacts with the other models through coupling terms. The coarse-grained model is introduced to drive efficient sampling of large conformational space and the all-atom model can serve to conduct accurate conformational sampling. Equations of motion for MuSTAR MD consists of Cartesian spaces and CV space,

$$\begin{aligned} m_i^\alpha \ddot{\boldsymbol{x}}_i^\alpha &= -\frac{\partial V^\alpha(\boldsymbol{x}^\alpha)}{\partial \boldsymbol{x}_i^\alpha} - \frac{\partial W^\alpha(\boldsymbol{x}^\alpha, \boldsymbol{z})}{\partial \boldsymbol{x}_i^\alpha} \\ &\quad + (\mathrm{thr}, \beta^\alpha) \\ &= -\frac{\partial U^\alpha(\boldsymbol{x}^\alpha, \boldsymbol{z})}{\partial \boldsymbol{x}_i^\alpha} \\ &\quad + (\mathrm{thr}, \beta^\alpha), \end{aligned} \quad (2)$$

$$m^z \ddot{z}_l = -\sum_{\alpha}^{N}\frac{\partial W^\alpha(\boldsymbol{x}^\alpha, \boldsymbol{z})}{\partial z_l} + (thr, \beta^z). \quad (3)$$

where $\boldsymbol{x}_i^\alpha$ and $V^\alpha(\boldsymbol{x}^\alpha)$ are the position vector in Cartesian coordinate for the i-th atom of model α and potential energy functions in each model, respectively, and $W^\alpha(\boldsymbol{x}^\alpha, \boldsymbol{z})$ is the coupling terms

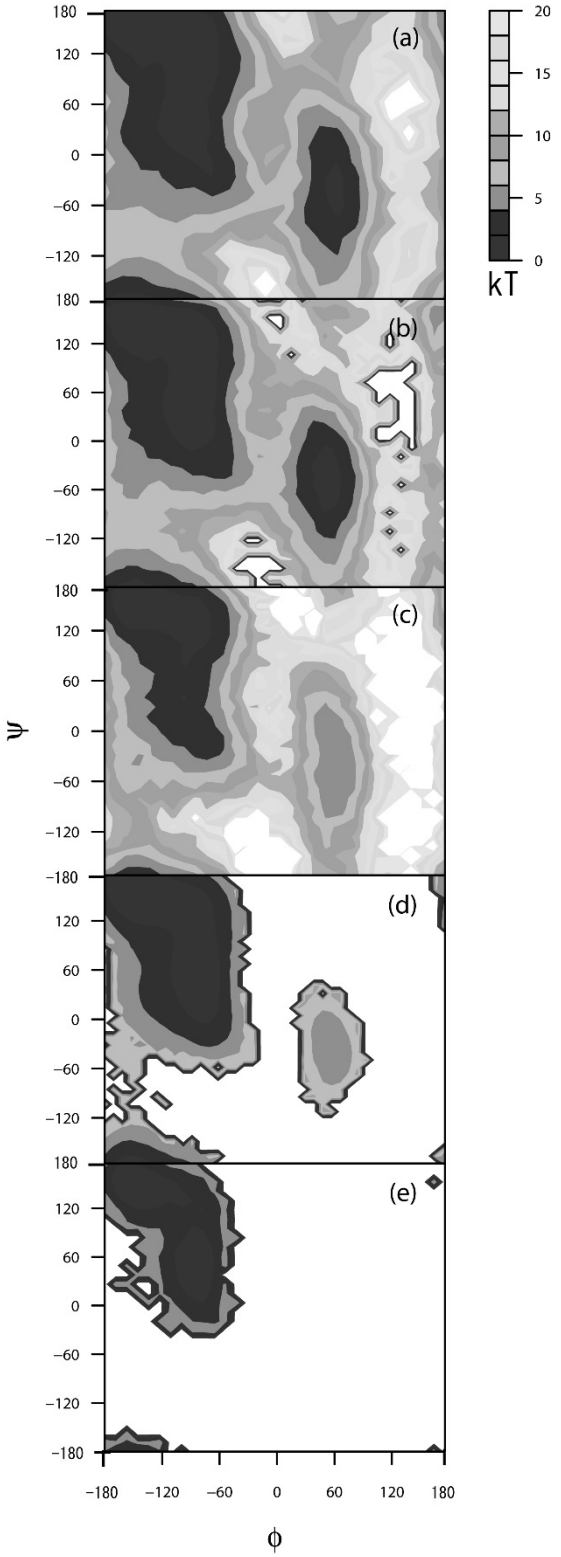

Figure FEL of Ala-dipeptide in vacuum using the AMBER force field parm99SB with respect to backbone dihedral angles ϕ and ψ. The results from (a) MuSTAR MD (10 ns×8 replicas), (b) TAMD (80ns),(c) REMD (10 ns×8 replicas), (d) REUS (5nsx16), (e) CMD (80 ns).

between model α and the CV system. α can represent either fine-grained or coarse-grained model. The thermostat parameters are related to temperatures as $\beta^{\alpha} = 1/k_B T^{\alpha}$ and $\beta^{z} = 1/k_B T^{z}$. The coupling terms are defined as:

$$W^{\alpha}(\boldsymbol{x}^{\alpha}, \boldsymbol{z}) = \frac{K^{\alpha}}{2} \sum_{l=1}^{L} (\theta_l(\boldsymbol{x}^{\alpha}) - z_l)^2, \qquad (4)$$

$$U^{\alpha}(\boldsymbol{x}^{\alpha}, \boldsymbol{z}) = V^{\alpha}(\boldsymbol{x}^{\alpha}) + W^{\alpha}(\boldsymbol{x}^{\alpha}, \boldsymbol{z}), \qquad (5)$$

where K^{α} is the coupling-strength between model α and the CV system. The parameters are exchanged between neighboring replicas in some interval obeying the Metropolis method.

We applied MuSTAR MD for typical test cases, Ala-dipeptide in vacuum. Figures (a)-(e) are FELs at 300 K calculated from the results of MuSTAR MD, TAMD, REMD, replica-exchange umbrella sampling (REUS) and conventional MD (CMD), respectively. The sampled conformational space obtained from same simulation time is broader in the order of MuSTAR MD>TAMD> REMD>REUS>CMD. In addition, among five methods examined, MuSTAR MD showed the closest results to that obtained from long-time umbrella sampling simulation.

MuSTAR MD shows the high performance in sampling efficiency and accuracy compared to established enhanced sampling methods. The advantageous features of MuSTAR MD are: 1) High temperature of the CV system enhances conformational sampling. 2) Multiple coarse-grained models can be introduced to guide the system to move to multiple structures. 3) Applications to larger system are expected to be relatively easy. The proposed methods are expected to be applied to the further computational studies of biological phenomena including large conformational change, such as allosteric transition.

References

[1] Y. Yamamori and A. Kitao, J. Chem. Phys., **139**, 145105(2014).

Data Analyses and Visualization of Bubbles

Hiroshi WATANABE
Institute for Solid State Physics, University of Tokyo
Kashiwa-no-ha, Kashiwa, Chiba 277-8581

A rapid increase in computational power allows us to simulate huge scale systems. However, as the size of simulation increases, the amount of data also increases and becomes quite huge which is difficult to process for further analysis. Therefore, some device is required to process such huge data. Visualization of data is also important. Appropriate visualization not only allows us to understand physical phenomena in an intuitive way, but may serve as a trigger of new discoveries. However, there is no general guide of visualization and we have to appropriate method according to problems. In this manuscript, we report on some devices to process huge data and their visualization.

We perform molecular dynamics simulations of multi-bubble nuclei involving up to 730 million particles on K-computer. If we store all data of position of particles, it requires 17GB per frame. Since one run involves about 1000 frames, the total amount of data could be 17TB per run, which is not impossible but unrealistic. Therefore, some kinds of compression are compression to store data for further analysis. While it is preferable to reduce the total amount of data, the important information should not be lost. We therefore divide the system into small subcells and count the number of particles in each subcell and store it as an integer (data type `unsigned char` in C language) instead of storing the local density with floating-point variables. The size of the subcells are determined so that the number of particles will not exceed 255, which is the maximum value of `unsigned char`. The number of subcells of the largest run is 32768000, *i.e.*, 32.7MB per fame. Therefore, we have succeeded to compress the data by 500 times. Additionally, we do not have to care about the byte order, since we use `unsigned char` which is free from the byte-order problem.

The picture is a visualization of bubbles using our data format. We define a subcell to be in the *gas state* when its density is less than some threshold, and identify the bubbles using the site-percolation criterion on the simple cubic lattice [1]. After identifying bubbles, we compute a center of inertia and volume of each bubble and draw bubble as sphere. From the information of the spheres, the image is produced by POV-Ray [2]

References

[1] H. Watanabe, M. Suzuki, and N. Ito: Comput. Phys. Commun. **184** (2013) 2775.

[2] ⟨http://www.povray.org⟩

Theoretical Study on Magnetic Refrigeration using Ising Model

Ryo TAMURA
International Center for Young Scientists, National Institute for Materials Science
1-2-1, Sengen, Tsukuba-city, Ibaraki, 305-0047

Magnetic refrigeration is a cooling technology which has attracted attention in energy science as an alternative to gas refrigeration. Magnetic refrigeration uses magnetocaloric effect which is a cross correlated phenomenon between the heat and the magnetic degree of freedom. In most experimental studies, magnetic refrigeration efficiency was estimated by the entropy change when the magnetic field is changed from 0 to finite H in isothermal process. Magnetic materials with large entropy change are regarded as a good material since these absorb large amount of heat. From this point, ferromagnets near the Curie temperature is a good magnetic refrigeration material. Experimental studies on magnetic refrigeration have been aggressively done throughout the world.

Our purpose is to propose a method that utilizes the underlying magnetic refrigeration effect in magnetic materials including nonferromagnets. We considered the Ising model on a cubic lattice:

$$\mathcal{H} = -J_{ab} \sum_{\langle i,j \rangle_{ab}} s_i s_j - J_c \sum_{\langle i,j \rangle_c} s_i s_j - H \sum_i s_i,$$
$$s_i = \pm \frac{1}{2},$$

where the first and second terms represent nearest-neighbor interactions on ab-plane and along c-axis, respectively, and the third term denotes the Zeeman term.

We considered four types of signs of interactions: (a) $J_{ab} > 0, J_c > 0$; (b) $J_{ab} < 0, J_c > 0$; (c) $J_{ab} > 0, J_c < 0$; (d) $J_{ab} < 0, J_c < 0$. The ground states of each case are (a) Ferromagnetic state (the corresponding wave vector is (000)), (b) A-type antiferromagnetic state (the corresponding wave vector is $(\pi\pi 0)$), (c) C-type antiferromagnetic state (the corresponding wave vector is (00π)), and (d) G-type antiferromagnetic state (the corresponding wave vector is $(\pi\pi\pi)$). We calculated the magnetic entropy as a function of temperature and magnetic field of this model whose linear dimension is up to $L = 16$ using the Wang-Landau method[2]. The Wang-Landau method can directly calculate the density of states and the absolute value of magnetic entropy without integrating the specific heat. In ferromagnetic phase and paramagnetic phase, the magnetic entropy decreases as the magnetic field increases at fixed temperature. However, the magnetic entropy as a function of magnetic field at fixed temperature T has a peak at finite magnetic field $H_{\max}(T)$ in antiferromagnetic phases. From the obtained results, we proposed a new protocol to obtain the maximum magnetic refrigeration efficiency in the isothermal process: *The magnetic field should be changed from $H_{\max}(T)$ to H.* This method can be applied not only antiferromagnets but also general types of magnetic materials. Furthermore, the proposed protocol is the same as the conventional one for ferromagnets and paramagnets.

This work was done in collaboration with Takahisa Ohno (NIMS) and Hideaki Kitazawa (NIMS).

References

[1] R. Tamura, T. Ohno, and H. Kitazawa: Appl. Phys. Lett. **104** (2014) 052415. [**This topic was reported in Press Release in NIMS (March 10, 2014), MyNavi News (March 12, 2014), The Chemical Daily (March 19, 2014), The Science News (March 28, 2014).**]

[2] F. Wang and D. P. Landau: Phys. Rev. Lett. **86** (2001) 2050.

Investigation of Phase Transitions and Their Microscopic Mechanisms in Frustrated Spin Systems

Ryo TAMURA
International Center for Young Scientists, National Institute for Materials Science
1-2-1, Sengen, Tsukuba-city, Ibaraki, 305-0047

Geometrically frustrated spin systems often exhibit unconventional phase transitions and dynamic behaviors, which are not observed in unfrustrated spin systems. We investigated phase transition nature in two geometrically frustrated spin systems[1, 2].

– **Simultaneous occurrence of Z_2 vortex dissociation and second-order phase transition**[1]

We considered the Heisenberg model with the nearest-neighbor and the third nearest-neighbor interactions on a distorted triangular lattice. We focused on the case that the order parameter space is described by SO(3) × Z_2. SO(3) and Z_2 correspond to global rotation symmetry of spins and lattice rotation symmetry, respectively. The long-range order of spins at finite temperatures is prohibited by the Mermin-Wagner theorem[3]. Instead, the Z_2 vortex dissociation related to SO(3) symmetry occurs at finite temperature, which was first pointed out by Kawamura and Miyashita[4]. We considered finite-temperature properties of the model using Monte Carlo simulations. A second-order phase transition with Z_2 symmetry breaking was observed. In addition, it was found that Z_2 vortex dissociation occurs at the second-order phase transition point. By the finite-size scaling, we concluded that the second-order phase transition belongs to the two-dimensional Ising universality class, which suggests that the Z_2 vortex dissociation does not affect the critical phenomena. To our knowledge, this is the first example to exhibit Z_2 vortex dissociation at the critical point.

This work was done collaboration with Shu Tanaka (The University of Tokyo, Kyoto University) and Naoki Kawashima (Institute for Solid State Physics, The University of Tokyo).

– **Strange behavior of latent heat in a geometrically frustrated spin system**[2]

We studied phase transition behavior of the Heisenberg model with the nearest-neighbor and the third nearest-neighbor interactions on a stacked triangular lattice. This is three-dimensional version of the studies in Refs.[5, 6, 7]. We focused on the case that the order parameter space is represented by SO(3)×C_3. SO(3) and C_3 correspond to global rotation symmetry of spins and lattice rotation symmetry, respectively, which is similar with two-dimensional case as described before. Temperature dependence of each order parameter was obtained by Monte Carlo simulations, which indicates that the first-order phase transition with SO(3)×C_3 symmetry breaking occurs at finite temperature. We also considered interlayer interaction dependence of transition temperature and latent heat. As the interlayer interaction increases, the transition temperature increases but the latent heat decreases. The latter behavior is not observed in usual unfrustrated spin systems such as the ferromagnetic Potts model.

This work was done collaboration with Shu Tanaka (The University of Tokyo, Kyoto University).

References

[1] R. Tamura, S. Tanaka, and N. Kawashima: Phys. Rev. B **87** (2013) 214401. [**Selected as Physical Review B Kaleidoscope**]

[2] R. Tamura and S. Tanaka: Phys. Rev. E **88** (2013) 052138.

[3] N. D. Mermin and H. Wagner: Phys. Rev. Lett. **17** (1966) 1133.

[4] H. Kawamura and S. Miyashita: J. Phys. Soc. Jpn. **53** (1984) 9, *ibid.* **53** (1984) 4138.

[5] R. Tamura and N. Kawashima: J. Phys. Soc. Jpn. **77** (2008) 103002.

[6] R. Tamura and N. Kawashima: J. Phys. Soc. Jpn. **80** (2011) 074008.

[7] R. Tamura, S. Tanaka, and N. Kawashima: JPS Conf. Proc. **1** (2014) 012125.

Multiscale Simulation for Soft Matter:
Sol-Gel Transition in Wormlike Micellar Solution during Flow

Takahiro Murashima

Department of Physics,Tohoku University,

Aramaki-Aza-Aoba, Aoba-Ward, Sendai, Miyagi 980-8578

Surfactant is an important material for our daily life. Surfactants spontaneously aggregate in a solvent because it consists of a hydrophilic head group and a hydrophobic tail group and shows a variety of complex structure: sphere, cylinder, lamellar, cubic and sponge structures. Self-assembled surfactants in a solvent make a curved membrane with a hydrophilic and hydrophobic layer. According to the concentration of surfactants, the size of the membrane changes, and the structure of micelle is selected in order to minimize the elastic curvature energy. A particle-field hybrid method implementing the kinetic Monte-Carlo method taking account of the Helfrich's bending energy of a membrane with Langevin thermostat [1] has succeeded in describing the sol-gel phase diagram of dilute micellar solution in equilibrium and a shear-induced instability which is found as an negative slope in shear stress. This instability comes from the breakup process of micellar branches and will lead to shear banding [1]. However, it is tough to simulate a macroscopic flow behavior such as shear banding in a particle-field hybrid method because a quite large number of degrees of freedom are needed to simulate a fluid dynamic behavior.

We have developed multi-scale simulation technique bridging the macroscopic fluid dynamics and microscopic (mesoscopic) molecular dynamics to simulate a fluid dynamic behavior of entangled polymer melt [2, 3]. Applying this method to the particle-field hybrid method, we can simulate a fluid dynamic behavior of the micellar solution [4, 5]. In the multi-scale simulation, the microscopic simulator is used as a constitutive equation in general fluid dynamic simulation. Applying a shear to the microscopic simulator, the stress tensor is obtained according to the structure of micelles. The updated stress tensor drives the flow to balance the stress tensors among the fluid elements. The multi-scale simulation alternately updates mactorsopic flow field and microscopic micellar structure.

We have investigated a channel flow of the micellar solution. The macroscopic fluid system is divided into Ne fluid elements and each fluid element has Ns simulators. The total number of the microscopic simulators in this system is $Nt = Ne \times Ns$. When the number of

CPUs is equal to *Nt* or the integral multiple of *Nt*, the multi-scale simulation is most efficient. On System B (SGI Altix ICE 8400EX) with 1024 cores, the weak scaling parallel efficiency of our multi-scale simulation is almost 100 % as shown in Fig 1 because the microscopic simulators are independent of the others during a time-interval of a fluid dynamic simulation and the time of communication is negligibly small in a total computation time.

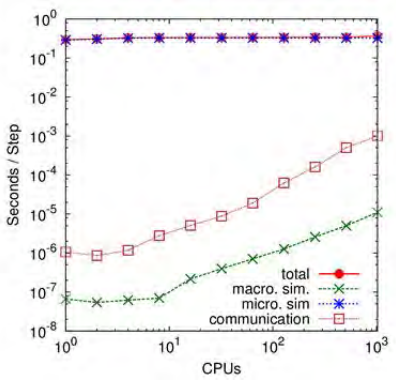

Fig:1 Weak scaling parallel efficiency

To decrease the noise coming from the low number of static samples (the number of molecules in a simulation box), we need more than 100 simulation box per one fluid element. To resolve the macroscopic fluid dynamics in a channel, we need to divide a channel into more than 20 fluid elements. Thus, we select *Ne* = 24 and *Ns* = 128, namely *Nt* = 3,072. Each simulation box has 3,000 particles which represent spherical micelles and then each fluid element is described by using 384,000 particles. On System B with 1024 cores, this simulation takes 0.75 sec per unit time interval. The noise in stress tensor is sufficiently small and we can investigate the time evolution of the multiscale simulation of micellar solution. Initial condition of the micellar solution is sol state where the spherical micelles are randomly distributed. The micelles spontaneously aggregate and make wormlike micelles during a flow in a channel. The growth of wormlike micelles results in a gel state. This situation mimics a real process where miceller solution starts to flow immediately after surfactants are put into water. Even if we apply high pressure difference between upstream and downstream, this initial transition from sol to gel is observed. The velocity gradient increases near the wall. The state of micellar solution near the wall changes from gel to sol under the high velocity gradient field. The sol region develops from the vicinity of the wall to the bulk. The transition from gel to sol in the vicinity of the wall is clearly observed as increasing the pressure difference between upstream and downstream.

References

[1] M. Toda, T. Kawakatsu, AIP Conf. Proc. **1518**, (2013) 419-423.

[2] T. Murashima, T. Taniguchi, EPL, 96 (2011) 18002.

[3] T. Murashima, S. Yasuda, T. Taniguchi, R. Yamamoto, JPSJ, 82 (2013) 012001.

[4] T. Murashima, M. Toda, T. Kawakatsu, AIP Conf. Proc. 1518, (2013) 436-439.

[5] T. Murashima, M. Toda, T. Kawakatsu, NIC Series, 46 (2013) 187-192.

Numerical Study of Coulomb Glass

Takamichi TERAO

Department of Electrical, Electronic and Computer Engineering,

Gifu University, Yanagido 1-1, Gifu 501-1193

Electronic states in Coulomb glass, in which the disorder and many-body electron-electron interaction are incorporated, have been extensively studied during the last few decades. The properties of compensated doped semiconductors, ultrathin films, and granular metals are well described by these Coulomb-glass models. Most of the past numerical studies have been devoted to examining the properties of Coulomb glasses in equilibrium, and they have shown the existence of a Coulomb gap at the Fermi level. Recent experiments have demonstrated the non-equilibrium nature of Coulomb glasses, such as logarithmic relation, aging, and memory effects below some critical temperature.

In this study, kinetic Monte Carlo simulations of disordered thin films, in which strongly interacting electrons hopping between randomly distributed sites that correspond to the localization centers of the single-electron wave functions, have been performed [1,2]. At first, the two-time autocorrelation function $C(t,t_W)$ has been calculated to clarify the non-equilibrium nature of interacting electrons in disordered thin films. The waiting time t_W is the time elapsed since the quenching from an infinite temperature. The function $C(t,t_W)$ is the overlap of the charge configurations at times $t+t_W$ and t_W. We have confirmed aging phenomena in the autocorrelation function $C(t,t_W)$ (Figure 1).

In addition, the temperature dependence of the mean square displacement (MSD) of electrons has been investigated to clarify the microscopic dynamics of electrons, and a crossover from diffusive to subdiffusive behavior has been observed. These results imply that there is a characteristic temperature T_c in this system, and the dynamical behavior such as the relaxation and diffusive motion of electrons changes at $T \approx T_c$, which reflects the glassy behavior of this system with lower temperature regime.

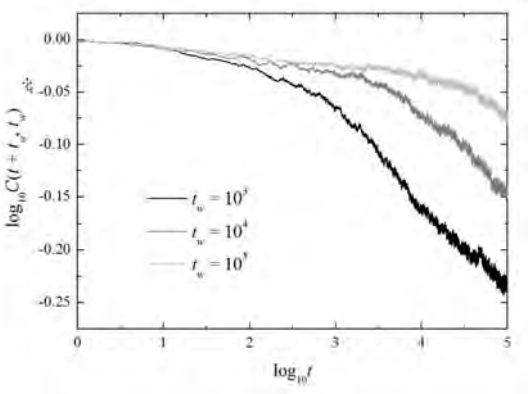

Fig. 1: Two-time autocorrelation function $C(t,t_W)$

References

[1] T. Terao, A. Kono, and W. Takahashi: AIP conference proceedings **1518**, (2013) 320.

[2] T. Terao: Philos. Mag. **89**, (2009) 405.

Physical properties of low-dimensional electron systems created on solid surfaces and their control

Takeshi INAOKA
Department of Physics and Earth Sciences, Faculty of Science, University of the Ryukyus, 1 Senbaru, Nishihara, Okinawa 903-0213

This academic year, we investigated collective excitations of two-dimensional electron systems with ultralow density and the strain effect on the band structure of bulk silicon (Si) and germanium (Ge). The latter investigation of the strain effect forms a basis to understand the strain effect on subbands formed at surfaces or interfaces.

(1) Exchange-correlation and temperature effects on plasmons in stronglycorrelated two-dimensional electron systems [1]

In two-dimensional (2D) electron systems with ultralow density, electrons are strongly correlated, which has striking exchange-correlation (XC) effects on the 2D plasmons (PLs) in these systems. By means of the finite-temperature local-field correction, we examined the 2DPLs in a density-parameter range of $9.1 \leq r_s \leq 21.8$ and a temperature range of $0.5 \leq T/T_F \leq 8.4$ (normalized by Fermi temperature T_F). We analyzed the PL dispersions that were observed from single quantum wells by Raman spectroscopy. With increasing wave number q, the XC effects start to operate to lower the PL energy strikingly. This operation is more remarkable at lower electron densities. Even in our strongly correlated and extremely nondegenerate 2D electron systems, the size of the XC holes can be well normalized by inverse Fermi wave number k_F^{-1}. From comparison with the experiment, the finite-temperature localfield correction (Singwi-Tosi-Land- Sjölander approximation) is expected to describe the PLs quantitatively in a smaller q range of $q \lesssim k_F$, but in a larger q range of $q \gtrsim k_F$, this correction begins to overestimate the XC effect. With an increase in temperature, the PL dispersion curve goes up strikingly in a larger q range. This remarkable T dependence can be ascribed largely to the T dependence of the constituent electronic transitions of the PLs through the Fermi-Dirac distribution function. We performed the above calculation on the system A.

(2) Internal-strain effect on the valence band of strained Si [2]

Now that performance enhancement of Si devices due to downsizing begins to show its limitations, one promising solution is to change the band structure by applying strain in order to realize higher mobility. By means of the local density-functional method including the spin-orbit interaction, we examined the effect of internal strain, namely, relative atom displacement of two atoms in the crystal unit cell on the valence band of strained Si. We analyzed the [111] ([110]) band dispersion for [111] ([110]) uniaxial compression and (111) ((110)) biaxial tensility, because the hole effective mass m^* becomes conspicuously small in the [111] ([110]) direction for these strain types [3]. Under the practical condition of no normal stress, uniaxial compression (biaxial tensility) entails additional normal tensility (compression) and internal strain. We achieved the total-energy minimum with a change in both normal and internal strain. The above uniaxial compression or biaxial tensility lifts degeneracy of the upper two valence bands at the Γ point, and the band with a conspicuously small $m*$ value projects above the other two around the Γ point. With increasing internal strain, the energy separation between the

highest and second-highest bands, E_1 E_2, becomes dramatically larger, and the band with the effective-mass ratio $m^*/m_e = 0.10$ 0.11 extends remarkably down to a lower energy region, until it crosses or gets admixed with the second-highest band. This holds true to all the strain types and strain orientations considered here. We found that this band variation due to internal strain is strongly correlated with the change in the specific bond angles in the tetrahedral unit cell. Some angles are closely related to the highest valence band which includes stronger coupling in the [111] or [110] direction, namely, which has stronger dispersion in this direction, while other angles are strongly correlated with the second-highest valence band which involves stronger coupling in the (111) or (110) plane, namely, which has weaker dispersion in the [111] or [110] direction. The change in these two types of bond angles due to internal strain can reasonably explain the conspicuous growth in E1-E2. Details are given in [2]. To do the above calculation, we used the program package 'ABINIT' [4,5] on the system B.

(3) Indirect-to-direct band gap transition of Ge induced by tensile strain [6]

Tensile strain is reported to induce an indirect-to-direct band gap transition of Ge where the conduction-band bottom shifts from the L point to the Γ point. This transition producing the direct gap enhances photoabsorption intensity in a lower energy region, and this strained Ge becomes a good candidate for solar-cell materials. According to first-principles calculations, uniaxial tensility in the [111] direction induces the transition at 4.2% strain [7], and biaxial tensility in the (001) plane does at 2.0% strain [8]. In [8], they evaluated the decreasing rate of the Land Γ-point energies with small strain coefficient for uniaxial and biaxial tensility with various orientations, predicted that biaxial tensility in the (001) plane induces the transition at the smallest strain, and estimated the critical strain as 2.0% for this strain type. These two studies take no account of internal strain. We employed a hybrid density-functional method (HSE06) where exchange terms due to the Hartree-Fock approximation are incorporated into those in the local localdensity approximation (LDA) and which remarkably improves underestimation of the band gap in the LDA. Taking the internal strain into consideration, we analyzed the transition for uniaxial and biaxial tensility with various orientations. According to our evaluation for room temperature, uniaxial tensility in the [001] and [111] directions gives rise to the transition at 4.2% and 3.7% strain, respectively. Biaxial tensility in the (001) and (110) planes causes the transition at 1.5% and 2.3% strain, respectively. No transition occurs for uniaxial tensility in the [110] direction and biaxial tensility in the (111) plane. Corresponding to [8], biaxial tensility in the (001) plane induces the transition at the smallest strain, though our critical strain coefficient is somewhat smaller that that in [8]. To carry out the above calculation, we used the program package 'Vienna Ab initio Simulation Package' (VASP) [9,10] on the system B.

References

[1] T Inaoka, Y. Sugiyama, and K. Sato: Phys. Status Solidi B (2014) published online, Doi: 10.1002/pssb.201350147. (11pages).
[2] T Inaoka, S. Yanagisawa, and Y. Kadekawa: J. Appl. Phys. **115** (2014) 063702 (14 pages).
[3] T. Inaoka, Y. Kinjyo, S. Yanagisawa, and K. Tomori: J. Appl. Phys. **113** (2013) 183718 (13 pages).
[4] X. Gonze et al., Z. Kristallogr. **220** (2005) 558-562.
[5] X. Gonze et al., Comput. Phys. Commun. **180** (2009) 2582-2615.
[6] T. Inaoka, T. Furukawa, R. Toma, and S. Yanagisawa: in preparation.
[7] F. Zhang, V. H. Crespi, and P. Zhang, Phys. Rev. Lett. **102** (2009) 156401 (4 pages).
[8] Y. Hoshina, K. Iwasaki, A. Yamada, and M. Konagai: Jpn. J. Appl. Phys. **48** (2009) 04C125 (6 pages).
[9] G. Kresse and J. Hafner. Phys. Rev. B **47** (1993) 558-561.
[10] G. Kresse and J. Furthmüller. Comput. Mat. Sci. **6** (1996) 15-50.

Ground-State Phase Diagram of a Spin-1/2 Anisotropic Rung-Alternating Ladder

Takashi Tonegawa

Professor Emeritus, Kobe University

With the help of some physical considerations, we [1] have numerically investigated the ground-state phase diagram of a spin-1/2 anisotropic rung-alternating ladder, which is described by the Hamiltonian,

$$\begin{aligned}\mathcal{H} = J_{\rm l} \sum_{l=1}^{L} \{\vec{S}_{l,a} \cdot \vec{S}_{l+1,a} + \vec{S}_{l,b} \cdot \vec{S}_{l+1,b}\} \\ + J_{\rm r} \sum_{l=1}^{L/2} [\vec{S}_{2l-1,a}, \vec{S}_{2l-1,b}]_{\delta} \\ + J'_{\rm r} \sum_{l=1}^{L/2} [\vec{S}_{2l,a}, \vec{S}_{2l,b}]_{\delta}\end{aligned} \quad (1)$$

with

$$\begin{aligned}&[\vec{S}_{l,a}, \vec{S}_{l,b}]_{\delta} \\ &\equiv \delta_{\rm r}^{xy}(S_{l,a}^{x}S_{l,b}^{x}+S_{l,a}^{y}S_{l,b}^{y}) + \delta_{\rm r}^{z}S_{l,a}^{z}S_{l,b}^{z}.\end{aligned} \quad (2)$$

Here, $\vec{S}_{l,\lambda}$ ($\lambda = a$ or b) is the spin-1/2 operator at the l-th site of the λ leg; L is the number of spins in each leg, being assumed to be even; $J_{\rm l}$ is the magnitude of the isotropic leg interaction; $J_{\rm r}$ and $J'_{\rm r}$ are those of the two kinds of anisotropic rung interactions which are alternating; $\delta_{\rm r}^{xy}$ and $\delta_{\rm r}^{z}$ are the XXZ-type anisotropy parameters of the rung interactions. This system has a frustration when $J_{\rm r}J'_{\rm r} < 0$ irrespective of the sign of $J_{\rm l}$. In Fig.1 the present spin-1/2 rung-alternating ladder is schematically sketched. For simplicity, we study in this report only the case where $J_{\rm l} = 0.2$, $J_{\rm r} = -1$ and $|J'_{\rm r}| \leq 1$. As regards the anisotropy of the rung interactions, however, we treat both the case where it is of the Ising-type ($\delta_{\rm r}^{z} = 1$ and $0 \leq \delta_{\rm r}^{x,y} \leq 1$) and the case where it is of the XY-type ($\delta_{\rm r}^{x,y} = 1$ and $0 \leq \delta_{\rm r}^{z} \leq 1$).

When $J'_{\rm r} = -1$, by performing the degenerate perturbation calculations, we can map the present spin-1/2 ladder onto the one-dimensional spin-1 chain governed by the effective Hamiltonian,

$$\mathcal{H}_{\rm eff,1} = \frac{J_{\rm l}}{2}\Big\{\sum_{l=1}^{L} \vec{T}_l \cdot \vec{T}_{l+1} + D\sum_{l=1}^{L} (T_l^{z})^2\Big\} \quad (3)$$

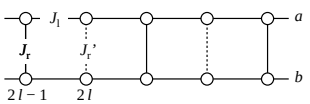

Figure 1: Sketch of the present spin-1/2 rung-alternating ladder.

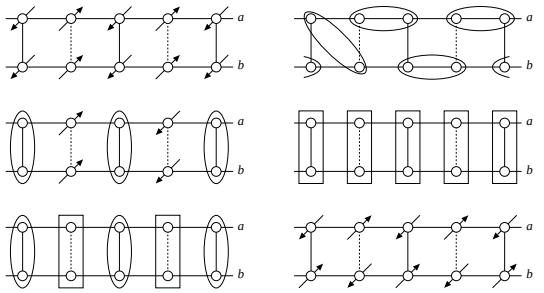

Figure 2: Schematic representations of various phases appearing in the ground-state phase diagrams of the present spin-1/2 rung-alternating ladder; the antiferromagnetic stripe Néel (top left), Haldane (top right), 'ferromagnetic'-'singlet dimer' (central left), triplet dimer (central right), 'triplet dimer'-'singlet dimer' (bottom left) and Néel (bottom right) phases. Ellipses show the singlet dimer pairs and rectangles the triplet dimer pairs.

with

$$D = (\delta_{\rm r}^{xy} - \delta_{\rm r}^{z})/J_{\rm l}\,, \quad (4)$$

where $\vec{T}_l$ is the pseudo $S = 1$ operator at the l-th site. Chen *et al.* [2] have already determined the ground-state phase diagram of this spin-1 chain, and showed that as the value of D increases, the phase transition from the Néel phase to the Haldane phase takes place at $D \sim -0.4$ and that from the Haldane phase to the large-D phase at $D \sim 1.0$. From these results, we may conclude that in our spin-1/2 ladder with $J'_{\rm r} = -1$, the phase transition from the antiferromagnetic stripe Néel (ASN) phase (see the top left of Fig.2) to the Haldane phase (the top right of Fig.2) occurs at $\delta_{\rm r}^{xy} \sim 0.9$ when $\delta_{\rm r}^{z} = 1$ and that from the Haldane to the triplet dimer (TD) phase (the central right of Fig.2) at $\delta_{\rm r}^{z} \sim 0.8$ when $\delta_{\rm r}^{xy} = 1$. It is noted that the Néel and large-D phases in the spin-1 chain correspond, respectively, to the ASN and TD phases in the spin-1/2 rung-alternating ladder.

When $J'_{\rm r} = 1$, on the other hand, it is naturally expected that a pair of $S = 1/2$ spins at the $(2l)$-th site of the a and b legs is in the singlet dimer state $\frac{1}{\sqrt{2}}\big(|\uparrow_a\downarrow_b\rangle - |\downarrow_a\uparrow_b\rangle\big)$, while a pair of $S = 1/2$

spins at the $(2l-1)$-th site of the a and b legs is in one of the ferromagnetic states $|\uparrow_a\uparrow_b\rangle$ and $|\downarrow_a\downarrow_b\rangle$ or in the triplet dimer state $\frac{1}{\sqrt{2}}\left(|\uparrow_a\downarrow_b\rangle+|\downarrow_a\uparrow_b\rangle\right)$ depending upon whether the anisotropy of the rung interactions is of the Ising-type or of the XY type. We have carried out a third-order perturbation calculation to obtain the effective interaction between two ferromagnetic states in a neighboring pair of spins at the $(2l-1)$-th and $(2l+1)$-th sites; the result shows that it is antiferromagnetic when $J_1>0$. Thus, the ground state in the case of Ising-type rung interactions is the 'ferromagnetic'-'singlet dimer' (F-SD) state (the central left of Fig.2), and that in the case of XY-type rung interactions is the 'triplet dimer'-'singlet dimer' (TD-SD) state (the bottom left of Fig.2).

We show in Fig.3 our results for the ground-phase diagrams; the left one is that on the $\delta_{\rm r}^{xy}$-$J_{\rm r}'$ plane in the case of Ising-type rung interactions where $\delta_{\rm r}^{z}=1$, and the right one is that on the $\delta_{\rm r}^{z}$-$J_{\rm r}'$ plane in the case of XY-type rung interactions where $\delta_{\rm r}^{xy}=1$. We first discuss the former phase diagram. By examining the $J_{\rm r}'$-dependence of the finite-L (up to $L=14$) excitation spin gap within the $M=0$ subspace, M being the total magnetization, calculated by the exact diagonalization (ED) method for a given value of $\delta_{\rm r}^{xy}$ as well as the l-dependence of the finite-L site magnetization $m_{l,\lambda}(L)$ (up to $L=192$), calculated by the density-matrix renormalization-group (DMRG) method [3] for a given set of $J_{\rm r}'$ and $\delta_{\rm r}^{xy}$, we have reached the conclusion that the Haldane phase appears in the frustrated region where $0<J_{\rm r}'<1$. The appearance of the Haldane phase in the case of Ising-type interactions is contrary to the ordinary situation [2], and this is called the inversion phenomenon concerning the interaction anisotropy [4]. Examining the Fourier transform of $m_{l,\lambda}(L)$, we have also shown that the incommensurate state becomes the ground state within the region of the Haldane phase. The solid lines are the second-order (2D Ising) phase boundary lines, which is determined by the phenomenological renormalization group analysis [5]. The dotted lines separate the commensurate and incommensurate regions; the region between these lines is the incommensurate one.

Let us move to the discussions on the latter phase diagram. Similarly to the above case, we have confirmed that the Néel phase (the bottom right of Fig.2) appears in the frustrated region. The appearance of the Néel phase in the case of XY-type interactions is also the inversion phenomenon concerning the interaction anisotropy [4]. The results of our DMRG calculations show that jump anomalies from zero to a finite value occur in the $m_{l,\lambda}(L)$ versus $J_{\rm r}'$ curve for a given value of $\delta_{\rm r}^{xy}$. From

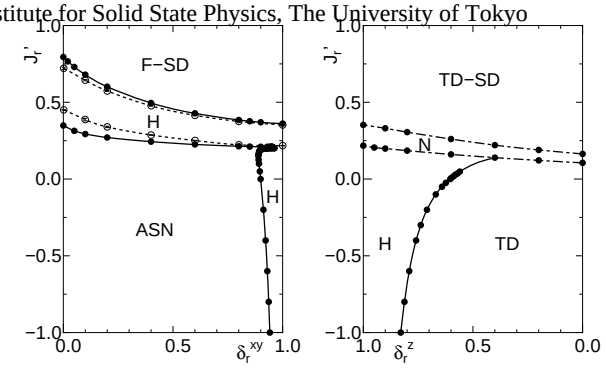

Figure 3: Ground-state phase diagram in the case of Ising-type rung interactions (left) and that in the case of XY-type rung interactions (right). In the left phase diagram, the 'ferromagnetic'-'singlet dimer' (F-SD), Haldane (H) and antiferromagnetic stripe Néel (ASN) phases appear. In the right phase diagram, the 'triplet dimer'-'singlet dimer' (TD-SD), Néel (N), Haldane (H) and triplet dimer (TD) phases appear. See the text for more details.

these results, we may conclude that the phase transition between the Néel phase and one of the other three phase are of the first-order, although, strictly speaking, it is difficult to come to a right and final conclusion from the finite-size calculations. The dot-dashed lines are the first-order phase boundary lines. On the other hand, the solid line is the second-order (Gaussian) phase boundary line; this line is determined by Kitazawa's level spectroscopy analysis [6], which has very recently been modified to some extent [1,7].

This work has been done in collaboration with K. Okamoto, T. Hikihara, T. Sakai, J. Morishige and K. Nomura. Performing the ED calculations, we have used the fortran program package KOBEPACK [8], which is very well vectorized for the NEC SX-9 system.

[1] T. Tonegawa, K. Okamoto, T. Hikihara, T. Sakai, J. Morishige and K. Nomura: in preparation.
[2] W. Chen, K. Hida and B. C. Sanctuary: Phys. Rev. B **67** (2003) 104401.
[3] S. R. White: Phys. Rev. Lett. **69** (1992) 2863.
[4] K. Okamoto and Y. Ichikawa: J. Phys. Chem. Solids **63** (2002) 1575.
[5] M. P. Nightingale: Physica A **83** 561 (1976).
[6] A. Kitazawa: J. Phys. A **30** (1997) L285.
[7] K. Nomura, J. Morishige, T. Tonegawa, K. Okamoto, T. Hikihara, T. Sakai: in preparation.
[8] M. Kaburagi, T. Tonegawa and T. Nishino: *Computational Approaches in Condensed Matter Physics*, Springer Proc. Phys., ed. S. Miyashita, M. Imada and T. Takayama (Springer, Berlin, 1992) p.179.

Phonon Effects and Frustration in Quantum Spin Systems

Chitoshi YASUDA
Department of Physics and Earth Sciences, Faculty of Science, University of the Ryukyus, Nishihara, Okinawa 903-0213, Japan

In frustrated quantum spin systems with competing interactions (frustration systems), novel spin states are often formed due to the strong quantum effects and have attracted considerable attention. In this project, we derived effective Hamiltonians of coupled systems of spins and phonons (phonon systems) by performing a unitary transformation [1]. Since the effective Hamiltonians describe the frustrated quantum spin systems, we can investigate relations between the phonon and frustration systems. For one-dimensional quantum Heisenberg-like models with a spin-phonon interaction, we consider a next-nearest-neighbor spin interaction in addition to a nearest-neighbor interaction and a spin-phonon interaction with a parameter to control a change of a geometric structure. In order to perform a unitary transformation for phonon systems, we use the computational software program 'Mathematica' and also check the results by hand calculation whenever it is possible. The effective Hamiltonian we obtained is expanded by the strength of the spin interaction J and that of the spin-phonon interaction g and can be theoretically derived for all order of the series expansion. If the order becomes large, the source memory we need becomes large. In the present work, we derived the effective Hamiltonian of fourth order in g and investigate the properties. The Hamiltonian consists of spin interactions up to fifth-nearest-neighbor and four-body interactions. The eigen values of the effective Hamiltonian are calculated by the exact diagonalization in the $\sum_i S_i^z = 0$ and $k = \pi$ subspace and the Berezinskii-Kosterlitz-Thouless-type phase transition points are evaluated by level-spectroscopy analysis. The agreement between results of system-size $N = 12$ and 16 suggests that the size dependence is negligible. Furthermore, the results for small J agree with phase transition points estimated by using $J_2/J_1 = \alpha$, where J_1 and J_2 are the strengths of the nearest- and next-nearest-neighbor interactions of the effective Hamiltonian and α_c is the phase transition point of the J_1-J_2 model. Thus, this phase transition is driven between the spin-liquid and spin-gapped phases. We can control the ground state for $g = 0$ by changing the strength of the next-nearest-neighbor spin interaction. In the system where the ground state is in the spin-liquid phase for $g = 0$, the spin-phonon interaction causes the usual phase transition to the spin-gapped phase. In the system where the ground state is in the spin-gapped phase for $g = 0$, on the other hand, the spin-phonon interaction causes the novel phase transition to the spin-liquid phase for some geometric structures. This work is done in collaboration with Satoru Akiyama (Wakayama National College of Technology).

References

[1] S. Akiyama and C. Yasuda: J. Phys. Soc. Jpn. **80** (2011) 104709.

Characterization of thermal transport at nanostructure interface

Junichiro SHIOMI

Department of Mechanical Engineering,

The University of Tokyo, 7-3-1, Hongo, Bunkyo-ku, Tokyo, 113-8656

Since interfacial thermal transport determines heat exchange, dissipation, thermoelectric efficiency and so on, it is a key property for the development of thermal management. Recently the non-equilibrium Green's function (NEGF) method with non-empirical force fields[1] has been applied to the silicon-germanium solid-solid interface, and microscopic and quantitative calculations of interfacial phonon transport were reported[2]. Although NEGF tells us the mode-dependent interfacial phonon transport, it cannot cover the effect of inelastic scattering process on thermal boundary conductance (G_{TBC}) since it is based on harmonic theory. For the comprehensive understanding and quantitative evaluation of the interfacial thermal transport in terms of phonons, the contribution of the inelastic scattering process to G_{TBC} needs be investigated.

In this work, considering the lead-telluride and lead-sulfide (PbTe-PbS) system exhibiting high thermoelectric efficiency, we calculated the phonon transmission function[3] by means of equilibrium molecular dynamics (EMD) simulation with a non-empirical force field[4].

Figure 1 shows the frequency dependence of the calculated phonon transmission function, $\Theta(\omega)$, at the PbTe-PbS interface and 300 K. Contributions of phonons below the cutoff frequency of PbTe (ω=3.45 THz) to G_{TBC} are dominant, whereas it can be seen that phonons (ω>3.45 THz) also contribute to G_{TBC}. Note that the latter contribution is caused by inelastic scattering at the interface and is not included in the NEGF calculation.

G_{TBC} can be calculated by simply integrating $\Theta(\omega)$ over frequency space. The calculated G_{TBC} is 0.34 $GWm^{-2}K^{-1}$, which is in excellent agreement with the result of non-equilibrium MD simulation that we also performed (0.33 $GWm^{-2}K^{-1}$). As shown in Fig.1, the inelastic contribution to G_{TBC} is around 10% and is not negligible.

To summarize, we calculated the phonon transmission function at PbTe-PbS solid-solid interface by performing EMD simulations. Phonons with a frequency above the cutoff frequency of PbTe transport across the interface and contribute to the G_{TBC} through inelastic scattering at the interface. We found that the inelastic contribution to G_{TBC} is around 10%, and thus cannot be neglected in the calculation of G_{TBC}.

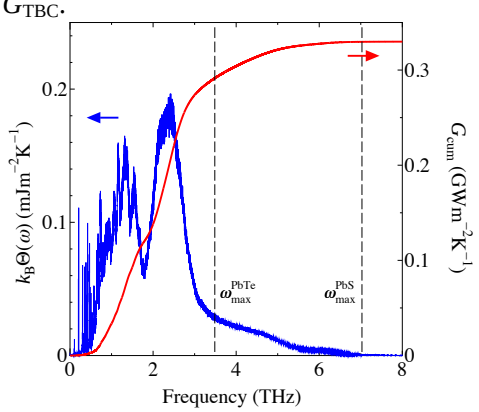

Fig. 1 Frequency dependence of phonon transmission function, $\Theta(\omega)$, at PbTe-PbS interface at 300 K. Vertical lines denote the maximum frequencies of PbTe and PbS crystals (3.45 and 7.06 THz), respectively. The solid line is the cumulative of $k_B\Theta(\omega)$.

References

[1] W. Zhang, T. S. Fisher, and N. Mingo, Numeriacal Heat Transfer, **51**, 333 (2007).

[2] Z. Tian, K. Esfarjani, and G. Chen, Phys. Rev. B **86**, 235304 (2012).

[3] Y. Chalopin, and S. Volz, Appl. Phys. Lett. **103**, 051602 (2013).

[4] T. Murakami, *et al.*, Eurphysics Lett. **102**, 46002 (2013)

Numerical analysis of field theory with non-trivial topological structure

Michikazu Kobayashi

Department of Physics and Astronomy, Graduate School of Science, Kyoto University

Oiwakecho, Sakyo-ku, Kyoto 606-8502

As a non-trivial topological structure, I have picked up the "knotted structure" of the field theory in the project. Knotted structures broadly appear in physics such as fluid mechanics, superfluid helium, Bose-Einstein condensates, non-equilibrium systems, soft matter, quantum chromodynamics, and so on. One of the most famous field theory for knot is the Hopf map $\pi_3(S^2) \simeq \mathbb{Z}$ which is the continuous map from S^2 to S^3 spaces. Because S^3 can be expressed as the fiber bundle $S^3 \simeq S^2 \rtimes S^1$ with the base space S^2 and the fiber S^1, one S^2 point is mapped to a knotted or unknotted loop in the S^3 space under the Hopf map. The simplest knot structure is the torus knot characterized by the number of string twists P along the torus and the number of strings Q, and the relation between the Hopf charge C for the Hopf map and the torus knot is $C = PQ$. The well known classical field model giving stable structure with $C \geq 1$ is the Faddeev-Skyrme model:

$$\begin{aligned} &\mathcal{L}_{\rm FS} = \frac{1}{2}\partial_\mu \boldsymbol{n} \cdot \partial^\mu \boldsymbol{n} - \kappa F^{\mu\nu} F_{\mu\nu}, \\ &\boldsymbol{n} \cdot \boldsymbol{n} = 1, \quad F_{\mu\nu} = \boldsymbol{n} \cdot (\partial_\mu \boldsymbol{n} \times \partial_\nu \boldsymbol{n}). \end{aligned} \tag{1}$$

The stable structure in the Faddeev-Skyrme model, however, cannot be classified as the torus knot because the structure is determined only for C. In particular, the stable structure is trivial unknotted one for $1 \leq C \leq 6$, and non-trivial knotted structure appears for $C \geq 7$ in the Faddeev Skyrme model. In this work, I have explicitly constructed stable structure classified (P, Q) rather than C [1]. Here I have considered the following extended Faddeev-Skyrme model:

$$\begin{aligned} &\mathcal{L}_{\rm TN} = \mathcal{L}_{\rm FS} - m^2(1 - n_3^2) + \beta^2 n_1 \\ &m \gg \beta > 0. \end{aligned} \tag{2}$$

The second and third terms in the right-hand-side make $n_3 = \pm 1$ and $n_1 = 1$ states favorable respectively. Under these terms, I expect the toroidal shape of the domain wall interpolating $n_3 = \pm 1$ states, and $n_1 = -1$ appears as a soliton string winding on the toroidal domain wall. As a consequence, I can obtain the torus knot of the $n_1 = -1$ state.

I numerically obtain the stable structure for the $\mathcal{L}_{\rm TN}$ in the 3-dimensional semi infinite space. For the time, the steepest descent method is used for finding the stable state. The condition $\boldsymbol{n} \cdot \boldsymbol{n} = 1$ is satisfied by introducing the Lagrange multiplier. For the space, to approximately treat the infinite space, I use the following scaling transformation:

$$\begin{aligned} &x_a = L \tan^{-1} X_a, \quad a = 1, 2, 3, \\ &(x_1, x_2, x_3) = (x, y, z), \end{aligned} \tag{3}$$

for $-1 < X_a < 1$, and consider the dependence of n_i on X_a instead of x_a, where L is the scaling parameter. I use the cubic with the $(N+1)^3$ grid points with $N = 1024$. On the l-th point in the x_a-direction, the value of $n_i(\{(l)_a\})$ is defined as

$$n_i(\{(l)_a\}) = n_i(\{(\cos(l\pi/N))_a\}), \qquad (4)$$

where $n_i(\{X_a\})$ is the value of n_i at $\{X_a\} = (X_1, X_2, X_3)$. For $l = 0$ or N, which corresponds to infinity, the value of n_i is fixed to the ground state:

$$n_1 = n_2 = 0, \quad n_3 = 1. \qquad (5)$$

To calculate the spatial derivative of n_i, I use the spectral collocation method. Under the discrete forward cosine transformation of n_i, I obtain the coefficients for the Chebyshev spectrum, and can easily calculate the first and second spatial derivatives of n_i through the forward and backward cosine transformations..

For the actual numerical procedure, I parallelize the task along the one direction to 128 core with 32 nodes through the standard MPI parallelization in the system B. The discrete cosine transformation for the Chebyshev spectrum is done with the FFT routine included provided by the Intel Math Kernel Library.

Figure 1 shows different stable solution of Eq. (2) for $C \leq 6$: $(P,Q) = (1,1)$, $(2,1)$, $(3,1)$, $(4,1)$, $(5,1)$, $(6,1)$, $(1,2)$, $(3,2)$, $(1,3)$, $(1,4)$, $(1,5)$, and $(1,6)$. Although there is no stable solution for $(P,Q) = (2,2)$ or $(2,3)$, I find configurations with different sets of (P,Q) for torus knots are topologically distinct even then they have the same Hopf charge C being different from the original Faddeev-Skyrme model. Especially, the state with $(P,Q) = (3,2)$ is non-trivial trefoil knot showing that knotted state appears even for $C = 6$.

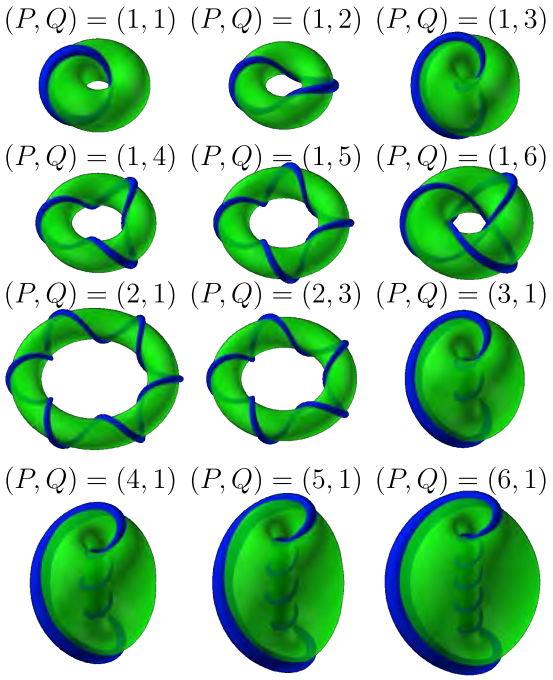

図 1: Toroidal domain wall (transparent green surface) and soliton string for $n_1 = -1$ (blue string). I fix $\beta^2/m^2 = 0.01$, and $\kappa m^2 = 1 \times 10^{-6}$.

参考文献

[1] M. Kobayashi and M. Nitta, Phys. Lett. B **728** (2014) 314.

Numerical Study of One Dimensional Frustrated Quantum Spin Systems

Kazuo HIDA
Division of Material Science, Graduate School of Science and Engineering
Saitama, Saitama 338-8570

1 Anisotropic Mixed Diamond Chains with Spins 1 and 1/2

Effects of single-site and exchange anisotropies on the ground state of the mixed diamond chain with spins 1 and 1/2 are investigated. The Hamiltonian is given by

$$\mathcal{H} = \sum_{l=1}^{L} \Big[J(\boldsymbol{S}_l + \boldsymbol{S}_{l+1}) \cdot (\boldsymbol{\tau}_l^{(1)} + \boldsymbol{\tau}_l^{(2)}) + DS_l^{z2} + \lambda \Big\{ \Delta \tau_l^{z(1)} \tau_l^{z(2)} + \tau_l^{(1)x} \tau_l^{(2)x} + \tau_l^{(1)y} \tau_l^{(2)y} \Big\} \Big] \tag{1}$$

where $\boldsymbol{S}_l$ is the spin-1 operator, and $\boldsymbol{\tau}_l^{(1)}$ and $\boldsymbol{\tau}_l^{(2)}$ are the spin-1/2 operators in the lth unit cell. The total number of unit cells is denoted by L. As in the case of $\lambda = 1$[1, 2], this model can be treated exactly by virtue of a series of conservation laws: $\forall l, [\boldsymbol{T}_l^2, \mathcal{H}] = 0$, where $\boldsymbol{T}_l \equiv \boldsymbol{\tau}_l^{(1)} + \boldsymbol{\tau}_l^{(2)}$. Therefore, each eigenstate has a definite set of $\{T_l\}$.

The ground state consists of an array of clusters called cluster-n each containing n successive bonds with $T_l = 1$ separated by singlet dimers with $T_l = 0$. We call this state DCn (dimer-cluster-n) state. A cluster-n is equivalent to a spin-1 chain with length $2n + 1$ and alternating single-site anisotropy.

For $1 \leq n < \infty$, DCn phase has $n + 1$-fold spontaneous translational symmetry breakdown. The ground state is nonmagnetic or paramagnetic depending on the magnitude of two types of anisotropies[3].

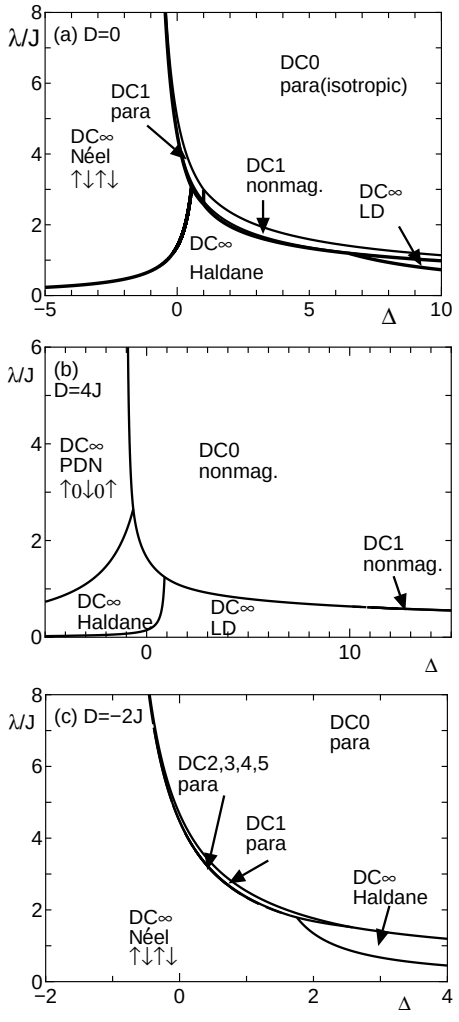

Figure 1: Ground-state phase diagram of the Hamiltonian (1) with (a) $D = 0$, (b) $D = 4J$, and (c) $D = -2J$.

For $n \to \infty$, the translational symmetry is recovered. The DC∞ phase is realized for small λ. Actually, this phase consists of four different phases; Néel, period-

doubled Néel(PDN), Haldane, and large-D(LD) phases. The ground state energy of the DCn phase is calculated by numerical exact diagonalization (NED) of a cluster-n. For the DC∞ phase, the ground state energy is calculated by the infinite size DMRG method. The phase boundaries shown in Fig. 1 are determined by comparing the ground state energy of each phase.

2 Antiferromagnetic Heisenberg Chains with Uniform and Alternating Single-site Anisotropies

The ground-state phase diagram of $S = 2$ antiferromagnetic Heisenberg chains with coexisting uniform and alternating single-site anisotropies described by the Hamiltonian

$$\mathcal{H} = \sum_{l=1}^{N} J\boldsymbol{S}_l\boldsymbol{S}_{l+1} + (D_0+\delta D)\sum_{l=1}^{N/2} S_{2l-1}^{z2} + (D_0-\delta D)\sum_{l=1}^{N/2} S_{2l}^{z2}, \quad (2)$$

is investigated[4]. Here $\boldsymbol{S_i}$ is the $S = 2$ spin operator on the i-th site. We consider the antiferromagnetic case $J > 0$. The case of $D_0 = 0$ has been investigated in [5]. We also take $\delta D > 0$ without the loss of generality. We investigate this model using NED and DMRG methods.

As shown in Fig. 2, we find the Haldane, LD, Néel, PDN, gapless spin fluid (SF), quantized ferrimagnetic(QF), and partial ferrimagnetic I and II (PFI and PFII) phases. In contrast to the case of $S = 1$[3], the Haldane phase is limited to the close neighborhood of the isotropic point. Within the numerical accuracy, the transition from the SF phase to the PDN phase is a direct transition. Nevertheless, the presence of a narrow spin-gap phase between these two phases is suggested on the basis of the low-energy effective theory. The ferrimagnetic ground state is present in a wide parameter range.

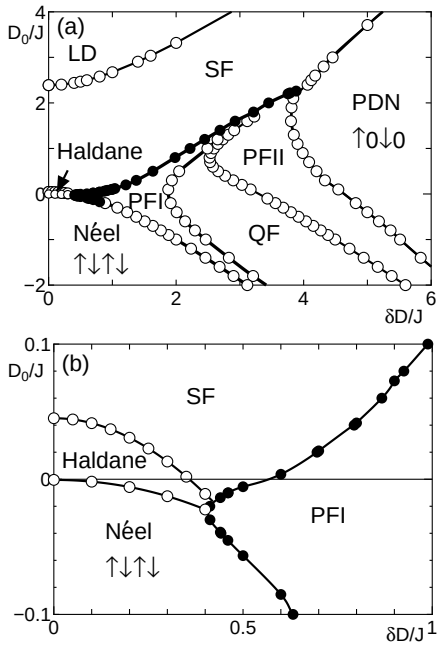

Figure 2: Ground-state phase diagram of the Hamiltonian (2). Open symbols are determined by extrapolation from the NED data for $4 \le N \le 12$. Filled symbols are determined from DMRG data with $N = 60$. (a) Overall phase diagram. (b) Enlarged phase diagram around $(D_0, \delta D) \sim (0, 0)$.

This work is supported by KAKENHI (C) (Nos. 25400389 and 21540379) from JSPS. The numerical diagonalization program is based on TITPACK ver.2 coded by H. Nishimori.

References

[1] K. Takano, H. Suzuki and K. Hida : Phy. Rev. B**80**, 104410 (2009).

[2] K. Hida and K. Takano : J. Phys. Soc. Jpn. **80**, 104710 (2011).

[3] K. Hida and W. Chen : J. Phys. Soc. Jpn. **74**, 2090 (2005).

[4] K. Hida: J. Phys. Soc. Jpn. **83**, 034707 (2014).

[5] K. Hida : J. Phys. Soc. Jpn. **76**, 024714 (2007).

Robustness of Scale-free Networks against Cascading Overload Failures

KOUSUKE YAKUBO
Department of Applied Physics, Hokkaido University
Sapporo 060-8628, Japan

Availability of functional networks is supported by the global connectivity of the network. The robustness of complex networks against damages is then a significant issue from a practical viewpoint. The network robustness has been extensively studied in context of the percolation problem. One of the most important node removal processes in actual network failures is cascading overload failures. In this work, we study the resilience of scale-free networks to cascading overload failures.

In our model, temporally fluctuating loads on a network are modeled by random walkers on the network. In order to estimate the percolation transition point in the node removal process by overload failures, we must determine the relation between the overload probability and network topology. Considering that the probability to find a random walker at the node i in the steady state is proportional to the degree of the node i, the overload probability of the degree-k node is given by the regularized incomplete beta function [1]. The cascading process based on the random-walk model is treated as follows.

1. Calculate the overload probability for the initial total load W_0 and remove nodes with this probability.
2. For the reduced-size network with N_t nodes, the total load W_t is updated. Under the new total load W_t, the overload probability is recalculated and nodes are further removed from the reduced network with this overload probability.
3. Repeat the above procedure until the expectation number of newly removed nodes becomes less than unity.

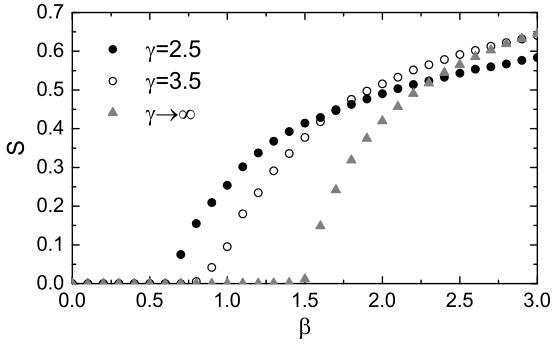

Figure 1: Relative size of the giant component in the final network as a function of the load renewal parameter β.

Figure 1 shows the relative size S of the giant component in the finally survived network as a function of the load renewal parameter β which characterizes the relation between W_t and N_t, for scale-free networks with different values of γ. It is clear that there exist the critical value β_c below which overload failures induce the global breakdown of the network. It should be noticed that the value of β_c for smaller γ is lower than that for larger γ. This implies that scale-free networks are robust against cascading overload failures modeled by random walkers, which is opposed to previous results based on the betweenness centrality [2].

References

[1] V. Kishore, M. S. Santhanam, and R. E. Amritkar, Phys. Rev. Lett. **106**, 188701 (2011).

[2] S. Boccaletti, V. Latora, Y. Moreno, M. Chavez, and D.-U. Hwang, Phys. Rep. **424**, 175 (2006).

Conformations of polymer chains in nematic liquid crystals

Takayuki UCHIDA and Takeaki ARAKI
Department of Physics, Kyoto University
Kitashirakawa-oiwake-cho, Sakyo, Kyoto 606-8502

The conformation of polymer chains dissolved in a simple solvent has been studied intensively. With changing the solvent quality, or χ parameter, a coil-globule transition is induced [1]. It is also interesting to study the conformation of polymers in an anisotropic liquid. It was reported that the conformation of polymers can be anisotropic in a nematic liquid crystal in experiments [2,3]. A mean-field theory on the conformation of semiflexible polymers in the vicinity of the nematic-isotropic (NI) phase transition point is also proposed [4]. Nevertheless, it is poorly understood what microscopic conformation is preferred in nematic liquid crystals. In this work, we studied the conformation of a polymer chain in a nematogenic liquid by means of Monte Carlo simulations. We adopt a spring-beads model to describe a polymer chain (Kremer-Grest and Weeks-Chandler-Andersen potentials) [5] and Gay-Berne potential for monomer-mesogen and mesogen-mesogen interactions [6]. The rigidity of the semi-flexible polymer is contolled with changing the bending modulus for angles between neighbour bonds. We employ NVT ensemble and control the temperature in order to change the phases of the background liquid.

If the chain is flexible, the conformation becomes anisotropic in nematic environment (see Fig. 1). However, the chain is not completely stretched there. If the polymer chain is semiflexible, on the other hand, the globule-stretched transition of the chain is observed in vicinity of the NI transition temperature. As the rigidity of polymer is enlarged, the globule-stretched transition point is increased far above the NI transition temperature. Here the solvent remains isotropic and the pretransitional nematic layer is formed around the stretched chain.

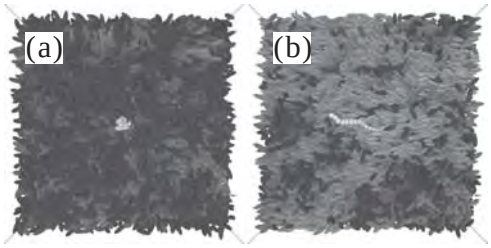

Figure 1: Snapshots of the polymer chain (a) far above and (b) in the vicinity of the NI transition temperature. The white chain represents the polymer. The ellipsoids are the nematogenic molecules and their brightness represent the local nematic order.

References

[1] P. G. de Gennes, *Scaling Concepts in Polymer Physics*, (Cornel Univ. Press., New York, 1979).

[2] J. F. D'Allest *et al.*, Phys. Rev. Lett. 61, 2562 (1988).

[3] Z. Dogic *et al.*, Phys. Rev. Lett. 92, 125503 (2004).

[4] A. Matsuyama, Phys. Rev. E 67, 042701 (2003).

[5] K. Kremer and G. S. Grest, J. Chem. Phys. 92, 5057 (1990).

[6] J. G. Gay and B. J. Berne, J. Chem. Phys. 74, 3316 (1981).

Collective Dynamics of Active Particles

Takaaki KAWAGUCHI
Department of Physics, School of Medicine, Toho University
5-21-16 Omorinishi, Ota-ku, Tokyo 143-8540, Japan

We investigate the directed motion of a one-dimensional particle array on a symmetric periodic potential by introducing spatiotemporally periodic modulation of the natural length between particles. Under certain conditions the particle array moves unidirectionally with finite velocity and shows directed motion for any finite value of the potential amplitude. Novel collective dynamics of the directed motion are observed.

The model considered here is an extended version of the one-dimensional Frenkel-Kontorova model, which consists of an array of particles interacting with each other via a linear spring on a periodic substrate. No directed external force works on the particles and no spatial asymmetry exists. We introduce spatiotemporally periodic modulation of the natural length between adjacent particles. The natural length between i-th and $(i+1)$-th particles is given by $c_{i,i+1}$. We assume sinusoidal modulation with an amplitude α, a time period T and a wave length λ.

The equation of motion of the i-th particle in the array is given by

$$\ddot{u}_i + \gamma \dot{u}_i = u_{i+1} - 2u_i + u_{i-1} - c_{i,i+1} + c_{i-1,i} - U \sin\left(2\pi u_i / c_b\right),$$

where u_i is the one-dimensional coordinate of the $i-$th particle. The equations of motion are solved under the periodic boundary condition by assuming overdamped motion of particles.

Figure 1 shows the time-evolution of the coordinates of the particles $u_i(t)$ for a certain condition. There appears spatiotemporally correlated motion of the particles. Each particle repeats oscillatory motion with different phases and as a whole moves forward. The motion resembles that of measuring worms, that is, the system repeats extension and contraction of its body part by part and moves forward as a whole.

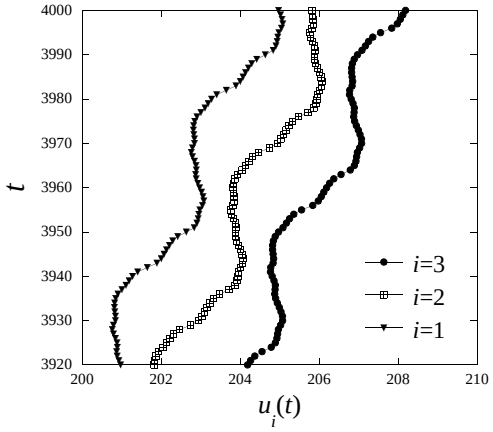

Figure 1: Time evolution of the coordinate of each particle.

The directed motion shows interesting behaviors against the change in the parameters of the modulation. In fig. 2 we show a reversal phenomenon of the direction, i.e., current reversal, against the change in the modulation amplitude α. The velocity v is normalized with $v_0 = c_b/T$. For $0.05 < \alpha/c_0 \leq 0.46$ the particle array moves in the positive direction with $v/v_0 = 1$. As α/c_0 is increased, reversal of motion appears twice. The first reversal occurs at $\alpha/c_0 \approx 0.47$ from $v/v_0 = 1$ to $v/v_0 = -2$, and the second one does at $\alpha/c_0 \approx 0.71$ and the value of v/v_0 returns to the same with that for $\alpha/c_0 \leq 0.46$. This may be called the dynamical reentrance of the directed motion. It is characteristic of the directed motion in this system that the strengthening of the modulation amplitude does not increase velocity, but causes the reversal of motion.

We investigate the changes of the system against increasing U for a suitable constant value of T. Figure 3 shows a diagram of the dy-

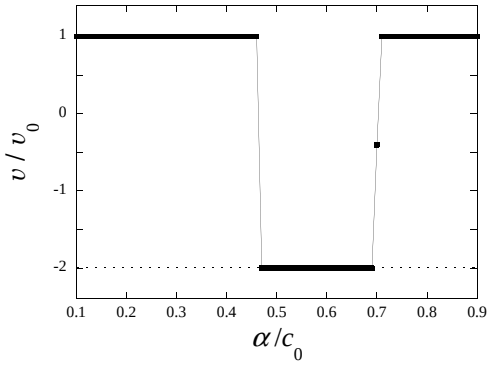

Figure 2: Modulation amplitude dependence of the normalized velocity of the particle array.

namical states for $T = 40$ in the $v/v_0 - U$ plane where the normalized velocity v/v_0 is plotted against U for $\alpha/c_0 = 0.5$ and $\lambda/L = 0.25$. The absolute magnitude of v/v_0 vanishes at

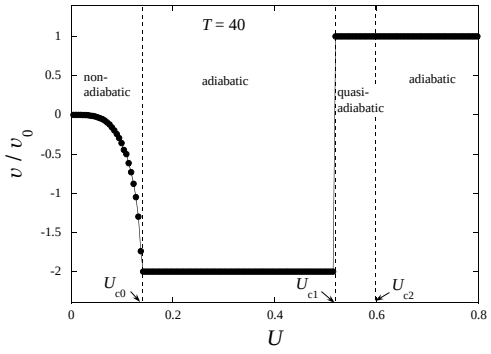

Figure 3: Diagram of dynamical states plotted in the $v/v_0 - U$ plane.

$U = 0$, i.e., no barrier cause no directed motion, and increases with U. The substrate potential yields barrier and frictional force for each particle. The directed motion observed in the present model is, hence, a sort of barrier-assisted and friction-induced motion. The velocity is locked to $v/v_0 = -2$ when U is larger than $U_{c0} \simeq 0.14$, where U_{c0} is the critical strength of U for the occurrence of the velocity locking. For $0 < U < U_{c0}$ the motion of the system is out of the range of the adiabatic motion. In this regime, hence, the motion is nonadiabatic and the velocity is not locked.

There exist another two critical strengths of U between the adiabatic and quasi-adiabatic regimes, which are denoted by U_{c1} and U_{c2}. In the range $U_{c0} < U < U_{c1}$ the motion becomes adiabatic and the velocity locking at certain value appears. In $U_{c1} < U < U_{c2}$ the new state appears as a quasi-adiabatic state. The velocity locking still occurs, that is "quasi-adiabatic locking", but the locked value is different from that for $U_{c0} < U < U_{c1}$. When we increase T, the transition from a quasi-adiabatic state with $v/v_0 = 1$ to an adiabatic one with $v/v_0 = -2$ occurs at a critical value of T in $U_{c1} < U < U_{c2}$. For $U \geq U_{c2}$ an adiabatic state with $v/v_0 = -2$ appears. In the adiabatic regime the velocity locking is stable for $T \to \infty$.

We investigated novel dynamical phenomena of directed motion in a particle array on a periodic substrate potential with no spatial asymmetry and no direct external driving force. The directional motion appears by introducing the spatiotemporally periodic modulation of the natural length between particles. The magnitude of the velocity is locked to multiple values of a unit velocity. The velocity locking behavior appears for adiabatic motion, and furthermore there appears a quasi-adiabatic locking behavior in a nonadiabatic regime.

References

[1] T. Kawaguchi and H. Matsukawa: *AIP Conf. Proc.*, **1518**, 737 (2013);

[2] T. Kawaguchi and H. Matsukawa: *JPS Conf. Proc.*, **1**, 012059 (2014);

Hydrodynamic effect on phase ordering

Ryotaro Shimizu, Hajime Tanaka

Institute of Industrial Science, University of Tokyo

Komaba 4-6-1, Meguro-ku, Tokyo, Japan

After shaking a salad dressing, we can see the collisions of oil droplets in vinegar. This coarse graining process is known as phase separation. In past decades researchers the kinetic process of phase separation phenomena have been intensively studied from both scientific and applications viewpoints, since this process is one of the most fundamental physical process of pattern formation[1].

For a binary liquid mixture, the relevant domain coarsening mechanism depends solely on the volume fraction of the minority phase. (1) For a small volume fraction, the evaporation-condensation mechanism is responsible for droplet coarsening. (2) Near a symmetric composition, the tube hydrodynamic instability proposed by Siggia[2] leads to rapid hydrodynamic coarsening. (3) For intermediate volume fraction, it has been believed that the Brownian-coagulation mechanism is responsible for the domain coarsening [2]. In this mechanism droplets grow by accidental collisions between droplets undergoing random Brownian motion.

Some time ago, we found in our microscopy observation of a droplet coarsening process that droplets are moving deterministically) rather than randomly [3,4]. Following trajectories of droplets, we noticed that droplets sometimes move directionally with a speed much faster than the expectation from random Brownian motion. We suggested that this may be due to a non-trivial coupling between composition and velocity fields. Droplets move around by thermal fluctuations while exchanging solutes with neighboring droplets via the surrounding matrix phase. The composition correlation between a pair of neighboring droplets should develop before an accidental collision between them by Brownian motion takes place. We speculated that this composition correlation may be an origin of rather deterministic motions of droplets.

This time we studied how this complex coupling leads to deterministic motions of droplets and efficient droplet coarsening, by numerically solving a fluid model (known as model H) for phase separation with and without thermal composition and force noises.

Figure 1 shows the snapshot of a binary fluid mixture undergoing droplet spinodal decomposition, which is simulated with thermal fluctuations. The interface of droplets is rough due to thermal fluctuation effects. We note that, to the best of our knowledge, this is the first example of model H simulation in three dimensions including full thermal noises. In the early stage, many small droplets are formed by fragmentations. We observed the growth of droplets by collisions with neighboring droplets in the late stage. We analysed the time evolution of average droplet size during the coarsening process. As the result, we found that the coarsening proceeds faster than the prediction by Brownian-coagulation (BC) theory, even though the coarsening exponent was close to 1/3, which is consistent with the BC theory.

To seek a cause of the faster coarsening mechanism, we analysed the displacements of droplets during the interval of two successive collisions. We found that the droplets move directionally towards a neighboring droplet. We consider that it is this fast directional motion that leads to the fast

coarsening process.

From the result of coarsening process without thermal noises, we can study about the composition correlation between droplets during the phase separation process, without suffering from noises that smear out all the details. We found that the interfacial profile of each droplet is not spherical symmetric but rather anisotropic, reflecting configuration of the neighboring droplets, even though the shape of droplets is almost perfectly spherical because of the action of the Laplace pressure. We also found that the deterministic flow field is induced at each droplet, reflecting the asymmetric interfacial profile of each droplet. This asymmetric interfacial profile leads to the intradroplet gradient of the interfacial tension and this gradient generates hydrodynamic motion of droplets.

In summary, we studied the coarsening process of droplet dispersions. We found that the coupling between diffusion and flow field plays a very important role for the phase separation process of asymmetric binary mixtures.

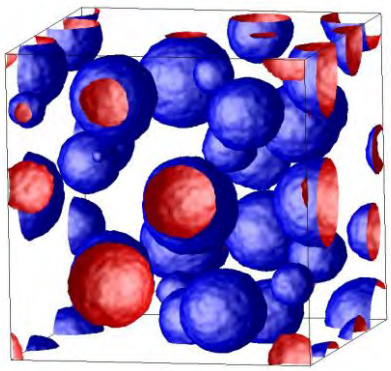

Figure 1: A snapshot during phase separation

References

[1] J.D.Gunton, M.San Miguel, and P.Sahni: in Phase Separation and Critical Phenomena, edited by C.Domb and J.H.Lebowitz, (Academic, London, 1983),Vol.8(1976)

[2] E.D.Siggia, Phys.Rev.A 20,595(1979)

[3] H.Tanaka, J.Chem.Phys. 103, 2361(1995)

[4] H.Tanaka, J.Chem.Phys. 107,3734(1997)

High precision computation of Feigenbaum constant.

Masanori SHIRO

HTRI, National Institute of Advanced Industrial Science and Technology

Umezono1-1-1 Central 2, Tsukuba, Ibaraki 305-8568

A purposes of our project is calculating the second Feigenbaum constant with high precision.

Properties of critical exponents between many type of phase transitions are not necessarily revealed, although the transitions are found in many solid-state materials. We think that phase transitions are able to treat as chaotic transitions. Feigenbaum constant is an universal value between simple chaotic models and fractals. A series expansion for the constant is not known yet. It is just found in almost two thousands digits in Briggs' thesis[1].

The most important signification of our project is to find a precise value of Feigenbaum constant for the phase-transition studies. In future, the value should be expanded in a series. Many digits provide more correct information whether the values is rational or not, transcendental or not, and so on.

Our project stated at the second half season in 2013. An universal function $g(x)$ which is required for calculation of the constant, has following properties,

1. $g(x)$ is an even function.
2. $g(\alpha x)/\alpha = g(g(x))$
3. $\alpha = 1/g(1)$
4. $g(0) = 1$

.

We did basis expansion of $g(x)$ and its coefficients as a vector and divided $x_i \in [0, 1]$ are constructed to a matrix.

Although required libraries as Eigen are not installed, we wrote a prototype in C++ and checked its workings, computational effort and required memory[2]. We found that a realistic digits is till later thousands order in our available resources.

Fortunately, our work will run on the next year. Required libraries such as Eigen and Mpreal will be modified for our computers, installed by the center staff and we want to do our task completely.

参考文献

[1] Doctor thesis: K. Briggs (1997)

[2] JPS abstracts in 2014 spring: 29pAD11, M. Shiro (2014)

Symmetry protection of disordered phases and phase transitions in spin chains

Yohei FUJI, Frank POLLMANN[a], and Masaki OSHIKAWA
Institute for Solid State Physics, University of Tokyo, Kashiwa, Chiba 277-8581
[a] *Max-Planck-Institut für Physik komplexer Systeme, D-01187 Dresden, Germany*

In recent decades, the study of topological phases is one of central interests in condensed matter physics. A special class of the topological phases is called "symmetry-protected topological (SPT)" phases [1], which are distinct only in the existence of certain symmetries. SPT phases are characterized by nontrivial entanglement structures. On the other hand, when the ground state is adiabatically connected to a direct product of local states, it is considered to be in a trivial phase. It appears that there is just one trivival phase. However, in the presence of certain symmetries, there can be distinct trivial phases.

In this work, we show such a symmetry-protected distinction between trivial phases in 1D spin systems in the presence of the symmetry with respect to the combined operation of the site-centered inversion and the π-rotation about one spin axis. [2] To illustrate this, we consider the spin-1 chain with a staggered magnetic field,

$$H = \sum_j \left[\vec{S}_j \cdot \vec{S}_{j+1} + D_z (S_j^z)^2 + D_x (S_j^x)^2 + h_z (-1) S_j^z \right],$$

which possesses the desired symmetry.

We numerically investigate its ground-state properties by the infinite density-matrix renormalization group (iDMRG) method [3], which provides an accurate variational ground-state wavefunction in the matrix-product representation with $\chi \times \chi$ matrices. We use Fortran90 on the ISSP Supercomputer with OpenMP parallelization in order to accelerate the contractions of tensors. In Fig. , we show the correlation length as a function of D_z for two sets of the parameters. Divergent behaviors of the correlation lengths as increasing χ correspond to phase transitions. These phase transitions indicate that two trivial phases are distinguished under the above symmetry.

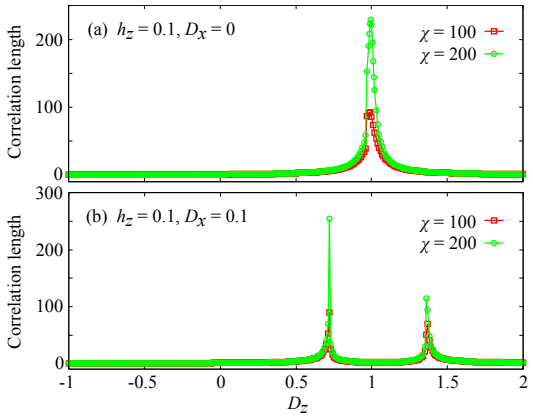

Figure 1: Correlation lengths are plotted against D_z.

References

[1] Z.-C. Gu and X.-G. Wen, Phys. Rev **80**, 155131 (2009); F. Pollmann, A. M. Turner, E. Berg, and M. Oshikawa, Phys. Rev. B **81**, 064439 (2010).

[2] Y. Fuji, F. Pollmann, and M. Oshikawa, in preparation.

[3] I. P. McCulloch, arXiv:0804.2509 (unpublished).

Fixed Scale Factor Finite-Size Scaling Analysis for Two-Dimensional Spin Systems

Yusuke TOMITA
Shibaura Institute of Technology
307 Fukasaku, Minuma-ku, Saitama-City, Saitama 337-8570

Critical phenomena in continuous spin systems on two-dimensional (2D) lattices have long been fertile soils for deep understanding of statistical physics. In particular, the Mermin-Wagner-Hohenberg theorem and the theory of the Berezinskii-Kosterlitz-Thouless (BKT) transition play roles of principal guides for investigating critical phenomena in 2D systems. Though the preceding studies are quite helpful to judge whether a system shows critical phenomena or not, a little number of systems yet annoy researchers by showing obscure *critical* behaviors. The obscureness hinders grasp of physics, and sometimes it may lead us to a misunderstanding of critical phenomena. A suitable example of such an obscureness is the 2D ferromagnetic Heisenberg model. The Heisenberg model exhibits exponentially large correlation lengths at low temperatures, and conventional finite-size scaling (FSS) analyses often lead to an erroneous conclusion that the model has the BKT phase.

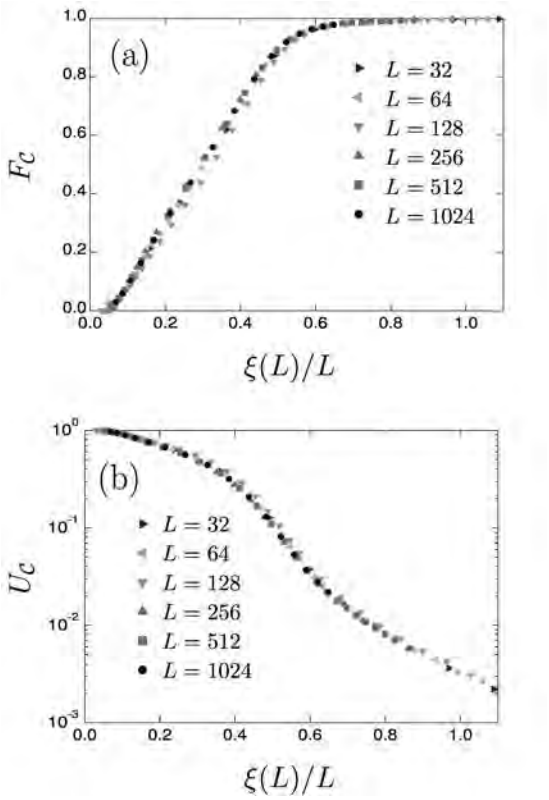

Figure 1: (a) An FSF-FSS plot of the correlation ratio for the 2D Heisenberg model. (b) A semi-logarithmic plot of an FSF-FSS function for the 2D Heisenberg model.

To improve accuracy of FSS analyses, I proposed a FSS analysis using a fixed scale factor[1]. A procedure of the FSS analysis is like as follows: (1) Calculate two two-point correlation functions, $G(\beta, L/2)$ and $G(\beta, L/4)$. The Correlation ratio $\mathcal{C}(\beta, L)$ is defined by $G(\beta, L/2)/G(\beta, L/4)$. (2) Calculate the ratio of the correlation ratio $F_{\mathcal{C}}(\xi(\beta, L)/L) = \mathcal{C}(\beta, sL)/\mathcal{C}(\beta, L)$. Here, s is a parameter named the fixed scale factor. Since the correlation ratio is a dimensionless quantity, the function $F_{\mathcal{C}}$ is equal to unity at the critical point. With usual procedure, a location of a critical point is estimated by a crossing point of a dimensionless FSS function, but the estimation of the crossing point is usually difficult task for systems under discussion. The conciseness in estimating a critical point ($F_{\mathcal{C}} = 1$) is a main advantage of the new FSS analysis. Even though the improved FSS analysis gives the concise measure, we need a further improvement to estimate criticalities of systems whose correlation lengths are exponentially large. The improvement is accomplished by introducing the form of the two-point correlation function in the critical region,

$G(\beta, r) \sim e^{-\kappa r}/r^{d-2+\eta}$. The parameter κ is proportional to the inverse of the correlation length; that is $G(\beta, r)$ gives the power law decaying correlation function at the critical point ($\kappa = 0$). Using the expression, the distance from unity $[U_{\mathcal{C}}(= 1 - F_{\mathcal{C}})]$ is approximately estimated as $(s-1)\kappa L/4$ in the critical region.

Figure 1 shows the FSS function $F_{\mathcal{C}}$ and the logarithm of the distance from unity for the 2D Heisenberg model. Since the correlation length of the model exponentially develops as lowering temperature, $F_{\mathcal{C}}$ is almost unity at low temperatures. However, the logarithmic plot of the function $U_{\mathcal{C}}$ manifestly shows the distance is finite at finite temperatures. Therefore, the correlation length of the 2D Heisenberg model never diverges at finite temperature.

I also applied the FSS analysis to the 2D XY and RP^2 models, and the results proved the analysis is quite helpful to judge whether a system exhibits a phase transition or not. The method can be applied to other systems straightforwardly. The applications will give firm evidences of existence or absence of the systems' criticalities.

References

[1] Y. Tomita, in preparation.

Large scale hard sphere molecular dynamics simulation in the nonequilibrium transport phenomena

Masaharu ISOBE
Nagoya Institute of Technology
Gokiso-cho, Showa-ku, Nagoya, 466-8555

In this project, we investigated several nonequilibrium phenomena in the simple model system by using event-driven molecular dynamics (EDMD) algorithm in hard core system [1] and other alternative methods.

(i) *Cluster Impact and Shock Wave Propagation in Freely Evolving Granular Gas*: Granular gas without any external force evolves from the initial homogeneous state to the inhomogeneous clustering state, at which the energy decay deviate from Haff's law. The asymptotic behavior of energy decay after the clustering regime have been predicted by two theories, which are based on mode coupling theory or extension of inelastic hard rods gas. In our study, we investigated this system especially in the clustering regime of freely evolving granular gas by a large-scale molecular dynamics simulation up to 16.7 million particles. We found novel regime regarding on collisions between"clusters" appearing after clustering regime spontaneously, which can be clearly identified more than a few million particles system. The volumetric dilatation patterns of semicircular shape originated from density shock propagation characterize the "cluster impact" during the aggregation process of clusters. The theories don't agree with our numerical results because of cluster collision. Our novel findings indicate that the freely cooling granular gas in quasi-elastic and thermodynamic limit is strongly related to Navier-Stokes incompressible turbulence (shearing regime), however, it eventually behaves as a compressible fluid (shock wave) after clustering regime (cluster collision regime) [2].

(ii) *Hard Disks Equation of State: First-Order Liquid-Hexatic Transition in Two Dimensions with Three Different Simulation Methods* [3]: Large-scale molecular simulations of the two dimensional hard disk system around the melting point are investigated with three different methods (i.e., event-chain Monte Carlo, a massively parallel Monte Carlo and EDMD). We reproduce the equation of state up to one million particles system. The relative performance of these methods is analyzed and the first-order melting transition in hard disks is confirmed, which were previously obtained using event-chain Monte Carlo method. Furthermore, the analyses of positional order confirms the existence of the hexatic phase in the one-million hard disk system.

References

[1] M. Isobe: Int. J. Mod. Phys. C **10** (1999) 1281.

[2] M. Isobe, Phys. Rev. E **68** (2003) 040301(R); Int. J. Mod. Phys. C **23** (2012) 1250032; J. Phys: Conf. Ser. **402** (2012) 012041; (2014) in preparation.

[3] M. Engel, J. A. Anderson, S. C. Glotzer, M. Isobe, E.P. Bernard and W. Krauth: Phys. Rev. E **87** (2013) 042134.

Study of the effect of the short-range interaction on critical phenomena driven by elastic interactions

Masamichi Nishino
Computational Materials Science Center, National Institute for Materials Science
Tsukuba, Ibaraki, Japan

Domain wall (interface) propagation is frequently seen in growth of a new ordered state. The structure of the interface has been studied extensively and the following scaling relation has been established: $W(L,t) \sim L^{\alpha} f(\frac{t}{L^z})$, where L is the system size parallel to the interface, t is time, and $f(x)$ is a scaling function. The critical exponents are established as $\alpha = 1/2$, $z = 3/2$ in KPZ universality class for one-dimensional interface, i.e., in two-dimensional systems. Various kinds of growth models such as Ising model, BD model, RSOS model, etc, are in this class. In the steady state of interface growth, i.e., when $\frac{t}{L^z} \gg 1$, the interface width is scaled as $W(L,t) \sim L^{\alpha}$.

Spin crossover (SC) materials show a wide variety of phase transitions and have attracted much attention in applicability to devices [1]. The SC system has bistable states, i.e., low spin (LS) state and high (HS) state and the size of each molecule depends on the states. The elastic interaction caused by the lattice distortion due to difference of the molecular sizes is important for the cooperative interaction. We modeled the cooperative interaction by constructing an elastic-interaction model, in which the changeable volume of the molecular unit is taken into consideration.

In this work we investigated domain wall propagation between HS and LS phases and the scaling property of the interface [2]. There exist two kinds of interfaces in SC systems. One is the interface of the spin states of molecules and the other is the interface of the lattice structure. The nature of the lattice interface width does not depend on the dynamics of the lattice and spin, and the shape is of macroscopic structure due to long-range nature of the elastic interaction. In contrast, the nature of the spin interface width changes depending on the dynamics of the lattice and spin. When the change of the spin state is fast and the lattice relaxation does not follow it sufficiently, the roughness exponent has the value $\alpha = 1/2$, which is commonly found in models of short-range interactions. In contrast, when the lattice relaxes well, the spin dynamics is influenced by the lattice dynamics, which leads to $\alpha = 1$ of the roughness exponent. In this case the macroscopic nature of the elastic interaction affects the spin interface.

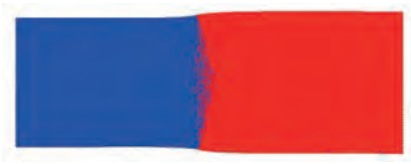

Figure 1: Snapshot of interface growth in the SC system. Blue and red parts denote LS and HS phases, respectively.

References

[1] "Theoretical Descriptions of Spin-Transitions in Bulk Lattice", C. Enachescu, M. Nishino, S. Miyashita in "Spin-crossover materials - properties and applications" M.A. Halcrow (ed) John Wiley & Sons, Chichester, UK, 2013, 455-474.

[2] "Crossover of the roughness exponent for interface growth in systems with long-range interactions due to lattice distortion", M. Nishino, T. Nakada, C. Enachescu, K. Boukheddaden and S. Miyashita, Phys. Rev. B 88, 094303 (2013).

Fracture dynamics and pattern formation

Satoshi YUKAWA and Shin-ichi ITO
Department of Earth and Space Science, Osaka University
Machikaneyama, Toyonaka, Osaka 560-0043

A fracture pattern of a thin layer is seen in everyday life. It is essentially caused by shrinkage of the paste; The fracture pattern of the dried mud is also caused by stress increment during the desiccation process of the paste. There are lots of interesting phenomena which have not been understood yet. Over the last few years, we have studied the fracture dynamics in a drying thin layer of the paste numerically and analytically.[1] The main result of this study is that the dynamical scaling law of the fragment size distribution is found; The bare distribution of the fragment size S at time t, $P(S,t)$, can be scaled by its average, $P(S,t) \sim \widetilde{P}(S/\langle S\rangle_t)$. This result resembles the Vicsek-Family scaling for the aggregation process,[2] but the direction of time is opposite.

In this year, in order to understand the dynamical scaling property, we study the stochastic model based on the Gibrat process,[3] which is called the modified Gibrat process. Original Gibrat process is a discrete-time dividing stochastic process with the multiplicative noise. For the modified Gibrat process, we introduce the concept of the lifetime of the fragments. Thus the discrete-time stochastic process becomes continuous-time one. The lifetime is a function of the area of the fragments, which is analytically evaluated by equations of motion for elastic continuum.

In the last year, we found that the modified Gibrat process obeyed the dynamical scaling law in the case that the lifetime is a power-law function on the area. In this year, on the ISSP super computers, we performed numerical simulations with parameter parallelization to survey the large parameter space. In Fig. 1, several scaled distributions are shown. In addition, we analyzed the Markovianized stochastic model of the modified Gibrat process. Further theoretical and experimental investigation are now in progress.

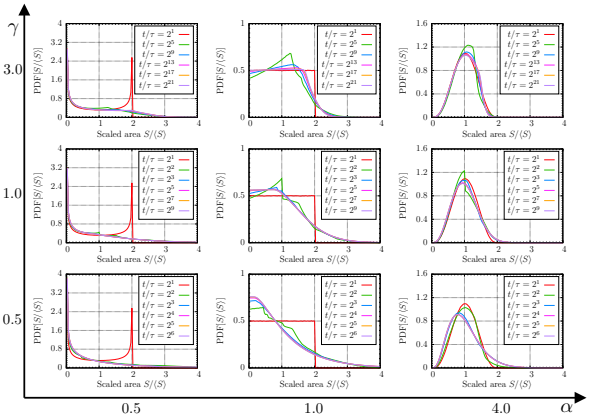

Figure 1: Scaled distributions for several parameters. Shapes of the final scaled distributions are different, but all distributions are scaled.

References

[1] S. Ito and S. Yukawa: arXiv:1209.6114.

[2] T. Vicsek and F. Family, Phys. Rev. Lett., **52**, b 1669, (1984).

[3] E. W. Crow and K. Shimizu ed, "Log-normal distributions: theory and applications" (Marcel Dekker, New York, 1988).

Multifractality near a Point Defect at Topological Phase Transitions

Hideaki OBUSE
Department of Applied Physics, Hokkaido University
Sapporo 060-8628, Japan

Multifractality at Anderson transitions, which reflects non-trivial self-similar structures of wave functions due to the absence of characteristic lengths, has attracted much attentions for its importance to understand the phase transitions[1]. Multifractality also exposes interesting natures when a topological insulator with disorder undergoes a phase transition into a metal or a topological insulator with the different topological number[2, 3]. On one hand, multifractality in the bulk region is determined by only symmetries and the spatial dimension of the system even for topological phase transitions. Thereby, bulk multifractality observed at topological phase transition is identical with bulk multifractality of one of the conventional Anderson transitions. On the other hand, multifractality near (straight) boundaries, called boundary multifractality, of the topological phase transition depends on the topological number of the adjacent topological insulating phase together with symmetries and the spatial dimension. Therefore, boundary multifractality of the topological phase transition is different from that of the conventional Anderson transitions. In this work, we study multifractality near a point like topological defect.

We focus on the two-dimensional square lattice with random hoppings. We note that there is no on-site disorder so that the system retains chiral symmetry. A vacancy, in other words, a point defect in this system is a topological defect and generates a zero energy state. We have

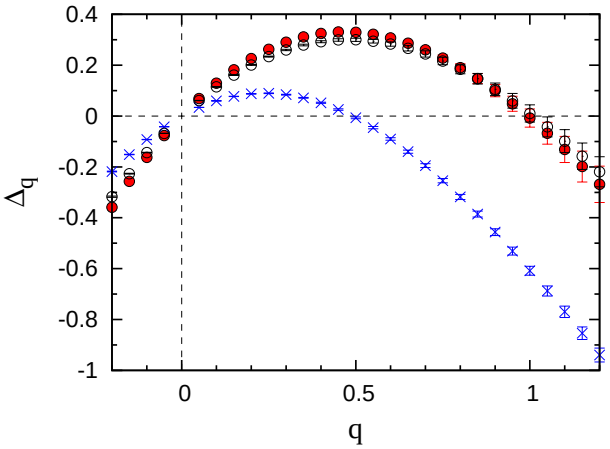

Figure 1: The q dependence of anomalous dimensions Δ_q. The blue crosses and red filled circles represent anomalous dimensions calculated from wave function amplitudes near and far from the defect, respectively. For comparison, the anomalous dimension for systems with no point defects is shown by the black open circles.

numerically calculated the wave function $\psi(\boldsymbol{r})$ at the zero energy of the system with the linear size L for many disorder realizations. The system size L is changed from 40 to 1000 and the number of disorder realizations is 10^6 for each L. Then, multifractality is quantitatively calculated from the size L dependence of the relation, $L^{2q}\overline{|\psi(\boldsymbol{r})|^{2q}} \propto L^{-\Delta_q}$, where Δ_q is an anomalous dimension and the overline represents the ensemble averaging. We have calculated Δ_q from the wave function amplitudes far from and close to the point defect.

Figure 1 shows Δ_q in case the position of wave function amplitude $\boldsymbol{r}$ is close to or far from the point defect. We have confirmed that Δ_q from wave function amplitude far from the point defect is the same with Δ_q calculated from a system with no point defect. We have also found that Δ_q from wave function amplitudes close to the point defect exhibits new multifractality which is different from Δ_q in the bulk.

References

[1] F. Evers and A. D. Mirlin: Rev. Mod. Phys. **80** (2007) 1355.

[2] H. Obuse, A. Furusaki, S. Ryu, and C. Mudry: Phys. Rev. B **78** (2008) 115301.

[3] R. Bondesan, I. A. Gruzberg, J. L. Jacobsen, H. Obuse, and H. Saleur: Phys. Rev. Lett. **108** (2012) 126801.

Molecular Simulation Study of Supramolecular Structure Formation by Amphiphilic Molecules

Susumu FUJIWARA

Graduate School of Science and Technology, Kyoto Institute of Technology

Matsugasaki, Sakyo-ku, Kyoto 606-8585

Amphiphilic molecules such as lipids and surfactants are composed of hydrophilic and hydrophobic parts. In aqueous solutions, amphiphilic molecules spontaneously self-assemble into various structures such as micelles, vesicles, and bicontinuous structures [1-3]. Although numerous computer simulation studies have so far been done on structure formation of amphiphilic molecules, each of which consists of a hydrophilic head group and a hydrophobic tail group, there have been few theoretical and simulation studies on structure formation of bolaamphiphilic molecules, each of which contains a hydrophobic stalk and two hydrophilic ends. The purpose of this study is to clarify the effect of hydrophilicity on the phase behavior of bolaamphiphilic solutions. With a view to investigating the phase behavior of bolaamphiphilic solutions at the molecular level, we perform the molecular dynamics (MD) simulations of coarse-grained bolaamphiphilic molecules with explicit solvent molecules and systematically analyze the formation processes of micelles and mesophases.

A bolaamphiphilic molecule is modeled as a semiflexible chain which consists of a hydrophobic stalk with three particles and two hydrophilic ends (H1 and H2), each of which contains one particle. The solvent molecules are modeled as hydrophilic particles. As bonded potentials, we consider the bond-stretching potential and the bond-bending potential. The interaction between hydrophilic and hydrophobic particles is modeled by the repulsive soft core potential and all other interactions are modeled by the Lennard-Jones (LJ) potential. Note that the LJ interaction parameter $\varepsilon^*_{\mathrm{hs2}}$ between a hydrophilic end particle (H2) and a solvent particle can be varied whereas the LJ interaction parameter $\varepsilon^*_{\mathrm{hs1}}$ between a hydrophilic end particle (H1) and a solvent particle is fixed constant.

The numerical integrations of the equations of motion for all particles are carried out using the velocity Verlet algorithm at constant temperature with a time step of 0.0005. We apply the periodic boundary conditions and the number density is set at 0.75. Initially, we prepare homogeneous bolaamphiphilic solutions at high temperature ($T^* = 10$) for various values of the amphiphilic

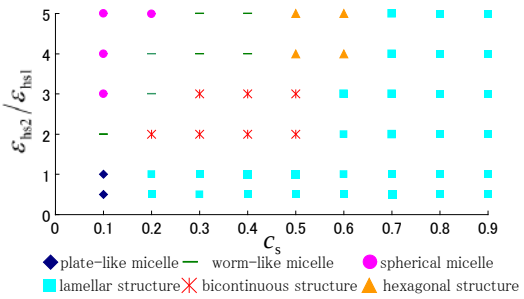

Fig. 1: $\varepsilon_{hs2}/\varepsilon_{hs1}$ vs c_s "phase diagram".

concentrations c_s and the LJ interaction parameters ε^*_{hs2}. The system is then quenched to $T^* = 1.3$ and MD simulations of 5.0×10^7 time steps are performed for each simulation run.

Our simulations show that various kinds of higher-order structures such as worm-like micelles, hexagonal structures and bicontinuous structures are obtained (Fig.1). We also clarified that, at low amphiphilic concentrations ($c_s = 0.1$), a plate-like micelle changes to worm-like micelles, and then to spherical micelles as the interaction parameter ε^*_{hs2} increases. At intermediate amphiphilic concentrations ($c_s = 0.5$), on the other hand, it is ascertained that the lamellar structure changes to the bicontinuous structure, and then to the worm-like or hexagonal structures as the interaction parameter ε^*_{hs2} increases.

References

[1] J. N. Israelachvili: *Intermolecular and Surface Forces*, 2nd ed. (Academic Press, London, 1992).

[2] *Micelles, Membranes, Microemulsions, and Monolayers*, edited by W. M. Gelbart, A. Ben-Shaul and D. Roux (Springer-Verlag, New York, 1994), pp. 1-104.

[3] I. W. Hamley: *Introduction to Soft Matter*, Rev. ed. (J. Wiley, ChichSester, 2007).

Phase Diagram of the Spin-1/2 Heisenberg Antiferromagnets on the Cairo-Pentagon Lattice

Makoto ISODA[1], Hiroki NAKANO[2], and Tõru SAKAI[2,3]
[1]*Department of Science Education, Faculty of Education, Kagawa University Takamatsu 760-8522*
[2] *Graduate School of Material Science, University of Hyogo, 3-2-1 Kouto, Kamigori-cho, Akou-gun, Hyogo 678-1297, Japan*
[3] *Japan Atomic Energy Agency, SPring-8, Sayo 679-5148, Japan*

Two-dimensional frustrated spin-1/2 Heisenberg antiferromagnet on the Cairo-pentagon lattice[1,2] is investigated by the numerical diagonalization method on the finite-size clusters up to 36 sites[3] with the periodic boundary condition. The lattice is constituted with the three-coordinated A-sites and the four-coordinated B-sites in the occupation ratio of 2 to 1. Hence the Heisenberg-type Hamiltonian requires two-types of nearest neighbor interactions, such as $J = J_{\rm AA}$ and $J' = J_{\rm AB}$, at least.

The magnetization under the magnetic field has been calculated. The so-called 1/3-plateau is observed for every value of $x \equiv J/J'$, with the exceptional narrow region around $x \sim 0.8$, where the plateau may vanish or survive with a narrow width in the thermodynamic limit. The magnetization jumps accompanying the change of the total spin $\Delta S_{\rm t} \geq 2$ are observed at the upper-field edge of the 1/3-plateau for $0 < x < 0.8$ and at the lower-field edge of the 1/3-plateau for $0.8 < x < 2.0$. Such jump in the isotropic spin system is peculiar and has been found in some spin frustrated systems. The mechanism is attributed to the spin flop transition under the isotropic spin system[3] and is confirmed by the drastic change in the correlation function as a function of x or the total magnetization m.

From the results of the magnetization process and the nn correlation functions for the longitudinal (z-axis) and the transverse components, the magnetic phase diagram was derived in the plane of $x - h/J$, where h is the magnetic field applied along the z-axis. The phase diagram is shown in Fig.1. The phase I is the disordered state, which emerges between the orthogonal dimer state at $x \gtrsim 0$ and the ferrimagnetic ordered state for $x \gtrsim 2.0$, under the absence of the magnetic field. The phases II and III are the 1/3-plateau states, which states are continued to each state at $x \sim 0$ and $x \gtrsim 2.0$, respectively. In the former phase, the 1/3-magnetization at $h = 0$ is attributed to the free 1/3 spins and in the latter phase, it is to the resultant ferrimagnetic magnetization.

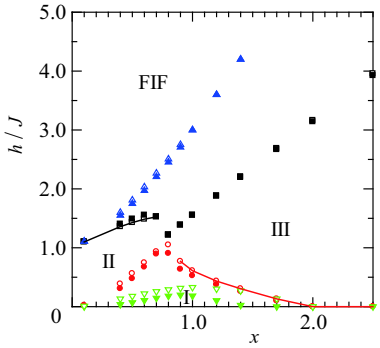

Fig. 1 The phase diagram under the magnetic field h. Reverse triangle, circle, square, and triangle denote the level-crossing field between the lowest energy state within the multiplet of $S_t = 0$ and $S_t = 1$ for the total spin S_t, the lower-field-edge (LFE) of the 1/3-plateau, the higher-field-edge (HFE) of the plateau, and the full polarization field, respectively. The solid and the vacant ones in those symbols denote data for the system sizes $N = 30$ and $N = 24$ systems, respectively. The phase FIF designates the field-induced ferromagnetic phases. The solid curves at the HFE of the phase II and the LFE of the phase III denote the regime of x where the magnetization jump of $\Delta S^z_{\rm t} \geqq 2$ emerges in the magnetization process, for the case of $N = 24$ as an example.

References

1) E. Ressouche et al.: Phys. Rev. Lett. **103** (2009) 267204.

2) I. Rousochatzakis et al.: Phys. Rev. B **85** (2012) 104415.

3) H. Nakano, M. Isoda, and T. Sakai: J. Phys. Soc. Jpn. **83** (2014) 053702.

3.5 CMSI projects

Nonadiabatic electron dynamics and many-body nuclear dynamics in molecules

Satoshi TAKAHASHI and Kazuo TAKATSUKA
Department of Basic Science, Graduate School of Arts and Sciences, University of Tokyo
Komaba, Meguro, Tokyo 153-8902

To understand the quantum effects of heavy particles (nuclei) in chemical reactions, it is necessary to track the wavepacket dynamics during the reaction. However, with the modern massive parallel computers, it is still prohibitive to perform a primitive fully-quantum wavepacket dynamics simulations, because the required amount of calculation grows exponentially with the number of degrees of freedom. To overcome such a situation, we have been continuing researches based on the action decomposed function (ADF) [1, 2].

In the theoretical framework of ADF, wavepacket dynamics is described in terms of an ensemble of classical trajectories. Starting from the fundamental equation of ADF, it is found that dynamics is decomposed into two terms. One is proved to represent geometrical change of small spatial region around the reference trajectory, and the other is the "diffusion operator" with a pure imaginary diffusion constant.

So far, our preliminary numerical studies have already shown that the geometrical change around the reference path is described well with the nearby running ones, and also that quantum effects are able to be well incorporated thereby. These facts provide a significant advantage for the calculations of real systems with many dimensions, because a reference trajectory is reused as a nearby for some other nearby paths.

Although we have not embarked on practical massive parallel computations based on this theory, we are going to make a start of many-body nuclear dynamics simulation, further proceeding to the connection to nonadiabatic electron dynamics. Numerical results successfully obtained for test systems are shown in Fig. 1.

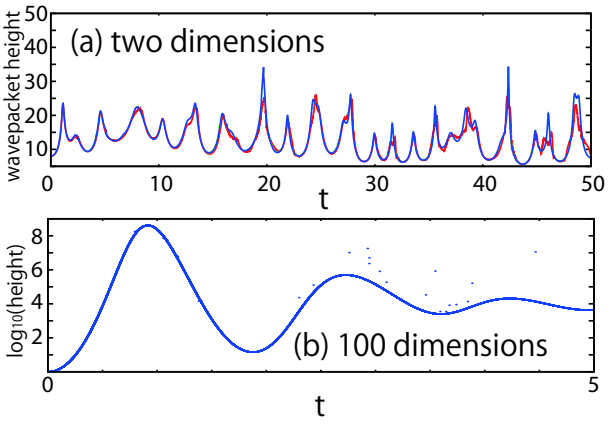

Figure 1: ADF wavepacket height carried on a classical trajectory. (a) For a two-dimensional system, it is confirmed that the ADF wavepacket component (blue) reproduces the fully-quantum result (red) very well. (b) ADF wavepacket calculation is applicable for a 100-dimensional test system.

References

[1] S. Takahashi and K. Takatsuka: Phys. Rev. A **89** (2014) 012108.

[2] K. Takatsuka and S. Takahashi: Phys. Rev. A **89** (2014) 012109.

Density-Matrix Renormalization Group Study of Effective Spin Models for Na_2IrO_3

Takami TOHYAMA*
Yukawa Institute for Theoretical Physics, Kyoto University
Kyoto 606-8502

The Kitaev-Heisenberg honeycomb lattice model has recently been proposed to describe magnetic properties in A_2IrO_3 (A= Na, Li). The model includes an isotropic Heisenberg term and strongly anisotropic Kitaev terms. The Kitaev terms give a spin-liquid ground state. With increasing the strength of Heisenberg coupling, the ground state firstly turns into a stripy antiferromagnetic phase and then into a Néel antiferromagnet. The x-ray and neutron scattering experiments indicated that the ground state of Na_2IrO_3 is most likely characterized by a zig-zag spin structure. However, this type of magnetic order cannot be explained theoretically by the Kitaev-Heisenberg model. It is necessary to introduce further neighbor Heisenberg couplings and/or trigonal distortion of the oxygen octahedra.

In this project, we have studied extended Kitaev-Heisenberg models including these additional terms by using two-dimensional density-matrix renormalization group method (2D-DMRG). Firstly, we have included the second- and third-neighbor Heisenberg exchange interactions into the Kitaev-Heisenberg model and examined the ground-state phase diagram by calculating spin-spin correlation functions. From a previous classical-spin calculation of the model, it has been reported that there appears a zig-zag phase at a region where the second- and third-neighbor exchange interactions are large. Similarly, our 2D-DMRG calculations up to 6x6 lattice with both cylindrical and periodic boundary conditions have shown the presence of the zig-zag phase. Overall phase diagram including stripy and Néel phases is also consistent with the classical-spin calculation. However, such a large value of the long-range exchange interactions might be unrealistic for A_2IrO_3.

We have also performed 2D-DMRG calculations for another extended Kitaev-Heisenberg mode proposed recently [1]. A zig-zag phase is found, being consistent with exact-diagonalization calculations [1]. This project is now in progress.

This works was done in collaboration with K. Shinjo and S. Sota.

参考文献

[1] Y. Yamaji, Y. Nomura, M. Kurita, R. Arita, and M. Imada: arXiv:1402.1030.

*Present Address: Department of Applied Physics, Tokyo University of Science, Tokyo 125-8585

Possibility of deconfined criticality in SU(N) Heisenberg models at small N *

Naoki KAWASHIMA
Institute for Solid State Physics, University of Tokyo
Kashiwa-no-ha, Kashiwa, Chiba 277-8581

The regular Heisenberg model, i.e., the SU(2) symmetric quantum spin model can be easily generalized to the SU(N) symmetry for arbitrary N by replacing the Pauli spin operators by SU(N) generators. Thus we obtain SU(N) Heisenberg model. While the ground state of this model is the Néel state for $N = 2$, as is well-known, its nature at higher values of N had not been known until 1989 when Read and Sachdev predicted the valence-bond solid state as the ground state. The numerical confirmation of this prediction did not follow immediately. Absence of the magnetic order, and spontaneous braking of the lattice-rotational symmetry were confirmed more than ten years later. Even then, there was a remaining question concerning the nature the pattern of the singlet-pair covering of the lattice; whether it is columnar, plaquette, zigzag, etc. The distribution function of the dimerization order parameter was almost circular symmetric, making the question hard to answer. This was due to the proximity to the quantum transition point at which $U(1)$ symmetry emerges. Concerning this model, there is another fundamental question regarding the nature of the quantum phase transition. While a field theory predicts a second order transition of a peculiar nature, a numerical study suggests the first order transition.

In the present study, we tried to solve this issue and carried out a series of quantum Monte Carlo simulations. We studied the SU(N) Heisenberg model with the four-body and six body interaction terms for the square lattice and the honeycomb lattice, respectively. The size of the system ranges from $L = 8$ to $L = 256$. For a limited size range, the finite-size scaling (FSS) works well and the resulting data collapse looked fine. However, we also discovered that depending upon the system sizes used in the FSS analysis, the resulting scaling exponents systematically drift. For example, the estimated exponent $y \equiv 1/\nu$ was $y \sim 1.5$ for $L = 8, 12, 16, 24$ whereas it was $y \sim 2.2$ for $L = 96, 128, 192, 256$, in the case of SU(3) model on the square lattice. The correlation decay exponent η_ψ was estimated as $\eta_\psi \sim 1.5$ for $L = 8, 12, 16, 24$ whereas it was $\eta_\psi \sim 1.2$ for $L = 96, 128, 192, 256$. From this observation, the apparent good scaling plots may not necessarily guarantee the 2nd order nature of the transition. On the other hand, if the transition is of the first order, the exponents should converge to $y \to 3$ and $\eta_\psi \to 0$, which are still far from what are actually observed in the numerical calculation.

Therefore, we must say that the true nature of the transition is still elusive and seems to demand even larger computation.

References

[1] K. Harada, T. Suzuki, T. Ohkubo, H. Matsuo, J. Lou, H. Watanabe, S. Todo and N. Kawashima: Physical Review B **88**, 220408(R) (2013).

*This report is based on a collaboration of [1].

Multi-scale simulation of nano-structured devices from electronic structures to mechanical properties

Shuji OGATA

Nagoya Institute of Technology

Gokiso-cho, Showa-ku, Nagoya 466-8555, Japan

In this fiscal year, we have treated two subjects. One is the Li-ion transfer mechanisms through the inteface between the solid-electrolyter interface (SEI) and liquid electrolyte in the Li-ion secondary battery (LIB) [1]. The other is the heat transfer mechanisims through the interface between the alumina-filler and polymer in a heat-dissipation material for high-power electronic devices [2].

The LIB is one of the most promising secondary batteries due to its higher energy density, high voltage, cycle performance, etc. The basic components of the electrolyte for the current LIB are ethylene carbonate (EC) for solvent and $LiPF_6$ for salt. The EC-based electrolytes are known to form a stable SEI on the graphite anode of the LIB in its first charging stage. The SEI transfers Li-ions but blocks electron current, and works to prevent further decomposition of the electrolyte. The SEI that is 10^1-10^2 nm in depth makes a major contribution to the overall resistivity in transferring Li-ions in the LIB. Despite the importance of the Li-ion transfer through the SEI, little is known about its microscopic mechanisms. Although the detailed composition of the SEI on the graphite anode depends on the settings and conditions of the electrolyte, the SEI is basically composed of inorganic solids (Li_2O, Li_2CO_3, LiF, etc.) and organic solids such as dilithium ethylene dicarbonate (Li_2EDC). The Li-ions are expected to diffuse through the relatively soft organic region.

We here investigate theoretically the microscopic mechanisms of the Li-ion transfer through the boundary between the SEI formed on the graphite anode and liquid electrolyte in the Li-ion battery [1]. A simulation system (about 2400 atoms) for the boundary is modeled using Li_2EDC, EC, and $LiPF_6$ for the SEI, solvent, and salt, respectively. After inserting Li-ions in the Li_2EDC region, we perform the first-principles molecular dynamics simulation for 4.8 ps using the divide-and-conquer-type real-space grid DFT code (DC-RGDFT) [3]. Enhanced stability of the Li-ions at the boundary where EDC^{2-} and EC contact with each other is thereby found in the runs without salt, which acts to impede the Li-ion transfer through the boundary. It is also found that inclusion of 1.0 M $LiPF_6$ salt in the liquid EC weakens such impedance effect significantly. Physical reasons for those phenomena are explained in combination with separate DFT calculations (see, Fig. 1)

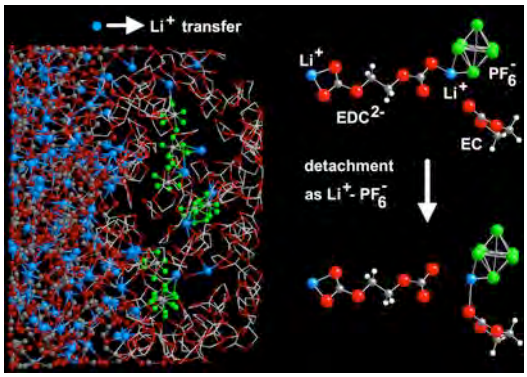

Fig. 1: (left) The snapshot at time 4.7 ps of the present DFT simulation run at 825 K. (right) The schemetic of the proposed mechanims for the ehnamcenet of the Li-ion tranfer rate between the SEI and EC liquid due the $LiPF_6$ salt.

The integrated circuit (IC)-utilized modular packaging of electronic components for automobiles has advanced remarkably in recent years. It is beneficial to automobiles not only for their compactness but also for reliability and functionality. Such modular packaging has been essential particularly for the electric and plug-in hybrid automobiles. Further improvement of the packaging toward higher densities is therefore desired. One of the important techniques that should be realized in developing the higher-density

packaging is efficient dissipation of intense heat generated locally, e.g., in a power IC. Heat-dissipation material for that purpose in the forms of adhesive and bulking agent needs be soft to cover an IC without gaps. Composite systems of soft polymers and hard filler-particles (called fillers) are often used for such heat-dissipation materials. The fillers, which are about 1-10 micrometer in size, are made of the materials with higher thermal conductivities than the polymers for enhanced effective thermal conductivity of the heat-dissipation material. For its application to IC's, the heat-dissipation material should be electrically insulating. Automobile-parts companies have been putting great effort to design a novel heat-dissipation material with a few times higher thermal conductivity than the current ones under the conditions that it is electrically insulating, durable, and low cost.

We here address the enhancement mechanisms of the heat conductance of the polymer-filler interfaces by adding the surface-coupling agent in such a polymer composite material through through the non-equilibrium molecular dynamics (MD) simulation. A simulation system is composed of alpha-alumina as the filler, bisphenol-A epoxy molecules as the polymers, and model molecules for the surface-coupling agent. The inter-atomic potential between the alpha-alumina and surface-coupling molecule, which is essential in the present MD simulation, is constructed to reproduce the calculated energies with the electronic density-functional theory. Through the non-equilibrium MD simulation runs, we find that the thermal resistance at the interface decreases significantly by increasing either number or lengths of the surface-coupling molecules and that the effective thermal conductivity of the system approaches to the theoretical value corresponding to zero thermal-resistance at the interface. Detailed analyses about the atomic configurations and local temperatures around the interface are performed to identify heat-transfer routes through the interface (see, Fig. 2).

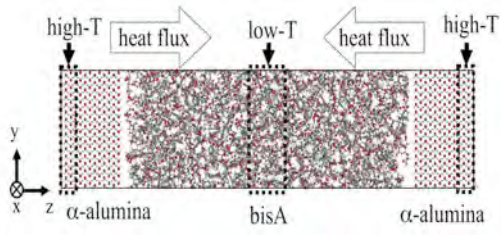

Fig. 2: Schematic of the atomic configuration of the present system with no surface-coupling molecule.

References

[1] S. Ogata, N. Ohba, and T. Kouno, J. Phys. Chem. C. 117 (2013) 17960-17968.
[2] K. Tanaka, S. Ogata, et al., J. Appl. Phys. 114 (2013) 193512-1-8.
[3] N. Ohba, S. Ogata, T. Kouno, et al., Comput. Phys. Commun. 183 (2012) 1664-1673.

Density Functional Study on Prediction of Electronic Properties of Nanostructures

Atsushi Oshiyama[1] and Tomoya Ono[2]
[1]*Department of Applied Physics, The University of Tokyo*
[2]*Department of Precision Science and Technology, Osaka University*

The aim of this project is to develop theoretical methodologies and computational techniques suitable for the current and future computer architectures, and apply thus obtained new schemes in order to clarify and predict properties of nanostructures on the basis of the quantum theory. The project is a part of research activities on "Next-generation Advanced Device Science" under Computational Materials Science Initiative (CMSI) conducted by MEXT, Japan. Currently four computational schemes are developed and tuned in this project: RSDFT (Real-Space Density-Functional-Theory) code, CONQUEST (Concurrent O(N) QUantum Electronic Simulation Technique) code, RSPACE (Real Space) code and RS-CPMD (Real Space Car-Parrinello Molecular Dynamics) code. The principal researchers to develop these four codes include Jun-ichi Iwata, Kazuyuki Uchida, Yasuteru Shigeta, Kenichi Koizumi and Shinnosuke Furuya for the RSDFT and RS-CPMD, Tsuyoshi Miyazaki, David Bowler for the CONQUEST, and Tomoya Ono for the RSPACE. We here report only a part of the achievements using RSDFT and RSPACE due to the limitation of the allotted length.

1. RSPACE: Electronic Structures and Magnetic Anisotropy Energies of Graphene with Adsorbed Transition-Metal Adatoms

Graphene has been one of the most promising candidates for future electronic and spintronic devices. Recent scanning tunneling microscopy experiment reported that it is possible to deposit single Fe, Co, or Ni adatom on graphene, tuning the electronic structures and realizing the spin texture of the graphene. The experiment pointed out that both the Fe and Co adatoms prefer an out-of-plane easy magnetization axis [1]. On the other hand, previous density functional theory studies suggested that the Co adatom exhibits an out-of-plane easy axis, whereas the Fe adatom exhibits an in-plane easy axis [2]. The number of theoretical studies is limited and do not provide sufficient results to discuss the problems in details. We study the electronic structures and magnetic anisotropy energies (MAEs) of graphene adsorbed with an Fe, Co, or Ni adatom in the presence of spin-orbit coupling (SOC).

The electronic band structures of graphene with adsorbed Fe, Co, and Ni adatoms in the absence of SOC are plotted in Fig. 1. The spin polarizations of Fe, Co, and Ni adatoms are 2.0, 1.0, and 0.0 μ_B, respectively. In the case of Ni adsorption, the Rashba effect is observed as a result of SOC with a **k**-dependent energy shift of π bands at the bottom of the Fermi surface (around -8.41 eV).

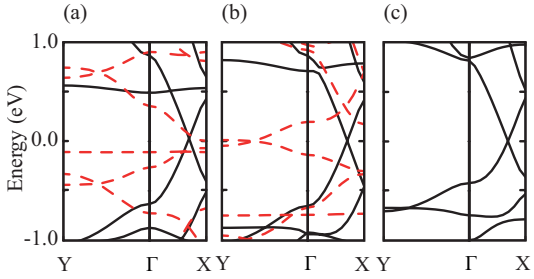

Figure 1: Band structures of graphene adsorbed with (a) Fe, (b) Co, and (c) Ni adatoms. The solid (dashed) curves indicates spin-up (spin-down) electronic bands. Zero energy is taken to be the Fermi level.

We found that the Fe adatom exhibits an in-plane easy axis with an MAE of 1.6 meV, in contradiction with the experimental result, and the Co adatom shows an out-of-plane easy magnetization axis with an MAE of 5.6 meV, in agreement with the experimental observation [1]. For Co adsorption, the E_1 orbitals, which contain d_{xz} and d_{yz} orbitals, are occupied leading to the out-of-plane easy axis of the Co adatom. The E_1 orbitals are unoccupied in the case of Fe adsorption, resulting in an in-plane easy axis.

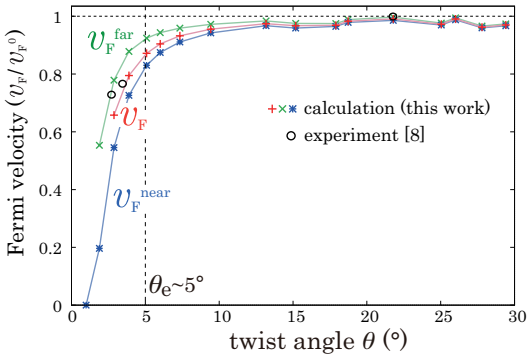

Figure 2: Fermi velocity normalized to the velocity of single layer graphene v_F^0, as a function of θ. The velocities in the optimized structures (v_F) and those for the flat structures with the interlayer distances of 3.61 Å (v_F^{far}) and 3.34 Å (v_F^{near}) are plotted.

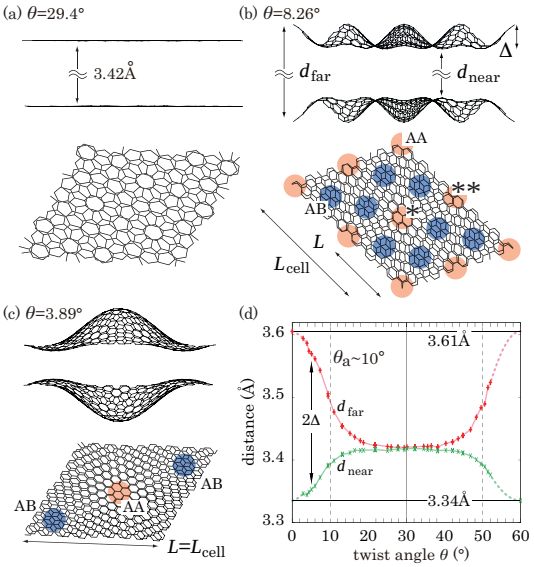

Figure 3: The side and top views of the total-energy optimized tBLG with the twist angle θ of (a) 29.4°, (b) 8.26°, and (c) 3.89°. In (b) and (c), the corrugation Δ is visible with the longest distance d_{far} and the shortest distance d_{near}. In (d), the distances d_{far} and d_{near} as functions of the twist angle θ are shown. The orange and blue circles in the top views in (b) and (c) depict the AA and AB stacking regions, respectively.

2. RSDFT: Electron Localization due to Moiré Patterns in Twisted Bilayer Graphenes

Interference of two waves causes rich phenomena in nature. Beat patterns in sounds and Moiré patterns in sights are commonly recognized in human life. In condensed matter, two periodicities in atomic arrangements slightly different to each other induce a Moiré pattern: *e.g.*, turbostratic stacking of surface layers of graphite leads to a Moiré pattern which is observed by scanning tunneling microscope (STM). How electron waves sense Moiré patterns of atomic arrangements is an intriguing issue which has never been pursued before.

Bilayer graphene (BLG) is produced by exfoliation of graphite or by heat treatments of SiC surfaces. Typical stacking of the two layers is either AB (Bernal) or AA. However, the two graphene layers are often twisted to each other in their basal planes. The two layers with a tiny twist angle θ generate a Moiré pattern with its period $L = \sqrt{3}d/(2\sin\frac{\theta}{2})$, where d is the C-C bond length.

The first-principles electronic-structure calculations for such twisted bilayer graphene (tBLG) have been regarded formidable: Even if we confine ourselves to tBLGs where the Moiré period L is commensurate with the period of SLG, the number of atoms in a unit cell increases tremendously with decreasing θ, reaching tens of thousands for $\theta \leq 1°$. We here apply our newly developed RSDFT code which has been optimized for current massively parallel multi-core supercomputers and enables us to perform the total-energy electronic-structure calculations for unprecedentedly large systems consisting of 10 - 100 thousands atoms in the density-functional theory (DFT).

We have found that there is a critical twist angle $\theta_e \sim 5°$ from either the AA or the AB stacking, below which the Fermi velocity v_F decreases dramatically toward zero to cause flat bands at the Fermi level E_F [Fig.2]. This v_F reduction is a consequence of localization of electrons sensing the Moiré patterns in tBLGs. We have also found that the two graphene layers are corrugated below another critical angle $\theta_a \sim 10°$ [Fig.3]. The two critical angles θ_e and θ_a are *unequal* to each other, reflecting the difference in the sensitivity to the Moiré pattern between the electron waves near E_F and the valence-electron density in the honeycomb lattice which decides the atomic structure.

References

[1] T. Eelbo *el al.*, PRL **110**, 136804 (2013).
[2] M. Sargolzaei and F. Gudarzi, JAP **110**, 064303 (2011).
[3] K. Uchida, Z.-X. Guo, J.-I. Iwata and A. Oshiyama, Proc. JSAP-MRS Joint Symposia **1595**, 1190 (2013).

Materials design for spintronics/multiferroics applications

Mineo SAITO, Tasuki, ODA and Fumiyuki ISHII

Institute of Science and Technology,

Kanazawa University, Kakuma, Kanazawa, 920-1192 Japan

In this project, we have developed codes which enable the study of spintronics and multiferroics materials. We have developed a program code of newly parallelized density functional electronic structure calculations (CPVO). We also made a program that enables drawing spin textures by using numerical results which are calculated by using the OpenMX code (Fig. 1). This program is useful to analyze the results of fully-relativistic density functional theory calculations.

We study the electronic structures of ZnO which is a hopeful material for spintronics application. We analyze the lowest conduction band. We find the Rashba rotation near the conduction band bottom (Fig. 1). When the biaxial strain is introduced, the drection of the Rashba rotation can be reversed. We study the cases of tensile stress (ε_{xx}=4%) and compressive one (ε_{xx}=-4%).

To find the mechanism of the inversed Rashba effect、 we calculate the electric polalization of the bulk ZnO. We find that the directions of the electric field in the cases of the tensile and compressive stresses are different (Fig. 2). This opposite direction of the electric field is the origin of the inversed Rashba effect. We expect that an effective spin filter is achieved by using the above mentioned inversed Rashba effect [1].

We also investigate the stable atomic structures of Tl-adsorbed surface of Tl/Si(111); Tl1/3/Tl/Si(111). For the system, the adsorbed Tl has four typical sites; T4, H3, bridge, and T1 models. After the atomic structure optimizations, the T4 model, in which there exist three nearest neighbors between the adsorbed and substrate Tl atoms, is found to be the most stable. According to our calculation, the bridge model is also comparably stable as the T4 model. The realistic surface configuration can be verified by experimental observation.

For the T4 model, the electronic structure is investigated. Fig, 3 shows the band dispersion curves in Tl1/3/Tl/Si(111) and those in Tl/Si(111) along the symmetry lines of 1st Brillouin zone. The dispersion curves which indicate folding characters are of Tl1/3/Tl/Si(111). The important result is that just below the Fermi level at K-bar point, there is the p-orbital component which comes from the Tl atoms in the 2nd layer of system. This means that the absorbed Tl atom provides electrons to the conduction band where the spin-polarization

is induced by the spin-orbit interaction in Tl atoms. This spin-polarization is found to be along the vertical direction of surface both in experimental and theoretical approaches [2]. These properties in the electronic structure may imply that such surface like Tl1/3/Tl/Si(111) is available for spintronics applications.

References

[1] M. A. Adhib, H. Kotaka, F. Ishii, and M. Saito: Appl. Phys. Exp. 7 (2014) 053002.

[2]K. Sakamoto et al.: Nat. Commun 4 (2013) 2073.

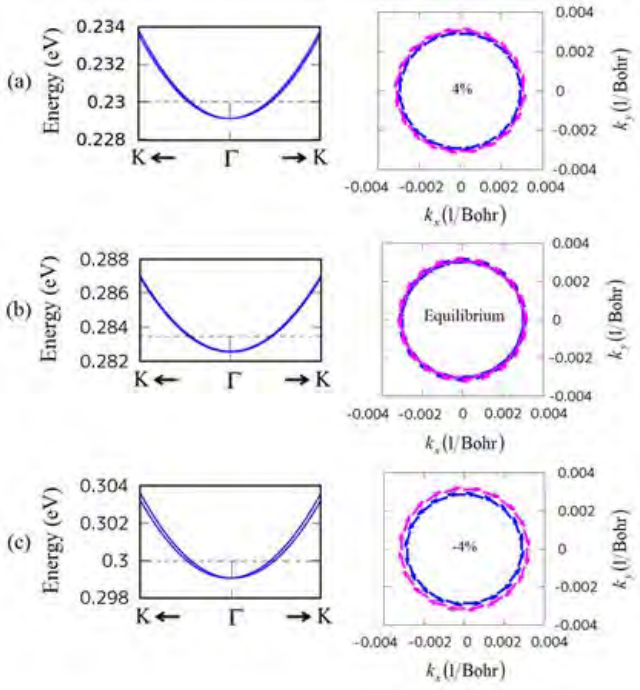

Fig. 1: Lowest conduction bands and spin textures of ZnO.

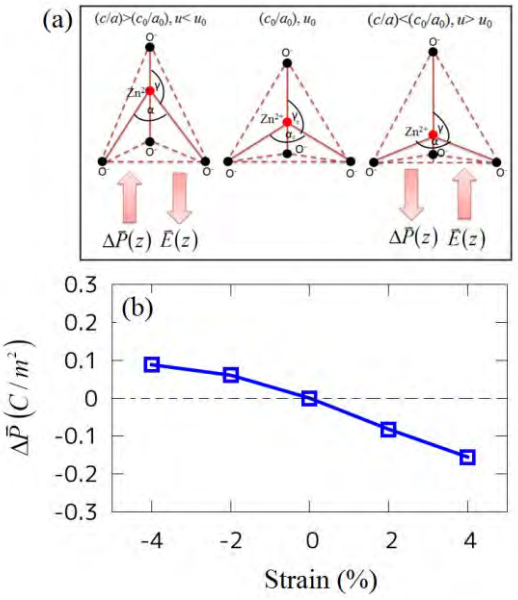

Fig. 2: Electric polarization of ZnO.

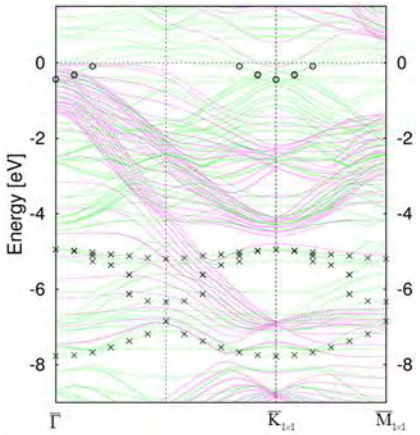

Fig. 3: Band dispersion curves in Tl1/3/Tl/Si(111) (dotted red) and in Tl/Si(111)(broken green). The circle symbols indicate the p-orbital component and the crosses s-orbital on the Tl atoms in the 2nd layer.

Large-scale molecular dynamics calculation study of viruses

Susumu Okazaki

Department Applied Chemistry,

Nagoya University, Furo-cho, Chikusa-ku, Nagoya, 437-8603

In the initial stage of infection, virus is recognized by a receptor. This causes entry of the virus into the cell by endocytosis mechanism. Then, the virus is uncoated and releases the RNA. In this study, in order to investigate the interaction between the poliovirus capsid and the receptor, all-atom molecular dynamics (MD) simulation has been performed for the system consisting of poliovirus capsid, the receptor (CD155-D1D2 domain), and aqueous electrolyte solution. To our knowledge, this is the first calculation to investigate the virus infection at a molecular level by using MD calculations. Then, CHARMM force field with CMAP for proteins and TIP3P model for water are used. The fast multi-pole method (FMM) combined with Ewald method is used to evaluate long-ranged Coulomb interaction. The total number of atom in the box is over ten million (see Fig.1).

The distance r between the virus capsid and CD155-D1D2 was fixed at several r. The calculations have been performed using our highly parallelized general-purpose molecular dynamics simulation program for large-scale systems,,MODYLAS [1]. Then, the calculated mean forces and free energy profile of binding of the virus capsid to the receptor as a function of r between their centers of mass are obtained. The calculations showed that attraction interaction works between the virus capsid and the receptor in aqueous electrolyte solution in spite of the same negative sign of the total net charge of each capsid and receptor.

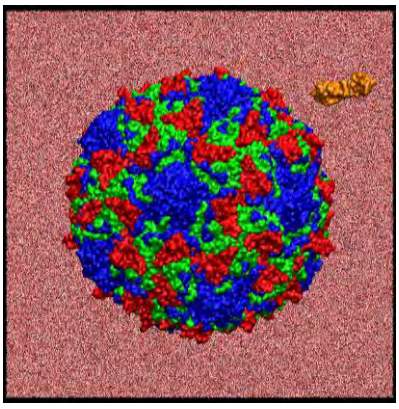

Fig.1 A snapshot of a poliovirus capsid particle (blue, red, and green represent VP1, VP2, and VP3 proteins) and D1 and D2 domains of the CD155 receptor (brown) in solution.

References

[1] Y. Andoh, N. Yoshii, K. Fujimoto, K. Mizutani, H. Kojima, A. Yamada, S. Okazaki, K. Kawaguchi, H. Nagao, K. Iwahashi, F. Mizutani, K. Minami, S. Ichikawa, H. Komatsu, S. Ishizuki, Y. Takeda, and M. Fukushima, *J. Chem. Theory Comput.*, **9**, 3201 (2013)

Theoretical simulation of thermoelectric figure of merit ZT of organic composite materials and nanostructured materials

Yoshihiro ASAI, Hisao NAKAMURA, and Marius E BÜRKLE
Nanosystem Research Institute, AIST
Umezono 1-1-1, Central 2, Tsukuba 305-8568

In our group, non-equilibrium transport theories of electron and phonon have been studied and developed, some of which have been extended with first principle density functional methods. While the theory has been tested for some models representing nanostructured/molecular junctions, it has been applied for various channel materials including bulk thin films as well. In this FY, we have focused our attentions to thermoelectric properties of organic materials.

The basic start point of our theory comes from the previous theory treating electron and phonon currents including the coupling between them. [1-5] The low energy transport physics such like the local heating effect and the temperature dependent conductance has been discussed thereby. Based on this background, we studied organic thermoelectric materials in this FY. We have studied the problem without taking into account the electron-phonon coupling for simplicity, in order to make parallel discussions with the standard linear response theory familiar in the condensed matter physics textbooks, which do not include the coupling effect.

Firstly, we studied the general conditions requisite for large values of the thermoelectric figure of merit ZT.[6] We have used a single chain tight-binding model bridging the two semi-infinite electrodes defined on the cubic lattice and have explored various values of the energy gap $\Delta E=E_F-\varepsilon$ where E_F is the Fermi energy of the electrode and ε is the atomic site energy. Along with the figure of merit ZT, Z_eT which is defined by $ZT=Z_eT[1/(1+\kappa_{ph}/\kappa_e)]$where κ_{ph} and κ_e represent phonon and electron heat conductance, was also examined. Z_eT gives the upper limit of ZT realized only when κ_{ph} is 0. The result summarized in Fig.1 indicates that ZT and Z_eT get enhanced when the Fermi energy comes close to the "band edge" of the single chain. Another important information is that ZT is largely reduced from Z_eT due to the finite value of κ_{ph}.

The formalism used for the model calculation has been converted to first principle methods. We have developed first principle density functional codes to calculate the phonon transport. Thermoelectric properties of molecular junctions with small single molecules and organometallic thin films have been investigated so far. In Fig.2., ZT of organometallic multilayers is shown. In this case only,[7] we simplified the phonon transport calculation using a rigid body approximation for the multilayer to reduce the computational cost for this system size. Because of the finite layer size effect, the Seebeck coefficient can change its sign as we increase temperature leading to the zero value of ZT at around $T=220K$ in the case of the Ruthenium complex with the layer size $L=3$. We found a strong metallic atom dependence on the magnitude of ZT, however. Fully systematic first principle calculations of the phonon heat conductance and ZT have been made a lot for a series of single molecular junctions, which will be published soon as well as phonon-phonon scattering effects significant at high temperature.

Electric heat transported to the source (S) and the drain (D) electrodes were analyzed both theoretically and experimentally.[8] The nanoscale thermocouple integrated scanning tunneling probes (NTISTPs) were used for the experimental analysis. The asymmetry in the heat transported to the S and the D electrode denoted by Q_S and Q_D is found and is shown in terms of the $Q_S(V)$ vs $Q_{Total}(V)=Q_S(V)+Q_D(V)$ plot. In the case of symmetry, i.e., $Q_S(V)=Q_D(V)$ or $Q_{S,D}(V)=Q_{S,D}(-V)$,

the slope of the plot should be 0.5. Deviations from 0.5 indicate the asymmetry, which depend on the bias voltage V. Both experimental and theoretical results indicate the asymmetry in quantitative agreement each other. The asymmetry comes from the electron-hole asymmetry and then depends on the sign of the Seebeck coefficient.

Not only for single molecular junction, but also for high-K hafnium oxide thin films exhibiting the resistive random access memory (ReRAM) behavior have been investigated in terms of the first principle transport calculations.[9,10] The success demonstrate that the usefulness of the theory for both academic and industrial researches.

REFERENCES

[1] Y. Asai, *Nonequilibrium phonon effects on transport properties through atomic and molecular bridge junctions*, **Phys. Rev. B** 78, 045434-1-24 (2008).

[2] Y. Asai, *Theory of inelastic electric current through single molecule*, **Phys. Rev. Lett**. 93, 246102-1-4 (2004).

[3] Y. Asai, *Theory of local heating in single molecular bridge junctions*, **Phys. Rev. B**, 84, 085436-1-7 (2011).

[4] Y. Asai, *Theory of zero-bias anomaly in low-temperature inelastic tunneling spectroscopy*, **Phys. Rev. B** 86, 201405(R)-1-4 (2012): **Rapid Communications**.

[5] S. K. Lee, R. Yamada, S. Tanaka, G.S. Chang, Y. Asai, and H. Tada, *Universal Temperature Crossover Behavior of Electrical Conductance in a Single Oligothiophene Molecular Wire*, **ACS Nano**, 6, 5078-5082 (2012).

[6] Y. Asai, *Length and energy gap dependences of thermoelectricity in nanostructured junctions*, **J. Phys. Cond. Matt.** 25, 155305-1-5 (2013).

[7] H. Nakamura, T. Ohto, T. Ishida, and Y. Asai, *Thermoelectric Efficiency of Organometallic Complex Wires via Quantum Resonance Effect and Long-Range Electric Transport Property*, **J. Am. Chem. Soc.** 135, 16545−16552 (2013).

[8] L.A. Zotti, M. Bürkle, F. Pauly, W. Lee, K. Kim, W. Jeong, Y. Asai, P. Reddy and J.C. Cuevas, *Heat dissipation and its relation to thermopower in single-molecule junctions*, **New J. Phys.** 16, 015004-1-25 (2014).

[9] T. Hines, I. Díez-Pérez, H. Nakamura, T. Shimazaki, Y. Asai and NJ Tao, *Controlling Formation of Single-Molecule Junctions by Electrochemical Reduction of Diazonium Terminal Groups*, **J. Am. Chem. Soc.** 135, 3319−3322 (2013): **Communication**.

[10]T. Miyazaki, H. Nakamura, K. Nishio, H. Shima, H. Akinaga, and Y. Asai, *First-Principles Transport Modeling for Metal/Insulator/Metal Structures*, JPS Conf. Proc. 012075 (2014).

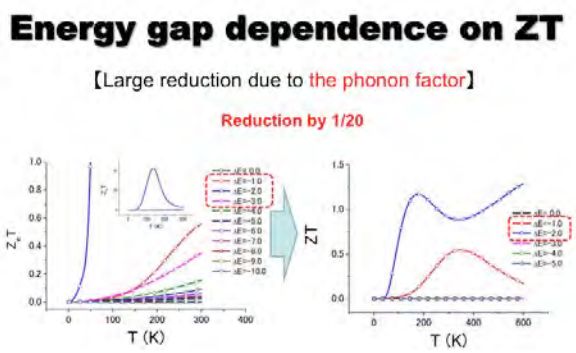

Fig. 1. The energy gap (ΔE) and the temperature dependences on Z_eT and ZT. When E_F comes close to the "band edge", Z_eT and ZT get enhanced. ZT is largely reduced about by a factor of 1/20 due to the finite phonon heat conductance κ_{ph}.

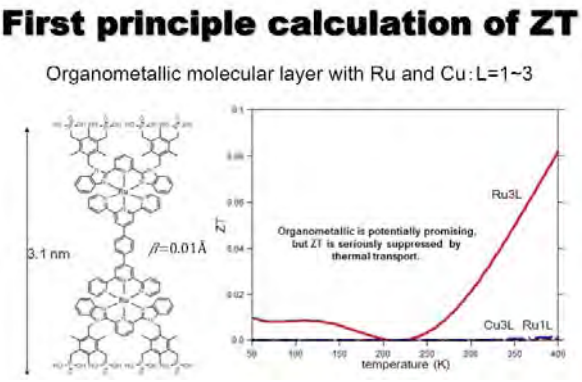

Fig. 2. First principle calculation results of ZT for a class of organometallic multilayers. There clearly is a layer size (L) dependence. The result also depends strongly on central metals, i.e., larger value of ZT is obtained for Ru but not for Cu.

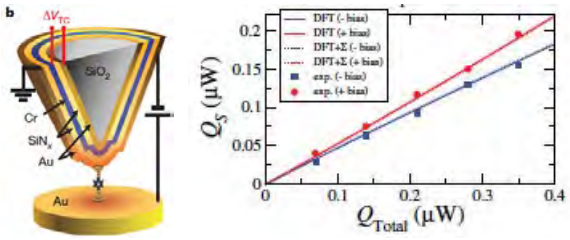

Fig. 3. Collaboration between first principle theory and experiment using the NTISTP shows asymmetry in electric heat transported to the electrodes, which well correlates with the sign of the Seebeck coefficient.

Large scale calculations on the fundamental processes of solar cells and their optimization in conversion efficiency and long lifetime

Koichi Yamashita

Department of Chemical System Engineering,

The University of Tokyo, Hongo, Bunkyo-ku, Tokyo 113-8656

1. Density functional based molecular dynamics study on redox potential of $Cu^{2+/+}$ and $I^{0/-}$ in non-aqueous solution

The redox potential calculation using density functional based molecular dynamics simulation (DFT-MD) have been applied and revealed the changes of solvent coordinations of redox reaction in aqueous solution. The method is now applicable to directly compare experimentally observed redox potentials with the help of reference electrode calculation[1]. We establish the calculation method of redox potentials in non-aqueous solution, especially aprotic solvent for understanding and predicting the efficient organic synthesis and devices related electrochemistry because aqueous solution is mere one of solutions.

All the thermodynamic integral method were performed by using CP2K software package. The dummy / proton atom, $I^{0/-}$ or $Cu^{2+/1+}$ were immersed in 44 explicit acetonitrile molecules under periodic boundary condition. The side length of cubic unit cell is 15.74 Å and is determined to reproduce the experimentally observed density of AN solution (0.786 g cm^{-1}) for 45 AN molecules system. All quantum chemical calculations were performed with PBE functional, DZVP-MOLOPT-GTH basis set, Goedecker-Teter-Hutter type potential and 280 Ry for cutoff energy of the finest grid level under Gaussian and plane wave mixed basis method (QUICKSTEP). The MD simulations were performed for 6 ps after equilibrium to determine the constraint parameters of dummy atom and for 2.0 ps for each electronic state .

The calculated redox potential of $I^{0/-}$ and $Cu^{2+/+}$ in AN are in good agreement with experiments[2,3]. The redox potential calculated by using linear response is also good approximation for $I^{0/-}$ half reaction in AN because the solvation structure is almost same except for the range $r < 4$ Å. On the other hand, the radial distribution functions from Cu atom show that acetonitrile molecules strongly solvate both $Cu^{2+/+}$ ions. The solvation numbers of acetonitrile molecule for Cu^{2+} and Cu^{+} are 5 and 4 in DFT-based MD simulation. This change of coordination number in AN is smaller than that in

aqueous solution but affects the redox potential to stray from linear response regime.

2. Theoretical investigations on the structure and the charge transfer state (CTS) of poly-3-hexyl thiophene / phenyl-C61-butyric acid methyl ester (PCBM/P3HT) as organic photovoltaic (OPV) cells

Recently, there are many studies about organic photovoltaic (OPV) cells that are expected to be used as energy conversion materials from the solar energy to electric energy. Because the OPV cells are thin-film, they are expected to be printed on various soft commodities Moreover, OPV can be made at low temperatures, about 420 K. So, OPVs enable to decrease the production cost. Up to present, many candidates to realize these features are introduced. Especially, PCBM/P3HT complex is thought as one of the most promising materials of OPV cells from the viewpoint of conversion efficiency. In this study, therefore, we investigated the structure of the interfaces of PCBM/P3HT complex and charge transfer states (CTs) that act as first key state in the course of energy conversion processes.

First, we obtained stable structures consisting of a few PCBMs and a P3HT with DFT-D method. Then, CTs of these structures are investigated with constrained DFT and time-dependent DFT implemented. All calculations were carried NWChem code. In detail settings, B3LYP/6-31G* was used in the usual DFT and constrained DFT. CAM-B3LYP/6-31G* was used in the excited state calculation.

After we had investigated the stable structure and structural relaxation caused by the charge migration, we analyzed the lifetime of the CTs by the Marcus theory. From results of these calculations, we concluded that the lifetime of charge transfer state becomes longer by structural relaxation due to the charge migration. To make sure of this estimation, we investigated same calculation in interfaces of one PCBM and one MEH-PPV. As a result, we obtained the common feature.

3. Parallelization of a new open source software for excited state dynamics.

We are developing a new open source software for electronic-excited-state-dynamics based on semiempirical quantum calculations, which is named as MolDS[4]. Especially, The Molds aims to simulate electronic nonadiabatic dynamics in the energy conversion processes. By using the System C, the MolDS was hyper-parallelized with openMP & MPI.

References

[1] M. Sulpizi, M. Sprik: Phys. Chem. Chem. Phys. **10** (2008) 5238.

[2] X. Wang, D. M. Stanbury: Inorg.Chem. **45** (2006) 3415

[3] J. K. Senne, B. Kratochvil: Anal.Chem. **44 (**1972) 585

[4] MolDS is distributed through: http://en.sourceforge.jp/projects/molds/

Particle catalysis and nano-scale fluctuation

Osamu SUGINO

Institute for Solid State Physics,

The University of Tokyo, Kashiwa-no-ha, Kashiwa, Chiba 277-8581

Nano-particles have been attracting attention because of their enhanced activity, but its origin has not been well understood. The enhanced activity has often been attributed to the larger surface/bulk ratio and the existence of many steps and apexes, but here we point out that the solvent fluctuation plays an important role [1].

Effect of the solvent fluctuation was investigated using the first-principles molecular dynamics (FPMD) simulation combined with the effective screening medium (ESM) [2, 3]. The investigation was done first for a planar platinum/water interface, which was modeled using a slab geometry. The solvent fluctuation was found to affect the interface dipole and thus the interface potential drop, and importantly, the fluctuation of the potential was found to occur faithfully as expected from the Marcus theory. The theory is based on the simple argument on the polarization of the solvent, such that the electronic polarization is assumed to occur adiabatically and the geometric polarization occurs much slower causing therefore the fluctuation of potential.

The fluctuation is stronger as the surface area is made smaller relative to the thickness of the solvent. The situation corresponds to reducing the size of the particle; the fluctuation is enhanced more as the size is reduced.

The Marcus theory was then combined with the Butler-Volmer equation to see an effect on the exchange current, i.e., an index of the catalytic activity. The exchange current i was found to have a large size effect: i for a nano-particle of diameter 3 nm is 15 times larger than that for infinite diameter (the bulk catalyst). This enhancement factor is indeed a large value which is comparable to (or larger than) the one achieved by the nano-shell method, i.e., a technique to enhance the activity by alloying the subsurface Pt. We expect the fluctuation effect as found here may be used to explain the known discrepancy between the experiments and existing theories.

In addition to this topic [1], we have also done several activities regarding the fuel-cell research. We have polished up the FPMD-ESM code to make the simulation more robust and efficient when run in the massively parallel supercomputers. Using this code, we have continued to study in detail the oxygen reduction (oxidation) reaction at the stepped Pt surface, which is considered as a key to identifying the reaction center of Pt. We have also done another

activity to combine the simulation results with the most recent experimental data. By this hybrid theoretical and experimental study, we have excluded several important candidates for the oxygen reduction reaction pathways, thus considerably narrowing the possibility [4]. The ESM method has also been improved at the interface between the solution and the continuum region [3], so that the simulation can be robustly done at the constant potential conditions [5]. Establishing a microscopic theory for electrochemistry is a challenging theme, but to that aim, we have made important advances in this fiscal year.

References

[1] N. Bonnet, O. Sugino, and M. Otani, J. Chem. Phys. 140 044703 (2014).

[2] M. Otani and O. Sugino, Phys. Rev. B 73, 115407 (2006).

[3] I. Hamada, O. Sugino, N. Bonnet, and M. Otani, Phys. Rev. B 88 155427 (2013).

[4] N. Bonnet, O. Sugino, and M. Otani, *submitted.*

[5] N. Bonnet, T. Morishita, O. Sugino, and M. Otani, Phys. Rev. Lett. 109, 266101 (2012)

Massively Parallel Implementation of 3D-RISM Calculation with Volumetric 3D-FFT

Norio YOSHIDA

Department of Chemistry, Graduate School of Sciences,

Kyushu University, 6-10-1, Hakozaki, Higashi-ku, Fukuoka 812-8581

We have developed a new computational algorithm for solving the three-dimensional reference interaction site model (3D-RISM) theory for massively parallel machines and test it on the RIKEN K supercomputer and the supercomputer of the Institute for Solid State Physics, University of Tokyo.[1] The computational time and speedup of the calculation are improved by introducing the MPI/OpenMP hybrid parallelization with the volumetric 3D-FFT.[2] The program achieves good parallelization on hundreds of thousands of CPU cores with good scalability on the RIKEN K supercomputer.

To show the efficiency of the new program, the oligomerization process of the chymotrypsin inhibitor 2 in solution has been considered as a example. The massive parallel implementation realized the analysis for extra-large biological systems, because the numerous 3D-RISM calculations of each sampled monomer and oligomer structure with fine and large grid were required. Although our results of the analysis shown here were still preliminary, qualitative agreements with the previous calculations was observed, and the efficiency of the program was successfully demonstrated.

References

[1] Y. Maruyama, N. Yoshida, H. Tadano, D. Takahashi, M. Sato, F. Hirata, J. Comput. Chem., ***In Press***. DOI: 10.1002/jcc.23619

[2] D. Takahashi, in Proceedings of the 8th International Conference on Parallel Processing and Applied Mathematics (PPAM 2009), Part I, Workshop on Memory Issues on Multi- and Manycore Platforms, Lecture Notes in Computer Science, Wroclaw, Poland, Sept 13-16, 2009; R. Wyrzykowski, J. Dongarra, K. Karczewski, J. Wasniewski, Eds.; Springer-Verlag: Berlin Heidelberg, 2010.; FFTE: A Fast Fourier Transform Package, http://www.ffte.jp (accessed March 11, 2014).

All electron spectra and dynamics of functional materials from nanoclusters to crystals

Kaoru OHNO
Department of Physics, Yokohama National University
Tokiwadai, Hodogaya-ku, Yokohama 240-8501

It is well known that local density approximation or generalized gradient approximation in density functional theory signi cantly underestimates the energy band gap. In contrast, *GW* approximation on the basis of many-body perturbation theory provides reliable results compared to hybrid method and is highly desirable. It is our aim to calculate XPS, UPS spectra, impurity levels, photoabsorption spectra, Auger spectra, and so on of molecules, clusters, and crystals such as TiO_2 by using all-electron *GW* approach and solving the Bethe–Salpeter equation systematically.

In this theme, we use our all-electron mixed basis code, TOMBO, which expresses quasiparticle wave functions as the linear combination of numerical atomic orbitals (AOs) and plane waves (PWs); see Figure 1. This is an unique and purely original rst-principles program, which can describe all electrons from core to free electrons of both isolated and periodic (crystal) systems as complete eigenstates of quasiparticle Hamiltonian and enables us to calculate various spectra of electronic excited states by using *GW* approximation and solving the Bethe–Salpeter equation. The program is hybrid parallelized both with MPI and OpenMP. The parallel e ciency of the *GW* + Bethe–Salpeter part is excellent.

In this scal year, we ported in our latest crystal version of TOMBO (1) Conjugate gradient + RMM-DIIS + Davidson iterative diagonalization, (2) Broyden charge mixing, and (3) Broyden structural relaxation routines

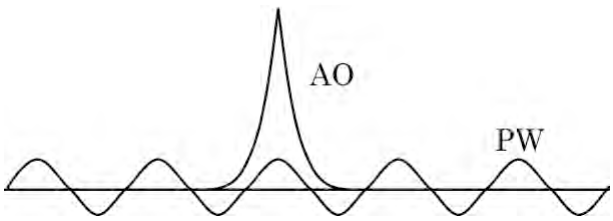

Figure 1: All-electron mixed basis representation of quasiparticle wave functions.

from an earlier di erent simple-cubic version of TOMBO developed by Prof. Marcel Sluiter (Delft Univ. of Tech.) in our group. This was done by the support (supplementary budget) from CMSI. We also accelerated the code by introducing (4) Fitting of self-consistent potentials inside atomic spheres by means of the Chebyshev polynomial and (5) Approximate optimization of 3D $\leftrightarrow$ 2D Fourier transformation for inclined unit cells. We have used System C (Fujitsu FX10) at the Institute for Solid State Physics of the University of Tokyo mainly for the debugging procedures and test runs of this new version of TOMBO in these implementations.

Already more than 18 years have past since the rst development of the all-electron mixed basis code by ourselves, now the code is having variety of useful routines and still being improved. The LDA part of this latest version of TOMBO is planed to be open to the public, although the schedule is delayed because Ohno was hospitalized with illness during December 2013 to March 2014.

Direct molecular dynamics simulation of electrocaloric effect in ferroelectrics

Takeshi Nishimatsu
Institute for Materials Research (IMR), Tohoku University, Sendai 980-8577, Japan

The electrocaloric effect (ECE) is an adiabatic change in the temperature, ΔT, of a material upon applying an external electric field. In particular, if an electric field is applied to a ferroelectric material at just above its phase transition temperature, $T_{\rm C}$, and the field is then removed, a large reduction in temperature is expected. It is widely believed that this effect is applicable to solid-state refrigeration.

Recent developments in the techniques of vapor deposition enable the production of defect-free single-crystal ferroelectric thin films. Such high-quality films allow for the application of large external electric fields, which cannot be applied to bulk polycrystalline specimens. Consequently, this advance in processing allows for investigation of the ECE in these ferroelectric thin films.

There have been several computational simulations of the ECE published in the literature. Ponomareva and Lisenkov have investigated the ECE of $Ba_{0.5}Sr_{0.5}TiO_3$ using Monte Carlo methods[1]. Rose and Cohen[2] have used molecular dynamics (MD) simulations and core-shell interatomic potentials to model the ECE in bulk $LiNbO_3$. Also using this form of atomic potential, Chen and Fang[3] have simulated the ECE in $BaTiO_3$ nanoparticles.

Here, we present a method to calculate the ECE directly by molecular dynamics simulations[4].

The effective Hamiltonian, constructed from first-principles calculations, and used in the present MD simulations is essentially the same as that in Refs. [5, 6]

$$\begin{aligned} H^{\rm eff} = & \frac{M^*_{\rm dipole}}{2}\sum_{\boldsymbol{R},\alpha}\dot{u}^2_\alpha(\boldsymbol{R}) + \frac{M^*_{\rm acoustic}}{2}\sum_{\boldsymbol{R},\alpha}\dot{w}^2_\alpha(\boldsymbol{R}) \\ & + V^{\rm self}(\{\boldsymbol{u}\}) + V^{\rm dpl}(\{\boldsymbol{u}\}) + V^{\rm short}(\{\boldsymbol{u}\}) \\ & + V^{\rm elas,\,homo}(\eta_1,\ldots,\eta_6) + V^{\rm elas,\,inho}(\{\boldsymbol{w}\}) \\ & + V^{\rm coup,\,homo}(\{\boldsymbol{u}\},\eta_1,\ldots,\eta_6) + V^{\rm coup,\,inho}(\{\boldsymbol{u}\},\{\boldsymbol{w}\}) \\ & - Z^*\sum_{\boldsymbol{R}}\boldsymbol{\mathcal{E}}\cdot\boldsymbol{u}(\boldsymbol{R})\ . \quad (1) \end{aligned}$$

The true atomic structure has properties determined by the complex chemical bonding between the atoms, but in the model system the complexity is reduced; the collective atomic motion is coarse-grained by local soft mode vectors, $\boldsymbol{u}(\boldsymbol{R})$, and local acoustic displacement vectors, $\boldsymbol{w}(\boldsymbol{R})$, of each unit cell located at $\boldsymbol{R}$ in a simulation supercell. Each term in the Hamiltonian is described in Ref. [6].

The procedure to estimate ΔT involves two steps: first constant-temperature MD is performed for a fixed external electric field, $\mathcal{E}$, in the canonical ensemble using the velocity-scaling thermostat. This allows the system to equilibriate. Next, the external electric field is switched off and the system is simultaneously changed to a constant-energy MD in the micro-canonical ensemble that is allowed to evolve using the leapfrog method. The final state at the end of the constant-temperature MD is used as the initial state of the constant energy MD. All MD simulations are performed with our original `feram` software. `feram` is distributed freely under the GNU General Public License (GPL) and can be found at `http://loto.sourceforge.net/feram/` .

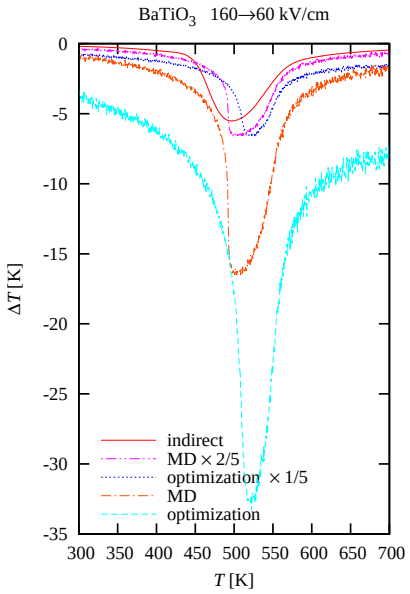

Figure 1: A comparison of the three MD methods to simulate the ECE. The temperature dependence of the ECE ΔT of $BaTiO_3$ is plotted versus ambient temperature for switching the applied external electric field from 160 to 60 kV/cm in the [001] direction.

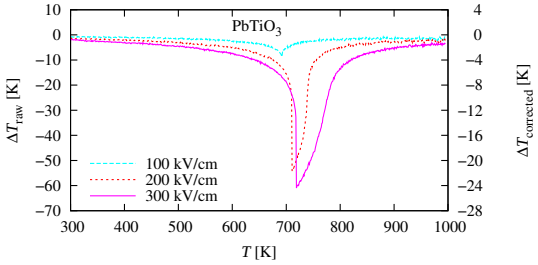

Figure 2: The temperature dependence of ΔT for $PbTiO_3$. There is an ordinate for both the raw data ΔT and for the corrected data $\Delta T_{\mathrm{corrected}} = \frac{2}{5}\Delta T$ that accounts for the underestimated specific heat capacity.

The ECE response is calculated using the *indirect* method[7], *direct MD* method, and *direct optimized* method and are compared in Fig. 1. The values of ΔT, corrected for the underestimated heat capacity in the *direct* methods, are also given in the figure. More detailed results are described in Ref. [4].

In Fig. 2, the temperature dependence for the ECE ΔT of $PbTiO_3$, under various initial external electric fields is compared.

References

[1] I. Ponomareva and S. Lisenkov: Phys. Rev. Lett. **108** (2012) 167604.

[2] M. C. Rose and R. E. Cohen: Phys. Rev. Lett. **109** (2012) 187604.

[3] X. Chen and C. Fang: Physica B: Condensed Matter **415** (2013) 14 .

[4] T. Nishimatsu, J. A. Barr and S. P. Beckman: J. Phys. Soc. Jpn. **82** (2013) 114605.

[5] U. V. Waghmare and K. M. Rabe: Phys. Rev. B **55** (1997) 6161.

[6] T. Nishimatsu, U. V. Waghmare, Y. Kawazoe and D. Vanderbilt: Phys. Rev. B **78** (2008) 104104.

[7] S. P. Beckman, L. F. Wan, J. A. Barr and T. Nishimatsu: Materials Letters **89** (2012) 254.

Structure Formation of Surfactant Membranes under Shear Flow

Hayato SHIBA
Institute for Solid State Physics, University of Tokyo
Kashiwa-no-ha, Kashiwa, Chiba 277-8581

We have been developing simulation of non-ionic surfactant membrane assemblies to reveal the mechanism of formation of onion structures that have been observed in the experiments for more than 20 years[1]. To realize simulations of such multi-layered systems, a highly coarse-grained model is necessary. In this project, we adopt the meshless membrane model, forming a monolayer surface representing bilayer membranes exhibiting bending rigidity and other standard membrane properties. The size of each particle corresponds to the membrane thickness *i.e.* around 10 nanometers, and simulation of a large number of particles can represent a membrane system with many layers. I have simulated as many as one million membrane and solvent particles that can contain 30 layers of the membranes. Their rolling up instability has been found out in agreement with the experiment. Please see our invited article in this Activity Report and Refs. [2, 3] for details.

While we could successfully reproduce the instability experimentally observed on the course of onion formation, the final onion structure could not be reproduced. One of the reasons can be attributed to the short of system size. In the experiments, diameters of the onion structures typically exceed 10 μm, and thus, they are composed of at least 100 layers. To realize this order of system size, the simulation size should be made far larger to sub-billion particles scale, with the use of superparallel computers.

I have been continuing our efforts to develop our code, bringing optimization on the SPARC processors into view. The performance of our code has turned out to be less than 5% compared with the theoretical peak FLOPS at the bottleneck (*i.e.* force calculation part) on System C. Since optimization by the C++ compiler has turned out to be quite unreasonable, I have asked for consultation through CMSI in last September. The support staff has promised to work on improvement of the compiler to achieve the same performance as FORTRAN for standard two-body force calculation. Howevr, I have not received the result from them as of May 2014. Improvement on the performance of our code is still going on.

References

[1] O. Diat, D. Roux, and F. Nallet, J. Phys. II France **3** (1993) 1427.

[2] H. Shiba, H. Noguchi, and G. Gompper, J. Chem. Phys. **139** (2013) 014702.

[3] H. Shiba and H. Noguchi, Ensemble (Bulletin of Molecular Simulation Society of Japan) **16**-1 (2014) 59.

Computational-Science Study of Frustrated Magnets

Hiroki NAKANO
Graduate School of Material Science, University of Hyogo
3-2-1 Kouto, Kamigori-cho, Ako-gun, Hyogo 678-1297, Japan

It is well known that a quantum spin system is a typical many-body problem that is di cult to be investigated. Computational approaches are quite useful to study it. Among them, however, quantum Monte Carlo method faces with a so-called negative sign problem when a system includes frustrations in it. Density matrix renormalization group method is a powerful to a one-dimensional system; on the other hand, the application to systems in dimensions larger than one is now under developing. When one wants to study a two-dimensional frustrated magnet, therefore, numerical-diagonalization method is a reliable way although this method can treat only very small systems. Under circumstances, we developed an MPI-parallelized code of numerical diagonalizations based on the Lanczos algorithm[1]; thereby, we can treat systems that are as large as possible beyond limitations determined by computer resources when a user carries out calculations in a single node.

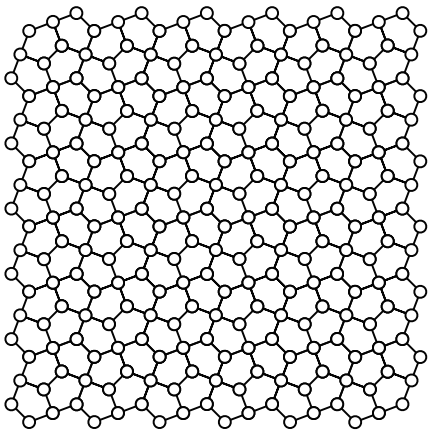

Figure 1: Cairo-pentagon lattice

The primary study of the present project is to clarify the behavior of the Heisenberg antiferromagnet on the Cairo-pentagon lattice[2] by means of the Lanczos-diagonalization code mentioned in the above. The Cairo-pentagon lattice is illustrated in Fig. 1. A noticeable feature is that the lattice is composed of only pentagons although the pentagons are not regular polygons. There are two kinds of vertices in this lattice: one is the vertices with the coordination number $z = 3$ and the other is the vertices with $z = 4$. From the two kinds of vertices, the system includes two kinds of antiferromagnetic interactions. We study the magnetization process of this model when the ratio of the two interactions is tuned; we focus our attention on the behavior around $m/m_{\rm s} = 1/3$, where m and $m_{\rm s}$ denote the magnetization and its saturation, respectively. We nd that a magnetization plateau appears at $m/m_{\rm s} = 1/3$ and that there exist two regions where the states at $m/m_{\rm s} = 1/3$ show properties that are di erent from each other. The boundary between the two regions is about 0.78. We clarify that the plateau is accompanied by a magnetization jump on one side among the edges and that which side the jump appears depends on the ratio. The behavior is related to the occurrence of the spin- op phenomenon, which is similar to the case of the Heisenberg antiferromagnet on the square-kagome lattice[3].

References

[1] H. Nakano and A. Terai: J. Phys. Soc. Jpn. **78**, 014003 (2009).

[2] H. Nakano, M. Isoda, and T. Sakai: J. Phys. Soc. Jpn. **83**, 053702 (2014).

[3] H. Nakano and T. Sakai: J. Phys. Soc. Jpn. **82**, 083709 (2013).

First-principles electronic structure calculation of permanent magnets using the screened KKR Green's function method

Shotaro DOI
Institute for Solid State Physics, University of Tokyo
Kashiwa-no-ha, Kashiwa, Chiba 277-8581

The KKR Green's function method is a method for first-principles electronic structure calculations. In this method, instead of solving eigenvalue problems as in most of band calculation codes, Green's function of the Kohn-Sham equation is directly calculated. By taking the imaginary part of the Green's function, we can obtain the electron density very accurately and efficiently.

The Green's function is calculated from that of an arbitrary reference system by solving the Dyson-type equation. In the process of solving the Dyson equation, inversions of matrices of a dimension proportional to N (N: the number of atoms in a unit-cell) is required. In the usual KKR method, the free space is chosen as the reference system. When N becomes large, the computational cost increases drastically. This is because $O(N^3)$ operations are required to invert a $N \times N$ matrix. To overcome this difficulty, the concept of screened KKR was proposed. In the screened KKR method, a system with repulsive muffin-tin potentials of a constant height is chosen as the reference system. In this reference system, the Green's function decays exponentially in real-space if the energy range is sufficiently lower than the repulsive potential height. Then we can ignore long range propagations without sacrificing the accuracy. In this case, the matrix that we must invert becomes sparse. Therefore, one can expect large improvement of the calculational efficiency by use of an efficient sparse matrix solver. This technique has been mainly applied to the multilayered systems which extend to only one dimensional direction assuming two-dimensional periodicity. For such systems, the matrix becomes block tridiagonal and the computational cost is exactly proportional to the layer thickness.

It is desirable to apply the screened KKR technique to more general and complex systems which extend to all three dimensional directions. For such general large super-cells, we must treat general non-Hermitian block sparse matrices. As a sparse matrix solver, the iterative method, which is often used to solve linear simultaneous equations with sparse coefficient matrices, is more efficient than the direct method such as the LU-factorization. This algorithm is also suitable for the parallel computing.

We developed a full-potential based screened KKR code which can treat such large super-cells by combining the iterative method for solving the Dyson equation with parallel computing techniques [**?**]. Through the test calculations, it was shown that our code is reliable and well parallelized w.r.t the number of atoms in the super-cell. we also confirmed that our code runs on the FX10 computer without any trouble. By the use of our code, it is possible to execute the all-electron level first-principles electronic structure calculations for super-cells which include thousands of atoms within a reasonable time. Our code should be useful for our research project: Elements Strategy Initiative Center for Magnetic Materials(ESICMM).

References

[1] S. Doi *et al*: J. Phys.: Conf. Ser. **454** (2013) 012019.

Ordering in frustrated spin systems

Tsuyoshi Okubo
Institute for Solid State Physics, University of Tokyo
Kashiwa-no-ha, Kashiwa, Chiba 277-8581

Several two-dimensional frustrated Heisenberg spin systems have a topologically stable point defect, a Z_2 vortex. About 30 years ago it was proposed that a thermodynamic phase transition driven by binding-unbinding of the Z_2 vortices occurred at a finite temperature $T = T_v$ [1]. In constast to the case of the Kosterliz-Thoulses transion in two dimensional XY spin systems, the Z_2 vortex transition occurs keeping the spin correlation length finite.

The ordering of Z_2-vortices has been studied mainly on the triangular lattice Heisenberg AF. Although recent Monte Carlo simulation up to $L = 1536$ has suggested the occurrence of Z_2 vortex transition at a finite temperature, the existence of "true" phase transition has not been resolved because the spin correlation length at the estimated transition temperature was longer than the system size. In order to clarify the nature of the Z_2 vortex transition through numerical simulations, we need larger system beyond the spin correlation length.

In order to perform larger scale Monte Carlo simulation, we consider an effective *non-frustrated* $SO(3)$ model of two-dimensional frustrated Heisenberg magnets. The Hamiltonian of the model is give by

$$\mathcal{H} = -\frac{J}{4}\sum_{\langle i,j\rangle} \mathrm{Tr} R_i R_j^t \qquad (J > 0), \quad (1)$$

where R_i is a $SO(3)$ rotation matrix on the site i, and $\sum_{\langle i,j\rangle}$ means the sum over the nearest-neighbor pairs. Although this effective model does not have frustrated interactions, it has a topological Z_2 vortex similar to the frustrated magnets.

We have implemented parrallelized Wolff-Swendsen-Wang type cluster algorithm and parformed an extensive Monte Carlo simulation of the model. The lattice is a $L \times L$ *square lattice* with periodic boundary conditions. By extrapolating an characteristic temperatures of the volticitly modulus to the thermodynamic limit, we estimate the Z_2 vortex transition temperature as $T_v/J \simeq 0.275$. However, because the spin correlation length at T_v is estimated about from 5000 to 10000 lattice spacings, the presetnt system size $L = 4096$ is too small to conclude the presence of true phase transition. In order to have the conclusive evidence of the Z_2 vortex transition, we need larger system such as $L = 8192$ or $L = 16384$.

References

[1] H. Kawamura and S. Miyashita: J. Phys. Soc. Jpn. **53** (1984) 4138.

[2] H. Kawamura, A. Yamamoto, and T. Okubo: J. Phys. Soc. Jpn. **79** (2010) 023701.

Search for New Structures and Functions of Nano-sized Molecules

Kazuya Ishimura

Theoretical and Computational Chemistry Initiative,

Institute for Molecular Science, 38 Nishigo-Naka, Myodaiji, Okazaki 444-8585

Recent super computers consist of a huge number of CPU cores and nodes, and high performance parallel algorithms and programs are necessary to use such computers efficiently. The development of a new quantum chemistry program started with MPI and OpenMP for inter- and intra-node parallelization in 2012. Geometry optimization calculations are significant to analyze and predict molecular structures and functions. Therefore, a parallel program for energy gradient calculations is developed in this study.

Based on the parallel algorithm [1] for Hartree-Fock energy calculations, an MPI/OpenMP parallel algorithm for DFT energy gradient calculations is developed. The calculation for the derivative terms of two-electron integrals is the most time-consuming step, and the algorithm is shown in Fig. 1.

```
!$OMP parallel do reduction(+:gradient)
do μ=n, 1, -1  <--- Distribution by OpenMP
 do ν=1, μ
  λstart=mod(μ*(μ+1)/2+ν+mpi_rank,nproc)+1
  do λ=λstart, μ ,nproc  <--- Distribution by MPI
   do σ=1, λ
     Calculation of derivative of 2e-integrals
     (μν|λσ) +Add them into gradient array
   enddo
  enddo
 enddo
enddo
call mpi_allreduce(gradient)
```

Fig. 1: Parallel Algorithm for Derivative Terms of Two-Electron Integrals.

CPU and parallel performances of the program were analyzed with FUJITSU FX10 and its profiler. The source codes were modified according to the profiler data.

DFT energy gradient calculations were performed on the K Computer with $C_{150}H_{30}$ (cc-pVDZ basis, 2250 functions). The speed-up is almost linear even on 16384 CPU cores as shown in Table 1. It is now practical to calculate geometries and functions of nano-sized molecules.

Table 1: Elapsed Time (sec) and Speed-up (in parentheses) for DFT Energy Gradient Terms.

# of Cores	1024	8192	16384
One-electron term	60.0 (1024.0)	7.9 (7777.2)	4.2 (14628.6)
Two-electron term	342.0 (1024.0)	42.9 (8163.4)	21.3 (16441.7)
Total	402.0 (1024.0)	50.8 (8103.3)	25.5 (16143.1)

References

[1] K. Ishimura, K. Kuramoto, Y. Ikuta, S. Hyodo, J Chem. Theory Comput. **6**, 1075 (2010).

4 PUBLICATION LIST

Example:

LASTNAME, Firstname [project class; # points (A), # points (B), # points (C)] (Page #)

— *Project title*

1. First paper
   Names of Authors, etc.
2. Second paper
   ...

□ ISSP Joint Research Projects

ADACHI, Takahiro [C class; 10000 (A), 500 (B), 500 (C)] ()
— *Heat Transfer Characteristics of Condensate Film Flow along Vertical Plates with Microscopic Grooves*

AKAGI, Kazuto [C class; 0 (A), 6000 (B), 1500 (C)] (93)
— *Microscopic understanding of electric double layer at solid-liquid interfaces*

AMEZAWA, Koji [C class; 0 (A), 1500 (B), 0 (C)] (126)
— *First principles calculation on defect structures in mixed conducting Perovskite oxides*

ANDO, Yasunobu [E class; 0 (A), 5500 (B), 1800 (C)] (95)
— *Study on material search and electrode interfaces for next-generation secondary batteries*

AOKI, Hideo [C class; 0 (A), 5000 (B), 0 (C)] (154)
— *Numerical study of various phases and non-equilibrium phase transitions in correlated electron systems*

1. Supersolid states in a spin system — phase diagram and collective excitations
   Yuta Murakami, Takashi Oka and Hideo Aoki: Phys. Rev. B **88** (2013) 224404.
2. Ordered phases in the Holstein-Hubbard model: Interplay of strong Coulomb interaction and electron-phonon coupling
   Yuta Murakami, Philipp Werner, Naoto Tsuji, and Hideo Aoki: Phys. Rev. B **88** (2013) 125126.
3. Nonequilibrium dynamical mean-field theory and its applications
   Hideo Aoki, Naoto Tsuji, Martin Eckstein, Marcus Kollar, Takashi Oka, and Philipp Werner: Rev. Mod. Phys. (2014), to be published (arXiv:1310.5329).

ARAKI, Takeaki [B class; 800 (A), 700 (B), 0 (C)] (236)
— *Conformations of polymer chains in nematic liquid crystals*

1. Defect science and engineering of liquid crystals under geometrical frustration
   Takeaki Araki, Francesca Serrab and Hajime Tanaka: Soft Matter **9** (2013) 8107.
2. Electro-osmotic flow of semidilute polyelectrolyte solutions
   Yuki Uematsu and Takeaki Araki: J. Chem. Phys. **139**, (2013) 094901.

EGAMI, Yoshiyuki [C class; 0 (A), 2000 (B), 2500 (C)] (120)
— *Development and application of first-principles electron-transport simulators for massively parallel computer*

1. First-Principles Study on Dynamic Electron-Transport Property through Low Dimensional System
   Y. Egami and K. Hirose: JPS Conf. Proc. **1** (2014) 016012.
2. Ballistic electron transport through nanostructure junctions from a real-space finite-difference

approach
S. Tsukamoto, T. Ono and Y. Egami: Quantum Matter, in press.

3. First-principles calculation method for electron transport based on grid Lippmann-Schwinger equation
Y. Egami, S. Tsukamoto, T. Ono and K. Hirose: submitted to Phys. Rev. B.

FEDERICI, Filippo [C class; 0 (A), 5000 (B), 0 (C)] ()
— *Molecular Dynamics study of frictional properties of confined ionic liquids*

FUCHIZAKI, Kazuhiro [C class; 22000 (A), 5000 (B), 0 (C)] (179)
— *Slow Dynamical Processes in Nonequilibrium Metastable States*

1. Predicting the Thermodynamic Properties of the Modified Lennard-Jones Fluid from the Lennard-Jones Equation of State
K. Fuchizaki and Y. Asano: J. Phys. Soc. Jpn. **82** (2013) 124001.
2. Melting behavior of SnI_4 reexamined
K. Fuchizaki: J. Chem. Phys. **139** (2013) 244503.
3. Modified Benedict–Webb–Rubin Equation of State for the Modified Lennard-Jones Fluid
Y. Asano and K. Fuchizaki: J. Phys. Soc. Jpn. **83** (2014) 034601.

FUJII, Hitoshi [C class; 0 (A), 2000 (B), 700 (C)] ()
— *First-principles calculations of X-ray absorption spectroscopy for Transition-Metal Oxides*

FUJIMOTO, Yoshitaka [C class; 11500 (A), 0 (B), 0 (C)] (79)
— *Effects of doping on atomic structures and electronic properties of nanocarbon materials*

1. Electronic structures of carbon-doped hexagonal boron nitride sheet: A density-functional study
Y. Fujimoto, T. Koretsune and S. Saito: JPS Conference Proceedings **1**, 012066 (2014)
2. Hydrogen adsorption and anomalous electronic properties of nitrogen-doped graphene
Y. Fujimoto and S. Saito: Journal of Applied Physics, Accepted.
3. Pyridine-Type Defects in Graphene: Stability, Reactivity and Electronic Property
Y. Fujimoto: Advances in Materials Science Research (Nova Science Publishers, New York), Submitted.
4. Electronic structures of hexagonal boron-nitride monolayer: strain-induced effects
Y. Fujimoto, T. Koretsune, and S. Saito: Journal of the Ceramic Society of Japan, Accepted.

FUJIWARA, Susumu [B class; 0 (A), 600 (B), 0 (C)] (250)
— *Molecular Simulation Study of Supramolecular Structure Formation by Amphiphilic Molecules*

1. Shape transition of micelles in amphiphilic solution: A molecular dynamics study
S. Fujiwara, M. Hashimoto, T. Itoh, H. Nakamura and Y. Tamura: J. Phys.: Conf. Ser. **454** (2013) 012024.
2. Nucleation and polymorphism of trans-1,4-polyisoprene containing copper phthalocyanine
T. Tsuboi, M. Harada, K. Ishii, S. Fujiwara and T. Itoh: Polymer J. **45** (2013) 915-920.
3. One-, Two-, and Three-Dimensional Hopping Dynamics
K. M. Aoki, S. Fujiwara, K. Sogo, S. Ohnishi and T. Yamamoto: Crystals **3** (2013) 315-332.
4. Molecular Dynamics Simulations of One-, Two-, Three-dimensional Hopping Dynamics
K. M. Aoki, S. Fujiwara, K. Sogo, S. Ohnishi and T. Yamamoto: JPS Conf. Proc. **1** (2014) 012038.
5. Molecular Dynamics Simulation of Micellar Shape Transition in Amphiphilic Solution
S. Fujiwara, M. Hashimoto, Y. Tamura, H. Nakamura and R. Horiuchi: Plasma Fusion Res., in press.

FUJIWARA, Takeo [C class; 3500 (A), 3500 (B), 0 (C)] (97)
— *Expansion of the first principle electronic structure calculation with hybrid method*

1. Nanoseconds Quantum Molecular Dynamics Simulations of Lithium Superionic Conductor $Li_{4-x}Ge_{1-x}P_xS_4$
Shinya Nishino, Takeo Fujiwara and Hisatsugu Yamasaki, submitted to Phys. Rev. B.
2. Parametrization scheme with accuracy and transferability for tight-binding electronic structure

calculations with extended Hückel approximation and molecular dynamics simulations
S. Nishino and T. Fujiwara, J. Molecular Modelling. Vol.19, 2363-2373 (2013).

FUKUI, Ken-ichi [E class; 0 (A), 9500 (B), 2900 (C)] (72)
— *First-principles calculation of electrochemical properties of redox-active monolayers*
— *Counter-ion effects of First-principles calculation of electrochemical properties*

FURUKAWA, Akira [C class; 13500 (A), 5000 (B), 2000 (C)] (184)
— *Nonequilibrium dynamics of complex colloidal suspension*

1. Simple picture of the supercooled liquid dynamics: Dynamic scaling and phenomenology based on clusters
   A. Furukawa: Phys. Rev. E **87** (2013) 062321.
2. Nonequilibrium critical Casimir interactions
   A. Furukawa, A. Gambassi, S. Dietrich, and H. Tanaka: Phys. Rev. Lett. **111** (2013) 055701.
3. Activity-induced clustering in model dumb-bell swimmers:
   The role of hydrodynamic interactions
   A. Furukawa, D. Marrenduzo, and M.E. Cates: submitted to Phys. Rev. E

FUSEYA, Yuki [B class; 1500 (A), 0 (B), 0 (C)] (166)
— *Theory of dynamical spin fluctuation in iron-based superconductors*

GOHDA, Yoshihiro [C class; 0 (A), 5000 (B), 2200 (C)] (96)
— *Itinerant electronic states at rare-earth-magnet interfaces*

1. Strain effects on the magnetic anisotropy of $Y_2Fe_{14}B$ examined by first-principles calculations
   Z. Torbatian, T. Ozaki, S. Tsuneyuki, and Y. Gohda: Appl. Phys. Lett., in press.

HARADA, KENJI [C class; 2500 (A), 5500 (B), 2700 (C)] (198)
— *Numerical study of quantum liquid phase using tensor network variational method*

1. Symmetry-protected topological order and negative-sign problem for SO(N) bilinear-biquadratic chains
   Kouichi Okunishi and Kenji Harada, Physical Review B **89**, 134422 (2014).

HAMADA, Ikutaro [C class; 8000 (A), 0 (B), 0 (C)] (91)
— *Density functional theory study of stability and dynamics of metal nanoclusters on a silicon surface*

HATSUGAI, Yasuhiro [C class; 10000 (A), 3000 (B), 2000 (C)] (145)
— *Numerical study of topological order*

1. Characterization of Dimers in Graphene Flakes
   D. Seki, Y. Hamamoto and Y. Hatsugai, JPS Conf. Proc. 1, 012068 (2014).
2. Sharp Zero-Energy Landau Levels in Multilayer Graphene
   H. Sakamoto, Y. Hatsugai, H. Aoki and T. Kawarabayashi, JPS Conf. Proc. 1, 012069 (2014).
3. Emergence of Topologically Stable Dirac Dispersions in a Fermionic Shastry-Sutherland Model
   T. Kariyado and Y. Hatsugai, JPS Conf. Proc. 1, 012001 (2014).
4. Symmetry-protected quantization and bulk-edge correspondence of massless Dirac fermions: Application to the fermionic Shastry-Sutherland model
   T. Kariyado and Y. Hatsugai, Phys. Rev. B 88, 245126 (2013).
5. Chiral symmetry and fermion doubling in the zero-mode Landau levels of massless Dirac fermions with disorder
   T. Kawarabayash1, T. Honda, H. Aoki and Yasuhiro Hatsugai, AIP Conf. Proc. 1566, 283 (2013).
6. Spin-resolved chiral condensate as a spin-unpolarized quantum Hall state in graphene
   Y. Hamamoto, T. Kawarabayashi, H. Aoki and Y. Hatsugai, Phys. Rev. B 88, 195141 (2013).
7. Chiral Symmetry and Many-Body Effect in Multilayer Graphene
   Y. Hatsugai; Y. Hamamoto; H. Aoki; T. Kawarabayashi, J. Phys. Conf. Ser. 456, 012013 (2013).
8. Stability of zero-mode Landau levels in bilayer graphene against disorder in the presence of the trigonal warping

T. Kawarabayashi, Y. Hatsugai and H. Aoki, J. Phys. Conf. Ser. 456, 012020 (2103).

9. Symmetry Protected Weak Topological Phases in a Superlattice
   T. Fukui, K.-I. Imura and Y. Hatsugai, Journal of the Physical Society of Japan 82, 073708 (2013).

HATTORI, Kazumasa [C class; 0 (A), 1500 (B), 0 (C)] (165)
— *Anomalous transport properties induced by Fermi surfaces variations*

HATTORI, Ken [B class; 1400 (A), 0 (B), 0 (C)] (127)
— *Model calculations in Si surfaces with adsorbates*

HIDA, Kazuo [B class; 800 (A), 700 (B), 0 (C)] (233)
— *Numerical Study of One Dimensional Frustrated Quantum Spin Systems*

1. Ground-State Phase Diagram of S=2 Heisenberg Chains with Alternating Single-Site Anisotropy
   K. Hida: J. Phys. Soc. Jpn. **83** (2014) 034707.
2. Topological Phases of the Spin-1/2 Ferromagnetic-Antiferromagnetic Alternating Heisenberg Chain with Frustrated Next-Nearest-Neighbour Interaction
   K. Hida, K. Takano, and H. Suzuki: J. Phys. Soc. Jpn. **82** (2013) 064703

HIRAI, Kunitomo [B class; 0 (A), 400 (B), 500 (C)] (135)
— *Electronic State and Proximity Effects around Interface in Layered Superlattices*

HIROSE, Kenji [C class; 2000 (A), 1500 (B), 800 (C)] ()
— *Multi-Scale Electric and Thermal Transport Calculations*

HOSHI, Takeo [E class; 0 (A), 16000 (B), 2300 (C)] (15)
— *Parallelized ultra-large-scale electronic-structure theory based on first principle calculation and novel numerical method*

HOSHINO, Shintaro [B class; 0 (A), 800 (B), 0 (C)] (169)
— *Quantum Monte Carlo Approach to Odd-Frequency Superconductivity*

1. Anisotropic Magnetic Response in Kondo Lattice with Antiferromagnetic Order
   Taku Kikuchi, Shintaro Hoshino and Yoshio Kuramoto: arXiv:1404.5718 (2014)
2. Composite Orders and Lifshitz Transition of Heavy Electrons
   Shintaro Hoshino and Yoshio Kuramoto: arXiv:1403.5634, to appear in J. Phys. Soc. Jpn. (2014)
3. Superconductivity of Composite Particles in a Two-Channel Kondo Lattice
   Shintaro Hoshino and Yoshio Kuramoto: Phys. Rev. Lett. **112** (2014) 167204
4. Strong Quasi-Particle Renormalizations in Heavy-Electron Magnets
   Shintaro Hoshino and Yoshio Kuramoto: to appear in JPS Conference Proceedings (2014)
5. Continuous-Time Quantum Monte Carlo Study of Strong Coupling Superconductivity in Holstein-Hubbard Model
   Satoshi Yamazaki, Shintaro Hoshino and Yoshio Kuramoto: to appear in JPS Conference Proceedings (2014)
6. Itinerant Versus Localized Heavy-Electron Magnetism
   Shintaro Hoshino and Yoshio Kuramoto: Phys. Rev. Lett. **111** (2013) 026401

HOTTA, Takashi [C class; 13500 (A), 0 (B), 0 (C)] (148)
— *Research for superconductivity in strongly correlated multi-orbital systems*

1. Key role of hybridization between actinide 5f and oxygen 2p orbitals for electronic structure of actinide dioxides
   Yu Hasegawa, Takahiro Maehira and Takashi Hotta: J. Mod. Phys. **4** (2013)1574-1582.
2. Kondo effect emerging from a spin-vibronic state
   Takahiro Fuse and Takashi Hotta: J. Phys.: Conf. Ser. **428** (2013) 012013.
3. Fermi-Surface Topology and Superconductivity Induced by Jahn-Teller Phonons
   Yuji Shiba and Takashi Hotta: J. Phys.: Conf. Ser. **428** (2013) 012038.
4. Electric Dipolar Susceptibility of the Anderson-Holstein Model

Takahiro Fuse and Takashi Hotta: J. Korean Phys. Soc. **62** (2013) 1874.

HUKUSHIMA, Koji [C class; 1500 (A), 11000 (B), 2300 (C)] (190)
— *Equilibrium simulations in spin glasses*

1. Dynamics of One-Dimensional Ising Model without Detailed Balance Condition
   Y. Sakai and K. Hukushima: J. Phys. Soc.Jpn **82** (2013) 064003-1-15
2. A List Referring Monte-Carlo Method for Lattice Glass Models
   M.Sasaki and K. Hukushima: J. Phys. Soc.Jpn **82** (2013) 094003-1-15
3. Response to a twist in systems with Z_p symmetry: The two-dimensional p-state clock model
   Y. Kumano, K.Hukushima, Y.Tomita, M.Oshikawa: Phys. Rev. B **88** (2013) 104427-1-6
4. An irreversible Markov-chain Monte Carlo method with skew detailed balance conditions
   M.Sasaki and K. Hukushima: J. Phys.: Conf. Ser. **473** (2013) 12012-1-9
5. Typical Behavior of the Linear Programming Method for Combinatorial Optimization Problems: A Statistical – Mechanical Perspective
   S. Takabe and K. Hukushima: J. Phys. Soc.Jpn **83** (2014) 043801-1-4

IGARASHI, Ryo [C class; 0 (A), 1000 (B), 1400 (C)] ()
— *Development of ALPS/MPS and its application to strongly correlated electron systems*

IKUHARA, Yuichi [C class; 13000 (A), 7000 (B), 3000 (C)] (53)
— *Local Quantum Design of Materials Fabricated by Bicrystal Technique*Metal-insulator Transition at Perovskite Oxide Interfaces

1. Spontaneous Structural Distortion and Quasi-One-Dimensional Quantum Confinement in a Single-Phase Compound
   Z. Wang, L. Gu, M. Saito, S. Tsukimoto, M. Tsukada, F. Lichtenberg, Y. Ikuhara, and J. G. Bednorz: Adv.Mater. **25** (2013) 218.
2. Ferromagnetic Dislocations in Antiferromagnetic NiO
   I. Sugiyama, N. Shibata, Z. Wang, S. Kobayashi, T. Yamamoto, and Y. Ikuhara: Nat. Nanotech. **8** (2013) 266.
   titleRegulating Infrared Photoresponses in Reduced Graphene Oxide Phototransistors by Defect and Atomic Structure Controla H. X. Chang, Z. H. Sun, M. Saito, Q. H. Yuan, H. Zhang, J. H. Li, Z. C. Wang, T. Fujita, F. Ding, Z. J. Zheng, F. Yan, H. K. Wu, M. W. Chen, and Y. Ikuhara: ACS NANO **7** (2013) 6310.

IMADA, Masatoshi [C,E class; 0 (A), 22000 (B), 2200 (C)] (23)
— *Numerical studies on ab initio low-energy effective models for high-Tc cuprates*
— *Variational Monte Carlo studies of electron correlation effects on topological insulators*

1. Atomically resolved spectroscopic study of Sr_2IrO_4: Experiment and theory
   Qing Li, Guixin Cao, Satoshi Okamoto, Jieyu Yi, Wenzhi Lin, Brian C. Sales, Jiaqiang Yan, Ryotaro Arita, Jan Kunes, Anton V. Kozhevnikov, Adolfo G. Eguiluz, Masatoshi Imada, Zheng Gai, Minghu Pan, David G. Mandrus: Scientific Reports **3** (2013) 3073.
2. Quantum Monte Carlo Simulations for Stacked Spin-Ladder Systems Containing Low Concentrations of Nonmagnetic Impurities: Application to the Low-Temperature Broadening of NMR Spectra in $SrCu_2O_3$
   Robert Achleitner, Hans Gerd Evertz, Masatoshi Imada, Ralf Gamillscheg, Peter Mohn: Phys. Rev. B **88** (2013) 214422.
3. Improved Multi-Variable Variational Monte Carlo Method Examined by High-Precision Calculations of One-Dimensional Hubbard Model
   Ryui Kaneko, Satoshi Morita, Masatoshi Imada: J.Phys.Conf.Ser. **454** (2013) 012046.
4. Theory of Pseudogap in Underdoped Cuprates
   M. Imada, S. Sakai, Y. Yamaji and Y. Motome: J. Phys. Conf. Ser. **449** (2013) 012005.
5. Derivation of Static Low-Energy Effective Models by *ab initio*Downfolding Method without Double Counting of Coulomb Correlations: Application to $SrVO_3$, FeSe and FeTe
   M. Hirayama, T. Miyake and M. Imada: Phys. Rev. B **87** (2013) 195144.
6. Raman-scattering measurements and theory of the energy-momentum spectrum for underdoped

$Bi_2Sr_2CaCuO_8 + \delta$ superconductors: Evidence of an *s*-wave structure for the pseudogap

Shiro Sakai, Sebastien Blanc, Marcello Civelli, Yann Gallais, Maximilien Cazayous, Marie-Aude Measson, Jinsheng Wen, Zhijun Xu, Genda Gu, Giorgio Sangiovanni, Yukitoshi Motome, Karsten Held, Alain Sacuto, Antoine Georges, and Masatoshi Imada: Phys. Rev. Lett. **111** (2013) 107001.

7. Phase diagram structure of topological Mott transition for zero-gap semiconductors beyond conventional Landau-Ginzburg-Wilson scenario
   Moyuru Kurita, Youhei Yamaji, and Masatoshi Imada: Phys. Rev. B **88** (2013) 115143.

INAGAKI, Kouji [C class; 19000 (A), 5500 (B), 2200 (C)] (49)
— *Clarification of reaction process in CRAE method*
— *Clarification of reaction process in CARE method for GaN, SiC and SiO2 materials*

INAOKA, Takeshi [C class; 2000 (A), 500 (B), 400 (C)] (225)
— *Physical properties of low-dimensional electron systems created on solid surfaces and their control*

1. Anisotropy of the silicon valence band induced by strain with various orientations
   T. Inaoka, Y. Kinjyo, S. Yanagisawa, and K. Tomori: J. Appl. Phys. **113** (2013) 183718 (13 pages).
2. Exchange-correlation and temperature effects on plasmons in strongly-correlated two-dimensional electron systems: finite-temperature local-field-correction theory combined with angle-resolved Raman spectroscopy
   T. Inaoka, Y. Sugiyama, and K. Sato: Phys. Status Solidi B, published online (2014) Doi: 10.1002/pssb.201350147 (11 pages).
3. Internal-strain effect on the valence band of strained silicon and its correlation with the bond angles
   T. Inaoka, S. Yanagisawa, and Y. Kadekawa: J. Appl. Phys. **115** (2014) 063702 (14 pages).

ISHIHARA, Sumio [B class; 0 (A), 1500 (B), 0 (C)] (163)
— *Non-linear and non-steady dynamics in correlated electron systems*
— *Response and non-linear dynamics in correlated electron system*

1. Dynamical Jahn-Teller effect in a spin-orbital coupled system
   J. Nasu and S. Ishihara: Phys. Rev. B **88** (2013) 094408
2. Vibronic excitation dynamics in orbitally degenerate correlated electron system
   J. Nasu and S. Ishihara: Phys. Rev. B **88** (2013) 205110
3. Transient carrier dynamics in a Mott insulator with antiferromagnetic order
   E. Iyoda and S. Ishihara: Phys. Rev. B **89** (2014) 125126

ISHII, Fumiyuki [B class; 0 (A), 1300 (B), 900 (C)] (121,122)
— *First-Principles Calculation of Spin Splitting at Oxide Surfaces and Interfaces*
— *First-Principles Calculation of Transition Metal Oxide Superlattices*

1. First-principles study of carrier-induced ferromagnetism in bilayer and multilayer zigzag graphene nano ribbons
   K. Sawada, F. Ishii, and M. Saito: Appl. Phys. Lett. **104** (2014) 14311.
2. Tunable Rashba effect on strained ZnO: First-principles density-functional study
   M. A. Adhib, H. Kotaka, F. Ishii, and M. Saito: Appl. Phys. Exp. **7** (2014) 053002.
3. Spin-Orbit Interaction Effects in the Electronic Structure of B20-type CoSi: First-Principles Density Functional Study
   F. Ishii, T. Onishi, and H. Kotaka: JPS Conf. Proc., in press.
4. Contribution of Berry Curvature to Thermoelectric Effects
   Y.P. Mizuta and F. Ishii: JPS Conf. Proc., in press.
5. First-principles study of Exchange Interaction in Ising-type Multiferroic Ca3CoMnO6
   M. Nishida, F. Ishii, and M. Saito: JPS Conf. Proc., in press.

ISOBE, Masaharu [B class; 400 (A), 300 (B), 0 (C)] (245)
— *Large scale hard sphere molecular dynamics simulation in the nonequilibrium transport phenomena*

1. Hard Disks Equation of State: First-Order Liquid-Hexatic Transition in Two Dimensions with Three Different Simulation Methods
   M. Engel, J. A. Anderson, S. C. Glotzer, M. Isobe, E.P. Bernard and W. Krauth: Phys. Rev. E **87** (2013) 042134.

ISODA, Makoto [B class; 500 (A), 0 (B), 0 (C)] (252)
— *Finite temperature properties of 2-dimensional frustrated system*
1. A microscopic modeling of the instant coffee effect
   M. Isoda and Y. Nishimori: J. Phys.: Conf. Ser. 490 (2014) 012030.

KAKEHASHI, Yoshiro [C class; 0 (A), 1000 (B), 0 (C)] (168)
— *Development of Nonlocal Dynamical CPA and Numerical Study of Long-Range Magnetic Correlations*
1. Nonlocal Excitations and 1/8 Singularity in Cuprates
   Y. Kakehashi, M.A.R. Patoary, S. Chandra: J. Korean Phys. Soc. **62** (2013) 1827-1831.
2. First-Principles Molecular Dynamics Study on the Magnetic Structure of Mn_3Pt
   T. Uchida, N. Kimura, and Y. Kakehashi: J. Korean Phys. Soc. **62** (2013) 1748-1752.
3. Momentum Dependent Local-Ansatz with Hybrid Wavefunction from Weak to Strong Electron Correlations
   M. Atiqur R. Patoary and Y. Kakehashi: J. Phys. Soc. Jpn. **82** (2013) 084710.

KAMIYA, Katsumasa [C class; 13000 (A), 3000 (B), 0 (C)] ()
— *Quantum theoretical study of the relationships among function, atomic structure, and electronic structure of bio-nano-materials*

KASAI, Hideaki [C class; 0 (A), 5500 (B), 2700 (C)] (89)
— *First principles based analysis of reactions on solid surfaces/interfaces*
1. Interplay between Plasmon Luminescence and Vibrationally Resolved Molecular Luminescence Induced by Scanning Tunneling Microscopy
   Kuniyuki Miwa, Mamoru Sakaue, Hideaki Kasai: Journal of the Physcial Society of Japan, **82**, 069715/1-5 (2013).
2. Vibration-assisted upconversion of molecular luminescence induced by scanning tunneling microscopy
   Kuniyuki Miwa, Mamoru Sakaue, Hideaki Kasai: Nanoscale Research Letters, **8**, 204 (2013).
3. First-principles study on surface structure, thickness and composition dependence of the stability of Pt-skin/Pt3Co oxygne-reduction reaction
   Mary Clare Sison Escaño, Hideaki Kasai: Journal of Power Sources, **247**, 562-571 (2013).
4. Hydrogen absorption and hydrogen-induced reverse segregation in palladium-silver surface
   Allan Abraham B. Padama. Hideaki Kasai, Yogi Wibisono Budhi:International Journal of Hydrogen Energy, **38**, 14715-14724 (2013).
5. Comparative Study on the Catalytic Activity of the TM-N2 Active Sites (TM= Mn, Fe, Co, Ni) in the Oxygen Reduction Reaction: Density Functional Theory Study
   Adhitya Gandaryus Saputro, Hideaki Kasai, Koichiro Asazawa, Hirofumi Kishi, and Hirohisa Tanaka: Jouranl of the Physical Society of Japan, **82**, 114704 (2013).
6. First Principles Study on the Electronic Structure and Properties of Sr- and Mg- Doped $LaGaO_3$
   Triati Dewi Kencana Wungu, Mamoru Sakaue, Susan Meñez Aspera, Tran Linh PhanThuy, Musa Alaydrus, Hideaki Kasai, Tatsumi Ishihara: ECS Transactions, **57**(1), 2715-2722 (2013).
7. First-principles Study of the Lattice Strain Effects on the Ionic Migration Barrier of Sm-doped Ceria
   Musa Alaydrus, Mamoru Sakaue, Susan Meñez Aspera, Triati Dewi Kencana Wungu, Tran Linh PhanThuy, Hideaki Kasai, Tatsumi Ishihara: ECS Transactions,, **57**(1), 2733-2739 (2013).
8. Development of Novel Materials Through Computational Materials Design (CMD)
   Hideaki Kasai, Susan Meñez Aspera, Adhitya Gandaryus Saputro: ECS Transactions, **53**(37), 1-6 (2013).
9. Investigations on the Structural and Electronic Properties of Pure and Doped Bulk Pr_2NiO_4 through First Principles Calculations

Susan Meñez Aspera, Mamoru Sakaue, Musa Alaydrus, Triati Dewi Kencana Wungu, Tran Linh PhanThuy, Hideaki Kasai, Tatsumi Ishihara: ECS Transactions, **57**(1), 2753-2762 (2013).

10. Computational Studies on Ionic and Electronic Conduction of Rare-Earth-Based Oxides Based on Density Functional Theory
    Mamoru Sakaue, Hideaki Kasai, Tatsumi Ishihara:ECS Transactions, **57**(1), 2411-2418 (2013).
11. Alkaline-earth doped effect on oxygen vacancy migration in monoclinic lanthanum germanate: first-principles calculation
    Tran Phan Thuy Linh, Mamoru Sakaue, Musa Alaydrus, Triati Dewi Kencana Wungu, Susan Menez Aspera, Hideaki Kasai, Tatsumi Ishihara: ECS Transactions, **57**(1), 1077-1083 (2013).
12. Mechanistic insight into the Au-3d metal alloy-catalyzed borohydride electro-oxidation: From electronic properties to thermodynamics
    Ryan Lacdao Arevalo, Mary Clare Sison Escano, Hideaki Kasai: ACS Catalysis, **3** 3031-3040 (2013).
13. Dynamics of Mu, H, D, and T Absorption into Pd(111): Isotope Effects
    Koji Shiizu, Wilson Agerico Dino, Hideaki Kasai: Journal of the Physical Society of Japan, **83**, 013601 (2014).
14. Density functional theory study on the interaction of O_2 and H_2O_2 molecules with the active sites of cobalt-polypyrrole catalyst
    Adhitya Gandaryus Saputro, Hideaki Kasai: Journal of the Physical Society of Japan, **83**, 24707-1 (2014).
15. A density functional theory-based study on the dissociation of NO on CuO(110) surface
    Joaquin Lorenzo Valmoria Moreno, Allan Abraham Bustria Padama, Hideaki Kasai: CrystEngComm, **16**, 2260-2265 (2014).
16. Analysis of the changes in electronic structures and work function variation in alkali metal - metal surface systems
    Allan Abraham B. Padama, Kohei Oka, Wilson Agerico Dino, Hideaki Kasai: Journal of the Vacuum Society of Japan, **57**(1), 27-31 (2014).
17. Adsorbed oxygen-induced cluster reconstruction on core-shell Ni@Pt and Pt clusters
    Ferensa Oemry, Hiroshi Nakanishi, Hideaki Kasai, Hiroyoshi Maekawa, Kazuo Osumi, Kaoru Sato: Journal of Alloys and Compounds, **594**(1), 93-101 (2014).
18. Initial stages of $Cu_3Au(111)$ oxidation: oxygen induced Cu segregation and the protective Au layer profile.
    Yasutaka Tsuda, Kohei Oka, Takamasa Makino, Michio Okada, Wilson Agerico Dino, M. Hashinokuchi, Akitaka Yoshigoe, Yuden Teraoka, Hideaki Kasai: Physical Chemistry Chemical Physics, **16**(8), 3815-3822 (2014).
19. Hydrogen atom absorption in hydrogen-covered Pd(110) (1x2) missing-row surface
    Allan Abraham B. Padama, Bhume Chantaramolee, Hiroshi Nakanishi, Hideaki Kasai: International Journal of Hydrogen Energy, **39**(12), 6598-6603 (2014).
20. A Theoretical Study of Ligand Effects on the Electronic Structures of Ligated Zinc Porphyrin using Density Functional Theory
    Febdian Rusydi, Mohammad Kemal Agusta, Adhitya Gandaryus Saputro, Hideaki Kasai: Journal of the Vacuum Society of Japan, **57**(3), 102-110 (2014).

KAWAGUCHI, Takaaki [B class; 1400 (A), 0 (B), 0 (C)] (237)

— *Collective dynamics of active particles*

1. Directed motion and novel dynamics of interfacial systems
   T. Kawaguchi and H. Matsukawa: JPS Conf. Proc. **1** (2014) 012059.

KAWAKAMI, Norio [C class; 0 (A), 10000 (B), 0 (C)] (150,151)

— *Phase formation and dynamics in correlated cold atom systems*

— *Analysis of Topological Phases in Strongly Correlated Systems*

1. Disorder Effects on Superfluidity in the Attractive Hubbard Model
   M. Sakaida, K. Noda and N. Kawakami, J. Phys. Soc. Jpn. **82**, 074715 (2013).
2. Reentrant topological transitions with Majorana end states in 1D superconductors by lattice modulation

M. Tezuka and N. Kawakami, Phys. Rev. B **88**, 155428 (2013).

3. Charge order in Kondo lattice systems
   R. Peters, S. Hoshino, N. Kawakami, J. Otsuki, and Y. Kuramoto, Phys. Rev. B **87**, 165133 (2013).
4. Kondo effect in f-electron superlattices
   Robert Peters, Yasuhiro Tada, Norio Kawakami, Phys. Rev. B **88**, 155134 (2013).
5. The surface density of states of layered f-electron materials
   R. Peters and N. Kawakami, Phys. Rev. B **89**, 041106(R) (2014).

KAWAMURA, Hikaru [B,C class; 32400 (A), 9400 (B), 0 (C)] (173,175)
— *Numerical simulations on statistical models of earthquakes*
— *Novel order in frsutrated magnets*

1. Monte Carlo simulations of the three-dimensional XY spin glass focusing on the chiral and the spin order
   T. Obuchi and H. Kawamura: Phys. Rev. B **87**, 174438 (2013)
2. Quantum Spin-Liquid Behavior in the Spin-1/2 Random Heisenberg Antiferromagnet on the Triangular Lattice
   K. Watanabe, H. Kawamura, H. Nakano, and T. Sakai: J. Phys. Soc. Jpn. **83**, 034714 (2014)
3. Earthquake nucleation process as a precursor of a mainshock
   Y. Ueda, S. Morimoto, S. Kakui, T. Yamamoto and H. Kawamura: arXiv:1401.3247

KAWASHIMA, Naoki [E class; 0 (A), 32000 (B), 4400 (C)] (181)
— *Simulation of Cold Atoms with Parallelized Worm Algorithm*

1. Parallelized Quantum Monte Carlo Algorithm with Nonlocal Worm Updates
   Akiko Masaki-Kato, Takafumi Suzuki, Kenji Harada, Synge Todo, Naoki Kawashima: Physical Review Letters **112** (2014) 140603 (5 pages)
2. Phase Transitions with Discrete Symmetry Breaking in Antiferromagnetic Heisenberg Models on a Triangular Lattice
   Ryo Tamura, Shu Tanaka, and Naoki Kawashima: JPS Conf. Proc. — Proceedings of the 12th Asia Pacific Physics Conference (APPC12) (2014) 012125.
3. Possibility of Deconfined Criticality in SU(N) Heisenberg Models at Small N
   Kenji Harada, Takafumi Suzuki, Tsuyoshi Okubo, Haruhiko Matsuo, Jie Lou, Hiroshi Watanabe, Synge Todo, Naoki Kawashima: Phys. Rev. B **88** (2013) 220408(R)(4 pages)
4. Second-Order Phase Transition in Heisenberg Model on Triangular Lattice with Competing Interactions
   Ryo Tamura, Shu Tanaka and Naoki Kawashima: Phys. Rev. B **87** (2013) 214401(5pages)

KITAO, Akio [C class; 0 (A), 5000 (B), 2200 (C)] (215)
— *Efficient sampling simulation of the soft modes significantly contribute to protein properties*

1. Mechanism of Deep-Sea Fish α-Actin Pressure Tolerance Investigated by Molecular Dynamics Simulations.
   N. Wakai, K. Takemura, T. Morita, and A. Kitao: PLoS One, **9** (2014) e85852.
2. MuSTAR MD: Multi-scale sampling using temperature accelerated and replica exchange molecular dynamics.
   Y. Yamamori and A. Kitao: J. Chem. Phys., **139** (2013) 229902.
3. Parallel cascade selection molecular dynamics (PaCS-MD) to generate conformational transition pathway.
   R. Harada and A. Kitao: J. Chem. Phys., **139** (2013) 035103.
4. CyClus: A fast, comprehensive cylindrical interface approximation clustering/reranking method for rigid-body protein-protein docking decoys.
   S. Omori and A. Kitao: Proteins, Structure, Function and Bioinformatics, **81** (2013) 1005.

KIZAKI, Hidetoshi [E class; 0 (A), 1000 (B), 900 (C)] (125)
— *First-principles Calculations of Photocatalytic Solid-liquid Interfaces*

KOBAYASHI, Katsuyoshi [B class; 1000 (A), 100 (B), 0 (C)] (133)
— *Search for electronic properties of new nanoscale interfaces*

1. Anisotropic electronic conduction in metal nanofilms grown on a one-dimensional surface superstructure
   N. Nagamura, R. Hobara, T. Uetake, T. Hirahara, M. Ogawa, T. Okuda, K. He, P. Moras, P. M. Sheverdyaeva, C. Carbone, K. Kobayashi, I. Matsuda and S. Hasegawa: Phys. Rev. B **89** (2014) 125415.

KOBAYASHI, Michikazu [B class; 1300 (A), 300 (B), 0 (C)] (231)
— *Numerical analysis of field theory with non-trivial topological structure*

1. Sine-Gordon kinks on a domain wall ring
   M. Kobayashi and M. Nitta: Phys. Rev. D **87** (2013) 085003
2. Fractional vortex molecules and vortex polygons in a baby Skyrme model
   M. Kobayashi and M. Nitta: Phys. Rev. D **87** (2013) 125013
3. Winding Hopfion on $\mathbf{R}^2 \times S^1$
   M. Kobayashi and M. Nitta: Nucl. Phys. B **876** (2013) 605
4. Kelvin modes as Nambu-Goldstone modes along superfluid vortices and relativistic strings: finite volume size effects
   M. Kobayashi and M. Nitta: Prog. Theor. Exp. Phys. (2014) 021B01
5. Vortex polygons and their stabilities in Bose-Einstein condensates and field theory
   M. Kobayashi and M. Nitta: J. Low Temp. Phys. **175** (2014) 208
6. Torus knots as Hopfions
   M. Kobayashi and M. Nitta: Phys. Lett. B **728** (2014) 314
7. Toroidal domain walls as Hopfion
   M. Kobayashi and M. Nitta: submitted to Phys. Rev. D
8. Color Magnetism in Non-Abelian Vortex Matter
   M. Kobayashi E. Nakano and M. Nitta: submitted to Phys. Rev. Lett.
9. Non-relativistic Nambu-Goldstone modes propagating along a skyrmion line
   M. Kobayashi and M. Nitta: submitted to Phys. Rev. Lett.
10. Non-relativistic Nambu-Goldstone modes associated with spontaneously broken space-time and internal symmetries
    M. Kobayashi and M. Nitta: submitted to Phys. Rev. B

KOBAYASHI, Nobuhiko [C class; 5000 (A), 7500 (B), 3600 (C)] (64)
— *First-principles study of quantum transport in nanostructures*

1. Strong anisotropy of momentum-relaxation time induced by intermolecular vibrations of single-crystal organic semiconductors
   H. Ishii, N. Kobayashi, K. Hirose, Phys. Rev. B 88 205208 (2013).
2. Influence of strong electron-phonon coupling and dynamic lattice disorder on the Hall effect in organic crystals
   H. Tamura, M. Tsukada, H. Ishii, N. Kobayashi, K. Hirose, Phys. Rev. B 87, 155305 (2013).
3. Thermal Conductance Calculations of Silicon Nanowires -Comparison with Diamond Nanowires-
   K.Yamamoto, H.Ishii, N.Kobayashi, and K.Hirose, Nano. Res. Lett. 8 256 (2013).
4. Crossover to quantized thermal conductance in nanotubes and nanowires
   K. Yamamoto, H. Ishii, N. Kobayashi, and K. Hirose: Open J. Comp. Mat. 3 48-54 (2013).
5. On phononic band of carbon nanotubes
   K. Yamamoto, H. Ishii, N. Kobayashi, K. Hirose, J. Nanomaterials 2013 525070 (2013).
6. Electric and Thermal Transport Calculations through Interface and Applications to Thermoelectric Energy Conversion
   K. Hirose, K. Kobayashi, M. Shimono, H. Ishii, N. Kobayashi, e-Journal Surf. Sci. Nanotechnol. 12 (2014) 115-118a
7. Quantum transport calculations for nanosystems
   K. Hirose and N. Kobayashi, (Pan Stanford Publishing, 2014).
8. 熱伝導・熱電性能
   広瀬賢二、小林伸彦、ナノワイヤ最新技術の基礎と応用展開第 II 編 7 章、(CMC 出版, 2013)

KOGA, Akihisa [C class; 5500 (A), 8500 (B), 2800 (C)] (144)
— *Stability of the superfluid state in fermionic optical lattices*
— *Stability of the superfluid state in three components fermionic optical lattices*

1. Stability of the Superfluid State in Three-Component Fermionic Optical Lattice Systems
   Y. Okanami, N. Takemori and A. Koga, arXiv:1401.5610.

KUNISADA, Yuji [C class; 0 (A), 3000 (B), 600 (C)] (106)
— *First principles based analysis of electronic structures and reactions on surfaces/interfaces*

1. Pd/ZnO 極性界面の HRTEM·EELS に基づく構造評価と第一原理電子状態計算
   坂口紀史，渡辺圭，國貞雄治: 顕微鏡 48 (2013) 195.

KUROKI, Kazuhiko [C class; 15000 (A), 2000 (B), 1600 (C)] (142)
— *Study on the correlation between the Fermi surface and T_c in iron-based and cuprate superconductors*

1. Understanding the re-entrant superconducting phase diagram of an iron-pnictide $Ca_4Al_2O_6Fe_2(As_{1-x}P_x)_2$
   H. Usui, K. Suzuki, K. Kuroki, N. Takeshita, P.M. Shirage, H. Eisaki, A. Iyo, Phys. Rev. B **87** (2013) 174528 (1-9).
2. Robust spin fluctuations and $s\pm$ pairing in the heavily electron doped iron-based superconductors
   K. Suzuki, H. Usui, K. Kuroki, S. Iimura, Y. Sato, S. Matsuishi, H. Hosono: J. Phys. Soc. Jpn. **82** (2013) 083702 (1-4).
3. Three-orbital study on the orbital distillation effect in the high Tc cuprates
   H. Sakakibara, K. Suzuki, H. Usui, K. Kuroki, R. Arita, D.J. Scalapino, H. Aoki: Physics Procedia **45** (2013) 13-16.
4. First-principles band structure and FLEX approach to the pressure effect on T_c of the cuprate superconductors
   H. Sakakibara, K. Suzuki, H. Usui, K. Kuroki, R. Arita, D.J. Scalapino, H. Aoki: J. Phys.: Conf. Ser. **454** (2013) 012021 (1-8).

KUSAKABE, Koichi [C class; 0 (A), 2000 (B), 600 (C)] (157)
— *Electronic state calculations of metal compounds showing quantum mechanical order*

1. Fermi surface shape controlling by element substitution in Tl-based cuprates
   Satoaki Miyao, Hirofumi Sakakibara, Isao Maruyama, Kazuhiko Kuroki, and Koichi Kusakabe: J. Phys. Soc. Jpn. Suppl. **83** (2014) in press.
2. Orbital mixture effect on the Fermi surface-Tc correlation in the cuprate superconductors - bilayer vs single layer
   Hirofumi Sakakibara, Katsuhiro Suzuki, Hidetomo Usui, Satoaki Miyao, Isao Maruyama, Koichi Kusakabe, Ryotaro Arita, Hideo Aoki, and Kazuhiko Kuroki: arXiv:1403.2497.
3. Direct imaging of monovacancy-hydrogen complexes in a single graphitic layer
   Maxim Ziatdinov, Shintaro Fujii, Koichi Kusakabe, Manabu Kiguchi, Takehiko Mori, and Toshiaki Enoki: Phys. Rev. B 89, 155405 (2014).

MATSUSHITA, Katsuyoshi [C class; 11000 (A), 3000 (B), 0 (C)] (191)
— *Clarification of magnon turbulence in nano-contacts*
— *Clarification of Emergence Conditions of Magnon Turbulence in Ferromagnet*

1. Swing Casting Boost for Confined Domain Wall Breathing
   atsuyoshi Matsushita, Munetaka Sasaki and Tsuyoshi Chawanya Journal of the Physical Society of Japan 83, 013801 (2014).
2. Magnon Turbulence in Ferromagnetic Nanocontact
   atsuyoshi Matsushita, Munetaka Sasaki, Jun Sato, and Hiroshi Imamura Journal of the Physical Society of Japan 82, 033801 (2013).

MASAKI, Akiko [C class; 4000 (A), 2000 (B), 1600 (C)] (212)
— *Development and application of a new quantum Monte Carlo Algorithm for lattice bosons*

1. Parallelized Quantum Monte Carlo Algorithm with Nonlocal Worm Updates
   Akiko Masaki-Kato, Takafumi Suzuki, Kenji Harada, Synge Todo, Naoki Kawashima: Physical

Review Letters

MATSUKAWA, Hiroshi [C class; 6000 (A), 1000 (B), 0 (C)] ()
— *Physics of Friction*

MATSUURA, Hiroyasu [C class; 14000 (A), 5000 (B), 2200 (C)] (141)
— *Theoretical Study of Novel Electronic Systems in Strongly Correlated Electron Systems*

1. Competition between the Spin Fluctuations for the d_{xy} orbital around $\mathbf{q} = (0, 0)$ and $\mathbf{q} \sim (\pi, 0)$ in $Ca_{2-x}Sr_xRuO_4$ around $x = 0.5$
   N. Arakawa and M. Ogata: Phys. Rev. B **87** (2013) 195110.
2. Magnetic Instability in $Ca_{2-x}Sr_xRuO_4$ with $x = 0.5$
   N. Arakawa and M. Ogata: J. Korean Phys. Soc. **63** (2013) 390.
3. Orbital-cooperative spin fluctuation and orbital-dependent transport in Ru oxides
   N. Arakawa, in preparation for publication in PRL.

MISAWA, Takahiro [C class; 0 (A), 6000 (B), 2400 (C)] (152)
— *Ab initio calculations for iron-based superconductors FeTe and FeSe*

1. 3D Dirac Electrons on a Cubic Lattice with Noncoplanar Multiple-Q Order
   S. Hayami, T. Misawa, Y. Yamaji, and Y. Motome: Phys. Rev. B 89 (2014) 085124
2. Origin of High-T_c Superconductivity in Doped Hubbard Models and Their Extensions - Roles of Uniform Charge Fluctuations -
   T. Misawa and M. Imada, arXiv:1306.1434

MIYAKE, Takashi [C class; 0 (A), 2500 (B), 0 (C)] (116)
— *First-principles study of magnetic materials and magnetism*

1. Derivation of Static Low-energy Effective Models by ab initio Downfolding Method without Double Counting of Coulomb Correlations: Application to $SrVO_3$, FeSe and FeTe
   Motoaki Hirayama, Takashi Miyake and Masatoshi Imada: Phys. Rev. B **87** (2013) 195144.
2. Spin-orbital frustration in molybdenum pyrochlores $A_2Mo_2O_7$ (A=rare earth)
   H. Shinaoka, Y. Motome, T. Miyake and S. Ishibashi: Phys. Rev. B **88** (2013) 174422.
3. First-principles study of magnetocrystalline anisotropy and magnetization in $NdFe_{12}$, $NdFe_{11}Ti$ and $NdFe_{11}TiN$
   Takashi Miyake, Kiyoyuki Terakura, Yosuke Harashima, Hiori Kino and Shoji Ishibashi: J. Phys. Soc. Jpn. **83** (2014) 043702.
4. Second-order Perturbation Formula for Magnetocrystalline Anisotropy using Orbital Angular Momentum Matrix
   Taichi Kosugi, Takashi Miyake, and Shoji Ishibashi: J. Phys. Soc. Jpn. **83** (2014) 044707.

MIYASHITA, Seiji [C class; 3000 (A), 4000 (B), 1200 (C)] (203)
— *Novel ordered phase and dynamical response under driving field*

1. Complex magnetic phase diagram of a geometrically frustrated Sm lattice: Magnetometry and neutron diffraction study of SmPd2Al3
   J.Pospisil,G.Nenert,S.Miyashita,H.Kitazawa,Y.Skourski,M.Divis,J.Prokleska,V.Sechovsky:Phy.Rev.B **87** (2013) 21.
2. Exantness of the mean-field dynamics in optical cavity sysytems
   T.Mori:J.Stat.Mech.**10**(2013)1088.P06005
3. Effect of the short-range interaction on critical phenomena in elastic interaction systems
   M.Nishino,S.Miyashita:Phy.Rev.B.**88**(2013)1.
4. Nonadditivity in Quasiequilibrium States of Spin Systems with Lattice Distortion
   T.Mori:Phy.Rev.Lett.**111**(2013)020601
5. Comment on "Experimental Test of an Event-Based Corpuscular Model Modification as an Alternative to Quantum Mechanics"
   K.Michielsen,T.Lippert,B.Barbara,S.Miyashita,H.De Raedt:J.Phys.Soc.Jpn.**82**(2013)8
6. Crossover of the roughness exponent for interface growth in systems with long-range interactions due to lattice distortion

M.Nishino,T.Nakada,C Enachescu,K.Boukheddaden, S.Miyashita:Phy.Rev.B.**88** (2013) 9
7. Phase transisions in sysytems with non-additive long-range interactions
T.Mori:J.Stat.Mech.**10**(2013)1088.P10003
8. Properties of the low-spin high-spin interface during th relaxation of spin-crossover materials,investigated though an electro-elastic model
A.Slimani,K.Boukheddaden,F.Varret,M.Nishino,S.Miyashita:J.Chem.Phys.**139**(2013)19
9. Novel symmetry-broken phase in a driven cavity system in the thermodynamic limit
T.Shirai,T.Mori,S.Miyashita:J. of Phy.B:At. Mole. and Opt. Phy.**47**(2014) 025501

MIYATA, Naoyuki [C class; 0 (A), 0 (B), 700 (C)] ()
— *Numerical calculation of the critical exponent of localization length in a quantum Hall system*

MIYAZAKI, Kunimasa [B class; 1600 (A), 0 (B), 0 (C)] ()
— *Mean Field Picture of the Glass Transition*

MIYAZAKI, Kunimasa [B class; 1800 (A), 0 (B), 0 (C)] ()
— *Mean Field Picture of the Glass Transition*

MIZOGUCHI, Teruyasu [B class; 0 (A), 1400 (B), 0 (C)] (128,129)
— *First principles study on homo and hetero interface of photovoltaic materials*
— *Large scale first principles calculation of core loss spectroscopy*

1. The atomic structure, band gap, and electrostatic potential at the (112)[1-10] twin grain boundary of CuInSe2
H. Yamaguchi, H. Hiramatsu, H. Hosono, and T. Mizoguchi Appl. Phys. Lett., 104, 153904-1-5 (2014).
2. Mn L2,3-edge X-ray absorption spectroscopic studies on charge-discharge mechanism analysis of Li2MnO3
K. Kubobuchi, H. Ikeno, M. Mogi, I. Tanaka, H. Imai, and T. Mizoguchi Appl. Phys. Lett., 104 (2014) 053906-1-4.
3. An estimation of molecular dynamic behaviour in a liquid using core-loss spectroscopy
Y. Matsui, K. Seki, H. Hibara, T. Mizoguchi Scientific Reports, 3 (2013) 3503-1-7.
4. The influence of neighboring vacancies and their charge state on the atomic migration of LaAlO3
T. Yamamoto and T. Mizoguchi Appl. Phys. Lett., 102 (2013) 211910-1-4.
5. Effect of local coordination of Mn on Mn-L2,3 edge electron energy loss spectrum
S. Nishida, S. Kobayashi, A. Kumamoto, H. Ikeno, T. Mizoguchi, I. Tanaka, Y. Ikuhara, T. Yamamoto J. Appl. Phys., 114,(2013)054906-1-6.
6. Defect formation energetics at the grain boundary in CuInSe2 using first-principles calculations
H. Yamaguchi and T. Mizoguchi J. Ceram. Soc. Jpn, (2014) in press.
7. Impact of local strain on Ti-L2,3 electron energy-loss near-edge structures of BaTiO3: A first-principles multiplet study
S. Ootsuki, H. Ikeno, Y. Umeda, H. Moriwake, A. Kuwabara, O. Kido, S. Ueda, I. Tanaka, Y. Fujikawa, and T. Mizoguchi Microscopy, (2014) in press.

MOMIDA, Hiroyoshi [C class; 3000 (A), 4000 (B), 1600 (C)] (84)
— *First-principles calculations of electron and spin properties in solid materials*

1. Physical Guiding Principles for High Quality Resistive Random Access Memory Stack with Al_2O_3 Insertion Layer
M. Y. Yang, K. Kamiya, B. Magyari-Köpe, H. Momida, T. Ohno, M. Niwa, Y. Nishi and K. Shiraishi: Jpn. J. Appl. Phys. **52** (2013) 04CD11.
2. First-Principles Study of X-Ray Absorption Spectra of FeS_2
T. Oguchi and H. Momida: J. Phys. Soc. Jpn. **82** (2013) 065004.
3. Hydrogen-Enhanced Vacancy Embrittlement of Grain Boundaries in Iron
H. Momida, Y. Asari, Y. Nakamura, Y. Tateyama and T. Ohno: Phys. Rev. B **88** (2013) 144107.

MORIKAWA, Yoshitada [E class; 0 (A), 37500 (B), 4700 (C)] (45)

— *First-principles simulations of atomic geometries, electronic properties and chemical reactions at interfaces*
— *First-principles simulations of atomic geometries, electronic properties, and chemical reactions at interfaces*

1. Search for a Self-Regenerating Perovskite Catalyst Using ab Initio Thermodynamics Calculations
   S. Yanagisawa, A. Uozumi, I. Hamada, and Y. Morikawa: J. Phys. Chem. C, **117** (2013) 1278.
2. First-principles investigation on the segregation of Pd at $LaFe_{1-x}Pd_xO_{3-y}$ surfaces
   Z.-X. Tian, A. Uozumi, I. Hamada, S. Yanagisawa, H. Kizaki, K. Inagaki, and Y. Morikawa: Nanoscale Res. Lett., **8** (2013) 203.
3. First-principles theoretical study of hydrolysis of stepped and kinked Ga-terminated GaN surfaces
   M. Oue, K. Inagaki, K. Yamauchi, and Y. Morikawa: Nanoscale Res. Lett., **8** (2013) 323.
4. HOMO band dispersion of crystalline rubrene: Effects of self-energy corrections within the *GW* approximation
   S. Yanagisawa, Y. Morikawa, and A. Schindlmayr: Phys. Rev. B, **88** (2013) 115438.
5. Intermolecular Interaction as the Origin of Red Shifts in Absorption Spectra of Zinc-Phthalocyanine from First-Principles
   S. Yanagisawa, T. Yasuda, K. Inagaki, Y. Morikawa, K. Manseki, and S. Yanagida: J. Phys. Chem. A, **117** (2013) 11246.
6. Search for a Self-Regenerating Perovskite Catalyst with Ab Initio Thermodynamics II: Cu-Doped Layered Perovskites with K_2NiF_4 Structure
   S. Yanagisawa, A. Takeda, K. Inagaki, I. Hamada, and Y. Morikawa: Catal. Lett., **144** (2014) 736.
7. Theoretical investigation of the band structure of picene single crystals within the *GW* approximation
   S. Yanagisawa, Y. Morikawa, and A. Schindlmayr: Jpn. J. Appl. Phys., **53** (2014) 05FY02.

MURASHIMA, Takahiro [E class; 0 (A), 4500 (B), 50 (C)] (222)
— *Multiscale Simulation for Soft Matter*

MUTOU, Tetsuya [C class; 6000 (A), 1000 (B), 0 (C)] (153)
— *Effect of fluctuation near the ordered state in strongly correlated electron systems*

1. Dynamical density and spin response functions of two-dimensional correlated fermion systems: Self-consistent second-order perturbation theory
   A. Kotani and D. S. Hirashima: Phys. Rev. B **88** (2013) 014529.
2. Validity of Fermi-Liquid Description of Low-Energy Magnetic Excitation in Electron-Doped Cuprate Superconductors
   T. Mutou and D. S. Hirashima: J. Phys. Soc. Jpn. **82** (2013) 094703.
3. Self-Consistent Second-Order Perturbation Theory of Correlation Effect in bcc Iron at Finite Temperatures
   M. Nishishita, D. S. Hirashima, and S. Pandey: J. Phys. Soc. Jpn. **82** (2013) 114705.

NADA, Hiroki [C class; 11000 (A), 0 (B), 0 (C)] (197)
— *Molecular Dynamics Simulation Study of Nucleation Mechanism of Calcium Carbonate Crystal in the Presence of Impurities*

1. Effects of Magnesium Ions and Water Molecules on the Structure of Amorphous Calcium Carbonate: A Molecular Dynamics Study
   H. Tomono, H. Nada, F. Zhu, T. Sakamoto, T. Nishimura and T. Kato: J. Phys. Chem. B, **117** (2013) 14849.
2. Tunning the Stability of $CaCO_3$ Crystals with Magnesium Ions for Formation of Aragonite Thin Films on Organic Polymer Templates
   F. Zhu, T. Nishimura, T. Sakamoto, H. Tomono, H. Nada, Y. Okumura, H. Kikuchi and T. Kato: Chem. Asian J., **8** (2013) 3002.

NAKAMURA, Kazuma [C class; 0 (A), 4000 (B), 2000 (C)] (98)
— *Development of ab initio GW code*Ab initio GW calculations for alkali-cluster-loaded zeolite

1. GW calculation of plasmon excitations in the quasi-one-dimensional organic compound (TMTSF)2PF6
   Kazuma Nakamura, Shiro Sakai, Ryotaro Arita, and Kazuhiko Kuroki: Physical Review B **88** (2013) 125128.
2. Effect of Electron-Phonon Interactions on Orbital Fluctuations in Iron-Based Superconductors
   Yusuke Nomura, Kazuma Nakamura, and Ryotaro Arita: Phys. Rev. Lett. **112** (2014) 027002.

NAKAMURA, Kohji [C class; 12000 (A), 0 (B), 0 (C)] ()

— *First principles calculations on magnetism and transport properties at surfaces/interfaces and in nanostructures*

1. Excited Cr impurity states in Al_2O_3 from constraint density functional theory
   Y. Kitaoka, K. Nakamura, T. Akiyama, T. Ito, M. Weinert, and A.J. Freeman: Phys. Rev. B **87**, (2013) 205113.
2. Electric field-driven hole carriers and superconductivity in diamond
   K. Nakamura, S.H. Rhim, A. Sugiyama, K. Sano, T. Akiyama, T. Ito, M. Weinert, and A.J. Freeman: Phys. Rev. B **87**, (2013) 214506.
3. Atomic-layer alignment tuning for giant perpendicular magnetocrystalline anisotropy of $3d$ transition-metal thin films
   K. Hotta K. Nakamura, T. Akiyama, T. Ito, T. Oguchi, and A.J. Freeman: Phys. Rev. Lett. **110**, (2013) 267206.
4. Role of electronic structure on solubility of magnetic Mn impurity in GaInAs semiconductor alloys
   Y. Kitaoka, M. Miyake, K. Nakamura, T. Akiyama, and T. Ito: J. Magn. Soc. Jpn. **37**, (2013) 227.
5. Magneto-transport properties of Fe thin films in an external electric field
   K. Nakamura, T. Akiyama, and T. Ito, M. Weinert, and A.J. Freeman: J. Korean Phys. Soc. **63**, (2013) 612.
6. Magnetism and multiplets in Fe-phthalocyanine molecules
   Y. Kitaoka, K. Nakamura, T. Akiyama, T. Ito, M. Weinert, and A.J. Freeman: J. Korean Phys. Soc. **63**, (2013) 695.
7. Structural and elastic properties of magnetic shape memory $Ni_2MnGa_{1-x}In_x$ alloy
   F. Kitanishi, K. Nakamura, T. Akiyama, and T. Ito: J. Korean Phys. Soc. **63**, (2013) 329.
8. Role of interfacial B impurity in magnetocrystalline anisotropy at MgO/Fe interface
   K. Hotta, K. Nakamura, T. Akiyama, and T. Ito: J. Korean Phys. Soc. **63**, (2013) 762.
9. Structural and magnetic stabilities of Fe thin films on Cu(111)
   K. Masuda, K. Nakamura, T. Akiyama, and T. Ito: e-J. Surf. Sci. Nanotech. **12**, (2014) 102.
10. Electronic structures and induced-hole carriers of covalent semiconductors in external electric field
    A. Sugiyama, K. Nakamura, T. Akiyama, and T. Ito: e-J. Surf. Sci. Nanotech. **12**, (2014) 109.
11. Electronic and structural investigations of Fe-phtalocyanine crystal
    T. Sakai, Y. Kitaoka, K. Nakamura, T. Akiyama, and T. Ito: e-J. Surf. Sci. Nanotech., in press.

NAKANO, Hiroki [E class; 0 (A), 7000 (B), 1900 (C)] (199)

— *Numerical study on low-energy states of quantum spin systems*

1. The Magnetization Process of the $S = 1/2$ Heisenberg Antiferromagnet on the Cairo Pentagon Lattice
   H. Nakano, M. Isoda, and T. Sakai: J. Phys. Soc. Jpn. **83** (2014) 053702.
2. Anomalous Quantum Magnetization Behaviors of the Kagome and Triangular Lattice Antiferromagnets
   H. Nakano and T. Sakai: to be published in JPS Conf. Proc.
3. Quantum Spin-Liquid Behavior in the Spin-1/2 Random Heisenberg Antiferromagnet on the Triangular Lattice
   K. Watanabe, H. Kawamura, H. Nakano and T. Sakai: J. Phys. Soc. Jpn. **83** (2014) 034714.
4. The Two-Dimensional $S = 1/2$ Heisenberg Antiferromagnet on the Shuriken Lattice - a Lattice Composed of Vertex-Sharing Triangles -
   H. Nakano and T. Sakai: J. Phys. Soc. Jpn. **82** (2013) 083709.
5. Crystal Structure and Magnetic Properties of the Verdazyl Biradical m-Ph-V2 Forming a Ferromagnetic Alternating Double Chain

K. Iwase, H. Yamaguchi, T. Ono, T. Shimokawa, H. Nakano, A. Matsuo, K. Kindo, H. Nojiri, and Y. Hosokoshi: J. Phys. Soc. Jpn. **82** (2013) 074719.
6. Nontrivial ferrimagnetism of the Heisenberg model on the Union Jack strip lattice
Tokuro Shimokawa and H. Nakano: J. Kor. Phys. Soc. **63** (2013) 591.
7. Novel Field-Induced Quantum Phase Transition of the Kagome-Lattice Antiferromagnet
Toru Sakai and H. Nakano: J. Kor. Phys. Soc. **63** (2013) 601.
8. Crystal structure and magnetic properties of honeycomb-like lattice antiferromagnet p-BIP-V2
H. Yamaguchi, S. Nagata, M. Tada, K. Iwase, T. Ono, S. Nishihara, Y. Hosokoshi, T. Shimokawa, H. Nakano, H. Nojiri, A. Matsuo and K. Kindo, and T. Kawakami: Phys. Rev. B **87** (2013) 125120.
9. Long-Range Order of the Three-Sublattice Structure in the S = 1 Heisenberg Antiferromagnet on a Spatially Anisotropic Triangular Lattice
H. Nakano, Synge Todo, and Toru Sakai: J. Phys. Soc. Jpn. **82** (2013) 043715.
10. Unconventional Magnetic and Thermodynamic Properties of S=1/2 Spin Ladder with Ferromagnetic Legs
H. Yamaguchi, K. Iwase, T. Ono, T. Shimokawa, H. Nakano, Y. Shimura, N. Kase, S. Kittaka, T. Sakakibara, T. Kawakami, and Y. Hosokoshi: Phys. Rev. Lett. **110** (2013) 157205.

NAKAYAMA, Takashi [C class; 18000 (A), 0 (B), 0 (C)] (62)
— *Electronic properties of impurity defects in organic molecular semiconductors*

1. First-principles study of Pt-film stability on doped graphene sheets
T. Park, Y. Tomita, T. Nakayama: Surf. Sci. **621** (2014) 7.
2. First-principles study of oxygen-doping states in II-VI semiconductors
M. Ishikawa, T. Nakayama: Physica St. Sol. (C) **10** (2013) 1385.
3. First-Principles Study of Schottky Barrier Behavior at Fe3Si/Ge(111) Interfaces
K. Kobinata, T. Nakayama: Jpn. J. Appl. Phys. **53** (2014) 035701.
4. First-principles evaluation of penetration energy of metal atom into Si substrate
T. Hiramatsu, T. Yamauchi, M. Y. Yang, K. Kamiya, K. Shiraishi, T. Nakayama: Jpn. J. Appl. Phys. **53** (2014) 058006.
5. Energetics and electron states of Au/Ag incorporated into crystalline/amorphous silicon
M. Y. Yang, K. Kamiya, T. Yamauchi, T. Nakayama, K. Shiraishi: J. Appl. Phys. **114** (2013) 063701.
6. Surface Stability and Growth Kinetics of Compound Semiconductors: An Ab Initio-Based Approach
Y. Kangawa, T. Akiyama, T. Ito, K. Shiraishi, T. Nakayama: Materials **6** (2013) 3309.

NISHIDATE, Kazume [C class; 5000 (A), 3000 (B), 500 (C)] (88)
— *Theoretical investigation of the initial growth process of organic semiconductor thin films*

1. Improved Organic Thin Film Transistor Performance Utilizing a DH-α 6T Submonolayer
Y. Fujinaka, R. Ye, K. Ohta, K. Nishidate, and M. Baba: Mol. Cryst. Liq. Cryst., **580**: pp. 110-116, (2013)

NISHINO, Masamichi [B class; 0 (A), 700 (B), 0 (C)] (246)
— *Study of the effect of the short-range interaction on critical phenomena driven by elastic interactions*

1. Crossover of the roughness exponent for interface growth in systems with long-range interactions due to lattice distortion
M. Nishino, T. Nakada, C. Enachescu, K. Boukheddaden and S. Miyashita: Phys. Rev. B. **88** (2013) 094303.
2. Effect of the short-range interaction on critical phenomena in elastic interaction systems
M. Nishino and S. Miyashita: Phys. Rev. B. **88** (2013) 014108.
3. Properties of the low-spin high-spin interface during the relaxation of spin-crossover materials, investigated through an electro-elastic model
A. Slimani, K. Boukheddaden, F. Varret, M. Nishino, and S. Miyashita: J. Chem. Phys. **139** (2013) 194706.

NOGAWA, Tomoaki [B class; 0 (A), 1500 (B), 0 (C)] ()
— *Search of close packing states of multicomponent hard-sphere systems by the parallelized Wang-Landau sampling*

NOGUCHI, Hiroshi [C class; 0 (A), 5000 (B), 2300 (C)] (34,214)
— *Structure changes of biomembranes induced by membrane proteins*

1. Structure formation of surfactant membranes under shear flow
   H. Shiba, H. Noguchi, and G. Gompper: Journal of Chemical Physics **139** (2013) 014702.
2. Entropy-driven aggregation in multilamellar membranes
   H. Noguchi: EPL **102** (2013) 68001.
3. Mechanical properties and microdomain separation of fluid membranes with anchored polymers
   H. Wu, H. Shiba, and H. Noguchi: Soft Matter **9** (2013) 9907.
4. Morphological variation of lipid vesicle confined in spherical vesicle
   A. Sakashita, M. Imai, and H. Noguchi: Physical Review E **89** (2014) 040701(R). A. Sakashita, M. Imai, and H. Noguchi: arXiv:1405.3076 [cond-mat.soft].

NOGUCHI, Yoshifumi [C class; 2000 (A), 4000 (B), 1900 (C)] (92)
— *First-principles calculation for Fullerene derivative under external electric field*

1. First-Principles Inverstigation on Structural and Optical Properties of $M^{+}@C_{60}$ (Where M=H, Li, Na, and K)
   Y. Noguchi, O. Sugino, H. Okada, and Y. Matsuo: J. Phys. Chem. C. **117**, 15362 (2013)

NOZAWA, Kazuki [C class; 2000 (A), 2000 (B), 700 (C)] (104)
— *First-principles study for adsorbed metallic atoms on quasicrystal surface*

1. Templated three-dimensional growth of quasicrystalline lead
   H. R. Sharma, K. Nozawa, J. A. Smerdon, P. J. Nugent, I. McLeod, V. R. Dhanak, M. Shimoda, Y. Ishii, A. P. Tsai, R. McGrath, Nat. Commun. **4**(2013) 2715.

OBATA, Shuji [C class; 9000 (A), 0 (B), 200 (C)] (82)
— *Electronic structure calculations of carbon materials*

1. The Barkhausen effects and Nano-System Magnetizations in Fe
   Shuji Obata: Materials Transactions 54(2013) 1661-1666
2. Analysis of the Barkhausen Effect and B-H Characteristics using the Retarded Trace Method
   Shuji Obata: IEEJ Trans. FM, Vol.133, No.9 (2013) 489-499

OBUSE, Hideaki [B class; 0 (A), 700 (B), 0 (C)] (248)
— *Multifractality near point defects in topological insulators*

ODA, Tatsuki [E class; 0 (A), 18000 (B), 1300 (C)] (59,61)
— *Analyses on magnetic anisotropy and its electric field effect for magnetic thin films*
— *Analyses on atomic structure, magnetism, and electronic structure in spintronics materials*

1. Valley filter by extraordinary Rashba spin on silicon
   K. Sakamoto, T.-H. Kim, T. Kuzumaki, B. Müller, Y. Yamamoto, M. Ohtaka, J. Osiecki, K. Miyamoto, Y. Takeichi, A. Harasawa, S. D. Stolwijk, A. B. Schmidt, J. Fujii, R. I. G. Uhrberg, M. Donath, H. W. Yeom and T. Oda: Nat. Commun., **4** (2013) 2073.
2. Implementation of Parallel Matrix Diagonalization for Ab-Initio Molecular Dynamics Program using ScaLAPACK
   I. Gunawan, M. Obata, M. Nakamura, M. A. Martoprawiro, T. Oda: Recent Development in Computational Science (ISSN 2223-0785),**4** (2013) 39.
3. Magnetic, structural, and electronic properties of Co doped Fe/MgO interface: Density functional approach
   N. Ikhsan, Y. Taguchi, M. Obata, M. Nakamura, Suprijadi, T. Oda: Recent Development in Computational Science (ISSN 2223-0785), **4** (2013) 95.
4. Tight-Binding Molecular Dynamics with Fermi Operator Expansion: Application to Vacancy Defects in Silicon

S. A. Wella, M. Nakamura, M. Obata, Suprijadi, T. Oda: Recent Development in Computational Science (ISSN 2223-0785), **4** (2013) 145.

5. Implementation of van der Waals density functional approach to the spin polarized system: interaction potential between oxygen molecules
   M. Obata, M. Nakamura, I. Hamada, and T. Oda: J. Phys. Soc. Jpn., **82** (2013) 093701.
6. An ab initio approach to free-energy reconstruction using logarithmic mean force dynamics
   M. Nakamura, M. Obata, T. Morishita, T. Oda: J. Chem. Phys., submitted for publication.

ODAGAKI, Takashi [C class; 0 (A), 3500 (B), 1000 (C)] ()
— *Computer simulaiton on discharge process*

OGUCHI, Tamio [C class; 1500 (A), 5500 (B), 1900 (C)] (83)
— *First-Principles Calculation of Transition-Metal Compounds*

OHMURA, Satoshi [C class; 0 (A), 3500 (B), 0 (C)] (108)
— *Dissociation mechanism of multiple-charged molecules irradiated by X-FEL: first-principles molecular-dynamics simulation*

1. Dynamic asymmetry of self-diffusion in liquid $ZnCli_2$ under pressure: *ab initio* molecular dynamics study
   A. Koura, S. Ohmura, and F. Shimojo: J. Chem. Phys.**138** (2013) 134504
2. Dynamic Structure of a Molecular Liquid $Si_0.5Cl_0.5$: ab initio Molecular-Dynamics Simulations
   S. Ohmura, H. Shimakura, Y. Kawakita, F. Shimojo, and M. Yao: J. Phys. Soc. Jpn.**82** (2013) 074602
3. *Ab initio* Molecular-Dynamics Study of Dissociation Mechanism of Highly Charged Molecules
   S. Ohmura, K.Nagaya, F. Shimojo and M. Yao: J. Phys.: Conf. Ser. (2013) accepted
4. A divide-conquer-recombine algorithmic paradigm for large spatiotempor quantum molecular dynamics simulations
   F. Shimojo, S. Hattori, R. K. Kaila, M. Kunaseth, W. Mou, A. Nakano, K. Nomura, S. Ohmura, P. Rajak, K. Shimamura, and P. Vashishta : J. Chem. Phys.**140** (2014) 18A529

OHSAWA, Kazuhito [C class; 0 (A), 2000 (B), 0 (C)] (124)
— *Study of hydrogen in intermetallic compound*

OHTO, Tatsuhiko [C class; 0 (A), 1500 (B), 700 (C)] (119)
— *Ab initio study of thermoelectric properties of molecules between magnetic electrodes*

1. Thermoelectric Efficiency of Organometallic Complex Wires via Quantum Resonance Effect and Long-Range Electric Transport Property
   H. Nakamura, T. Ohto, T. Ishida and Y. Asai: JACS 2013, 135, 16545

OHTSUKI, Tomi [C,D class; 0 (A), 8000 (B), 0 (C)] (205,206)
— *Critical behavior of metal-insulator transition in disordered systems using density functional theory*
— *Transport phenomena in disordered topological insulators*

1. Disordered weak and strong topological insulators
   K. Kobayashi, T. Ohtsuki, K.-I. Imura: Physical Review Letters **110** (2013), 236803
2. Experimental proof of universal conductance fluctuation in quasi-one-dimensional epitaxial Bi2Se3 wires
   S. Matsuo, K. Chida, D. Chiba, T. Ono, K. Slevin, K. Kobayashi, T Ohtsuki, C.-Z. Chang, K. He, X.-C. Ma, Q.-K. Xue: Physical Review B **88** (2013), 155438
3. Density of States Scaling at the Semimetal to Metal Transition in Three Dimensional Topological Insulators
   K. Kobayashi, T. Ohtsuki, K.-I. Imura, I.F. Herbut: Physical Review Letters **112** (2014), 016402
4. Critical exponent for the Anderson transition in the three-dimensional orthogonal universality class
   K. Slevin, T. Ohtsuki: New Journal of Physics **16** (2014), 015012
5. Near-field optical imaging of light localization in GaN nanocolumn system

M. Sakai, Y. Inose, T. Ohtsuki, K. Ema, K. Kishino, T. Saiki: Japanese Journal of Applied Physics **53** (2014) 030301

6. Critical exponent of metal-insulator transition in doped semiconductors: the relevance of the Coulomb interaction
   Y. Harashima, K. Slevin: arXiv:1308.1191

OKA, Takashi [C class; 7500 (A), 5500 (B), 0 (C)] (193)

— *Theoretical study of non-equilibrium phase transitions in strongly correlated superconductors*

1. Nonequilibrium dynamical mean-field theory and its applications
   H. Aoki, N. Tsuji, M. Eckstein, M. Kollar, T. Oka, and P. Werner, to appear in Rev. Mod. Phys.

OKADA, Susumu [C class; 6000 (A), 1500 (B), 0 (C)] (94)

— *Design of nanoscale carbon materials*

1. Two-dimensional Metallic Molecular Sheet of Fused C_{26} Fullerene
   Mina Maruyama and Susumu Okada: Journal of the Physical Society of Japan, Vol. 82, 043708 (2013).
2. Anomalous Electric-Field Screening at Edge Atomic Sites of Finite-length Zigzag Carbon Nanotubes
   Ayaka Yamanaka and Susumu Okada: Applied Physics Express Vol. 6, 045101 (2013).
3. Energetics and Electronic Structures of Alkanes and Polyethylene Adsorbed on Graphene
   Katsumasa Kamiya and Susumu Okada: Japanese Journal of Applied Physics, Vol. 52, 04CN07 (2013).
4. Magnetic Properties of Deca-Methyl Fullerenes: Radical Spin Interaction on Chemically Functionalized Fullerenes
   Haruna Nitta, Yutaka Matsuo, Eiichi Nakamura, and Susumu Okada: Applied Physics Express, Vol. 6, 045102 (2013).
5. High-Efficient Photoelectric Conversion in Graphene-Diamond Hybrid Structures: First-principles and Model Calculations
   Satoru Konabe, Nguyen Thanh Cuong, Minoru Otani, and Susumu Okada: Applied Physics Express Vol. 6, 045104 (2013).
6. Massless Electrons on Hexagonal Dangling Bond Network on Hydrogen Deposited Diamond (111) and Si(111) Surfaces
   Junki Sone and Susumu Okada: Journal of the Physical Society of Japan, Vol. 82, 064706 (2013).
7. Energetics and Electronic Structures of Alkanes Adsorbed on Carbon Nanotubes
   Katsumasa Kamiya and Susumu Okada: Japanese Journal of Applied Physics, Vol. 52, 06GD10 (2013).
8. Electronic Properties of Capped Carbon Nanotubes under an Electric Field: Inhomogeneous Electric-Field Screening Induced by Bond Alternation
   Ayaka Yamanaka and Susumu Okada: Japanese Journal of Applied Physics Vol. 52, 06GD04 (2013).
9. Energetics and Electronic Structures of C_{60} Included in $[n]$Cyclacene Molecules
   Shota Kigure and Susumu Okada: Journal of the Physical Society of Japan, Vol. 82, 094717 (2013).
10. A Two-dimensional sp^2 Carbon Network of Fused Pentagons: All Carbon Ferromagnetic Sheet
    Mina Maruyama and Susumu Okada: Applied Physics Express Vol. 6, 095101 (2013).
11. Tuning the Chemical Reactivity of Graphene by Mechanical Strain
    Mark A. Bissett, Satoru Konabe, Susumu Okada, Masaharu Tsuji and Hiroki Ago: ACS Nano, Vol. 7, pp. 10335 – 10343 (2013).
12. Design of New Carbon Allotropes of Fused Small Fullerenes
    Mina Maruyama and Susumu Okada: Physica Status Solidi (c), Vol. 10, pp. 1620 – 1623 (2013).
13. Electrostatic Potential of Hydrogenated Finite-length Carbon Nanotubes under an Electric Field
    Ayaka Yamanaka and Susumu Okada: Physica Status Solidi (c), Vol. 10, pp. 1624 – 1627 (2013).

OKAMOTO, Yuko [E class; 0 (A), 20500 (B), 200 (C)] ()

— *Study on complex systems by generalized-ensemble algorithms*

OKITSU, Kouhei [C class; 10000 (A), 3000 (B), 1900 (C)] (188)
— *Study on phase determination of protein crystals based on an n-beam X-ray dynamical diffraction theory for an arbitrary number of n*

OKUBO, Tsuyoshi [C class; 3000 (A), 7000 (B), 3500 (C)] (192)
— *Ordering and dynamics of topological excitations in frustrated magnets*
— *Topological order in frustrated spin systems*

1. Possibility of deconfined criticality in SU(N) Heisenberg models at small N
   K. Harada, T. Suzuki, T. Okubo, H. Matsuo, J. Lou, H. Watanabe, S. Todo, and N. Kawashima: Phys. Rev. B **88** (2013) 220408(R).
2. Various regimes of quantum behavior in an $S = 1/2$ Heisenberg antiferromagnetic chain with fourfold periodicity
   H. Yamaguchi, T. Okubo, K. Iwase, T. Ono, Y. Kono, S. Kittaka, T. Sakakibara, A. Matsuo, K. Kindo, and Y. Hosokoshi: Phys. Rev. B **88** (2013) 174410
3. Kagome-Triangular Lattice Antiferromagnet $NaBa_2Mn_3F_{11}$
   H. Ishikawa, T. OKubo, Y. Okamoto, and Z. Hiroi: J. Phys. Soc. Jpn. **83** (2014) 043703

ONO, Tomoya [C class; 1000 (A), 9000 (B), 4000 (C)] (68)
— *Development of first-principles electronic-structure and transport calculation method based on real-space finite-difference approach*

1. First-principles study of spin-dependent transport through graphene/BNC/graphene structure
   T. Ota and T. Ono: Nanoscale Res. Lett. **8** (2013) 199.
2. Convergence of the Broyden density mixing method in noncollinear magnetic systems
   M. Heide and T. Ono: J. Phys. Soc. Jpn. **82** (2013) 114706.
3. Doping Effect on Magnetism and Transport Property of Heterojunction between Carbon and Boron Nitride Nanotubes
   H. D. Nguyen and T. Ono: J. Phys. Chem. C **117** (2013) 24115.
4. First-principles electronic-structure and transport calculation formalism using real-space grid based method
   T. Ono: AIP Conf. Proc. **1558** (2013) 1524.

OSHIKAWA, Masaki [B class; 0 (A), 800 (B), 0 (C)] (242)
— *Topological selection rules in one-dimensional critical phases*

1. Response to a twist in systems with Z_p symmetry: The two-dimensional p-state clock model
   Y. Kumano, K. Hushima, Y. Tomita and M. Oshikawa: Phys. Rev. B **88** (2013) 104427.
2. Entanglement spectra between coupled Tomonaga-Luttinger liquids: Applications to ladder systems and topological phases
   R. Lundgren, Y. Fuji, S. Furukawa and M. Oshikawa: Phys. Rev. B **88** (2013) 245137.
3. Quantum criticality in an asymmetric three-leg spin tube: A strong rung-coupling perspective
   Y. Fuji, S. Nishimoto, H. Nakada and M. Oshikawa: Phys. Rev. B **89** (2014) 054425.

OSHIYAMA, Atsushi [E class; 0 (A), 27000 (B), 4100 (C)] (47)
— *Atomic Structures and Electronic Properties of Hard- and Soft-Nanomaterials*

1. Atom-Scale Reaction Pathways and Free-Energy Landscapes in Oxygen Plasma Etching of Graphene
   K. Koizumi, M. Boero, Y. Shigeta, and A. Oshiyama: J. Phys. Chem. Letters **4** (2013) 1592
2. Absence of Dirac Electrons in Silicene on Ag(111) Surfaces
   a Z.-X. Guo, S. Furuya, J.-I. Iwata and A. Oshiyama: J. Phys. Soc. Jpn. **82** (2013) 063714
3. Atomic Reconstruction and Electron States at Interfaces between 3C-SiC(111) and Si(110)
   E. K. K. Abavare, J.-I. Iwata and A. Oshiyama: Phys. Rev. B **87** (2013) 235321
4. Absence and Presence of Dirac Electrons in Silicene on Substrates
   Z.-X. Guo, S. Furuya, J.-I. Iwata and A. Oshiyama: Phys. Rev. B **87** (2013) 235435
5. Firtst-Principles Study of Nanofacet Formation on 4H-SiC(0001) Surface
   K. Sawada, J.-I. Iwata and A. Oshiyama: Proc. Int. Conf. Silicon Carbide and Related Materials (ICSCRM) **778-780** (2013) 201

6. Diameter-Selective Alignment of Carbon Nanotubes on Si(001) Stepped Surfaces
   B. Enkhtaivan, M. Yoshimura, J.-I. Iwata, and A. Oshiyama: J. Chem. Phys. **140** (2013) 044713
7. Magic Angle and Height Quantization in Nanofacets on SiC(0001) Surfaces
   K. Sawada, J.-I. Iwata and A. Oshiyama: Appl. Phys. Lett. **104** (2014) 051605
8. Interstitial Channels that Control Band Gaps and Effective Masses in Tetrahedrally Bonded Semiconductors
   Y. Matsushita and A. Oshiyama: Phys. Rev. Lett. **112** (2014) 136403
9. Structural Tristability and Deep Dirac States in Bilayer Silicene on Ag(111) Surfaces
   Z.-X. Guo and A. Oshiyama: Phys. Rev. B **89** (2014) 155418
10. 結晶性半導体エピタキシャル成長の量子論 -
    押山淳: ポストシリコン半導体：ナノ成膜ダイナミクスと基板・界面効果 (エヌ・ティー・エス、2013) pp32 - pp42

OTANI, Minoru [E class; 0 (A), 10000 (B), 2000 (C)] (75)
— *First-principles molecular dynamics simulation of electrode/electrolyte interface with constant bias potential method.*
Effect of thermal motion on catalytic activity of nanoparticles in polar solvent

1. Effect of thermal motion on catalytic activity of nanoparticles in polar solvent
   N. Bonnet, O. Sugino, and M. Otani:J. Chem. Phys. **140** (2014) 044703.
2. Improved modeling of electrified interfaces using the effective screening medium method
   I. Hamada, O. Sugino, N. Bonnet and M. Otani:Phys.Rev. B **88** (2013) 155427.

OTOMO, Junichiro [B,C class; 1300 (A), 3600 (B), 0 (C)] (100,102)
— *Synthesis of proton conducting electrolyte and evaluation of ion conductivity of interfaces*
— *Development of proton conducting solid electrolyte for inter mediate temperature fuel cells*
— *Study on physicochemical properties for proton conductivity in lanthanum tungstate*

OZEKI, Yukiyasu [C class; 0 (A), 7000 (B), 1300 (C)] (201)
— *Numerical study on critical universalities for random systems including KT transition*
— *Dynamical scaling for nonequilibrium relaxation functions by the use of Bayesian inference and kernel method*

1. Numerical studies on critical properties of the Kosterlitz-Thouless phase for the gauge glass model in two dimensions
   Y. Ozeki, S. Yotsuyanagi, T. Sakai and Y. Echinaka: Phys. Rev E **89** (2014) 022122

RAEBIGER, Hannes [C class; 8500 (A), 2500 (B), 0 (C)] ()
— *Theory of self-organized nano-interfaces for electronic devices*

SAITO, Mineo [C class; 0 (A), 8500 (B), 0 (C)] (85)
— *First-Principles Calculations Concerning Spintronics*

1. Hydrogen Adsorption in Capped Armchair Edge (5,5) Carbon Nanotubes
   A. Setiadi, M. S. Alam, F. Muttaqien, and M. Saito: Jpn. J. Appl. Phys. **52** (2013) 125105.
2. First-principles study of carrier-induced ferromagnetism in bilayer and multilayer zigzag graphene nano ribbons
   K. Sawada, F. Ishii, and M. Saito: Appl. Phys. Lett. **104** (2014) 14311.
3. Tunable Rashba effect on strained ZnO: First-principles density-functional study
   M. A. Adhib, H. Kotaka, F. Ishii, and M. Saito: Appl. Phys. Exp. **7** (2014) 053002.
4. Spin polarized positron lifetimes in ferromagnetic metal
   J. Lin, T. Yamasaki, and M. Saito: Jpn. J. Appl. Phys. **53** (2014) 053002.

SAKAI, Toru [C class; 23500 (A), 8000 (B), 3800 (C)] (176,178)
— *Numerical Study on Spin Liquid in Frustrated Systems*Novel Spin Flop Transition in Low-Dimensional Quantum Spin Systems

1. Quantum Critical Magnetization Behaviors of the Kagome- and Triangular-Lattice Antiferromagnets

T. Sakai and H. Nakano: Physica Status Solidi. B **250** (2013) 579.

2. Anomalous behavior of the spin gap of a spin-1/2 two-leg antiferromagnetic ladder with Ising-like rung interations
   T. Tonegawa, K. Okamoto and T. Sakai: Physica Status Solidi. B **250** (2013) 575.
3. Long-Range Order of the Three-Sublattice Structure in the S=1 Heisenberg Antiferromagnet on the Spatially Anisotropic Triangular Lattice
   H. Nakano, S. Todo and T. Sakai: J. Phys. Soc. Jpn. **82** (2013) 043715
4. Novel Field-Induced Quantum Phase Transition of the Kagome-Lattice Antiferromagnet
   T. Sakai and H. Nakano: J. Korean Phys. Soc. **63** (2013) 601
5. Quantum Critical Magnetization Behaviors of the Kagome- and Triangular-Lattice Antiferromagnets
   T. Sakai and H. Nakano: J. Low Temperature Phys. **170** (2013) 255
6. The Two-Dimensional S=1/2 Heisenberg Antiferromagnet on the Shuriken Lattice -a Lattice Composed of Vertex-Sharing Triangles
   H. Nakano and T. Sakai: J. Phys. Soc. Jpn. **82** (2013) 083709
7. Transitions in 1/3 Plateau of the Quantum Spin Tube
   K. Okunishi, M. Sato, T. Sakai, K. Okamoto and C. Itoi: J. Korean Phys. Soc. **63** (2013) 596
8. Ground-state phase diagram of an S=1/2 two-leg Heisenberg spin ladder system with negative four-spin interaction
   K. Hijii and T. Sakai: Phys. Rev. B **88** (2013) 104403
9. Exotic Quantum Phenomena in the Spin Nanotubes
   T. Sakai and K. Okamoto: JPS Conf. Proc. **1** (2013) 012025
10. Exotic Magnetism of the Quantum Spin Nanotube
    T. Sakai and K. Okamoto: JPS Conf. Proc. **2** (2013) 010208
11. Quantum Spin-Liquid Behavior in the Spin-1/2 Random Heisenberg Antiferromagnet on the Triangular Lattice
    K. Watanabe, H. Kawamura, H. Nakano and T. Sakai: J. Phys. Soc. Jpn. **83** (2014) 034714
12. Anomalous Quantum Magnetization Behaviors of the Kagome and Triangular Lattice Antiferromagnets
    H. Nakano and T. Sakai: to appear in JPS Conf. Proc.
13. Edge Modes in the Intermediate-D and Large-D Phases of the S=2 Quantum Spin Chain with XXZ and On-Site Anisotropies
    K. Okamoto, T. Tonegawa, T. Sakai and M. kaburagi: to appear in JPS Conf. Proc.
14. The Magnetization Process of the S=1/2 Heisenberg Antiferromagnet on the Cairo Pentagon Lattice with Distortion
    H. Nakano, M. Isoda and T. Sakai: to appear in J. Phys. Soc. Jpn.

SAKASHITA, Tatsuya [B class; 0 (A), 1600 (B), 0 (C)] ()
— *Parallelization and High Precision Computation of Exact Diagonalization Package for Spin Systems*

SAKURAI, Masahiro [B class; 0 (A), 1300 (B), 900 (C)] (123)
— *A study of electron self-energy using first-principles calculations*
— *First-principles calculations for electron self-energy*

SATO, Toshihiro [C class; 0 (A), 5000 (B), 0 (C)] (159)
— *Thermal transport property in strongly correlated electronic system*
— *Electronic properties of multi-orbital electronic system with strong spin-orbit coupling*

SATO, Yukio [B class; 0 (A), 1100 (B), 0 (C)] (131,132)
— *First-principles calculations on atomic and electronic structure at oxide grain boundaries*
— *First-principles calculations of the atomic arrangement at the interfaces in crystalline solids*

1. Atomic structure of ZnO S13 [0001]/13-40 symmetric tilt grain boundary
   J.-Y. Roh, Y. Sato, and Y. Ikuhara, Journal of the American Ceramic Society, 97, 617-621 (2014).
2. Grain-boundary structural transformation induced by the geometry and chemistry
   Y. Sato, J.-Y. Roh, and Y. Ikuhara, Physical Review B 87, 141001-1-4 (2013).

3. Investigation of microstructure and its impact on physical property in electroceramics
   Y. Sato, Journal of the Ceramic Society of Japan, 121, 825-830 (2013).

SHIBA, Hayato [E class; 0 (A), 17000 (B), 2400 (C)] (34)
— *Spatiotemporal inhomogeneity of glasses at large scales - low-frequency vibrations, finite size effect, and continuum entropy*

1. Spatiotemporal heterogeneity of local free volumes in highly supercooled liquid
   H. Shiba and T. Kawasaki: J. Chem. Phys. **139** (2013) 184502.

SHIGETA, Yasuteru [C class; 8500 (A), 4000 (B), 0 (C)] (71)
— *Theoretical analyses on self-splicing mechanism of Nyl C*

1. A Nylon-oligomer Hydrolase Promoting Cleavage Reactions in Unnatural Amide Compounds
   K. Kamiya, T. Baba, M. Boero, T. Matsui, S. Negoro, Y. Shigeta, J. Phys. Chem. Lett, 5, 1210 (2014)

SHIMIZU, Akira [B,C class; 9200 (A), 2500 (B), 1200 (C)] (195)
— *Analysis of the spin system using the canonical thermal pure quantum state at finite temperature*
— *Thermodynamics and statistical mechanics of systems with long-range interactions*

SHIMOJO, Fuyuki [C class; 0 (A), 8000 (B), 3700 (C)] (78)
— *First-Principles Molecular-Dynamics Study of Structural and Electronic Properties of Covalent Liquids under Pressure*

1. Concentration dependence of the dynamic properties of liquid Tl_xSe_{1-x} based on *ab initio* molecular-dynamics simulations
   A. Koura and F. Shimojo: J. Phys. Soc. Jpn. **82** (2013) 094602.
2. Dynamic Structure of a Molecular Liquid $S_{0.5}Cl_{0.5}$: *ab initio* Molecular-Dynamics Simulations
   S. Ohmura, H. Shimakura, Y. Kawakita, F. Shimojo, and M. Yao: J. Phys. Soc. Jpn. **82** (2013) 074602.
3. Dynamic asymmetry of self-diffusion in liquid $ZnCl_2$ under pressure: an *ab initio* molecular-dynamics study
   A. Koura, S. Ohmura, and F. Shimojo: J. Chem. Phys. **138** (2013) 134504.
4. Bonding and Structure of Ceramic-Ceramic Interfaces
   K. Shimamura, F. Shimojo, R. K. Kalia, A. Nakano, and P. Vashishta: Phys. Rev. Lett. **111** (2013) 066103.
5. *Ab initio* study of dissociation reaction of ethylene molecules on Ni cluster
   K. Shimamura, T. Oguri, Y. Shibuta, S. Ohmura, F. Shimojo, and S. Yamaguchi: J. Phys.: Conf. Ser. **454** (2013) 012022.

SHIOMI, Junichiro [B class; 1400 (A), 600 (B), 400 (C)] (230)
— *Characterization of thermal transport at nanostructure interface*

SHIRAISHI, Kenji [C class; 13500 (A), 5000 (B), 900 (C)] ()
— *Guiding Principles towards Fabricating SiC-MOSFET for Future Power Devices*

SHIRO, Masanori [B class; 900 (A), 0 (B), 0 (C)] (241)
— *High precision computation of Feigenbaum constant*

SHOJI, Mitsuo [C class; 0 (A), 4000 (B), 0 (C)] ()
— *Theoretical elucidation on the reaction mechanism in Nitrite Reductase*

SHUDO, Ken-ichi [C class; 3000 (A), 500 (B), 300 (C)] (105)
— *Local structure organo-complex adsorbed on metallic surface*

1. Molecular Motion Induced by Multivibronic Excitation on Semiconductor Surface
   Tatsuya Momose, Ken-ichi Shudo, Hannes Raebiger, Shin-ya Ohno, Takeshi Kitajima, Masanobu Uchiyama, Takanori Suzuki, Masatoshi Tanaka: J. Phys. Chem. **C 114**, 15671–77 (2014).

2. Electronic Excited States in Strongly Correlated Organic Radical 1,3,5-trithia-2,4,6-triazapentalenyl (TTTA) Adsorbed on Si(001) Surface
   K. Shudo, T. Satake, T. Shimatsu, M. Uchiyama, Y. Morikawa, J. Takeda: Phys. Chem. Chem. Phys. **15**, 19213–19220 (2013).
3. Atomic-scale structures and electronic states of defects on Ar+ -ion irradiated MoS2
   Akihiro Inoue, Takahiro Komori, Ken-ichi Shudo: Journal of Electron Spectroscopy and Related Phenomena **189**, 11–18 (2013).
4. Titanium-induced charge of Si(001) surface dependent on local configuration
   K. Shudo, T. Aoki, S. Ohno, K. Yamazaki, F. Nakayama, M. Tanaka, T. Okuda, A. Harasawa, I. Matsuda, T. Kakizaki, M. Uchiyama: J. Electr. Specrosc. Rel. Phenom. **192**, 35–39 (2014).
5. Ultrafast Measurements of Coherent Vibrations in Benzenethiol Monolayer Film
   K. Shudo, K. Doi, I. Katayama, M. Kitajima, J. Takeda: Ultrafast Phenomena **XVIII** 05013 (pp.3), EDP Sciences (2013 Les Ulis Cedex, France). ISBN: 978-2-7598-0956-1
6. Coherent phonon and surface-enhanced Raman scattering dynamics in solids
   J. Takeda, K. Ikufumi, K. Shudo, M. Kitajima: Journal of Luminescence, *in press* (2014).
7. Thermally Formed Ru-Si Nanostructures Grown on Silicon (001) Surface
   K.Shudo, S. Ohno, N. Kawamura, M. Toramaru, N. Kobayashi, Y. Miyamoto: Surface Review and Letters **20**, 1350018 (2013).
8. Nanoscale Relaxation in Ru-Si Growth on a Silicon (111) Surface
   M. Toramaru, N. Kobayashi, N. Kawamura, S.Ohno, Y. Miyamoto, K.Shudo: Surface and Interface Analysis **45**, 1109–1112 (2013).

SUGINO, Osamu [E class; 0 (A), 7500 (B), 2300 (C)] (80)
— *Oxide electrocatalysts*

1. First-principles thermodynamic description of hydrogen electroadsorption on the Pt(111) surface
   T. T. T. Hanh, Y. Takimoto and O. Sugino: Surface Science **625** (2014) 104.

SUZUKI, Takafumi [E class; 0 (A), 12500 (B), 2500 (C)] (186)
— *Edge state in 2d quantum spin and bosonic systems*

1. Possibility of deconfined criticality in SU(N) Heisenberg models at small N
   K. Harada, T. Suzuki, T. Okubo, H. Matsuo, J. Lou, H. Watanabe, S. Todo, and N. Kawashima: Phys. Rev. B 88, 220408(R) (2013).

TAKAGI, Noriaki [B class; 0 (A), 2500 (B), 200 (C)] (113,114)
— *Exploring two-dimensional honeycomb materials*

1. Symmetry-Driven Novel Kondo Effect in a Molecule
   E. Minamitani, N. Tsukahara, D. Matsunaka, Y. Kim, N. Takagi, and M Kawai: Phys. Rev. Lett **109** (2012) 086602.
2. Structural transition of silicene on Ag(111)
   R. Arafune, C. -L. Lin, K. Kawahara, N. Tsukahara, E. Minamitani, Y. Kim, N. Takagi, and M. Kawai: Surf. Sci. **608** (2013) 297.
3. Structure of Silicene grown on Ag(111)
   C.-L. Lin, R. Arafune, K. Kawahara, M. Kanno, N. Tsukahara, E. Minamitani, Y. Kim, M. Kawai, and N Takagi: Phys. Rev. Lett., **110** (2013) 076801.
4. Mode-selective electron-phonon coupling in laser photoemission on Cu(110)
   E. Minamitani, R. Arafune, M. Q. Yamamoto, N. Takagi, M. Kawai, and Y. Kim: Phys. Rev. B, **88** (2013) 224301.
5. Comment on ‘‘ Evidence for Dirac Fermions in a Honeycomb Lattice Based on Silicon ’’
   R. Arafune, C.-L. Lin, R. Nagao, M. Kawai, and N. Takagi: Phys. Rev. Lett., **110** (2013) 229701.

TAMARIBUCHI, Tsuguhiro [B class; 1600 (A), 700 (B), 500 (C)] ()
— *Development of fast algorythms for sparse Pfaffians and their applications to Ising systems*

TAMURA, Ryo [C class; 0 (A), 4000 (B), 1400 (C)] (218,220)
— *Theoretical Study for Magneto Caloric Effect using Spin Models*

— *Investigation of phase transitions and their microscopic mechanisms in frustrated spin systems*

1. Network-Growth Rule Dependence of Fractal Dimension of Percolation Cluster on Square Lattice
   S. Tanaka and R. Tamura: J. Phys. Soc. Jpn. **82** (2013) 053002.
2. Quantum Annealing for Dirichlet Process Mixture Models with Applications to Network Clustering
   I. Sato, S. Tanaka, K. Kurihara, S. Miyashita, and H. Nakagawa: Neurocomputing **121** (2013) 525.
3. Second-Order Phase Transition in Heisenberg Model on Triangular Lattice with Competing Interactions
   R. Tamura, S. Tanaka, and N. Kawashima: Phys. Rev. B **87** (2013) 214401.
4. A Useful Way to Obtain the Central Charge of Entanglement Hamiltonian – Nested Entanglement Entropy –
   S. Tanaka: Interdisciplinary Information Sciences **19** (2013) 101.
5. Interlayer-Interaction Dependence of Latent Heat in the Heisenberg Model on a Stacked Triangular Lattice with Competing Interactions
   R. Tamura and S. Tanaka: Phys. Rev. E **88** (2013) 052138.
6. A Generalized Magnetic Refrigeration Scheme
   R. Tamura, T. Ohno, and H. Kitazawa: Appl. Phys. Lett. **104** (2014) 052415. [This topic was reported in Press Release in NIMS (March 10, 2014), MyNavi News (March 12, 2014), The Chemical Daily (March 19, 2014), The Science News (March 28, 2014).]
7. Phase Transitions with Discrete Symmetry Breaking in Antiferromagnetic Heisenberg Models on a Triangular Lattice
   R. Tamura, S. Tanaka, and N. Kawashima: JPS Conf. Proc. **1** (2014) 012125.
8. Entanglement Properties of a Quantum Lattice-Gas Model on Square and Triangular Ladders
   S. Tanaka, R. Tamura, and H. Katsura: Kinki University Series on Quantum Computing - Vol. 9, "Physics, Mathematics, And All That Quantum Jazz" (World Scientific), in press.
9. A Method to Change Phase Transition Nature – Toward Annealing Method –
   R. Tamura and S. Tanaka: Kinki University Series on Quantum Computing - Vol. 9, "Physics, Mathematics, And All That Quantum Jazz" (World Scientific), in press.

TANAKA, Hajime [B class; 0 (A), 900 (B), 0 (C)] (239)

— *Hydrodynamic effects on phase ordering 2*

1. A novel coarsening mechanism of droplets in immiscible fluid mixtures
   Ryotaro Shimizu and Hajime Tanaka: submitted.

TANAKA, Shu [C class; 0 (A), 3000 (B), 2600 (C)] (207,209)

— *Study on Statistical Physics Based on Quantum Information Theory*

— *Control of Phase Transition Behavior in Lattice Models*

1. Network-Growth Rule Dependence of Fractal Dimension of Percolation Cluster on Square Lattice
   S. Tanaka and R. Tamura: J. Phys. Soc. Jpn. **82** (2013) 053002.
2. Quantum Annealing for Dirichlet Process Mixture Models with Applications to Network Clustering
   I. Sato, S. Tanaka, K. Kurihara, S. Miyashita, and H. Nakagawa: Neurocomputing **121** (2013) 525.
3. Second-Order Phase Transition in Heisenberg Model on Triangular Lattice with Competing Interactions
   R. Tamura, S. Tanaka, and N. Kawashima: Phys. Rev. B **87** (2013) 214401.
4. A Useful Way to Obtain the Central Charge of Entanglement Hamiltonian – Nested Entanglement Entropy –
   S. Tanaka: Interdisciplinary Information Sciences **19** (2013) 101.
5. Interlayer-Interaction Dependence of Latent Heat in the Heisenberg Model on a Stacked Triangular Lattice with Competing Interactions
   R. Tamura and S. Tanaka: Phys. Rev. E **88** (2013) 052138.
6. A Generalized Magnetic Refrigeration Scheme
   R. Tamura, T. Ohno, and H. Kitazawa: Appl. Phys. Lett. **104** (2014) 052415. [This topic

was reported in Press Release in NIMS (March 10, 2014), MyNavi News (March 12, 2014), The Chemical Daily (March 19, 2014), The Science News (March 28, 2014).]

7. Phase Transitions with Discrete Symmetry Breaking in Antiferromagnetic Heisenberg Models on a Triangular Lattice
   R. Tamura, S. Tanaka, and N. Kawashima: JPS Conf. Proc. **1** (2014) 012125.
8. Entanglement Properties of a Quantum Lattice-Gas Model on Square and Triangular Ladders
   S. Tanaka, R. Tamura, and H. Katsura: Kinki University Series on Quantum Computing - Vol. 9, "Physics, Mathematics, And All That Quantum Jazz" (World Scientific), in press.
9. A Method to Change Phase Transition Nature – Toward Annealing Method –
   R. Tamura and S. Tanaka: Kinki University Series on Quantum Computing - Vol. 9, "Physics, Mathematics, And All That Quantum Jazz" (World Scientific), in press.

TANIGAKI, Kenichi [B class; 0 (A), 1100 (B), 0 (C)] ()
— *First principles analysis for suppression of grain boundary embrittlement of aluminum alloys by liquid metals*ab-initio theoretical analysis for low-temperature elastic anomaly of Pd and Pt

TATENO, Masaru [C class; 0 (A), 8500 (B), 0 (C)] (86)
— *Hybrid ab initio QM/MM calculations of biological macromolecular systems*

TATEYAMA, Yoshitaka [C,E class; 0 (A), 13500 (B), 1600 (C)] (66)
— *DFT statistical mechanics analysis of redox reaction mechanism at interfaces in catalysts and batteries*
— *DFT statistical mechanics analysis of redox reaction mechanisms at interfaces in catalysts and batteries*

1. Amplification of Conformational Effects via tert-Butyl Groups: Hexa-tert-butyl Decacyclene on Cu(100) at Room Temperature
   G. Pawin, A. Z. Stieg, C. Skibo, M. Grisolia, R. R. Schilittler, V. Langlais, Y. Tateyama, C. Joachim, and J. K. Gimzewski: Langmuir 29, 7309-7317 (2013).
2. Unusually Stable 100-Fold Reversible and Instant Swelling of Inorganic Layered Materials
   F. Geng, R. Ma, A. Nakamura, K. Akatsuka, Y. Ebina, Y. Yamauchi, N. Miyamoto, Y. Tateyama, and T. Sasaki: Nature Comm. 4, 1632 (2013).
3. High performance organic field-effect transistors based on single-crystal microribbons and microsheets of solution-processed dithieno[3,2-b:2',3'-d]thiophene derivatives
   Yu Seok Yang, Takuma Yasuda, Hayato Kakizoe, Hiroyuki Mieno, Hiori Kino, Yoshitaka Tateyama, and Chihaya Adachi: Chem. Commun., 49, 6483 - 6485, (2013).
4. Trimer effects in fragment molecular orbital-linear combination of molecular orbital calculation of one-electron orbitals for biomolecules
   Tomoki Kobori, Keitaro Sodeyama, Takao Otsuka, Yoshitaka Tateyama, and Shinji Tsuneyuki: J. Chem. Phys. 139, 094113 (2013).
5. Additive Effect on Reductive Decomposition and Binding of Carbonate-Based Solvent toward Solid Electrolyte Interphase Formation in Lithium-Ion Battery
   Keisuke Ushirogata, Keitaro Sodeyama, Yukihiro Okuno, and Yoshitaka Tateyama: J. Am. Chem. Soc. 135, 11967-11974 (2013).
6. Unusual Stability of Acetonitrile-Based Superconcentrated Electrolytes for Fast-Charging Lithium-Ion Batteries
   Y. Yamada, K. Furukawa, K. Sodeyama, K. Kikuchi, M. Yaegashi, Y. Tateyama, and A. Yamada: J. Am. Chem. Soc. 136 (2014).

TERAO, Takamichi [B class; 2400 (A), 1000 (B), 800 (C)] (224)
— *Numerical study of Coulomb glass*

1. Non-equilibrium dynamics of Coulomb glass: Kinetic Monte Carlo simulation
   T. Terao, A. Kono, and W. Takahashi: AIP conf. proc. **1518** (2013) 320.
2. Numerical study of two-dimensional metamaterial composites: the existence of a stop band
   T. Terao: J. Mod. Opt. **60** (2013) 1997.

TODO, Synge [C class; 0 (A), 5500 (B), 2400 (C)] (211)

— *Analysis of Quantum Phase Transitions with Large Finite-Size Effect*

1. Long-Range Order of the Three-Sublattice Structure in the $S = 1$ Heisenberg Antiferromagnet on the Spatially Anisotropic Triangular Lattice
   H. Nakano S. Todo and T. Sakai, J. Phys. Soc. Jpn. **82**, 043715 (2013).
2. レイテンシコアの高度化・高効率化による将来の HPCI システムに関する調査研究のためのアプリケーション最適化と異機種計算機環境での性能評価
   片桐孝洋, 大島聡史, 中島研吾, 米村崇, 熊洞宏樹, 樋口清隆, 橋本昌人, 高山 恒一, 藤堂眞治, 岩田潤一, 内田和之, 佐藤正樹, 羽角博康, 黒木聖夫, 情報処理学会研究報告 **HPC-139(4)**, 1–9 (2013).
3. 詳細つりあいを満たさないマルコフ連鎖モンテカルロ法とその一般化
   諏訪秀麿, 藤堂眞治, 数理解析研究所 講究録 **1848**, 93–107 (2013).
4. Possibility of Deconfined Criticality in SU(N) Heisenberg Models at Small N
   K. Harada, T. Suzuki, T. Okubo, H. Matsuo, J. Lou, H. Watanabe, S. Todo and N. Kawashima, Phys. Rev. B **88**, 220408(R) (2013).
5. Geometric Allocation Approaches in Markov Chain Monte Carlo
   S. Todo and H. Suwa, J. Phys.: Conf. Ser. **473**, 012013 (2013).
6. Monte Carlo simulation with aspect ratio optimization: Anomalous anisotropic scaling in dimerized antiferromagnet
   S. Yasuda and S. Todo, Phys. Rev. E **88**, 061301(R) (2013).
7. Numerical Analysis of Quantum Phase Transitions with Dynamic Control of Anisotropy
   S. Yasuda and S. Todo, JPS Conf. Proc. **1**, 012127 (2014).
8. Path-Integral Monte Carlo for the Gauge-Fixed Berry Connection and the Local Z_2 Berry Phase
   Y. Motoyama and S. Todo, JPS Conf. Proc. **1**, 012130 (2014).
9. Parallelized Quantum Monte Carlo Algorithm with Nonlocal Worm Updates
   A. Masaki, T. Suzuki, K. Harada, S. Todo, and N. Kawashima, Phys. Rev. Lett. **112**, 140603 (2014).

TOHEI, Tetsuya [B class; 0 (A), 600 (B), 0 (C)] (136)

— *First principles calculations of complex defect structures in oxide ceramics*

TOHYAMA, Takami [E class; 0 (A), 13500 (B), 0 (C)] (147)

— *DMRG Study of Triangular Lattice Hubbard Model*

1. Magnetic Raman scattering study of spin frustrated systems, κ-(BEDT-TTF)$_2$X
   Y. Nakamura, N. Yoneyama, T. Sasaki, T. Tohyama, A. Nakamura, and H. Kishida: J. Phys. Soc. Jpn. in press.

TOMITA, Yusuke [B class; 0 (A), 700 (B), 0 (C)] (243)

— *Application of a cluster algorithm to the RP^2 model*

1. Relaxor Behavior and Morphotropic Phase Boundary in a Simple Model
   Y. Tomita and T. Kato: J. Phys. Soc. Jpn. **82** (2013) 063002.

TONEGAWA, Takashi [C class; 25000 (A), 3000 (B), 0 (C)] (227)

— *Numerical Study of the One-Dimensional Quantum Spin Systems with Spatial Structures*

1. Edge Modes in the Intermediate-D and Large-D Phases of the $S = 2$ Quantum Spin Chain with XXZ and On-Site Anisotropies
   K. Okamoto, T. Tonegawa, T. Sakai, and M. Kaburagi: JPS Conf. Proc. in press.

TSUNEYUKI, Shinji [C class; 6000 (A), 4000 (B), 2000 (C)] (77)

— *First-principles investigation on thermophysics of nano structures*

1. Optimization of the Jastrow factor using the random-phase approximation and a similarity-transformed Hamiltonian: Application to band-structure calculation for some semiconductors and insulators
   M. Ochi, K. Sodeyama and S. Tsuneyuki: J. Chem. Phys. **140** (2014) 074112.
2. Improved tetrahedron method for the Brillouin-zone integration applicable to response functions
   M. Kawamura, Y. Gohda and S. Tsuneyuki: Phys. Rev. B **89** (2014) 094515.
3. Anharmonic force constants extracted from first-principls molecular dynamics: applications to

heat transfer simulations
T. Tadano, Y. Gohda and S. Tsuneyuki: J. Phys. Condens. Matter, in press.

4. Trimer effects in fragment molecular orbital-linear combination of molecular orbitals calculation of one-electron orbitals for biomolecules
T. Kobori, K. Sodeyama, T. Otsuka, Y. Tateyama and S. Tsuneyuki: J. Chem. Phys. **139** (2013) 094113.

UCHIDA, Takashi [C class; 0 (A), 1000 (B), 300 (C)] (130)
— *Analysis of the temperature dependence of the magnetic and electronic structures of Mn_3Pt on the basis of the first-principles molecular dynamics theory*

1. First-principles Molecular-dynamics Study on the Magnetic Structure of Mn_3Pt
T. Uchida, N. Kimura and Y. Kakehashi: J. Korean Phys. Soc. **62** (2013) 1748.

UDA, Yutaka [B class; 0 (A), 400 (B), 0 (C)] (137)
— *Wear mechanism of diamond tool*

UDAGAWA, Masafumi [C class; 0 (A), 4000 (B), 0 (C)] ()
— *Multipole ordering and magnetic, phononic and conduction properties of conduction systems*

WATANABE, Hiroshi [C class; 0 (A), 5000 (B), 1800 (C)] (217)
— *Numerical analysis on interbubble interaction in multibubble nuclei*

1. Huge-scale Molecular Dynamics Simulation of Multibubble Nuclei
H. Watanabe, M. Suzuki, and N. Ito: Comput. Phys. Commun., **184**, (2013) 2775–2784.

WATANABE, Kazuyuki [C class; 18000 (A), 4500 (B), 700 (C)] (50)
— *Ab Initio Study of Excited Electronic States and Nonadiabatic Processes of Nanostructures under External Fields*

1. Optical Properties of Boron Nitride and Graphene Nanoribbons: A Time-Dependent Density Functional Theory Simulation
S. Hagiwara, H. Goto, C. Hu, and K. Watanabe, JPS. Conf. Proc. **1**, 012072 (2014).
2. Time-Dependent Density Functional Theory Simulation of Electron Wave-Packet Scattering with Nanoflakes
K. Tsubonoya, C. Hu, and K. Watanabe, submitted.
3. Patterns of Field Electron Emission from Carbon Nanotubes: Ab initio Simulations by Time-Dependent Density Functional Theory
C. Hu, R. Mori, and K. Watanabe, JPS Conf. Proc. **1**, 012067 (2014).
4. Performance of Tamm-Dancoff Approximation on Nonadiabatic Couplings by Time-Dependent Density Functional Theory
C. Hu, O. Sugino, and K. Watanabe, J. Chem. Phys. **140**, 054106 (2014).

WATANABE, Satoshi [C class; 1500 (A), 9000 (B), 1600 (C)] (73)
— *Theoretical Analyses on Electron/Ion/Thermal Transport Properties toward Nano-devices*

1. Design principle for increasing charge mobility of π-conjugated polymers using regularly localized molecular orbitals
J. Terao, A. Wadahama, A. Matono, T. Tada, S. Watanabe, S. Seki, T. Fujihara and Y. Tsuji: Nat. Commun. **4** (2013) 1691.
2. Non-equilibrium thermal transport simulation of conical carbon nanofibers
D. A. Thomas, T. Yamamoto, T. Tada and S. Watanabe: Trans. Mater. Res. Soc. Jpn. **38** (2013) 183.
3. Wavelet Analysis of Quantum Transient Transport in a Quantum Dot
K. Sasaoka, T. Yamamoto and S. Watanabe: Appl. Phys. Lett. **102** (2013) 233107.
4. Highly Conductive $[3 \times n]$ Gold-Ion Clusters Enclosed within Self-Assembled Cages
M. Kiguchi, J. Inatomi, Y. Takahashi, R. Tanaka, T. Osuga, T. Murase, M. Fujita, T. Tada and S. Watanabe: Angew. Chem. Int. Ed. **52** (2013) 6202.
5. Nonvolatile three-terminal operation based on oxygen vacancy drift in a $Pt/Ta_2O_{5-x}/Pt$ structure

Q. Wang, Y. Itoh, T. Hasegawa, T. Tsuruoka, S. Yamaguchi, S. Watanabe, T. Hiramoto, and M. Aono: Appl. Phys. Llett. **102** (2013) 233508.

6. Anomalous metallic-like transport of Co-Pd ferromagnetic nanoparticles cross-linked with π-conjugated molecules having a rotational degree of freedom
   Y. Ito, K. Takai, A. Miyazaki, V. Sivamurugan, M. Kiguchi, Y. Ogawa, N. Nakamura, S. Valiyaveettil, T. Tada, S. Watanabe and T. Enoki: Phys. Chem. Chem. Phys. **16** (2014) 288.
7. Conduction Paths in Cu/Amorphous-Ta_2O_5/Pt Atomic Switch: First-Principles Studies
   B. Xiao, T. Gu, T. Tada and S. Watanabe: J. Appl. Phys. **115** (2014) 034503.
8. Two types of on-state observed in the operation of a redox-based three-terminal device
   Q. Wang, Y. Itoh, T. Tsuruoka, T. Hasegawa, S. Watanabe, S. Yamaguchi, T. Hiramoto and M. Aono: Key Eng. Mater. **596** (2014) 111.
9. Anomalous Satellite Inductive Peaks in AC Response of Defective Carbon Nanotubes
   D. Hirai, T. Yamamoto and S. Watanabe: J. Appl. Phys., in press.
10. Spin Polorlized Currents through a Quantum Dot: Non-Equilibrium Green's Function Simulations under Hartree Approximation
    K. Sasaoka, T. Yamamoto and S. Watanabe: submitted to Jpn. J. Appl. Phys.
11. Oxygen Vacancy Effects in Amorphous-TaO_x-Based Resistance Switch: First Principle Study
    B. Xiao and S. Watanabe: submitted to Nanoscale.

YABANA, Kazuhiro [E class; 0 (A), 21000 (B), 2100 (C)] (52)
— *First-principles calculation for light-matter interactions*

1. First-principles simulation of the optical response of bulk and thin-film alpha-quartz irradiated with an ultrashort intense laser pulse
   K.-M. Lee, C. M. Kim. S. A. Sato, T. Otobe, K. Yabana, T. M. Jeong: J. Appl. Phys. **115** (2014) 053519.
2. Numerical pump-probe experiments of laser-excited silicon in nonequilibrium phase
   S.A. Sato, K. Yabana, Y. Shinohara, T. Otobe, G.F. Bertsch: Phys. Rev. B**89** (2014) 064304.

YAKUBO, Kousuke [B class; 1500 (A), 0 (B), 0 (C)] (235)
— *Robustness of Scale-free Networks against Overload Failures*

1. Structural robustness of scale-free networks against overload failures
   S. Mizutaka and K. Yakubo: Phys. Rev. E **88** (2013) 012803.
2. Network robustness to overload failures
   S. Mizutaka and K. Yakubo: Topologica **3** (2014) in press.
3. Self-organized Criticality in Catalytic Reaction Dynamics
   A. Watanabe and K. Yakubo: Topologica **3** (2014) in press.
4. A Network Model for Urban Scaling
   K. Yakubo and Y. Saijo: Topologica **3** (2014) in press.
5. Overload Network Failures: An Approach from the Random-Walk Model
   S. Mizutaka and K. Yakubo: J. Comp. Net. **2** in press.
6. Catalytic reaction dynamics in inhomogeneous networks
   A. Watanabe and K. Yakubo: submitted to Phys. Rev. E

YAMAJI, Youhei [C class; 0 (A), 4500 (B), 500 (C)] (156)
— *Numerical studies on topological and spin liquid phases of iridium oxides*

1. Metallic Interface Emerging at Magnetic Domain Wall of Antiferromagnetic Insulator: Fate of Extinct Weyl Electrons
   Youhei Yamaji and Masatoshi Imada: Phys. Rev. X, in press; arXiv:1306.2022
2. Honeycomb Lattice Iridates Na2IrO3 under Strong Spin-Orbit Interaction and Electron Correlation Studied by Ab Initio Scheme
   Youhei Yamaji, Yusuke Nomura, Moryuru Kurita, Ryotaro Arita, and Masatoshi Imada: arXiv:1402.1030

YAMAMOTO, Takahiro [C class; 0 (A), 2500 (B), 0 (C)] (118)
— *First-principles modeling of next-generation functional materials*

1. Asymmetric behavior of current-induced magnetization switching in magnetic tunnel junction:

Non-equilibrium first-principles calculations
Masaaki Araidai, Takahiro Yamamoto and Kenji Shiraishi: Appl. Phys. Express 7 (2014) 045202.

2. Conductance fluctuation of edge-disordered graphene nanoribbon: Crossover from diffusive transport to Anderson localization
   Kengo Takashima and Takahiro Yamamoto: Appl. Phys. Lett. 104, 093105 (2014).
3. Giant Seebeck Coefficient in Semiconducting Single-Wall Carbon Nanotube Film
   Yusuke Nakai, Kazuya Honda, Kazuhiro Yanagi, Hiromichi Kataura, Teppei Kato, Takahiro Yamamoto and Yutaka Maniwa: Appl. Phys. Express 7 (2014) 025103.
4. Water Encapsulation Control in Individual Single-Walled Carbon Nanotubes by Laser Irradiation
   Shohei Chiashi, Tateki Hanashima, Rhota Mitobe, Kotaro Nagatsu,Takahiro Yamamoto and Yoshikazu Homma: J. Phys. Chem. Lett. 5 (2014) 408-412.
5. Non-Equilibrium Thermal Transport Simulation of Conical Carbon Nanofibers
   Derek Ashley Thomas, Takahiro Yamamoto, Tomofumi Tada, and Satoshi Watanabe: Transactions of the Materials Research Society of Japan 38 (2013) 183.
6. Wave Packet Dynamics Simulation on Electronic Transport in Carbon Nanotubes with Randomly Distributed Impurities
   Yasuhiro Takada and Takahiro Yamamoto: Jpn. J. Appl. Phys. 52 (2013) 06GD07.
7. Nanostructural Effects on Thermoelectric Power of Graphene Nanoribbons
   Teppei Kato, Shinji Usui, and Takahiro Yamamoto: Jpn. J. Appl. Phys. 52 (2013) 06GD05.
8. Wavelet Analysis of Quantum Transient Transport in a Quantum Dot
   Kenji Sasaoka, Takahiro Yamamoto, and Satoshi Watanabe: Appl. Phys. Lett. 102 (2013) 233107.
9. Photoluminescence Measurements and Molecular Dynamics Simulations of Water Adsorption on the Hydrophobic Surface of a Carbon Nanotube in Water Vapor
   Yoshikazu Homma, Shohei Chiashi, Takahiro Yamamoto, Kaname Kono, Daiki Matsumoto, Junpei Shitaba, and Shintaroh Sato: Phys. Rev. Lett. 110 (2013) 157402.

YAMASHITA, Koichi [C class; 0 (A), 3000 (B), 0 (C)] (109,111)
— Large scale ab initio calculations on the fundamental processes of energy convergence devices and on their optimization for high conversion efficiency

1. Small Photocarrier Effective Masses Featuring Ambipolar Transport in Methylammonium Lead-Iodide Perovskite: A Density Functional Analysis
   G. Giorgi, J. Fujisawa, H. Segawa, K. Yamashita: J. Phys. Chem. Lett. **4** (2013) 4213.
2. Ab initio theory for current-induced molecular switching: Melamine on Cu(001)
   T. Ohto, I. Rungger, K. Yamashita, H. Nakamura, and S. Sanvito: Phys. Rev. B **87** (2013) 205439.
3. Unraveling Adsorption Mechanism of Aromatic and Aliphatic Diols on TiO2 Surface by Density Functional Theory Analysis
   G. Giorgi, J. Fujisawa, H. Segawa, and K. Yamashita: Phys. Chem. Chem. Phys. **15** (2013) 9761.
4. The origin of the strong interfacial charge-transfer absorption in the surface complex between TiO_2 and dicyanomethylene compounds
   R. Jono, J. Fujisawa, H. Segawa, and K. Yamashita: Phys. Chem. Chem. Phys. **15** (2013) 18584.
5. Effect of Isotopic Substitution on Elementary Processes in Dye-Sensitized Solar Cells: Deuterated Amino-Phenyl Acid Dyes on TiO_2
   S. Manzhos, H. Segawa fand K. Yamashita: Computation **1** (2013) 1.
6. Theoretical studies on the stabilities and reactivities of Ta_3N_5 surfaces
   E. Watanabe, H. Ushiyama, K. Yamashita: Chem. Phys. Lett. **561-562** (2013) 57.
7. Dynamics of interband transitions in triangular quantum wells due to static and laser fields
   B. Dahiya, V. Prasad, K. Yamashita: J. Luminescence **136** (2013) 240.
8. Effect of nuclear vibrations, temperature, co-adsorbed water, and dye orientation on light absorption, charge injection and recombination conditions in organic dyes on TiO_2
   S. Manzhos, H. Segawa and K. Yamashita: Phys. Chem. Chem. Phys. **15** (2013) 1141.
9. Chirality dependence of quantum thermal transport in carbon nanotubes at low temperatures: A first-principles study

T. Hata, H. Kawai, T. Ohto, and K. Yamashita: J. Chem. Phys. **139** (2013) 044711.

10. Small Photocarrier Effective Masses Featuring Ambipolar Transport in Methylammonium Lead-Iodide Perovskite: A Density Functional Analysis
    G. Giorgi, J. Fujisawa, H. Segawa, K. Yamashita: J. Phys. Chem. Lett. **4** (2013) 4213.
11. Ab initio theory for current-induced molecular switching: Melamine on Cu(001)
    T. Ohto, I. Rungger, K. Yamashita, H. Nakamura, and S. Sanvito: Phys. Rev. B **87** (2013) 205439.
12. Unraveling Adsorption Mechanism of Aromatic and Aliphatic Diols on TiO2 Surface by Density Functional Theory Analysis
    G. Giorgi, J. Fujisawa, H. Segawa, and K. Yamashita: Phys. Chem. Chem. Phys. **15** (2013) 9761.
13. The origin of the strong interfacial charge-transfer absorption in the surface complex between TiO_2 and dicyanomethylene compounds
    R. Jono, J. Fujisawa, H. Segawa and K. Yamashita: Phys. Chem. Chem. Phys. **15** (2013) 18584.
14. Effect of Isotopic Substitution on Elementary Processes in Dye-Sensitized Solar Cells: Deuterated Amino-Phenyl Acid Dyes on TiO_2
    S. Manzhos, H. Segawa fand K. Yamashita: Computation **1** (2013) 1.
15. Theoretical studies on the stabilities and reactivities of Ta_3N_5 surfaces
    E. Watanabe, H. Ushiyama, K. Yamashita: Chem. Phys. Lett. **561-562** (2013) 57.
16. Dynamics of interband transitions in triangular quantum wells due to static and laser fields
    B. Dahiya, V. Prasad, K. Yamashita: J. Luminescence **136** (2013) 240.
17. Effect of nuclear vibrations, temperature, co-adsorbed water, and dye orientation on light absorption, charge injection and recombination conditions in organic dyes on TiO_2
    S. Manzhos, H. Segawa and K. Yamashita: Phys. Chem. Chem. Phys. **15** (2013) 1141.
18. Chirality dependence of quantum thermal transport in carbon nanotubes at low temperatures: A first-principles study
    T. Hata, H. Kawai, T. Ohto, and K. Yamashita: J. Chem. Phys. **139** (2013) 044711.

YAMAUCHI, Jun [B class; 1600 (A), 700 (B), 500 (C)] (112)

— *First-principles study on the defects in semiconductors*

1. First-principles calculation on the XPS spectra of boron defects in silicon crystal
   J. Yamauchi: KOTAIBUTSURI (AGNE GIJUTSU CENTER, Tokyo) **48** (2013) 215.
2. A first-principles core-level XPS study on the boron impurities in germanium crystal
   J. Yamauchi, Y. Suwa and Y. Yoshimoto: AIP Conference Proceedings **1566** (2013) 41.
3. First-principles core-level X-ray photoelectron spectroscopy calculation on arsenic defects in silicon crystal
   H. Kishi, M. Miyazawa, N. Matsushima, and J. Yamauchi: AIP Conference Proceedings **1583** (2014) 226.

YAMAUCHI, Kunihiko [C class; 3500 (A), 8000 (B), 1700 (C)] (70)

— *Ab-initio search of novel multiferroics based on manganites*

1. Mechanism of Ferroelectricity in Half-Doped Manganites with Pseudocubic and Bilayer Structure
   K. Yamauchi and S. Picozzi: J. Phys. Soc. Jpn. **82** (2013) 113703.
2. Ab initio study of magnetic coupling in $CaCu_3B_4O_12$ (B = Ti, Ge, Zr, and Sn)
   M. Toyoda, K. Yamauchi, and T. Oguchi: Phys. Rev. B **87** (2013) 224430.
3. First-Principles Calculation of X-ray Absorption Spectra for the A-Site Ordered Perovskite $CaCu_3Fe_4O_12$
   T. Ueda, M. Kodera, K. Yamauchi, and T. Oguchi: J. Phys. Soc. Jpn. **82** (2013) 094718.
4. Influence of lone pair doping on the multiferroic property of orthorhombic HoMnO3: ab initio prediction
   S. S. Subramanian, K. Yamauchi, T. Ozaki, T. Oguchi and B. Natesan: J. Phys.: Condens. Matter **25** (2013) 385901.
5. Electronic ferroelectricity induced by charge and orbital orderings
   K. Yamauchi and P. Barone: J. Phys.: Condens. Matter **26** (2014) 103201.

YANAGISAWA, Susumu [B,C class; 14300 (A), 5100 (B), 0 (C)] (55,57)

— *Theoretical investigation on electronic structures of organic molecular aggregates*
— *Investigation of cluster, and surface electronic properties relevant to dye sensitized solar cells*
— *Theoretical investigation on the magnetic polarization induced at organic/metal interfaces*

1. Theoretical investigation of the band dispersion of picene single crystals within the GW approximation
   S. Yanagisawa, Y. Morikawa and A. Schindlmayr: Jpn. J. Appl. Phys. **53** (2014) 05FY02
2. Search for a self-regenerating perovskite catalyst with ab initio thermodynamics II: Cu-doped layered perovskites with K_2NiF_4 structure
   S. Yanagisawa, A. Takeda, K. Inagaki, I. Hamada and Y. Morikawa: Catal. Lett. **144** (2014) 736
3. Internal-strain effect on the valence band of strained silicon and its correlation with the bond angles
   T. Inaoka, S. Yanagisawa and Y. Kadekawa: J. Appl. Phys. **115** (2014) 063702
4. Intermolecular interaction as origin of red shifts in absorption spectra of Zinc-Phthalocyanine from first-principles
   S. Yanagisawa, T. Yasuda, K. Inagaki, Y. Morikawa, K. Manseki and S. Yanagida: J. Phys. Chem. A **117** (2013) 11246
5. HOMO band dispersion of crystalline rubrene: Effects of self-energy corrections within the GW approximation
   S. Yanagisawa, Y. Morikawa and A. Schindlmayr: Phys. Rev. B **88** (2013) 115438
6. Anisotropy of the silicon valence band induced by strain with various orientations
   T. Inaoka, Y. Kinjyo, S. Yanagisawa and K. Tomori: J. Appl. Phys. **113** (2013) 183718
7. First-principles investigation on the segregation of Pd at $LaFe_{1-x}Pd_xO_{3-y}$ surfaces
   Z.-X. Tian, A. Uozumi, I. Hamada, S. Yanagisawa, H. Kizaki, K. Inagaki and Y. Morikawa: Nanoscale Res. Lett. **8** (2013) 203

YANAGISAWA, Takashi [B class; 600 (A), 1000 (B), 700 (C)] (161)

— *Quantum Monte Carlo simulations and electronic state calculations in correlated electron systems*
— *Quantum Monte Carlo simulation and electronic state calculations in correlated electron systems*

1. Enhanced pair-correlation functions in the two-dimensional Hubbard model
   T. Yanagisawa: New J. Physics **15** (2013) 033012.a
2. Systematics of T_c studied on the basis of the d-p model of cuprate superconductors
   K. Yamaji and T. Yanagisawa: Physica C**494** (2013) 5.
3. Effective Coulomb interaction in multiorbital system
   I. Hase and T. Yanagisawa: J. Phys. Conf. Series **428** (2013) 012013.
4. Electronic band calculation of $BaPd_2Sb_2$: which polymorph is stable?
   I. Hase and T. Yanagisawa: Physica C**404** (2011) 27.
5. Valence Skipping driven Superconductivity and Charge Kondo Effect
   T. Yanagisawa and I. Hase: Physica c**494** (2013) 24.
6. Correlated Electron Systems and High-Temperature Superconductivity
   T. Yanagisawa, M. Miyazaki and K. Yamaji: J. Mod. Phys. **4**, No.6A (2013) 33.a
7. Gauge fields, massless modes and topology in multi-band superconductors
   T. Yanagisawa, Y. Tanaka and I. Hase: JPS Conference Proceedings **1** (2014) 012121.
8. Electronic structure of novel superconductor $AuSb_6Te$
   I. Hase, T. Yanagisawa, A. Iyo and H. Eisaki: JPS conference Proceedings **1** (2012) 012114.
9. Massless modes and abelian gauge fields in multi-band superconductors
   T. Yanagisawa and I. Hase: J. Phys. Soc. Jpn. **82** (2013) 124704.
10. Soft confinement in 3D spin systems
    K. Odagiri and T. Yanagisawa: Euro. Phys. J. C**73** (2013) 124704.
11. Systematics of the strength of superconductivity of the d-p model in relation to cuprates
    K. Yamaji and T. Yanagisawa: Physica C**497** (2013) 93.
12. Mott transition in cuprate superconductors - Role of t'_d in the three-band d-p model -
    T. Yanagisawa, M. Miyazaki and K. Yamaji: JPS Conference Proceedings (2014) in press.a
13. Electronic structure of $LaTSb_2$ (T=Cu, Ag,Au)
    I. Hase and T. Yanagisawa: Physics Procedia (2014) in press.
14. Material-parameter dependence of superconductivity in high-temperature cuprates

T. Yanagisawa, M. Miyazaki and K. Yamaji: Physics Procedia (2014) in press.
15. Stripes and superconductivity in the two-dimensional Hubbard model
M. Miyazaki, K. Yamaji and T. Yanagisawa: Physics Procedia (2014) in press.
16. Electron correlation in high temperature superconductors
T. Yanagisawa, M. Miyazaki and K. Yamaji: J. Applied Math. Phys. **2** (2014) 72.
17. Mott transition in cuprate high temperature superconductors
T. Yanagisawa and M. Miyazaki: to be submitted.a

YANASE, Youichi [C class; 12500 (A), 4500 (B), 0 (C)] ()
— *Theoretical study of novel superconducting state with exotic symmetry*

YASUDA, Chitoshi [C class; 500 (A), 1500 (B), 400 (C)] (229)
— *Phonon Effects and Frustration in Quantum Spin Systems*

YOSHINO, Hajime [C,D class; 0 (A), 20500 (B), 0 (C)] (183)
— *Analysis of collective plastic events at the jamming transition*
— *Analysis of the dynamical critical phenomena at the jamming transition*
— *Analysis of the hierarchy of thermal fluctuations and replica symmetry breaking in a jamming system*

1. Rigidity of thermalized soft repulsive spheres around the jamming point
Satoshi Okamura and Hajime Yoshino, arXiv:1306.2777.
2. The shear modulus of glasses: results from the full replica symmetry breaking solution
Hajime Yoshino and Francesco Zamponi, arXiv:1403.6967.

YUKAWA, Satoshi [B class; 0 (A), 700 (B), 0 (C)] (247)
— *Fracture dynamics and pattern formation*

HASHIMOTO, Tamotsu [C class; 6000 (A), 1000 (B), 700 (C)] ()
— *First-principles study of Pt adsorption on Ge(001)*

□ CMSI Projects

ASAI, Yoshihiro [R class; 0 (A), 0 (B), 3000 (C)] (265)
— *Theory and computer simulation studies of non-equilibrium transport phenomena*

1. Length and energy gap dependences of thermoelectricity in nanostructured junctions
   Y. Asai: J. Phys. Cond. Matt. 25, 155305-1-5 (2013).
2. Thermoelectric Efficiency of Organometallic Complex Wires via Quantum Resonance Effect and Long-Range Electric Transport Property
   H. Nakamura, T. Ohto, T. Ishida, and Y. Asai: J. Am. Chem. Soc. 135, 16545-16552 (2013).
3. Heat dissipation and its relation to thermopower in single-molecule junctions
   L.A. Zotti, M. Bürkle, F. Pauly, W. Lee, K. Kim, W. Jeong, Y. Asai, P. Reddy and J.C. Cuevas: New J. Phys. 16, 015004-1-25 (2014).
4. First-Principles Transport Modeling for Metal/Insulator/Metal Structures
   T. Miyazaki, H. Nakamura, K. Nishio, H. Shima, H. Akinaga, and Y. Asai: JPS Conf. Proc. 012075 (2014).

DOI, Shotaro [R class; 0 (A), 0 (B), 2000 (C)] (277)
— *First-principles Electronic Structure Calculation of Permanent Magnets using the Screened KKR Green's Function Method*

1. Development of a first-principles code based on the screened KKR method for large super-cells
   S. Doi, M. Ogura and H. Akai: J. Phys.: Conf. Ser. **454** (2013) 012019.

IMADA, Masatoshi [R class; 0 (A), 0 (B), 5000 (C)] (23)
— *New machanisms and controllability of real strongly correlated electron materials*

ISHIMURA, KAZUYA [R class; 0 (A), 0 (B), 2000 (C)] (279)
— *Search for new structures and functions of nano-sized molecules*

KAWASHIMA, Naoki [R class; 0 (A), 0 (B), 5000 (C)] (257)
— *Monte Carlo Study of Novel Quantum Phases and Critical Phenemena*

1. Parallelized Quantum Monte Carlo Algorithm with Nonlocal Worm Updates
   Akiko Masaki-Kato, Takafumi Suzuki, Kenji Harada, Synge Todo, Naoki Kawashima: Physical Review Letters **112** (2014) 140603 (5 pages)
2. Phase Transitions with Discrete Symmetry Breaking in Antiferromagnetic Heisenberg Models on a Triangular Lattice
   Ryo Tamura, Shu Tanaka, and Naoki Kawashima: JPS Conf. Proc. — Proceedings of the 12th Asia Pacific Physics Conference (APPC12) (2014) 012125.
3. Possibility of Deconfined Criticality in SU(N) Heisenberg Models at Small N
   Kenji Harada, Takafumi Suzuki, Tsuyoshi Okubo, Haruhiko Matsuo, Jie Lou, Hiroshi Watanabe, Synge Todo, Naoki Kawashima: Phys. Rev. B **88** (2013) 220408(R)(4 pages)
4. Second-Order Phase Transition in Heisenberg Model on Triangular Lattice with Competing Interactions
   Ryo Tamura, Shu Tanaka and Naoki Kawashima: Phys. Rev. B **87** (2013) 214401(5pages)

NAKANO, Hiroki [R class; 0 (A), 0 (B), 5000 (C)] (276)
— *Computational-Science Study of Frustrated Magnets*

1. The Magnetization Process of the $S = 1/2$ Heisenberg Antiferromagnet on the Cairo Pentagon Lattice
   H. Nakano, M. Isoda, and T. Sakai: J. Phys. Soc. Jpn. **83** (2014) 053702.
2. Anomalous Quantum Magnetization Behaviors of the Kagome and Triangular Lattice Antiferromagnets
   H. Nakano and T. Sakai: to be published in JPS Conf. Proc.
3. Quantum Spin-Liquid Behavior in the Spin-1/2 Random Heisenberg Antiferromagnet on the Tri-

angular Lattice
K. Watanabe, H. Kawamura, H. Nakano and T. Sakai: J. Phys. Soc. Jpn. **83** (2014) 034714.
4. The Two-Dimensional $S = 1/2$ Heisenberg Antiferromagnet on the Shuriken Lattice - a Lattice Composed of Vertex-Sharing Triangles -
H. Nakano and T. Sakai: J. Phys. Soc. Jpn. **82** (2013) 083709.
5. Crystal Structure and Magnetic Properties of the Verdazyl Biradical m-Ph-V2 Forming a Ferromagnetic Alternating Double Chain
K. Iwase, H. Yamaguchi, T. Ono, T. Shimokawa, H. Nakano, A. Matsuo, K. Kindo, H. Nojiri, and Y. Hosokoshi: J. Phys. Soc. Jpn. **82** (2013) 074719.
6. Nontrivial ferrimagnetism of the Heisenberg model on the Union Jack strip lattice
Tokuro Shimokawa and H. Nakano: J. Kor. Phys. Soc. **63** (2013) 591.
7. Novel Field-Induced Quantum Phase Transition of the Kagome-Lattice Antiferromagnet
Toru Sakai and H. Nakano: J. Kor. Phys. Soc. **63** (2013) 601.
8. Crystal structure and magnetic properties of honeycomb-like lattice antiferromagnet p-BIP-V2
H. Yamaguchi, S. Nagata, M. Tada, K. Iwase, T. Ono, S. Nishihara, Y. Hosokoshi, T. Shimokawa, H. Nakano, H. Nojiri, A. Matsuo and K. Kindo, and T. Kawakami: Phys. Rev. B **87** (2013) 125120.
9. Long-Range Order of the Three-Sublattice Structure in the S = 1 Heisenberg Antiferromagnet on a Spatially Anisotropic Triangular Lattice
H. Nakano, Synge Todo, and Toru Sakai: J. Phys. Soc. Jpn. **82** (2013) 043715.
10. Unconventional Magnetic and Thermodynamic Properties of S=1/2 Spin Ladder with Ferromagnetic Legs
H. Yamaguchi, K. Iwase, T. Ono, T. Shimokawa, H. Nakano, Y. Shimura, N. Kase, S. Kittaka, T. Sakakibara, T. Kawakami, and Y. Hosokoshi: Phys. Rev. Lett. **110** (2013) 157205.

NISHIMATSU, Takeshi [R class; 0 (A), 0 (B), 5000 (C)] (273)
— *Direct molecular dynamics simulation of electrocaloric effect in ferroelectrics*

1. Direct molecular dynamics simulation of electrocaloric effect in BaTiO3
Takeshi Nishimatsu, Jordan A. Barr and S. P. Beckman: J. Phys. Soc. Jpn. **82**, 114605 (2013)

OGATA, Shuji [R class; 0 (A), 0 (B), 5000 (C)] (258)
— *Multi-scale simulation of nano-structured devices from electronic structures to mechanical properties*

1. Multi-Thousand-Atom DFT Simulation of Li-Ion Transfer through the Boundary between the Solid-Electrolyte Interface and Liquid Electrolyte in a Li-Ion Battery
S. Ogata, N. Ohba, and T. Kouno: J. Phys. Chem. C. **117** (2013) 17960.
2. Enhanced Heat Transfer through Filler-Polymer Interface by Surface-Coupling Agent in Heat-Dissipation Material: A Non-equilibrium Molecular Dynamics Study
K. Tanaka, S. Ogata, R. Kobayashi, T. Tamura, M. Kitsunezuka, and A. Shinma: J. Appl. Phys. **114** (2013) 193512.

OHNO, Kaoru [R class; 0 (A), 0 (B), 5000 (C)] (272)
— *All electron spectra and dynamics of functional materials from nanoclusters to crystals*

OKUBO, Tsuyoshi [R class; 0 (A), 0 (B), 2000 (C)] (278)
— *Ordering of topological excitations of the frustrated magnets*

1. Possibility of deconfined criticality in SU(N) Heisenberg models at small N
K. Harada, T. Suzuki, T. Okubo, H. Matsuo, J. Lou, H. Watanabe, S. Todo, and N. Kawashima:Phys. Rev. B **88** (2013) 220408(R).
2. Various regimes of quantum behavior in an $S = 1/2$ Heisenberg antiferromagnetic chain with fourfold periodicity
H. Yamaguchi, T. Okubo, K. Iwase, T. Ono, Y. Kono, S. Kittaka, T. Sakakibara, A. Matsuo, K. Kindo, and Y. Hosokoshi: Phys. Rev. B **88** (2013) 174410.
3. Kagome-Triangular Lattice Antiferromagnet $NaBa_2Mn_3F_{11}$
H. Ishikawa, T. OKubo, Y. Okamoto, and Z. Hiroi: J. Phys. Soc. Jpn. **83** (2014) 043703.

OKAZAKI, Susumu [R class; 0 (A), 0 (B), 5000 (C)] (264)
— *Large scale molecular dynamics calculation study of viruses*

OSHIYAMA, Atsushi [R class; 0 (A), 0 (B), 5000 (C)] (260)
— *Density Functional Study on Prediction of Electronic Properties of Nanostructures*

1. Performance evaluation of ultra-largescale first-principles electronic structure calculation code on the K computer
   Y. Hasegawa, J.-I. Iwata, M. Tsuji, D. Takahashi, A. Oshiyama, K. Minami, T. Boku, H. Inoue, Y. Kitazawa, I. Miyoshi, M. Yokokawa: International Journal High Performance Computing Applications, online version Oct 17, 508163 (2013) DOI=10.1177/1094342013508163
2. Large-Scale Electronic-Structure Calculations in the Real-Space Scheme: Bilayer Graphene and Silicene
   K. Uchida, Z.-X. Guo, J.-I. Iwata and A. Oshiyama: Proc. JSAP-MRS Joint Symposia **1595** (2013) 1190
3. First-principles study of spin-dependent transport through graphene/BNC/graphene structure
   T. Ota and T. Ono: Nanoscale Res. Lett. **8** (2013) 199.
4. Convergence of the Broyden density mixing method in noncollinear magnetic systems
   M. Heide and T. Ono: J. Phys. Soc. Jpn. **82** (2013) 114706.
5. Doping Effect on Magnetism and Transport Property of Heterojunction between Carbon and Boron Nitride Nanotubes
   H. D. Nguyen and T. Ono: J. Phys. Chem. C **117** (2013) 24115.
6. First-principles electronic-structure and transport calculation formalism using real-space grid based method
   T. Ono: AIP Conf. Proc. **1558** (2013) 1524.

OTANI, Minoru [R class; 0 (A), 0 (B), 5000 (C)] ()
— *First-principles simulation of Li-ion battery*

SAITO, Mineo [R class; 0 (A), 0 (B), 5000 (C)] (262)
— *Materials design for spintronics/multiferroics applications*

1. Hydrogen Adsorption in Capped Armchair Edge (5,5) Carbon Nanotubes

   A. Setiadi, M. S. Alam, F. Muttaqien, and M. Saito: Jpn. J. Appl. Phys. **52** (2013) 125105
2. First-principles study of carrier-induced ferromagnetism in bilayer and multilayer zigzag graphene nano ribbons

   K. Sawada, F. Ishii, and M. Saito: Appl. Phys. Lett. **104** (2014) 14311.
3. Tunable Rashba effect on strained ZnO: First-principles density-functional study

   M. A. Adhib, H. Kotaka, F. Ishii, and M. Saito: Appl. Phys. Exp. **7** (2014) 053002.
4. Spin polarized positron lifetimes in ferromagnetic metals

   J. Lin, T. Yamasaki, and M. Saito: Jpn. J. Appl. Phys.**53** (2014) 053002.
5. Valley filter by extraordinary Rashba spin on silicon
   K. Sakamoto, T.-H. Kim, T. Kuzumaki, B. Müller, Y. Yamamoto, M. Ohtaka, J. Osiecki, K. Miyamoto, Y. Takeichi, A. Harasawa, S. D. Stolwijk, A. B. Schmidt, J. Fujii, R. I. G. Uhrberg, M. Donath, H. W. Yeom and T. Oda: Nat. Commun., **4** (2013) 2073.
6. Implementation of van der Waals density functional approach to the spin polarized system: interaction potential between oxygen molecules

   M. Obata, M. Nakamura, I. Hamada, and T. Oda : J. Phys. Soc. Jpn. **82** (2013) 093701.
7. An ab initio approach to free-energy reconstruction using logarithmic mean force dynamics

   M. Nakamura, M. Obata, T. Morishita, T. Oda: J. Chem. Phys., submitted for publication.
8. Spin-Orbit Interaction Effects in the Electronic Structure of B20-type CoSi: First-Principles Den-

sity Functional Study
F. Ishii, T. Onishi, and H. Kotaka: JPS Conference Proceedings, in press.
9. Contribution of Berry Curvature to Thermoelectric Effects
Y.P. Mizuta and F. Ishii: JPS Conference Proceedings, in press.
10. First-principles study of Exchange Interaction in Ising-type Multiferroic Ca3CoMnO6
M. Nishida, F. Ishii, and M. Saito: JPS Conference Proceedings, in press.

SHIBA, Hayato [R class; 0 (A), 0 (B), 5000 (C)] (34,275)
— *Structure Formation of Surfactant Membranes under Shear Flow*
1. Mechanical properties and microdomain separation of fluid membranes with anchored polymers
H. Wu, H. Shiba and H. Noguchi: Soft Matter **9** (2013) 9907.
2. Structure formation of surfactant membranes under shear flow
H. Shiba and H. Noguchi: J. Chem. Phys. **139** (2013) 014702.

SUGINO, Osamu [R class; 0 (A), 0 (B), 5000 (C)] (269)
— *Basic processes in the electrode catalysis*
1. Effect of thermal motion on catalytic activity of nanoparticles in polar solvent
Nicephore Bonnet, O. Sugino, and M. Otani: J. Chem. Phys. **140**, 044703 (2014).
2. Improved modeling of electrified interfaces using the effective screening medium method
I. Hamada, O. Sugino, B. Nicephore, and M. Otani: Phys. Rev. B **88**, 155427 (2013).

TAKATSUKA, Kazuo [R class; 0 (A), 0 (B), 2500 (C)] (255)
— *Nonadiabatic electron dynamics and many-body nuclear dynamics in molecules*

TOHYAMA, Takami [R class; 0 (A), 0 (B), 5000 (C)] (256)
— *Double-Pulse Deexcitations in a One-Dimensional Strongly Correlated System*
1. Effects of frustration on magnetic excitations in a two-leg spin-ladder system
T. Sugimoto, M. Mori, T. Tohyama and S. Maekawa:Phys. Rev. B **87**, (2013) 155143.
2. Photoinduced spin-order destructions in one-dimensional extended Hubbard model
H. Lu, S. Sota, H. Matsueda, J. Bonca and T. Tohyama: J. Phys.: Conf. Ser. **454** 012079.
3. Double-pulse deexcitations in a one-dimensional strongly correlated system
H. Lu, J. Bonca and T. Tohyama: EPL **103**, (2013) 57005.
4. Nonequilibrium photo dynamics of low-dimensional strongly correlated electron systems
T. Tohyama: Eur. Phys. J. Special Topics **222**, (2013) 1065-1075.

TSUNEYUKI, Shinji [R class; 0 (A), 0 (B), 5000 (C)] ()
— *Development of first-principles simulation software for exploration of new materials*

YAMASHITA, Koichi [R class; 0 (A), 0 (B), 5000 (C)] (267)
— *Large scale calculations on the fundamental processes of solar cells and their optimization in conversion efficiency and long lifetime*
1. Unraveling Adsorption Mechanism of Aromatic and Aliphatic Diols on TiO2 Surface by Density Functional Theory Analysis
G. Giorgi, J. Fujisawa, H. Segawa, and K. Yamashita: Phys. Chem. Chem. Phys. **15** (2013) 9761.
2. The origin of the strong interfacial charge-transfer absorption in the surface complex between TiO_2 and dicyanomethylene compounds
R. Jono, J. Fujisawa, H. Segawa and K. Yamashita: Phys. Chem. Chem. Phys. **15** (2013) 18584.
3. Effect of Isotopic Substitution on Elementary Processes in Dye-Sensitized Solar Cells: Deuterated Amino-Phenyl Acid Dyes on TiO_2
S. Manzhos, H. Segawa fand K. Yamashita: Computation **1** (2013) 1.
4. Effect of nuclear vibrations, temperature, co-adsorbed water, and dye orientation on light absorption, charge injection and recombination conditions in organic dyes on TiO_2
S. Manzhos, H. Segawa and K. Yamashita: Phys. Chem. Chem. Phys. **15** (2013) 1141.

YOSHIDA, Norio [R class; 0 (A), 0 (B), 5000 (C)] (271)

— *Theoretical analysis of hydrolysis of pyrophosphate by 3D-RISM-SCF*

1. Extended Molecular Ornstein-Zernike Integral Equation for Fully Anisotropic Solute Molecules: Formulation in a Rectangular Coordinate System
   R. Ishizuka, N. yoshida: J. Chem. Phys. **139** (2013) 084119.
2. Solvent dependence of Stokes shift for organic solute-solvent systems: A comparative study by spectroscopy and reference interation-site model-self-consistent-field theory
   K. Nishiyama, Y. Watanabe, N. Yoshida, F. Hirata: J. Chem. Phys. **139** (2013) 094503.
3. Theoretical Study of Salt Effects on Diels-Alder Reaction of Cyclopentadiene With Methyl Vinyl Ketone Using RISM-SCF Theory
   N. Yoshida, H. Tanaka, F. Hirata: J. Phys. Chem. B **117** (2013) 14115.
4. Probing “ambivalent” snug-fit sites in the KcsA potassium channel using three-dimensional reference interaction site model (3D-RISM) theory
   S. Phongphanphanee, N. Yoshida, S. Oiki, F. Hirata: Pure and Applied Chem. **86** (2014) 97.
5. Theoretical Characterization of the “Ridge” in the Supercritical Region in the Fluid Phase Diagram of Water
   M. Matsugami, N. Yoshida, F. Hirata: J. Chem. Phys. **140** (2014) 104511.
6. Massively Parallel Implementation of 3D-RISM Calculation with Volumetric 3D-RFFT
   Y. Maruyama, N. Yoshida, H. Tadano, D. Takahashi, M. Sato, F. Hirata: J. Comput. Chem. In Press, DOI: 10.1002/jcc.23619.
7. Theory and Efficient Computation of Differential Vibrational Spectra
   S. Sakaguchi, T. Ishiyama, A. Morita: J. Chem. Phys. **140** (2014) 144109.
8. Computation of the Free Energy due to Electron Density Fluctuation of a Solute in Solution: A QM/MM Method with Perturbation Approach Combined with a Theory of Solutions
   D. Suzuoka, H. Takahashi, A. Morita: J. Chem. Phys. **140** (2014) 134111.
9. Theoretical Studies of Structures and Vibrational Sum Frequency Generation Spectra at Aqueous Interfaces
   T. Ishiyama, T. Imamura, A. Morita: Chem. Rev. (2014) in press.
10. Reply to "Comment on 'Surface Acidity of Water Probed by Free Energy Calculation for Trimethylamine Protonation'"
    Y. Tabe, N. Kikkawa, H. Takahashi, A. Morita: J. Phys. Chem. C **118** (2014) 2895-2895.
11. Surface Acidity of Water Probed by Free Energy Calculation for Trimethylamine Protonation
    Y. Tabe, N. Kikkawa, H. Takahashi, A. Morita: J. Phys. Chem. C **118** (2014) 977-988.
12. Real-Time Observation of the Destruction of Hydration Shells
    A. Yamakata, E. Soeta, T. Ishiyama, M. Osawa, A. Morita: J. Am. Chem. Soc. **135** (2013) 15033-15039.
13. Tip-Enhanced Raman Spectroscopy of 4,4'-Bipyridine and 4,4'-Bipyridine N, N'-Dioxide Adsorbed on Gold Thin Films
    I. I. Rzeznicka, H. Horino, N. Kikkawa, S. Sakaguchi, A. Morita, S. Takahashi, T. Komeda, H. Fukumura, T. Yamada, M. Kawai: Surf. Sci. **617** (2013) 1-9.
14. Molecular Dynamics Study of Water Transfer at Supercooled Sulfuric Acid Solution Surface Covered with Butanol
    S. Sakaguchi, A. Morita: J. Phys. Chem. A **117** (2013) 4602-4610.
15. A Molecular Dynamics Study on Inner Pressure of Microbubbles in Liquid Argon and Water
    H. Takahashi, A. Morita: Chem. Phys. Lett. **573** (2013) 35-40.
16. Computational Analysis of the Quadrupole Contribution in the Second-Harmonic Generation Spectroscopy for the Water/Vapor Interface
    K. Shiratori, S. Yamaguchi, T. Tahara, A. Morita: J. Chem. Phys. **138** (2013) 064704.

□ Doctor theses

1. **Andraus Robayo Sergio Andres**
   Multiple-particle diffusion processes from the viewpoint of Dunkl operators: relaxation to the steady state
   The University of Tokyo, 2014-03-24

2. **THOMAS, Derek**
   Theoretical study of thermoelectric properties of conical carbon nanofibers
   The University of Tokyo, 2014-03-24

3. **ASANO, Yuta**
   Phase diagram and equation of state of modified Lennard-Jones system
   Ehime University, 2014-03-24

4. **TAE-UK, Park**
   First-principles Study of Metal-atom Adsorption on Carbonic Systems
   Chiba University, 2014-03-25

5. **KOBINATA, Kyousuke**
   First-principles Study of Schottky Barrier at Metal/Semiconductor Interfaces
   Chiba University, 2014-03-25

6. **SAKAKIBARA, Hirofumi**
   Study on the correlation between the transition temperature and the crystal structure in the cuprate superconductors
   The University of Electro-Communications, 2014-03

7. **SUZUKI, Katsuhiro**
   Theoretical analysis of superconductivity in multi-orbital systems
   The University of Electro-Communications, 2014-03

8. **ASPERA, Susan**
   Theoretical Study on Nitric Oxide Adsorption and Oxidation on Metallo-Macrocycles and Ceria-Supported Platinum Cluster
   Osaka University, 2014-09-25

9. **QUANG, Nguyen**
   Density Functional Theory-based Studies on Oxygen Interaction with Varied Catalytic Environments for Nano Technological Applications
   Osaka University, 2014-09-25

10. **HARASHIMA, Yosuke**
    Critical phenomena of the metal-insulator transition in doped semiconductors using density functional theory and local density approximation
    Osaka University,

11. **KYOGOKU, Shinya**
    Microscopic study on nano-scale deformation and electronic state of carbon nanotube
    The University of Tokyo, 2014-03-24

12. **SHIMIZU, Ryotaro**
    Hydrodynamic effects on structure formation of soft matter
    The University of Tokyo, 2014-03-24

13. **MOTOYAMA, Yuichi**
Quantum Monte Carlo approach to the quantum phase transition in low-dimensional antiferromagnets in terms of the Berry phase
The University of Tokyo, 2014-03-31

□ Master Theses

1. **MIYAO, Satoaki**
Study of cuprate superconductors by element-substitution simulation
Osaka University, 2014-03-25

2. **Sunnardianto Gagus Ketut**
Charge distribution of hydrogenated graphene with a vacancy
Osaka University, 2014-03-25

3. **ONISHI, Takashi**
First-principles study of spin-orbit interaction in ferroelectrics
Kawazawa University, 2014-03-22

4. **SATO, Kosuke**
Quantum dissociation processes of exciton at semiconductor hetero-interfaces
Chiba University, 2014-03-25

5. **HIRAMATSU, Tomoki**
Atom diffusion, segregation, and mixing at metal/semiconductor interfaces
Chiba University, 2014-03-25

6. **YOSHIDA, Kazuyuki**
Metal-atom diffusion in self-assembled monolayer molecules
Chiba University, 2014-03-25

7. **KIRII, Tomohiro**
Critical phenomena of hierarchical model based on droplet picture
The University of Tokyo,

8. **KOJIMA, Yuhei**
Stability of the Superfluid State in Three-Component Fermionic Optical Lattice Systems
Tokyo Institute of Technology,

9. **MORI, Kouta**
Study on thermoelectric effect and superconductivity based on an effective model derived from first-principle band calculations
The University of Electro-Communications, 2014-03

10. **MATSUSHIMA, Kyohei**
Theoretical study on nuclear magnetic resonance of iron-based superconductors
The University of Electro-Communications, 2014-03

11. **TAKASAKI, Eriko**
Theoretical study on Sb_2Te topological insulator using first-principle calculations

Osaka University,

12. **OBATA, Masao**
Development and application of electronic state calculation method based on the van der Waals density functional
Kawazawa University, 2014-03-22

13. **SUGIHARA, Hiroki**
First-principle calculations of superlattice crystal structures
The University of Tokyo, 2014-03-24

14. **HAGINO, Shota**
First-principle calculations of lattice thermal conductivity: silicon crystals and nanowires
The University of Tokyo, 2014-03-24

15. **HYUGA, Masahiko**
Scaling Law of the Systems with Long-Range Interactions
The University of Tokyo, 2014-03-31

16. **MOHRI, Souitirou**
The universality class of a quantum phase transition in the J_1–J_3–J_4 model
The University of Tokyo, 2014-03-24

17. **HORITA, Toshiki**
Critical exponents and universality class of Ising model with long range interactions
The University of Tokyo, 2014-03-31